Proceedings of COSPAR Symposium on Solar Particle Event of November 1969 / James C. Ulwick, editor.

Ulwick, James C.

AFCRL-72-0474
11 AUGUST 1972
SPECIAL REPORTS, NO. 144

IONOSPHERIC PHYSICS LABORATORY PROJECT 7663

AIR FORCE CAMBRIDGE RESEARCH LABORATORIES

L. G. HANSCOM FIELD, BEDFORD, MASSACHUSETTS

Proceedings of COSPAR Symposium on Solar Particle Event of November 1969

JAMES C. ULWICK, Editor

AIR FORCE SYSTEMS COMMAND
United States Air Force

Abstract

A COSPAR-sponsored Symposium on Solar Particle Events was held at Boston College at Chestnut Hill, Massachusetts on 16, 17, and 18 June 1971. The purpose of the symposium was to present measurements and observations made during the November 1969 Solar Proton Event. This particular event was unique in that extensive solar, magnetospheric and aeronomic measurements by rocket, satellite and ground based techniques were made to provide a comprehensive picture of the phenomenology and morphology of this event. In addition, present knowledge of solar proton events and their effects on the polar ionosphere was reviewed and discussed. This included theoretical studies as well as results from investigations of other solar proton events. The symposium comprised invited as well as contributed papers. A total of 49 papers presented at the symposium are included in these proceedings.

Preface

The COSPAR-sponsored Symposium on the November 1969 Solar Particle Event was held at Boston College at Chestnut Hill, Massachusetts, on 16, 17, and 18 June 1971. The purpose of the symposium was to present measurements and observations made during the November 1969 solar particle event and to review and discuss present knowledge of solar particle events and their effects on the polar ionosphere. The November 1969 event was of particular significance because of the comprehensive rocket and ground measurement program called PCA-69 conducted during the event and the extensive satellite and ground experimental coverage available. Of the 49 papers presented at the Symposium, 39 were concerned with the November 1969 event including 20 based on rocket results, 10 on ground and aircraft observations and 9 on satellite results. The Symposium program was divided into 5 subject areas with an invited speaker for each. The categories and the session chairmen were: The Solar Proton Flare of 2 November 1969 (R. Carovillano, Boston College); Energetic Particles and Magnetospheric Effects (J. Ortner, European Space Research Organization); Ionospheric Effects (W. Berning, Defense Nuclear Agency and W. Pfister, Air Force Cambridge Research Laboratories); Aeronomy Effects (C. Blank, Defense Nuclear Agency); and the Disturbed D-Region (W. Heikkila, University of Texas). These proceedings contain the papers presented at the symposium. Since the results of the program called PCA-69 are the subject of the majority of the papers of the proceedings, a summary of the total program is also presented in Appendix A as a reference and to provide continuity to the reader.

Acknowledgments

As Technical Director and Field Director of Operation PCA-69, I would like to acknowledge the outstanding support received which made this program successful. I cannot acknowledge every individual who contributed but I will at least try to name their organizations and the principal personnel. The Defense Nuclear Agency and the Air Force Cambridge Research Laboratories jointly sponsored this program. Dr. Charles Blank and Lt. John Schroeder of the Defense Nuclear Agency provided the program management. The complicated and extensive logistics for the program was accomplished by the Operational Services Division at AFCRL with Mr. Tangredo J. Maltacea mainly responsible. Mr. Charles Reynolds and Mr. Philip Gustafson of the Aerospace Instrumentation Laboratory at AFCRL were responsible for coordination of the required rocket and range support. Special mention must be made of the outstanding support this program received at the Churchill Rocket Range operated by the National Research Council of Canada. At the managerial level Dr. James H. Brandy, the General Superintendant, Mr. Douglas A. Fretts, Chief of Plans and Operations, and Mr. James O. Hillis, the Project Manager were most cooperative. The operational phase of the program could not have been accomplished without the two range test conductors, Mr. Lyn C. Batstone and Mr. Donald G. Burrows. These two gentlemen were responsible for organizing and conducting the launch phase of the program. For their cooperation, talent and especially their patience in a long and complicated program, the range users are extremely grateful. Significant contributions to the scientific and technical planning and direction of the program were received from Dr. Kenneth Champion and Dr. Rocco Narcisi of AFCRL, Mr. John Mester of the Ballistic Research Laboratories and Mr. Warren Berning of the Defense Nuclear Agency and especially from Dr. Wolfgang Pfister of AFCRL.

James C. Ulwick, Editor

Contents

Contents

1. Characteristics of Strong Particle Sources of the Sun

Z. Švestka ≠
Space Science Department, ESTEC
Noordwijk, The Netherlands

1-1 TYPES OF PARTICLE EVENTS

As the sensitivity of spacecraft detectors increase, we discover more and more sources of particle events on the sun. Table 1-1 demonstrates the variety of phenomena we encounter when dealing with particle emission from the sun.

Permanent emission of protons with energy of about 1 MeV, and electrons with energy of several tens of keV, is associated with some specific active regions (Fan et al 1968). This permanent flux is fairly continuous at low energies, but shows an impulsive behavior at energies above ~10MeV. It is suspected, therefore, that even this so-called permanent flux is produced by a series of individual acceleration processes, and that particle storage in the solar corona or in space then produces the seemingly permanent flux at lower energies. Regardless of the explanation of the phenomenon, it gives an evidence that the active region in question is very capable of producing accelerated

≠ On leave from the Astronomical Institute of the Czechoslvak Academy of Sciences, Ondřejov, Czechoslovakia.

(Received for publication 11 August 1972)

Table 1-1

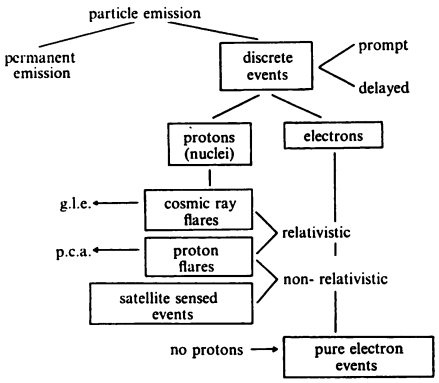

particles, and the regions of this type also are the seats of discrete particle events which we intend to discuss in this review (Švestka 1970a).

The discrete particle events can be classified from two points of view. The prompt events set in tens of minutes or a few hours after the particle ejection on the sun, and are directly connected with an acceleration process in the solar atmosphere. Delayed events, on the other hand, occur tens of hours after the suspected flare on the sun, and often their association with acceleration processes in the solar atmosphere is not clear. We will discuss them in more detail later on.

The second classification is according to the species of the recorded particles. These may be either atomic nuclei, protons being the most common sort among these, or electrons. Among the proton events, we distinguish cosmic-ray flares which cause a ground-level effect, and in which there must be enough protons with energy above 500 MeV at the earth distance from the sun. These are extremely rare phenomena; since 1942, less than 20 cosmic-ray flares have been recorded (McCracken and Rao 1970). Next we distinguish events which produce polar cap absorptions in the polar ionosphere, which means that there must be a strong flux of protons with energy above 10 MeV close to the earth, even when relativistic protons are absent. Particle emission of this type have been called proton flare events, and approximately 180 such events were recorded between 1956 and the end of 1969 (Fritzová and Švestka 1971). These proton flares will be the main subject of my discussion. Apart from them, of course, there are hundreds of similar satellite-sensed events which could never be recognized at ground-based stations. For example, in the year 1966, a year of moderate solar activity, a total of 30 proton events were recorded, and 5 of them belonged to the category of strong events which will be discussed in this review (Švestka 1970a).

There has also been observed a great number of non-relativistic electron events, in the range of energy above 20 keV. Such electrons are almost always present in proton events, and very few cases are known where electrons were obviously missing. Such "pure proton events" appear to be quite anomalous phenomena. In the strongest one of these events, on 4 October 1965, other

anomalies were observed as well. As Arnoldy et al (1968) pointed out, there was no X-ray burst associated with the flare, and the microwave radio component was extremely weak, as well. Hence, the production of electrons seemed to be very low in that flare.

On the other hand, pure electron events appear to be very frequent phenomena, and they obviously reflect an acceleration process on the sun, different from that which produces proton flares (Lin 1970). An evidence for this is an association of pure electron events with relatively small flares and radio bursts of Type III plus V, while proton flares generally are of great importance and are associated with a Type IV radio burst.

In the last few years, relativistic electrons have been detected in space. With the very rare exceptions of some delayed events, they are always associated with strong proton events (Lin 1970), and according to Datlowe (1971), their behavior strongly resembles that of 100 MeV protons. They seem to be associated with the same flares as proton events and to be produced by the same acceleration process.

1-2 PROPERTIES OF PROTON ACTIVE REGIONS

After some ten years of intense study we now know that proton flares occur in active regions which are characterized by several specific properties.

The proton active region is always of magnetically complex type, which means that sunspots of different magnetic polarities are mixed in at least a part of the active center. Of course, only some of these magnetically complex sunspot groups produce particle events of a recognizable size. A necessary condition of producing particle events is a substantial increase of the gradient of the magnetic field in the active region, as has been shown by Severny and his coworkers (Severny 1964, Gopasyuk et al 1965). Without any magnetic measurements, an easily recognizable manifestation of this fact is a close approach of at least two big spots of opposite magnetic polarity in the sunspot groups (Avignon et al 1965). Another important characteristic feature is the formation of a common penumbra, embedding spots of different polarities, the so-called β-configuration of a complex sunspot group (Warwick 1966). Both these characteristics can be seen, for example, in the group shown in Figure 1-2, in which a great proton flare appeared on 23 May 1967. A particularly favorable situation, and the highest probability of a proton event, appears when a high gradient of the magnetic field forms within a large portion of the active region, which is manifested optically by two rows of spots of opposite polarity. We speak then about the so-called A-configuration (Avignon et al 1963).

Such a development of an active region is associated with an intensification and a hardening both of the microwave and x-ray spectrum. In the microwave range, the radio emission strongly increases, and the usual flux maximum close to 10 cm is suppressed by the greatly increased flux at shorter wavelengths so that the microwave spectrum flattens, as has been shown by Tanaka et al (1969, Tanaka and Kakinuma, 1964). At the same time the x-ray flux also increases. According to Friedman and Kreplin (1969), this increase often exceeds one order of magnitude in the spectral range of a few Angstroms, decreases with the increasing wavelength, and becomes insignificant for wavelengths above 40 Å.

All these characteristic features begin to develop about three days before the proton flare occurrence. As soon as this happens, even small flares in the active region usually begin to be accompanied by radio bursts, and also the association of flares with x-ray bursts increases, which indicates that favorable conditions for acceleration processes have been formed in the active region (Eliseev and Moiseev 1965, Křivský and Nestorov 1968, Švestka and Simon 1969). Therefore, when such a behavior of an active region is observed, a proton flare actually occurs there. The region may decay again without producing any strong particle event. But we may be fairly certain that there will be no proton flare on the visible solar hemisphere for the following two or three days if such conditions do not exist in any of the visible sunspot groups. On the other hand, if such conditions develop and a proton flare is produced, one can expect occurrences of other proton flares in the same region, sometimes for a fairly long period.

Such a development of an active region, of course, can also occur behind the limb. If this happens behind the western limb, we do not know anything about it, and then a particle event may occur when nobody expects it. If it happens behind the eastern limb, the active region already appears fully developed on the visible hemisphere, and usually within one or two days it becomes conspicuous through a permanent flux of low-energy protons which reach the earth's surroundings.

1-3 COMPLEXES OF ACTIVITY

As Martres (1968) has shown, the magnetically complex active regions in which the proton flares occur, originate when a new active region forms within the remnants of an older one, and the complexity of the newly born region depends on the age of the remnants. The younger is the old active region, the more complex is the newly born one. Therefore, as solar activity is never distributed quite uniformly on the solar surface, there are always some parts of the sun where the probability of occurrence of a magnetically complex active

region is higher, and other parts where this probability is lower. In particular, there exists the so-called complexes of activity which produce many active regions in a limited area on the solar disc for a fairly long time (Bumba and Howard 1965). In these complexes, therefore, the probability of occurrence of magnetically complex and particle-producing active regions is very high.

Figure 1-1 shows two examples of such complexes of activity (Švestka 1968a) or active longitudes, as they are called by some authors (Warwick 1965, Sakurai 1966, Dodson and Hedeman 1969, Vitinsky 1969, Švestka 1970a). On the horizontal axis are dates, and on the vertical axis the subsequent solar rotations. Squares denote active regions that produced particles. One can see that several active regions producing particles are subsequently formed in a similar position on the solar disk, so that for many months, or even more than one year, the particle production is predominantly confined to approximately the same part of the solar surface. This might be quite helpful for long-term forecasts of proton events, but unfortunately, usually at least two such active longitudes are

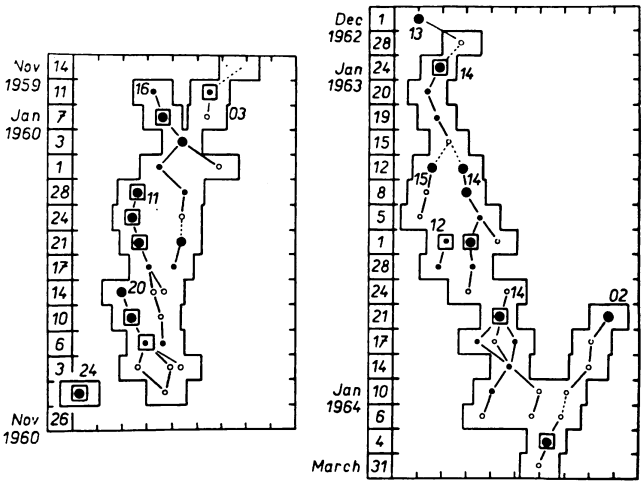

Figure 1-1. An Example of Two Complexes of Proton-Flare Activity on the Northern Hemisphere. Subsequent days are plotted on the horizontal axis, and subsequent 27-day rotations on the vertical one. Numbers on the left give the date, as 1960, 7 January, 3 February, 1 March, 28 March, etc., of the first day of each rotation. Circles denote the date of the central meridian passage of a proton-active region. Filled circles refer to sunspot groups, open circles to plages without sunspots, squares mark groups producing proton flares. (After Švestka 1968a)

present on the sun, and of course, we do not know when a particle-producing region might be formed in any of them, so that the practical use of this knowledge so far is fairly limited.

1-4 THE ACCELERATION PHASE

When a proton flare appears in an active region, it generally has the characteristic shape of two bright ribbons, which separate and move one from the other with decreasing velocity until the ribbons cover sunspot umbrae. These ribbons form along the line which separates the different magnetic polarities in the sunspot group, and one can consider them visible roots of a system of expanding loops, which form a hot thermal condensation above the active region. (Figure 1-2).

During the early phase of the expansion, before the flare reaches its maximum brightness in the Hα light, the acceleration process occurs. An evidence of it is an impulsive microwave burst produced by synchrotron radiation of mildly relativistic electrons, and the simultaneously occurring hard x-ray burst, produced by bremsstrahlung of electrons of about the same energy. We have no unambiguous proof that protons, too, are accelerated at the same time, but it seems reasonable to assume this to be so. At cosmic ray flares and very strong proton flares, we sometimes observe a short-lived white-light emission which exactly coincides in time with the microwave and hard x-ray bursts. This can most easily be explained by a penetration of energetic protons into the upper photosphere, which is then slightly heated and brightens in continuous light (Švestka 1970, Najita and Orrall 1970). Similar brightenings have been observed several times in the UV light (McClinton 1968, Friedman 1969, Donnelly 1970, Kane and Donnelly 1971) and one can explain these UV bursts in a similar way. Figure 1-3 shows the range of penetration of energetic protons, with zero pitch-angle, into the solar atmosphere below the flare (Švestka 1970b). The solid line corresponds to heights where the optical depth is unity, that is, approximately the heights where the continuous emission comes from. Thus, protons with energy of about 10 MeV can produce an increase in brightness in the UV region, while 100 MeV protons are needed for producing the white-light emission in the visible spectral region, which is very rarely observed.

If this hypothesis of the white-light origin is accepted, then the white-light emission areas show the roots of the loop-like region in which the impulsive acceleration process takes place. Figure 1-2 shows a part of the magnetically complex active region in which the flare of 23 May 1967 occurred. All the observed phenomena can be explained if the acceleration occurred in a volume of 5×10^{27} cm^3, which was only a small fraction of the whole hot flare-condensation,

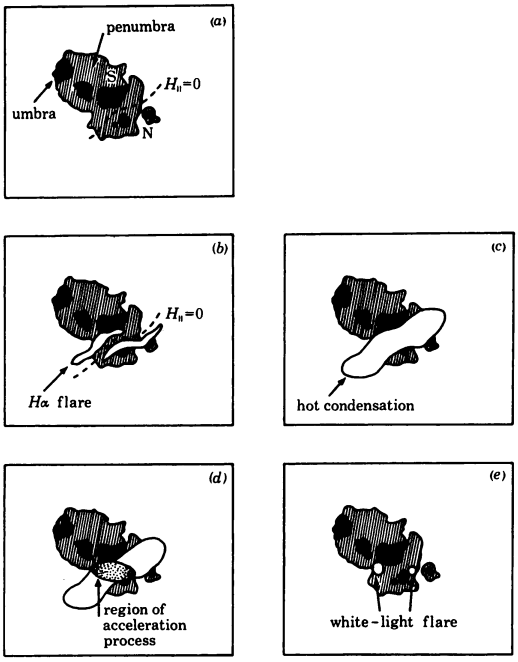

Figure 1-2. Drawings of the Sunspot Group That Produced the Proton Flares of 23 May 1967. All drawings refer to the same time, 1840 UT. (a) The magnetic configuration. (b) The brightest part of the two bright ribbons in the Hα line going parallel to the $H_{\parallel}=0$ line and partly covering the sunspots. (c) The core of the expanding hot condensation composed of a system of loops, the feet of which produce the bright ribbons in the Hα line. (d) The region of the impulsive acceleration process in the part of the condensation where the magnetic-field gradient was the highest. (e) White-light flare emission at position of the roots of loops inside of which the acceleration process occurred. (After Švestka 1971)

with a density of about 10^{10} particles per cm^3, which indicates that the acceleration process cannot occur too high in the atmosphere (Švestka 1970b). The same density is also obtained from analyses of the microwave bursts (Takakura 1969). If, on the other hand, the white-light emission is explained as being due to synchrotron radiation of highly relativistic electrons, one should need a number of particles two orders of magnitude higher (Najita and Orrall 1970), and these particles should produce more energetic x-ray bursts than actually is observed (Korchak 1967, Švestka 1970b).

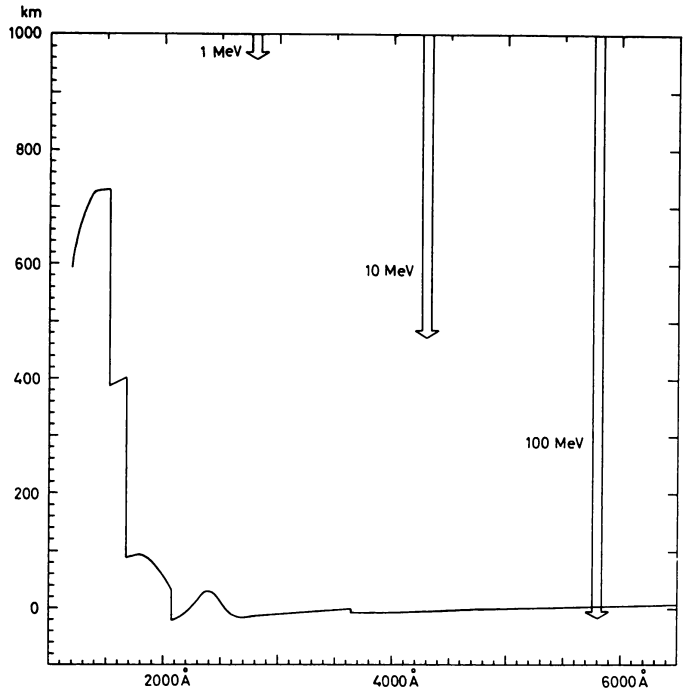

Figure 1-3. Height in the Solar Atmosphere at Which the Optical Thickness τ = 1 for Different Wavelengths. The arrows show the maximum depth to which protons of different energy penetrate in the solar atmosphere. (After Švestka 1970b)

Everything we observe later on in the flare development can be explained as a consequence of this initial acceleration process. The accelerated electrons thermalize and participate in the production of the thermal soft x-ray burst with a slow decay, and electrons escaping to higher layers give rise to a Type IV radio burst which is one of the most characteristic features of proton flares. As Castelli et al (1967) have shown, the burst spectrum has a typical V-shaped form with minimum flux near 2000 MHz in all strong particle events, with a very strong enhancement on millimeter wavelengths, as has been recently demonstrated by Croom (1971).

The acceleration process itself is not well understood as yet. So far, we do not know any mechanism effective enough to accelerate particles within some 100 seconds or less from their thermal energies to the relativistic energy range. With our present knowledge, one can help only by assuming a two-stage acceleration; the first one to energies of the order of 100 keV, which might be produced by induced electric fields, and the second one to higher energies, maybe in some

form of the Fermi mechanism (Wild et al 1963, De Jager 1969). The observations, however, strongly indicate that these two stages must immediately follow one another (Švestka 1970b, Frost and Dennis 1971).

1-5 THE SIZE OF A PARTICLE EVENT

The size of a particle event close to the earth is determined by three main factors. First, by the number of particles which take part in the acceleration process. This number obviously depends on the size of the region in which the acceleration occurs, and this size is determined by the magnetic configuration in the sunspot group. If this configuration is favorable, a high number of particles enter the acceleration process and are ejected, with different energies, into interplanetary space. In other more frequent events, the acceleration takes place in a much more restricted region and involves a substantially smaller number of particles. There may be many flares in which a small acceleration process occurs, but we do not record any particles in the vicinity of the earth, because the sensitivity of our detectors is insufficient to record the small number of accelerated particles ejected into space. Finally, there are probably many flares where no impulsive acceleration process occurs at all. An indication for this is the fact that some flares do, and other flares do not, show the impulsive hard x-ray component (Kane 1969). Figure 1-4a, taken from a paper by Anderson et al (1971) shows an example of an x-ray burst in which the impulsive component is clearly visible up to energy above 100 keV, while on Figure 1-4b, this component is entirely missing.

The other factor which determines the importance of a particle event is the shape of the energy spectrum. Figure 1-5 compares energy spectra of three large proton flares (Švestka 1971). The flares of 23 February 1956 and 2 September 1966 were characterized by approximately the same number of energetic particles in the energy range about 10 MeV, and accordingly, they also produced PCAs of about the same size. The energy spectra, however, greatly differed in these two events. While that of February 1956 was hard and produced an extremely strong ground level effect in neutron monitor records, the other was very soft and did not produce any ground level effect at all. On the other hand, the flare of 7 July 1966 was characterized by a small number of particles near 10 MeV, the PCA size being only two decibels. But its spectrum was extremely hard, so that even with this small total number of accelerated particles there were enough protons with energy above 500 MeV to produce a small neutron monitor increase.

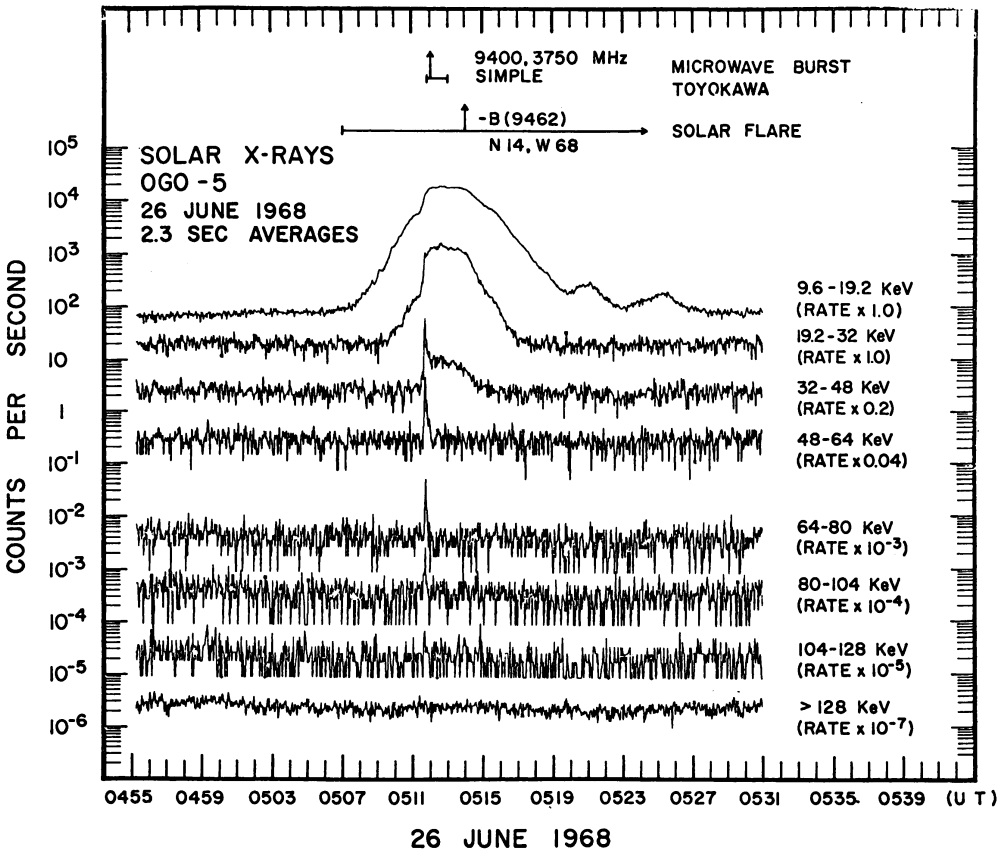

Figure 1-4a. An X-Ray Burst Composed of an Impulsive and a Gradual Component. (After Anderson et al 1971)

Finally, the size of the event, as observed at the earth, depends on the position of the particle source on the solar disc (Švestka 1971). The vast majority of all strong PCAs have their origin in flares situated between 10° east of the central meridian and the western limb. Weak PCA events, however, are recorded without any particular preference from about 70° east up to far behind the western solar limb, which is approximately the extent in longitude, from where the permanent particle emission is also recorded. There are some exceptions, of course, obviously due to anomalous diffusion either in the solor corona or in interplanetary space, when fairly strong events come from very unexpected positions, but these are relatively rare. Figure 1-6 shows a statistic based on 181 PCAs recorded from 1956 to 1969 (Fritzová and Švestka 1971). It shows the

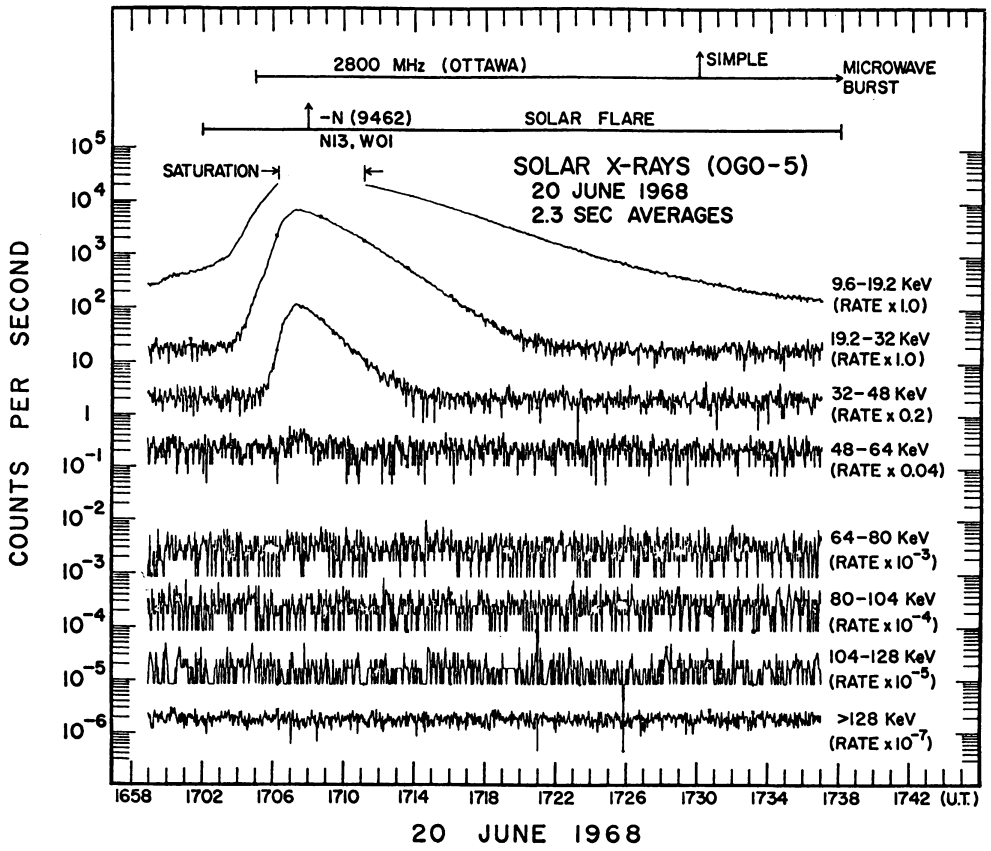

Figure 1-4b. An X-Ray Burst Without the Impulsive Component. (After Anderson et al 1971)

minimum and maximum number of PCAs of different importance, which might have been caused by flare sources on the invisible solar hemisphere; that is, predominantly behind the western solar limb. One can see from it that possibly all PCAs stronger than 8 dB originated in flares visible on the solar disk. On the other hand, more than 38% of PCAs with intensity less than 1 dB originated in sources behind the solar limb. A more detailed analysis shows that 25 - 30% is the most probable number of PCAs caused by flares on the invisible hemisphere, with the dependence on the PCA size shown in the figure.

1-6 DELAYED EVENTS

So far, we have been speaking about the prompt strong proton events, which directly reflect the acceleration process in a flare on the sun. Apart from these, however, as was mentioned previously, delayed events are also observed, at which the association with acceleration processes on the sun is not always clear.

First, we observe increases in particle flux, which are associated with sudden commencements at the earth or shock-waves in space. One example of such an event is shown on Figure 1-7 after Palmeira et al (1971). According to these authors, these delayed events only occur during the decay phase of an earlier prompt event, and are of a short duration, as one can see on the figure.

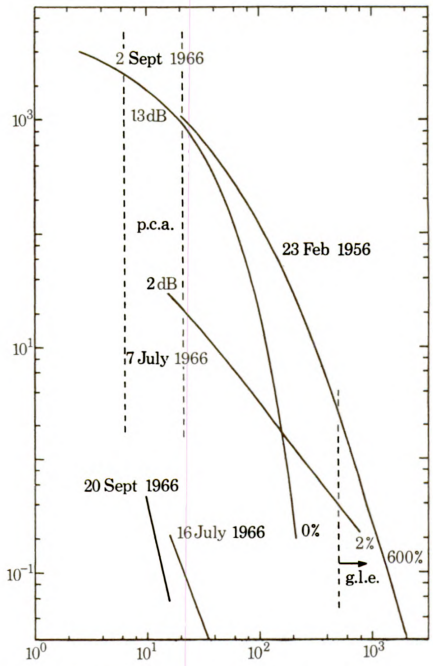

Figure 1-5. Energy Spectra of Three Selected Strong Particle Events. (After Švestka 1971)

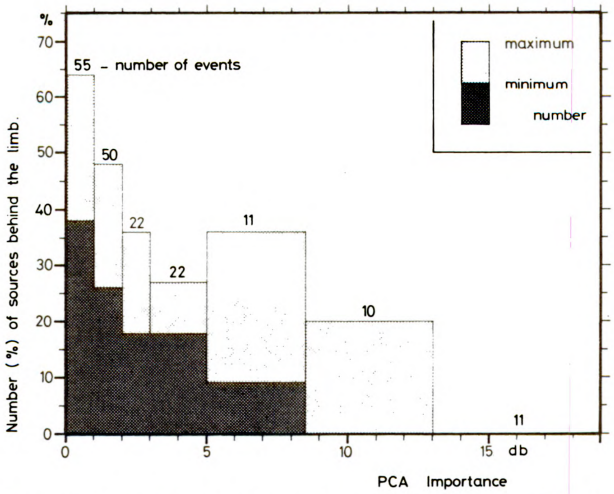

Figure 1-6. The Relative Number (in Percent) of PCAs of Different Importance (in Decibels) Caused by Flares on the Invisible Solar Hemisphere. Heavy shadings denotes clear, and light shadings suspected, events of this type

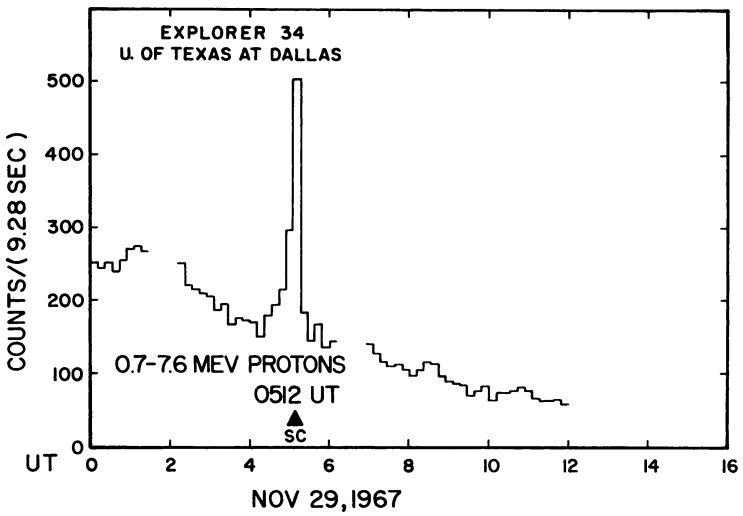

Figure 1-7. Examples of a Delayed Particle Event Associated With a Sudden Commencement. (After Palmeira et al 1971)

As for all delayed events, their energy spectrum is much softer than that of the prompt event particles. For this reason, the delayed event can be seen only at low energies. This phenomenon can be explained by a sweeping of low-energy particles by the propagating shock-wave. The particles are piled up ahead of the shock and swept away as the front passes the observer's position.

Sometimes, however, such an effect is observed without any associated sudden commencement. Figure 1-8 shows an example of such an event, for the flare of 7 July 1966 (Švestka 1968b). First we see the prompt event, and then a delayed event, which is very strong at 3 MeV, but completely disappears above 20 MeV. I have tried to explain this effect as being due to a sector boundary crossing the earth at that time, while Kahler et al (1968) interpret it as a special variation of the particle flux which reflects a particular injection profile at the sun.

In the lower part of Figure 1-8, one can see that the PCA also increased at that time, and this happens quite often in association with the delayed events. The curve represents a sum of the PCA records. When the recording stations are divided according to their geomagnetic latitude, the increase is found pronounced at low-latitude stations, but it is completely missing at high-latitude riometers. This indicates that the delayed PCA increase was not caused by an increased inflow of energetic protons into the polar region, but was due to a decrease of the geomagnetic cutoff and a subsequent shift of the polar-cap absorption to lower geomagnetic latitudes.

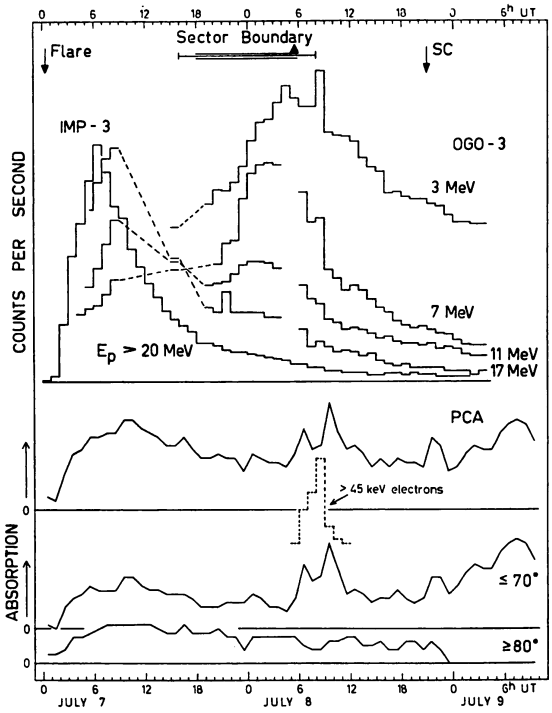

Figure 1-8. Counting Rates of Protons of Different Energies on 7 - 9 July 1966. Time of proton flare, sector boundary crossing, and sudden commencement are indicated at the top. In the lower part of the graph three PCA-curves are given: The first one is a sum of a absorption recorded at 15 stations in different geomagnetic latitudes. The second one only includes stations below 70 deg latitude, and the third one only stations above 80 deg latitude. (After Švestka 1968b)

Finally, there are delayed events which are not preceded by any prompt event, and sometimes are called "energetic storm particles". In some cases a flare on the eastern hemisphere, which appeared tens of hours earlier, may be tentatively associated with them, and sometimes no associated flare can be found at all. Figure 1-9 shows an example of one such event, after Anderson (1969), and one can see from it several typical properties of such a phenomenon.

It again is most pronounced at low energies, and occurs mostly in association with a decrease in the neutron flux and a magnetic storm. Sudden commencements, when present, reflect themselves in the recorded flux, but frequently in

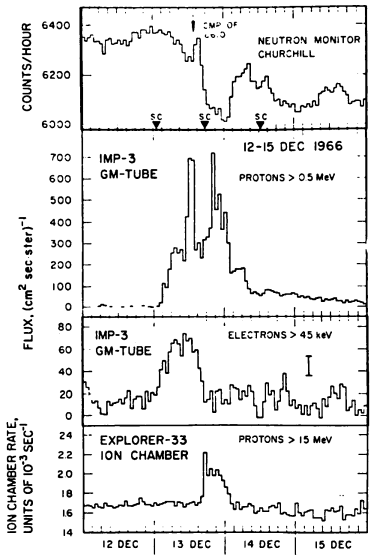

Figure 1-9. Example of an ESP (Energetic Storm Particles) Event. Three sudden commencements are marked in the upper part of the figure. The example illustrates the marked difference between the time histories of the electrons and protons. (After Anderson 1969)

a fairly curious way. Here, for example electrons appeared at the time of the first sudden commencement, and were completely swept away by the second one. Protons of higher energy, on the other hand, appeared just after this second sudden commencement, when electrons disappeared. According to Anderson, the time histories of electrons and protons mostly are different in delayed events of this type.

These all are problems which we do not yet understand, and obviously a further study of these delayed events is greatly needed.

References

Anderson, K.A. (1969) Solar Phys. 6: 111.

Anderson, K.A., Kane, S.R., and Lin, R.P. Paper presented at the Leningrad Seminar on Cosmic Ray Generation, December 1970, in press.

Arnoldy, R.L., Kane, S.R., and Winckler, J.R. (1968) Astrophys. J. 151: 711.

Avignon, Y., Martres, M.J., and Pick, M (1963) C. r. hebd. Seanc. Acad. Sci., Paris 256: 2112.

Avignon, Y., Caroubalos, C., Martres, M.J., and Pick, M. (1965) I.A.U. Symp. 22: 374.

Bumba, V. and Howard, R. (1965) Astrophys. J. 141: 1492.

Castelli, J.P., Aarons, J., and Michael, G.A. (1967) J. Geophs. Res. 72: 5491.

Croom, D.L. (1971) Solar Phys. in press.

Datlowe, D. (1971) Solar Phys. 17: 436.

De Jager, C. (1969) in Solar Flares and Space Research, p. 1.

Dodson, H.W. and Hedeman, E.R. (1969) Annals of IQSY. 4: 3.

Donnelly, R.F. (1970) ESSA Technical Report ERL 169 - SDL 14.

Eliseev, G.F. and Moiseev, I.G. (1965) Izv. Krymsk. Astrofiz. Observ. 34: 3.

Fan, C.Y., Pick, M., Pyle, R., Simpson, J.A., and Smith, D.R. (1968) J. Geophsy. Res. 73: 1555.

Friedman, H. (1969) in Solar Flares and Space Research, p. 87.

Friedman, H. and Kreplin, R.W. (1969) Annals of IQSY. 3: 78.

Fritzová - Švestkova, L. and Švestka, Z. (1971) Solar Phys. 17: 212.

Frost, K.J. and Dennis, B.R. (1971) Astrophys. J. 165: 655.

Gopasyuk, S., Ogir, M., Severny, A.B., and Shaposhnikova, E. (1963) Izv. Krymsk. Astrofiz. Observ. 29: 15.

Kane, S.R. (1969) Astrophys. J. 157: L 139.
Kane, S.R. and Donnelly, R.F. (1971) Astrophys. J. 164: 151.
Korchak, A.A. (1967) Soviet Astron. 11: 258.
Korchak, A.A. (1971) Solar Phys. in press.
Křivský, L. and Nestorov, G. (1968) Bull. Astron. Inst. Czech. 19: 197.
Lin, R.P. (1970) Solar Phys. 12: 266.
Lin, R.P., Kahler, S.W., and Roelof, E.C. (1968) Solar Phys. 4: 338.
Martres, M.J. (1968) IAU Symp. 35: 25
McClinton, A.T. (1968) NRL Space Research Seminar (April 17, 1968) p. 63.
McCracken, K.G. and Rao, U.R. (1970) Space Sci. Reviews. 11: 155.
Najita, K. and Orrall, F.Q (1970) Solar Phys. 15: 176.
Palmeira, R.A.R., Allum, F.R., and Rao, U.R. (1971) Solar Phys., in press.
Sakurai, K. (1966) Rep. Ionosph. Space Res. Japan. 20: 33.
Severny, A.B. (1964) AAS - NASA Symp. on the Physics of Solar Flares, p. 95.
Švestka, Z. (1968a) Solar Phys. 4: 18.
Švestka, Z. (1968b) Solar Phys. 4: 361.
Švestka, Z. (1970a) Space Research. X: 797.
Švestka, Z. (1970b) Solar Phys. 13: 471.
Švestka, Z. (1971) Phil. Trans. Roy. Soc. London A, in press.
Švestka, Z. and Simon, P. (1969) Solar Phys. 10: 3.
Takakura, T. (1969) Solar Phys. 6: 133.
Tanaka, H. and Kakinuma, T. (1964) Rep. Ionosph. Space Res. Japan. 18: 132.
Tanaka, H., Kakinuma, T., and Enome, S. (1969) Annals of IQSY. 3: 63.
Vitinsky, J.I. (1969) Solar Phys. 7: 210.
Warwick, C.S. (1965) Astrophys. J. 141: 500.
Warwick, C.S. (1966) Astrophys. J. 145: 215.
Wild, J.P., Smerd, S.F. and Weiss, A.A. (1963) Ann. Rev. Astron. Astrophys. 1: 291.

2. Typical Characteristics of the Active Region With Proton Flare Behind the Limb (2 November 1969) and Accompanying Effects

V. Bumba, L. Krivsky, A. Tlamicha
Astronomical Institute of the Czech. Acad. of Sci.
Ondrejov near Prague

J. Sykora
Astronomical Institute of the Slovak. Acad. of Sci.
Skalnate Pleso

J. Halenka, J. Lastovicka, P. Triska
Geophysical Institute of the Czech. Acad. of Sci.
Prague

S. Pinter
Geophysical Institute of the Slovak. Acad. of Sci.
Hurbanovo

A flare with a fast particle emission occurred in a spot group with the flare base 8 - 10° behind the western limb of the disc (N 14°) on 2 November 1969.

The active region in which the proton flare studied was generated, developed in a very typical situation of a large-scale distribution of solar magnetic fields. This situation was created in one of the two "active longitudes" existing at the time on the sun, and it is characterized by a special pattern of magnetic field distribution, which was described by Bumba and Howard (1965), Ambroz et al (1971); this pattern practically extended over half of the solar surface (Figure 2-1).

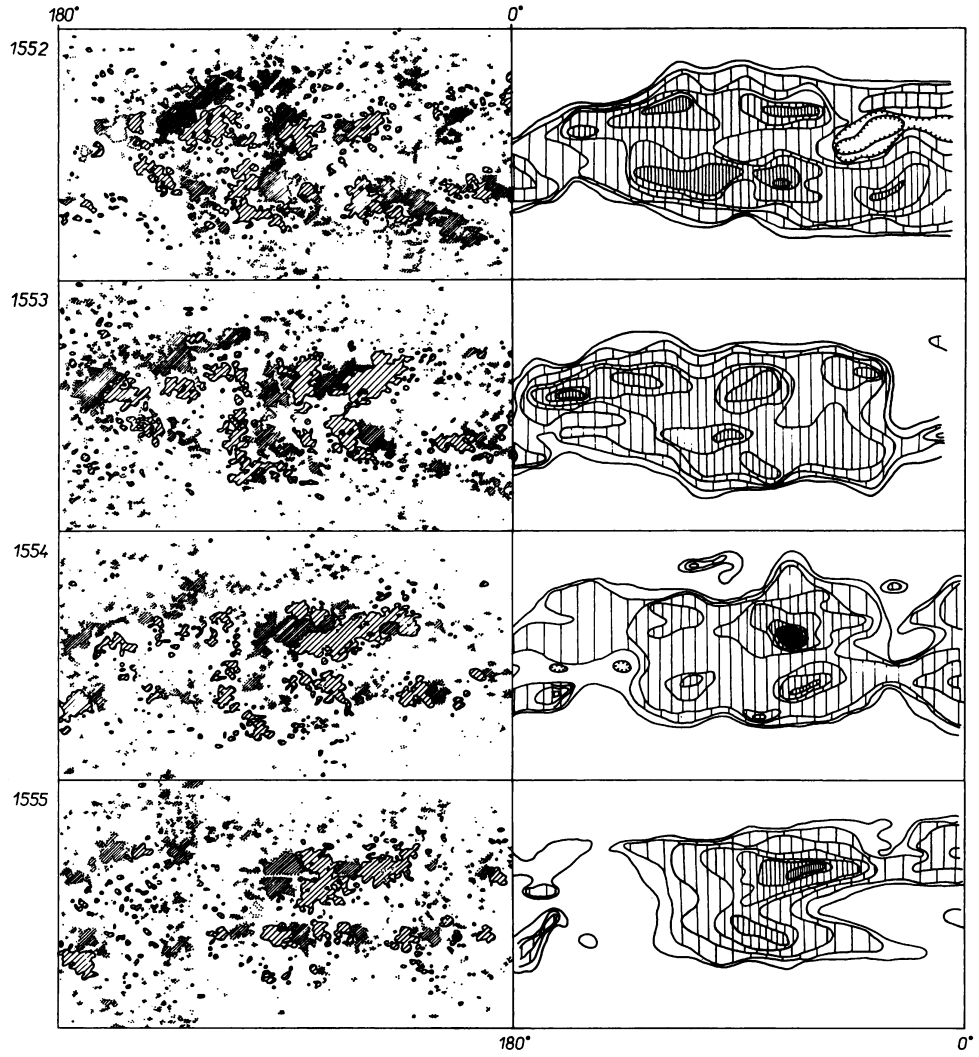

Figure 2-1. Typical Large-Scale Pattern in the Distribution of the Magnetic Field (Left) and of the Green Coronal Emission (Right) for Heliographic Longitude 180° - 0° and Rotations Nos. 1552 - 1555. The positive polarity of the magnetic field is shown by full lines and more widely spaced shading, the negative polarity by dots and denser shading. The active region with the proton flare developed around 70° longitude and 13° northern latitude during the rotation No. 1553

The active region with the flare is located in the eastern part of this formation, as has already been shown for a number of flares emitting particles (Bumba 1971). Moreover, the flare region is created at a time when the center of activity is shifting from the "head" (western) part of the large-scale formation to its tail (eastern) part, and the whole configuration of the head part disintegrates during the rotations following the flare.

The shift of the activity center can also be observed in the distribution of the coronal emission in the green line, where the green coronal emission attains a significant maximum (Figure 2-1) during the rotation following the flare. A shift of the activity towards the east can also be observed in the slowly varying component of the radio emission, as observed at the Pulkovo Observatory.

It seems that the complex of activity, which develops in the eastern part of the "supergiant" structure reaches its maximum on the invisible solar hemisphere. During this period, its whole activity is concentrated into two active regions only, which clearly interact. After the maximum, the number of regions increases rapidly with the simultaneous disintegration of the complex. However, the magnetic situation at the time of the passage of both active regions on the visible disc is not complicated. Its assumed complication was probably caused by the development of new activity adjacent to these regions near the limb of the solar disc.

During the critical period of 0930 - 1515 UT on 2 November 1969, when an unusually long and intense x-ray burst was recorded by the satellites, a number of active phenomena could be observed on the disc as well as behind the limb, so that the whole observed burst could not be attributed to a single phenomenon and a single source. The occurrence and duration of the individual active phenomena is indicated in Figure 2-2 by the lengths of the abscissas.

It is possible to consider the proton flare of the flare-channel type (loop tunnel), which began to develop impetuously behind the limb between 1030 and 1036 UT, as the source of the sub-cosmic radiation indicated by satellites (ATS-1, 20 - 70 MeV protons, beg. 1045 UT, ESSA, Sol. Geophys. Data, No. 304, Boulder 1969), on the one hand, and by a PCA effect (beg. about 12^h UT), on the other; the upper nodes of the loop structure began to ascend above the disc at about 1040 UT, when the μIV-type burst also reached its maximal value. The spatial development of the flare displayed a number of properties typical for similar flares (Figure 2-3). The emission of the fastest particles occurred between about 1030 and 1036 UT.

In connection with the present theoretical considerations of the mechanisms of rapid energy release by way of instabilities and in coincidence with observational data, one may assume that the energy was released in three parts of the

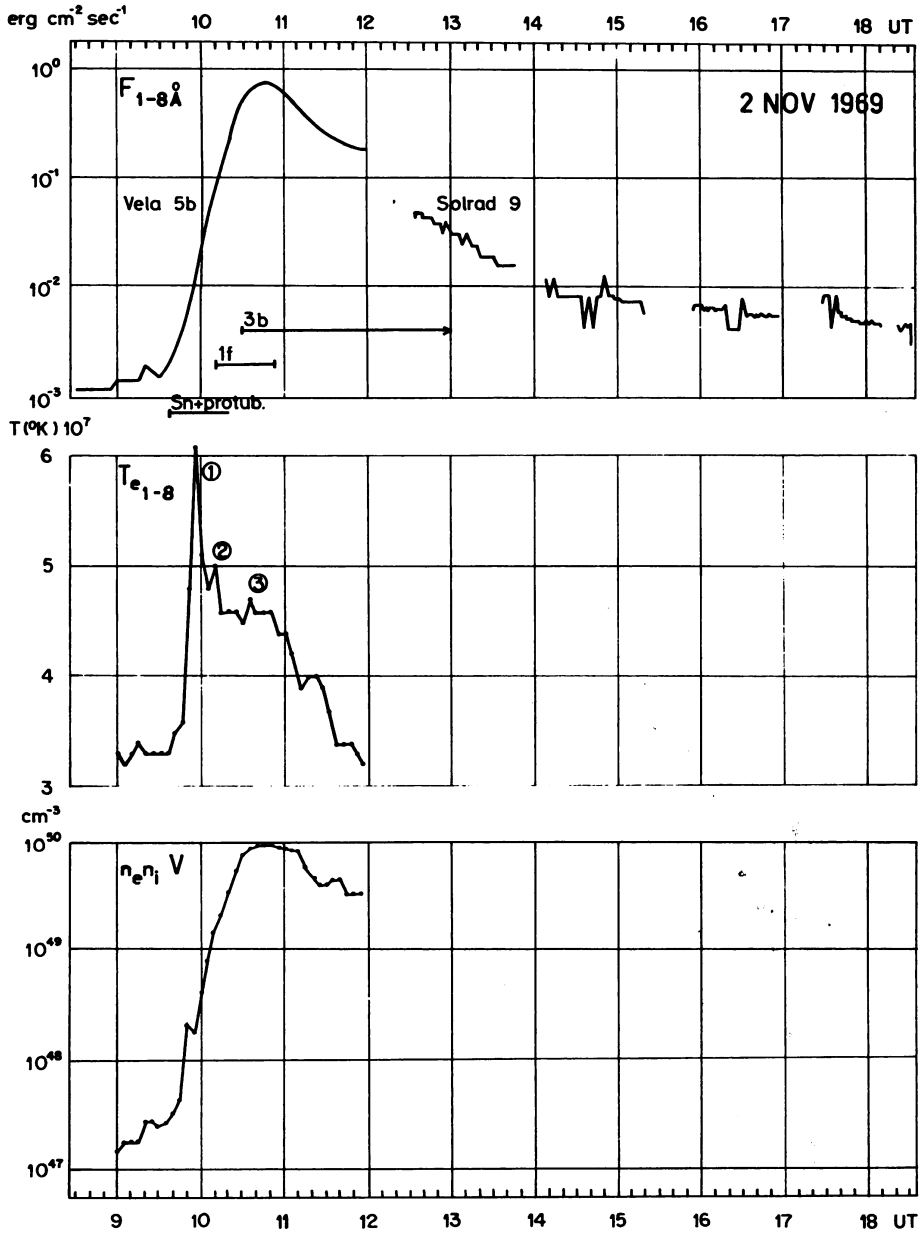

Figure 2-2. The X-Emission, the Computed Temperature $T_{e_{1-8}}$ and the Emission Measure. Below the x-emission curve the duration of the discussed active phenomena is indicated by the length of the abscissas. The individual peaks are marked by numbers on the $T_{e_{1-8}}$ temperature curve

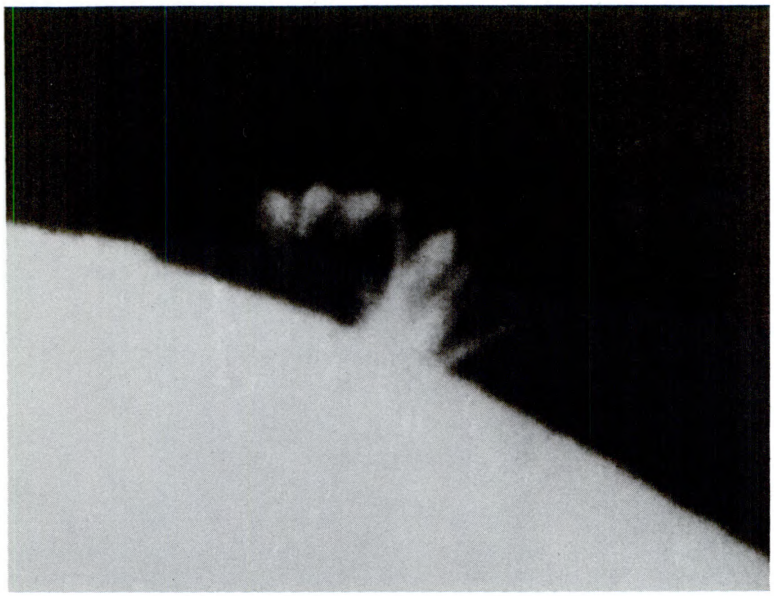

Figure 2-3. A Picture of the Proton Flare Tunnel in Hα at $12^h\ 00^m\ 15^s$ (Submitted From the Abastumani Observatory, USSR)

flare channel (Krivsky 1970): (1) along the two horizontal zero lines at both sides of the flare-channel (this process is of an explosive nature); (2) generation of fast particles and plasma flows in the region of the reconnection of the magnetic lines of force above and below both zero lines [the injection of particles upwards into the loop formations is also substantiated by Teske's results (1971)]; (3) a less significant acceleration of particles in the regions of the top nodes of the individual tunnel loops (only at the beginning of the development), where the plasma is concentrated and MH-waves of different types probably interact.

The anomalous x-ray burst, observed by satellites Vela 5A and 5B and by Explorer 37, and also displayed in ionspheric effects, presents a number of peculiarities: an extraordinary long ascent to considerable intensity, and a slow decrease of long duration (Figure 2-2). The curve of the x-ray burst is formed by the superposition of several sources on the sun, and it reaches its maximum at 0.5 - 3Å at 1042, and somewhat later in the softer channels.

At the same time when the loop tunnel of the proton flare appeared above the limb, the electron temperature T_{e1-8} showed a secondary maximum of $4.7 \times 10^{7}\ ^{\circ}K$, which means that this temperature was lower than at the time of the preceding activity, observed on the disc in the form of a small bright field connected with a prominence ($6.1 \times 10^{7}\ ^{\circ}K$ was the value of the main maximum). It seems that the T_{e1-8}-curve always displays a peak when another x-emission source is being created on the sun. The computed emission measure reached a maximum of $9.6 \times 10^{49}\ cm^{-3}$ between 1040 and 1055 UT, that is, at the time the upper parts of the Hα flare channel appeared above the limb of the disc (Figure 2-2).

The radio emission demonstrates two temporally and spectrally differing phenomena: the type III bursts series (234 - 30 MHz) are related with the small flare at the disc limb accompanied by an ascending prominence (1014 - 1017), and the short-wave continuum μIV (>10,000 - 510 MHz) with its maximum at 1040 - 1043 seems to be related to the appearance of the peak regions of the proton flare above the disc (Figure 2-4).

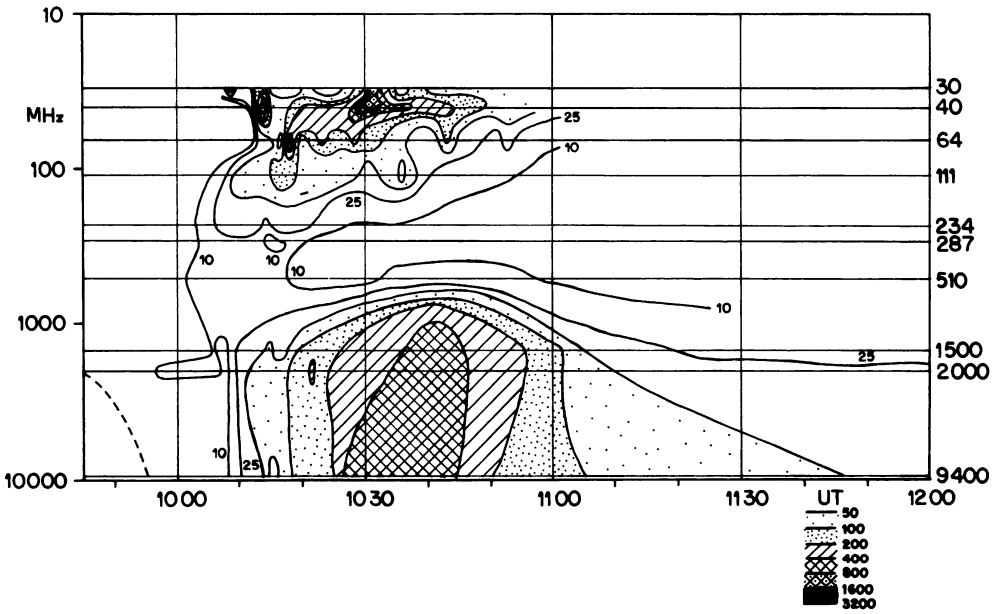

Figure 2-4. Radio Spectral Diagram of the Proton Event of 2 November 1969 (Heinrich-Hertz-Institute, by Courtesy of Dr. F. Fürstenberg)

The records of ionospheric SFA (155 kHz) and SEA (27 kHz) effects indicate that the maximum of the effects occurred between 1044 and 1049, preceded by a gradual increase lasting for about one hour; the importance, including the SWF effect (2,775 kHz), being 3.

From the geomagnetic activity pattern on and around 4 November 1969, when the effects due to the solar plasma should have been observed, it can be seen that no exceptional disturbance occurred, and also that the slight degree of disturbance has a clearly recurrent tendency, which is incompatible with a sporadic phenomenon like a flare. The only slightly peculiar event during the period

following the flare, is a bpsB-type bay disturbance in the 7th interval on 3 November 1969, which displays a shift in the Z-component record after a recovery (Budkov Observatory, Czechoslovakia).

The ionospheric conditions were investigated at large zenith distances of the sun, when the corpuscular ionization can already be effective in the lower ionosphere, since it is no longer blanketed by the short-wave ionizing radiation of the sun. The ionosphere was quiet on and around the day of the flare. Only in the lower ionsphere, an anomalous increase of night absorption on long waves was recorded between 19 and 20 UT on November 2 (A_o disturbance), which is sometimes the case on the first night following a proton flare (Nestorov et al 1964). As far as we know this anomaly has a local character only. The parallel measurement of absorption on 185 kHz (point of reflection 51° 09'N, 14° 06'E) also showed increased absorption (but not anomalous), but no increase of absorption was observed on the LF records of the Kuhlungsborn Observatory (Germany). What concerns the delayed corpuscular effects in the ionosphere the proton flare was practically negative, which is apparently due to the fact that it was not accompanied by a geomagnetic storm, as opposed to the storm event of 8 March 1970 (Triska and Lastovicka 1971).

References

Ambroz P., Bumba V., Howard R., Sykora J. (1971) Proc. of the Paris IAU Symp. No. 43 on Solar Magnetic Fields, ed. Howard, Dordrecht-Holland, in press.

Bumba V. (1971) Submitted to the Proceedings of the Solar Wind Conference, Asilomar, Pacific Grove, California, March 21-26.

Bumba V., Howard R. (1965) Astrophys. J. 141: 1502.

Krivsky L. (1970) Bull. Astr. Inst. Czech. 21: 67.

Nestorov G., Krivsky L., Letfus V. (1964) Geomagn. Aeronomia (USSR). 4: 1059.

Teske R.G. (1971) Sol. Phys. 17: 76.

Triska P., Lastovicka J. (1971) Rep. UAG-12 II, Boulder. 211.

Contents

3. The Radio Event Associated With the Polar Cap Absorption Event of 2 November 1969

J. P. Castelli and D. A. Guidice
Air Force Cambridge Research Laboratories
Bedford, Massachusetts

Abstract

A comprehensive picture of the solar radio disturbance associated with the polar cap absorption event of 2 November 1969 is presented. Although the probable center of gravity of the flare-burst was 12 to 25° beyond the west limb, a "Great Burst" type radio event was observed in the microwave region. Though some attenuation of the burst signal due to its limb location is apparent, the peak flux density spectrum in the dm-cm λ range produced a characteristic U-shaped spectrum satisfying criteria which have been identified with proton events. The dekameter emission was apparently obscured by directivity considerations. In terms of total emission, the radio event resembled other proton flare bursts producing an integrated flux density quantitatively identified with satellite observed proton flux densities and riometer absorptions. The radio burst-time intensity profiles are discussed in terms of a probable sequence of events on the sun and are compared with those of a much earlier event having similar radio absorption and particle density characteristics. Finally, a brief discussion of the peak flux-density U-shaped spectrum (and several other significant burst parameters) is presented. Probable physical mechanisms producing it and the justification for its use in prediction of proton events are suggested.

3-1 INTRODUCTION

It has long been recognized that solar radio astronomy provides a useful service to solar physicists and specialists in magneto-ionic research and solar-terrestrial relations. The time-intensity history of solar radio disturbances has been used alone and in conjunction with soft and hard x-ray data to study cosmic ray energies, and the acceleration of electrons and protons. A number of researchers have pointed out the excellent correlation between proton flux density and microwave burst energy (for example, Webber 1963). In the current sunspot cycle when prediction and warning of proton events became important to space efforts, the "tell-tale" signature of dm-cm bursts with proton correlation suggested by Castelli and Aarons (1967) has become an operational tool.

The 2 November 1969 event will be considered in relation to some of those points. A brief review will be made of the application of radio burst peak-flux spectra-principally in the dm-cm range, to the short term prediction of PCA events.

3-2 IDENTIFICATION OF PROTON EVENT SOURCES

One of the problems of proton and PCA event studies is the identification of the disturbance which triggers the event. There are a number of different criteria which have been used for identification with varying degrees of success. Of recent years, one of the most successful means of identification and, indeed, warning of impending events is found in the AFCRL-suggested U-shaped peak flux spectral signature. The spectrum is derived from discrete frequency observation of the associated flare-burst and later arrival of energetic particles in the earth's atmosphere, the signature provides short term prediction and warning of proton activity. The validity of this approach was pointed out by Castelli (1968); see Figure 3-1. In considering Bailey's (1964) list of 48 principal PCA events of the last sunspot cycle with unambiguous flare-burst association, the delay between burst start, burst maximum, and first onset of particles is plotted. It is clear that a minimum warning time of 12 minutes exists and that the mean delay is 4 hours to first onset. The mean delay to the time of maximum proton flux is 18 hours.

Although a distinction is made between principal (>2.0 dB absorption at 30 MHz) and weaker PCA events in the application of this warning device, the technique has been tested against both large and small PCA events of the present sunspot cycle and was found to be almost 100% successful when applied to large

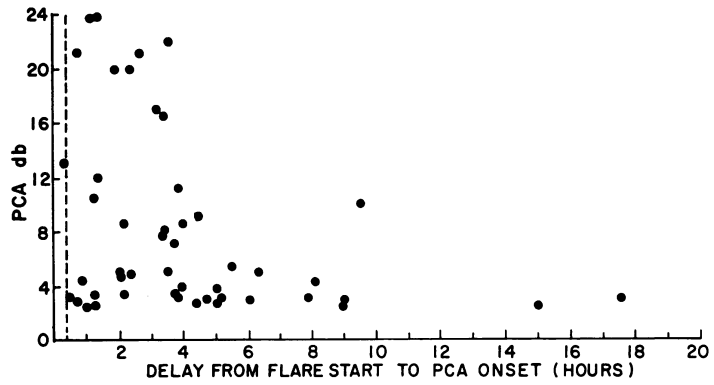

Figure 3-1. Distribution of Principal PCAs (>2 dB) 1952-1963 (Bailey 1964). Mean delay flare start to flare max (24 minutes) shown by broken line. Mean delay flare start to PCA onset 4 hours. Mean delay PCA onset to max, 18 hours

events whose parent disturbance was on the visible solar hemisphere. It cannot generally be applied to invisible hemisphere proton flare-bursts which certainly do occur; when applied to weaker PCA events (0.5 - 2.0 dB), only a small number would not have been predicted.

In addition to a low "miss" rate, a low "false alarm" prediction rate (which is a necessary consideration) has also prevailed. Though our statistics now are not current, over the three year period 1966-1968, no more than four false alarms would have occurred by utilization of the Sagamore Hill observations, and some of those were associated with proton activity if not PCA events.

A group of U-shaped spectral signatures associated with recent PCA events is shown in Figure 3-2. The curves reflect the following criteria: (1) flux density rising in the high frequency direction to values of greater than 1000 units of 10^{-22}W m^{-2} Hz^{-1} in the 9000 MHz regions, (2) a dip or minimum in the decimeter range between 500 and 2000 MHz, and (3) flux rising in the low frequency direction to large values in the meter wavelength range. It has also been noted that slow rise time from burst start to maximum (>5 minutes) is characteristic of principal PCA events >2.0 dB (O'Brien 1970). Additional discussion on these criteria can be found in Castelli and Aarons (1969).

3-3 CONSIDERATION OF TYPICAL RADIO-PROTON EVENTS

There is often tremendous complexity in the radio image of a proton event even at one frequency. The variation in the burst characteristics in the different

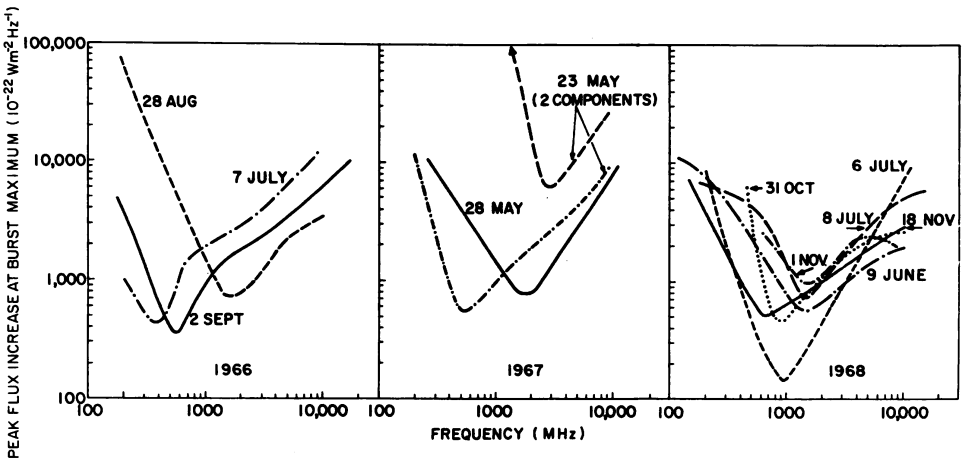

Figure 3-2. Spectra of Solar Radio Bursts Associated With Principal PCA Events (1966-1968). Flux values are based on published data from many sources

wavelength ranges (which are often inadequately monitored) differ greatly in a given event and from one event to another. Still, the observation of many different events leaves one with a general impression of what a typical event looks like. For discussion purposes, Figure 3-3 demonstrates the main characteristics. Shortly after the basic discharge, perhaps high in the chromosphere, the flare and microwave burst begins. (Even before the discharge, there may be some preheating which results in a gradual increase of the radio brightness temperature.) There is a moderately fast rise to maximum both in the Hα and in the cm-λ radio followed by a slower decay. In the radio ranges, this constitutes the Type IV μ. Starting at about the same time, there may be a weak decimeter component but a stronger meter wavelength component which has its first maximum at about the same time as the cm burst. This is the Type IV mA component. Somewhat later, a meter-and-dekameter component of considerably longer duration (possibly hours) begins. This is known as the Type IV mB. By that time, the microwave burst is all but over. The intensity of the IV mB may be relatively uniform for many minutes or even hours, but the event is not featureless from a spectral viewpoint, as it has a frequency of maximum emission.

The type information shown in Figure 3-3 may be plotted to give a three dimensional spectral plot as shown in the Fokker (1966) reduction of a proton event. Figure 3-4, showing intensity vs. frequency and time, is such a plot. The drawing lacks the frequency resolution of sweep frequency recording since it is constructed from discrete frequency observations. However, the intensity levels

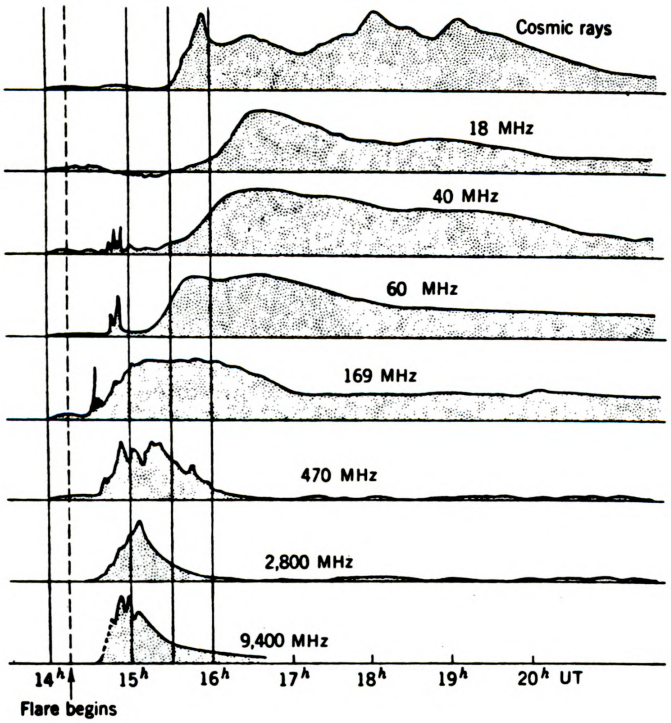

Figure 3-3. Type IV Burst Connected With a Flare of 22 August 1958 and the Cosmic-Ray Event Observed by Balloon. Flare importance 3 at N18, W10. Proton flux for >10 MeV particles $\cong$ 1010 cm^{-2} sec^{-1} str^{-1}

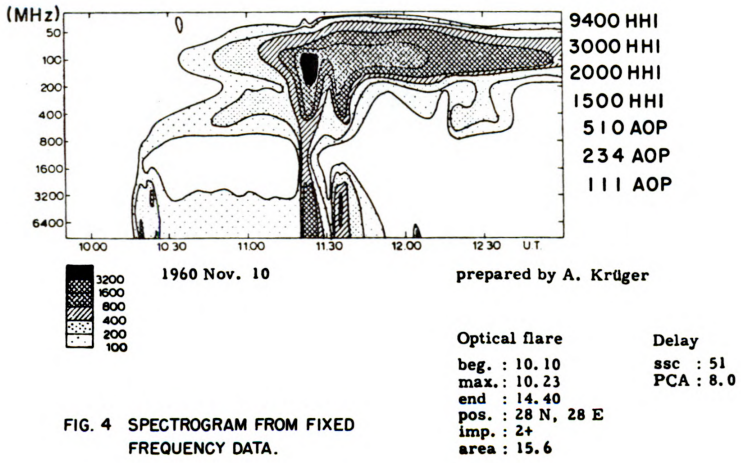

Figure 3-4. A Three-Dimensional Radio Spectrogram Prepared From Fixed Frequency Radio Data

are more accurate than could be derived from sweeping equipment. The lack of frequency resolution is unimportant in the microwave region, as bursts from one frequency to another are similar in shape - differing mainly in intensity.

From records, as shown in Figure 3-3, the general features of a fully developed Type IV event was conceived by Wild (1962). These are shown in Figure 3-5. Note start and maximum times of the various components in relation to each other. The strong decimeter component visualized by Wild seems to be missing in many of the large events with the Type IV μ and Type IV-m merging to produce a spectral minimum. Regardless, there will be two or three inverted U peak flux spectra with frequencies of maximum emission in the cm, dm-m, or deka-m wavelength regions (Kundu 1965).

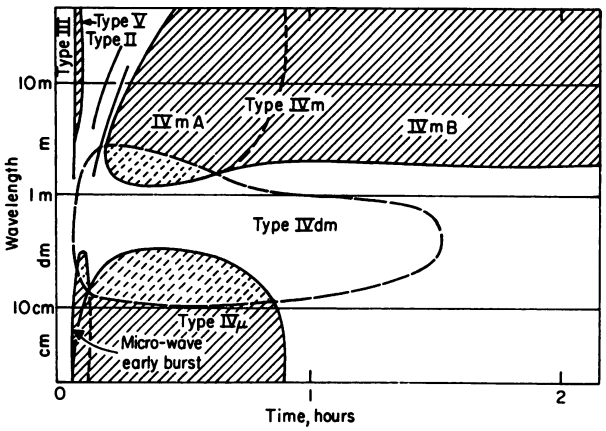

Figure 3-5. The Structure of a Fully Developed Type IV Burst (After Wild 1962). Frequently the decimeter component is missing or absorbed by the overlap of μ and m components

3-4 OBSERVED LIMIT OF GREAT BURSTS

The largest solar radio bursts go through a wide spread of intensities ranging from a factor of 10 times the quiet sun in the λ = 8 mm range to about 10^6 times the quiet sun in the meter λ range (see Figure 3-6). The very large bursts at the shorter wavelengths are accompanied by intense emission at the longer wavelengths. These all constitute fully developed Type IV events. However, there may be events with a strong meter λ component having little or no emission at

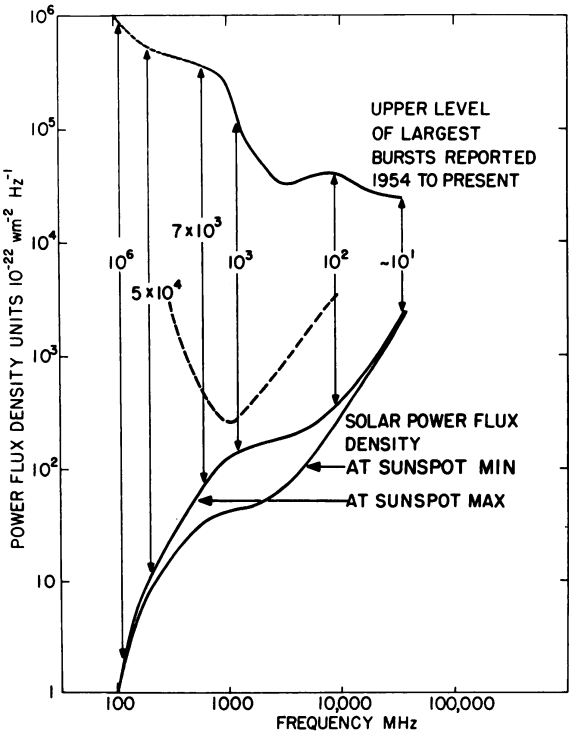

Figure 3-6. Spectrum of the Quiet Sun at Sunspot Max and Min. Larget bursts reported range between 10^1 and 10^6 times background sun at sunspot max. Threshold signature (generalized) for PCE's is shown by broken line

the short wavelengths. These are not indicative or proton activity. The figure also shows the threshold level for burst intensities in the cm range with proton activity via PCA events. No threshold above and below the limits of the broken line is shown since weather or other considerations preclude the formation of reliable criteria.

3-5 THE 2 NOVEMBER 1969 EVENT

The position of the present disturbance associated with the proton event in question was obviously beyond the west limb. The center of gravity of the probable flare was somewhere between 12 and 25° beyond the west limb, depending on which researcher one favors. It is clear that proton flare-bursts occur on the invisible

as well as visible solar hemisphere. It is also clear that identification of the source becomes extremely difficult if neither the radio nor optical emission can be observed. It is most disturbing in these situations that the proton event which is strongly detected might be falsely identified with an insignificant radio burst or flare on the visible solar disk which happens accidentally to fit within the time frame of the proton event. All near-the-limb events are difficult to interpret though there are different considerations for east or west limb events.

The question arises whether beyond-the-limb radio bursts with proton association can be detected and interpreted. One might ask, how far beyond the limb can bursts be observed and still furnish valid data? The 2 November 1969 event apparently from plage 385/381 (Ulwick 1970) was so far beyond the west limb that the flare which must surely have occurred was not observed per se, but only associated loops which rose to heights of 10^5 km. The microwave data fared much better judging from reported measurements. The timing of the event was such that both the Sagamore Hill and Manila Observatories of the Air Force were in darkness. The many radio observatories in Europe which recorded the event have provided data to reconstruct the event. One would have concluded that as the data satisfied PCA event criteria, one was in the offing.

We are indebted particularly to Professor Kruger and his colleagues at the Heinrich Hertz Institute for furnishing us with excellent time intensity profiles of the radio event.

3-6 THE BURST

Figures 3-7 and 3-8 are copies of the burst profile at multiple discrete frequencies between 9500 MHz and 30 MHz. Because of the position of the disturbance, the starting times at all frequencies are somewhat in doubt. Nevertheless, radio burst data indicate a probable flare starting time of 0934-0936 UT. From a proton prediction standpoint, the peak flux intensities in the dm-cm range in this case (and in all instances) are the most useful. Although they may require some corrections, and are certainly less intense than they would be if the event were on the visible disk, they meet our minimum criteria for identification.

The burst at all frequencies had a slow rise time, $\gg$ 5 minutes from start to peak. This characteristic has been observed in all bursts associated with principal PCA events in the present and previous sunspot cycle (O'Brien 1970). Actually, it may have been considerably longer than the record shows; especially at cm wavelengths. The present event, which was a "Great Burst" (by the morphological classification), appears to have started as early as 0936 UT and to

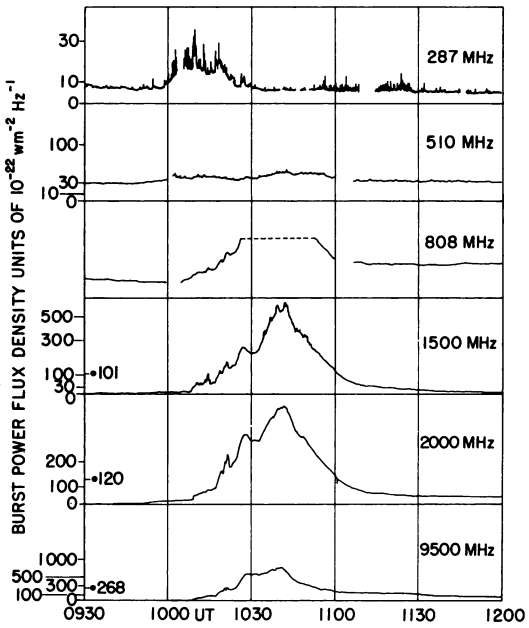

Figure 3-7. Solar Radio Burst (287-9500 MHz) Associated With 2 November 1969 Event (Courtesy of Heinrich Hertz Institute)

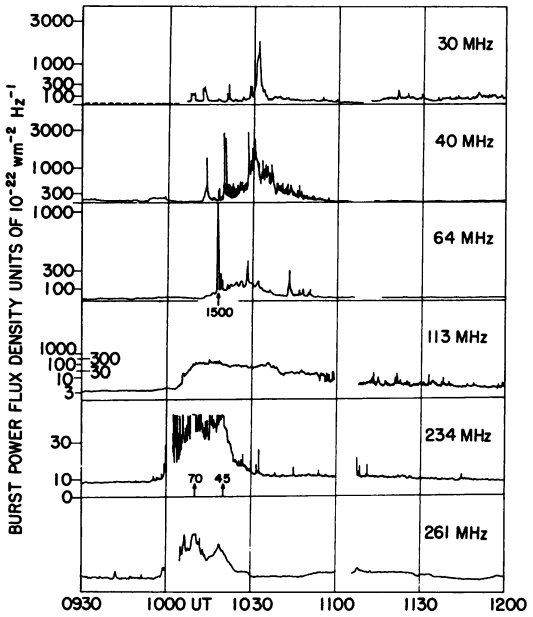

Figure 3-8. Solar Radio Burst (30-361 MHz) Associated With the Proton Event of 2 November 1969 (Courtesy of Heinrich Hertz Institute)

have reached a maximum generally near 1041 UT at all cm wavelengths. (This part of the event is shown as Type IV μ in Figure 3-5.) Emission remained enhanced in this band for several hours before returning to the preburst level. In comparison with a typical visible-hemisphere cm burst, the general form is similar except that here the burst may have been attenuated 10 dB in the 3-10 cm λ range in passing obliquely through the more dense lower solar atmosphere toward the observer. If we assume that the burst source in this range was at a height of 30,000 to 35,000 km (0.05 R_o) as suggested by Kai (1965) as the average burst height for IV μ, it would have been well above the critical plasma heights for the 3-10 cm λ. Hence, the burst radio emission would not be reflected significantly, but would propagate through the lower more dense regions suffering mainly attenuation. However, the source could not have been more than 18° beyond the limb, or it would have been eclipsed by the photosphere. The attenuation would also reduce small increases to values lower than the minimum detectable flux density at these wavelengths and, hence, artificially create an apparent delay in the start of the radio burst. (Compare the start of the 9500 MHz burst with that at 2000 MHz in Figure 3-7.)

In the very short cm range, extremely small burst values (see Table 3-1) suggest even greater attenuation. The complete lack of emission in the mm λ range during this period of confirmed monitoring suggests either high attenuation of these signals or eclipsing of the mm burst signal by the photosphere.

In the decimeter range, a proton event typically has a spectral minimum (see Figure 3-2). In the present instance, the flux density increase is so small as to be almost negligible. This may result from a combination of causes; attenuation and reflection. The precise altitudes of the bursts (in relation to the critical plasma layers for these layers) and the varying electron density in the ray path through the solar atmosphere between the burst and the observer are important. Considering the present observations in relation to Figure 3-5, no important dm component is apparent and in fact may not have existed, judging by its absence in many of the proton events which have been examined (Fokker 1966).

In the meter and dekameter ranges, small components of emission are apparent which occurred relatively early in the sequence. These are identified with the normal Type IV mA (early) component. However, this source must have been considerably east of the sun center - cm burst position radial line. Judging from the timing, it might also have been somewhat lower than the 0.3 to 1.0 R_o distance normally given for Type IV bursts in the 200-50 MHz range (Kai 1965). Since no one observed a Type IV mB dekameter event (late Type IV m in the normal sense), though one certainly must have existed, we conclude that the burst position was sufficiently rotated beyond the west limb, precluding

Table 3-1. Compilation Radio Burst Data Associated With Proton Event of 2 November 1969

FREQUENCY MHz	START TIME UT	MAX TIME UT	DURATION MINUTES	TYPE BURST	PEAK FLUX F.U.	MEAN FLUX F.U.	OBSERVATORY
19000	--	1040	--	--	163	--	Slough
9500	0955	1041.0	240.0	G.B.	720	--	H.H.I.
9500	1017.6	1041.0	27.4	C	155%	75%	NERA
9400	--	1038.7	--	--	1150	--	Slough
9400	1041.0*	1042.7	17.2	46	1767.2	200.9	Huancayo
5000	0949	1042	--	--	1523	--	Canary
3000	0944	1041	--	--	1589	--	Canary
3000	1007.8	1040	38.7	C	1275	700	NERA
2800	--	1040	--	--	1065	--	Slough
1470	0936	1042.5	300	G.B.	750	--	H.H.I.
~1500	0943	1043	--	--	704	--	Canary
1000	--	--	--	--	150	--	Weissenau
610	1018	1041.7	36	--	30	--	NERA
610	--	--	--	--	35	--	Weissenau
536	0950	1043	70	--	55	--	Ondrejov
260	1005	1010	25	---	50	--	Ondrejov
234	0954*	1010*	41*	C	75	--	H.H.I.
111	1006*	1016*	106*	C	250	--	H.H.I.
86-32	SPORADIC DEKMETER TYPE III's 1016-1030 UT						Weissenau
106-600	VERY WEAK CONTINUUM 1003-1026 UT						Weissenau

Symbols and Abbreviations:

- H.H.I. - Heinrich Hertz Institut
- * - uncertain
- G.B. - great burst
- C. - complex burst
- 46 - complex burst with fluctuation
- F.U. - flux unit 10^{-22}w $M^{-2}Hz^{-1}$

its detection. Bursts in this frequency range take place relatively closer to (though slightly above) the critical plasma heights for those frequencies than bursts in the microwave frequency range, for example. Because of this, there can be no penetration of lower altitudes, but only refraction outward and away from the sun-observer path.

Sweep-frequency spectral indications in this range scarcely appear. Sporadic Type III bursts in the 111 MHz area are suggested to have come possibly from another source (Urbarz 1970). The weak continuum between 1000 UT and 1030 UT between 160 and 540 MHz (Urbarz 1970) is suggested in Figures 3-7 and 3-8.

To summarize and explain the anomalous radio spectrum of this event, see Figure 3-9. The key factor in interpreting the spectrum is that the radio burst took place behind the west limb of the sun. Although the protons managed to reach the earth (protons from west limb events have a favorable probability of accomplishing this feat), the radio emission at certain radio frequencies could not. (Protons from east limb events as we shall see, often fail to arrive at the earth; note for example, the radio event of 6 July 1968, where only a small proton flux was recorded at the earth.) Radio emission at frequencies less than the ambient plasma frequency results in evanescent wave propagation and complete attenuation within a few wavelengths. Even where the emission comes from a height such that its frequency (f) is greater than the plasma frequency (f_o), any attempt to propagation in a direction along which f_o increases results in severe refraction; thus radiation at these lower frequencies cannot reach the observer on earth (as illustrated in Figure 3-9).

For centimeter wavelengths, $f_o \ll f$ all along the path toward the observer. The refractive index $n = \sqrt{1 - f_o^2/f^2} \approx 1$, and we have:

$$\tau = \int K \, dl = \int \frac{1}{nc} \frac{f_o^2}{f^2} \nu \, dl = \frac{0.054}{f^2 T^{3/2}} \int N^2 \, dl$$

where ν is the collision frequency (a function N and T), T is the electron temperature (°K) and N is the electron density (cm^{-3}). For an Allen-Baumbach distribution of solar electron density $N = 10^8 (1.55 \rho^{-6} + 2.99 \rho^{-16})$, we have $\int N^2 \, dl = 2R_o 10^{16}$ (4.15). If we assume the centimeter radiation comes from a height of about 42×10^3 km ($\rho_{cm} = 1.06$), then the nearest approach of the line-of-sight of the radiation $\rho_m = \rho_{cm} \cos 18° = 1.008$. For the height corresponding to ρ_m (about 5600 km), at which most of the attenuation takes place, the solar temperature is about 30,000°K. Using this value for T, we find for f = 5 GHz that the attenuation $e^{-\tau} \approx e^{-2.4} = 0.09 = -10.5$ dB. We shall see later that this is a realistic value considering the uncertainties of both source height and angular distance beyond the west limb.

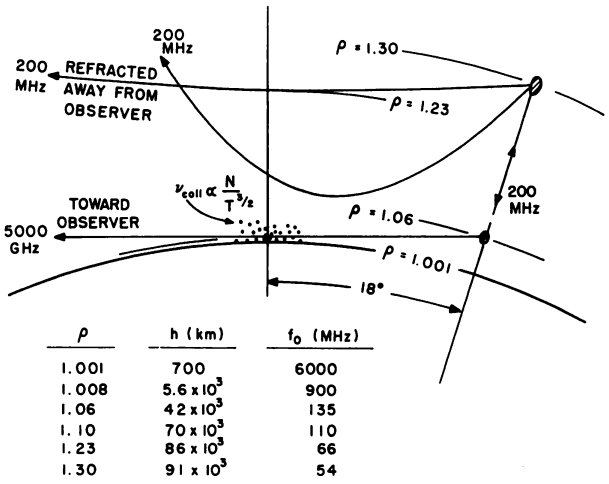

ρ	h (km)	f_0 (MHz)
1.001	700	6000
1.008	5.6×10^3	900
1.06	42×10^3	135
1.10	70×10^3	110
1.23	86×10^3	66
1.30	91×10^3	54

Figure 3-9. Propagation of Radio Emission From a Burst Behind the Limb. Meter and cm radiation arise from different levels in the solar atmsophere

3-7 BURST SPECTRA AND THE PROTON SPECTRAL SIGNATURE

There are several general types of emission spectra associated with the solar bursts in the dm-cm range. They are: (1) those with only a low frequency component without cm emission, which are not associated with proton events, (2) those with only a high frequency component which also lack proton association, and (3) those with both high and low frequency components. When in the last case the two components are strong and satisfy criteria set forth earlier whether from visible or invisible hemisphere sources, proton activity may be expected.

Figure 3-10 is the peak flux spectrum of the present event with the data points taken from Table 3-1. The characteristic U-shaped signature is present in spite of the unfavorable position of the source and probable attenuation. The part of the spectrum in which we are interested for source identification is shown within the broken lines. The short cm and mm waves, which might be useful for visible hemisphere events, are badly compromised by positions beyond the limb.

For visible hemisphere events, Castelli and Barron (1968) found (though it is difficult to prove rigorously) no serious attenuation effects as a function of source central meridian distance.

The slope steepness values in both directions (normally indicative of the energy distribution for synchrotron emission), the harmonic drop-off in the gyrosynchrotron emission case, and the absorption mechanisms present are of little value in the present case because of the data distortion.

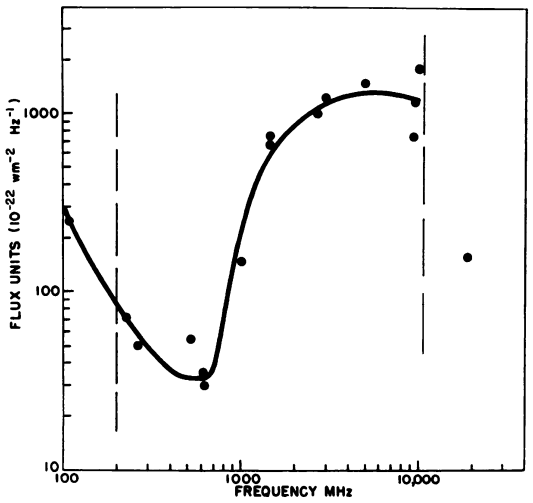

Figure 3-10. Peak Flux Radio Spectrum of Burst at Approximately 1041 UT, 2 November 1969, With PCA Association, Data Sources - Slough, Nera, HHI, ESSA Canary Island, Weissenau, Ondrejov and Huancayo

3-8 BURST INTEGRATED FLUX DENSITY

While the burst peak flux U-shaped spectrum is an excellent identifier of principal PCA events and many of the small ones as well, it does not provide a useful quantitative correlation with the associated polar cap absorption (dB) or the satellite measured particle flux density at different energy levels. However, considerable success has come from correlating burst integrated flux density with proton flux (Straka 1970). Figure 3-11 based on Straka's work shows 8800 MHz burst integrated flux density vs proton flux of >10 MeV particles for a group of current sunspot cycle events. The events were selected if they first met the peak flux criteria. Except for a few events, the overall correlation coefficient (0.73) is quite reasonable. One of the events at N14, E89 (6 July 1968) referred to earlier, was in an unfavorable position for producing a PCA event based on current ideas on particle directivity. We can assume that the burst integrated flux densities are valid since these are all for visible hemisphere events not requiring any correction as a function of central meridian distance.

On the same figure, the typical event shown in Figure 3-3 has been added. The plot of the 9400 MHz 2 November 1969 event indicates the expected high proton flux density, but the radio burst integrated energy is perhaps a factor of 10 lower (as discussed in previous section) than it would be if the same event

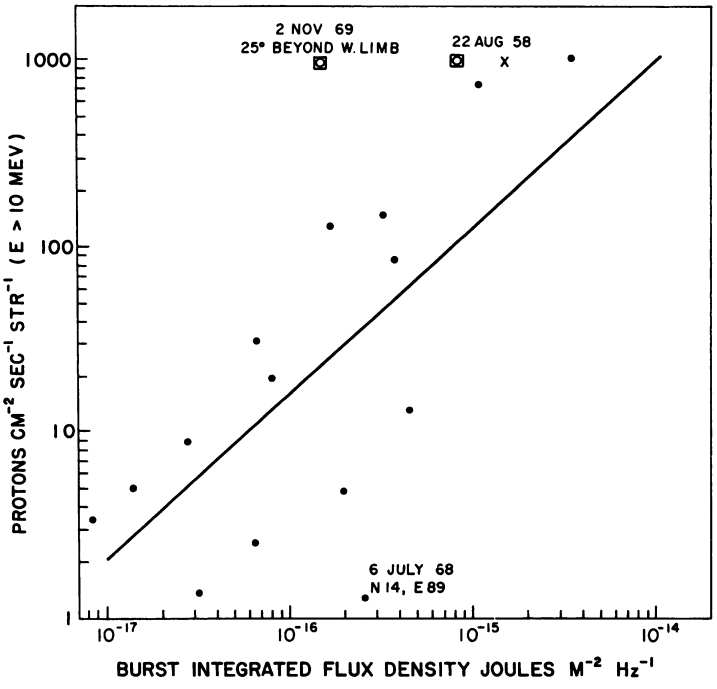

Figure 3-11. Burst Integrated Flux Density at 8800 MHz vs. Proton Flux (From Table 3-1, Straka 1970). Note position of 6 July 1968 event. Boxed points have been added

occurred on the visible disc. With this correction, the point might be replotted at the location indicated by the "x" and thus compare favorably with earlier events.

3-9 THE U-SHAPED SPECTRUM – DISCUSSION

The correlation between radio bursts with a U-shaped peak flux spectral signature in the dm-cm range and proton events has been well established. The device makes possible a prediction accuracy of almost 100% for PCA events with absorptions greater than 2.0 dB that are associated with visible hemisphere events. Frequently one asks for an explanation of the U-shaped spectrum, whence it comes, and why it works.

In the first place, the spectrum exhibits a crossover frequency. Below the crossover, the burst intensity increases with decreasing frequency for some unspecified interval of bandwidth, while above the crossover the intensity

generally increases with frequency. Hence, in the case of particle associated bursts, the spectral characteristics may be divided into two domains; that above and that below the crossover frequency. The portion below the crossover frequency may be considered a coronal event and that above it a chromospheric event. To adequately explain the entire event, one must consider emission spectra of bursts in general in relation to a plausible model.

3-10 THE HIGH FREQUENCY SIDE OF THE "U"

Assume, within an active region or coronal condensation, the whole sequence of events is triggered by some sort of a discharge resulting from magnetic field instability. During the pre-discharge period, ambient electrons may be randomly spiraling around field lines at different heights. At the time of the discharge, an acceleration of these ambient electrons takes place in some manner by particles actually moving downward into the chromosphere or by some transfer of acceleration. This process may produce emission either by bremsstrahlung or gyro-synchrotron process. The former would produce a burst peak flux spectrum which would increase with frequency and then level off (as the plasma becomes optically thin at higher frequencies). One might assume that some gradual rise-and-fall type bursts are caused by this mechanism. Nevertheless, since this type spectrum is observed only infrequently, it must be assumed that it is not a dominant process for cm bursts.

The spectrum which is most common in the cm range is one which rises rather steeply to some maximum between 1400 and 15,000 MHz (and possibly higher) and then falls off in the higher frequency direction. As the event becomes more intense, there is a spectral hardening with the frequency of maximum emission shifting toward the higher frequencies (Castelli and Guidice 1970). This type spectrum is observed through a wide range of intensities. Its form suggests the gyro-synchrotron process of sub-relativistic electrons, even for the most intense events – though for the larger events the high frequency end may have a less steep slope, which is indicative of higher particle energies. We may consider emission at different frequencies as coming from an inhomogeneous and extended medium. The peak frequency may be a composite of spectra of individual particles at different energies in different media. The frequency of maximum emission, f_{max}, is empirically related to the gyro-frequency f_H; $f_{max} \approx 3.5\ f_H$, where $f_H = 2.8$ H with the magnetic field H in gauss and f_H and f_{max} in MHz.

The slope in the high frequency region above the cm λ peak would indicate the energy distribution of the radiating electrons only in the relativistic case. The steep spectral indices observed can only be related to the drop-off of harmonics of the gyro frequency. The form of the spectrum in this range is consistent with magnetic fields at burst heights in the order of 500-1500 gauss. The slope on the low frequency side of the cm λ max and sharpness of the low frequency cutoff indicates the absorption mechanism.

This part of the curve constitutes the upper part of the U-shaped signature. For many bursts, there is no low frequency emission, for example, below 1500 MHz. If the radiation takes place at a height lower than the critical plasma density for a given frequency, the radiation cannot escape and hence is not observed. If electrons are not accelerated outward, but are prevented by closed magnetic field lines, there can be no radiation at longer wavelengths in the corona. The foregoing, in agreement with observations, indicates that there may be a discontinuity of radio emission even with dropouts between different portions of the radio spectrum, though there is a continuity of mechanism. For centimeter bursts whether large or small, whether there is another emission band below 1500 MHz or not, no MeV electrons have been observed to coincide with the microwave Type IV, and only sub-relativistic electron velocities are present. We might conclude also that no MeV protons came from this region or from anywhere in the time interval of the first acceleration.

There are a number of reasons why we can be sure that there are no MeV particles created in this first acceleration. First, Arnoldy et al (1967) demonstrated that correlation exists between hard x-ray bursts and microwave emissions in time integrated intensity, peak flux, and decay shape. These observational characteristics strongly support the hypothesis that x-rays and centimeter wavelengths are generated in the same region. De Jager (1969) notes that no solar x-ray bursts have yet been observed with energies above 1 MeV. Also, Holt and Ramaty (1969) have shown that hard x-rays and microwave bursts are consistent with a single source of non-thermal electrons, where both emissions arise from electrons with energies $<m_o c^2$. De Jager (1969) also notes that Type III radio bursts occur in the first phase of flares and are due to electron jets progressing through the corona with speeds c/6 to c/2 (average), with a maximum velocity of 0.9c (that is, ~700 keV). If MeV electrons were produced in this first phase, we would see Type III's with velocities very nearly the speed of light, but we do not.

Protons are not accelerated to MeV energies in this first acceleration because, if they were, we would also have MeV electrons, but there are none present.

3-11 THE LOW FREQUENCY SIDE OF THE "U"

Some particles accelerated in the discharge region move upward and out along open field lines to produce a continuum Type IV burst with only the tail visible in the 500-and-above MHz region. The tail may be shifted to higher or lower frequencies. Events of this type, while important in themselves and often correlated with certain classes of geophysical phenomena, are not relevant to proton considerations when they stand alone without cm emission, as they sometimes do. Events in this group have slopes in the high frequency direction which are generally smaller than for cm events. They also have a f_{max} and low frequency slopes which we have not investigated in detail. The spectrum in the m-dm range is generally assumed to be produced by the synchrotron process by relativistic electrons in weak magnetic fields.

This type event alone without a high-frequency cm component may exist. Field strengths in the order of 25 gauss can be assumed with electron energies of 1 or 2 MeV. In this situation there is no evidence of an outpouring of highly energetic protons. When coupled with the cm components, it is more plausible to assume weaker fields (for example, 1 gauss) and more energetic electrons - and protons, which are, in fact, measured.

With the outward acceleration of electrons, a cloud of gas travels radially outward with a velocity of about 1000 km/sec (higher than the velocity of sound in the corona) resulting in the formation of a shock wave. The shock front is assumed to excite plasma oscillations resulting in Type II radiation. High energy electrons and protons are produced abundantly due to Fermi-like acceleration by hydromagnetic shocks (Kundu 1965). As the gas column is strongly ionized and highly conducting, the sunspot magnetic fields will be "frozen in" and carried along by the gas. The 10 to 100 MeV protons will escape. Electrons accelerated to the same energies will give rise to m - λ Type IV radiation, possibly at greater heights than the non-cm-associated m - λ Type IV.

3-12 THE CONNECTION BETWEEN THE TWO COMPONENTS

The connection between the cm and m λ radio components appears to be a physical one where the acceleration process is a two-step affair (De Jager 1969). In the former case, a large quantity of electrons at low energies (0.2 - 0.7c) is present. This is suggested by the value of the radio burst integrated flux density at a given frequency, the quantity of electrons being related to the integrated flux density.

This same volume of moderately low energy particles is indicative of the quantity (which must be much smaller) of electrons accelerated to high energies by the Fermi-like process following a Type II disturbance which may or may not be observed.* Hence, without the former emission with large burst integrated flux density thresholds (for example, 10^{-17} joules m^{-2} Hz^{-1}), we do not have m - λ bursts with energetic proton association. If there is an insufficient quantity of lower energy electrons to produce a shock wave, etc., then there is no m - λ Type IV to produce the low frequency side of the "U" signature.

*Since the plasma frequency coincides with the critical frequency at which the refractive index is zero, there will be difficulties of escape (Kundu 1965). If the emission taken place from a localized region in which only the plasma frequency is excited, the radiation can escape only within an infinitely narrow cone normal to the surface of zero refractive index. The prerequisite shock may be present without the Type II.

References

Arnoldy, R.L., Kane, S.R., and Winckler, J.R. (1967) A Study of Energetic Solar Flare X-rays, Solar Physics. 2 (No. 2): 171-178, September.

Bailey, D.K. (1964) Polar Cap Absorption, Planetary Space Science, 12: 495-541.

Castelli, J.P., Aarons, J., and Michael, G.A. (1967) Flux Density Measurements of Radio Bursts of Proton-Producing Flares and Non-Proton Flares, J. Geophys. Res., 72 (No. 21): 5491-5498.

Castelli, J.P. (1968) Observation and Forecasting of Solar Proton Events, AFCRL-68-0104.

Castelli, J.P. and Barron, W.R. (1969) Statistical Consideration of Centimeter Wavelength Solar Burst Directivity, Bulletin of the A.A.S. 1 (No. 3): 274 (Abstract).

Castelli, J.P. and Aarons, J. (1969) Short Term Prediction of Solar Proton Events. Proc. of Symp. on Ionospheric Forecasting, Grey Rock, Canada, Conf. Proc. (No. 49).

Castelli, J.P. and Guidice, D.A. (1970) On the Classification, Distribution and Interpretation of Microwave Solar Burst Spectra, Proc. G-AP International Symp., Columbus, Ohio, 70C-36-4P, 88-93.

De Jager, C. (1969) Solar Flares-Properties and Problems in Solar Flares and Space Research, Proc. of COSPAR Symp., Tokyo, May 1968. Ed De Jager and Svestka, North Holland Pub. Co., Amsterdam.

Fokker, A.D., Goh, T., Landre, E. and Roosen, V. (1966) A Collection of Spectral Diagrams of Solar Radio Type IV Events, Utrechtse Sterrekundige Overdrukken (No. 23).

Holt, S.S. and Ramaty, R. (1969) Microwave and Hard X-ray Bursts from Solar Flares, Solar Physics. 8 (No. 1): 119-141.

Kai, K. (1965), Publ. of the Astron. Soc. of Japan. 17 (No. 3).

Kruger, A. (1971) Private Communication.

Kundu, M.R. (1965) Solar Radio Astronomy, Interscience Pub., New York.

O'Brien, W.E. (1970) The Prediction of Solar Proton Events Based on Solar Radio Emissions, AFCRL 70-0425.

Straka, R.M. (1970) Unpublished Report - to appear.

Ulwick J. and Blank, C.A. (1970) Proc. of Meeting on Operation PCA-1969, AFCRL 70-0625, Special Report No. 110.

Urbarz, H. (1970) Private Communication.

Webber, W.R. (1963) AAS-NASA Symp. on the Physics of Solar Flares, NASA-SP-50, W.N. Hess, Editor, 215.

Wild, J.P. (1962) J. Phys. Soc. Japan, Supplement AII 17: 249.

Contents

4. Origins of the 2 November Proton Event

C. J. Thomas, Major, USAF
Aerospace Environmental Support Center
12th Wea Sq
Air Weather Service
Ent AFB, NCMC, Colorado

Abstract

The solar region that eventually evolved into the source of the particle event of 2 November 1969 is traced from its inception to the 2 November flare. The flare event is described in terms of optical, radio and x-ray responses. The real time successful forecast of this PCA event is discussed with respect to the data available to the Aerospace Environmental Support Center.

4-1 INTRODUCTION

This paper presents the data that were available to the Aerospace Environmental Support Center (AESC) in tracing the responsible solar active region from its inception to the flare that gave rise to the 2 November 1969 PCA events. The flare event is described in terms of optical, radio, and x-ray responses. These data are also discussed with respect to their availability and use in making the real time successful forecast of the ensuing PCA event.

4-2 HISTORY OF THE REGION

The solar region that eventually evolved into the source of the particle event of 2 November 1969 was born on the visible disc, apparently as a result of the splitting of McMath Region 10245. Figure 4-1 illustrates this development. The only significant fact in relation to its beginnings is that development of a new region in close proximity with an existing region at a heliographic longitude that is associated with a high flare incidence suggests dynamic development. No significant development was apparent before the region's first west limb transit, however.

The region returned for its first complete disc transit on 27 August as McMath Region 10293, but remained relatively simple in structure and generally unimpressive (see Figure 4-2). Activity was limited to 15 subflares during this first transit. Upon its return for its second disc transit as McMath Region 10335, the most salient developmental feature within the region was a growth in calcium plage. The activity level increased slightly (22 subflares and a single Importance 1 flare), but few of the dynamic features generally associated with energetic activity were apparent. Evidence indicates that the development of these dynamic features occurred after the region had passed the west limb following its second disc transit. The evidence, based upon Pioneer spacecraft data, is not direct, but is fairly conclusive.

NASA's Pioneer spacecraft are in heliocentric orbit, similar to that of the earth. At the time the solar region in question was on the nonvisible hemisphere of the sun, the Pioneer 6 and 7 spacecraft were in a position to detect particle enhancements resulting from energetic activity from regions on the nonvisible disc. Enhancement in proton counting rates were sensed by both the spacecraft, and, considering the position of the region relative to the spacecraft, it appears likely that the enhancements resulted from a "proton flare" within the region. The relatively unimpressive history of other regions on the nonvisible disc at the time lends credence to the conclusion as to the origin of the event. The region's subsequent appearance on the east limb further substantiates the conclusion.

Before the region returned, coronal emissions became enhanced on the limb, usually indicative of the emergence of an active region. The coronal enhancements were followed by frequent reports of surge and spray activity, up to Importance 2, and the region began to transit the limb as McMath Region 10385. The region had grown to the extent that it required 36 hours to completely clear the limb, and many of the characteristics of proton-producing regions were then in evidence. The region was large in calcium plage (7500 millionths of the hemisphere) and contained a correspondingly large Zurich Type "F" spot group (880

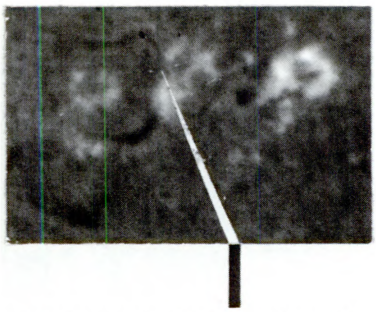

MC MATH REGION 10245
BEGINNING TO SEPARATE
ON 4 AUG

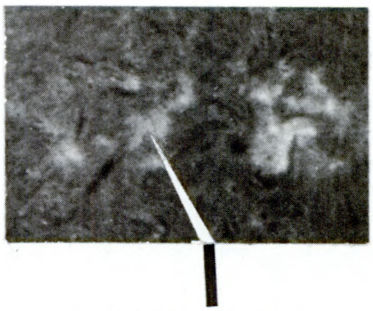

FURTHER PLAGE
SEPARATION ON
6 AUG

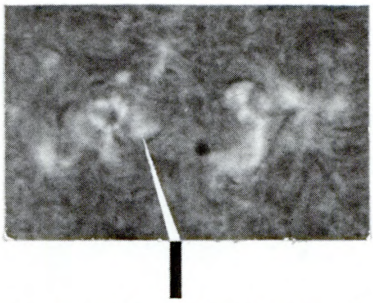

BY 8 AUG A SUNSPOT IS
BEGINNING TO FORM
IN THE NEW REGION

Figure 4-1. This is the Birth of the Region Which Ultimately Gave Rise to the 2 November 1969 PCA Event

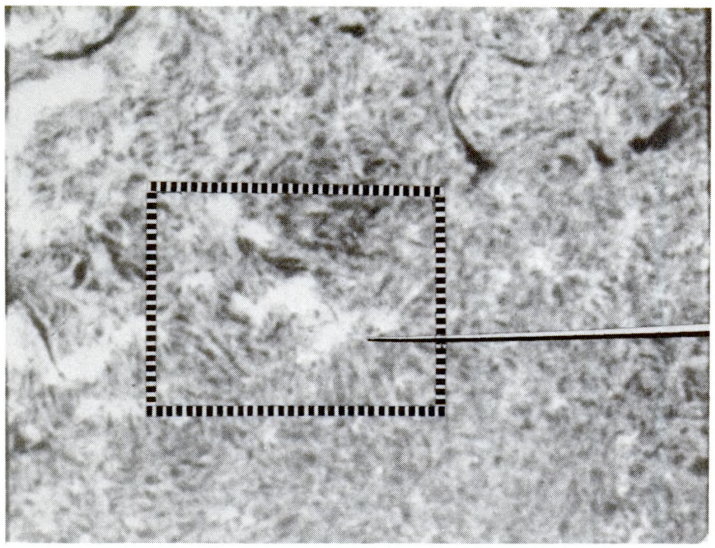

FIRST VISIBLE DISK TRANS
AS
MC MATH REGION 10293
BEGAN ON 27 AUG

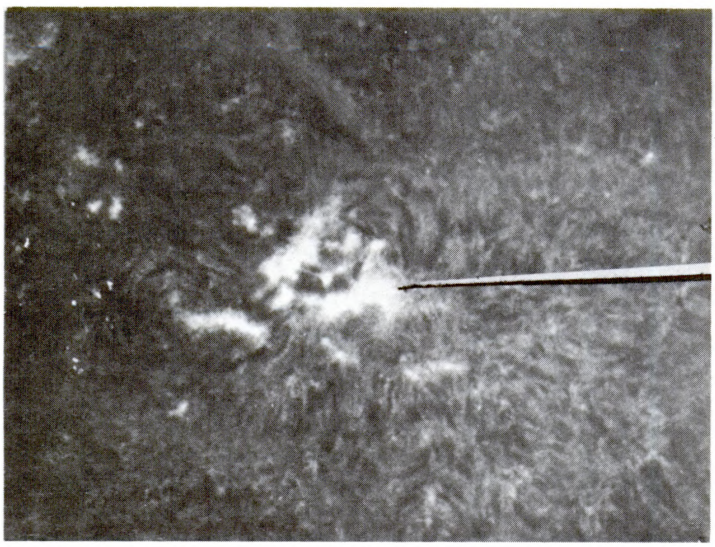

BACK FOR ITS SECOND DIS
TRANSIT WHICH STARTED O
22 SEP
AS
MC MATH REGION 10336

Figure 4-2. The Active Region During its First and Second Visible Disc Transit. Note in the lower picture that the region is becoming more structured

millionths). Magnetically, the region was classified as complex bipolar, containing at least two Delta configurations. The region was also a strong 9.1 cm radio noise source. The development in these parameters is indicated by the curves in Figures 4-3 and 4-4.

The most impressive developmental stage, in terms of optical and magnetic parameters, occurred on 25 October as the region was near the solar central meridian (CM), as shown in Figure 4-3. The region appeared to be extremely complex and dynamic in H-α light and its associated Zurich Type "F" spot group sprawled across 23 degrees of longitude. The group was characterized by several Delta configurations and a maximum magnetic field strength of 2900 Gauss. Correlatively, the activity level during this development phase was fairly impressive. The region produced five optical Importance 1 flares and 111 subflares during the first half of this third transit. Eleven of the events proved sufficiently energetic to have produced short-lived ionospheric effects.

After 25 October, observations indicated that the region had entered a period of decline. Figures 4-3 and 4-4 show this general decline after the region's CM passage. Much of the intricate filament network within the region disappeared and a decrease in H-α brightness was evident. The activity level, however, diminished only slightly. During the second half of its transit, the region produced six Importance 1 and 101 subflares, seven of which resulted in slight sudden ionospheric disturbances.

As the region approached the west limb, many of its features became distorted or obscured. Nevertheless, some restructuring and redevelopment again began. Figure 4-3 shows a marked increase in sunspot and calcium plage area or 31 October. No significant change was observed by the Mt. Wilson observatory in the region's magnetic structure; however, magnetic observations are severely hampered by a region's close proximity with the limb. The magnetic field structure inferred from neutral-line analysis of the H-α spectroheliogram (after McIntosh 1969) suggested that a newly developed bipolar sunspot existed in the leading portion of the region on 31 October. Intense coronal emission in the green line of iron (FeXIV) at 5303A on the west limb indicated an active corona. Type III fast-drift radio bursts in the dekametric and metric wavelengths, resulting from coronal excitation by streams of electrons accelerated to approximately half the speed of light, were observed at Boulder, Colorado and Weissenau, Germany. The solar observatory at Athens, Greece, reported that a large embedded filament (probably defining a neutral line between large umbrae) was strongly and persistently enhanced in the blue wing of H-α just prior to the region's west limb passage.

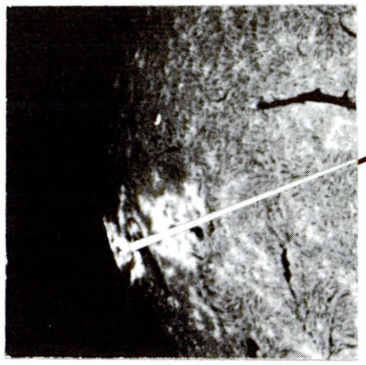

MC MATH REGION 10385 20 OCT

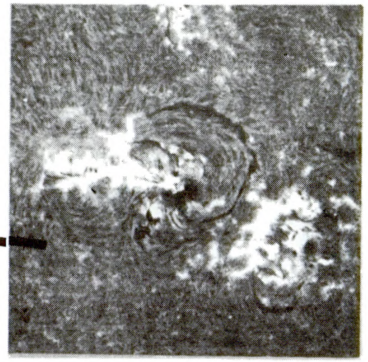

25 OCT

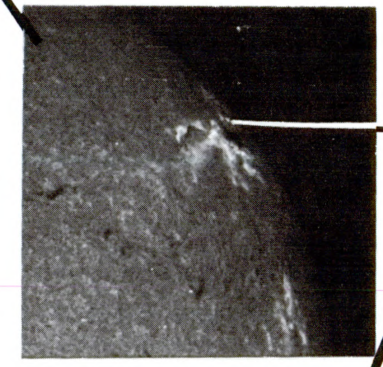

31 OCT
NOTE NEW BIPOLAR GROUP

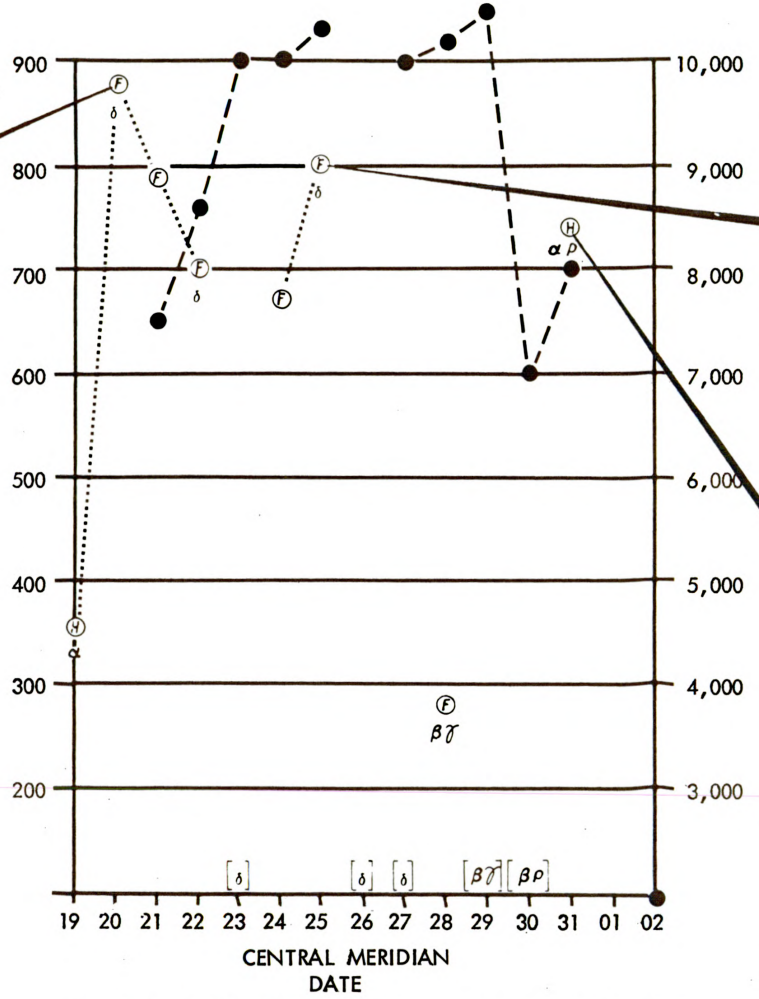

Figure 4-3. The Optical Characteristics of the Region on its Third Disc Transit

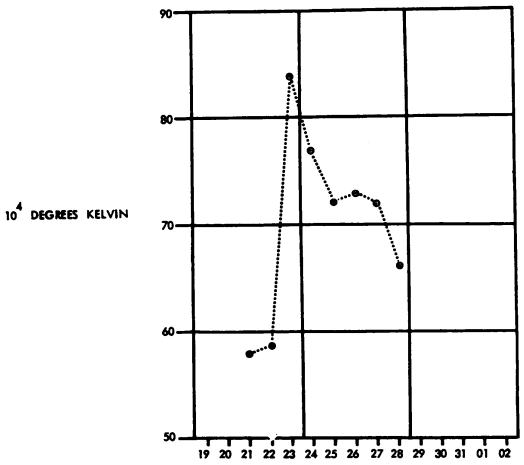

Figure 4-4. The 9.1 cm Radio Brightness Graph of the Region on its Third Transit

Thus, in spite of the region's limb proximity, there were several indications that Region 10385 was undergoing dynamic changes both in size and complexity before and during its west limb transit.

4-3 THE SOLAR FLARE EVENT

At 0934Z, 2 November 1969, after one full day's rotation beyond the limb, the region produced a major flare. Although the event was visible at the limb, its actual optical importance is unspecified due to limb shielding. Importance 2 loops (a post-flare phenomenon related to very energetic proton flares) were observed extending outward to 0.15 solar radius (see Figure 4-8). The energetic aspects of the event were manifested by an x-ray burst whose maximum intensity at 1038Z exceeded 2.2×10^{-1} ergs cm^{-2} sec^{-1} (or >997 fold increase above background) on the Vela 0.5 to 5.0 Ångstrom detector, and a major 10 cm radio burst whose maximum reached 1589 flux units (see Figure 4-6). The Naval Research Laboratory's SOLRAD 9 satellite recorded the event as the largest x-ray burst of the year. As further reports became available, it was obvious that the immediate ionospheric effects were major in magnitude. The observatory in the Canary Islands reported a short wave fade at 1040Z with propagation not recovering until after 1100Z, correlating well with the x-ray event.

4-4 PCA CONSIDERATIONS

Solar-geophysical events for which there are delays in the terrestrial response, such as polar cap absorption (PCA) events, allow for the application of various prediction methods. Several techniques are employed by the AESC in attempting to arrive at a prediction of the occurrence, magnitude and duration of PCA events. One such technique, developed by Castelli et al (1967), involves consideration of radio burst data.

Castelli has identified a characteristic burst signature as associated with flares causing PCA. He describes this burst profile in terms of flux density at

various discrete frequencies across the microwave spectrum. That profile most conducive to PCA is one in which the minimum flux density occurs at approximately 1000 MHz, with increasing flux densities at higher frequencies, exceeding 1000 flux units near 10,000 MHz. He describes this as a "negative spectral index." The occurrence of large flux densities at the lower (that is, less than 1000 MHz) frequencies (so as to cause the burst to assume a "U" shape) enhances the proton association of the burst. The association is further enhanced by Type IV dekametric emission. Radio burst data alone, however, may not be conclusive PCA predicators, since the data do not relate directly to the longitudinal location of the event at the sun. One of the considerations built into the proton event-PCA study conducted by Smart and Shea (1968) is precisely that of longitudinal location and the interplanetary propagation considerations implied by flare location.

The Smart-Shea study is programmed to yield computer printouts of proton flux envelopes and riometer absorption curves based upon radio burst configuration, optical flare importance and propagation factors. Unfortunately, optical flare importance data are not always available (as was the case on 2 November) requiring a subjective assessment of the probable magnitude of the optical event.

Another study in use at the AESC was conducted by Captain Kuck of the Air Force Weapons Laboratory (Kuck, 1969). The study takes a different approach in that it relates the integrated x-ray intensity with proton flux and associated riometer absorption. The Kuck study also takes flare location and propagation factors into account.

Optical data when available are also used to their fullest extent in predicting PCA. Use is made of the empirical relationships between flare magnitude, flare configuration, degree of umbral coverage, and other flare/region characteristics that the literature describes as being proton-flare associated. Generally, the approach to PCA forecasting is eclectic, with the emphasis on objective measures of the energetic aspects of a flare event, that is, x-ray and radio burst spectra.

4-5 THE PCA EVENT

Assessment of the flare event of 2 November in terms of PCA prediction was complicated by the lack of optical data (other than an indication as to the location at the sun), sparsity of radio data, and the nonavailability of x-ray data in real time. Radio burst data were available at only three discrete frequencies (1420, 2700, 5000 MHz) from the NOAA observatory in the Canary Islands. The burst profile nominally satisfied the Castelli criteria in that the minimum flux density occurred at 1420 MHz (704 flux units) and the maximum occurred at 5000 MHz (1523 flux units), describing a negative spectral index in the burst profile.

Whether the burst might have been the "U" shape characterized by an increase in flux density at any lower frequency than 1420 MHz could not be determined. Dekametric emission, if any, was also an unknown factor.

Neither the Smart-Shea nor the Kuck study could be used immediately because of the limited availability of data; however, subjective evaluation of propagation conditions based upon solar wind data and the assumption that the radio data available suggested at least marginally favorable conditions for particle acceleration led to the expectation of a PCA. A first order approximation of the interplanetary magnetic field structure, based upon a solar wind speed of 307 km sec^{-1} recorded at 1 au at Pioneer 8, was that of a "tightly wound" Archimedean spiral configuration. High energy particles ejected from a west limb event into such an interplanetary field structure would have a high probability of intercepting the earth.

As x-ray data become available, the Kuck study yielded a prediction of 460 counts per second above background for protons of E > 25 MeV. This count rate represents a flux of approximately 1700 particles cm^{-2} sec^{-1} $ster^{-1}$ of protons of E >10 MeV, equating with a prediction of approximately 13 dB absorption on a sunlit, 30 MHz polar riometer within one to three hours following the flare.

Before the ionosphere had recovered from the immediate effects of the x-ray burst, proton enhancements began to be detected by the Vela satellite system and by the ATS-1 satellite. Earliest detections were approximately one hour after the flare event. Counting rates of protons differed significantly among the Vela satellites, with Vela 5 reaching a maximum of 692 CPS at 1152Z. The Vela 4 vehicle detected a maximum of 1500 CPS at 1302Z, while the Vela 3 satellite showed a maximum of only 126 CPS at 1744Z. The ATS-1 satellite reached a maximum of 580 flux units at 2000Z (see Figures 4-5, 4-6, 4-7). Riometer absorption did indeed ensue, with one site (Shepherd Bay, Canada) responding with a maximum of approximately 11 dB absorption.

4-6 SUMMARY

Recapping some of the salient features of the region's history it is seen that:

(1) The region's major development occurred on its second transit of the nonvisible disc.

(2) It returned for its third visible disc transit as one of the largest, most impressive groups of the current solar cycle.

(3) The region continued to develop until 25 October after which a general decline occurred for the next four days. The long-awaited major geophysical event did not occur during the visible disc transit.

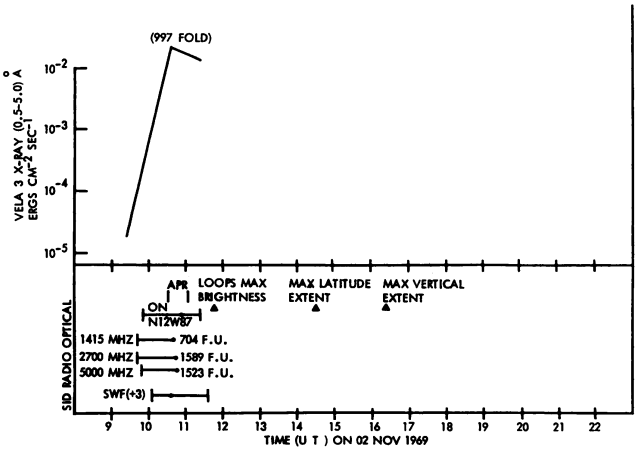

Figure 4-5. Optical, Radio and X-Ray Response to the 020943Z Solar Event

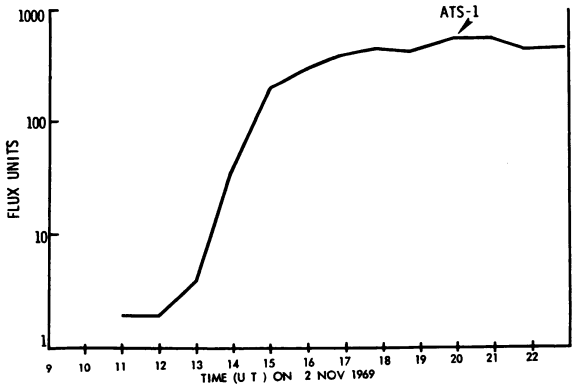

Figure 4-6. The ATS-1 20 to 70 MeV Proton Detection

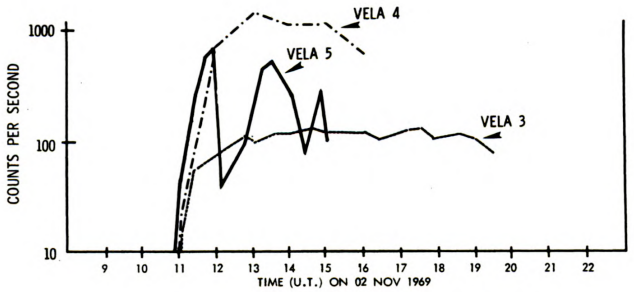

Figure 4-7. Vela 3, 4 and 5 Protons 25 MeV Counting Rates

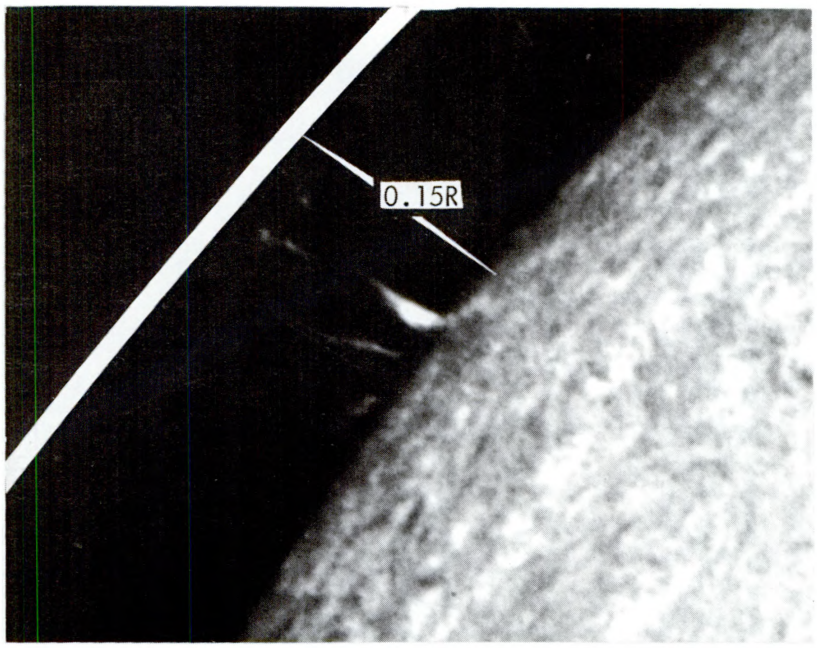

Figure 4-8. Importance 2 Loops Associated With the 020943Z Solar Event

(4) Marked redevelopment was observed during the region's west limb passage. The emergence of the bipolar spot in the leading portion of the group on 31 October may have contributed to the destabilizing of the magnetic fields that eventually led to the violent solar eruption and ejection of high energy particles into interplanetary space on 2 November 1969.

4-7 EPILOGUE

Region 10385 returned on 15 November and was very active during the Apollo 12 manned space flight. The region produced six Importance 2 flares, 26 Importance 1 flares and 348 subflares. None of these events presented a hazard to the astronauts, although HF communications were often disrupted by flare-associated SWFs. The region continued for three more transits, but in a very subdued fashion, finally dying on its seventh transit.

Acknowledgements

The author is grateful to the Aerospace Environmental Support Center for making the data available. Also, special thanks to Lt. Col. Kenneth E. German and SMSgt George Krause for their critical reading and editorial assistance of the manuscript.

References

Castelli, J.P., Aarons, J., and Michael, G. A. (1967) Flux Density of Radio Bursts of Proton-Producing Flares and Non Proton Flares, J. Geophys. Res. 72: 5491.

ESSA Research Laboratories 1969, Solar Geophysical Data, Number 303 to 305.

Kuck, G. A. (1969) Prediction of Polar Cap Absorption Events, Technical Note WLRTH 69-8, August 1969.

McIntosh, P. S. (1969) Inference of Solar Magnetic Fields from H-alpha Structures, A Manual for Observers, Unpublished.

Smart, D. F., and Shea, M. A. General Description of Current Procedure for Estimating Solar Proton Intensities, Revised June 1969, Air Force Cambridge Research Laboratory, Bedford, Mass., Unpublished.

Contents

5. A Review of the Magnetospheric Characteristics of Solar Flare Particles

J. R. Burrows
National Research Council of Canada
Ottawa, Canada

Abstract

The time dependence, composition and spectrum of several representative solar flare particle events in the interplanetary medium are discussed briefly. Modification of these parameters caused by propagation through the magnetosphere are considered. Some new data from the polar orbiting satellite ISIS-1 are used to identify features of the morphology in the polar cap and auroral zone that occur frequently during quiet and disturbed magnetic conditions. The effects of pitch angle anisotropy and the variation of particle flux with latitude are discussed and their influence on ionospheric observations is noted.

5-1 INTRODUCTION

This review will touch briefly on the characteristics of solar flare particles in the interplanetary medium as a background for considering their propagation characteristics in the magnetosphere. Section 2 will discuss composition and spectra and Section 3 will touch on their temporal evolution. For a recent more comprehensive review of these subjects the reader is referred to Kavanagh et al (1970).

The subject of particle access to the magnetosphere is considered in Section 4 from the contrasting points of view of the 'open' and 'closed' tail models. The low latitude boundary of the polar cap region is considered in Section 5, and differences between various calculations and measurements are noted. In Section 6, mechanisms for penetrating the closed field region are discussed, using new data from the 13 April and 2 November 1969 solar particle events. The importance of considering time dependent changes in the configuration of the magnetosphere is emphasized. The review tends to favor the low energy proton and electron propagation problem.

5-2 SOLAR FLARE PARTICLE COMPOSITION AND SPECTRA

5-2.1 Composition

Most of the particles observed from solar flares are protons, electrons, and alphas. Higher-Z elements (C, N, O) are present as about 1-1/2% of the alpha flux or as about 0.1% of the proton flux (Fichtel, 1970, Armstrong and Krimigis, 1971, Durgraprasad et al 1968). They will not be considered further in this review. Protons are the predominant particles although some flares, such as the ones on 7 July 1966 and 10 April 1969, have also produced very large fluxes of electrons. The alpha particle abundance is often expressed as a ratio of differential intensity relative to the proton flux. There is a large variation in alpha/proton ratio for different flares but typical values are 0.04 and 0.006 at 50 MeV/nucleon and 100 MeV/nucleon respectively (Durgraprasad et al 1968). Measurements during the 24 May 1967 flare (Lanzerotti and Robbins 1969) at lower energies yield ratios of 0.01 at 8 MeV/nucleon. Somewhat different numbers are obtained if the ratios are taken at equal energies or equal energy/charge instead of at equal energy/nucleon.

5-2.2 Proton Spectra

Proton spectra from different flare events vary widely and usually the spectrum changes during the event. Proton differential intensities above 80 MeV (or ~400 MV rigidity) are often fitted well by a spectral form that is exponential in the proton rigidity (Freier and Webber, 1963). An upper energy cutoff as high as 4.3 ± 0.5 GeV has been determined for protons in the large 28 January 1967 event (Heristchi and Trotter 1971). However, there are many proton events where the high energy component is negligibly small. When a wide energy range is present, the spectrum below about 20 MeV is often different from the higher energy both in its shape and in its time evolution (Lanzerotti 1969, 1971). Figure 5-1 from

Imhof et al (1971) shows proton spectra in this energy range for three flares in 1969. None of the events is an exact power law. The fitted curves vary from the extreme steep slope in the June event to the much shallower slope in the November event. All data were taken near the maxima of the events.

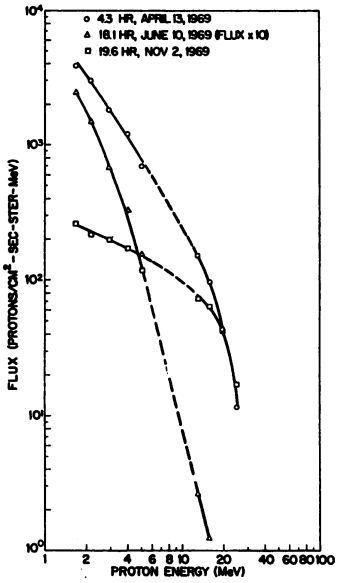

Figure 5-1. Proton Spectra Measured on a Low Altitude Polar Satellite for Three Events in 1969, From Imhof et al (1971). The contrast between spectra for different events is apparent

5-2.3 Electron Spectra

There are fewer published examples of good electron spectra. Lin (1970) has compiled some for several events in 1967. The spectrum near the peak of the intense 11 April 1969 event has been measured by West and Vampola (1971) from relativistic energies down to 53 keV. Figure 5-2 shows the combined data from two spacecraft. OGO-5 is outside the magnetosphere while OVI-19 is over the polar caps. There is no consistent difference between the two satellites' measurements. The spectrum is steep with a small departure from a power law. The differential intensity is comparable to protons of the same energy but the ionospheric effects will be different, since the maximum ionization loss will occur at a lower height for the electrons. In Figure 5-3, this spectrum has been replotted as a line and data from the ISIS-1 satellite spectrometers, (Burrows, unpublished; Winningham and Heikkila, unpublished) taken over the north polar cap at the same time, has been added to extend the spectrum to 1 keV. Altogether, over the three decades of energy, the differential flux has a range of seven decades. The energy deposition over a large altitude range from the electron fluxes should not be ignored in studying the ionospheric effects of flares similar to the April 1969 flare.

5-3 TIME DEPENDENCE OF SOLAR PARTICLE FLUXES

The time evolution of solar particle fluxes and the relative importance of particle storage near the sun and diffusion in the interplanetary field (Krimigis and Verzariu 1971) is too complex a subject to do more than touch on here.

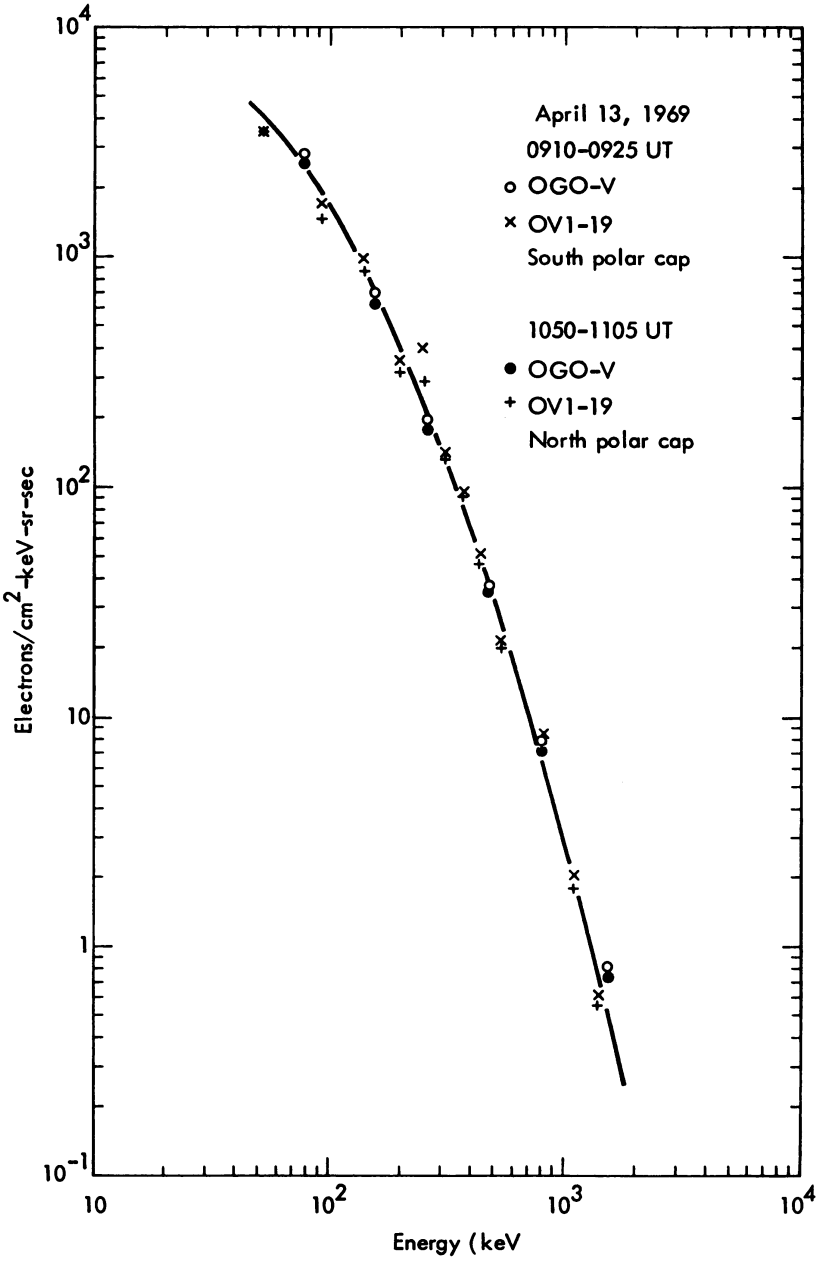

Figure 5-2. Solar Electron Spectra Over the North and South Polar Caps and in Interplanetary Space Near Maximum Intensity on 13 April 1969 From West and Vampola (1971)

However, one should mention first the different rise times of events resulting from the different longitudes of the parent flares on the sun; second the tendency for higher velocity particles to arrive first and to decay faster (Cline and McDonald 1968) resulting in a softening spectrum as the event proceeds; and third the tendency for protons and alphas below about 10 MeV/nucleon to be modulated more effectively by structure in the interplanetary magnetic field and in the solar wind.

Figure 5-4 takes ten days of data from the 11 April 1969 flare to show the proton flux for four integral thresholds. Hourly averages are used from Explorer 34 in interplanetary space, and passes over the polar cap every two hours are taken from ISIS-1. It presents several contrasts to the 2 November 1969 event (Lincoln and Bucknam 1971, Lanzerotti and Maclennan 1971). The April event is from an east limb flare, and the flux does not peak until more than two days after the flare, compared to six hours in November which was a west limb flare event. In April, all of the energy channels have a similar profile in contrast to the November event when a greater variability is observed in the flux between 30 MeV. However, there is an evolution of the spectrum even in the well-behaved April event in which the flux has been smoothed as it diffused across the interplanetary field. Notice that near noon on 12 April, a change in the rate of increase occurs. During

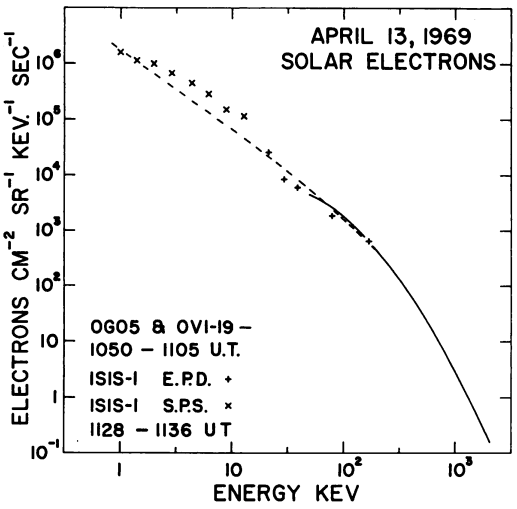

Figure 5-3. Solar Electron Spectrum Over the North Polar Cap Corresponding to Figure 5-2 and Extended in Energy to 1 keV

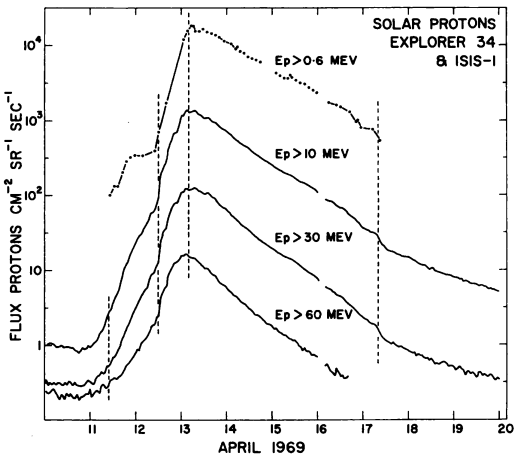

Figure 5-4. Hourly Averages of Integral Proton Fluxes (E>60, 30, 10 MeV) From Explorer 34 From Solar-Geophysical Data No. 303 - Part II, November 1969 and Flux (E>0.6 MeV) Over the Northern Polar Cap From ISIS-1 Satellite at ~3000 km Altitude

the decay phase on 17th April, there is a discontinuity in the nearly exponential decays, with slower decays thereafter. During the increasing portion, the lower energy components have a steeper slope than the higher energies due to the later arrival of the slower protons. This results in a softening spectrum. Also the E >0.6 MeV components peak about 4 hours after the E > 60 MeV component. On the decaying portion, further spectral softening occurs since the nearly exponential decays are slightly faster at higher energies.

Figure 5-5 shows the corresponding electron profile for the April event and the shapes are very similar, rising slowly, peaking at the same time as the protons and decaying nearly exponentially, with less energy dispersion than the protons.

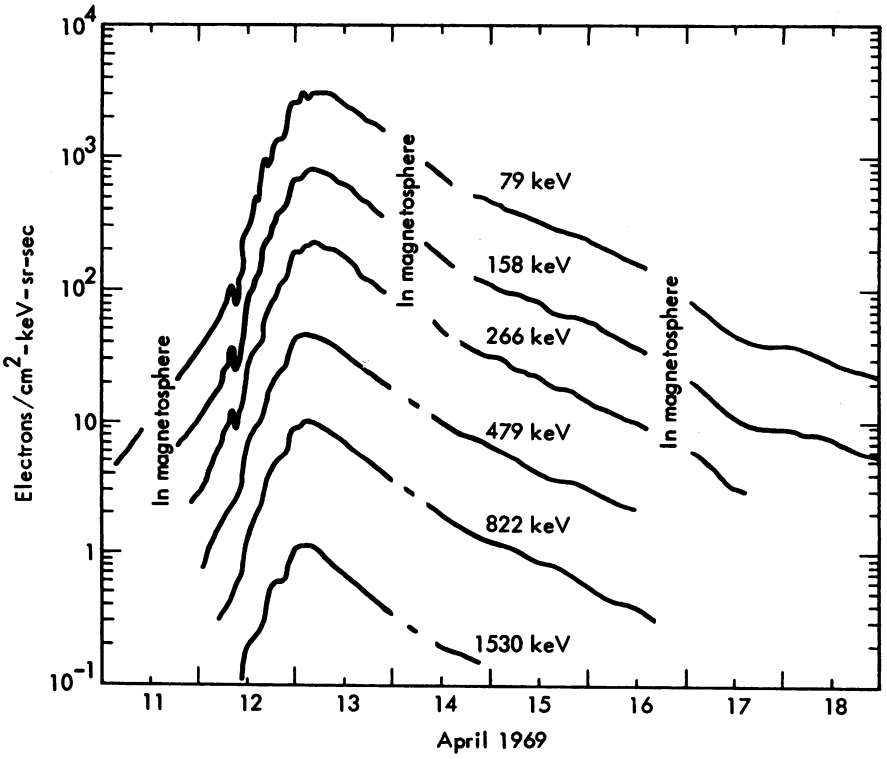

Figure 5-5. Differential Electron Fluxes in Interplanetary Space During the 11 April 1969 Solar Particle Event, From West and Vampola (1971). Normally the solar fluxes could be identified well inside the magnetosphere, with no sign of discontinuity at the magnetospheric boundary except for the superposition of trapped radiation

5-4 PARTICLE ACCESS TO THE MAGNETOSPHERE

The entry of solar protons via the sunlit magnetopause has been calculated by trajectory tracing in the Williams and Mead (1965) model field by Gall et al (1968) as a function of energy. The cutoffs for protons vertically incident on the atmosphere were found to occur at significantly higher latitudes than they would in the undistorted internal dipole field. For example, 100 MeV and 10 MeV protons would penetrate to 71.5° and 77° invariant latitude respectively. Lower energy protons gain access almost entirely via the magnetotail.

One might postulate two extreme configurations for the magnetotail which have been characterized by the terms 'open' or 'closed'. Entry into an open tail would be by adiabatic motion along the field lines while entry into a closed tail would be accomplished by diffusion across field lines. In fact, experimental evidence supports neither extreme model consistently, since the tail appears open for some particle tracers at some times while for other particle species it appears more nearly closed at other times. Some evidence for both cases is presented below.

5-4.1 The Open Tail

Figure 5-6 from Van Allen et al (1971) shows the idealized model of the open configuration. The field lines connect smoothly and directly from the interplanetary medium to the tail. Three types of observation support this model.

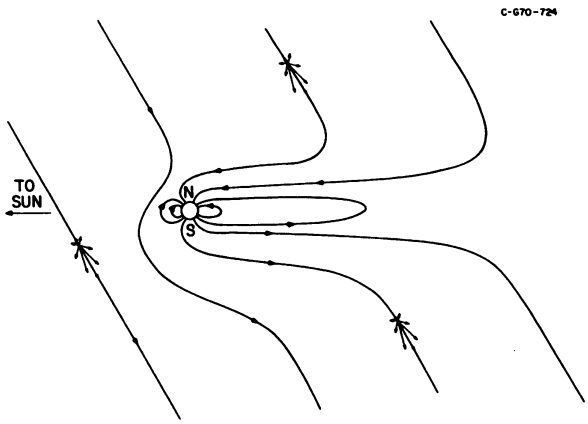

Figure 5-6. Postulated Model of the Open Magnetotail From Van Allen et al (1971). The diagram schematically represents the noon-midnight meridian cross-section at a time of strong southward directed interplanetary field and anisotropic solar proton fluxes on 24 January 1969

First, as was mentioned above, West and Vampola's measurements of the electron intensity and spectrum show that they are equal outside and inside the magnetosphere to within 10%. This, and the absence of any discontinuity in the solar electron flux when OGO-V crossed the magnetospheric boundary supports the picture of adiabatic motion into an open tail. Adiabatic motion implies that energy is conserved as the particles spiral along the field lines, and Liouville's theorem requires that, when the flux is iostropic in the interplanetary medium, there should be an equal iostropic flux on field lines over the polar cap. This is generally observed for electron fluxes.

A second type of experiment supporting an open tail is based on the lunar shadowing of solar electrons in the magnetotail (Van Allen and Ness 1969, Anderson and Lin 1969, Van Allen 1970). The occultation of field lines by the moon causes sharply defined voids in the electron flux between the moon and the earth and the amount of diffusion into these voids has been used by Van Allen (1970) to establish that the cross-B diffusion rate is less than 100 km/sec between the moon and the earth. This value is much too small to allow diffusion into a closed magnetotail to be a major access mechanism for electrons at distances closer than the orbit of the moon (64 Re). An upper limit to the distance at which electrons gain access to the magnetotail was also determined by Van Allen (1970) using the delay time between the occurrence of the same identifiable features of the electron flux in interplanetary space and in the magnetotail. This limit indicates prompt access into the magnetotail at distances less than 900 earth radii.

A third observation, first reported by Evans and Stone (1969), is that different solar proton fluxes are observed at the same time over the north and south polar caps. During the 24 January 1969 event, Van Allen et al (1971) correlated similar differences with aniostropies in the interplanetary flux. The open field model that they have used to interpret the data is shown in Figure 5-6 in which anisotropies measured perpendicular to the ecliptic plane are represented by the vector groupings on the field lines. Their data showed that anisotropies perpendicular to the ecliptic plane existed in the interplanetary proton flux for an interval of about six hours on 24 January, during which time the proton flux was depressed over the south polar cap in both the 0.3 - 9.2 MeV and 3.4 - 74 MeV channels. On 25 January, both the polar asymmetries and the interplanetary anisotropies were negligible. The northern polar region received a higher intensity on 24 January because it was directly connected to the maximum flux flowing outward from the sun. Similar ideas were used by Engelmann et al (1971) to explain intensity fluctuations over the northern polar cap in the 25 February 1969 event.

All of these observations are most easily interpreted by the model of an open tail although West and Vampola's observations are consistent with strong loss-free scattering by magnetic inhomogeneities in an essentially closed field configuration.

5-4.2 The Closed Tail

The evidence for a closed tail is strongest for the magnetopause region close to the earth and for proton propagation. It should be noted that an MeV proton with its greater rigidity and larger gyroradius may be scattered in a moderately disordered field where a 100 keV electron may trace out a more adiabatic path along the field. Measurements by Montgomery and Singer (1969) from Vela 4 at 19 earth radii show a marked change in the proton flux anisotropy in three energy channels from 0.65 to 6.1 MeV as the spacecraft crosses the magnetopause on the evening side at a S.M. latitude of 38°. In the magnetosheath the maximum flux is from the sun direction, but it does not continue across the magnetopause as a purely open field model would predict. Such observations are normal in the Vela data and are in contrast to the observations of Van Allen et al discussed above, but it should be recognized that the Vela orbit at 19 Re is in the near magnetotail. Another common Vela observation, indicative of diffusion into a quasi-closed tail, is shown in Figure 5-7. Here one Vela satellite (4A) is in the magnetosheath and solar wind, while the other is in the tail. There is clearly not only a delay in access to the magnetotail, but some smoothing of the interplanetary fluctuations and a tendency to lower intensities. Typically, delays of 15 minutes to an hour were observed.

In summarizing the considerations of the mode of particle access to the magnetotail, it should be noted that the observations of Van Allen et al (1971) of the asymmetric access to the north and south polar caps were made at a time of very strongly southward directed interplanetary field, a configuration that is most favorable for direct connection. In its 'average condition', the magnetotail probably has a magnetopause discontinuity which provides some scattering for protons, but which becomes more transparent as one progresses down the tail. The distant tail field may become more 'filamentary' with regions of strong field intermixed with solar wind plasma, and the concepts of pure field line tracing or pure diffusion across field lines become applicable only to specific times and to selected particle species which minimize or maximize the amount of scattering.

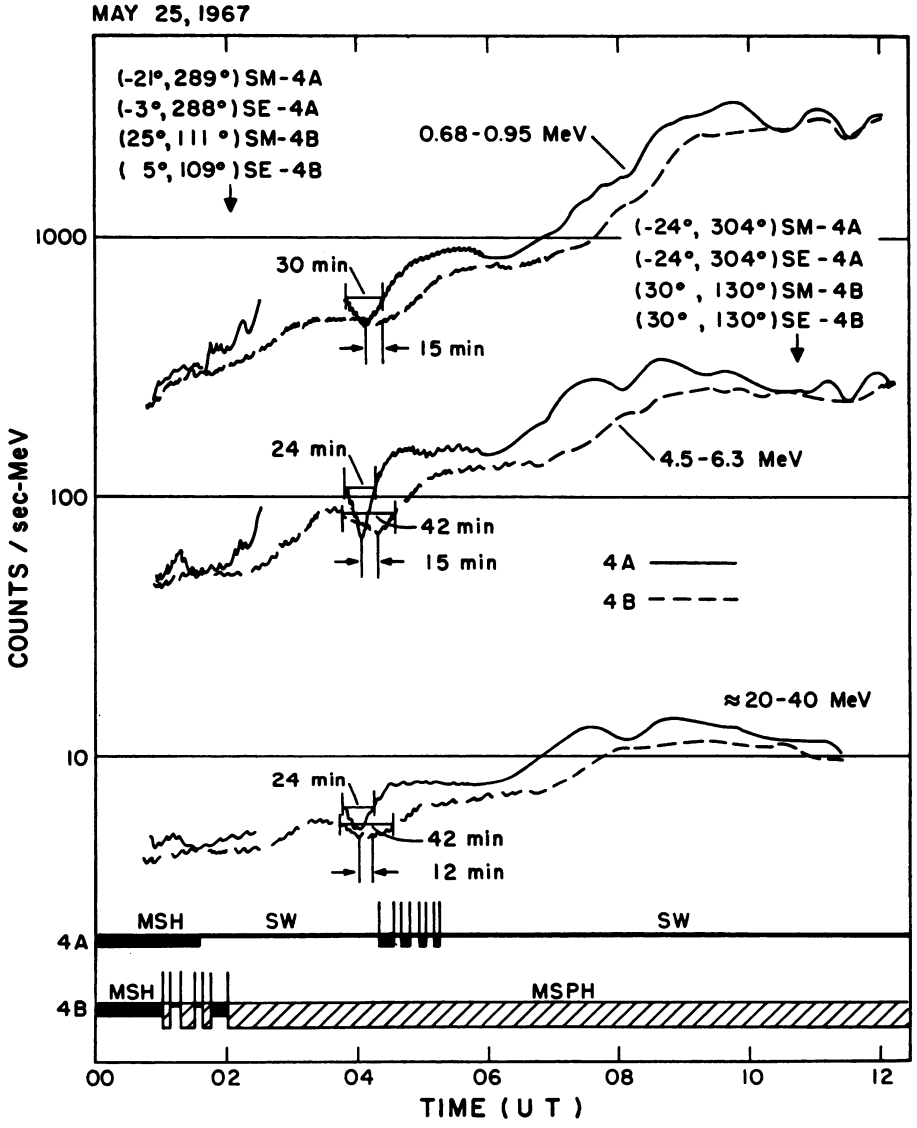

Figure 5-7. Count Rates in Three Differential Proton Channels on Two Vela Satellites During the 25 May 1967 Event, From Montgomery and Singer (1969). Delays between Vela 4A in interplanetary space and Vela 4B in the magnetotail are evident at all energies

5-5 THE LOW LATITUDE BOUNDARY OF THE POLAR CAP REGION

All current models for low energy solar particle access to the magnetosphere consider a polar cap region consisting of tail field lines and a low latitude dipole-like field region which excludes solar particles. The polar cap is more or less accessible as discussed above. In the transition region between, there is a latitude range on the day side to which Reid and Sauer (1967) and Taylor (1967) have postulated that lower energy protons gain access via drift from the night side neutral sheet. Williams and Bostrom (1969) have proposed that latitudes corresponding to plasma sheet and magnetopause field lines tend to have the full interplanetary flux, while diffusion results in lower proton flux over the polar caps. Other authors have favored a form of fast radial diffusion into the closed field region (McDiarmid and Burrows 1969, Lanzerotti 1968, 1970). Thus, it is necessary to consider this low latitude boundary of the polar cap and to identify to what extent and by what mechanisms the various particle species penetrate from the magnetotail to closed field lines.

Three factors influence the penetration. First, in a smooth field, free of any scattering centers, the particles of higher rigidity are deflected less and penetrate deeper into the closed field. A number of calculations of this type have been made using different field models (Reid and Sauer 1967, Taylor 1967, Gall et al 1968, Smart et al 1969). The answers obtained depend considerably on the static field configuration which is selected for three calculations. The models use parameters specifying the day side compression by the solar wind and the strength and position of the current in the plane of the neutral sheet required to generate the tail. A more sophisticated model should specify the morning and evening extension of the plasma sheet.

Second, evidence from low altitude proton latitude profiles strongly indicates that some scattering is necessary even during the quietest magnetic conditions, since no realistic static field can explain the amount of proton penetration (McDiarmid and Burrows 1969, McDiarmid et al 1971, Imhof et al 1971). However, Vampola (1971) has rejected scattering and radial diffusion for electrons ($E \sim 300$ keV) and has interpreted the observed anisotropic solar electrons as quasi-trapped fluxes gradient-drifting onto closed field lines from the tail.

Third, some observations suggest that time-dependent processes occur in addition to the diffusion caused by scattering centers. Protons often penetrate to lower latitudes during magnetic disturbances (Stone 1964). At other times, they are partially excluded from the night side plasma sheet. Proton acceleration also may occur as they are transported inward.

Five proton flux versus latitude profiles of the boundary region are shown in Figure 5.8 near midnight at an altitude of about 500 km. One notes that the cutoff region is depressed about three degrees in latitude when the kp index is larger. The slopes in the cutoff latitude intervals are fitted by straight lines to provide e-folding latitudes ranging from 0.25° to 0.7°. The slopes have no apparent relationship to the magnetic index. In order to define the boundary of the polar cap, some consistent criterion must be selected. Imhof et al (1971) have chosen the cutoff latitude as the latitude at which the flux is 1/e of the maximum flux in the adjacent polar cap. In Figure 5-9, they have compared the 1/e cutoff latitudes to two static model calculations for a range of rigidities from 50 - 200 MV (1 - 20 MeV). They find that the measured cutoffs are more equatorward and less energy dependent than either model predicts. The two models differ in their choice of the magnetosphere's shape with the later

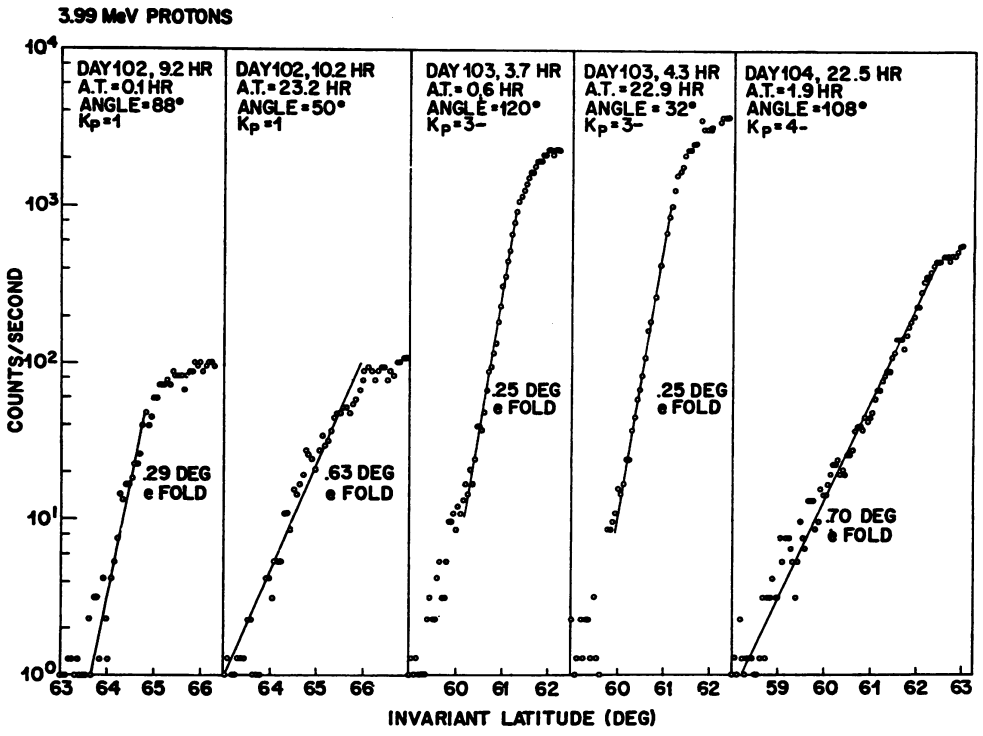

Figure 5-8. Examples of E-Folding Fits to the Low Latitude Boundary of 3.99 MeV Solar Protons at Low Altitudes During the 12-14 April 1969 Event From Imhof et al (1971). Auroral time (AT) and detector pitch angle with respect to the magnetic field are indicated for each pass

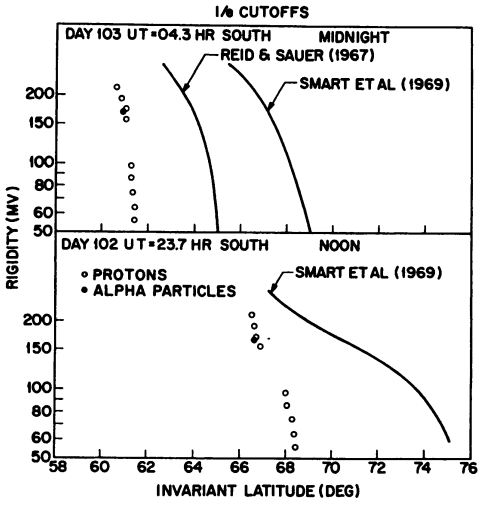

Figure 5-9. 1/e Cutoffs as a Function of Rigidity for a Midnight and a Noon Pass on 12 and 13 April 1969, From Imhof et al (1971). The measured cutoffs are compared to two different mode model calculations and a considerable discrepancy is observed

calculations of Smart et al (1969) being more realistic. Experimental evidence for the intrusion of low energy protons onto closed field lines has been given in Figure 5-10 from McDiarmid and Burrows (1969). They showed by simultaneous measurement of outer zone electron and solar proton latitude profiles, that at all local times the solar protons remain at or above the polar cap intensity for about 5° equatorward of the limit of closed field lines determined from the outer zone background boundary.

The observation that the intensity in the boundary region is frequently higher than the adjacent polar cap intensity has been reported from a number of polar orbiting, low altitude satellites (Blake et al 1968, Williams 1969, Paulikas et al 1970, Bostrom 1970, Engelmann et al 1971). Many of these measurements may correspond to the observations of Evans and Stone (1969) and Van Allen (1971) discussed above, where the higher intensity arrives via closed field lines from the opposite hemisphere which is directly connected to the flux flowing out from the sun. The close correspondence of the high latitude limit of these 'enhancements' to the limit of closed field lines, reported by McDiarmid and Burrows (1969) would be consistent with this interpretation. However, at this stage, one should be cautious about interpreting all observations of relatively higher flux in the boundary region as being due to interplanetary anisotropies.

The diurnal dependence of the latitude knee was first reported by Stone (1964) for solar protons of energy ~1 MeV. In Figure 5-10, one notes the strong diurnal asymmetry in the proton knee latitude. If one postulates that the knee latitude is the point where diffusion becomes weaker, and a pitch angle anisotropy develops in the proton flux, the mid-day recovery observed on riometers by Leinbach (1962) and others is qualitatively explained for stations in the invariant latitude range 65° to 73° (Reid and Sauer 1967).

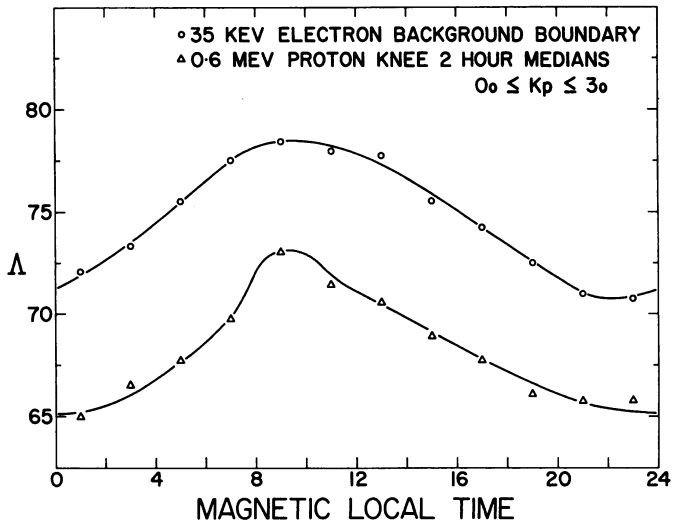

Figure 5-10. The Penetration of Solar Protons Onto Closed Field Lines as a Function of Local Magnetic Time From McDiarmid and Burrows (1969). The proton knee latitude is taken at the point where the proton flux falls below the polar cap flux. About 200 passes are used. The electron background boundary is determined from ~1000 passes

5-6 MECHANISMS FOR PENETRATING THE CLOSED FIELD REGION

It is of special interest for ionospheric studies to enquire whether the particle fluxes measured by satellites are isotropically distributed in pitch angle, thereby assuring a flux incident on the atmosphere that is equal to that at the satellite. Generally, isotropy is observed over the high latitude polar cap, but in the boundary region near to and equatorwards of the knee latitude, quasi-trapping may occur, resulting in the development of a loss cone and anisotropic flux (Paulikas et al 1968).

Quasi-trapped particles are those which execute a limited number of bounces between hemispheres on closed field lines but are unable to execute stably trapped orbits, including complete drift around the earth, due to the violation of one or more of the adiabatic invariants of trapped motion. Quasi-trapping results from the particle gyroradius being large compared to the magnetic field gradient (that is, $\rho > \frac{1}{B}\frac{dB}{dr}$) or from the non-dipole configuration of the smooth geomagnetic field. Particles are lost into the absorbing atmosphere or out through the neutral sheet or the magnetopause (Roederer 1967). Magnetic scattering is not included in such a model except for those effects that may be caused by the sharp curvature of the model field near the neutral sheet (Taylor 1967).

The next few figures are taken from previously unpublished ISIS-1 data. They provide good examples of pitch angle measurements to determine the anisotropy and hence to deduce quasi-trapping. They are selected as illustrative cases differing from each other and in some points differing from the statistical picture developed above. Figure 5-11 is a sample of the format used. Invariant latitude is the linear abscissa. At the top are indicated magnetic local time and the angle between the spacecraft spin axis and the magnetic field vector (θz). A proton and an electron detector are mounted perpendicular to the spacecraft spin axis. As the spacecraft spins with a 20 second period, they sample pitch angles between $90 \pm \theta z$. The upper curve is a useful spectral index which helps to distinguish auroral zone and outer zone electron fluxes from the harder solar electron fluxes. Two contrasting regions are apparent. In the polar cap, the electron and proton fluxes are both very uniform and iostropic except when the detectors look down the field line into the loss cone at particles returning from the atmosphere. At low latitudes below 60°, both fluxes are strongly anisotropic looking both up and down the field line in the loss cones. This indicates stable trapping. In both regions the spectral index is nearly unity. In between, near 70° latitude, there is a strong, sharply defined burst of auroral type electrons with a spectral ratio greater than 20. These are probably associated with a substorm near the midnight sector. The field is most definitely closed out to the arrows at 68° and detailed analysis shows electron anisotropies up to 71.5°. The solar electrons appear to have freely penetrated the closed field lines associated with the auroral flux as far as 68°. This is probably the inner edge of the plasma sheet extending to the late afternoon sector. The proton knee occurs at 62° and the proton anisotropy develops suddenly between 62° and 61° where the solar protons merge with outer zone. At ionospheric altitudes or even at 500 km, this knee would be sharp

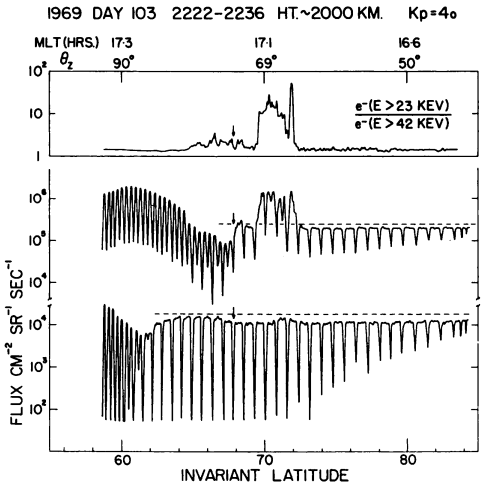

Figure 5-11. ISIS-1 Data Over the Northern Hemisphere, 13 April 1969 2222 UT. The bottom curve is the proton flux ($0.5 < E < 3.8$ MeV) measured with a collimator half angle of 10.2°. The middle curve is electron flux ($E \geq 36$ keV) with collimator half angle of 8.8°. The upper curve is a spectral index for electrons taken from two axially mounted Geiger counters looking at angle θz to the magnetic field

and none of the highly anisotropic stably trapped outer zone protons would be observed. There are two enhancements above the uniform isotropic intensity in the polar cap. Between 63° and 68°, the flux is about 30% greater, while between 71° and 72.5°, a somewhat smaller enhancement occurs coincident with the active auroral region. These enhancements give rise to the speculation that there may be some dynamic acceleration occurring if one assumes that the polar cap fluxes have entered the tail adiabatically from the interplanetary medium. Quasi-trapping may be present below the knee at 62°. If there is a quasi-trapping between 68° and 62°, it is insufficient to lead to the development of a loss cone.

In contrast to this example near 17 hours MLT, Figure 5-12 is near 13 hours MLT from 2 November 1969. The solar electrons are uniform over the polar cap to ~72.5°, where the anisotropy clearly establishes closed field lines. The proton intensity between 73° and 81° is also the most common in the remainder of the pass which has not been plotted on the other side of the pole, but near 82° there is a reduced intensity of no known cause. The proton knee occurs at 73°, although there is no clear evidence of anisotropy until 64° where the solar protons overlap the outer belt protons. The lower intensity between 73° and 64° may result from quasi-trapping, but strong pitch angle diffusion must be occurring to keep the incoming flux isotropic. Although Kp = 3o, the spectral index is low and uniform suggesting negligible acceleration and injection of auroral fluxes.

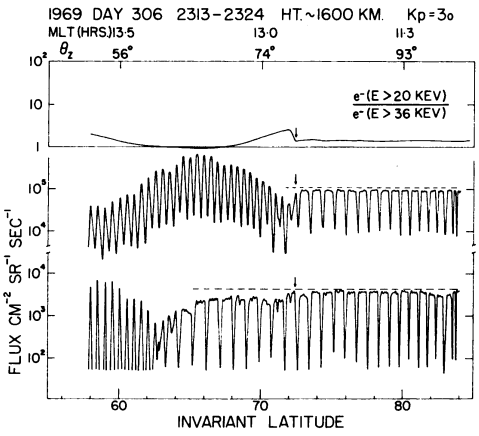

Figure 5-12. ISIS-1 Data Similar to Figure 5-11 From 2 November 1969 2213 UT. The electron spectral ratio is taken from two radial Geiger counters

In Figure 5-13, one day later near noon MLT, the profiles are less uniform. The spectral index increases at 81°, although consistent electron anisotropy does not occur until ~78°; between 78° and 69° the spectral index is high and there are mixed regions of strong and weak electron precipitation. The pre-flare stably-trapped outer zone proton fluxes are overlapped near 64° by solar protons with well developed anisotropies up to 74°. In contrast to the two previous examples when kp was higher, these protons appear to be quasi-trapped with relatively weak pitch angle scattering, and

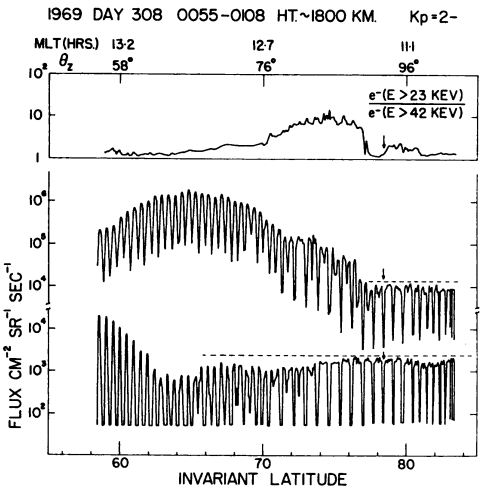

Figure 5-13. ISIS-1 Data Similar to Figure 5-11 From 4 November 0055 UT. Although the kp index is lower than Figure 5-12, there is more prominent low energy outer zone electron flux. The polar cap proton flux is not constant, suggesting a partially closed tail configuration.

a marked mid-day recovery should be apparent on riometer records. Only above 74° are nearly-isotropic fluxes found on closed field lines.

In contrast to the three previous examples, Figure 5-14 is on the night side at ~4 hours MLT and the pitch angle scan is very limited. The electron spectral index is characteristic of an auroral substorm, and outer zone fluxes meet the polar cap electrons at 74°. At this 3000 km altitude, the protons remain nearly at the polar cap level until they join up with the outer zone protons near 64°. No recognizable knee can be identified, although a low altitude pass or a complete pitch angle scan would undoubtedly observe one near 64° coincident with a transition from an isotropic to an anisotropic regime. Certainly the substorm does not impede access of the protons at this time.

Figure 5-15 provides a complete pass from the afternoon side to near midnight. It violates, in almost all respects, the simplistic average picture of uniform access over the polar cap; access near midnight to 65° or 69° latitude and quasi-trapped anisotropic fluxes on the day side on closed field lines. The solar electron flux and spectrum is uniform and isotropic over the polar cap from 74° near midnight to 76-1/2° in the afternoon. However, the solar electron knee and a consistent anisotropy do not develop until 72-1/2°. First among the atypical features, the solar proton flux is not uniform over the polar cap, being 30% higher in the central region between 81° and 76°. This 30% higher flux occurs at all energies up to 30 MeV; yet Explorer 42 during this time in the northern magnetotail, measured the proton flux above 10 MeV and found only a 9% increase. This suggests spatial inhomogeneities in the polar cap. Second, the electron knee is at 72-1/2° on the afternoon side, but the proton fluxes are essentially equal on either side of it and isotropic to 65° without a proton knee being reached. However, fifteen minutes later near midnight, the proton flux seems to start being excluded at 76° latitude and it is reduced by a factor of three below 74° where some night side magnetospheric electron fluxes have appeared. In this case the midnight field

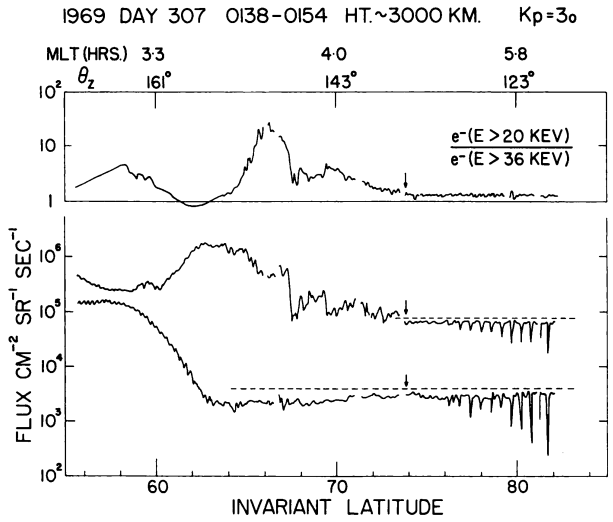

Figure 5-14. ISIS-1 Data Similar to Figure 5-12

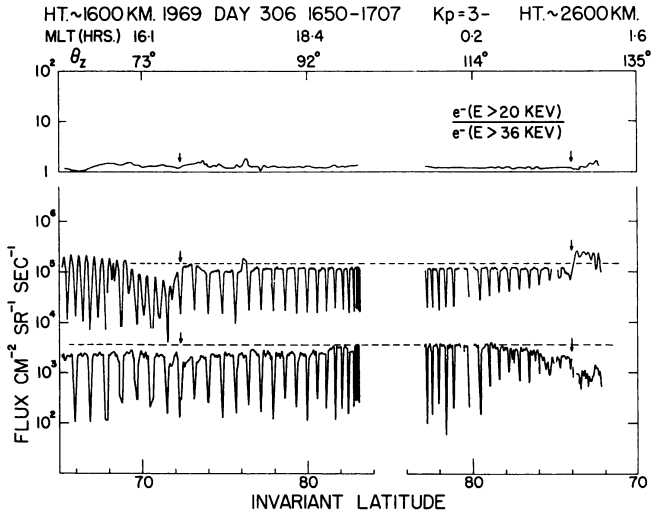

Figure 5-15. A Continuous Oblique Pass Across the Polar Cap. A maximum invariant latitude is reached at 83°. The spin modulation is very compressed as the satellite goes from the evening to the midnight sector at nearly constant latitude

lines seem less accessible than the afternoon sector. This is probably because the satellite has crossed the midnight sector during the late expansion phase of a substorm and has found the field lines closed to latitudes of 74° to 76° with a considerable northward component across the neutral sheet. This would exclude protons more than the inflated plasma sheet typical of the growth phase of a substorm.

One can see from these examples that the problem of the boundary of the polar cap region is not easily described, particularly during disturbed magnetic conditions. However, McDiarmid et al (1971) have plotted the kp dependence of the solar proton and solar electron knee latitudes on the day side (08 - 14 hours LMT) using about 40 data points for each. The least squares fits have their Kp = 0o intercepts at 73.1° and 79.0° respectively and slopes of -0.255° and -0.44°/ unit kp. It is probable that the region between the electron and proton knees corresponds to a region of strong diffusion both in pitch angle giving rise to iostropic fluxes and across field lines, thereby maintaining polar cap intensities. The latitudes below the proton knee have much less scattering and quasi-trapping and anisotropies occur. The sharper knees observed on the average on the night side are consistent with more direct access and a sharper boundary between a diffusion region and a diffusion-free region. Magnetospheric processes such as substorms, storm-inflation of the ring current etc., give rise to a large variability in the size of the diffusion region and the amount of diffusion occurring on closed field lines near the boundary of the polar cap. When observations are made at sufficiently high altitudes, it is apparent that the solar protons merge with the outer belt protons (for example, Figures 5-11, 5-12, 5-14). This occurs most often during high magnetic activity, resulting in a possible source for the trapped proton belt. It is also apparent that the diffusion region which enables solar protons to gain access far on to closed field lines also limits the lifetime of the trapped protons, thereby establishing the average high latitude boundary for the trapped proton belt.

5-6.1 Note Added in Proof

Additional calculations of electron and proton geomagnetic cutoffs by Smart and Shea (1972) lead them to conclude that trajectory tracing in a static model magnetosphere must be supplemented by taking account of dynamic and stochastic processes in the magnetosphere. Morfill and Scholer (1982) and Gall et al (1972) have used models of the tail and anisotrophic interplanetary proton fluxes to interpret structure observed in the polar cap of the type noted in Figures 5-12 and 5-13. Useful recent bibliographies are contained in these papers. Faneslow and Stone (1972) have completed a comprehensive study of proton cutoffs observed

from low altitude polar orbit and Verzariu and Krimigis (1972) have reported solar proton spectra in the polar cap. Datlowe (1972) has discussed the effect of the interplanetary field structure on propogating solar particles.

Acknowledgments

The author would like to thank Dr. I.B. McDiarmid for many useful discussions. He would like to thank Dr. D.J. Williams and Dr. D. Winningham for the use of Explorer 41 and ISIS-1 data.

References

Anderson, K.A. and Lin, R.P. (1968) Observation of interplanetary field lines in the magnetotail. J. Geophys. Res. 74: 3953.

Armstrong, T.P. and Krimigis, S.M. (1971) Statistical study of solar protons alpha particles, and $Z \geq 3$ nuclei in 1967-1968. J. Geophys. Res. 76: 4230.

Blake, J.B., Paulikas, G.A. and Freden, S.C. (1968) Latitude-intensity structure and pitch angle distributions of low energy solar cosmic rays at low altitudes. J. Geophys. Res. 73: 4927.

Bostrom, C.O. (1970) Entry of low energy solar protons in the magnetosphere, in Intercorrelated Satellite Observations Related to Solar Events, edited by V. Manno and D.E. Page, D. Reidel, Dordrecht, Holland.

Cline, T.L. and McDonald, F.B. (1968) Relativistic electrons from solar flares. Solar Phys. 5: 507.

Datlowe, D. (1972) Association between Interplanetary Shock Waves and Delayed Solar Particle Events, J. Geophys. Res. 77: 5374.

Durgraprasad, N., Fichtel, C.E., Guss, D.E. and Rehmes, D.V. (1968) Nuclear charge spectra and energy in the September 2, 1966, solar particle event. Astrophys. J. 154: 307.

Engelmann, J., Hynds, R.J., Morfill, G., Axisa, F., Bewick, A., Durney, A.C. and Koch, L. (1971) Penetration of solar protons over the polar cap during the February 25, 1969 event. J. Geophys. Res. 76: 4245.

Evans, L.C. and Stone, E.C. (1969) Access of solar protons into the polar cap: A persistent north-south asymmetry. J. Geophys. Res. 74: 5127.

Faneslow, J.L. and Stone, E.C. (1972) Geomagnetic Cutoffs for Cosmic Ray Protons for Seven Energy Intervals Between 1.2 and 39 MeV, J. Geophys. Res. 77: 3999.

Fitchtel, C.E. (1970) Solar cosmic rays. GSFC Preprint X-662-70-134, Goddard Space Flight Center.

Freir, P.S. and Webber, W.R. (1963) Exponential rigidity spectrums for solar flare cosmic rays. J. Geophys. Res. 68: 1605.

Gall, R., Bravo, S. and Orozco, A. (1972) Model for the Uneven Illumination of Polar Caps by Solar Protons, J. Geophys. Res. 77: 5360.

Gall, R., Jimenez, J. and Camacho, L. (1968) Arrival of low energy cosmic rays via the magnetotail. J. Geophys. Res. 73: 1593.

Heristchi, D.J. and Trottet, G. (1971) Upper cutoff in the spectrum of solar particles. Phys. Rev. Letters 26: 197.

Imhof, W.L., Reagan, J.B. and Gaines, E.E. (1971) Solar particle cutoffs as observed at low altitudes. J. Geophys. Res. 76: 4276.

Kavanagh, L.D., Schardt, A.W. and Roelof, E.C. (1970) Solar wind and solar energetic particles: properties and interactions. Rev. Geophys. Space Phys. 8: 389.

Krimigis, S.M. and Verzariu, P. (1971) Implications on particle storage at the sun from observations of solar flare proton spectrums. J. Geophys. Res. 76: 792.

Lanzerotti, L.J. (1968) Penetration of solar protons nnd alphas to the geomagnetic equator. Phys. Rev. Letters 21: 929.

Lanzerotti, L.J. (1969) Report UAG-5 World Data Center A. 56: Feb. 1969.

Lanzerotti, L.J. (1970) Access of solar particles to synchronous altitude, in Intercorrelated Satellite Observations Related to Solar Events, edited by V. Manno and D.E. Page, D. Reidel, Dordrecht, Holland.

Lanzerotti, L.J. (1971) Solar flare particle radiation, presented at the National Symposium on Natural and Manmade Radiation in Space, March.

Lanzerotti, L.J. and Maclennan, C.G. Relative importance of solar electrons, protons and alphas in the November 1969 PCA event, presented at this conference.

Lanzerotti, L.J. and Robbins, M.F. (1969) Solar flare alpha to proton ratio changes following interplanetary disturbances. Solar Phys. 10: 212.

Leinbach, H. (1961) Some observations of daytime recoveries during polar cap absorption events. Arkiv Geofysik 3: 427.

Lin, R.P. (1970) The emission and propagation of 40 keV solar flare electrons. I: The relationship of 40 keV to energetic proton and relativistic electron emission by the sun. Solar Phys. 12: 266.

Lincoln, J.V. and Bucknam, D.B. presetned at the COSPAR Symposium on November 1969 Solar Particle Event, June 1971 and Solar Geophysical Data Report No. 309, Part II, May 1970.

McDiarmid, I.B. and Burrows, J.R. (1969) Relation of solar proton latitude profiles to outer radiation zone electron measurements. J. Geophys. Res. 74: 6239.

McDiarmid, I.B., Burrows, J.R. and Wilson, Margaret D. (1971) Solar particles and dayside limit of closed field lines, to be published in J. Geophys. Res.

Montgomery, M.D. and Singer, S. (1969) Penetration of solar energetic protons into the magnetotail. J. Geophys. Res. 74: 2869.

Morfill, G. and Scholer, M. (1972) Reconnection of the Geomagnetic Tail Deduced from Solar Particle Observations, J. Geophys. Res. 77: 4021.

Paulikas, G.A., Blake, J.B. and Freden, S.C. (1968) Low energy solar-cosmic-ray cutoffs: diurnal variations and pitch angle distributions. J. Geophys. Res. 73: 87.

Paulikas, G.A., Blake, J.B. and Vampola, A.L. (1970) Solar particle observations over the polar cap, in Particles and Fields in the Magnetosphere, edited by B.M. McCormac, D. Reidel, Dordrecht, Holland.

Reid, G.C. and Sauer, H.H. (1967) The influence of the geomagnetic tail on low energy cosmic ray cutoffs. J. Geophys. Res. 72: 197.

Roederer, J.G. (1971) On the adiabatic motion of energetic particles in a model magnetosphere. J. Geophys. Res. 72: 981.

Smart, D.F. and Shea, M.A. (1972) Daily Variations of Electron and Proton Cutoffs Calculated for Ft. Churchill, Canada, J. Geophys. Res. 77: 4595.

Smart, D.F., Shea, M.A. and Gall, R. (1969) The daily variation of trajectory-derived high-latitude cutoff rigidities in a model magnetosphere. J. Geophys. Res. 74: 4731.

Stone, E.C. (1964) Local time dependence of non-Stormer cutoffs for 1.5 MeV protons in a quiet geomagnetic field. J. Geophys. Res. 69: 3577.

Taylor, H.E. (1967) Latitude local-time dependence of low-energy cosmic-ray cutoffs in a realistic geomagnetic field. J. Geophys. Res. 72: 4467.

Vampola, A.L. (1971) Access of solar electrons to closed field lines. J. Geophys. Res. 76: 36.

Van Allen, J.A. (1970) On the electric field in the earth's distant magnetotail. J. Geophys. Res. 75: 29.

Van Allen, J.A. and Ness, N.F. (1969) Particle shadowing by the moon. J. Geophys. Res. 71.

Van Allen, J.A. Fennell, J.F. and Ness, N.F. (1971) Asymmetric access of energetic solar protons to the earth's north and south polar cap.s J. Geophys. Res. 76: 4262.

Verzariu, P. and Krimigis, S.M. (1972) Several Observations of Low Energy Proton Spectra and Possible Interpretation, J. Geophys. Res. 77: 3985.

West, Jr., H.I. and Vampola, A.L. (1971) Simultaneous observations of solar flare electron spectra in interplanetary space and within the earth's magnetosphere. Phys. Rev. Letters 26: 458.

Williams, D.J. (1969) Solar proton observations, 1-10 MeV. NASA-GSFC Rep. X 612-69-258.

Williams, D.J. and Bostrom, C.O. (1969) Proton entry into the magnetotail on May 26, 1967. J. Geophys. Res. 74: 3019.

Williams, D.J. and Mead, G.D. (1965) Nightside magnetospheric configuration as obtained from trapped electrons at 1100 km. J. Geophys. Res. 70: 3017.

Contents

6. Relative Importance of Solar Electrons, Protons, and Alphas in the November 1969 PCA Event

L. J. Lanzerotti and C. G. Maclennan
Bell Laboratories
Murray Hill, New Jersey, U.S.A.

Abstract

The fluxes of electrons ($E > 0.35$, > 0.6, and > 1.1 MeV), protons (0.47-19.7 MeV in ten differential channels), and alpha particles (1.0-21.4 MeV/nucleon in six differential channels) produced by the 2 November 1969 west limb flare were measured in interplanetary space by a semiconductor particle telescope on the Explorer 41 satellite. Intense fluxes of electrons arrive at the earth ~1 hour after the flare and prior to the arrival of the higher energy protons. Calculations indicate that these electrons produce approximately 50% of the intense (~14 dB) riometer absorption observed near the beginning of the event. The calculated electron and proton total riometer absorption agrees well throughout most of the event with that measured at 30 MHz at McMurdo, Antarctica. The alpha-to-proton ratios are presented for several different values of particle energy-per-nucleon. These ratios are quite low and indicate that the alphas were relatively insignificant contributors to the ionization of the PCA event.

6-1 INTRODUCTION

Beginning with the ionospheric effects observed during the great solar cosmic ray event of 23 February 1956 (Bailey, 1957), polar cap absorption events (PCA events) have been studied extensively in recent years both as distinct ionospheric phenomena and as diagnostic tools for solar-magnetospheric processes (see reviews by Reid 1970a, b). In recent years, with the advent of satellite measurements with good time-resolution and good spectral information on the solar proton fluxes, satisfactory agreement has frequently been achieved in calculating the expected excess riometer cosmic noise absorption due to the stopping of these solar protons in the high-latitude terrestrial atmosphere (Potemra et al 1967, 1969, 1970, Potemra and Lanzerotti 1971).

Although alpha particles and electrons are also constituents of the solar flare-produced cosmic rays, quantitative examination of their relative contributions to the PCA ionization has not previously been reported (Reid 1970b). Hakura (1967) originally suggested that electrons may play a role in the initial stages of a PCA event. Masley and Goedeke (1969) qualitatively attributed a part of the absorption during the July 1966 event to solar electrons. This paper demonstrates quantitatively that intense fluxes of high energy solar electrons incident on the polar ionosphere contributed approximately 50% of riometer absorption in the southern polar cap for the first several hours of the 2 November 1969 PCA event. In contrast, it is concluded that alpha particles contributed only a few percent to the total absorption measured in the southern polar cap.

In this paper, a discussion is first presented of the solar particle fluxes measured during the PCA event. The data are then used to compute the expected riometer absorption due to the assumed incidence of these particles on the polar ionosphere. This predicted absorption is then compared with actual absorption measurements made during the event at McMurdo, Antarctica.

The solar particle data used in this study were obtained by the Bell Laboratories particle telescope on the Explorer 41 (IMP-G) spacecraft. The details of the solid state telescope and associated electronics, which consist of coincidence circuitry and a particle identifier to separate protons, alpha particles, and electrons, have been described previously (Lanzerotti et al 1969). The 30 MHz riometer data was obtained by the McDonnell-Douglas observatory at McMurdo (79°S, 294.9°E geomagnetic; L ~32). These observations have been reported by Masley et al (1970).

6-2 OBSERVATIONS

6-2.1 Solar Particle Fluxes

The fluxes of solar protons, alpha particles, and electrons measured on Explorer 41 during the November 1969 PCA event are presented in Figure 6-1. Figure 6-1a contains a plot of the one-half hour average proton fluxes in eight of the ten differential energy channels of the experiment. These protons were apparently produced by a solar flare behind the west limb of the sun (Thomas 1970, Masley et al 1970). The lower-energy proton fluxes increase slowly to a peak intensity which does not occur until approximately one day after the initial particle onsets. In contrast, the higher energy protons increase more rapidly to a peak intensity (the exact time and intensity of which is somewhat uncertain due to a perigee pass of the satellite). The proton decay at the lower energies is approximately exponential; the decay appears more like a power-law in time at the higher energies.

Plotted in Figure 6-1b are the one-half hour average alpha particle fluxes measured in the six differential alpha channels of the experiment. The overall temporal appearance of the alpha fluxes resembles that of the proton fluxes in Figure 6-1a. The lower energy fluxes increase more slowly to a peak intensity and have an approximately exponential decay. At higher energies, the peak intensities are reached within several hours of the first particle observations. The high energy alpha fluxes decay with a power-law time dependence.

The one-half hour averaged electron fluxes measured in three integral channels are plotted in Figure 6-1c. The temporal profiles of the electron fluxes resemble those of the highest energy alphas and protons. The electron fluxes increase rapidly to a peak intensity soon after the first particles are observed, and then exhibit a predominantly power-law decay in time. The electron fluxes were quite intense during the onset of the event with $\sim 10^4$ electrons $(cm^2 \text{ sec ster})^{-1}$ of energy >350 keV measured at the peak of the event.

6-2.2 Particle Onsets

During the onset of the solar particle event, the IMP-G satellite was approaching the perigee of its orbit. The satellite entered the high latitude magnetosphere at ~0700 UT 2 November and remained within the magnetosphere until ~1300 UT on 3 November (D. H. Fairfield, private communication). The period when the satellite was within 10 earth radii (10 R_E) of the center of the earth is indicated on Figure 6-1a-c by the heavy bars. At 1100 UT on 2 November (shortly after the particle onsets), the satellite was located ~18 R_E from the earth at a solar - magnetosphere latitude of ~45° and longitude of ~125°. Hence, during the solar

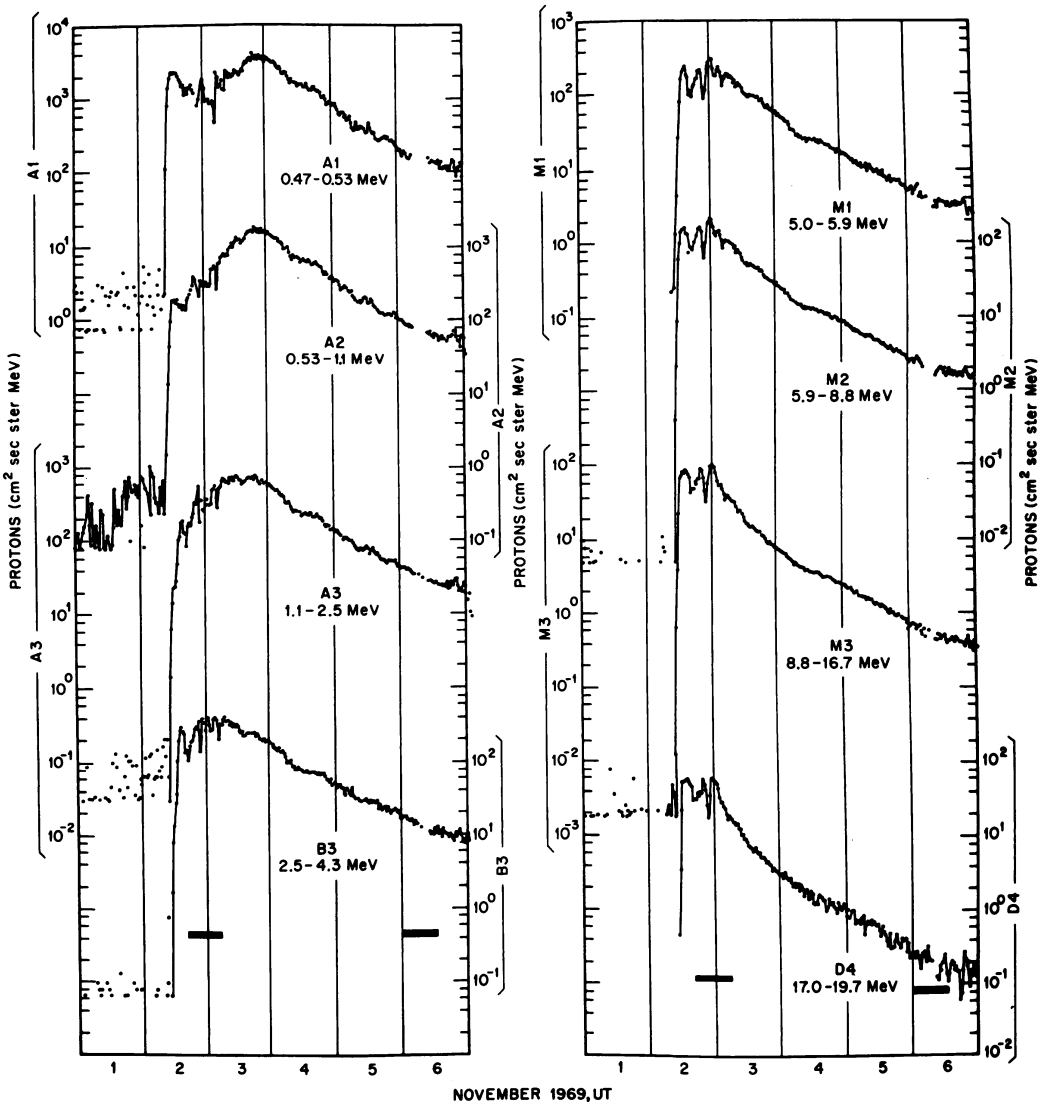

Figure 6-1a

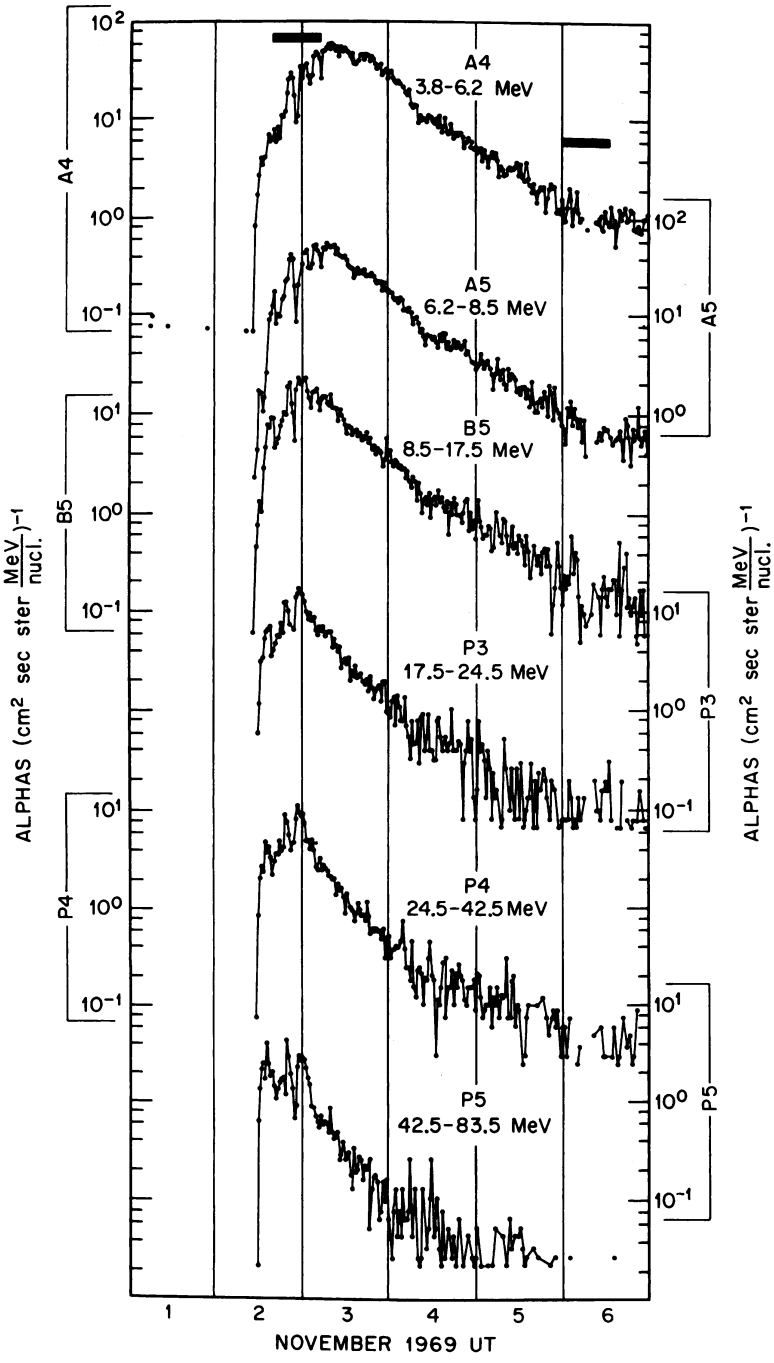

Figure 6-1b

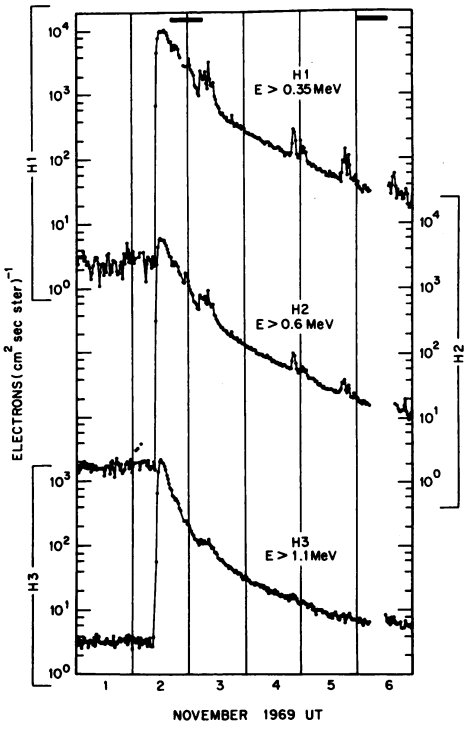

Figure 6-1c

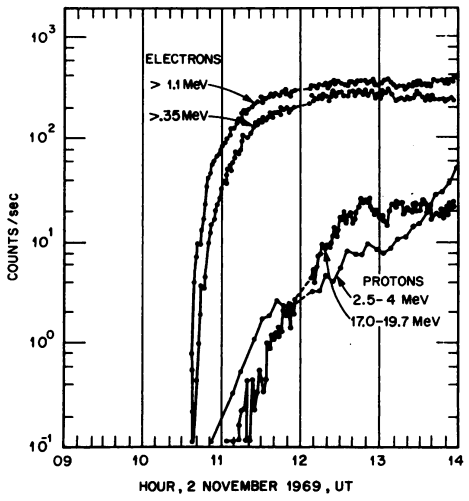

Figure 6-2

particle onset, the satellite was entering perigee ~35° behind the dawn meridian at high latitudes in the northern hemisphere.

Although the solar flare that produced the PCA event occurred behind the west limb and thus could not be optically classified, its onset time could nevertheless be estimated from optical, radio, and X-ray measurements (Thomas 1970, Castelli 1970). Evidence of the flare was first observed on 2 November optically at 0943 UT and in the 10 cm band at 0944 UT (Thomas 1970). An X-ray burst was reported by Vela 3 beginning at 0934 UT (Thomas 1970).

The solar particle enhancements at 1 au occurred quite late after the flare with the first electrons not observed on Explorer 41 until ~1037 UT. The energetic protons began arriving even later. These time relationships are seen in Figure 6-2, where high time resolution counting rates in two of the integral electron channels and two of the differential proton channels are plotted for 0900-1400 UT on 2 November. Each data point represents a 9.28 second spin-averaged counting rate. An electron channel sample is made approximately once each 1.2 minutes. The higher energy proton channel plotted in Figure 6-2 is sampled as frequently as the electron channel. The lower energy proton channel is sampled once every ~5 minutes.

The slow proton onsets measured by Explorer 41 at the beginning of the event, and the proton velocity dispersions seen in Figure 6-2, could be due to proton

delays in entering the distant magnetosphere from interplanetary space. Such delays would be compatible with the Vela satellite measurements of solar particles made in the magnetotail by Montgomery and Singer (1969). In addition, there is evidence that the interplanetary proton fluxes increased more rapidly in intensity than did the proton fluxes measured by Explorer 41 (J. B. Blake, private communication).

In contrast to the proton measurements, the sharp onset profile of the electron fluxes suggest rapid access of these solar particles to the satellite location. Such a rapid access would be compatible with the observations of lower energy electrons (>40 keV) rapidly entering the magnetotail (Lin and Anderson 1966). The importance of these proton and electron measurements for studying solar particle access to the magnetosphere will be discussed in a future paper.

The relativistic electrons measured by Explorer 41 arrived essentially at the time of the first reported observations of riometer absorption between 1045-1055 at McMurdo (Masley et al 1970) and at 1048 UT at both Thule (the magnetic pole) and Godhaven (L~20.5) (Cormier 1970). Excess cosmic noise absorption was observed to begin somewhat later, ~1100 UT, in the auroral zone at Churchill (L ~ 8.6; Cormier 1970). It is clear from the quoted riometer onsets that the solar electrons played a major role in producing significant enhancements of polar cap ionization during the onset of the PCA event.

6-2.3 Alpha-to-Proton Ratios

The half-hour averaged alpha particle-to-proton ratios for four different values of equal particle energy per nucleon are plotted in Figure 6-3. Initially, the ratios are largest at the lowest energies. For example, at the beginning of 3 November, the ratio is ~0.13 for 2 MeV/nucleon particles and ~0.04 for 12 MeV/nucleon particles. Late in the event, the ratios for all energies are approximately the same; equal to about 2% of the proton fluxes.

The alpha-to-proton fluxes plotted in Figure 6-3 exhibit a distinctly different temporal structure than the same ratios measured following the west-limb flare of 18 November 1968 (Lanzerotti 1970). This is due to the fact that, unlike the 1968 event, the solar cosmic rays from the 1969 event apparently propagated to the earth unaccompanied by a flare-produced shock wave. Such a shock disturbance apparently affects differently the propagation characteristics of alphas and protons of equal energy per nucleon. This effect was first noted by Lanzerotti and Robbins (1969) and Lanzerotti and Graedel (1970), and is currently being studied further.

The daily-average alpha-to-proton ratios measured during 2 November to 5 November are plotted in Figure 6-4 as a function of particle energy per nucleon.

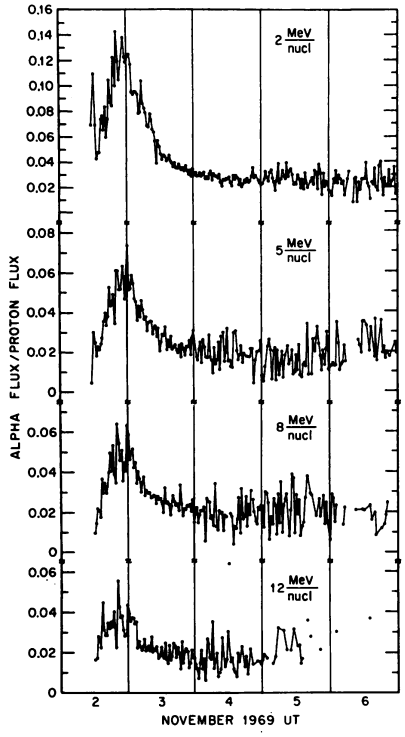

Figure 6-3

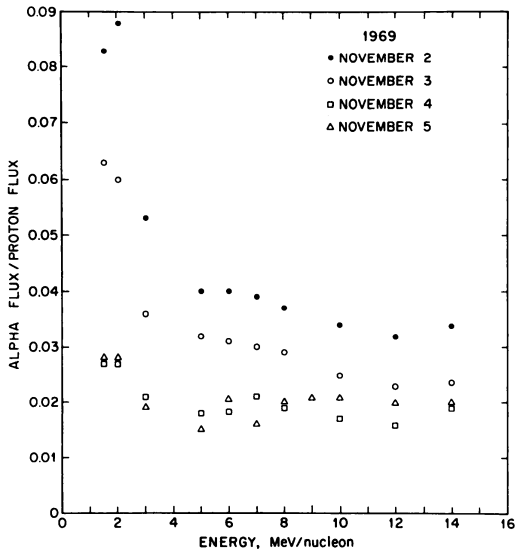

Figure 6-4

This figure clearly shows the relative enhancement of alphas at low energies early in the event. During the last two days plotted, the alpha-to-proton ratio is ~0.02 at all energies measured.

6-2.4 Particle Spectra

Half-hour average proton, alpha particle, and electron spectra are plotted in Figure 6-5 for three different periods during the PCA event. On 3 November and 4 November, both the proton and the alpha particle spectra had approximately power-law spectral dependences, particularly at the higher energies. However, the spectra of 2 November indicate a positive energy slope (in the case of the alphas) and definite evidence of a spectral turnover with a peak at ~7.5 MeV (in the case of protons). A turnover in both the alpha particle and proton spectra is observed until ~1100 UT 3 November.

The gradual change with time of the proton spectra and the peak in intensity during 3 November is shown in Figure 6-6 where six one-half hour average spectra are plotted. Another unusual aspect of these proton spectra is that not only is a peak (which shifts to lower energies in time) observed, but the spectra also turns upward at the lowest energy measured. (This increase in the proton spectra at ~500 keV has also been observed in the solar particles measured over the polar caps during this event; J. B. Blake, private communication.) These spectra are currently being studied in terms of particle access to the

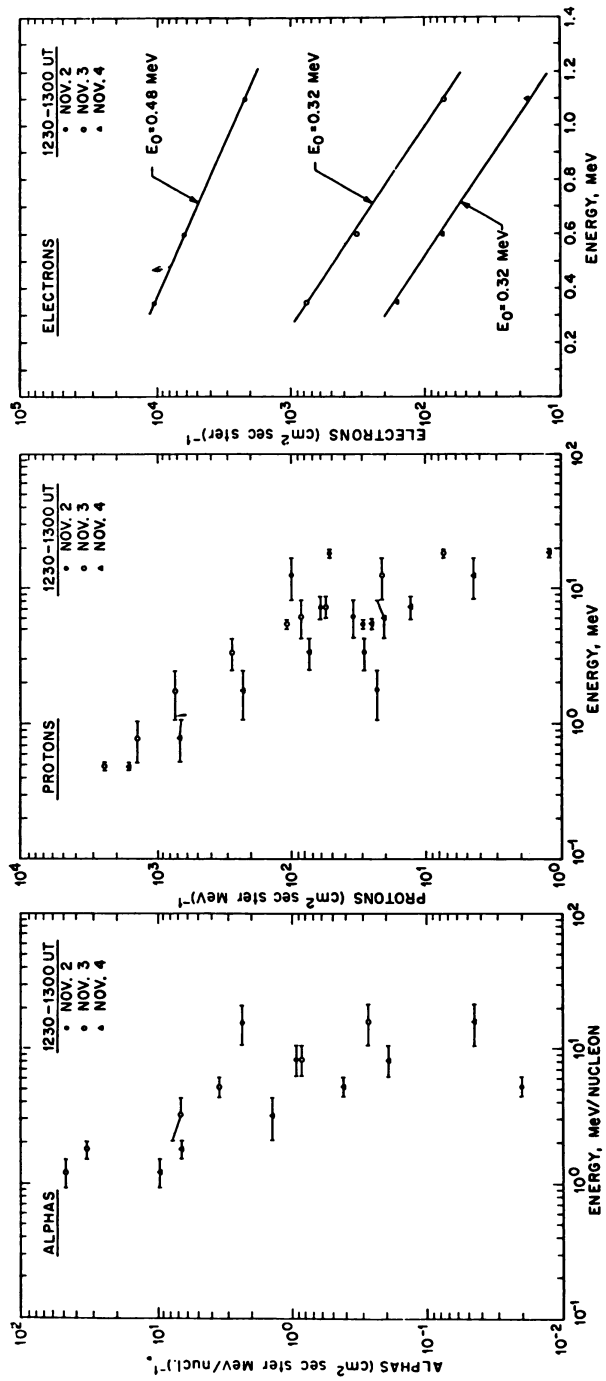

Figure 6-5

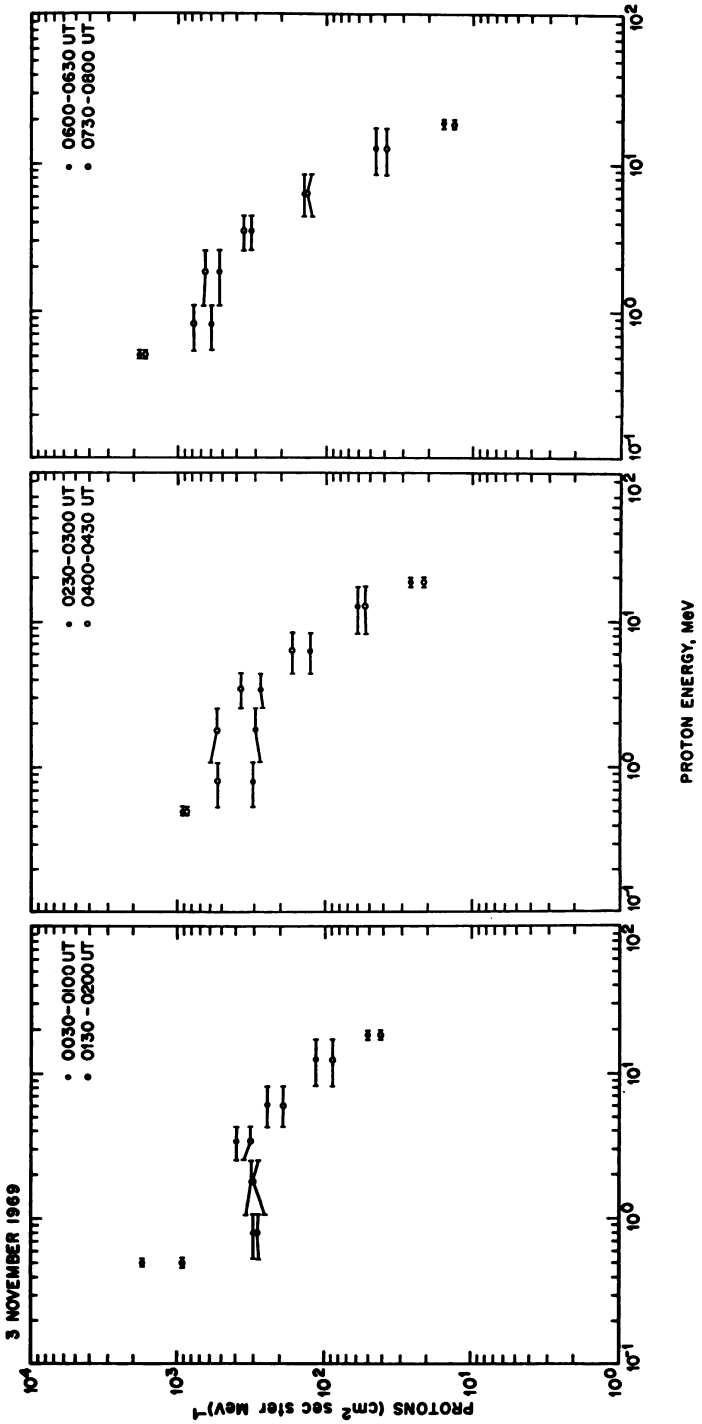

Figure 6-6

magnetosphere as well as propagation mechanisms at the sun and in interplanetary space.

The three-point electron spectra measured by Explorer 41 during the event could be well represented by an exponential spectral representation

$$J(>E) = J_o(E_o)\exp(-E/E_o)\ (cm^2\ sec\ ster)^{-1} \qquad (1)$$

over the energy range measured (c.f. Figure 6-5). The spectra were quite hard early in the event ($E_o \sim 0.5$ MeV) and softened during the later days of the event ($E_o \sim 0.3$ MeV). For the riometer calculations considered in the following section, it was assumed that exponential electron spectra such as those of Figure 6-5 could be extrapolated to zero energy.

Solar electrons of relativistic energies ($\gtrsim 1$ MeV) have been commonly represented quite well by power law spectral shapes (Cline and McDonald 1968, Simnett 1971). However, when electron fluxes from some events have been plotted for particle energies $\gtrsim 1$ MeV, the spectra appear to change slope and have less steep energy dependencies (Simnett 1971). Hence, the measured electron spectra in this event may be more like exponential distributions than power law distributions at the lower energies.

6-3 CALCULATED RIOMETER RESPONSE

6-3.1 Electrons

It was assumed that the measured solar electrons had unimpeded access to the earth's polar regions. From the work of Vampola (1971) and West and Vampola (1971) it would seem that this is a valid assumption, at least for electrons of energies as low as ~70 keV (the lowest energies measured and reported to date).

The expected riometer absorption due to these electrons was then determined from the daytime vertical-incidence 30 MHz absorption calculation results presented by Bailey (1968). Bailey calculated the expected absorption for auroral electrons assuming exponential energy spectra for the precipitating particles. As such, he presented results for relatively soft electron spectra ($E_o \leq 150$ keV). However, since his results showed that the absorption A(dB) could be given by

$$A(dB) = B\sqrt{J(>E_{min})} \qquad (2)$$

where B is a proportionality factor dependent upon E_{min}, it is possible to extend Bailey's work to the hard spectrum solar electrons discussed here.

The proportionality factor B for electrons in Equation (2) can be obtained from Bailey's absorption calculation results which are plotted as a function of incident particle flux (for values of E_o = 20, 40, 60, 100 and 150 keV). The relationship between the particle flux required to produce 0.1 dB absorption and the e-folding spectral energy E_o was determined from Bailey's results to be given by a power-law expression

$$J(.1\ dB, E_o) \sim 1.5 \cdot 10^7 E_o^{-2.8} \tag{3}$$

where $J(.1\ dB, E_o)$ has dimensions of electrons $(cm^2\ sec\ ster)^{-1}$ and E_o is in keV. Using this relationship, the expected riometer absorption in Equation (2) can be written as

$$A(dB) = \sqrt{\frac{0.01\ J_o}{J(.1\ dB, E_o)}} \tag{4}$$

where J_o is the measured electron flux extrapolated to E = 0 and

$$B(E > 0) = 2.6 \cdot 10^{-5} E_o^{1.4}\ dB(cm^2\ sec\ ster)^{1/2}\ .$$

The values of E_o and J_o were determined from the measured half-hour averaged electron spectra during the first five hours of the event. After that time, the hourly-averaged spectra were used. The estimates of the expected riometer absorption using Equations (3) and (4), and the measured (extrapolated) values of E_o (J_o), were multiplied by 1.6 in order to obtain the approximate absorption that would be observed by a broad-beam riometer such as that at McMurdo (Bailey 1968). These results are plotted as open circles in Figure 6-7a.

The calculations show that the measured integral electron fluxes are expected to produce significant absorption (~1 dB) during the period 1030-1100 UT. The calculated solar electron-produced absorption increases to a peak value of ~10 dB between 1230-1300 UT and then decreases during the remainder of the event.

6-3.2 Protons and Alphas

As indicated in the introduction, agreement has been achieved recently between the observed riometer absorption and that calculated due to solar protons using magnetoionic theory and an appropriate ionosphere model (Potemra et al 1967, 1969, 1970). In addition, in the past, a number of workers have investigated an

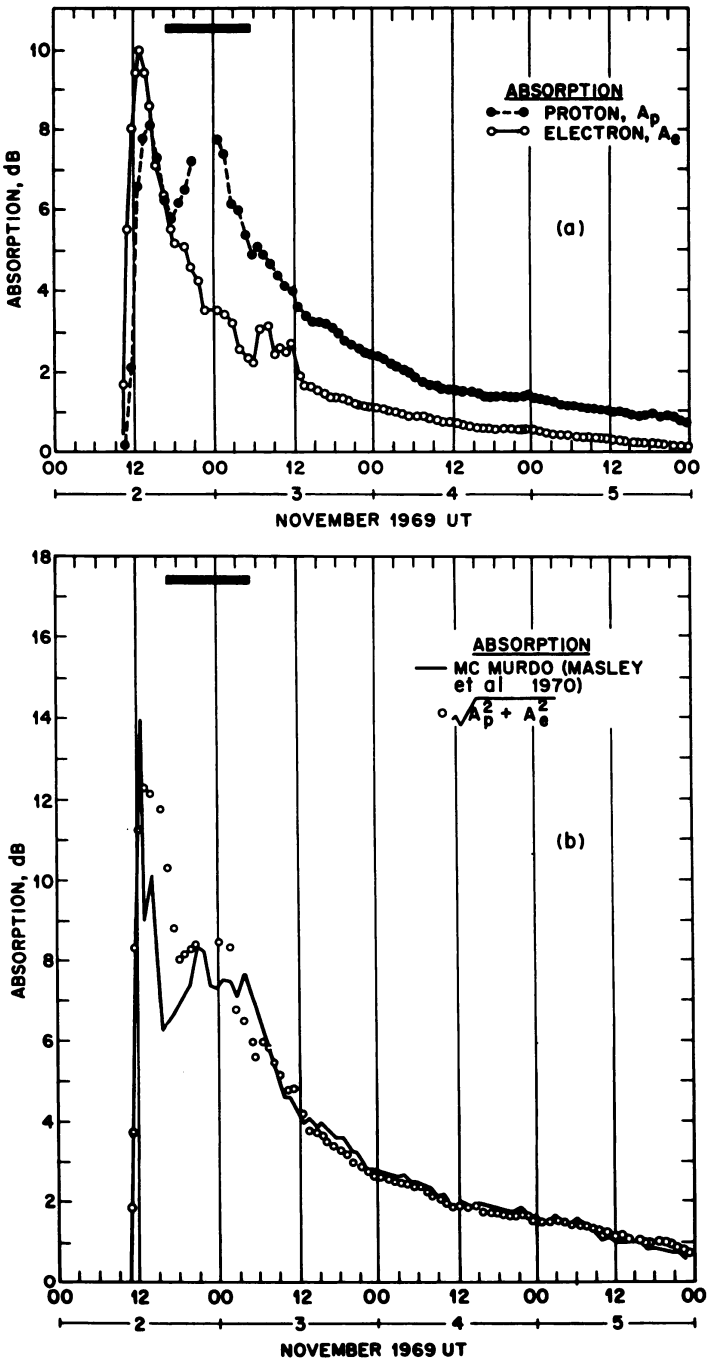

Figure 6-7

empirical relationship of the form of Equation (2) between the measured solar proton fluxes and the measured absorption (Fichtel et al 1963, Van Allen et al 1964, Juday and Adams 1969, Reid 1969, 1970a). Potemra and Lanzerotti (1971) were able to determine the proportionality factor B in Equation (2) for seven values of E_{min} (5, 10, 15, 20, 25, 30, and 50 MeV). They found Equation (2) to give an excellent fit to the data for all values of E_{min}, and concluded that this was due to the fact that the proton spectrum did not change appreciably during the event they analyzed.

Potemra (1971) has recently calculated, using the results of Potemra et al (1967, 1969), the proportionality factor B as a function of γ, the power-dependence in the proton differential spectrum when expressed as a power-law in energy

$$\frac{dJ(E)}{dE} \propto E^{-\gamma} . \tag{5}$$

He found that for a power-law proton spectrum, B was essentially independent of spectral shape (independent of γ) for E_{min} ~7 MeV. He found that

$$A(dB) = 0.083 \sqrt{2\pi J(E > 7 \text{ MeV})} . \tag{6}$$

The relationship in Equation (6) was used to calculate the expected riometer absorption due to the solar protons measured by Explorer 41 incident on the polar ionosphere. As in the case of the electrons, it was assumed that these solar protons had free access to the polar caps. This is not always true, of course, as frequently substantial asymmetries between north and south polar fluxes and the interplanetary fluxes are observed during an event (see recent reviews by Bostrom 1970, and Paulikas et al 1970).

The differential proton fluxes from the Bell Laboratories Explorer 41 experiment were used together with the integral fluxes of protons >30 MeV and >60 MeV measured by the monitoring experiment on the same satellite (Solar-Geophysical Data 1970) to give proton spectra from 0.5 to 60 MeV. The hourly average integral proton spectra for protons > 7 MeV were computed from these spectra. These computed integral spectra were used together with Equation (6) to give the expected riometer absorption due to the protons. These values of the absorption are plotted as solid points in Figure 6-7a.

It is seen from Figure 6-7a that electrons produce more absorption than the protons until hour 17 on 2 November. After that time, the protons are the dominant producers of the excess ionosphere ionization for the remainder of the event.

Equal fluxes of alpha particles and protons of the same energy per nucleon will produce the same amount of excess ionosphere absorption (for example, Adams and Masley 1966). From the data of Figures 6-3 and 6-4, it is clear that the integral alpha intensities for alphas of energy >7 MeV/nucleon are only a few percent of the proton intensities during this event. Hence, the alphas contributed less than 1 dB to the total absorption at the beginning of the event and substantially less later.

6-3.3 Total Absorption

The square root of the sum of the squares of the calculated electron and proton riometer absorption for the November 1969 event (Figure 6-7a) is plotted in Figure 6-7b together with the absorption measured at McMurdo. The most striking result in Figure 6-7b, of course, is the fact that the peak absorption observed near the beginning of the event can only be accounted for by including the substantial fluxes of solar electrons. For the duration of the event the general agreement between the calculations and the observations is quite satisfactory and attests to the importance of including the solar electrons in the absorption considerations.

6-4 DISCUSSION

The most significant result of this study is the conclusion that intense fluxes of solar electrons incident on the polar ionosphere early in the event provided approximately one-half the total measured polar cap absorption during the first few hours of the event. The electrons appear to have contributed a finite amount of ionization for producing the measured polar cap absorption throughout the entire event.

It should be stressed, that the calculated electron absorption in this paper was determined from the work of Bailey (1968), rather than by use of an empirical relationship between the measured absorption and electron precipitation such as has been derived by Jelly et al (1964), Parthasarathy et al (1966), or Hakura (1969). This was done because the empirical relationships in these references were obtained for electrons of energy >40 keV without reference to their spectral e-folding energies E_o. Bailey (1968) finds a strong energy dependence to the proportionality constant B (Equation 2), with B approaching unity for fluxes >40 keV and $E_o \sim 300$ keV (in contrast to an empirical $B \sim 10^{-3}$ for $E_o \sim 10$-100 keV as determined by Jelly et al 1964, Parthasarathy et al 1966 and Hakura 1969). All of the high-energy electron spectra measured during this event had values of $E_o \gtrsim 250$ keV.

From the measured alpha flux-to-proton flux ratios, it was concluded that the solar alpha particles never contributed more than a few percent to the total measured absorption. This conclusion would hold for other PCA events where alpha particle fluxes have been reported in detail (for example, Lanzerotti and Robbins 1969, Lanzerotti 1970).

The expected absorption was not calculated from solar fluxes measured directly over the polar cap station. Hence, it is reasonable that perfect agreement was not always achieved between the calculated and observed values.

In conclusion, it should be stressed that it is not possible to ignore the importance of hard-spectra solar electrons for producing significant early PCA riometer absorption following some solar flares. It would be of great value to study other PCA events that have occurred when the sun-earth propagation path was such that the electrons arrived appreciably prior to the protons. In addition to studying which flares produce copious fluxes of relativistic electrons, future investigations should consider the solar longitude of the parent flare to determine which longitudes tend to give rise to the greatest time differences between the arrival of the electrons and protons.

Acknowledgments

We would like to thank J. B. Blake and A. L. Vampola (Aerospace Corporation), A. J. Masley and M. B. Baker (McDonnell-Douglas Corporation), J.B. Reagan (Lockheed Research Labs), and T. A. Potemra (Applied Physics Laboratory) for profitable discussions of various aspects of this event and T. E. Graedel (Bell Laboratories) for comments on the manuscript.

References

Adams, G. W. and Masley, A. J. (1966) Theoretical study of cosmic noise absorption due to solar cosmic radiation, Planet. Space Sci. 14: 277.

Bailey, D. K. (1957) Disturbances in the lower ionosphere observed at VHF following the solar flare of 23 February 1956 with particular reference to auroral zone absorption, J. Geophys. Res. 62: 431.

Bailey, D. K. (1968) Some quantitative aspects of electron precipitation in and near the auroral zone, Rev. Geophys. 6: 289.

Bostrom, C. O. (1970) Entry of low energy solar protons into the magnetosphere, Intercorrelated Satellite Observations Related to Solar Events, ed. V. Manno and D. E. Page (D. Reidel, Holland): 229.

Castelli, J. P. (1970) Microwave burst spectra and PCA's, Proc. Meeting on Operation PCA 69, AFCRL-70-0625: 19.

Cline, T. L. and McDonald, F.B. (1968) Relativistic electrons from solar flares Solar Phys. 5: 507.

Cormier, R. J. (1970) Riometer observations during PCA's, Proc. Meeting on Operation PCA 69, AFCRL-70-0625: 21.

Fichtel, C. E., Guss, D. E., and Ogilvie, K. W. (1963) Solar Proton Manual, ed. F. B. McDonald, NASA Report, NASA-TRR-169.

Hakura, Y. (1967) Entry of solar cosmic rays into the polar cap atmosphere, J. Geophys. Res. 72: 1461.

Hakura, Y. (1969) The polar cap absorption on 7-10 July 1966, Annals IQSY 3: 337.

Jelly, D. H., McDiarmid, I. B., and Burrows, J. R. (1964) Correlation between intensities of auroral absorption and precipitated electrons, Canadian J. Physics 42: 2411.

Juday, R. D. and Adams, G. W. (1969) Riometer measurements, solar proton intensities and radiation dose rates, Planet. Space Sci. 17: 1313.

Lanzerotti, L. J. (1970) Protons, alpha particles, and electrons resulting from the 18 November 1968 solar flare, World Data Center A, Report UAG-9, 34, April.

Lanzerotti, L. J. and Graedel, T. E. (1970) Observations of solar electron, proton and alpha particle propagation, Bull. Am. Phys. Soc. 15: 610.

Lanzerotti, L. J., Lie, H. P., and Miller, G. L. (1969) A satellite solar cosmic ray spectrometer with on-board particle identification, I.E.E.E. Trans. Nucl. Sci. NS-16(1): 343.

Lanzerotti, L. J., and Robbins, M. F. (1969) Solar flare alpha to proton ratio changes following interplanetary disturbances, Solar Phys. 10: 212.

Lin, R. P. and Anderson, K. A. (1966) Evidence for connection of geomagnetic tail lines to the interplanetary field, J. Geophys. Res. 71: 4213.

Masley, A. J. and Goedeke, A. D. (1969) The 7 July 1966 solar cosmic-ray event, Annal IQSY 3: 353.

Masley, A. J., McDonough, J. W., and Satterblom, P. R. (1970) Solar cosmic-ray observations during 1969, Antarctic J. of the U. S. 5: 172.

Montgomery, M. D. and Singer, S. (1969) Penetration of solar energetic protons into the magnetotail, J. Geophys. Res. 74: 2869.

Parthasarathy, R., Berkey, F. T., and Venkatesan, D. (1966) Auroral zone electron flux and its relation to broadbeam radiowave absorption, Planet. Space Science 14: 65.

Paulikas, G. A., Blake, J. B., and Vampola, A. L. (1970) Solar particle observations over the polar caps, Intercorrelated Satellite Observations Related to Solar Events, ed. V. Manno and D. E. Page (D. Reidel, Holland): 193.

Potemra, T. A. (1971) The empirical connection of riometer absorption to solar protons during PCA events, submitted to J. Geophys. Res.

Potemra, T. A. and Lanzerotti, L. J. (1971) Equatorial and precipitating solar protons in the magnetosphere, 2. Riometer observations, J. Geophys. Res. 76.

Potemra, T. A., Zmuda, A. J., Shaw, B. W., and Haave, C. R. (1970) VLF phase disturbances, HF absorption, and solar protons in the PCA events of 1967, Radio Science 5: 1137.

Potemra, T. A., Zmuda, A. J. Haave, C. R., and Shaw, B. W. (1969) VLF phase disturbances, HF absorption, and solar protons in the events of August 28 and September 2, 1966, J. Geophys. Res. 74: 6444.

Potemra, T. A., Zmuda, A. J., Haave, C. R., and Shaw, B. W. (1967) VLF phase perturbations produced by solar protons in the event of February 5, 1965, J. Geophys. Res. 72: 6077.

Reid, G. C. (1969) Associate detachment in the mesosphere and the diurnal variation of polar cap absorption, Planet. Space Sci. 17: 731.

Reid, G. A. (1970a) Current problems in polar cap absorption, Intercorrelated Satellite Observations Related to Solar Events, ed. V. Manno and D.E. Page (D. Reidel, Holland): 319.

Reid, G.A. (1970b) The energetic particle environment of the polar caps, J. Franklin Inst. 290: 197.

Simnett, G. M. (1971) Relativistic electrons from the sun observed by IMP-4, Solar Phys, 22: 189.

Solar-Geophysical Data, U.S. Dept. Commerce, Boulder, Colorado, (No. 309), Part II, May 1970.

Thomas, C. J., History and characteristics of the active solar region that caused the proton event of 2 November 1969, Proc. Meeting on Operation PCA 69, AFCRL-70-0625, pg. 15, October 1970.

Vampola, A. (1971) Access of solar electrons to closed field lines, J. Geophys. Res. 76: 36.

Van Allen, J. A., Lin, W. C., and Leinback, H. (1964) On the relationship between absolute cosmic ray intensity and riometer absorption, J. Geophys. Res. 69: 4481.

West, H. I., Jr. and Vampola, A. L. (1971) Simultaneous observations of solar flare electron spectra in interplanetary space and within the earth's magnetosphere, Phys. Rev. Letters 26: 458.

Contents

7. Northern Polar Cap Particle Flux Variations Following the 2 November 1969 Event

V. Domingo, E. E. Page and M. L. Shaw
Space Science Department (ESLAB)
European Space Research and Technology Centre
Noordwijk, The Netherlands

Abstract

Some of the data available for the period following 2 November 1969 is presented with a view suitable for combining it with complementary results appearing at the Chestnut Hill Symposium.

The particle intensity differences observed between the ESRO IA satellite at 1000 km and ESRO IB at 300 km are discussed.

A notable feature was the apparent absence of auroral zone enhancements early in the event and the presence on the polar plateau of an intensity spike. The central plateau intensity rose in step with the interplanetary 45 keV electron intensity as measured by Explorer 35 (R.P. Lin), suggesting direct connection of that region with interplanetary space. When ESRO IA and IB were on one occasion simultaneously over the northern polar cap, but in slightly different places, in-phase intensity variations were seen by both satellites. These would suggest that at that time a large area of the polar cap region was experiencing coherent temporal fluctuations at about one minute intervals.

Chestnut Hill Conference, June 1971

7-1 INTRODUCTION

An aim of this paper is to present some illustrative data and make known what data is available so that following the Chestnut Hill conference it should be possible to combine the contributions of many experimenters to form an overall picture of the 2 November 1969 event. In addition, however, certain interesting phenomena seen during the period are discussed in the light of existing experimental evidence and theory.

7-2 SATELLITES AND DETECTORS

Two identical, magnetically stabilized, near earth polar orbiting satellites obtained data for us during the 2 November 1969 event. At that time ESRO IA/ Aurorae was crossing the north polar region at around 1000 kms while ESRO IB/ Boreas was just below 300 kms. Both orbits were close to the midday-midnight meridian. Detailed description of these satellites can be found in Jaeschke (1970).

The passive magnetic stabilization was such that, in general, alignment with the earth's magnetic field was better than 5°. Consequently, the geiger counter from which we obtained data and which was set to view perpendicular to the satellite axis, monitored pitch angles around 90°. (The geiger counter was supplied by the Norwegian Defence Research Establishment, Kjeller, as part of a high speed auroral zone experiment, and we supplied low speed electronics to permit a radiation belt survey.)

The geiger, an EON 6222, had a mica end window with a nominal 40% transmission of 40 keV electrons and a proton threshold around 500 keV. It was shielded so that protons not entering via the collimator needed at least 30 MeV to be registered. The geometric factor assuming detection via the collimator was 8.3×10^{-3} cm^2 sterad. The analogue ratemeter output was monitored each 12.8 seconds and reached a rate of 4.7×10^3 per second before saturation. When the detector with an opening angle of ±15° was pointed within 20° of the solar direction the data was automatically rejected. Solar radiation generally saturated the device in such configurations.

7-3 FLUX VARIATIONS

Our detector indiscriminately counts protons above 500 keV, electrons above 40 keV, which enter via the collimator at 90°, and, in addition, high energy particles which have the range of a 30 MeV proton and which may enter through the shielding.

Characteristically, after the first few hours of an event the count profile over the central polar cap is fairly level and uniform (Paulikas et al 1970, Thomas and Dalziel 1970, Krimigis and Verzariu 1971, and Krimigis and Van Allen 1967). Frequently, early in the event there is considerable enhancement of flux in the 'auroral' zones at the edge of the polar 'plateau' (Domingo and Page 1971, Thomas and Dalziel 1970, and Williams and Bostrom 1969).

After the first few hours, the 2 November 1969 event displayed a reasonably level central polar cap plateau. On this occasion, however, in the early stages no enhancement at the 'auroral' zone edges was seen; instead there was a considerable count rate spike over a limited region of the central polar cap. During the remainder of this paper, when we refer to plateau level, we mean value of the count rate observed at invariant latitudes above 78°.

Figure 7-1 shows the plateau count rates obtained from ESRO IA and ESRO IB data during the period 2 to 11 November 1969.

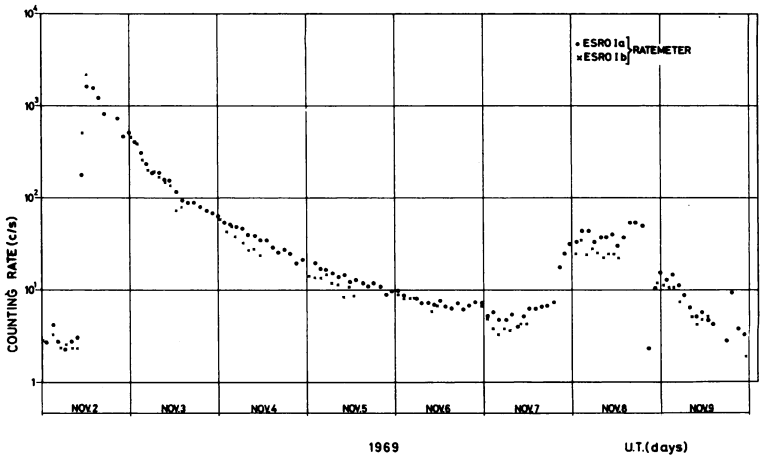

Figure 7-1. North Polar Cap 'Plateau' Level of the Particle Counting Rate Measured by the Satellites ESRO IA and ESRO IB During the 2 November 1969 Event. The 'plateau' levels have been defined as the median value of the counting rate measurement made over invariant latitude greater than 78°N.

7-4 COUNT RATE DIFFERENCE BETWEEN 1000 AND 3000 KMS

During the first few hours of the event, the ESRO IA plateau rate at around 975 km was essentially the same as the ESRO IB rate at 275 km. Later in the

event, the ESRO IA plateau rate became 40% above ESRO IB rate at times. The respective heights had changed very little to 1015 and 245 km respectively.

Large fluxes of protons above 30 MeV were present in interplanetary space during the first 36 hours of the event (Solar Geophysical Data 1970). In such a flux, the geiger counter becomes a complicated function of particle energy and arrival direction.

Protons with energies above 0.5 MeV are, of course, large in number per cm^2 second sterad. compared with the intensity above 30 MeV in the same units. However, to protons above 30 MeV, the geometric factor of the counter is ill-defined and probably greater than 1 cm^2 sterad. while the geometric factor for access via the window is 8×10^{-3} cm^2 sterad. Thus, early in the event, in the presence of protons above 30 MeV, it is not possible to discuss the difference in fluxes we measure at 300 and 1000 km in terms of loss cone variations.

Later in the event, however, and in particular, during the smaller secondary increase on 8 November 1969 when the 30 MeV intensity in interplanetary space remained at 'background' level, the 90° intensity differed by up to 40% from 300 to 1000 km. In these circumstances, it seems valid to conclude that the difference was largely due to a changing loss cone effect since most particles detected must have entered 'properly' via the collimator. Then the difference may be accounted for in terms of particles which mirror below 1000 but above 300 km, and it may be that the pitch angle distribution at the two heights changes with time as the whole topology of the region enclosing the field lines rooted in the tail changes.

The loss cone is also a function of energy since high energy particles can penetrate deep into the atmosphere and return with enough energy to be detected. The effective loss cone will therefore have changed during the event development for our integral energy detector, as the ratio of low energies to high energies increased.

Because of the integral energy detection and the geometric factor varying with energy, we can put in no useful numbers but can discuss the situation in case it is useful to compare with other results obtained by narrow band directional detectors. Clearly it would be of interest to see if there are pitch angle variations as the polar cap is crossed (Hudson and Anderson 1969) and if these are spatial or temporal.

7-5 POLAR CAP STRUCTURE DURING EVENT RISE

Figure 7-2 shows the count rates during the first two north pole passes after the start of the event. Superposed is a plot, in arbitrary units, of the count rate of electrons with energies greater than 45 keV obtained fromExplorer 35 (courtesy

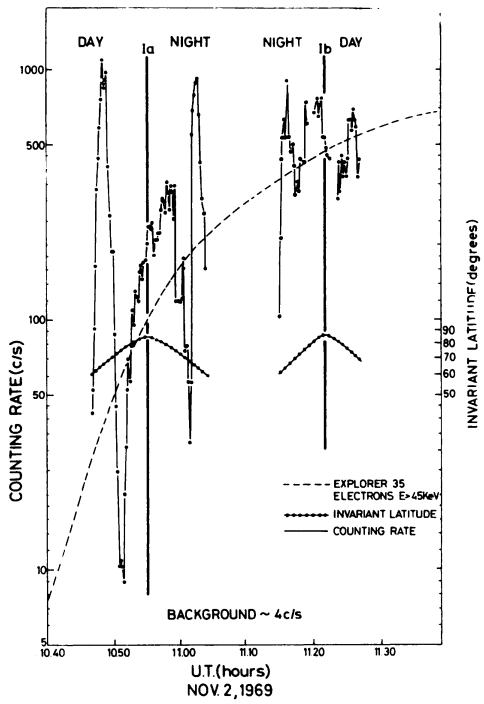

Figure 7-2. Protons (E >500 keV) and Electrons (E >40 keV) Counting Rate Versus Universal Time Registered Over the North Polar Cap by ESRO IA and ESRO IB on Their First Passage After the Start of the Event. For comparison the electron flux (E > 45 keV) measured by Explorer 35 outside the magnetosphere is shown on an arbitrary scale

of Dr. R. P. Lin, Space Science Lab., University of California, Berkeley) which was, at that time, outside the magnetosphere.

The ESRO IB pass centered at 0950 UT on 2 November 1969, showed the normal background rate of around 4 counts per second. The Explorer 35, 45 keV flux began to rise above background at 1030 UT and the ESRO IA satellite first recorded an increased flux at 1052 UT. During the 7 minute passage across the central polar cap, the intensity measured rose steeply - even more steeply than the extrapolated 45 keV intensity in interplanetary space. (We do not yet have interplanetary proton data with fine time resolution and can, therefore, only compare with the electron flux to which our detector was also sensitive.) This might be taken to suggest that particles were, in fact, on this occasion focussed into the central polar cap region. The degree to which the polar cap count rate follows the interplanetary rate would also suggest that the connection between the two regions provided almost instantaneous access.

In other events (Domingo and Page 1971) we have sometimes been able to see enhancements in the 'auroral zone' fluxes with one detector in spite of radiation belt contamination. In the present case, such enhancements appear to be absent. It has been observed on some occasions that the auroral enhancements appeared to follow the interplanetary flux variations better than did the central polar cap (Bostrom 1970).

In at least one other event, the auroral zone enhancement and a central polar cap spike were present together (Thomas et al 1970, Jakeways et al 1970, Durney et al 1972, and Engelmann et al 1971). The result of Jakeways et al (1970) shows that protons with energies of MeV can still find themselves channeled into a quite narrow region of the central polar cap.

The spike seen in the central polar cap during the November 1969 event is illustrated in the three passes of Figure 7-3. In all cases, the flux enhancement was at invariant latitudes contained between 76° and 86°. The persistence of the spike for several orbits suggests that it was a spatial rather than temporal phenomenon.

The picture is clearly very complicated but recently Domingo and Page (1971) and Engelmann et al (1970) have presented results which indicate that what is seen over over the polar cap is very dependent on the direction of the interplanetary magnetic field and on the interplanetary particle directional anisotrophy providing impact zones at the magnetosphere. It is to be hoped that the complementary interplanetary results become available at this symposium.

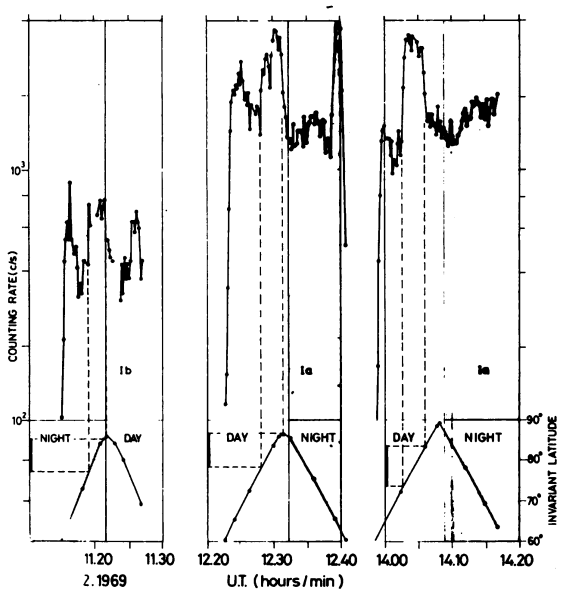

Figure 7-3. Counting Rate (E_o >500 keV, E_e >40 keV) Over the North Pole Showing the Central Polar Cap Intensity 'Spike' Persisting During Three Passes

7-6 SHORT TERM FLUCTUATIONS

As well as the gross effects described in the previous section, there were small but significant fluctuations in the particle count rate over the polar cap plateau region, which were of the order 10 to 20% in magnitude and had time scales of about one minute. There was no clear evidence of periodicity in the fluctuations, but it should be remembered that data samples were available only at 12.8 second intervals.

Usually such variations have been attributed to spatial effects (Bostrom 1970, Page 1971), that is, the satellite while over the polar region crossed 'bundles' of magnetic field lines with associated flux variations. Variations of about 1 minute would then suggest 'bundle' diameters of a few hundred kilometers.

In the November 1969 event, while the particle flux was high enough to allow the observation of statistically significant short term variations, there was one interval during which we received simultaneous data from both satellites. At the time these satellites were in slightly different regions of the northern central polar cap. The positions are shown in Figure 7-4. While ESRO IA moved from X' to Y', ESRO IB moved from X to Y.

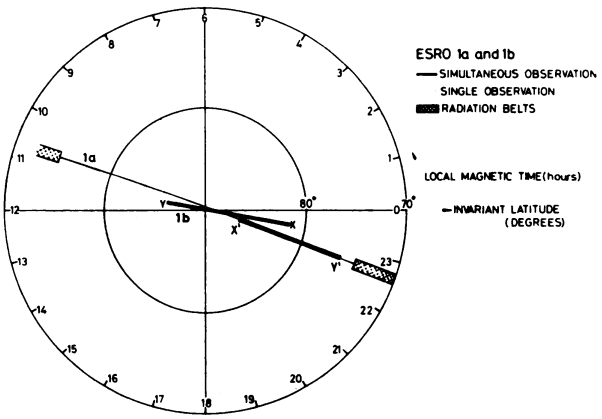

Figure 7-4. Spatial Position of ESRO IA and ESRO IB on an Invariant Latitude Versus Local Magnetic Time Map at the Time of the Existing Simultaneous Observation

The UT interval was approximately 1429 till 1433 on 3 November and the count rates observed are shown in Figure 7-5. It is apparent that these rates follow each other closely and in Figure 7-6 where we have plotted the count rate variations of ESRO IA versus those of ESRO IB, the alignment is evident. A simple statistical argument indicates that such a distribution of points has a 3% probability of arising by chance.

The separation of the two satellites above the polar cap is such as to persuade us that these variations are probably of a temporal rather than a spatial nature. It would be of interest to find micropulsation records for this period or

riometer records confirming the phonemena which, on the basis of the present evidence, must be taken as a coherent temporal fluctuation affecting a large area of the polar cap.

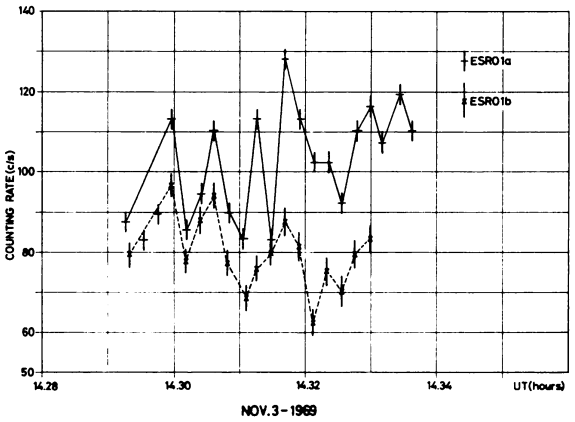

Figure 7-5. Counting Rate (E_p>500 keV) Versus Universal Time in a Simultaneous Pass of ESRO IA and ESRO IB Over the Central Part of the North Polar Region

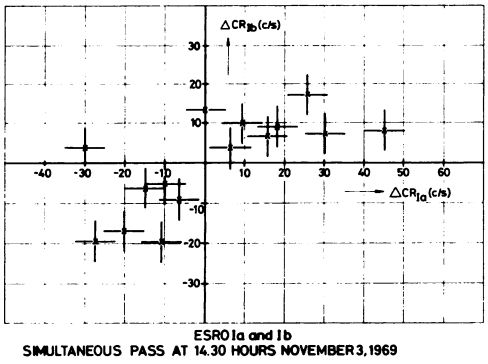

Figure 7-6. Proton Counting Rate (E_p>500 keV) Variations Observed by ESRO IB Versus Variations Observed Simultaneously by ESRO IA During the Coincident Pass Over the Polar Cap

Acknowledgments

We gratefully acknowledge the continuing encouragement from Dr. E. A. Trendelenburg. We wish to thank our ESRO colleagues engaged on the ERSO I project, technicians S. T. Ho and H. Huisman, and Dr. R. P. Lin, Berkeley, California for 45 keV electron data from Explorer 35.

References

Bostrom, C. O. (1970) Intercorrelated Satellite Observations related to Solar Events, ed. V. Manno and D. E. Page, p. 229. D. Reidel Publishing Co. Dordrecht, Holland.

Domingo, V. and Page D. E. (1971) J. Geophys. Res. 76: 8159.

Durney, A. C., Morfill, G.E., and Quenby, J. J. (1972) J. Geophys. Res. 77: 3345.

Engelmann, J., Hynds, R.J., Morfill, G.E., Axisa, F., Bewick, A., Durney, A.C., and Koch, L. (1971) J. Geophys. Res. 76: 4245.

Hudson, P. D. and Anderson, H. R. (1969) J. Geophys. Res. 74: 2881.

Jaeschke, R. (1970) ESRO SN-106 (ESTEC); ESRO, 1970.

Jackeways, R., Marsden, P. L., and Calder, I.R. (1970) Intercorrelated Satellite Observations related to Solar Events, ed. V. Manno and D. E. Page, p. 486. D. Reidel Publishing Co. Dordrecht, Holland.

Krimigis, S. M. and Verzariu, P. (1971) J. Geophys. Res. 76: 792.

Krimigis, S. M. and van Allen, J. A. (1967) J. Geophys. Res. 72: 4471.

Page, E. E. (1971) Space Research XI: 1189.

Paulikas, G. A., Blake, J. B., and Vampola, A. L. (1970) in Intercorrelated Satellite Observations related to Solar events. ed. V. Manno and D.E. Page, p. 193. D. Reidel Publishing Company, Dordrecht, Holland.

Solar Geophysical Data (1970) 309 part II: 78.

Thomas, G. R., and Dalziel, R (1970) Space Research X: 837.

Thomas, G. R., Dalziel, R., and Donaldson,W. (1970) Intercorrelated Satellite Observations related to Solar Events, ed. V. Manno and D. E. Page, p. 492. D. Reidel Publishing Co. Dordrecht, Holland.

Williams, D. J. and Bostrom, C. O. (1969) J. Geophys. Res. 74: 3019.

Contents

8. The 2 November 1969 Solar Proton Event Compared to Other West-Limb Flares

M. Gros, P. Masse*, J. Engelmann, E. Barouch*
Service d'Electronique Physique
Centre d'Etudes Nucleaires de Saclay
(*and C.N.R.S.)
(France)

Abstract

Observations of the 2 November 1969 solar proton event based on data from the HEOS A1 and ESRO II satellites are presented. The energy ranges covered are respectively 6 - 1500 and 26 - 400 MeV.

From an analysis of the active Carrington longitude at that time, and from H α cinephotographs of the sun, we could assign to this flare an heliographic longitude of 106° ±3° and estimate the flare time at ~ 0957.

The time profile for several energy windows between 5 and 1500 MeV is displayed. Its structure is compared with that observed for other flares situated near the west limb such as 18 November 1968 and 30 March 1969. For both November events, the time constant of the exponential decay is consistent with that calculated from convection dominated propagation, and the differential energy spectrum at late times has the same slope ~ 3.2. The 30 March event appears to have a quite different behavior.

8-1 INTRODUCTION

In this paper, we present data obtained aboard the ESRO spacecrafts HEOS A1 and ESRO II for the 2 November solar proton event.

We feel that one of the delicate points in interpreting this event is the identification of the responsible flare, and we have devoted some effort in this direction, using our own data on previous events of the same flare sequence, as well as optical data (kindly provided by Dr. Servajean of World Data Center 4, Meudon Observatory, whose patient collaboration is gratefully acknowledged). Some points concerning particle propagation theories in interplanetary space are discussed in the concluding section.

8-2 FLARE IDENTIFICATION

We have attempted to determine the location and time of the flare assumed to have given rise to the proton event by both a study of our own and published data. Due to a telemetry interruption from 0834 to 1159 on 2 November for the HEOS spacecraft, we are unable to determine the initial proton rise. Data from the ATS satellite published (Solar Geophysical Data) give the initial rise (>20 MeV) at 1045 2 November. We can, therefore, safely assume that the flare occurred before 1030. A number of flares are reported around this time (Solar Geophysical Data), but only one observatory interprets the observations as a 3 B flare starting at 1028, located N22W90 with a maximum at 1139. Other laboratories give lesser latitudes, typically N13.

Clues to the flare identification may be gathered from the sun's flare behavior during rotations 1553 and 1554. We have examined all flares and subflares in the region of the sun around the position of the 2 November flare. During rotation 1553, two "suspect" flare active longitudes may be distinguished: one, around Carrington 88°, which gave rise to 11 flares, and one around Carrington 68°, giving 43 flares, a few being of importance 1 or 2, between 17 October and 2 November. During rotation 1554, flare activity was predominantly around Carrington 78° giving over 120 flares, many of which were of importance 1 or 2, between 14 November and 30 November.

The longitude spread for these flares is quite small, about 3° to 4° rms deviation. Two trends may be noticed in the data for rotation 1553: (1) the number of flares around Carrington 88° decreased as a function of time, (2) the average longitude of the flares around 68° first declined, then rose sharply to about 73°. If we assume that the flare causing the 2 November event was part of this flare sequence (which we take to continue into rotation 1554), we can assign a Carrington

longitude of 104° to 109° on 2 November around 1000.

The H α cinephotographs of the sun (Figure 8-1) show ejecta appearing on the west limb at 1043. Bright loops have formed by 1139, at a projected height of 45,000 km above the limb. The brightness has decreased somewhat by 1230, when the maximum altitude of 60,000 km is achieved. These pictures may be compared to those presented by other workers for the 18 November 1968 and 10 November 1961 events (Krivsky 1969, Zirin 1966). The 18 November 1968 event, at longitude 87°W, displayed simultaneous brightening of the top and bottom ribbons. In the event under discussion, only the top brightens, enhancing our belief that the bottom is beyond the limb, and thus invisible.

When the prominence altitude is plotted as a function of time, the velocity v may be estimated (Figure 8-2). We estimate the velocity as 15 km/sec. approximately at 1043. This sets the flare time at a moment $R\ tg^2\theta/_{2v}$ earlier where R is the solar radius and θ the angular distance beyond the limb, that is, 24 to 26 minutes. Thus the flare time is estimated at 0957 to 1019. If we suppose that the bright spot visible at approximately 88°W at 1000 on Figure 8-1 is due to a sympathetic flare triggered by the surface wave (Moreton 1960) and assume a propagation velocity of 700 km/sec. to this wave, we obtain a flare time of 0955 to 0958.

This assignment leads to a very brief sun-earth transit time of energetic protons (~ 50 minutes for E >20 MeV protons). For the active region responsible for most of the proton flares of 1969, the transit time-longitude relationship has been discussed elsewhere (Barouch et al 1971), and it is not easy to fit the 2 November event point on the curve. Figures 8-3 and 8-4 show the solar flare activity in the northern hemisphere in 1968 to 1970, with the 1969 proton events picked out, and the transit time longitude relationship obtained for these solar flares. (The 2 November event was thought at the time to be at longitude 90°W approximately.)

8-3 PARTICLE OBSERVATIONS

The Saclay experiments aboard ESRO II and HEOS A1 have been previously described (Amram et al 1969, Barouch et al 1971). The energy ranges covered are respectively 26 - 400 and 6 - 1500 MeV. The hourly means observed by HEOS in four energy windows during rotation 1554 are displayed in Figure 8-5. From our data the rise time cannot accurately be determined due to a telemetry interruption, but it is of the order of one hour. A characteristic decay time of five hours fits all the data in the early phase of the decay, and is respectively 25, 18 and 13.5 hours in the 6 - 25, 24 - 63, 63 - 200 MeV windows at later times, on the

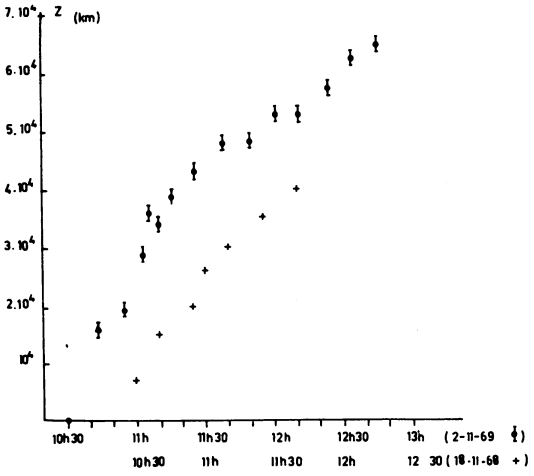

Figure 8-2. Projected Altitude of the Prominence as a Function of Time for the 2 November 1969 and 18 November 1969 Solar Flares. The 18 November data are derived from Krivsky (1969)

assumption of exponential decay. The decay is not exponential in the highest energy window. These characteristics are in qualitative agreement with convection dominated propagation as discussed by Forman (1971) and McCracken et al (1971).

After the main peak, a secondary peak, presumably associated with the same solar event, occurs (at low energies only) on 7 November at 2000, with its maximum on 8 November at 0400. This peak is preceded by an abrupt decrease of the low energy particle flux. Quite similar time profiles are visible on the Explorer 41 results (E > 10 MeV) (Solar Geophysical Data). We conclude that the maximum energy of the particles in the peak is between 10 and 25 MeV.

The energy spectra can best be obtained from our ESRO II data, which compensate the poor time coverage by good energy resolution (Figure 8-6). For energies less than ~ 100 MeV, the differential energy spectrum at late times is fitted by a power law in energy, with a γ index of 3.2 approximately (a good fit is obtained in a broader range of energies by an exponential in rigidity spectrum with a e-folding value of 55 MeV).

8-4 DISCUSSION

We have attempted to compare the observed time profiles with those of the 18 November 1968 and 30 March 1969 solar proton events which were also West-limb events. Figure 8-7 shows the observed time profiles (using both HEOS and ESRO II data) for these events in comparable energy windows. Striking similarities are seen for the November events, whereas the 30 March event is noticeably different: (1) the index of the differential spectrum is 1.6, compared to 3.2 for both November events, and (2) the characteristic decay time is much larger in all energy channels (about 3 times in the 63 - 200 MeV channel).

Probably a reasonable explanation for this behavior may be in the combined effect of two associated phenomena. The November events were both the first major events for the active region in question after a fairly long quiet period; on

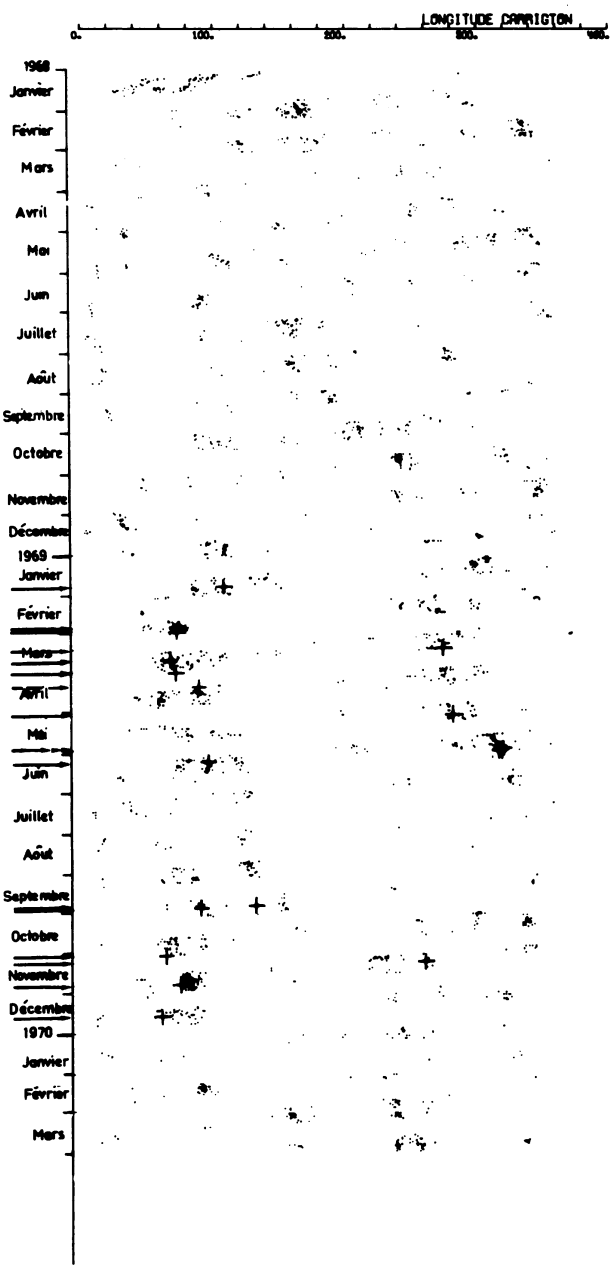

Figure 8-3. Solar Flares in the Northern Hemisphere in 1968, 69, 70 as a Function of Carrington Longitude and Time. All Flares and subflares are depicted. Crosses and arrows point out the proton events detected by HEOS in 1969

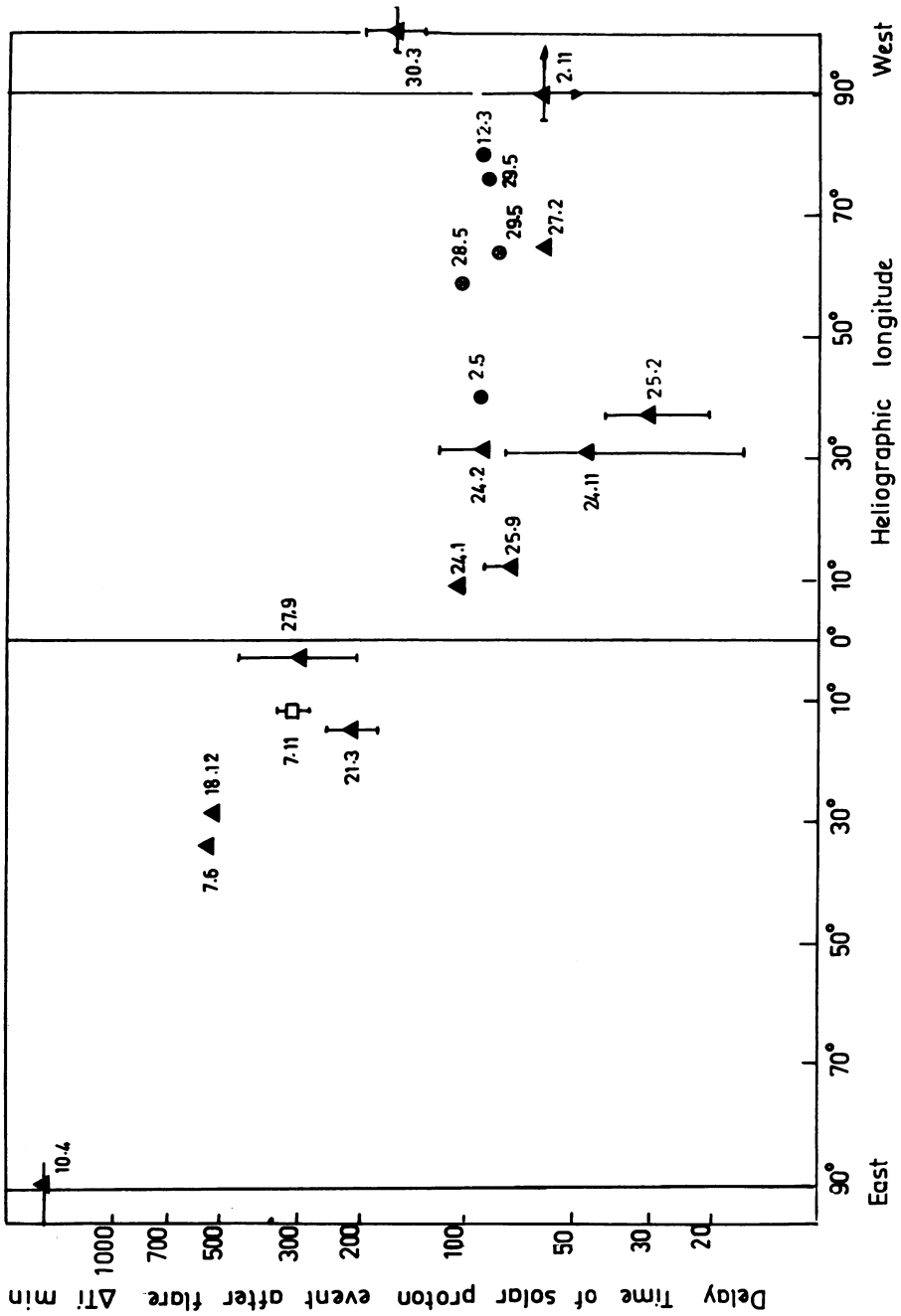

Figure 8-4. The Delay Time of the First Observed Particles as a Function of Heliographic Longitude for the Solar Flares of 1969, as Observed by HEOS

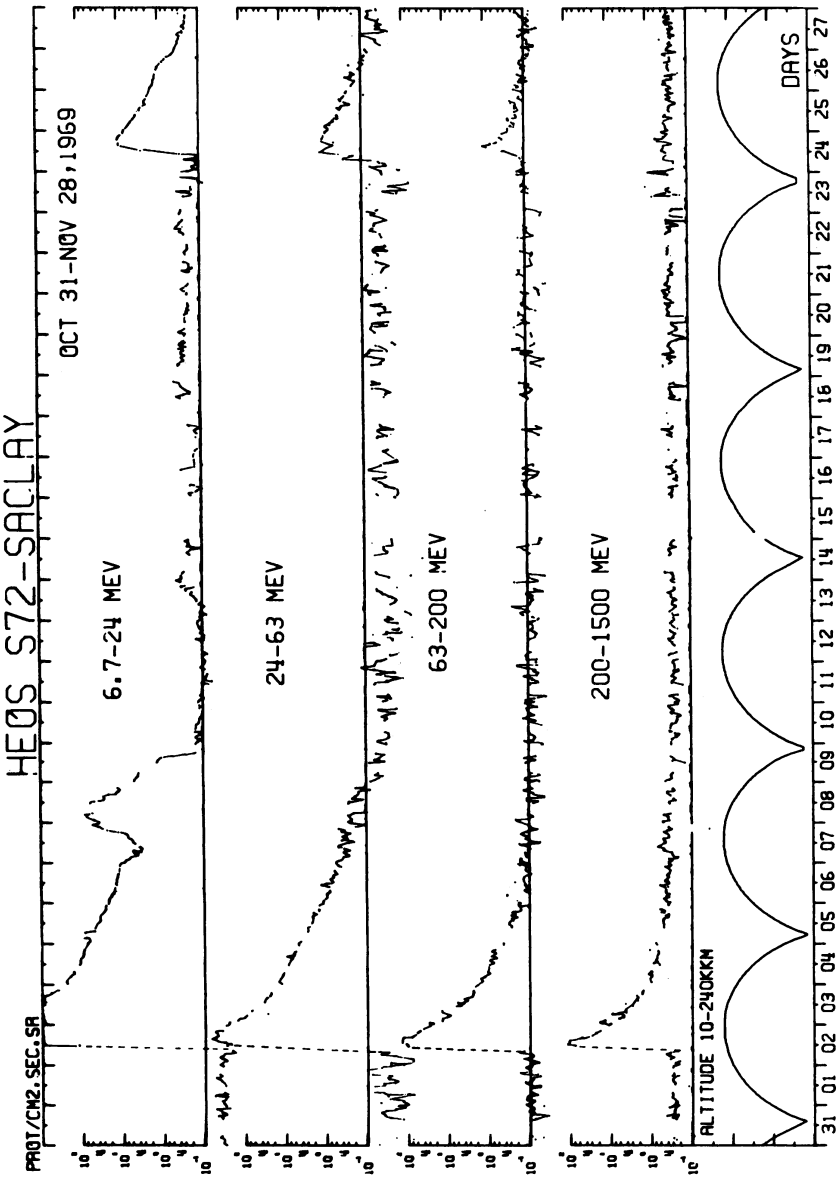

Figure 8-5. Hourly Mean Values of the Proton Intensity Observed by HEOS in the Energy Windows 6 - 25 MeV, 24 - 63 MeV, 63 - 200 MeV, 200 - 1 500 MeV. The intensity scale is logarithmic. The satellite altitude is shown on a linear scale below the intensity curves. Data around perigee correspond to passage through the earth's radiation belts

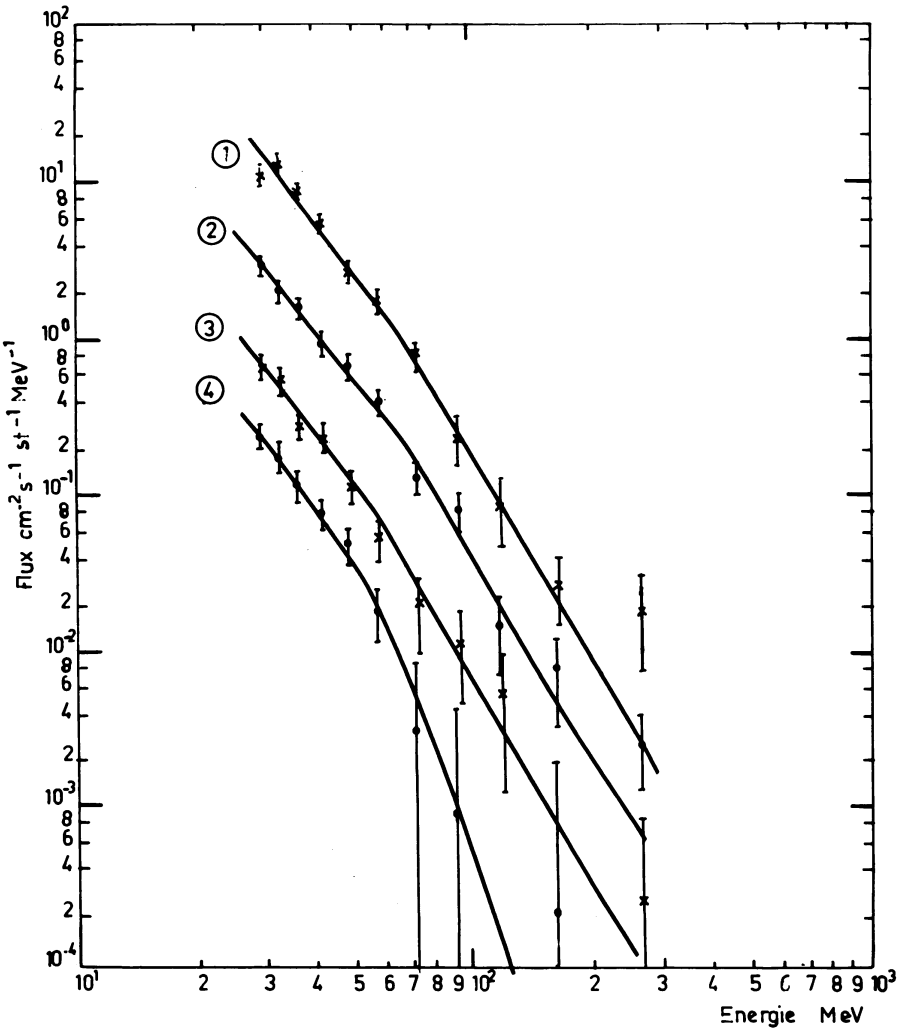

Figure 8-6. Energy Spectra of the 2 November 1969 Event as a Function of Time, as Observed by ESRO II. The spectra 1 to 4 were respectively registered on 2 November 2346, 3 November 1735, 4 November 0309, 4 November 2059, (that is, 13, 31, 41 and 58 hours after the assumed acceleration time)

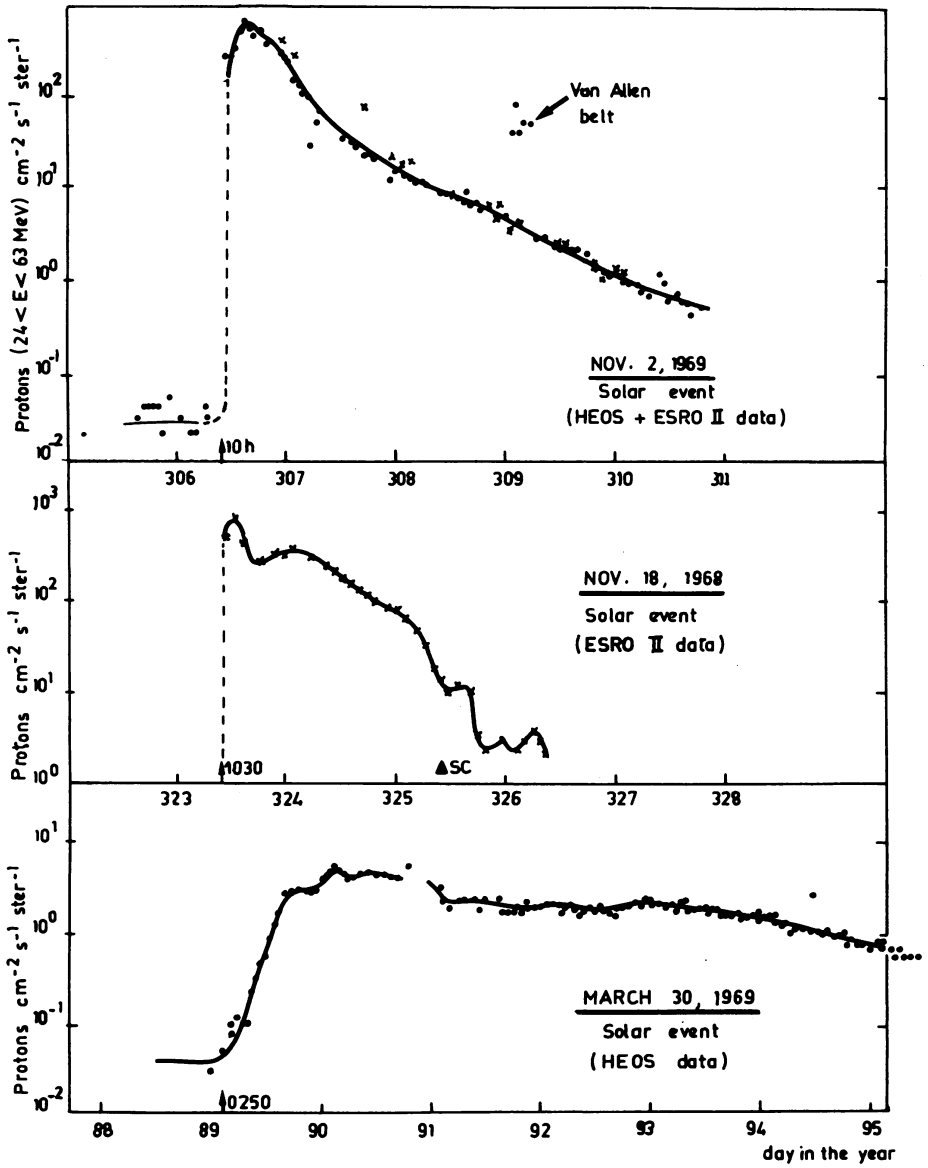

Figure 8-7a. Time Profiles in the 24 - 63 MeV Energy Range, as Observed by HEOS and ESRO II in the 2 November 1969, 18 November 1968 and 30 March 1969 Solar Proton Events. Crosses represent ESRO II data; circles HEOS data. The points are arbitrarily normalized to account for differences in instrumental calibration

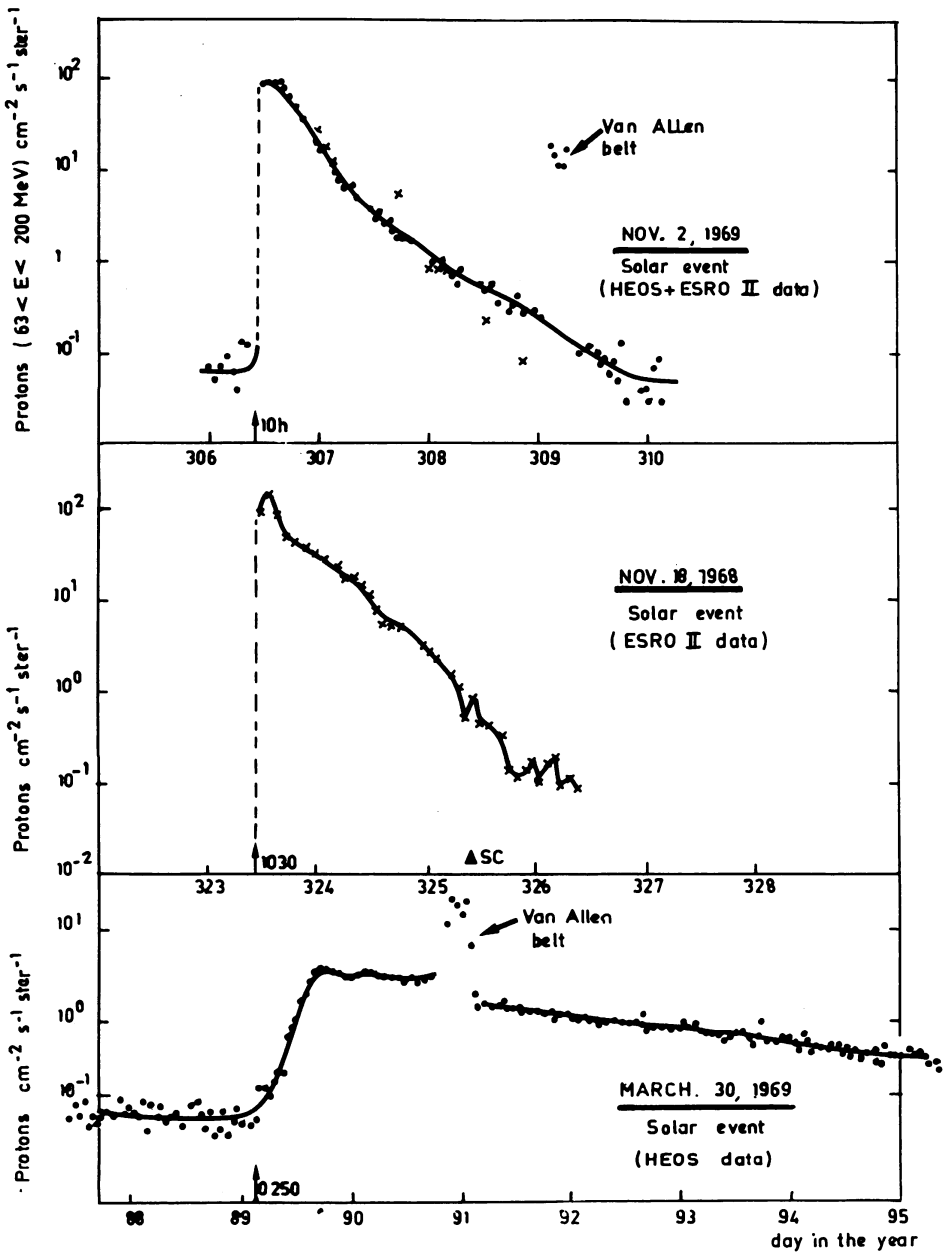

Figure 8-7b. As in a), for the 63 - 200 MeV Window

the contrary, the 30 March event was preceded by a proton event on 21 March on the same McMath plage. The consequences are twofold: (1) for the November events, the relatively low value of the solar wind velocity leads to a position of the interplanetary magnetic field line joining earth to sun far to the west of its average position, thereby ensuring "good connectivity" for flares far to the west, and (2) a very important role can be ascribed to the detailed physical characteristics of the sun at the time of the flare; a well developed magnetic regime may force the protons into complicated paths prior to their injection into interplanetary space ("diffusion" close to the sun, as the process can be called).

For simple conditions on the sun and interplanetary space as those prevailing for the November events, the data appear to support the convection dominated process in two respects: (1) the time constants we find for the later part of the decay are shorter than the "convective time constant" $\tau = 3r/2vc\ (2 + \alpha\gamma)$ (= 27 hours in our case) by an amount consistent with reduction by co-rotation effects in each energy window, and (2) the remarkable numerical agreement between the exponents of the energy spectra of the 2 November 1969 and 18 November 1968 events supports the view that the spectrum at late times is often determined in totality by the relative positions of observer and flare.

Another interesting feature of the comparison between these events is the neutron monitor behavior. The spectra for the 2 November 1969 and 18 November 1968 events as seen by satellite are very similar, both being power law in energy with $\gamma \sim 3.2$ under 100 MeV. The intensities are comparable, the solar situation quite close and the interplanetary conditions are not apparently very dissimilar. However, neutron monitors (at a cutoff >4.3 GeV) detected the 18 November event, whereas no neutron monitor increase is reported for 2 November.

One might look upon this fact as evidence for the hypothesis that states the solar acceleration mechanism has a high energy cutoff beyond which particles cannot be accelerated (Heristchi and Trottet 1971). However, it seems that for the 2 November event, the slope of the power law spectrum steepens above ~ 100 MeV, according to ESRO II observations; this can explain the absence of neutron monitor increase.

The complicated situation prevailing on 30 March is supported also by the neutron monitor data; the increase lasted for more than 28 hours and the peak maximum occurred some 6 hours after the arrival of the first neutrons. These times are respectively 0.2 and 1 hour for the 18 November event.

Once more we find that the 30 March 1969 event was quite different from both November events, although its location was roughly the same. This seems again to support the view that the solar conditions can play a very important role in the propagation process, particularly in the escape from the acceleration site.

As already discussed by Barouch et al (1971), the solar conditions were presumably quite similar for a number of proton flares in 1969. The accompanying table shows the main characteristics of the solar proton flares in 1969. The clustering of over half these flares around Carrington longitude 80°, together with the prevalence of a very large plage around this position for a large part of the year, lead us to suspect a semi-permanent "complex of activity" (Švestka 1969) lasting over several solar rotations and generating flares, some of which are observed as proton flares during its existence. We would therefore expect some similarities between these events since they are "related genetically". In fact, this was not found to be the case for the events discussed in the present study and the similarities, if they exist, can be revealed only by a statistical analysis of the characteristics of many proton events.

Table 8-1

OPTICAL FLARE					RADIO-EMISSION			X-RAYS		PROTON EVENT	
DATE	TIME (H.M.)	Importance	Carrington Longitude	Coordinates	Starting Time	Time of End	TYPE	Starting Time	Time of max	Onset Time H.M. ±mn	Delay Time mn
24. 1.69	0706	3N	106	N20 W09	0700	0850 est	IV est	0709	0730	0854 ±15	108
24. 2.69	2305	2B	72	N12 W31	2308	2430	IV	2306	2322	0030 ±30	90
25. 2.69	0900	2B	72	N12 W37	0904	1130	IV	0856	0918	930 ±10	30
27. 2.69	1348	2B	71	N13 W65	1405	1458	IV	1356	1412	1500 ± ?	72
12. 3.69	1739	2B	273	N12 W80	1731	1748	II, IV	1735	1750	1900 ±06	81
21. 3.69	0138	2B	66	N18 E15	0115	0210 est	IV est	0133	0208	1536 ±30	210
30. 3.69	0100	estimated	70	W100	0247	0400 est	IV est	0246	0302	0340 ±30	160
10. 4.69	0410		87	N11 E90	0352	0420	IV est II	0356	0404	0530(11.4.69)	1516
2. 5.69	1745	1B/2B	280	N08 W40	1748	1834	IV	1746	1758	1915 ±4	90
28. 5.69	1241	2B	318	N10 W59	1755	1800 est	IV ? V	1254	1301	1415 ±10	104
29. 5.69	0020	1B	316	N12 W64	0018	0025	V,III G	0019	0027	146 ± 6	86
29. 5.69	1939	1B	317	N10 W76	1938	1943	III GG	1938	1946	2114 ± 6	95
7. 6.69	0945	2N	94	N12 E34	0953	0959	IV		1007	1845 ±10	540
25. 9.69	0658	3N	130	N14 W13	0630	0740 est	IV est	0642 est	0720	0809 ± 7	71
37. 9.69	0350	3B	88	N10 E03	0359	0415	IV	0330 est	0430	0900 ±120	310
02. 11.69	1028 1102	1N	61	N13 W90	1000	1037	IV est	0939	1050	1159	90
07. 11.69	0324	2N ?	259	N13 E10 ?						0830 ±30	306
34. 11.69	0914	2B	73	N17 W31	0913	1050	IV est	0915	0929	1000 ±30	46
18. 12.69	0745	1N	58	N15 E28	0750	1105	III G	0732	0800	1622 ± 6	517

Acknowledgments

We acknowledge fruitful discussions with our co-experimenters aboard the ESRO II and HEOS A1 satellites, and with Dr. Servajean of Meudon Observatory. Our thanks are due to Prof. J. Labeyrie and Dr. L. Koch for their continual encouragement and help. This work was made possible through the efforts of the scientific and technical staff of the European Space Research Organization.

This work was supported in part by the Centre National d'Etudes Spatiales under contract 70/CNES/320.

References

Amram, Y., Axisa, F., Engelmann, J., and Koch L. (1969) Nucl. Inst. and Meth. 75: 181.

Barouch, E., Gros, M., and Masse, P. (1971) Solar Physics 19: 483.

Barouch, E., Englemann, J., Gros, M., Koch, L., and Masse, P. (1969) Proc. 11th Int. Conf. Cosmic Rays, Budapest.

Forman, M. (1971) J. Geophys. Res. 76: 759.

Heristchi, D. J., Trottet, G. (1971) Phys. Rev. Letters 26: 197.

Krivsky, L. (1969) Proc. 11th Int. Conf. Cosmic Rays, Budapest.

McCracken, K. G., Rao, U. R., Bukata, R. P., and Keath, E. P. (1971) Solar Physics (to be published).

Moreton, H. E. (1960) Astrophys. J. 65: 494.

Moreton, H. E. (1960) I. A. U. Symposium 22, North Holland, Amsterdam.
Solar Geophysical Data.
Švestka, Z. (1969) Solar Physics, 4: 18.
Zirin, H. (1966) The Solar Atmosphere, Blaisdell, Waltham.

Contents

9. Energetic Particle Measurements Aboard OV5-6 and OV1-19 Satellites

G. K. Yates and L. Katz
Air Force Cambridge Research Laboratories
Bedford, Massachusetts, U.S.A.

J. B. Blake, G. A. Paulikas, and A. L. Vampola
Space Physics Laboratory
The Aerospace Corporation
Los Angeles, California, U.S.A.

B. Sellers and F. A. Hanser
Panametrics, Inc.
Waltham, Massachusetts, U.S.A.

Abstract

Comparisons of solar particles fluxes during the event of 2 November 1969 as measured outside the magnetosphere (OV5-6) and over the polar caps (OV1-19) are presented. The onset times as a function of particle identity and energy are given. The temporal behavior of the alpha/proton ratio at 6.6 MeV/nucleon is shown.

9-1 INTRODUCTION

Comparisons of solar particle fluxes observed simultaneously by spacecraft within and outside the magnetosphere have been reported by numerous authors (Krimigis et al 1967, Van Allen et al 1971, Engelmann et al 1971). These earlier observations have established that solar particles reach the earth's polar caps with high efficiency. Occasionally strong north-south asymmetries are observed (Evans and Stone 1969, Van Allen et al 1971). These have been attributed to anisotropies in the particle flux in interplanetary space and a direct connection between the terrestrial field and the interplanetary field (Van Allen et al 1971).

The present report concerns a comparison between solar particle fluxes as observed interior to and exterior to the magnetosphere during the solar particle event of 2 November 1969. The purpose of this paper is to report a comparison of interplanetary and polar cap fluxes of solar particles (electrons, protons and alphas) over a broad energy range, the arrival times of various particle species, and the evolution of the alpha to proton ratio during the event.

9-2 SPACECRAFT AND INSTRUMENTATION

Observations are presented of solar particles during the 2 November 1969 event obtained from the satellites OV1-19 (1969-25C) and OV5-6 (1969-46B). Table 9-1 lists some pertinent orbital parameters. These spacecraft provide a

Table 9-1. Basic Orbital Parameters

	OV1-19	OV5-6
Perigee (km)	465	16,341
Apogee (km)	5,737	112,196
Inclination	104.7°	33.3°
Period (minutes)	154	3,115

comparison of the solar particle fluxes measured outside the magnetosphere with the fluxes above the polar regions. At 1000 UT, 2 November 1969 just before the arrival of solar particles, OV5-6 was at 106,400 km altitude, 79.7° west of the sun and 1.8° south of the ecliptic. It was outbound and near apogee during the onset of the 2 November event and was outside of the magnetosphere most of the day following the start of the event.

The relevant instruments aboard OV1-19 consisted of a pair of magnetic spectrometers which measured the electron spectra from 53 keV to 5.1 MeV in 24 channels, and two proton spectrometers which provided proton spectra from 430 keV to 126 MeV in 12 channels.

Data from two instruments on OV5-6 are reported here. One is an omnidirectional solar x-ray detector consisting of NaI (T1) scintillation crystal with four energy channels - 19.4 to 76.5, 76.5 to 232, 232 to 1175, and greater than 1175 keV. Electrons with energies $\gtrsim$ keV and protons with energies $\gtrsim$ 17 MeV can penetrate the shielding surrounding the scintillator. Proton events will appear mainly in channel 4; minimum ionizing protons are also counted in this channel.

The second OV5-6 instrument is a proton-alpha semi-conductor telescope with nine proton energy channels from 1.25 to 100 MeV and three alpha channels from 20 to 100 MeV. The lowest proton channel is also sensitive to electrons $\gtrsim$ 280 keV; this characteristic will be used in the following analysis. All fluxes are spin averaged.

9-3 PARTICLE ONSET TIMES

Data from the OV5-6 are available before, during and immediately following the beginning of the solar event of 2 November. Unfortunately, at these early times in the event, data on the solar particle fluxes over the polar caps are not available.

Particle arrival times are shown in Figure 9-1. The particles first observed are solar electrons. This is unambiguously determined by the observations that only the lowest channel of the proton-alpha telescope and the three lowest channels of the scintillation counter count. If the scintillation counter were detecting energetic protons, all channels would respond and the upper telescope channels would count; if the telescope were counting only low energy protons, the scintillation detector would not count. With reasonable assumptions of electron counting efficiencies, the rates of the two instruments agree. Because of the efficiency uncertainties, these fluxes are not given in absolute units.

No rise in the count rate of the high energy channel of the scintillation counter was observed until 1045 UT. This count rate can be due to electrons $\gtrsim$ 1.2 MeV and/or protons $>$ 100 MeV. Since the onset of the 40-100 MeV protons began at 1058 UT and substantial fluxes of $>$ 1.1 MeV electrons were present by 1045 (Lanzerotti and Maclennan, this volume) it is most probable that this initial response of the scintillation detector was due to electrons and not relativistic protons. That electrons with MeV-energies were produced in substantial numbers by the solar event is shown in Figure 9-2 from the OV1-19 polar cap data.

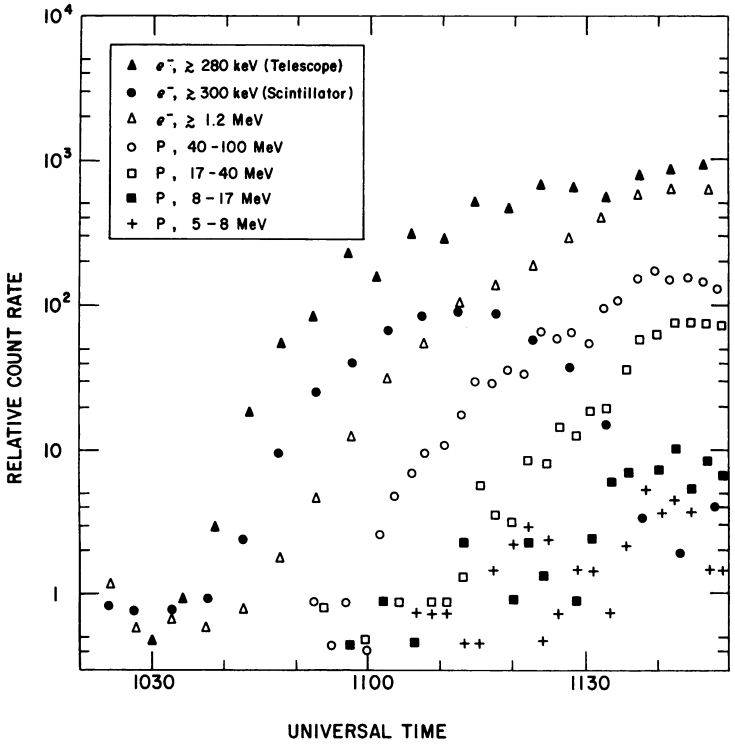

Figure 9-1. The Arrival Times of Particles at OV5-6, 2 November 1969

Solar X-rays as a source of the count rate in the scintillation detector are ruled out by the Solrad 9 results (World Data Center Report, 1971).

Table 9-2 summarizes the particle arrival times as measured by OV5-6.

9-4 PROTON SPECTRA NEAR THE EARTH AND OUTSIDE THE MAGNETOSPHERE

Figures 9-3 through 9-7 show the proton energy spectra at selected times in the days following the 2 November event. Observations from the OV1-19 during north polar passes are compared with the near coincident OV5-6 measurements outside the magnetosphere. The south polar cap data exhibited marked latitudinal structure (Blake et al 1970) for the first day, clearly indicative of impeded access of solar protons. Later in the event when the structure disappeared, the solar particle fluxes over the northern and southern polar caps were similar.

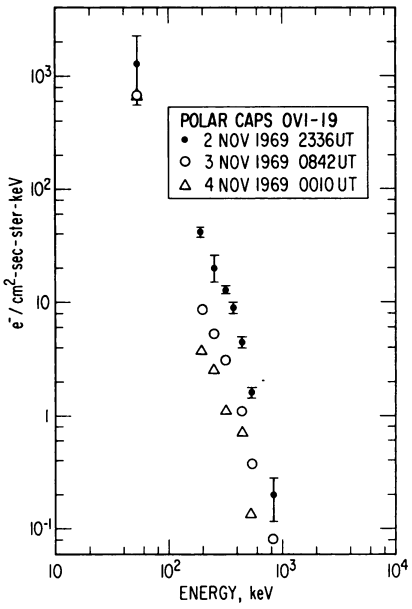

Figure 9-2. Spectrum of Solar Electrons as Observed by the Magnetic Electron Spectrometers Aboard OV1-19 at High Latitudes Over the North Polar Cap

The only apparent disagreement between the OV1-19 and OV5-6 observations is most clearly illustrated in Figure 9-3. At energies greater than 20 MeV, the OV5-6 flux is substantially greater than that observed over the polar caps by OV1-19. At the same time, there are no differences in the fluxes at the lower energies. The magnitude of the disagreement lessens later in the event when the spectrum softens. A problem with the efficiency calibrations of the upper channels of the OV5-6 instrument is suspected; a comparison of the OV1-19 data with OGO-6 shows good agreement (Mosley, this volume).

9-5 TEMPORAL BEHAVIOR OF PROTONS AND ALPHA PARTICLES

By 0115 UT, 4 November the proton spectrum had become softer and the flux was lower at all energies. Subsequently, the fluxes decayed monotonically with a time constant which was independent of energy. This decay is illustrated in Figure 9-8.

The alpha/proton flux ratio for 6.6 MeV/nucleon is shown in Figure 9-9 as a function of time. These results are from the OV5-6, except for the three open circles which were measured on rockets fired from Fort Churchill, Manitoba (reported by Sellers and Hanser, this volume). They also agree with the Explorer 41 results reported by Maclennan (this volume).

9-6 SUMMARY

9-6.1 Large fluxes of electrons were produced in this event. The electrons reached the vicinity of the earth substantially earlier than the protons and alpha particles.

9-6.2 The interplanetary and north polar cap intensities tracked well at energies $\gtrsim$20 MeV. The difference at higher energies observed early in the event is believed to be an instrumental effect.

Table 9-2. OV5-6 Particle Arrival Times

UT ± 1 min	Particle Species	Energy (MeV)
1036	Electrons	0.25
1045	Electrons	1.21
	Protons	100*
1058	Protons	40 - 100
1112	Protons	17 - 40
1120	Protons	8 - 17
1121	Protons	5.3 - 8
1125	Alphas	20 - 32

*Detector actually measures protons greater than 17.2 MeV but onset times of p < 100 are given in the following lines.

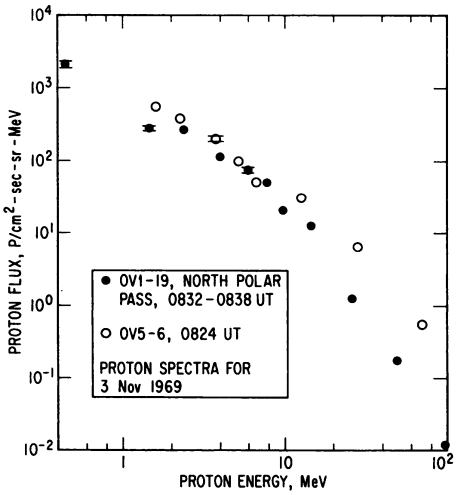

Figure 9-3. Spectra of Protons Observed Outside the Magnetosphere (OV5-6, Open Circles) and Inside the Magnetosphere Over the North Polar Cap (OV1-19, Solid Symbols) Between 0832 and 0838 UT on 3 November 1969

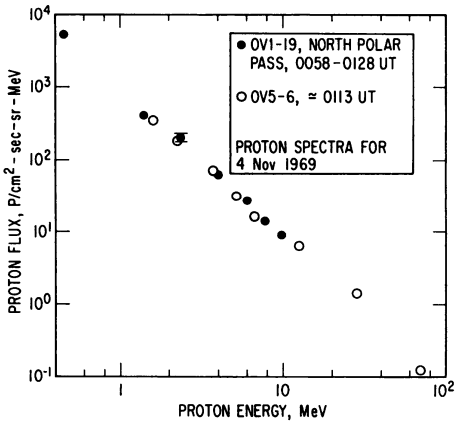

Figure 9-4. Same as 9-3, Except... Between 0058 and 0128 UT on 4 November 1969

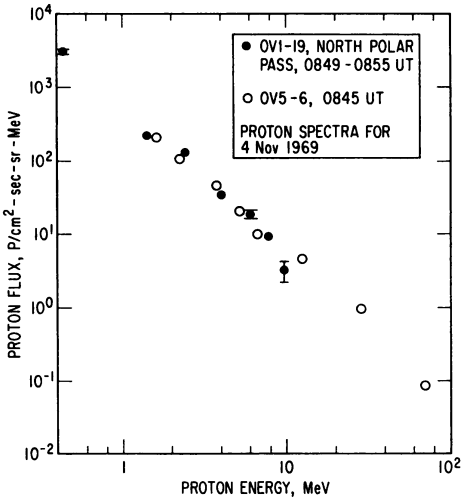

Figure 9-5. Same as 9-3, Except... Between 0849 and 0855 UT on 4 November 1969

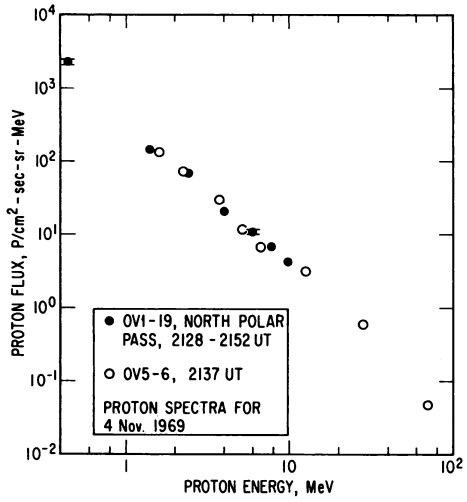

Figure 9-6. Same as 9-3, Except... Between 2129 and 2152 UT on 4 November 1969

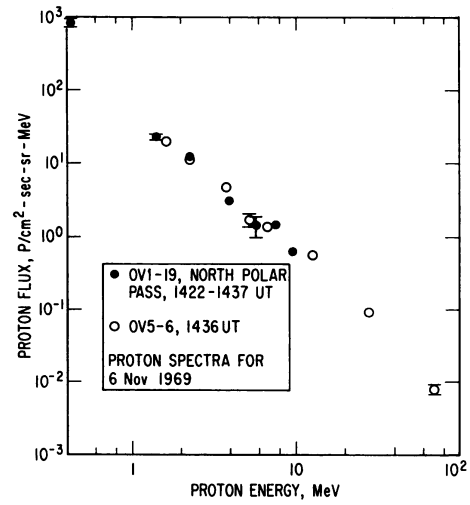

Figure 9-7. Same as 9-3, Except... Between 1422 and 1437 UT on 6 November 1969

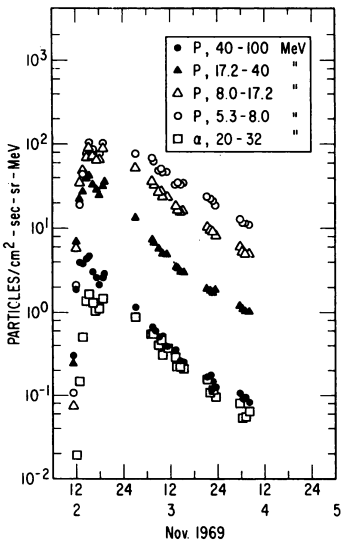

Figure 9-8. The Time History of the Proton Event of 2 November as Observed by Proton/Alpha Detector OV5-6 Outside the Magnetosphere

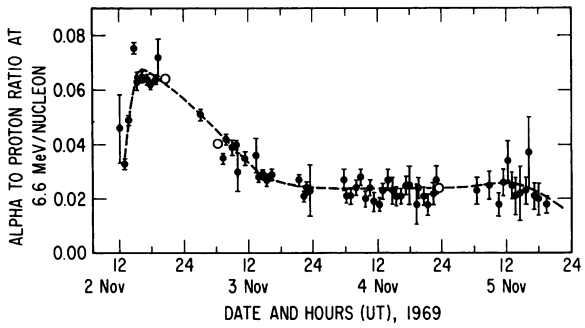

Figure 9-9. The Variation of the Alpha to Proton Ratio vs Time During Solar Particle Event of 2 November 1969. OV5-6 data are the solid symbols, while data from three rocket experiments fired from Ft. Churchill are indicated by open circle

9-6.3 The relative alpha abundance rose rapidly to ~ 7 percent shortly after the beginning of the event and then declined to ~ 2 percent after 36 hours.

References

Blake, J. B., Paulikas, G. A., and Vampola, A. L. (1970) A Compilation of the Latitudinal Profiles of Solar Protons and Electrons Over the Polar Caps during the Event Beginning 2 November 1969, EOS 51: 800.

Engelmann, J., Hynds, R. J., Morfill, G., Axisa, F., Bewick, A., Curney, A. C., and Koch, L. (1971) Penetration of Solar Protons Over the Polar Cap during the February 25, 1969 Event, J. Geophys. Res. 76: 4245.

Evans, L. C. and Stone, E. C. (1969) Access of Solar Protons into the Polar Cap: A Persistent North-South Asymmetry, J. Geophys. Res. 74: 5127.

Krimigis, S. M., Van Allen, J. A., and Armstrong, T. P. (1967) Simultaneous Observations of Solar Protons Inside and Outside the Magnetosphere, Phys. Rev. Letters 18: 1204.

Van Allen, J. A., Fennell, J. F., and Ness, N. F. (1971) Asymmetric Access of Energetic Solar Protons to the Earth's North and South Polar Caps, J. Geophys. Res. 76: 4262.

World Data Center A, Report UAG-13 (1971) Data on the Solar Proton Event of November 2, 1969 Through the Geomagnetic Storm of November 8-10, 1969.

Contents

10. Satellite Measurements of Energetic Solar Protons, Alpha Particles, Electrons, and Auroral Particles During the 2 November 1969 PCA Event

J. B. Reagan, W. L. Imhof, and E. E. Gaines
Lockheed Palo Alto Research Laboratory
Palo Alto, California 94304

Abstract

During the 2-5 November 1969 PCA event, high-resolution differential spectral measurements of energetic protons (1-46 MeV), alpha particles (7-22 MeV), and electrons (0.4 - 1.9 MeV) were made at altitudes of 466 to 583 km over both polar caps and in the vicinity of Fort Churchill, Canada, with the polar orbiting OV1-18 satellite. Simultaneous measurements of the auroral particle fluxes at several pitch angles and in several bands over the range 0.5-50 keV were also made aboard the same satellite.

Significant particle fluxes of energetic protons, alpha particles and electrons were observed over the poles and in the vicinity of Fort Churchill during the entire event. The solar protons exhibited significant spatial structure across the entire polar cap regions early in the event. A pronounced north-south asymmetry in both the protons and alpha particles below energies of approximately 20 MeV was observed on 2-3 November. On 3 November the north polar cap fluxes were a factor of 3 higher than those over the south polar cap. Complex proton spectra were obtained during this period which could not be described by a single power-law or exponential shape. Evidence of a peak in the proton spectra in the vicinity of 3.5 MeV was also observed. Comparisons of these with the Explorer 41 and Vela 5B satellite data show good agreement at all times throughout the event.

Solar electrons, in contrast, exhibited smooth spatial profiles across the polar caps ($\wedge > 72^\circ$), showed no evidence of north-south asymmetry, and their spectra could be described by a single power-law shape.

Comparison of the differential spectra over the polar caps ($\wedge > 80^\circ$) and in the vicinity of Fort Churchill ($\wedge = 68.7^\circ$) confirm that the latter location was within the polar plateau region during all of the local night-time passes of the satellite. On three of the four daytime passes, however, the latitude of Fort Churchill was well below the polar plateau and significantly different spectra were obtained at these times.

Precipitating fluxes were observed on every satellite pass, and the energy input to the atmosphere from auroral particles which could penetrate to altitudes below 95 km was often comparable to, or larger than, that from the energetic solar particles. Variations were observed in the magnetic latitudes at which the auroral fluxes were precipitated, but no systematic shift in latitude was observed during the PCA event. Data on the locations, intensities and integral energy fluxes of the auroral particles are included.

10-1 INTRODUCTION

Measurements associated with polar cap absorption events are complicated by the fact that the incident particle environment can be complex and can vary considerably from one event to another. These variations typically involve the intensities, energy spectra and particle compositions. During any given event the particle flux incident over the polar caps is often not describable by a few simple parameters. Solar protons have been observed to display pronounced spatial/temporal variations in flux over the polar caps (Reid and Sauer 1967, Williams and Bostrom 1967, Blake et al 1968) and the energy spectra are sometimes observed to display rapid spatial/temporal variations; the fluctuations perhaps being more pronounced at the lower energies (Reagan and Imhof 1969). In addition, large asymmetries in the solar proton fluxes as observed at the same time over both polar caps have been reported during certain solar particle events by Evans and Stone (1969) and by Van Allen et al (1971). The radiation environment is further complicated near the latitude of magnetic cutoff. For several years it has been known that the cutoff latitudes deviate significantly from the predictions of Stormer for a dipole field (Gall et al 1968, Smart et al 1969).

Alpha particles and electrons have also been observed over the polar caps during certain solar events in addition to protons. These so-called "contaminates" of the solar proton events have been less thoroughly measured due partly, in the case of alpha particles, to the lower intensities at comparable energies, and in the case of energetic electrons, to the fact that they appear to be always accompanied by energetic protons, but not vice versa (Vampola 1969, Reagan and Imhof 1969).

In addition, the instrumentation flown at both low altitudes and in interplanetary space has tended to favor observations of protons. Although electrons in the hundreds of keV energy range do not appear to be a common feature of the polar cap region, they may appear during PCA events with significant intensities and a hard spectrum. For example, in the solar flare event of 11 April 1969, appreciable fluxes of energetic electrons were observed, whereas in the next two events, solar electrons were present in considerably smaller numbers (Reagan and Imhof 1969). In contrast to protons, energetic solar electrons have displayed no spatial structure over the entire polar zone (Vampola 1969), that is, electrons of solar origin seem to have uniform access to the polar caps. However, the magnetic cutoffs for the electrons appear to be significantly different than for the protons (Imhof et al 1971). Solar alpha particles in the polar cap regions also appear to behave differently than protons. In particular, alpha particles have given no evidence of durable trapping (Blake et al 1968).

The "auroral contamination" of PCA events must also be considered, particularly at latitudes near the auroral zone, which includes Fort Churchill at 68.7° magnetic latitude. O'Brien (1962) has shown that this precipitation is a continuous phenomenon, and even on those occasions when the intensity is below the threshold for the production of a visible auroral form, the effects on the properties of the ionosphere may be considerable. In fact, the precipitation of those energetic electrons which can penetrate most deeply and will therefore have the most significant effects on the D-region experiments, is not well correlated with the precipitation of the softer electrons which are most effective in producing visible aurora. In addition, the position of the auroral zone changes with the geomagnetic activity. Generally, when the level of activity is low, the auroral precipitation may be confined to the region poleward of the normal auroral oval. Conversely, if the level of activity is sufficiently high, the auroral activity may all be equatorward of the region of the PCA-69 rocket experiments. Further complications in interpretation can result from the occurrence of relativistic electron precipitation events (Bailey 1968) which appear to be related to the trapped fluxes in the radiation belts. These electrons are precipitated in the vicinity of the boundary of the trapping region at L values of ~ 4 to ~ 8.

The intent of this paper is to present the characteristics of the particle radiation environment during the 2-5 November 1969 solar particle event as measured at low altitudes by instrumentation aboard the polar-orbiting satellite OV1-18. Satellite overpasses in the vicinity of Fort Churchill, Canada and the north polar cap region were specifically coordinated with Operation PCA 69 during this period. Data on the mass composition and energy spectra of the energetic solar particles, and on the temporal and spatial variations of these particles over both polar caps

and in the vicinity of Fort Churchill, have been obtained. The general locations, intensities, and energy input of the auroral particle fluxes during the PCA event have also been mapped.

10-2 SATELLITE INSTRUMENTATION

The OV1-18 satellite was launched on 18 March 1969 into a polar orbit with an apogee of 609 km, a perigee of 467 km, and an inclination of 98.8 degrees. A large complement of the satellite payload was provided by the Lockheed Palo Alto Research Laboratory. Several of the experiments contained particle detectors which were sensitive to the low-energy protons, electrons, and alpha particles observed during auroral activity. In addition, a high-sensitivity particle spectrometer was included which measured the higher energy protons, electrons, and alpha particles observed during polar-cap-absorption (PCA) events. Table 10-1 contains a list of the instruments in the OV1-18 payload that provided data on both high- and low-energy particle flux inputs to the polar regions during the period 2-5 November 1969.

The instrument payload provided both differential and integral measurements of electrons and protons. Low-energy differential measurements were performed with channel multiplier detectors in conjunction with magnetic analysis. The CME and CMP detectors are examples of this type of detector for electrons and protons, respectively. The typical $\Delta E/E$ for these detectors was 0.8. High-energy differential measurements for electrons from 0.4 to 1.9 MeV, and for protons from 1.2 to 46 MeV, were accomplished with a particle spectrometer (PRM) consisting of a semiconductor dE/dX detector and a plastic scintillation E-detector. Differential pulse-height analysis providing contiguous coverage with 15-channel resolution was performed on pulses from each of the two detectors. Sensitivities as high as 0.1 particles/cm^2-second have been achieved. Low-energy integral measurements were performed with either channel multiplier or scintillation detectors in conjunction with foil threshold determination. The CFE and CFP instruments and the VED, TED and TEP instruments are examples of these two types of detectors, respectively. A high-energy integral proton measurement above 70 MeV was also obtained with the particle spectrometer. Measurements of electrons in the energy range 0.2 to 19 keV, and of protons from 1 keV to greater than 38 keV, were performed at several orientations to provide an angular distribution of the incoming particles. Finally, alpha particles were measured at 1, 3 and 8 keV and in the interval 7-20 MeV.

Particle flux data on several PCA events have been obtained from the above instruments during the period 22 March 1969 to 24 August 1970. Continuous

Table 10-1. LMSC OV1-18 Experiment Payload

Instrument Payload	Particle Type	Differential Measurements Central Energy (keV)	Integral Measurements Threshold (keV)	Nominal Orientations With Respect to Zenith (deg)
VED	e		0.2, 1.2	0, 55, 90
CME	e	1.2		0, 55, 90, 180
CME	e	2.5		0, 55, 90
CME	e	3.5		180
CFE	e		7.5	90
CME	e	5.4		0, 55, 90
CFE	e		14	90
CME	e	10.5		180
CME	e	12.3		0, 55, 90
TED	e		21	55
CME	e	27		0
CME	e	31		180
CFE	e		40	90
CME	BKGD	--	--	0
CMP	p	1		55
CMP	p	3		55
TEP	p		3	55
CFP	p		5	55
CFP	p		7.5	55
CMP	p	8		55
CFP	p		8.8	180
CFP	p		9	0
CFP	p		14	90
CFP	p		24	55
CFP	p		27	180
CFP	p		38	0, 55, 90, 180
CFP	p		800	55, 180
CZU	UV BKGD	--	--	55
CFA	H^+,He^+,He^{++}	1		0
		3		
		9		
PRM	e	0.4-1.9 MeV		90
	p	1.2-5.0 MeV		
	p	10-46 Mev		
	p		70 MeV	
	α	7-20 MeV		

worldwide coverage was obtained through the use of an on-board tape recorder. Significant energetic fluxes of precipitating protons were observed on a large fraction of the polar crossings over the entire time period March through June 1969. Figure 10-1 shows the counting rates observed in several channels of the high-energy spectrometer during polar crossings between 22 March and 5 November 1969. Also shown are the 30 MHz riometer absorption data (Masley 1969)

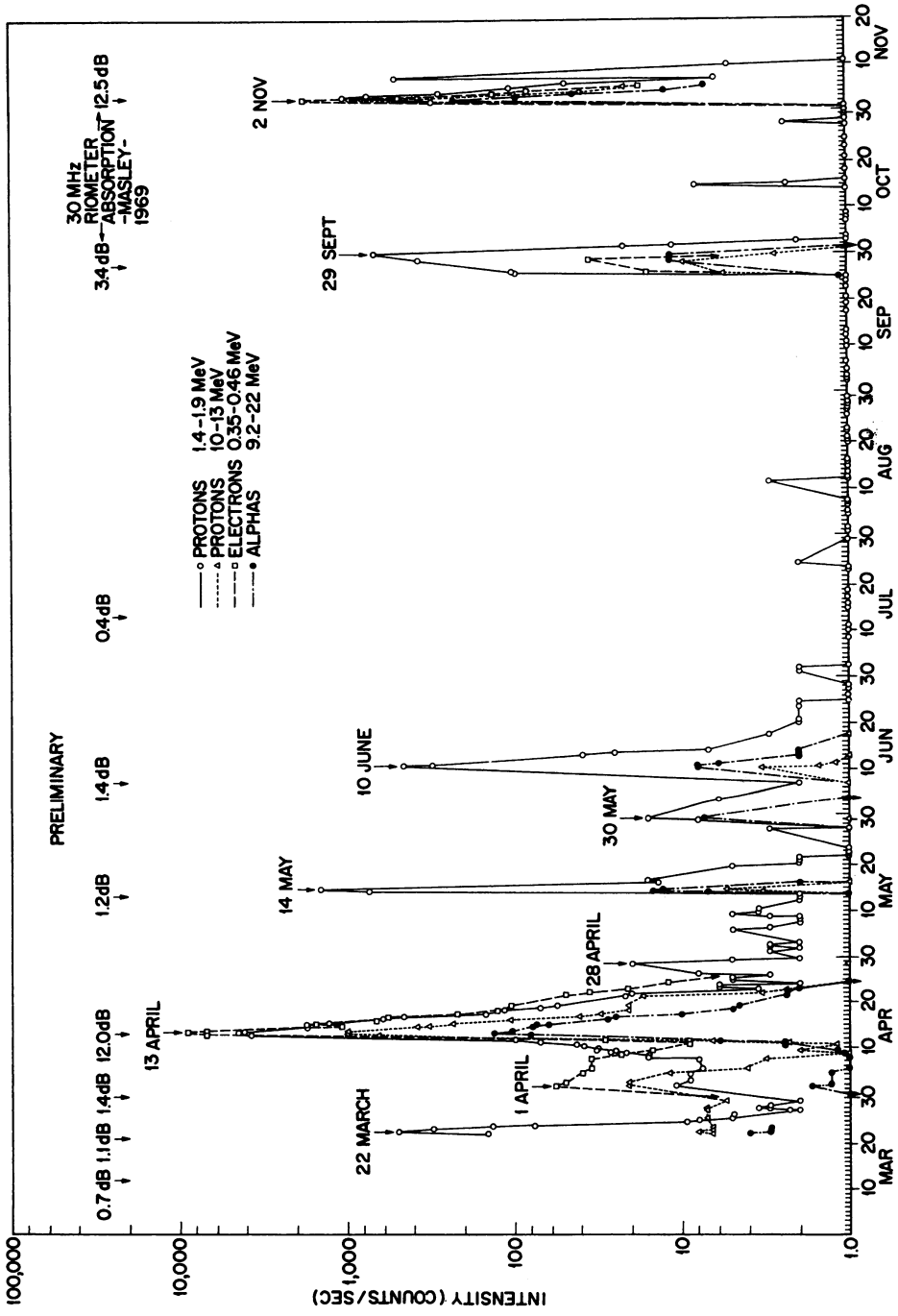

Figure 10-1. Observed Counting Rates With the OV1-18 Satellite of Protons, Electrons and Alpha Particles Over Both Geomagnetic Poles During the Period March to November 1969. The occurrence and magnitude of 30-MHz absorption in ground-based riometers in the polar region is also shown

from several polar stations over the same time period. The expected general correlation is found between the influx of the higher energy protons into the polar regions and the riometer absorption. The correspondence is less pronounced for the lower energy protons since the riometer has significantly reduced sensitivity to the ionospheric effect produced by these protons.

Figure 10-1 also illustrates the wide variations encountered during PCA events in regard to particle composition, intensity, and energy spectrum. During the intense event which reached a peak on 13 April, electrons and alpha particles were also observed with the protons over both polar regions for a 14-day period. During the less intense PCA events of 14 May and 10 June, the proton spectra were considerably softer than the above event. These latter events were also characterized by the absence of significant fluxes of higher energy electrons. These observations are consistent with the findings of Vampola (1969) who concluded that electrons in this energy range are not always present in PCA events, but that electrons are never present in the absence of comparable energy protons. Because of the wide variations encountered, the concept of an average polar-cap event is not an easily interpretable quantity. Accordingly, it is important to perform simultaneous measurements on the various particle types in any given event with high sensitivity and with high spatial, temporal and spectral resolution.

10-3 ENERGETIC PARTICLE DATA

In Figure 10-2 are shown the raw outputs of the high-energy particle channels for a typical pass over the north polar region. This plot is presented primarily to provide an indication of the nature of the data and the fact that the spectra and intensities undergo pronounced variations at times in the polar cap as well as near Fort Churchill. In addition to the spatial variations, one can see the fluctuations in counting rate associated with the slow spinning of the satellite. These energetic particle data were taken with the PRM instrument which detects protons in the energy range 1.2 to 46 MeV and integral above ~ 70 MeV, electrons in the range 0.4 to 1.9 MeV and alpha particles in the range 7 to 20 MeV. Acceptable pulses from the solid-state dE/dX-detector and the plastic scintillation E-detector as determined by various combinations of coincidence logic, were analyzed with separate 15-channel pulse-height analyzers of the analog-to-digital type. The binary-coded channel addresses were parallel shifted to two complementary readout systems; one being digital in nature and the other analog, each providing contiguous coverage in energy. The data shown in Figure 10-2 are the analog logarithmic ratemeter outputs. Analysis of pulses in the E-detector was accomplished in two alternate 16-second modes of operation corresponding to the

Figure 16-2. Raw Outputs of the High-Energy Particle Channels for a Typical Pass Over Fort Churchill

measurement of protons and of electrons. The occurrence of these two modes of operation is readily apparent in the outputs of channels E1, E2, E3, E7 and E8. The data shown at the left of each energy channel correspond to an automatic calibration sequence in the instrument.

Figure 10-2 illustrates that the magnetic latitude corresponding to the location of Fort Churchill, 68.7°, was within the proton and alpha particle polar plateau at 1938 UT on 2 November. Fort Churchill at this time, however, was not within the electron polar plateau. This is clearly evident in Figure 10-3, where the precipitating fluxes of energetic protons and electrons are plotted as a function of invariant latitude for the same time period. The spin of the satellite has been removed by accepting data only where the view angle was in the upper hemisphere near zero degree pitch angle. The precipitating electron fluxes at an average energy of 0.44 MeV exhibit a smooth flat profile over the high latitude region of the polar cap with sharp decreases evident at latitudes below about 72.5° on the dayside and 74.5° on the nightside. The smooth profile of the electron fluxes, in contrast to the structured proton profiles at high latitudes, is strongly suggestive of different access mechanisms for solar protons and electrons into the magnetosphere. Solar electrons appear to have ready access to the high latitude "open" field lines. This characteristic of the solar electrons has been observed in other solar particle events also (Imhof et al 1971). At a magnetic latitude of 68.7°, the electron fluxes were approximately a factor of 7 lower than in the electron polar plateau at this time.

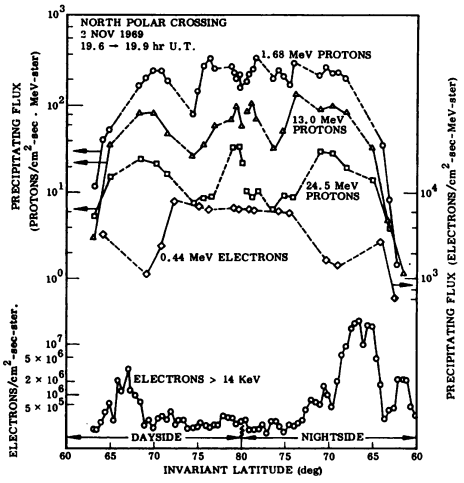

Figure 10-3. Precipitating Fluxes of Solar Protons at Energies of 1.68, 13.0, and 24.5 MeV and of Solar Electrons of Energy 0.44 MeV as a Function of Invariant Latitude in the Northern Polar Region at 19.6-19.9 Hours UT on 2 November 1969. The locations of the > 14-keV auroral electron fluxes are also shown

Variations in the proton fluxes by factors of 3 or more are evident at all proton energies at this time. The proton fluxes near the magnetic latitude of Fort Churchill on both the dayside and nightside are, however, approximately equal to the peak fluxes observed over the center of the polar cap. The decrease in solar proton fluxes to a level e^{-1} that of the polar cap, therefore, occurs at significantly lower latitudes than for the solar electrons. Because of this structure in

the solar protons, which appears to be spatial in nature and associated with particle entry into the magnetosphere, it is incorrect to adopt a simple, uniform access concept for a typical PCA event and equally incorrect to use interplanetary satellite fluxes and spectra to describe phenomena at low altitudes over the polar caps.

Figure 10-3 also shows the low energy electron fluxes >14 keV observed with the CFE instrument. These auroral fluxes which penetrate to altitudes lower than 96 km are peaked equatorward of the Fort Churchill latitude at this time with the nightside peak occurring at $\wedge = 66°$ and being more intense by an order of magnitude than the dayside fluxes, which peaked at $\wedge = 67°$. The low energy electron fluxes over the polar cap are only slightly above the sensitivity level of this instrument.

Figure 10-4 shows the measured angular distribution of 3.99-MeV protons over the invariant latitude interval 69° to 72° at 3.1 hours UT on 3 November. The pitch-angle data shown as open circles were obtained from the slow spin motion of the satellite in conjunction with measurements made with a three-axis magnetometer. The solid curve represents the expected count rate distribution for a source that is isotropic over all solid angles except for particles that might come back up from the loss cone. The good agreement between the experimental data on this and other passes with the calculated distribution illustrates the isotropic nature of the incoming solar protons, at least at high latitudes. Non-isotropic distributions near the lower latitude cutoff region, particularly on the dayside, have been observed (Paulikas et al 1968) and isotropy cannot be assumed at all latitudes.

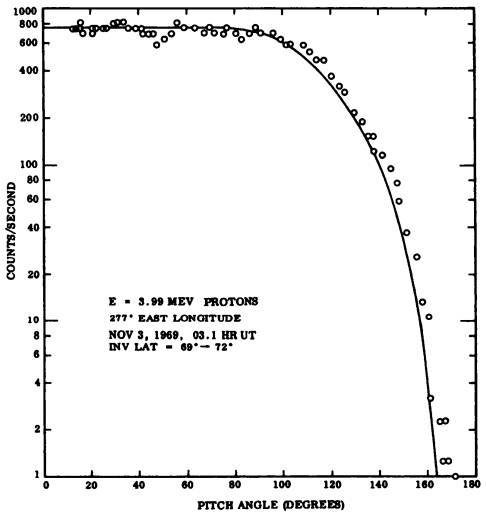

Figure 10-4. Counting Rate Versus Orientation Angle During a Satellite Pass Near Fort Churchill

A pronounced north-south asymmetry was also observed in the proton fluxes during the early portion of this event. Figure 10-5 shows the fluxes of 1.68-MeV protons as a function of invariant latitude on successive north-south polar cap crossings at 8.3 - 8.6 hours UT and 9.1 - 9.4 hours UT on 3 November. The flux in the north polar cap at $\wedge > 82°$ was a factor of three higher than the corresponding south polar cap flux at these times. Despite the depression at very high latitudes ($\wedge > 80°$) over the south pole the magnitude of the fluxes at the lower latitude cusp near $\wedge = 70°$ at both poles on both

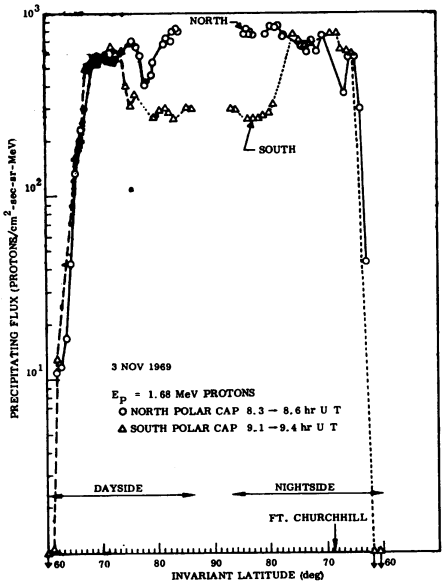

Figure 10-5. Fluxes of 1.68-MeV Solar Protons as a Function of Invariant Latitude on Successive North-South Polar Cap Crossings at 9.3-9.6 Hours UT and 9.1-9.4 Hours UT on 3 November 1969

the dayside and nightside are quite similar, and are within 25 percent of the maximum fluxes observed over the north pole. The steep cutoff of the proton fluxes below $\Lambda = 65°$ on the nightside can also be seen in Figure 10-5 in contrast to the less steep dayside cutoff.

The north-south polar asymmetry was most pronounced at the lower proton energies as shown in Figure 10-6 which is for the same time period as the previous figure. The ratio of north-to-south fluxes at $\Lambda > 83°$ decreased with increasing proton energy such that at 25 MeV the ratio was only 1.3. An asymmetry was also observed in the alpha particles which were measured at energies of 8.2 MeV and 15.4 MeV. While not totally unexpected, this is the first reported observation of solar alpha particle asymmetry over the polar caps. The magnitude of the asymmetry is comparable to that for the protons when considered on an MeV/nucleon basis. In contrast to the protons and alpha particles, the solar electrons showed no evidence of asymmetry at any time during this event.

In Figure 10-7, the absolute differential spectra of the protons, alpha particles, and electrons observed with the OV1-18 spectrometer at high latitudes ($\Lambda > 75°$) in the north polar cap throughout the 2-5 November period are shown. Also plotted are the data from the Explorer 41 (IMP-G) (Lanzerotti and Maclennan 1971) and the VELA-5B (Singer, private communication) satellites. During this period, the Explorer 41 satellite was generally in interplanetary space, with the exception that between 1600 hours UT on 2 November and 0600 hours UT on 3 November and also between 0000 UT and 1300 UT on 6 November, the satellite was within 10 R_E of the earth (Lanzerotti and Maclennan 1971). Despite the satellite transit in and out of the magnetosphere, the proton spectral data from the two satellites are in close agreement throughout the event. The VELA-5B data which were also obtained both within and beyond the magnetosphere are also in good agreement. In insert 3 of Figure 10-7 the energy widths of the various channels of the three satellite spectrometers are shown for comparison. The energy

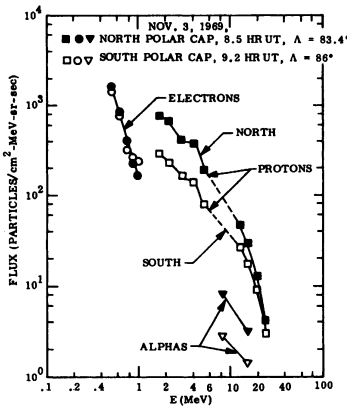

Figure 10-6. Energy Dependence of the North-South Polar Cap Asymmetry in the Solar Protons, Alpha Particles, and Electrons. The time period is identical to Figure 10.5

channels in the OV1-18 spectrometer are near contiguous and have widths corresponding to the data symbols.

The proton spectra as observed by all three satellites at 1942 hours UT on 2 November (insert 1) exhibited a complex shape characterized by an intense, steep rising component below about 1 MeV, and a relatively flat component out to approximately 20 MeV, above which a steep decline is observed. The proton spectrum as observed in the OV1-18 and Explorer 41 data shows evidence of a peak near 3.5 MeV that is greater than the statistical uncertainties in the data. This observation is also consistent with data obtained at the same time from the Cal-Tech spectrometer aboard the low-altitude polar-orbiting satellite OGO-6 (Stone, private communication). The electron spectra at this time could be well described by a power law of the form $\Phi = \Phi_o E^{-3.79}$.

By 0824 hours UT on 3 November, the low-energy proton flux had increased such that the complex, double-component spectral shape observed earlier was barely evident. By 1924 hours UT on the same day, the proton flux had reached a near power-law distribution and retained that shape as the flux at all energies continued to decrease throughout the remainder of the event. The electron flux could be described by a power-law spectral shape throughout the event. Also note the relatively small contribution of the alpha particles to the PCA event at all times. At 1942 hours on 2 November the proton-to-alpha ratio at 10 MeV was approximately 15 and remained between 10 and 15 throughout the event.

Figure 10-8 shows the differential spectra of protons, electrons and alpha particles measured near the magnetic latitude of Fort Churchill, $\Lambda = 68.7°$. Because the geomagnetic cutoff varies with local time and magnetic activity, one should expect to observe different spectra at this latitude than over the polar cap at certain times. In insert 1, for example, the electron flux at $\Lambda = 69°$ at 1336 hours local time was approximately a factor of seven lower than the polar cap fluxes at the same time. Significant differences between the polar cap and $\Lambda = 68.7°$ latitude proton fluxes at 1918 hours UT on 4 November, and at 1842 hours UT on 5 November, are also evident. At the latter two times, the low-energy protons (<5 MeV) at Fort Churchill were reduced by approximately a factor of 6 from the north polar cap values. Because of the cutoff feature of the geomagnetic

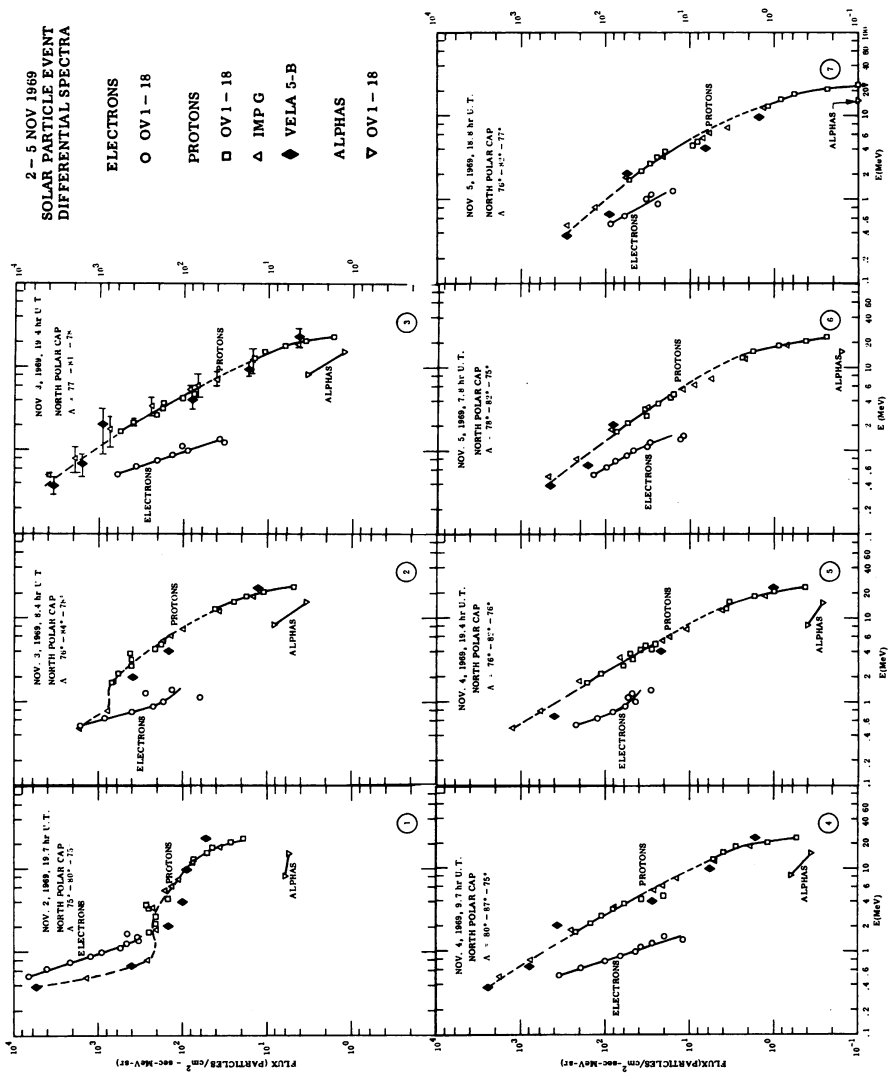

Figure 10-7. Differential Spectra of the Solar Protons, Alpha Particles and Electrons Observed With the OV1-18 Spectrometer Over the North Polar Cap During the 2-5 November Period. Data from the Explorer-41 and VELA-5B satellites are plotted for comparison

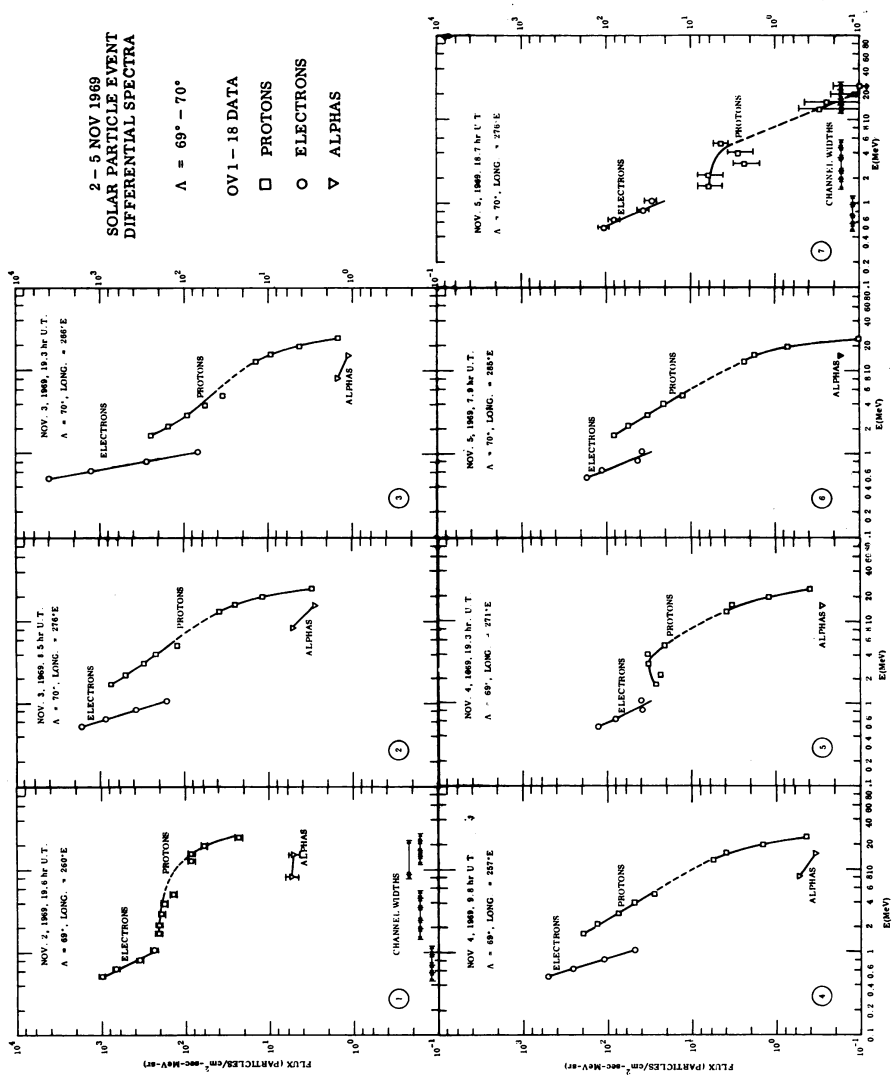

Figure 10-8. Differential Spectra of the Solar Protons, Alpha Particles and Electrons Observed With the OV1-18 Spectrometer in the Vicinity of the Magnetic Latitude of Fort Churchill, Canada, $\Lambda = 69^{o}$

field, caution must be exercised by rocket experimenters in utilizing interplanetary or even polar cap spectra to describe conditions in the vicinity of Fort Churchill.

The overall effect of the geomagnetic cutoff can be best seen in Figure 10-9, where the invariant latitude at which the fluxes of 2.16, 13.0, and 24.5 MeV protons have fallen to e^{-1} of the polar plateau values is plotted versus the universal time corresponding to the local daytime pass of the satellite. In general, the latitude of Fort Churchill is above the e^{-1}-cutoff level, except in the cases of the 2.16 MeV protons on 3, 4, and 5 November and the 13 MeV protons on 5 November. In contrast, Figure 10-10 shows the same plot for the local nighttime pass of the satellite. On the nightside, the e^{-1}-cutoff latitude is well below Fort Churchill at all energies measured and at all times during the event.

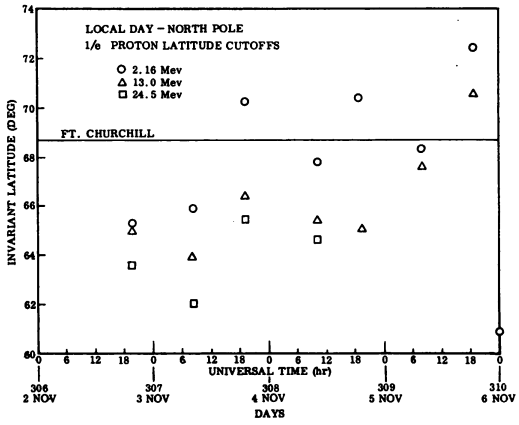

Figure 10-9. The Invariant Latitude at Which the Fluxes of 2.16-, 13.0-, and 24.5-MeV Protons Equal e^{-1} of the Polar Plateau Values Versus the Universal Time Corresponding to the Local Daytime Pass of the Satellite

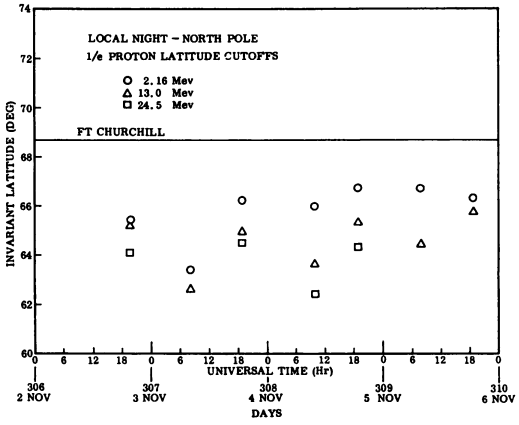

Figure 10-10. The Invariant Latitude at Which the Fluxes of 2.16-, 13.0-, and 24.5-MeV Protons Equal e^{-1} of the Polar Plateau Values Versus the Universal Time Corresponding to the Local Nighttime Pass of the Satellite

Finally, the time history of the 2-5 November event can be seen in Figure 10-11. In this figure, the fluxes of electrons, protons, and alpha particles measured in selected energy channels over the north and south polar caps are plotted as a function of time. The distinguishing features are the polar asymmetry in the proton and alpha particle data and the absence of asymmetry in the electron data, the buildup of the lower-energy protons over the first 24 hours, and the near-exponential decay of all three particle types.

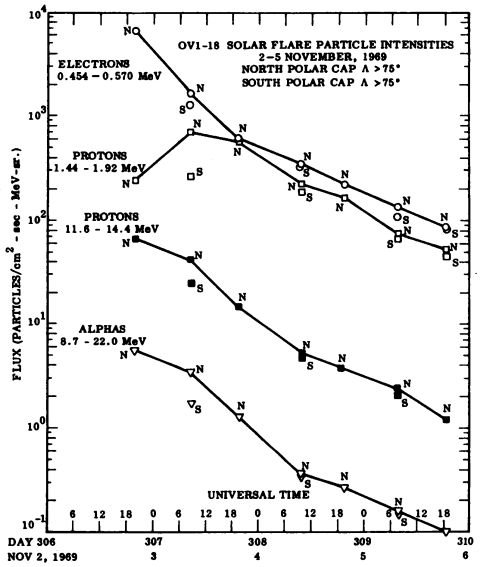

Figure 10-11. Fluxes of Solar Protons, Electrons and Alpha Particles Over the North and South Polar Caps as a Function of Time During the 2-5 November PCA Event

10-4 AURORAL ELECTRONS

Precipitating fluxes in the vicinity of the Fort Churchill magnetic latitude were observed on every pass of the satellite during the 2-5 November period. Figure 10-12 shows the response, on an approximately logarithmic scale, of one of the Total-Energy Detectors (TED) in the payload, on six of the satellite passes. For typical auroral spectra, this instrument measures the total energy deposition in plastic scintillation material above an equivalent electron energy threshold of 21 keV established by an evaporated aluminum window. Response in this instrument can be related to the energy deposited in the D-region by electrons, protons, and alpha particles at altitudes below approximately 92 km. The plots have been aligned to display the response at a north-magnetic latitude of 69° on both the dayside and nightside traversals of the satellite on each orbit. In each case, the central portion illustrates the maximum response in the detector to the solar particles present over the north polar cap. The periodic modulation in the data is due to the satellite spin at this time. At some point in the spin, one of the sets of low-energy particles detectors was pointing into the loss cone within 200 km of the indicated Fort Churchill overpass, in each case. On 2 November, the auroral particle energy inputs below 92 km at the Fort Churchill magnetic latitude were comparable with the solar particle fluxes over the polar cap region as uniquely identified by other detectors. As the PCA event decayed, the auroral particle contribution to the total energy response in this instrument became predominant, especially on the nightside.

In Figure 10-13, the integral electron number fluxes greater than 14 keV as measured with a channel multiplier detector are shown for the same series of satellite passes. Auroral activity in this detector remained fairly high throughout the event, particularly on the nightside, and the peak intensity shifted in latitude with time, as might be expected. The energy input and hence, the ionization profile throughout the high-altitude region of the D-ionosphere in the vicinity of Fort Churchill was, therefore, a complex function of the temporal and spectral

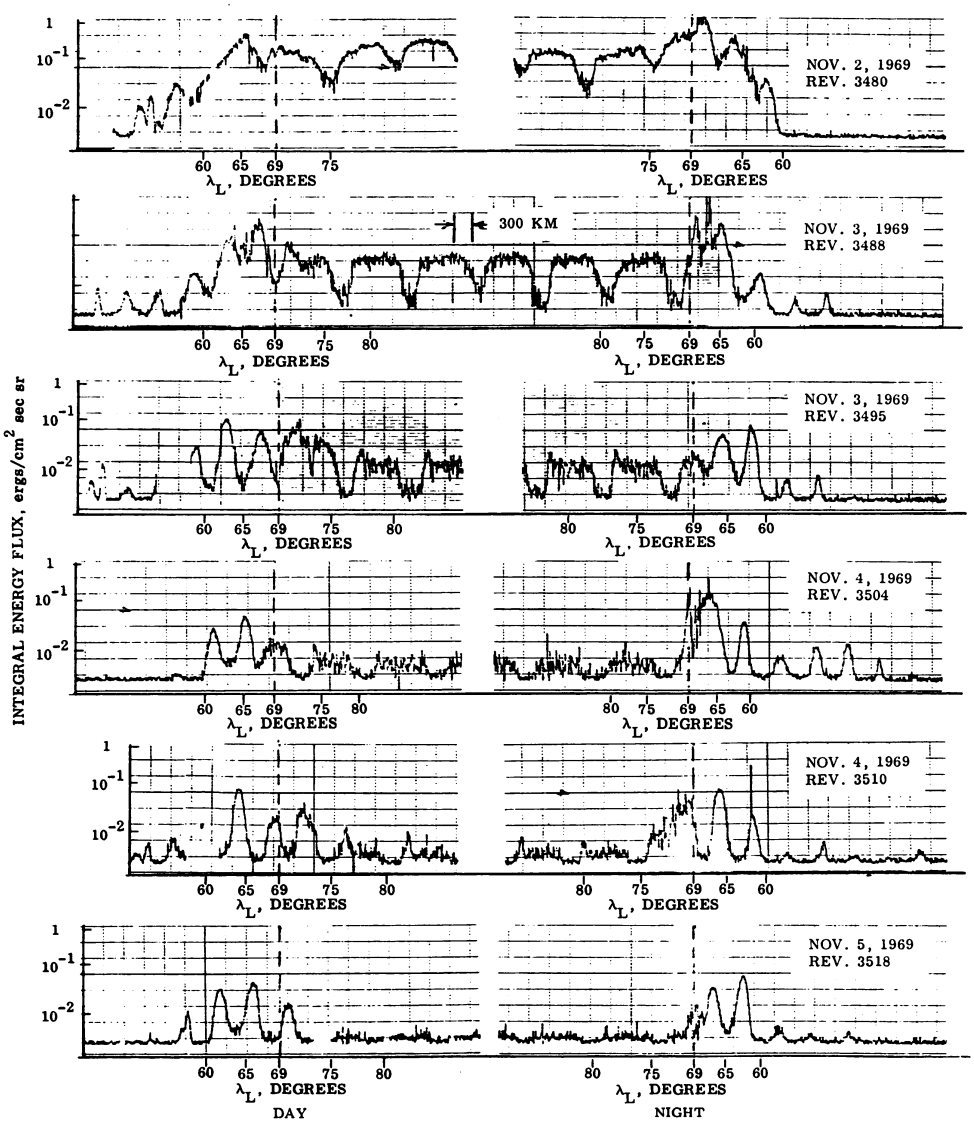

Figure 10-12. Integral Energy Flux of Auroral Electrons >21 keV as a Function of Time Near the Magnetic Latitude Corresponding to the Vicinity of Fort Churchill, Canada

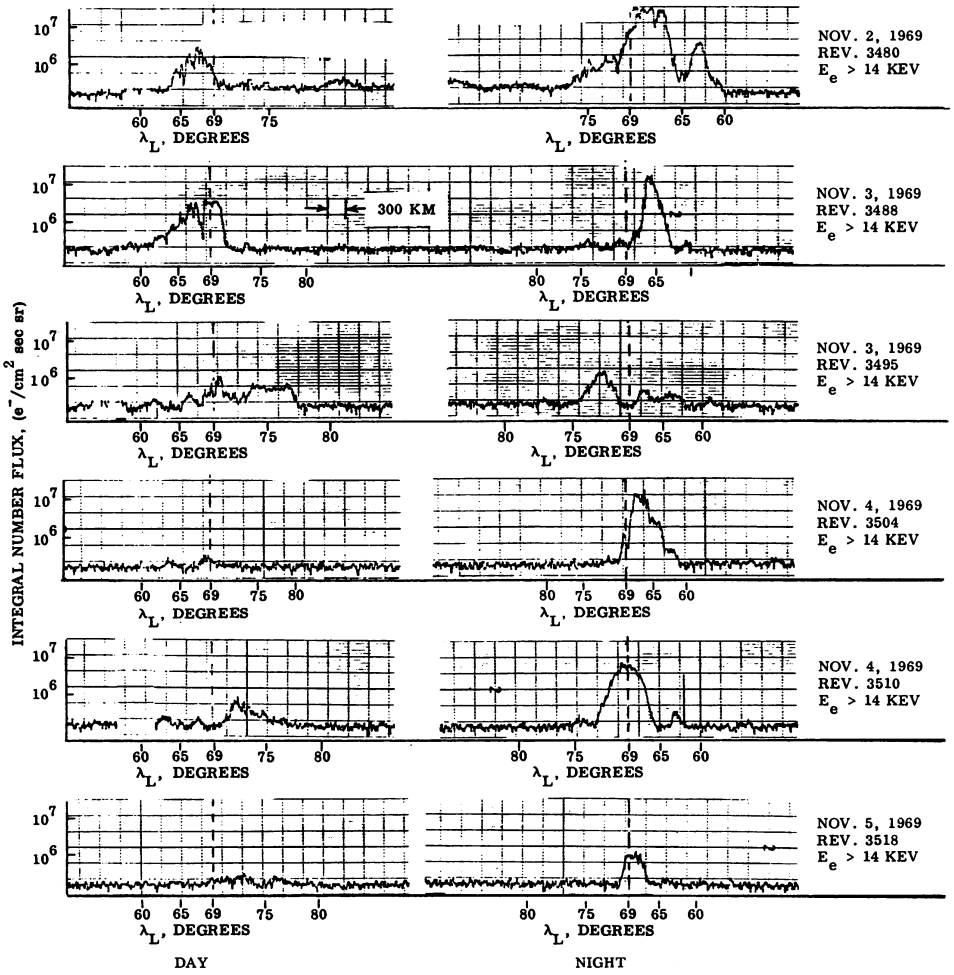

Figure 10-13. Integral Electron Number Fluxes > 14 keV as a Function of Time Near the Magnetic Latitude Corresponding to the Vicinity of Fort Churchill, Canada

variations in the solar particle fluxes and the intensity, spectral and spatial variations in the auroral fluxes during this period.

The principal conclusions to be drawn from the data illustrated are two-fold: (1) the auroral precipitation was not consistently displaced to the south of Fort Churchill, as might have been hoped, and (2) the general magnitudes of the fluxes, as measured at representative times during the period of interest, were such that they provided a significant source of ionization below about 92 km altitude. Since the auroral precipitation generally varies rapidly both in time and space, the fluxes measured on the satellite cannot be directly utilized to obtain the auroral produced ionization throughout the period of interest. The results, however, clearly indicate that the aurora particle produced ionization in the D-region was not negligible during the course of this event.

10-5 DISCUSSION

One of the most significant items in the energetic particle data is the contrast in the flux profiles between protons and electrons across the polar cap as seen in Figure 10-3. Early in the event the protons exhibited large variations (x 3) at magnetic latitudes >72 degrees. These variations are attributed to spatial rather than temporal phenomena associated with the proton access into the magnetosphere. The absence of large variations in the interplanetary flux (Lanzerotti and Maclennan 1971) and the generally excellent absolute agreement between the peak differential flux spectra over the north polar cap and in interplanetary space throughout the event, argue strongly that the variations are spatial in nature and originate near or within the magnetosphere.

In sharp contrast, the electron data show no significant spatial variations across the polar cap at the same time. In addition, the electron flux exhibits a significantly different latitudinal cutoff profile than the proton flux, with the protons extending to considerably lower latitudes than the electrons.

This evidence suggests that protons and electrons probably have different access paths into the magnetosphere. The smooth electron profiles confined to latitudes $>72^\circ$ indicate that electrons have highly-efficient direct access principally to the high-latitude polar cap field lines via the geomagnetic tail.

The drastically different proton latitudinal profiles and the flux variations evidenced in Figures 10-3 and 10-5 suggest that more complex processes are involved in the proton and alpha particle entry into the magnetosphere. The generally excellent agreement in absolute intensity between the polar cap differential proton spectra and the interplanetary spectra shown in Figure 10-7 indicates that the entry mechanism is highly efficient. The close temporal agreement also

argues for a near-earth entry point for the protons since distant-tail entry models (Michel 1965, Michel and Dressler 1970) require diffusion times of the order of 30 hours for a 5 MeV proton to enter the polar caps. Such long delay times are inconsistent with the time profiles of the interplanetary and north polar cap fluxes observed during this event.

The observed latitudinal profile of the 1.68 MeV protons at the time of the north-south asymmetry, as shown in Figure 10-5, also requires explanation. Despite the pronounced depression of the proton flux on the high-latitude ($\Lambda > 80$ degrees) south-polar-cap field lines, the flux levels at lower latitudes ($\Lambda > 73$ degrees) in the polar regions are approximately equal in both the north and south polar caps on both the dayside and nightside, and are within 25 percent of the peak north-polar cap (and interplanetary) flux values. These data indicate that while low-energy protons did not yet have access to the high-latitude portions of the south-polar cap, highly efficient and timely access was possible to the lower latitude field lines at both poles. This evidence suggests that multiple proton entry mechanisms were probably involved at this time. Comprehensive models of particle entry into the magnetosphere must therefore explain these latitudinal phenomena. Such models must also explain the observed proton and alpha particle energy dependence of the observed north-south asymmetry and the energy-independent symmetry of the solar electrons as shown in Figure 10-6.

The complex spectral shapes observed at the beginning of this event suggest that the energetic solar proton plasma consisted of two components, an intense, steep, lower-energy (~ 0.5 MeV) component superimposed on a much lower intensity, flat, energetic component. The good agreement in absolute differential flux between widely separated satellite observations both within and without the magnetosphere illustrates the extensive spatial uniformity of the fluxes. Magnetosphere entry models invoking diffusion of these particles into the polar caps from the distant tail must be able to explain the remarkable preservation of complex spectral shapes.

10-6 SUMMARY

The following items summarize the observations made by the OV1-18 satellite during the 2-5 November 1969 PCA event.

10-6.1 Significant fluxes of energetic protons (1-46 MeV) and electrons (0.4-1.9 MeV) were observed throughout the above period over both polar caps and in the vicinity of Fort Churchill, Canada. Both types of particles were important contributors to the enhanced D-region ionization during the event.

10-6.2 Alpha particles (7-22 MeV) were observed at considerably lower flux levels with the ratio of proton-to-alpha particles at 10 MeV remaining between 10 and 15 throughout the event. Alpha particles were therefore not prime contributors to the D-region ionization during this event.

10-6.3 A pronounced north-south asymmetry in both the protons and alpha particles below energies of approximately 20 MeV was observed on 2-3 November, with the north polar cap fluxes being a factor of three higher than those over the south polar cap on 3 November.

10-6.4 Complex proton spectra were obtained during the above period which could not be described by a single power-law or expoential shape. Evidence of a peak in the proton spectra in the vicinity of 3.5 MeV was also observed. Comparisons of these spectra with the Explorer 41 and VELA 5B satellites, both within and without the magnetosphere, show good agreement at all times throughout the event. The good temporal agreement between absolute differential proton flux in interplanetary space and over the polar caps argues for a near-earth entry point. Distant-tail entry models require long diffusion times that are inconsistent with the data obtained during this event.

10-6.5 The solar proton angular distribution over the polar caps and in the vicinity of Fort Churchill ($\wedge > 68.7^\circ$) was isotropic over all solid angles except for particles coming back up from the loss cone. Solar protons were observed to extend to significantly lower latitudes than the solar electrons.

10-6.6 Solar electrons exhibited smooth spatial profiles across the high-latitude polar caps ($\wedge > 72^\circ$), showed no evidence of north-south asymmetry at any energy observed, and their spectra could be described by a single power-law shape.

10-6.7 Large differences in the differential electron and proton spectra between the north polar cap and the magnetic latitude of Fort Churchill ($\wedge = 68.7^\circ$) were observed at times due to the geomagnetic cutoff. In general, the latitude of Fort Churchill was well above the e^{-1} cutoff latitude of the solar proton fluxes during the local nighttime passes of the satellite. On the dayside, the e^{-1} cutoff latitude of 2.16-MeV protons was occasionally above the Fort Churchill latitude.

10-6.8 Auroral precipitation was evident throughout the event in the vicinity of the magnetic latitude corresponding to Fort Churchill. The general magnitudes of the fluxes were such that they provided a major source of ionization below about 92 km altitude.

Acknowledgments

The authors wish to acknowledge the important contributions of Drs. R. G. Johnson and R. D. Sharp to this paper.

The authors also wish to acknowledge the invaluable assistance of Mr. J. C. Bakke to the design and operation of the OV1-18 payload and of Mr. D. L. Carr and Mrs. S. Spencer in the data analysis effort.

The authors would like to thank Dr. Sid Singer of the Los Alamos Scientific Laboratory for the use of previously unpublished VELA-5B particle data. Special acknowledgement is extended to Dr. Lou Lanzerotti of the Bell Telephone Laboratories for use of his Explorer 41 particle data and for many valuable discussions of the data. Helpful discussions were also had with Dr. E. Stone of the Calfornia Institute of Technology and Dr. A. J. Masley of the McDonnell-Douglas Laboratories.

The OV1-18 satellite payload, and operations during the PCA-69 rocket coordinations, were funded by the Advanced Research Projects Agency through the Office of Naval Research under Contract NOnr 4969(00) and this help is gratefully acknowledged. The detailed data analysis effort in conjunction with the Operation PCA-69 rocket coordination was supported by the Defense Nuclear Agency through the Office of Naval Research under Contract N00014-70-C-0334, Task NR087-172. This support is also graciously acknowledged in addition to the support of the Lockheed Independent Research Program in preparing this paper.

References

Bailey, D. K. (1968) Some Quantitative Aspects of Electron Precipitation In and Near the Auroral Zone, Rev. of Geophys 6: 289.

Blake, J.B., Paulikas, G.A., and Freden, S.C. (1968) Latitude-Intensity Structure and Pitch Angle Distributions of Low-Energy Solar Cosmic Rays at Low Altitude, J. Geophys. Res. 73: 4927.

Evans, L. C. and Stone, E. C. (1969) Access of Solar Protons into the Polar Cap: A Persistent North-South Asymmetry, J. Geophys. Res. 74: 5727.

Gall, R., Jimenez, J., and Camacho, L (1968) Arrival of Low-Energy Cosmic Rays Via the Magnetospheric Tail, J. Geophys. Res. 73: 1393.

Imhof, W. L., Reagan, J. B., and Gaines, E. E. (1971) Solar Particle Cutoffs as Observed at Low Altitudes, J. Geophys. Res. 76: 4276.

Lanzerotti, L. J. and Maclennan, C.G. (1971) Relative Importance of Solar Electrons, Protons and Alphas in the November, 1969 PCA Event, paper presented at the COSPAR Symposium on the November 1969 Solar Particle Event, June 1971.

Masley, A. J. (1969) Solar Cosmic Ray Events, Trans. Am. Geophys. U. 50: 666.

Michael, F. C. (1965) Effect of Magnetospheric Tail on Cosmic-Ray Cutoffs, Planet, Space Sci. 13: 753.

Michel, F. C. and Dessler, A. J. (1970) Diffusive Entry of Solar-Flare Particles into the Geomagnetic Tail, J. Geophy. Res. 75: 6061.

O'Brien, B. J., Van Allen, J. A., Laughlin, C., and Frank, L. (1962) Absolute Intensities in the Heart of the Earth's Outer Radiation Zone, J. Geophys. Res. 67: 397.

Paulikas, G. A., Blake, J. B., and Freden, S. C. (1968) Low Energy Solar-Cosmic-Ray Cutoffs: Diurnal Variations and Pitch Angle Distributions, J. Geophys. Res. 73: 87.

Reagan, J. B. and Imhof, W. L. (1969) High-Resolution Measurements of Polar Cap Protons in the 9 keV - 46 MeV Energy Range, Trans. Am. Geophys. U. 50: 662.

Reid, G. C. and Sauer, H. H. (1967) The Influence of the Geomagnetic Tail on Low-Energy Cosmic-Ray Cutoffs, J. Geophys. Res. 72: 197.

Smart, D. F., Shea, M. A., and Gall, R. (1969) The Daily Variation of Trajectory-Derived High-Latitude Cutoff Rigidities in a Model Magnetosphere, J. Geophys. Res. 74: 4731.

Vampola, A. L. (1969) Energetic Electrons at Latitudes Above the Outer-Zone Cutoff, J. Geophys. Res. 74: 1254.

Van Allen, J. A., Fennell, J. F., and Ness, N. F. (1971) Asymmetric Access of Energetic Solar Protons to the Earth's North and South Polar Caps, J. Geophys. Res. 76: 4262.

Williams, D. J. and Bostrom, C. O. (1969) Proton Entry Into the Magnetosphere on May 26, 1967, J. Geophys. Res. 74: 3019.

Contents

11. Particle Fluxes Associated With the PCA Event of November 1969

A. W. Waltner and G. J. Oliver
North Carolina State University
Raleigh, North Carolina

Abstract

Two instruments were flown on each of six NIKE Javelin rockets from Ft. Churchill, Canada subsequent to the onset of the PCA event of November 1969. The first instrument consisted of a three-counter telescope detecting electrons, protons, alphas, and gamma rays. Data were obtained at altitudes of about 40 to 130 kilometers with seven logic outputs representing various energy intervals for electrons, protons, alpha particles, and gamma rays. Flux variations with time are observed over a period of about 50 hours and are compared with available satellite data. The second instrument contained a silicon avalanche detector designed for low energy electrons. A magnetic field is cyclically applied to separate low energy electrons from high energy particulate or photon radiation. From this instrument is obtained count rate and spectral data for low energy electrons.

11-1 INTRODUCTION

Two instruments were flown on each of 6 NIKE Javelin rockets subsequent to the solar event of 2 November 1969. The first instrument contained a three

counter telescope consisting of a Si surface barrier ΔE counter, a CsI scintillator as an E counter, and a plastic scintillator as a veto counter. The second instrument contained a silicon avalanche counter designed primarily to measure low energy electron fluxes. Pulse rate as well as spectrum information is obtained from this instrument.

11-2 INSTRUMENTATION

11-2.1 High Energy Spectrometer (PCA)

The instrument was fabricated by Industrial Nucleonics of Columbus, Ohio in consultation with NCSU personnel.

The detector array consists of three detectors and the information is to be obtained from various combinations of coincidences and anticoincidences from the outputs of the three detectors. The first detector is a totally depleted silicon surface barrier detector with a depletion depth of about 300 microns and an area of 200 mm^2.

The second detector, hereafter referred to as the E counter, is a CsI(T1) scintillator optically coupled to a photomultiplier by means of a plastic light pipe.

It is recognized that response of CsI(T1) to different particles and to particles of different energies is a complex function and this needs to be taken into account in the data analysis.

The third detector, hereafter referred to as the veto counter, is a plastic scintillator in the form of a cup in which the ΔE and E counters are mounted. The function of this detector is to define the angle of acceptance and to reject those particles which pass through the E counter.

The physical arrangement of the three detectors is shown in Figure 11-1. The instrument operates in the following manner. Particles passing through the ΔE detector deposit an amount of energy depending on the energy of the particle and on its charge and mass. The energy loss for electrons, protons, and alpha particles in a 300μ Si detector is shown in Figure 11-2. A system of discriminators selects those events which deposit energies as indicated in the figure. This makes possible a discrimination between electrons, protons, and α particles in broad energy ranges. The logic system (Figure 11-3) provides signals from the various discriminators giving coincidence and anticoincidence outputs which are simultaneously applied to three rate meters which cover a range of about 3 to 10^5 counts/sec. (Figure 11-4). As an example, a coincidence indicated by $A_1 \bar{A}_2 B_1 B_2$ would represent electrons with energy in excess of 1 MeV but under 22 MeV.

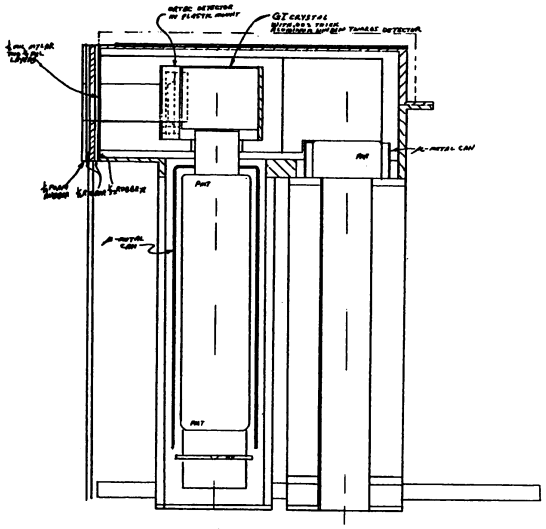

Figure 11-1. Detector Assembly

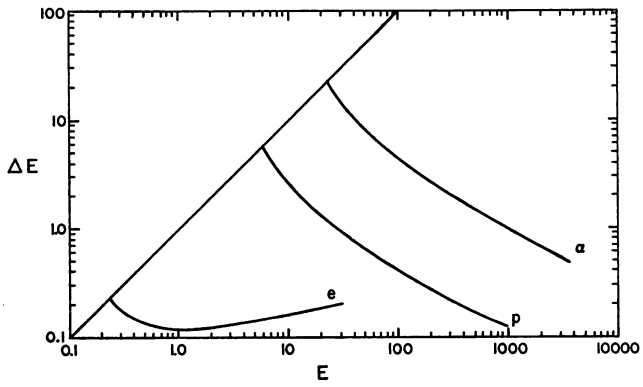

Figure 11-2. Energy Loss for p, α, and e- in 300μ Si Detector

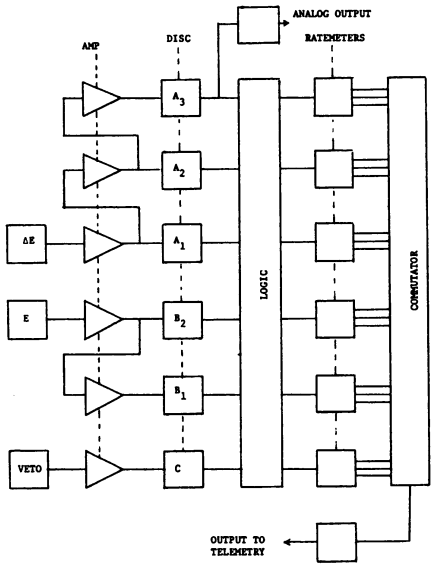

Figure 11-3. The Logic System

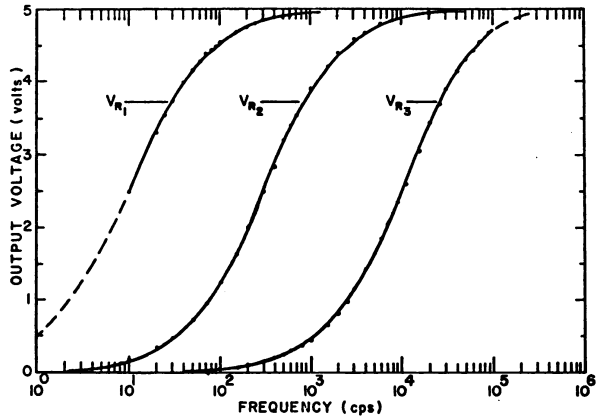

Figure 11-4. Rate Meter Calibration Curves

The effect of back-scatter of electrons from the CsI detector into the Si was measured by means of a dual-parameter coincidence experiment in which the ΔE for the Si detector is shown in Figure 11-5. The distribution shown is for an electron energy of 0.7 MeV and it fits rather closely to the modified Landau distribution. From this, one can conclude that there is, at this energy, relatively little back-scatter.

The counting rates are limited by the resolution of the logic system. A measure of 2τ yields a value of about $7\mu s$ which is approximately that expected from a simple overlap coincidence circuit with $3\mu s$ logic pulses. The dead time correction is approximately 10% at a counting rate of $\approx 4 \times 10^4$.

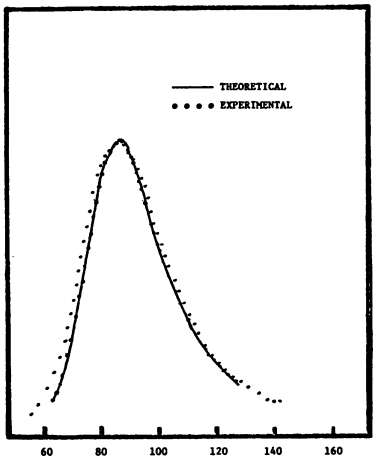

Figure 11-5. Energy Absorption of 700 keV Electrons in Si Detector

11-2.2 Low Energy Spectrometer (LEESA)

The low energy spectrometer was designed and fabricated by Industrial Nucleonics of Columbus, Ohio. The spectrometer contains a Si avalanche detector. This detector operates with internal amplification in a manner somewhat analagous to that of the proportional counters. The response of this detector was determined using internal conversion electrons of Au^{195} and Cd^{109} and the x-ray response was determined by means of Fe^{55} and Co^{57}.

The instrument is shown in block form in Figure 11-6. The "spectrum" output provides output signal proportional to the amplitude of the input pulses.

For low counting rates, the spectrum signal is updated to a new value for each pulse incident on the detector. Because of telemetry bandwidth limitations, the signal is inhibited for a period of 1 millisecond after a pulse is sampled. Therefore, at high count rates ($>10^3$ counts/sec.) the spectrum output consists of a random sample of the total incident pulses.

The rate output is obtained from the summed output of two scalers. At low count rates, all counts are transmitted. At high rates, only the major excursions are observed.

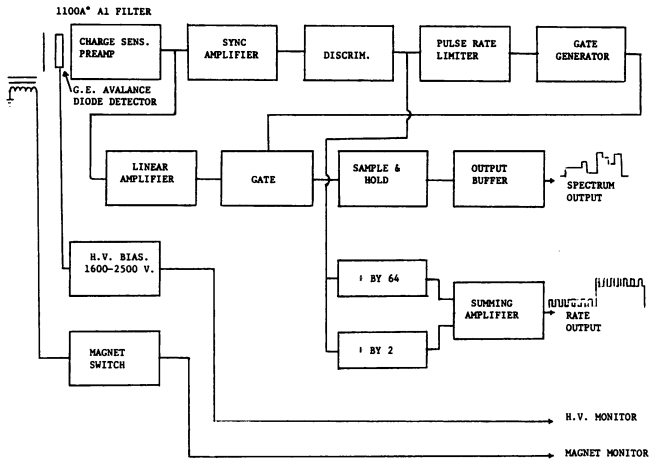

Figure 11-6. Electronics of Instrument in Block Form

11-2.3 Results

At the time of each flight, all data from the commutator outputs were stored on magnetic tape. From this magnetic tape, analog charts were prepared for each channel of the commutator. In turn, these charts were then inspected and a reading was taken at each sampling point (one reading per second). Once these voltage outputs were obtained, they were converted to count-rates. Due to the great volume of data and its complexity, this conversion was performed by means of a computer. The program for the conversion interpolated between table values at 0.1 volt intervals (150 data points for a logic group) and detected data of various illogical configurations. The illogical configurations are designated in the plotting routine.

Corresponding altitudes for each measurement have been assigned and are designated at the top of each graph. Typical graphs are shown in Figures 11-7, 11-8, and 11-9; uncorrected for dead time, random coincidence, etc.

Data was plotted by computer involving a Calcomp plotter. A smoothing routine giving relative weights of 4/7, 1/7, and 1/14 to each point and the two nearest adjacent points on each side was applied.

The various types of radiation and the observed maximum counting rates for the various logic groups are tabulated in Table 11-1. It is believed that excessive counting rates in the first logic group make this group essentially meaningless. The second two groups represent electrons in two energy categories and will be discussed in some detail in this report.

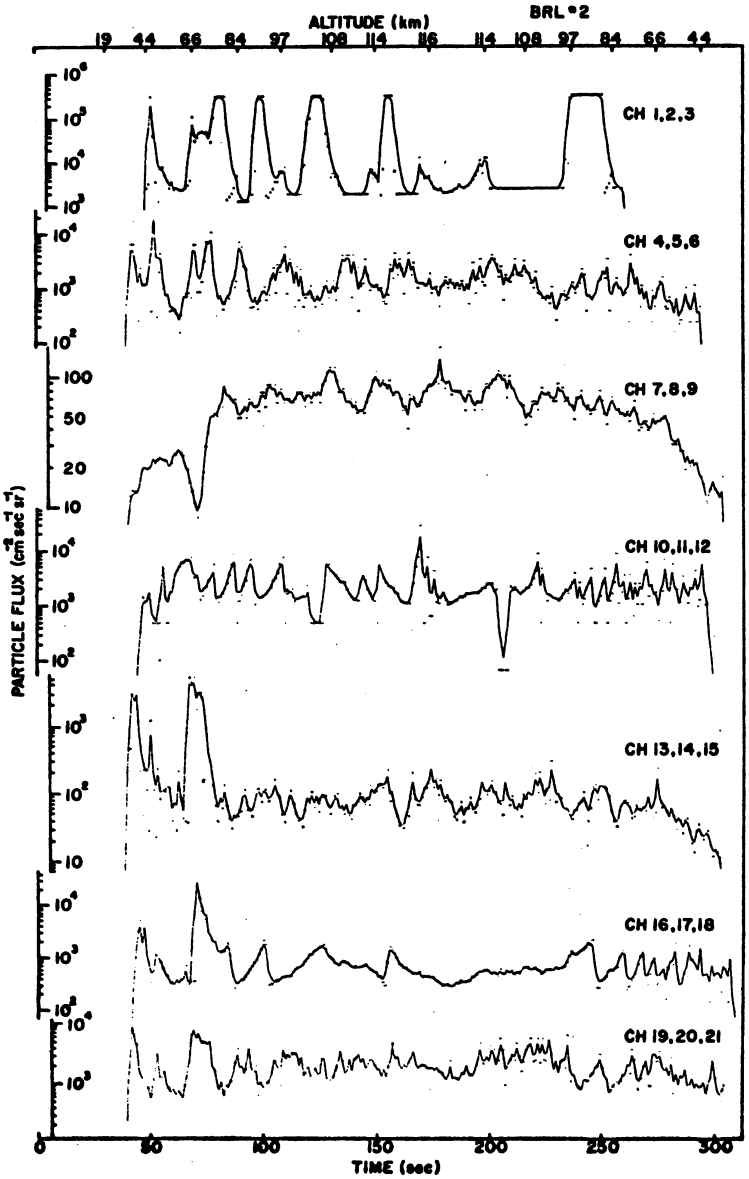

Figure 11-7. Particle Fluxes - Flight #2

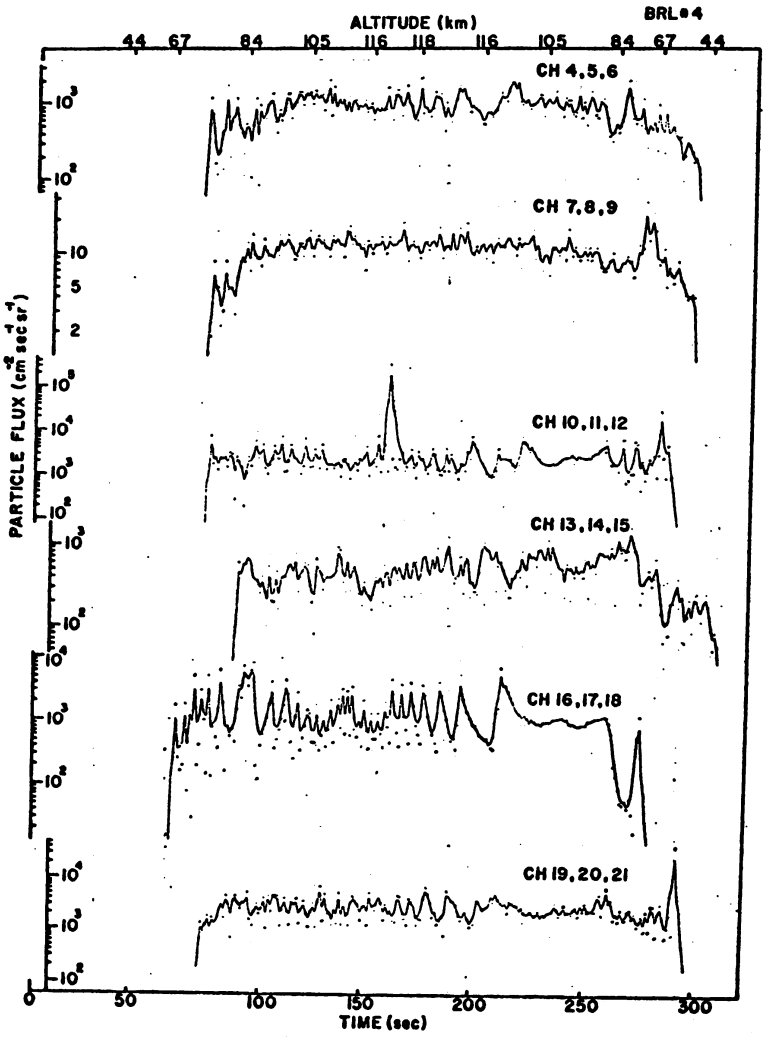

Figure 11-8. Particle Fluxes - Flight #4

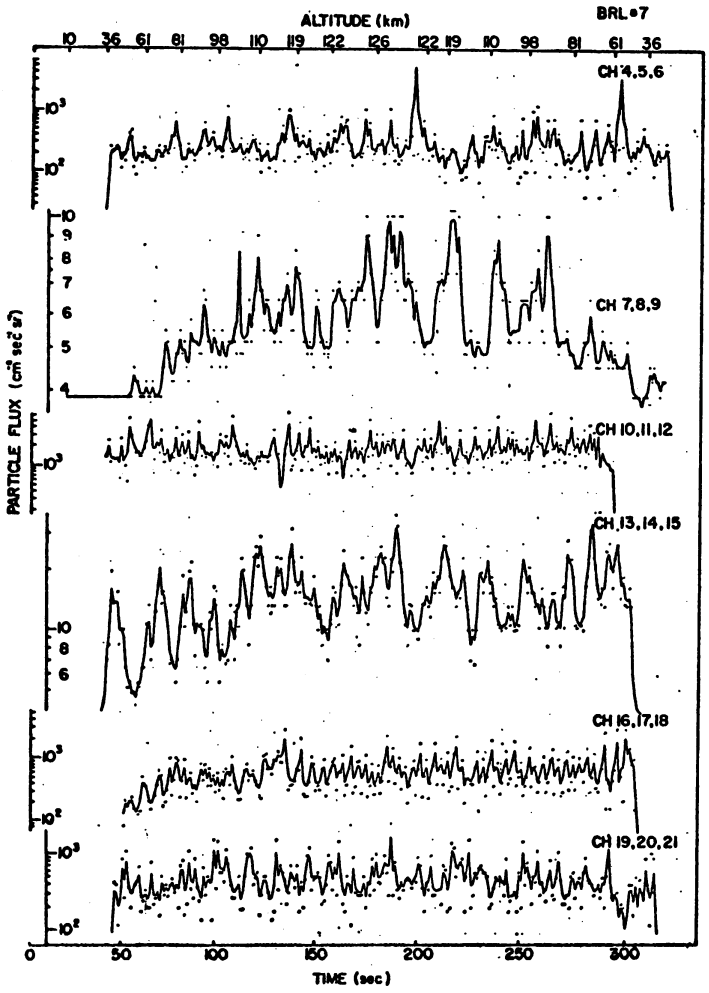

Figure 11-9. Particle Fluxes - Flight #7

Table 11-1

Logic	Commutator	Max Count Rate	Identification
S	4, 5, 6	1.50×10^3	$\bar{e}$, (350 keV - 1 MeV)
T	7, 8, 9	1.45×10^2	$\bar{e}$, (1 - 22 MeV)
U	10, 11, 12	(off scale) ($>10^5$)	p^+, α(350 keV - 6 MeV)
V	13, 14, 15	7.0×10^2	p^+, (6 MeV - 80 keV)
W	16, 17, 18	2.2×10^3	α(6 MeV - 350 MeV)
X	19, 20, 21	4.5×10^3	γ ($\geq$ 20 keV)

Electron flux as a function of altitude for the high energy category is shown in Figure 11-10.

An altitude of 110 kilometers was common to all flights, and was selected to illustrate a flux variation with respect to time during the life of the flare. It was observed that the low-energy electron flux decreased with time in approximately an exponential manner, and that the high-energy electron flux decreased in a similar manner, but at a different rate (as seen in Figure 11-11). The ratio of these fluxes changes with time, indicating a changing electron spectrum. The change indicates a gradually-decreasing electron energy, as expected from time-of-flight considerations.

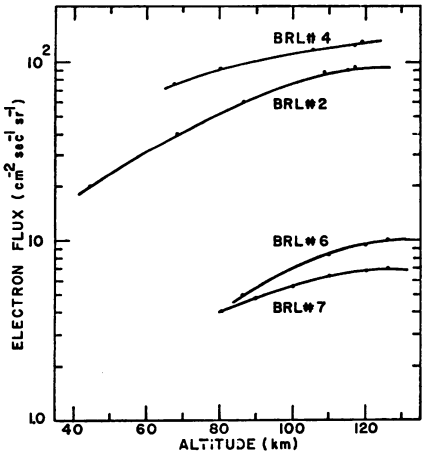

Figure 11-10. Electron Flux vs Altitude

Mozer (1965) states that the electron flux by energy at any one time is expressed as

$$N(E) = A_o e^{-E/E_o}.$$

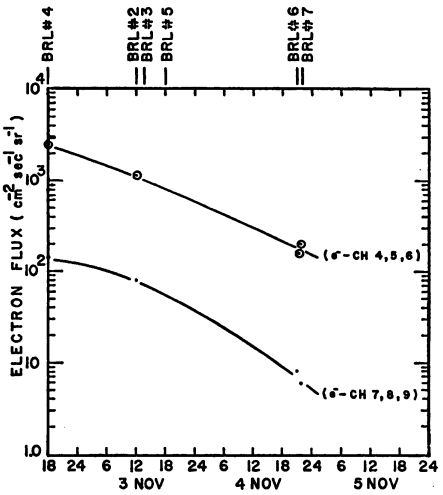

Figure 11-11. Electron Flux vs Time

Now, if we procede to evaluate these constants A_o and E_o, we get the following results.

Table 11-2

Flight	E_o	A_o	Time (NOV)
BrL #4	.271 MeV	4.70×10^5	2 - 2110
BrL #2	.241 MeV	2.17×10^5	3 - 1257
BrL #6	.188 MeV	5.26×10^4	4 - 2130
BrL #7	.184 MeV	6.47×10^4	4 - 2238

As we see, the two constants E_o and A_o do vary with time. It is possible then, to write a function to predict A_o and E_o.

$$A_o = A_o' e^{-c_1 T'}$$

where

$$T' = t - t_o$$

$$E_o = E_o' e^{-c_2 T'}.$$

Now expressing these results

$$N(E,T) = (A_o' \; e^{-c_1 T'}) \, e^{-E(e^{c_2 T'}/E_o)}.$$

For own data we find the following values for A_o', E_o', C_1, C_2

$$A_o' = 4.70 \times 10^5 \text{ cm}^{-2} \text{ sec}^{-1} \text{ MeV}^{-1}$$

$$E_o' = 0.271 \text{ MeV}$$

$$C_1 = 0.0905 \text{ hr}^{-1}$$

$$C_2 = 0.00809 \text{ hr}^{-1}.$$

It is important to choose an original starting time (t_o) at a time after the flare reaches maximum intensity (this means this model would only work for the electron fluxes after flare maximum).

In summary, this model properly takes into account the decrease in flux with time as well as the change in the energy distribution of the electron spectrum.

11-3 SUMMARY AND CONCLUSION

Electron fluxes have been measured over a period of 50 hours at altitudes of 40 to 120 km and show expected changes in intensity and energy with time and with altitude. Results are to be considered preliminary in that final random coincidence corrections have not yet been made.

11-3.1 Note Added in Proof

Subsequent analysis indicates that a strong dependence of counting rate on rocket orientation is observed in both the high and low energy spectrometer data. This effect accounts in part for the periodicity of the counting rates of Figures 11-7 - 11-9.

Acknowledgments

The following persons contributed to the work reported herein: J. M. Sanderson, T. A. Eaves, D. M. Peterson and L.S. Culler of North Carolina State University and R. J. Fowler, D. Cressman, B. Y. Cho and O. Utt of Industrial Nucleonics of Columbus, Ohio.

This work was supported under Contract DAAD05-69-Q-1151, Aberdeen Proving Grounds and Contract DAAD05-69-C-0294 by BRL.

Contents

12. Heavy Particle Ionization Rates

B. Sellers and F.A. Hanser
Panametrics, Inc.
Waltham, Massachusetts

Abstract

Proton and alpha particle fluxes in the approximate range 2 to 100 MeV were determined from measurements made on three Black Brant rockets launched at the following universal times: AJ17.602, 2 Nov/2020; AJ17.758, 3 Nov/0605; AJ17.617, 4 Nov/2308. Specific ionization rate expressions are derived for heavy particle spectra of the form $j(E,\alpha) \sim E^{-n}\cos^{\beta}\alpha$ and presented in a manner applicable to any atmosphere. When the spectrum is assumed to extend to infinite energy, a simple analytic result is obtained that is applicable to that region of the atmosphere in which the atmospheric depth exceeds the range of the minimum energy particles contained in $j(E,\alpha)$. Altitude profiles of proton induced ionization rate are given for the launch time of each of the three rockets.

12-1 INTRODUCTION

During PCA 69, five Black Brant rockets were instrumented to measure the heavy particles responsible for the ionization during most of the event. Included were instruments to measure protons and alpha particles in the range of about

2 to 100 MeV. Of these five rockets, three were complete successes and yielded particle measurements up to about 120 km. One rocket suffered a door ejection failure which resulted in complete loss of useful particle data, and the remaining rocket had door ejection occur shortly after launch which caused complete failure of the flight.

The three successful flights yielded particle data spanning a period of about two days, between 2 and 4 November 1969. Data from these flights have been reduced to yield the incident particle spectra, from which the altitude profiles of ionization rate have been calculated. Preliminary results have been reported previously (Sellers, 1970).

12-2 SYSTEM DESCRIPTION

The particle detection system consists of two spectrometers, labeled "high" and "low" energy (Hi and Lo, for brevity). Each of the spectrometers has an upper and lower energy integration range, as shown in Table 12-1. Limits of these integration ranges are determined in the usual manner by a combination of energy loss in the detectors and electronic thresholds. The principal measurement of interest is obtained from the lower range of Hi, which provides an integral measurement of protons between about 3.5 and 102 MeV, but it also includes alphas between about 6 and 20 MeV. The Lo spectrometer measures this alpha contribution in its upper energy range with no sensitivity to protons. Thus the alpha contribution can be measured separately. This spectrometer, which uses a partially depleted detector whose sensitive depth is determined by the applied bias, also measures protons in the approximate range 2 to 4 MeV in its lower window. This measurement is approximate only, however, and was not used in determining the incident proton energy spectra from which the ionization rates were calculated.

Both the approximate geometrical factor G and the actual factor G_a for each spectrometer are given in Table 12-1. G is found from

$$G = \pi S (c/r)^2 \tag{12-1}$$

and G_a from

$$G_a = 2 \pi S(1 - \cos \theta_{1/2}) \tag{12-2}$$

where S is the detector area, r the aperture plane-detection plane distance, c the aperture radius and $\theta_{1/2}$ the aperture half-angle, which was about 30^o for each spectrometer. The system detection geometry at any specific time is shown in Figure 12-

Table 12-1. Specifications for Flare Particle Spectrometers

Spectrometer, Detector	Avg. Thickness, Area Geometrical Factors	Integration Range (MeV)		
		Window	Particle Type	
			Protons	Alphas
Hi Si(Li)	2.17 mm, 0.8 cm^2 G=.82, G_a=.68cm^2-sr	Upper	does not detect	20-230
		Lower	3.5-102	6-20
Lo Surface barrier	81* micron, 0.8 cm^2 G=.85, G_a=.68cm^2-sr	Upper	does not detect	6-25
		Lower	2-4	4-5

* Includes estimate of about 30 microns due to back collection

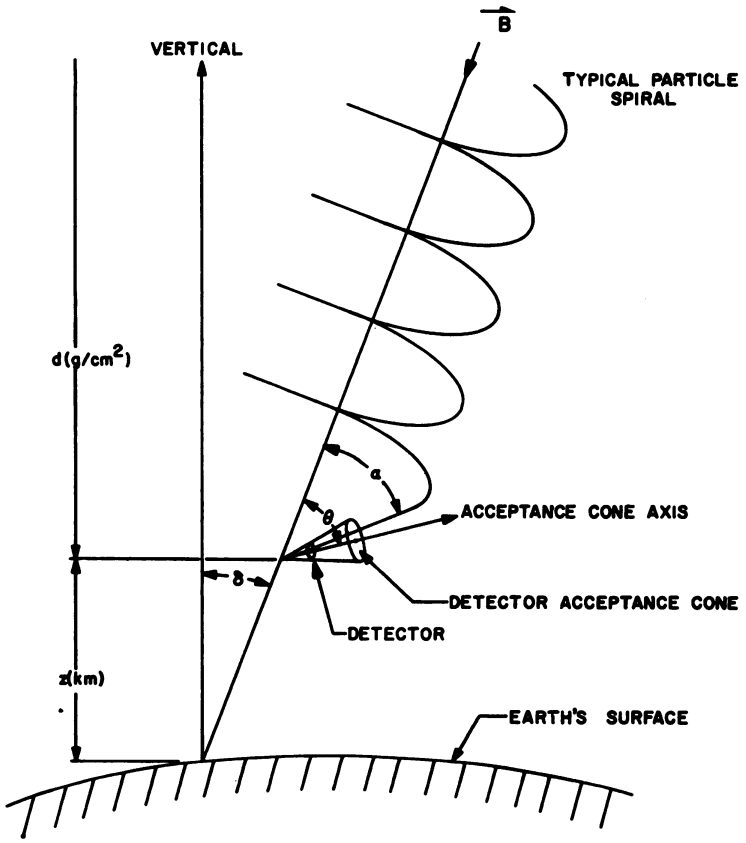

Figure 12-1. System Detection Geometry

The counting rate of the detectors is determined by the spiral path lengths $y(z,\alpha)$ of all the particles having pitch angles α such that they enter the acceptance cone, where

$$y(z,\alpha) = d(z)/\cos\alpha \cos\delta \ . \qquad (12\text{-}3)$$

The basic data are, therefore, the values of θ, as determined by an on-board single axis magnetometer, and the detector count rates for a series of altitudes between the point at which the doors are ejected, exposing the detectors, and apogee. For these flights the altitude range was about 60 to 120 km and the maximum θ range was about 30^{o} to 80^{o}.

12-3 ANALYTICAL PROCEDURE

The general method of spectral analysis consists of determining the incident differential energy spectrum shape that will yield the observed count rate variation with altitude and θ of the measured integral spectrum. This differential spectrum is then used to calculate the ionization rate altitude profile. There are, therefore, three steps in the entire procedure for each flight:

(1) Determination of count rate variation with z and θ,

(2) Determination of incident differential spectrum, and

(3) Calculation of ionization rate.

Here the general approach is discussed, and the results obtained are given in the following section.

12-3.1 Count Rate Variation with Altitude and Angle

Each detected pulse was telemetered in real time and subsequently associated with a pitch angle θ for the acceptance cone axis at that time. These pulses were then summed and sorted over 1--I fixed time increments into a series of 1--J pitch angle bins designated by central values θ_j. The altitude at the center of each time interval was designated z_i. Typically, I = 20 to 50 and J = 5 to 7. This then yields a set of count rates $C(z_i, \theta_j)$, some of which are zero, since all pitch angles are not scanned consistently throughout the flights. To allow straightforward utilization in the theoretical analysis the count rates were converted into a quantity defined as the "integral flux", $J(z_i, \theta_j)$, simply by dividing by the approximate geometrical factor G,

$$J(z_i, \theta_j) \equiv C(z_i, \theta_j)/G \ (\mathrm{cm}^2\text{-sec-sr})^{-1} \ . \qquad (12\text{-}4)$$

The actual incident integral flux, averaged over the 30^{o} half-angle aperture, is found by multiplying $J(z_i, \theta_j)$ by G/G_a .

12-3.2 Differential Energy Spectrum Determination

The values of $J(z_i, \theta_j)$ are utilized as follows to determine the incident differential spectrum at the top of the atmosphere. It is assumed that this spectrum is isotropically directed into the lower hemisphere, zero into the upper hemisphere, and can be written as a series

$$j(E,\alpha)\, d\Omega dE = \sum_n j_n(E,\alpha)\, d\Omega dE = \sum_n a_n E^{-n} d\Omega dE \ . \tag{12-5}$$

A set of values of n is assumed and the coefficients a_n are determined as those which produce the best fit to the entire set of $J(z_i, \theta_j)$. Using the spectrum Eq. (12-5) it is possible to calculate a theoretical value $J_c(z_i, \theta_j)$ for any z_i, θ_j (Sellers et al, 1970)

$$J_c(z_i, \theta_j) = \sum_n J_n K_n(z_i, \theta_j) \tag{12-6}$$

where the $K_n(z_i, \theta_j)$ are numerical integrals involving the detector characteristics, the atmospheric depth $d(z_i)$, and the electronic threshold energy E_o (MeV), and the coefficients J_n are related to a_n by

$$a_n = (n - 1)\, J_n\, E_o^{\,n-1} \tag{12-7}$$

and to the incident flux between any two limits E_1 and E_2 crossing the plane perpendicular to $\vec{B}$ by

$$\mathscr{F}(n, E_1, E_2) = \pi J_n \left[(E_o/E_1)^{n-1} - (E_o/E_2)^{n-1} \right] (cm^2\text{-sec})^{-1} \ . \tag{12-8}$$

The coefficients J_n are those which minimize, on a least square basis, the sum

$$\Sigma = \sum_i \sum_j \left[J(z_i, \theta_j) - J_c(z_i, \theta_j) \right]^2 / \Delta J(z_i, \theta_j)^2 \tag{12-9}$$

where the $\Delta J(z_i, \theta_j)$ are the uncertainties in $J(z_i, \theta_j)$ introduced by the statistics of the counting process. Substitution of Eq. (12-6) into Eq. (12-9) and minimizing produces a set of simultaneous equations for the J_n with coefficients calculable

in terms of the K_n, $J(z_i, \theta_j)$ and $\Delta J(z_i, \theta_j)$. Once the J_n have been found for any assumed set of n's, the a_n are given by Eq. (12-7) and the incident differential energy spectrum by Eq. (12-5).

12.3.3 Ionization Rate Calculation

For particles of energy E incident from angle α, the monoenergetic-monodirectional specific production rate at an altitude z where the density is $\rho(z)$ is

$$Q_o(z, E, \alpha) = \frac{\rho(z)}{Q} S\left[R(E) - y(z,\alpha)\right] \quad \frac{\text{e-ion pairs/cm}^3\text{-sec}}{\text{particle/cm}^2\text{-sec}} \tag{12-10}$$

where Q is the energy to produce one e-ion pair, taken here as 36×10^{-6} MeV, S(R) is the stopping power (MeV-cm^2/g) for particles of range R(g/cm^2) and $y(z,\alpha)$ is given by Eq. (12-3). The production rate for a differential spectrum $j(E,\alpha)$ is then

$$q(z, E_1, E_2) = \int_E \int_\Omega j(E,\alpha) Q_o(z, E, \alpha)\, d\Omega\, dE \tag{12-11}$$

where the energy integration is carried out between the limits E_1 and E_2 within which the incident spectrum is known, and the solid angle integration is taken over the region in which the incident flux is non-zero; here this is the lower 2π steradians.

We assume a spectrum of the form

$$j(E,\alpha) = \mathscr{F}\, k\, E^{-n} \cos^{\beta}\alpha \tag{12-12}$$

where $\mathscr{F}$ is the incident flux between E_1 and E_2 and k is the normalization constant

$$k = \left[(n-1)(\beta+2)/2\pi\right] \; E_1^{n-1} \Big/ \left[1 - (E_1/E_2)^{n-1}\right] . \tag{12-13}$$

If it is assumed that the stopping power S(E) can be written

$$S(E) = A\, E^{-m} \text{ MeV-cm}^2/\text{g} \tag{12-14}$$

where, for protons

$$A = 231.8 \text{ MeV}^{1+m} \text{ and } m = 0.775 \tag{12-15}$$

then the stopping power as a function of R is

$$S(R) = \left[1/(m+1)\right]\left[A(m+1)\right]^{1/(m+1)} R^{-m/(m+1)} . \qquad (12\text{-}16)$$

The constants Eq. (12-15) give S(E) to ± 3 percent of the values of Janni (1966) between 1.5 and 200 MeV. If it is assumed that α does not vary with altitude, Eq. (12-11) can be integrated to yield the specific ionization rate

$$\frac{q(z, n, E_1, E_2, \beta)}{\mathscr{E}} \equiv Q(z, n, E_1, E_2, \beta) = L\left(\frac{E_1}{Q}\right) \frac{X_1^{-a(n-2)}}{H_e(z)} \times \left[D(X_2, n, \beta) - D(X_1, n, \beta)\right] . \qquad (12\text{-}17)$$

Here

$$X_1 = W(z)/R_1, \quad X_2 = W(z)/R_2, \quad W(z) = d(z) \sec \delta \qquad (12\text{-}18)$$

$$L = a(n-1)/\left[1 - (E_1/E_2)^{n-1}\right] , \quad a = 1/(m+1) \qquad (12\text{-}19)$$

and

$$H_e(z) \equiv W(z)/\rho(z) \qquad (12\text{-}20)$$

is the density scale height that would exist along the magnetic field direction in an exponential atmosphere. In Eq. (12-18), R_1 and R_2 are the ranges in air for particles of energy E_1 and E_2, respectively. The function $D(x, n, \beta)$ is given by

$$D(x, n, \beta) = a(\beta+2) \int_x^1 X^{b+\beta} B_{1-x/X}(a, b)\, dX \qquad (12\text{-}21)$$

where

$$b = a(n-2) + 1 \qquad (12\text{-}22)$$

and $B_u(a, b)$ is the incomplete Beta Function as defined by Abramowitz and Stegun (1964). The integral in Eq. (12-21) can be carried out to yield a series which can be summed to any desired degree of accuracy on a digital computer. Results for $\beta = 0$ (isotropic) and $\beta = 10$ (nearly monodirectional) are shown in Figures 12-2 and 12-3.

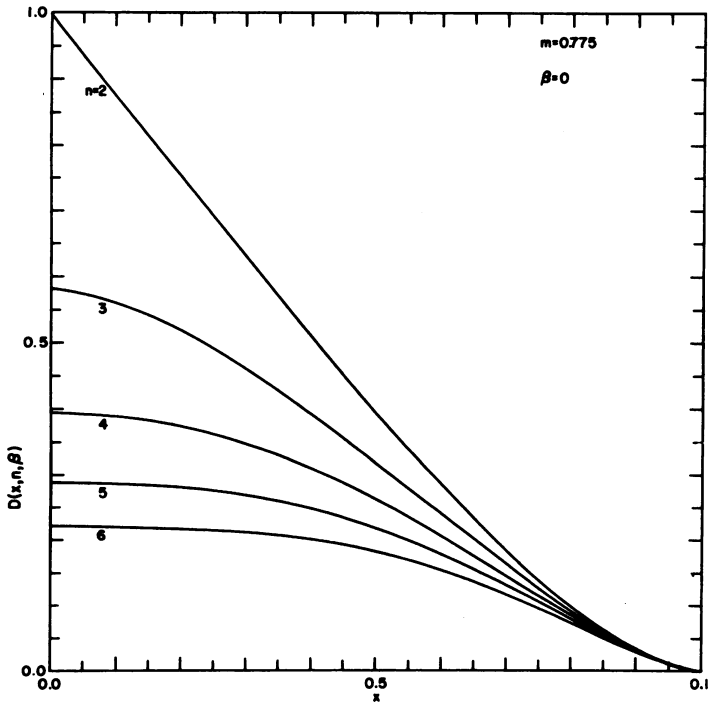

Figure 12-2. $D(x, n, \beta)$ for Heavy Particles With Isotropic Angular Distribution

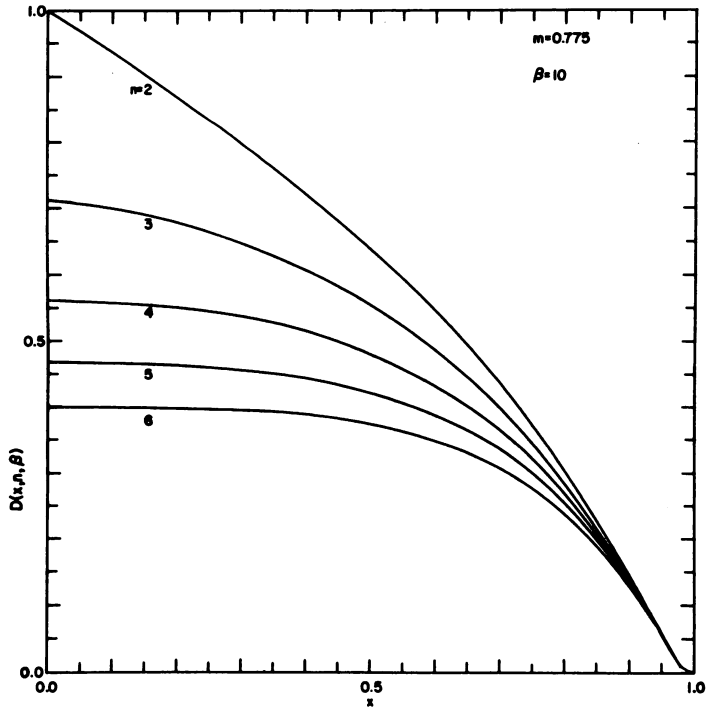

Figure 12-3. $D(x, n, \beta)$ for Heavy Particles With $\cos^{10}\alpha$ Angular Distribution

If $W(z) > R_1$, the second term of Eq. (12-17) is zero. Further, if $R_2 \to \infty$ so that $X_2 = 0$, then

$$Q(z, n, E_1, \infty, \beta) = \frac{(n-1)(\beta+2)}{b+\beta+1} a^2 B_1(a,b) \left(\frac{E_1}{Q}\right) \frac{X_1^{-a(n-2)}}{H_e(z)}; X_1 \geq 1 \qquad (12\text{-}23)$$

where $B_1(a,b) = \Gamma(a)\,\Gamma(b)/\Gamma(a+b)$ is the complete Beta Function. Here the altitude dependence is contained principally in the power law in X_1, since $H_e(z)$ is a very slowly varying function of altitude. For reference purposes, Table 12-2 gives values of $d(z)$ and $H_{eo} \equiv d(z)/\rho(z)$ for two model atmospheres. $H_e(z)$ is given by $H_e(z) = H_{eo}(z) \sec \delta$.

Table 12-2. Atmospheric Parameters*

Model ⟶	60^oN		Empirical	
z	d	H_{eo}	d	H_{eo}
km	g/cm^2	10^5cm	g/cm^2	10^5cm
40	2.32 + 0	6.97	2.29 + 0	6.85
45	1.15 + 0	7.32	1.12 + 0	7.10
50	5.92 - 1	7.71	5.67 - 1	7.70
55	3.11 - 1	7.72	2.97 - 1	7.80
60	1.61 - 1	7.49	1.56 - 1	7.48
65	8.23 - 2	7.41	8.00 - 2	7.46
70	4.35 - 2	7.63	4.11 - 2	7.40
75	2.09 - 2	7.04	2.08 - 2	7.53
80	1.01 - 2	6.73	1.09 - 2	7.56
85	4.72 - 3	6.41	6.00 - 3	9.60
90	2.12 - 3	6.09	3.34 - 3	7.11
95	9.50 - 4	6.38	1.57 - 3	6.55
100	4.45 - 4	6.73	7.34 - 4	6.55

*Entries in the table N ± n are to be read N x $10^{\pm n}$.

Model designations are as follows: 60^oN, U.S. Standard Atmosphere Supplements, 1966 (60^oN, January, pp. 124-125);

Empirical, by use of $\rho(z)$ for AT7.396 (A.C. Faire and E.A. Murphy, this volume) from 40-94 km, extrapolated above 94 km.

In most practical instances X_2 is very small, since q(z) calculations are not usually made at atmospheric depths close to the upper limit range R_2. Thus, Eq. (12-23) will usually be a valid approximation at all atmospheric depths exceeding the range R_1 of the minimum energy particles for which the spectrum is defined. At atmospheric depths less than R_1, q(z) can still be calculated by use of Eq. (12-17), but this only provides a lower limit to the production rate. This is true because the contribution due to particles of energy less than E_1 is not known.

For the present rocket flights a spectrum of the form Eq. (12-12) was assumed, with $\beta = 0$, so that the total ionization rate was obtained by use of Eq. (12-17) and

$$q(z, E_1, E_2) = \sum_n q(z, n, E_1, E_2, 0)$$

$$= \sum_n \mathcal{F}(n, E_1, E_2) Q(z, n, E_1, E_2, 0) \qquad (12\text{-}24)$$

where the fluxes $\mathcal{F}$ were found from Eq. (12-8).

12-4 RESULTS

12-4.1 General

Table 12-3 gives pertinent launch and spectral data for the three successful flights.

Table 12-3. Launch and Spectral Data

Rocket	Launch (Date/U. T.)	Apogee (km)	Incident Integral Flux, $(cm^2\text{-sec-sr})^{-1}$		
			p, 2-4 MeV	α, 6-25 MeV	p, 3.5-102 MeV
AJ17.602	2 Nov/2020	120	438 ± 9	48 ± 3	2138 ± 24
AJ17.758	3 Nov/0605	126	458 ± 9	34 ± 3	1186 ± 17
AJ17.617	4 Nov/2308	128	108 ± 4	4.1 ± .5	119 ± 5

The incident integral fluxes were found by 10 to 20-second averages near apogee of the "integral fluxes" $J(z_i, \theta_j)$ for all values of $\theta_j \leq 60^o$. As noted above, it is necessary to multiply $J(z_i, \theta_j)$ by G/G_a to obtain the actual integral flux, as given in the table. For $\theta_j > 60^o$, a portion of the 30^o half-angle viewing cone detects particles with $\alpha > 90^o$. Table 12-4 gives the pitch angle bins for the various rockets, which cover the maximum scanned range in each case.

Table 12-4. Pitch Angle Bins

Rocket:	AJ17.602		AJ17.758		AJ17.617	
Bin Width:	7^o		4^o		7^o	
	Bin #	θ	Bin #	θ	Bin #	θ
	1	39^o	1	52^o	1	46^o
	2	46^o	2	56^o	2	53^o
	3	53^o	3	60^o	3	60^o
	4	60^o	4	64^o	4	67^o
	5	67^o	5	68^o	5	74^o
	6	74^o				
	7	81^o				

Only 17.602 provided a large enough pitch angle scan to determine whether there were many particles incident with $\alpha > 90^o$. A comparison of the observed and calculated variation of flux with θ is given below.

12-4.2 Alpha/Proton Ratio

The data of Table 12-3 in the 2 to 4-MeV proton window and the 6 to 25-MeV alpha particle window can be used to obtain the ratio of differential fluxes at about 3 MeV/n. The resulting values are as follows:

Table 12-5. Rocket Measured Alpha/Proton Ratios at 3 MeV/Nucleon

Date/U. T.	Flux Ratio
2 Nov/2022	.047 ± .003
3 Nov/0607	.031 ± .002
4 Nov/2310	.016 ± .002

The errors listed are statistical only, and the fluxes have the units of $(cm^2\text{-sec-sr-MeV/n})^{-1}$. The data are plotted in Figure 12-4 along with some of the OV5-6 data at about 6.6 MeV/n (Yates et al., this volume). The trend in the ratio of the rocket data, at 3 MeV/n, is similar to that of the satellite data, at 6.6 MeV/n; however, the magnitude of the rocket measured ratio seems to be slightly lower.

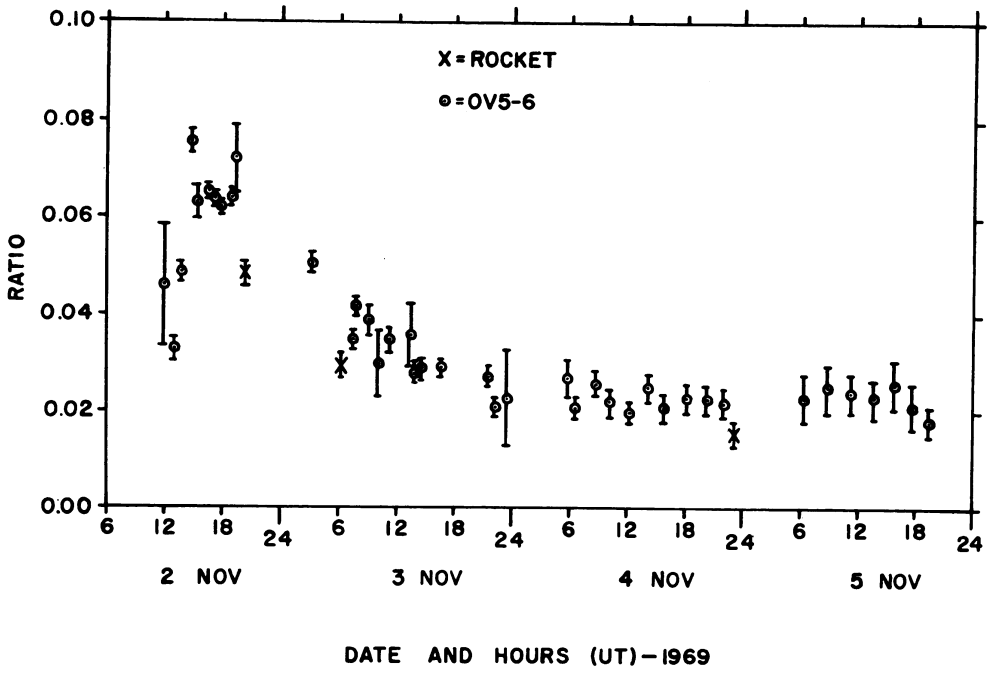

Figure 12-4. Alpha Particle to Proton Differential Flux Ratio Measured by Rockets at About 3 MeV/nucleon and by the OV5-6 Satellite at 6.6 MeV/nucleon Outside the Magnetosphere. Fluxes are in $(cm^2\text{-sec-sr-MeV/nucleon})^{-1}$

From these results it is evident that alphas contributed only a small amount of the ionization in this event, and their contribution was neglected in the q(z) calculations discussed below.

12-4.3 Differential Energy Spectra

Calculation of the $K_n(z_i, \theta_j)$ integrals requires an assumed profile for d(z). Although several flights were made to measure $\rho(z)$ during this event, only one was made at a time near one of these flights (AT7.396 was flown at 0642 U.T. on 3 November). Also none of them provided data significantly above 100 km, whereas, as seen in Table 12-3 particle data were obtained up to at least 120 km. Thus for all three flights the 60^{o}N atmospheric model was used, which gives data up to 118 km; d(z) for this model is shown in Table 12-2 up to 100 km. Use of a model such as this, rather than one such as the "Empirical" model in Table 12-2, which is based totally on one measured $\rho(z)$ profile, affects the shape of the derived incident differential spectrum somewhat, although not its integral value. The choice of $\rho(z)$ profile is not crucial to the q(z) calculation for these flights, since

the same profile used to determine the spectrum is also used to calculate q(z). If the spectrum were determined independently, say by satellite, the effect of the $\rho(z)$ profile on q(z) would be larger.

Particle data were recorded from about 60 km to apogee, and were used to determine the values of $J(z_i, \theta_j)$ by use of Eq. (12-4) for the pitch angle bins given in Table 12-4. About fifteen sets of values for n were used in the spectrum determination procedure for the 3.5 to 102 MeV window (telemetered on Link 2) for each rocket, with each set consisting of five to ten values of n between 1.5 and 6.5. For each n set, an optimum set of J_n was obtained by the procedure described above. The differential spectra produced in this way were then compared for consistency and were generally found to agree within about 10 to 20 percent in magnitude within the valid energy region. The choice of n set used for the q(z) calculation was based somewhat on the differential spectrum agreement with the incident integral spectra between 2 and 4 MeV as given in Table 12-3.

To determine how well this procedure actually fits the experimental data, the values of $J_c(z_i, \theta_j)$ obtained using the optimum J_n set in Eq. (12-6) can be compared with the experimental $J(z_i, \theta_j)$ from Eq. (12-4). This comparison is shown in Figure 12-5 for several pitch angle bins for 17.602. Due to the 30^o half-angle of the aperture, particles with $\alpha > 90^o$ are accepted when $\theta_j > 60^o$. The fit is generally good, although the experimental values exceed the theoretical values somewhat for the large values of θ_j at high altitudes. This suggests that there are actually some particles with $\alpha > 90^o$ that have mirrored below the rocket and are detected when $\theta_j > 60^o$, thus indicating a lack of total agreement with the assumption that α does not vary with altitude. The results given in Figure 12-5 were obtained using a set of five n values: 1.5, 2.0, 2.5, 3.0 and 3.5. Except for the systematic deviation due to mirrored particles, the observed scatter of the experimental fluxes is consistent with the statistical counting uncertainty of the data. Similar results were found for other n sets and for the other rockets. Figure 12-6 shows 10 to 20-second averaged experimental fluxes near apogee for both Lo and Hi as a function of θ_j. Effectively, these are also averages of the incident flux over the acceptance cone. The calculated best fit values obtained from $J_c(z_i, \theta_j)$ are also shown for Hi (this was not done for Lo). Again, it is clear that there are some mirrored particles present, but the assumption of isotropy for downward traveling particles is seen to be well substantiated over most of the angular range.

Our results for the spectra are given in Figure 12-7, including, for comparison, the result obtained for AJ17.758 using the "Empirical" model atmosphere of Table 12-2. In each case these were obtained using sets of five n values. The spectra from Hi are considered to be valid only down to about 3.5 MeV, to have an absolute upper limit of about 100 MeV, and to have maximum validity only up to

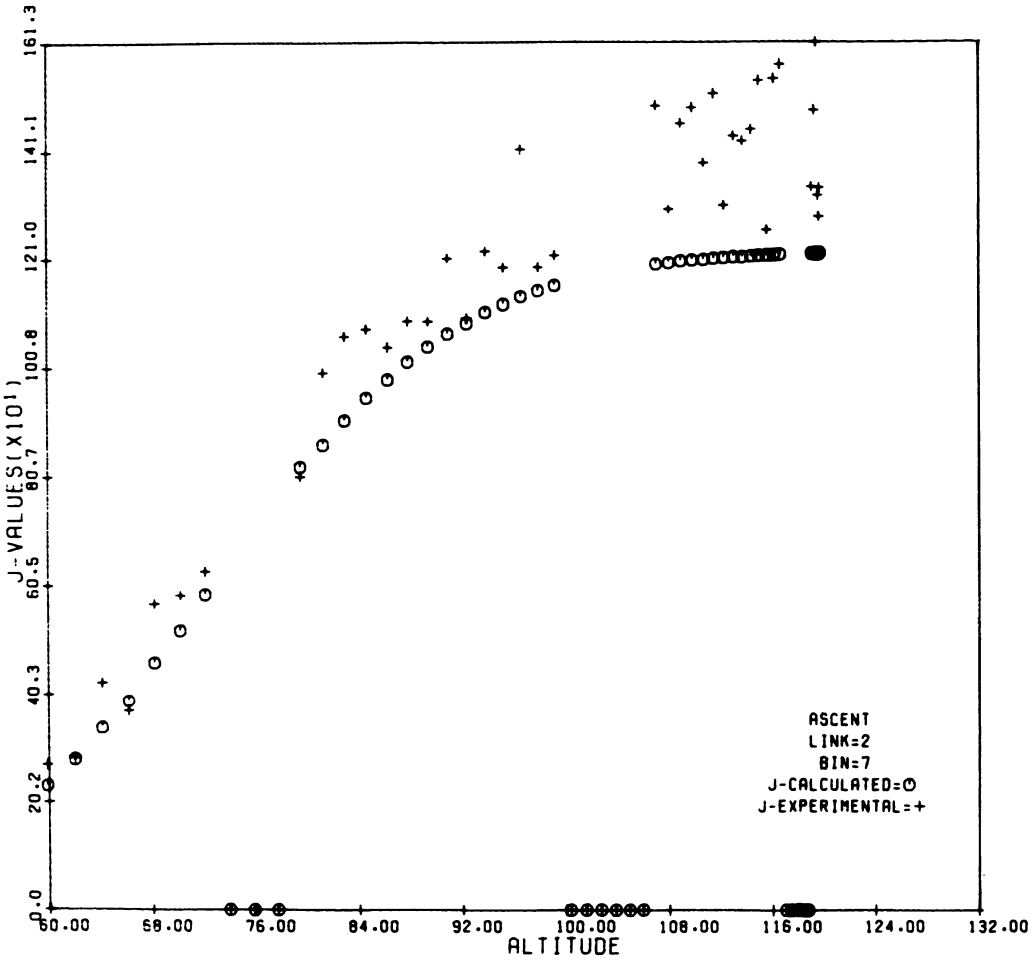

(a) $\theta = 81°$

Figure 12-5. Comparison of Calculated and Experimental Values of Hi Proton "Integral Flux" $J(z_i, \theta_j)$ for AJ17.602. Fluxes are in $(cm^2\text{-sec-sr})^{-1}$. Average statistical uncertainty in flux values is 10 percent; zero values indicate that no data were available for that pitch angle bin at that altitude

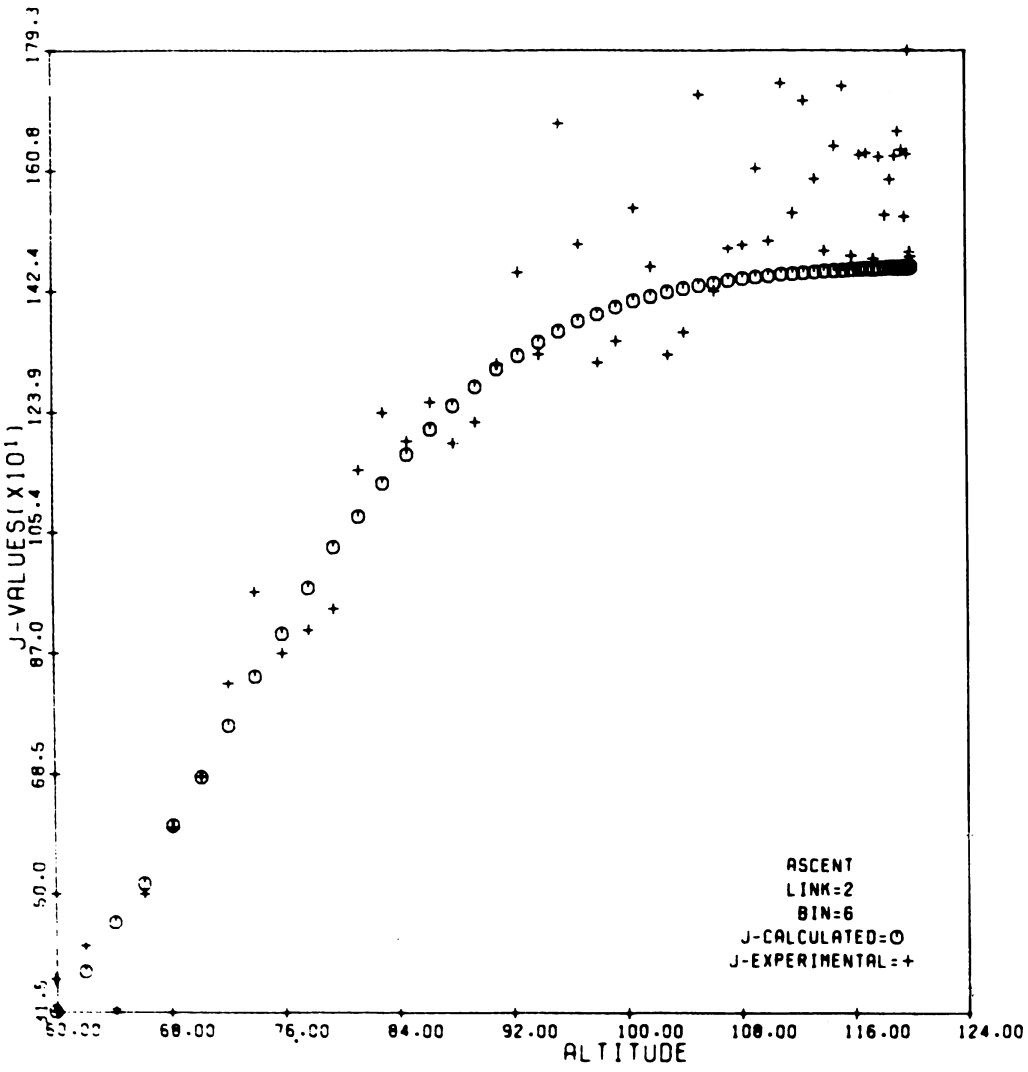

(b) $\theta = 74°$

Figure 12-5 (Contd.) Comparison of Calculated and Experimental Values of Hi Proton "Integral Flux" $J(z_i, \theta_j)$ for AJ17.602. Fluxes are in $(cm^2\text{-sec-sr})^{-1}$. Average statistical uncertainty in flux values is 10 percent; zero values indicate that no data were available for that pitch angle bin at that altitude

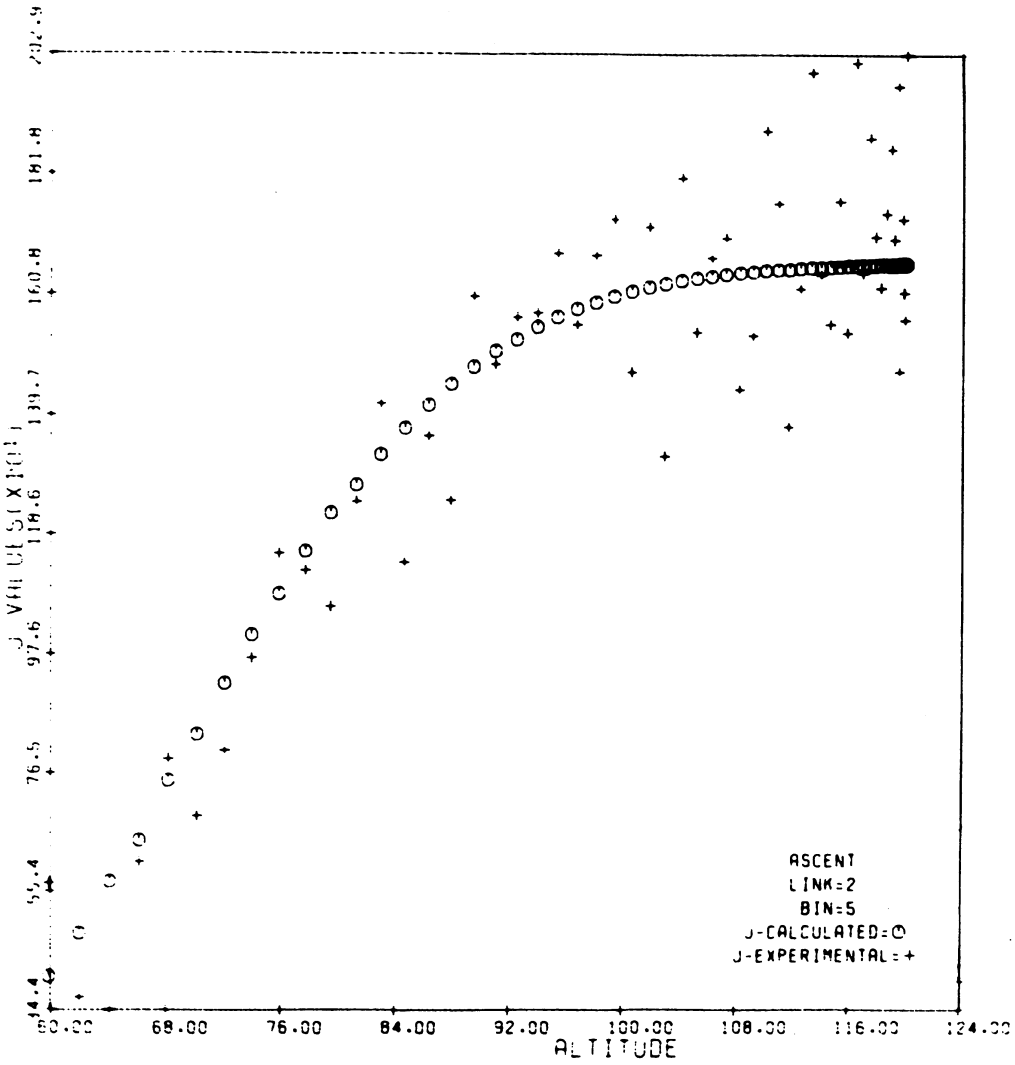

(c) $\theta = 67°$

Figure 12-5 (Contd.). Comparison of Calculated and Experimental Values of Hi Proton "Integral Flux" (Jz_i, θ_j) for AJ17.602. Fluxes are in $(cm^2\text{-sec-sr})^{-1}$. Average statistical uncertainty in flux values is 10 percent; zero values indicate that no data were available for that pitch angle bin at that altitude

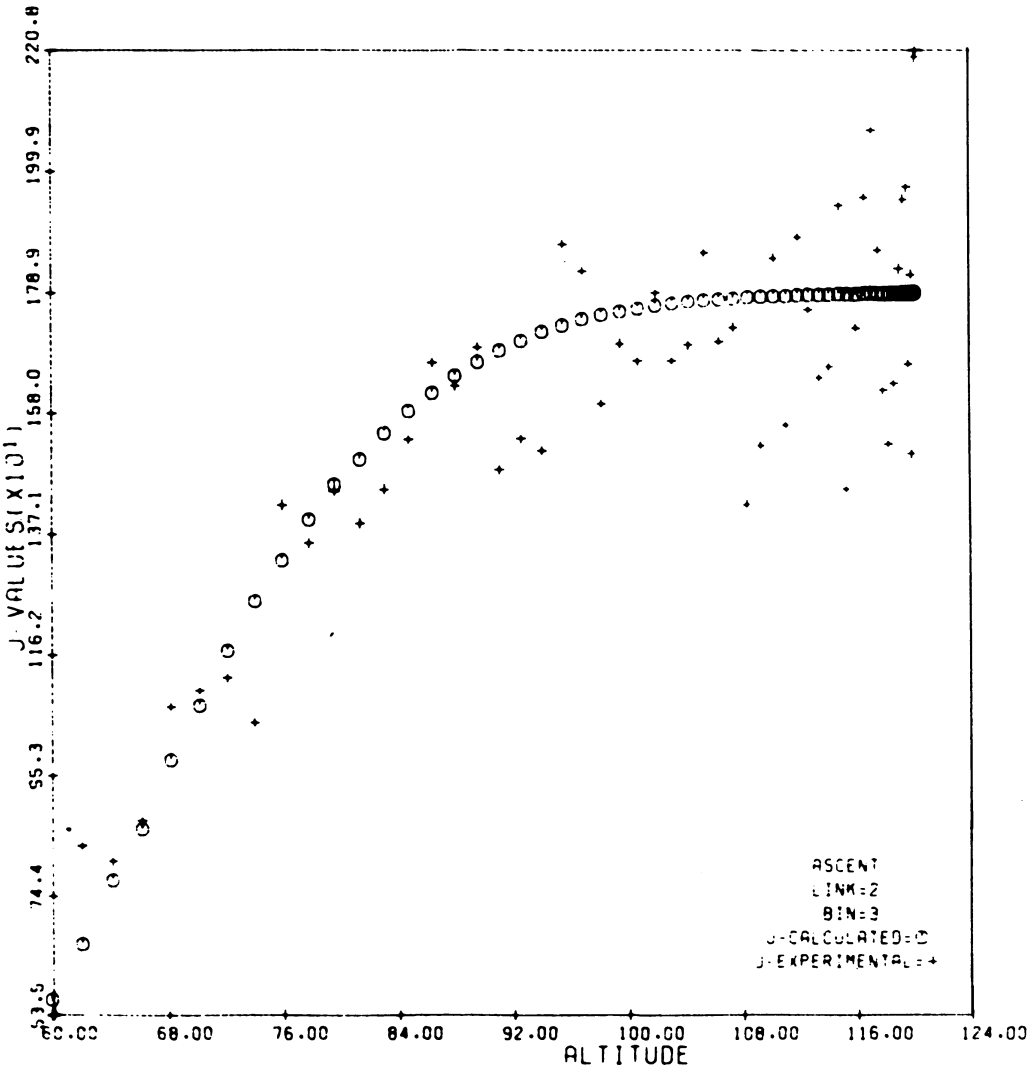

(d) $\theta = 53°$

Figure 12-5 (Contd.). Comparison of Calculated and Experimental Values of Hi Proton "Integral Flux" $J(z_i, \theta_j)$ for AJ17.602. Fluxes are in $(cm^2\text{-sec-sr})^{-1}$. Average statistical uncertainty in flux values is 10 percent; zero values indicate that no data were available for that pitch angle bin at that altitude

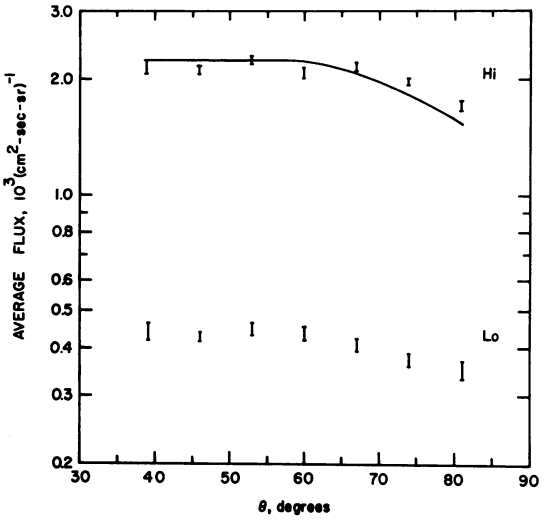

Figure 12-6. Angular Distribution of Calculated and Experimental Proton Integral Fluxes Near Apogee for AJ17. 602

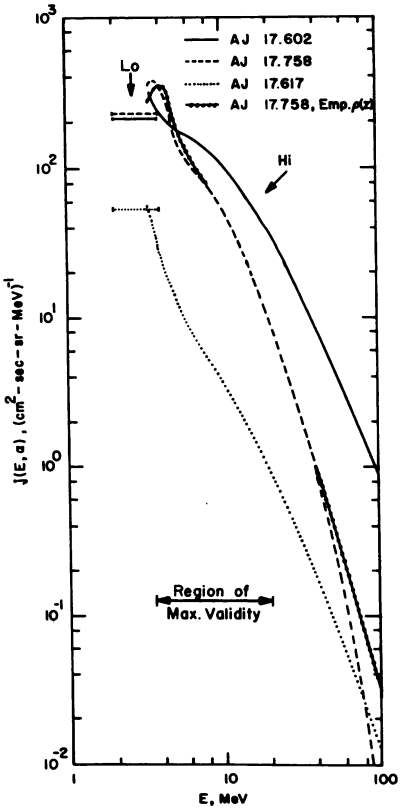

Figure 12-7 Proton Differential Energy Spectra for PCA69 as Deduced From Low (Lo) and High (Hi) Energy Spectrometers

about 20 MeV, since the maximum path length that occurred on ascent was about 0.5 g/cm^2 - corresponding to a range altitude of about 50 km. Also included in Figure 12-7 are the average results from Lo for the 2-4 MeV region as obtained from Table 12-3. As expected, the spectra are found generally to soften and reduce in intensity as time increases.

12-4.4 Ionization Rates

To obtain the ionization rates the values of J_n associated with the spectra of Figure 12-7 were used in Eq. (12-8), and $q(z, E_1, E_2)$ was calculated from Eq. (12-24) with E_1 = 3.5 MeV, E_2 = 100 MeV, and using the appropriate model in Table 12-2. In these models the range altitude for a vertically incident 3.5 MeV particle is about 75 km. Thus the ionization rates shown in Figure 12-8 above 75 km are lower limits only. If a geomagnetic cutoff existed just below 3.5 MeV, these rates would approximate the total value, but the spectra of Figure 12-7 suggest that if such a cutoff existed it was probably somewhat below 3 MeV. The disagreement in the 17.758 results above 85 km is due to the difference in density in this region for the two models. Below 50 km the divergence is caused by the difference in the spectra in Figure 12-7 above 40 MeV, where the spectrum is not well defined. Including all sources of uncertainty, we believe the results for q(z) are accurate to about ±15 percent within the region of validity, limited principally by the assemption that the pitch angle of incident particles does not vary with altitude.

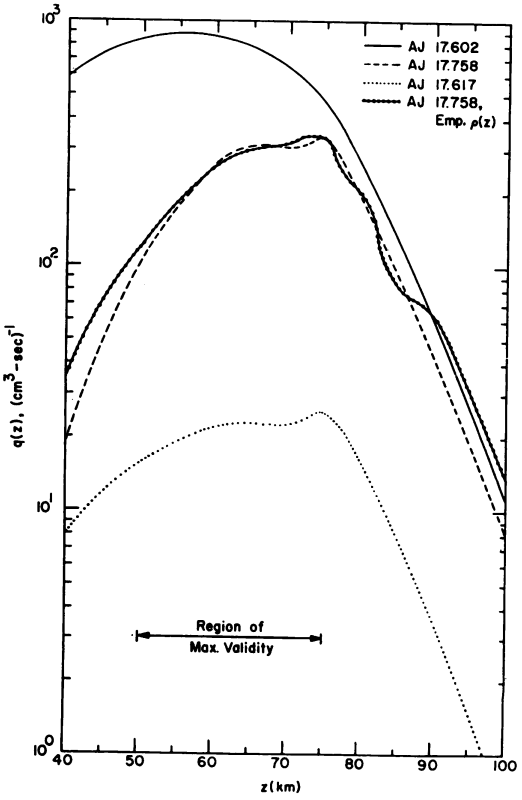

Figure 12-8. Proton Induced Ionization Rates for PCA69. Above 75 km the rates are lower limits only. δ (Figure 12-1) = 6°

12-5 CONCLUSIONS

The method of calculating the incident differential spectrum from the measured variation of integral flux with altitude was found to be generally accurate, although results for the spectrum would have been improved by a simultaneous measurement of air density to the required altitude.

The technique for calculation of q(z) by Eq. (12-17) was readily adapted to a digital computer, and the analytic function Eq. (12-23) was found to provide a useful check on the results.

Acknowledgments

The authors would like to express their appreciation to Mr. John A. Sandock and Mr. James C. Ulwick for their constant guidance during the course of this work, which was supported by AFCRL under Contract No.'s F19628-67-C-0208 and F19628-71-C-0086. Data processing was carried out by the Analysis and Simulation Branch (SUYA) of the Computation Center, AFCRL, under Contract No. F19628-71-C-0048 with RDP, Inc. and Contract No. F19628-70-C-0236 with ACSI, Inc.

References

Abramowitz, M. and Stegun, I.A., Editors (1964) Handbook of Mathematical Functions, U.S. Govt. Printing Office.

Janni, F.J. (1966) Calculations of Energy Loss, Range, Pathlength, Straggling, Multiple Scattering, and the Probability of Inelastic Nuclear Collisions for 0.1 to 1000 MeV Protons, AFWL-TR-65-150, AD643837.

Sellers, B. (1970) Preliminary Data Analysis of Solar Flare Rocket Flights of November, 1969, Proceedings of Meeting on Operation PCA 69, AFCRL-70-0625, pp 53-58.

Sellers, B., Hunerwadel, J.L., and Hanser, F.A. (1970) Research Directed Toward the Design, Development and Installation of Instrumentation to Study Energy Spectra of High Energy Solar Protons in Polar Cap Events; Vol. I. The Black Brant Payload and the 19 November 1968 PCA Event, Final Report submitted to AFCRL under Contract No. F19628-67-C-0208.

U.S. Standard Atmosphere Supplements (1966) U.S. Government Printing Office.

Contents

13. A Review of Ionospheric Radio-propagation Effects Associated With Solar-Proton Events

G.C. Reid
Aeronomy Laboratory
National Oceanic and Atmospheric Administration
Boulder, Colorado

Abstract

Solar-proton bombardment causes substantial increases in the concentration of ions and electrons throughout the polar ionosphere. The increases are particularly pronounced in the lower ionosphere, where normal ambient concentrations are small, and they give rise to a variety of effects on radio waves propagating through the ionosphere, allowing study of solar-proton events by purely ground-based techniques. This paper reviews the nature of these effects and the current status of our understanding of the mechanisms involved.

13-1 INTRODUCTION

Solar-proton events give rise to major effects in the earth's ionosphere. Some of these have important practical consequences in terms of the increasing needs for reliable radio-communication links at high latitudes, while several of them can be used as potential sources of important scientific information, both on the properties of the solar-particle fluxes themselves and on the mechanisms that

govern the production and loss of ionization in the polar upper atmosphere. Indeed, the first realization that the sun was a relatively plentiful source of sub-relativistic particles came about through interpretation of some of these ionospheric effects, and in the days before satellite monitoring became a reality the polar ionosphere was the major detector of the presence of solar protons in the vicinity of the earth.

Since these early days, the importance of the ionospheric effects as monitors of the particle flux has decreased as direct satellite data has become increasingly available over a steadily widening range of particle energies. The ionospheric techniques still have a role of this kind of play, however, since satellites are not always where one would like them to be, and satellite data is usually far from continuous in time over the rather long periods of several days during which solar-proton fluxes often persist. The major role of the ionospheric techniques nowadays, however, is in studying the response of the lower ionosphere to solar-proton ionization. In this kind of investigation there are essential complementary parts to be played by satellite data on particle fluxes, by rocket measurements made at discrete moments of time, and by the continuous monitoring supplied by the ionospheric techniques.

This paper is intended to provide a brief review of the influence of solar-proton bombardment on the ionosphere as revealed by radio-propagation techniques. The problems of ion chemistry and the details of the electron-density profile will not be considered, since they will be dealt with in other parts of the proceedings. It is worth saying at the outset that our understanding of most of the effects tends to be qualitative rather than quantitative, and the field is one of phenomenology and empirical relations rather than the precise quantitative relationships that most physicists like to deal with. Hopefully this situation is capable of improvement, and it is through detailed studies of the kind we are discussing at this conference that the improvement is likely to come.

13-2 RADIO-PROPAGATION EFFECTS AT HF AND VHF

The basic physical factor that gives rise to all the ionospheric effects is the great increase in ionization in the lower ionosphere; that is, at altitudes below about 100 km. At higher altitudes, the particles ionize much less efficiently and any effects that occur tend to be masked by the relatively intense ionization created by the normal sources. During the event of February 1969, a search for F-region effects was carried out using probe measurements on board the ESRO-1 satellite between 300 and 1300 km (Raitt, 1970), but no obvious effect was found.

At altitudes below 100 km, and at frequencies in the hf and vhf range, the principal effect is one of increased absorption of radio waves. This increased

absorption is particularly easy to measure in the case of waves that traverse the entire ionosphere along known ray paths, that is, at frequencies above the maximum critical frequency of the ionosphere. These strong absorption effects are easily recognized, and were, of course, responsible for the term 'polar-cap absorption' that is now widely used to describe the entire range of phenomena embracing the ionospheric response to solar-proton bombardment. The absorption is also the easiest of the ionospheric effects to interpret quantitatively and to understand physically. Briefly, the increased electron concentration means that there are more electrons available to pick up energy from the radio waves. The fact that the electrons are produced in regions where collisions are relatively frequent means that this energy can be efficiently transferred to the neutral atmosphere, resulting in absorption of the radio-wave energy. Quantitatively, the mechanism can be understood in terms of the magneto-ionic theory, and as a rough approximation the absorption, A, can be written as

$$A \propto \int_o^\infty \frac{N\nu}{\nu^2 + (\omega \pm \omega_L)^2}\, dh \qquad (13\text{-}1)$$

where N is the electron concentration, ν is the momentum-transfer collision frequency for electrons, ω is the radio-wave angular frequency, and ω_L is the component of the electron angular gyrofrequency along the ray path. There is no evidence for, nor reason to expect, any changes in ν during solar-proton bombardment, and the intense absorption effects arise purely from the great increase in N in the region where ν is significant.

The principal source of information on absorption has been the riometer, which simply monitors the intensity of cosmic noise, usually incident vertically. A frequency of 30 MHz has generally been used for these measurements, representing a suitable compromise between lower frequencies, at which the absorption is more intense but propagated interference becomes a serious factor; and higher frequencies, at which the absorption becomes smaller and more difficult to measure. In the early history of PCA events, riometer data was widely used as a source of information on solar-proton fluxes (Reid and Collins, 1959; Hultqvist, 1959; Leinbach and Reid, 1959). Riometers still provide a useful basis for long-term synoptic studies of solar-proton events (for example Goedeke et al, 1967) and for calibrating indices of solar-proton activity (Smart and Shea, 1970). The basic problem in interpreting riometer measurements quantitatively is the fact that they provide only an integrated measure of the response of the entire lower ionosphere, and the detailed relationship between proton flux and radio-wave abosrption depends on knowing the quantitative details of the ion chemistry involved in the loss of

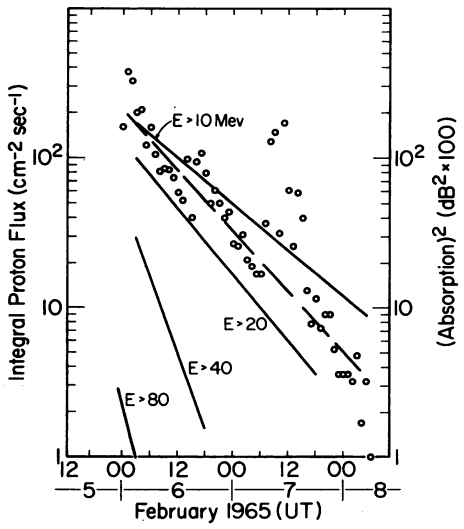

Figure 13-1. Decay of the Flux of Protons in Four Energy Channels During the Solar-proton Event of February 1965, Compared With the Decay of the 30-MHz Absorption Recorded at the South Pole. The proton flux data is taken from Paulikas et al (1966)

electrons. It is possible, however, to develop empirical relations between proton flux and absorption, and several such relations have appeared (Van Allen et al, 1964; Parthasarathy and Venkatesan, 1964; Adams and Masley, 1966; Juday and Adams, 1969; Potemra et al, 1969). Figure 13-1 shows an example of the relationship that can be found (Reid, 1970). This shows the time-history of the proton flux in four energy channels as observed by the satellite 1964-45A (Paulikas et al, 1966) over the polar caps (solid lines) and the 30-MHz absorption measured by a riometer at the South Pole during the event of February 1965. The dashed line is a least-squares fit to the riometer data (excluding the brief enhancement on 7 February), and indicates that the time-history of the absorption is closer to that of the protons with energy greater than 20 Mev than to that of the other channels. This particular piece of data gives the following relationship between 30-MHz vertical absorption and proton flux:

$$J(> 20 \text{ Mev}) = 60\, A^2 \qquad (13\text{-}2)$$

where A is the absorption in decibels and J is the 2π-omnidirectional proton flux in $cm^2\ sec^{-1}$. Although only strictly valid for this particular event, this relation can be used to examine the limits of usefulness of the riometer technique in an approximate way.

At the lower limit, it is not possible in practice to measure absorption of less than about 0.3 dB, so that the technique is restricted to proton fluxes above about 6 $cm^{-2}\ sec^{-1}$ (or about 1 $cm^{-2}\ sec^{-1}\ ster^{-1}$ in terms of directional flux). At the upper limit, the restriction is imposed by thermodynamic considerations, rather than by equipment sensitivity. The ionosphere emits thermal radiation in direct proportion to its power to absorb, and the power received by the riometer, P_r, is given by

$$P_r = \alpha P_c + (1 - \alpha) P_i \qquad (13\text{-}3)$$

where α is the fraction of the incident power transmitted by the ionosphere, P_c is the cosmic-noise power, and P_i is the thermal power corresponding to the temperature of the ionospheric electrons. When $\alpha = 1$, the riometer records pure cosmic noise, and when $\alpha = 0$ (complete absorption) the riometer still records a signal, but one originating from the ionosphere itself. In terms of effective temperatures, the cosmic noise signal at 30 MHz corresponds to a temperature of about 20,000°K, and the temperature of the electrons in the lower ionosphere is of the order of 200°K. Thus when absorption reduces the apparent cosmic-noise temperature to 200°K, the riometer runs into serious difficulties as far as quantitative measurements of absorption are concerned. This corresponds to a factor of 100 in transmitted power, or an absorption of 20 dB. The effect is illustrated in Figure 13-2, which shows the effective antenna temperature as a function of absorption by a uniform ionospheric layer. Ionospheric thermal radiation begins to be appreciable at 10 dB, and makes the absorption virtually unmeasurable much above 20 dB. From Eq. (13-2) above, this leads to a maximum observable proton flux of about 2.4×10^4 cm^{-2} sec^{-1} (directional flux of 4×10^3 cm^{-2} sec^{-1} ster^{-1}). Thus

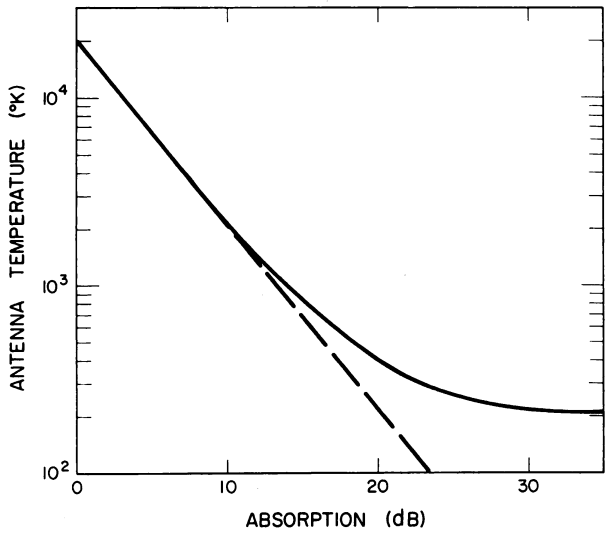

Figure 13-2. Antenna Temperature as a Function of Absorption by a Uniform Ionospheric Layer, Assuming a Source Temperature of 20,000°K and an Ionospheric Temperature of 200°K. The broken line shows the relationship that would exist if the ionospheric thermal emission were ignored; the solid curve includes this ionospheric contribution

regarded as a detector of solar protons, the riometer has an approximate dynamic range of 1 to 4000 protons cm^{-2} sec^{-1} $ster^{-1}$ with energies above 20 Mev. These values refer to daytime conditions—during the night the absence of solar photochemical effects make the lower ionosphere much less sensitive, and the primary response is greatly reduced, and is due to protons of considerably lower energies (Reid, 1969).

At frequencies above 30 MHz, thermal radiation from the ionosphere becomes an increasingly serious problem, since the cosmic-noise power decreases sharply with increasing frequency. In the neighborhood of 200 MHz the effective temperature of the galactic source becomes lower than that of the ionosphere, and absorption should be accompanied by an increase in received power, rather than a decrease, since the power is being received increasingly from the relatively hot ionosphere rather than from the relatively cold galaxy. Recently, experiments aimed at detecting such signal increases at VHF have been carried out in the auroral zone by Leinbach and Ecklund (1968), but no definitive observations of the effect have yet been obtained.

Strong absorption effects are also recorded by other techniques operating in the hf and lower vhf range, for example, by normal sweep-frequency ionospheric sounders operating at high magnetic latitudes. Ionosonde echoes are received only at frequencies below the maximum ionospheric critical frequency, and hence the magnitude of the absorption experienced is larger than in the case of riometers. The technique is thus more sensitive to weak events, which are revealed by abnormal increases in the minimum frequency at which detectable echoes are received. When this minimum frequency exceeds the F-region critical frequency, a complete blackout is recorded, and the technique has no quantitative sensitivity beyond that point, although in principle this limit could be extended by employing more sensitive receiving systems. Because of its dependence on equipment parameters, the technique has not proven to be a source of quantitative information on PCA events, but it has frequently been used to deduce information about the time of onset of events (Hakura, 1967), their qualitative morphology (Hakura, 1961), and their synoptic occurrence over long periods of time, particularly before the more modern techniques became available (Collins et al, 1961). Some of the early PCA events of the IGY period were indeed recognized as a distinct phenomenon solely on the basis of high-latitude ionosonde data (Hakura et al, 1958). Figure 13-3 shows an example (Collins et al, 1961) of the kind of information that has been deduced on the long-term solar-cycle occurrence of PCA events by use of ionosonde data.

Ionospheric sounding measurements have not produced any surprises as far as PCA is concerned, but studies of oblique hf propagation have revealed at least one puzzling feature. Egan (1963) investigated the propagation of 12-MHz signals

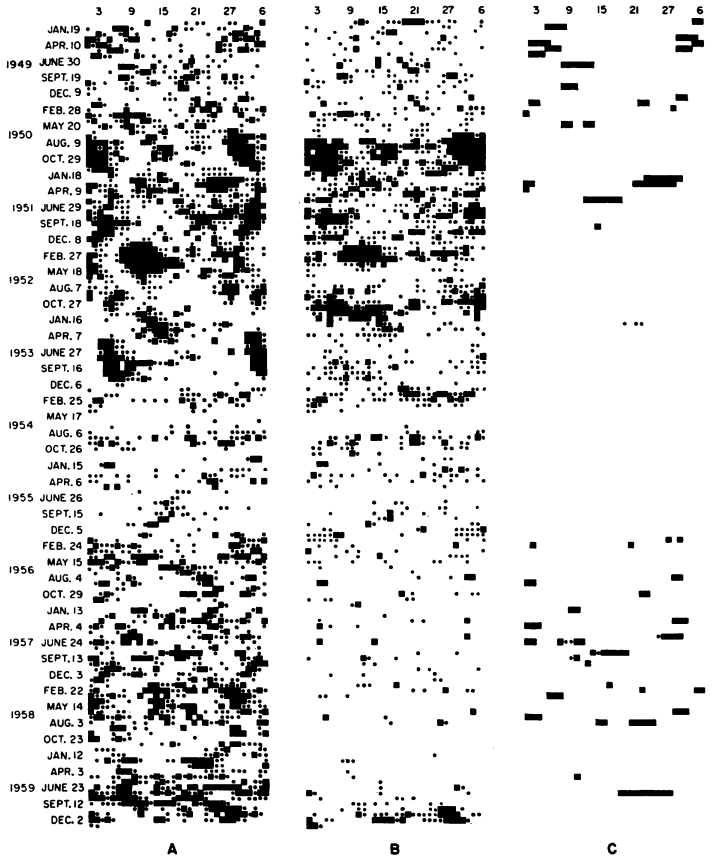

Figure 13-3. 27-day Recurrence Time Patterns of (A) Magnetic Activity at Meanook, (B) All Blackouts Recorded at Churchill, Excluding Polar-cap Blackouts, (C) Polar-cap Blackouts at Churchill. The diagram is taken from Collins et al (1961), and is reproduced by permission of the National Research Council of Canada

from Thule, Greenland, to College, Alaska, during the major PCA events of April and May 1960, and found that the signal strength over this polar-cap path was very much greater than would have been predicted on the basis of extrapolation of riometer measurements of vertical 30-MHz absorption. Riometers recorded absorption in excess of 10 dB at times during these events over the entire path, and the calculated oblique-incidence 12-MHz absorption would have been expected to reach over 400 dB. In fact the absorption never exceeded about 35 dB, reaching this value shortly after the start of the event and remaining at about the same level through the peak of the event as recorded by riometers.

It is possible that this anomalously high-signal strength can be explained by the greatly increased electron density of the lower ionosphere, leading to the possibility of propagation via reflection from the D region itself, with only slight penetration of the radio waves into the absorbing region. This explanation requires further investigation, however.

High-frequency radio-wave propagation during PCA events is actually helped by one factor. During PCA events the background atmospheric noise level is substantially decreased, since in polar regions most of this noise is due to integrated atmospherics generated by distant (mainly tropical) thunderstorms and propagated to high latitudes by ionospheric reflection. The reduction in noise level that occurs during PCA events has been studied by Herman (1962), and Jelly (1963) has shown that the signal-noise-ratio on arctic hf communications circuits is little affected by the presence of PCA events. Figure 13-4 shows a comparison between normal and PCA days as measured on a link between Resolute Bay and Ottawa.

At much higher frequencies, Pope and Leinbach (1970) have recently predicted the influence of PCA events on vhf communications links to synchronous satellites from high-latitude aircraft or ground stations. Because synchronous satellites are located vertically above the equator, the line-of-sight path from high-latitude locations penetrates the lower ionosphere quite obliquely, giving rise to substantial absorption effects even at vhf frequencies. The absorption at 137 MHz may be as much as half of the vertical 30-MHz absorption, that is, up to about 10 dB, depending on the latitude of the ground station or aircraft and the shape of the proton spectrum. Thus PCA events are likely to pose important communications problems

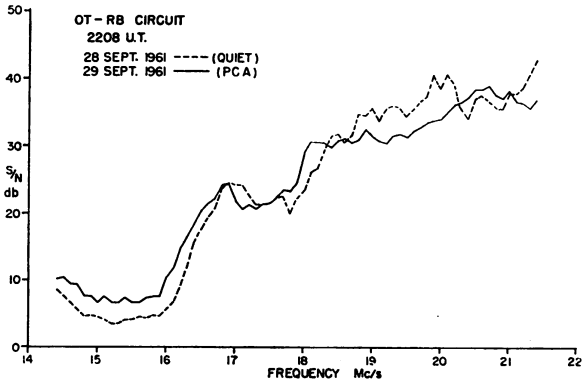

Figure 13-4. The Signal-to-noise Ratio Measured on an Oblique-incidence Ionosonde Circuit Between Ottawa and Resolute Bay on a Quiet Day (28 September 1961) and During a PCA Event (29 September 1961). From Jelly (1963)

even at frequencies that are normally considered as being well beyond those affected appreciably by the ionosphere.

In addition to regular ionospheric reflection, weak scatter of radio waves occurs from turbulent irregularities in the electron concentration of the lower ionosphere. This weak scattered signal gives rise to partial reflections in the mf and lower hf regions, and to forward scatter at upper hf and lower vhf frequencies where the phenomenon has formed the basis for forward-scatter communications links. The pioneering work on the influence of PCA events on vhf forward-scatter signals was carried out by Bailey (1957, 1959), who made the first serious study of solar-proton-induced ionization on the basis of the major effects observed during the relativistic proton event of February 1956. As a technique, vhf forward scatter shows similar effects to those observed by riometers, but quantitative interpretation is hampered by uncertainty in the height of the irregularities that are responsible for propagating the signal. If there is a substantial portion of the absorbing region below the altitude of the irregularities, the signal is strongly absorbed, but if most of the absorbing region lies above the irregularities the signal is enhanced due to the increased electron concentration in the neighborhood of the scatterers. The technique has, however, proved important in identifying events and in providing the basis for lists of past events (Bailey and Harrington, 1962).

The measurement of partial reflections at lower frequencies has more promise in a quantitative sense, since it can give us information on both electron concentration and collision frequency. Observations by Gregory (1963) using a frequency of 2.3 MHz at Scott Base, Antarctica, revealed the existence of several events in 1960 that were too weak to be recorded by riometers. The sensitivity to weak events is again a consequence of the low frequency, but this again leads to a disadvantage when intense events are observed. Since the signals are heavily absorbed near the bottom of the absorbing region, the electron-density profile can be measured only near the base. Figure 13-5 shows some profiles measured by

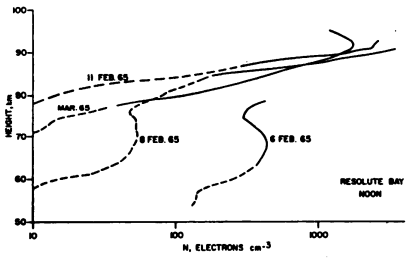

Figure 13-5. Electron-concentration Profiles Measured by the Partial-reflection Technique at Resolute Bay. The profiles are for three days in February 1965 and for an average day in March. The diagram is taken from Hewitt (1969), and is reproduced by permission of the National Research Council of Canada

Hewitt (1969) using a frequency of 2.66 MHz at Resolute Bay during the events of February 1965 and July 1966. Further results obtained with this technique will be presented in these proceedings.

13-3 RADIO-PROPAGATION EFFECTS AT LF AND VLF

Turning to the lower frequency ranges of the lf (30 to 300 kHz) and vlf (3 to 30 kHz) bands, we find a group of phenomena that can be understood qualitatively, but whose quantitative interpretation is not yet on firm ground.

Historically, the topic of PCA-associated vlf disturbances started with the relativistic event of 23 February 1956, which also marked the starting point for the entire field of polar-cap absorption. Severe disturbances in the amplitude and phase of vlf signals received at midlatitudes were observed over short paths (Belrose et al, 1956) and over long paths (Allan et al, 1957; Ellison and Reid, 1956; Pierce, 1956), and were generally attributed to the increased ionization produced by the relativistic solar cosmic rays in the lower ionosphere. Shortly after the existence of much more frequent non-relativistic solar-proton events was realized, it became evident that these events were also responsible for major disturbances on vlf circuits that crossed the polar caps (Ortner et al, 1960; Eriksen and Landmark, 1961). Since then several papers have presented data on vlf effects associated with PCA events, and have discussed the physical processes involved (for example, Bates, 1962; Belrose, 1963; Egeland et al, 1963; Albee and Bates, 1965; Crombie, 1966; Egeland and Naustvik, 1967). The most extensive recent study has been that of Westerlund et al (1969), who investigated eleven major PCA events in 1966 and 1967 by means of phase and amplitude measurements on several transpolar paths. Some of their conclusions were:

(1) In the absence of antipodal interference, and over paths longer than about 2000 km, phase advances were always seen, corresponding to a lowering of the reflection height.

(2) Amplitude variations were uncertain and relatively unpredictable - both increases and decreases of signal strength are seen, depending on unknown factors.

(3) Theory indicates that there should be an approximate linear relationship between the phase shift and the log log of the proton flux that affects the region of propagation. Figure 13-6 shows that this relationship is fairly well obeyed, but the observations show two distinct straight lines for the vlf data from different paths. The authors show that the dashed line corresponds to paths that cross the Greenland ice-cap, where the ground conductivity is low, while the solid curve corresponds to paths that lie mainly over the oceans, with a very high surface conductivity. The much larger effects over the ice-cap paths are related to the change

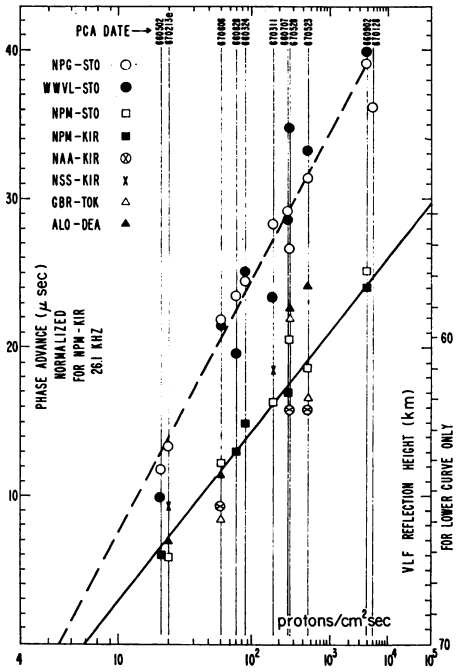

Figure 13-6. Daytime Phase Advance on High-latitude VLF Circuits as a Function of the Flux of Protons With Energy Greater than 25 MeV. Phase advances have been normalized to a frequency of 26.1 kHz and to a PCA-affected path portion of 5300 km. From Westerlund et al (1969)

in the phase velocity of the waves in the earth-ionosphere waveguide, and implies, for instance, that Antarctic vlf paths would be expected to be more sensitive to PCA effects than most arctic paths. The dependence on the log log of the proton flux (chosen here as the flux above 25 MeV) means that the vlf phase becomes much less sensitive to modulation in the proton flux when the flux is high, that is, near the peak of an event, than when it is low, that is, near the beginning or end of an event. Extrapolating the lines to zero phase shift indicates the lower limit of sensitivity of the technique as lying at about 5 protons cm^{-2} sec^{-1} (or about 1 cm^{-2} sec^{-1} $ster^{-1}$ directional flux).

This latter value for the minimum detectable flux is almost identical to the value quoted earlier for the minimum flux detectable by a vertical 30-MHz riometer, which leads to an anomalous situation. The statement has frequently been made that vlf phase shifts are a much more sensitive means of detecting solar-proton fluxes than the riometer. The data of Figure 13-6 appear to disprove this

statement, yet evidence certainly exists that vlf phase often shows a large effect at about the time of onset of an event as seen by satellites, and long before riometers record any appreciable PCA (for example, Crary and Diede, 1969). This is understandable if the riometer is in darkness, since its sensitivity is then much lower than its daytime value, but this has not always been the case when the comparisons have been made. It is possible that vlf phase is much more sensitive to weak fluxes at higher energies (for example, greater than 200 Mev), which predominate in the proton flux at the beginning of an event. This explanation would pose a problem, however, in the later phases of a major event, when it has been found that the vlf effects have a very long duration (for example Albee and Bates, 1965), also indicating a considerably more sensitive response to weak proton fluxes than that of the riometer. The particles responsible in the later stages of an event, however, are much more likely to be of lower energies, since the decay of the proton flux is usually more rapid at higher energies. Thus it appears that vlf phase measurements have roughly the same sensitivity to solar-proton fluxes as riometer measurements in the energy range to which riometer measurements apply, while their sensitivity to fluxes at both higher and lower energies is substantially greater than that of the riometer.

The magnitude of the effects experienced on a long-distance vlf path must depend in some way on the integrated properties of the entire portion of the earth-ionosphere waveguide that affects the path, and different regions are usually experiencing different conditions of sunlight and of proton flux at any given time. The complexity of the situation makes quantitative studies very difficult, if not impossible, except in very broad terms. Very-low-frequency measurements at vertical incidence are not nearly as subject to these problems, and vlf sounding has been carried out during PCA events by Helms and Swarm (1969) at Byrd Station, Antarctica, using a 34-km-long dipole antenna buried in the ice. These authors were able to make direct measurement of reflection phase height and its changes, and found typical drops in daytime reflection height from about 85 km under normal conditions to about 65 km during a PCA event. Long-distance vlf phase shifts have also been interpreted quantitatively by Potemra et al (1967, 1969), who have shown that they can be understood in terms of an exponential model for the conductivity of the D region (Wait and Spies, 1964).

In the lf (30 to 300 kHz) band of the radio spectrum, not much information is available. Observations on high-latitude paths at frequencies in the 70 to 80-kHz range during the November 1960 PCA events have been reported by Belrose and Ross (1961), who concluded that weak PCA events produced opposite effects on daytime and nighttime signal strengths, that is, daytime signals were stronger than usual, and nighttime signals were weaker. The transition between the two occurred quite suddenly at mid-path twilight. Strong PCA events tended to remove

the normal diurnal variation in signal strength entirely, and also removed the usual pronounced nighttime fading, indicating the presence of a homogeneous layer of ionization whose reflection properties were independent of the presence of sunlight.

13-4 SUMMARY

The ionization created in the high-latitude upper atmosphere by solar-proton fluxes can thus have major effects on the polar ionosphere, and these in turn cause abnormal phenomena to occur on ionospherically propagated radio signals over a very wide range of frequencies. An approximate threshold flux for appreciable ionospheric effects is 1 proton cm^{-2} sec^{-1} $ster^{-1}$ with energy above 20 Mev, though the possibility that vlf phase measurements are considerably more sensitive to weak fluxes of both higher and lower energies than this requires further investigation.

Of the various ionospheric effects that occur, the only one that lends itself to fairly precise quantitative interpretation is the absorption suffered by a radio wave that traverses the entire ionosphere without appreciable refraction, for example, as measured by a riometer. The other techniques tend to be hampered by such factors as uncertainties in reflection height (for example, vhf forward scatter), dependence on uncertain equipment parameters (for example, vertical-incidence ionospheric sounding), or integration of effects over long distances (for example, transpolar vlf effects). The use of partial reflections from D-region irregularities and of vertical sounding at VLF are promising, but a great deal of further work in these areas is needed. Until our understanding of the complex ion chemistry of the D region is more complete, it appears that the ionospheric effects of solar-proton bombardment will find their principal use in qualitative descriptions of the morphology and time-history of solar-proton events, and the important practical consequences of these effects for radio communication can best be predicted by the development of empirical relations.

References

Adams, G.W. and Masley, A.J. (1966) Theoretical study of cosmic noise absorption due to solar cosmic radiation, Planetary Space Sci. 14:277.

Albee, P.R. and Bates, H.F. (1965) VLF observations at College, Alaska, of various D-region disturbance phenomena, Planetary Space Sci. 13:175.

Allan, A.H., Crombie, D.D., and Penton, W.A. (1957) Long-path vlf frequency variations associated with the solar flare of 23 February 1956, J. Atmospheric Terrest. Phys. 10:110.

Bailey, D.K. (1957) Disturbances in the lower ionosphere observed at VHF following the solar flare of 23 February 1956 with particular reference to auroral-zone absorption, J. Geophys. Res. 62:431.

Bailey, D.K. (1959) Abnormal ionization in the lower ionosphere associated with cosmic-ray flux enhancements, Proc. IRE 47:255.

Bailey, D.K. and Harrington, J.M. (1962) A survey of polar cap absorption events (solar proton events) in the period 1952 through 1960, J. Phys. Soc. Japan 17(Suppl. A-II):334.

Bates, H.F. (1962) Very-low-frequency effects from the 10 November 1961 polarcap absorption event, J. Geophys. Res. 67:2745.

Belrose, J.S. (1963) The oblique reflection of low-frequency radio waves from the ionosphere, Propagation of Radio Waves at Frequencies below 300 Kilocycles, AGARDograph 74, Pergamon Press, p. 149.

Belrose, J.S., Devenport, M.H., and Weekes, K. (1956) Some unusual radio observations made on 23 February 1956, J. Atmospheric Terrest. Phys. 8:281.

Belrose, J.S. and Ross, D.B. (1961) Observations of unusual low-frequency propagation made on 12 November 1960, Can. J. Phys. 39:609.

Collins, C., Jelly, D.H., and Matthews, A.G. (1961) High-frequency radio-wave black-outs at medium and high latitudes during a solar cycle, Can. J. Phys. 39:35.

Crary, J.H. and Diede, A.H. (1969) Early detection at low latitudes of a polar cap event by its effect on vlf propagation, J. Geophys. Res. 74:362.

Crombie, D.D. (1966) On the use of vlf measurements for obtaining information about the lower ionosphere, especially during solar flares, Electron Density Profiles in Ionosphere and Exosphere, J. Frihagen, Ed., North-Holland Publishing Company, p. 118.

Egan, R.D. (1963) Thule to College 12 Mc propagation during the April and May 1960 intense polar cap absorption events, The Effect of Disturbances of Solar Origin on Communications, G.J. Gassmann, Ed., Macmillan Company, p. 47.

Egeland, A., Hultqvist, B., and Ortner, J. (1963) The influence of solar disturbances on VLF radio wave propagation over a long high-latitude path, The Effect of Disturbances of Solar Origin on Communications, G.J. Gassman, Ed., Macmillan Company, p. 79.

Egeland, A. and Naustvik, E. (1967) Influence of high-latitude disturbances on VLF propagation, Radio Sci. 2:659.

Ellison, M.A. and Reid, J.H. (1956) A long-wave anomaly associated with the arrival of cosmic-ray particles of solar origin on 23 February 1956, J. Atmospheric Terrest. Phys. 8:291.

Eriksen, K.W. and Landmark, B. (1961) Some results concerning the behaviour of long distance VLF circuits during polar cap absorption events, Ark. f. Geofysik 3:489.

Goedeke, A.D., Masley, A.J. and Adams, G.W. (1967) Riometer observations in the polar caps of the solar cosmic ray events during the IQSY, Solar Phys. 1:285.

Gregory, J.B. (1963) Particle influx at high latitudes. 2. Solar protons, J. Geophys. Res. 68:3097.

Hakura, Y. (1961) Development of ionospheric and geomagnetic storms caused by solar corpuscular emissions. I. Polar cap blackout and auroral zone blackout, Rept. Ionosphere and Space Res. Japan 15:1.

Hakura, Y. (1967) Entry of solar cosmic rays into the polar cap atmosphere, J. Geophys. Res. 72:1461.

Hakura, Y., Takenoshita, Y., and Otsuki, T. (1958) Polar blackouts associated with severe geomagnetic storms on 13 September 1957 and 11 February 1958, Rept. Ionosphere and Space Res. Japan 12:459.

Helms, W.J. and Swarm, H.M. (1969) VLF step frequency sounding of the polar lower ionosphere, J. Geophys. Res. 74:6341.

Herman, J.R. (1962) Polar-cap and auroral-zone absorption effects on 2.5- and 5.0-megacycles per second atmospheric radio noise, J. Geophys. Res. 67: 2299.

Hewitt, L.W. (1969) Ionization increases associated with the small solar proton events of 5 February 1965 and 16 July 1966, Can. J. Phys. 47:131.

Hultqvist, B. (1959) On the interpretation of ionization in the lower ionosphere occurring on both day and night side of the earth within a few hours after some solar flares, Tellus 11:332.

Jelly, D.H. (1963) The effects of polar-cap absorption on hf oblique-incidence circuits, J. Geophys. Res. 68:1705.

Juday, R.D. and Adams, G.W. (1969) Riometer measurements, solar proton intensities and radiation dose rates, Planetary Space Sci. 17:1313.

Leinbach, H. and Ecklund, W.L. (1968) VHF measurements of the ionospheric absorption of cosmic noise - pilot experiment, March 1967, unpublished ESSA Technical Memorandum.

Leinbach, H. and Reid, G.C. (1960) Ionization of the upper atmosphere by cosmic rays of solar origin, Phys. Rev. Letters 2:61.

Ortner, J., Egeland, A., and Hultqvist, B. (1960) A new sporadic layer providing vlf propagation, IRE Trans. on Antennas and Prop. AP-8 :621.

Parthasarathy, R. and Venkatesan, D. (1964) An empirical relationship between particle flux, energy spectrum, and radio wave absorption during a polar cap event, J. Geophys. Res. 69:549.

Paulikas, G.A., Freden, S.C., and Blake, J.B. (1966) Solar proton event of 5 February 1965, J. Geophys. Res. 71:1795.

Pierce, J.A. (1956) Vlf Phase shifts associated with the disturbance of 23 February 1956, J. Geophys. Res. 61:475.

Pope, J.H. and Leinbach, H. (1970) Effects of polar cap absorption events on geostationary satellite vhf communications systems, NOAA Technical Report ERL 196-OD 5.

Potemra, T.A., Zmuda, A.J., Haave, C.R., and Shaw, B.W. (1967) VLF phase perturbations produced by solar protons in the event of 5 February 1965, J. Geophys. Res. 72:6077.

Potemra, T.A., Zmuda, A.J., Haave, C.R., and Shaw, B.W. (1969) VLF phase disturbances, hf absorption, and solar protons in the events of 28 August and 2 September 1966, J. Geophys. Res. 74:6444.

Raitt, W.J. (1970) Ionospheric measurements by the ESRO-1 satellite during the February 25th 1969 solar proton event, Intercorrelated Satellite Observations Related to Solar Events, V. Manno and D.E. Page, Ed., Reidel Publishing Company, p. 535.

Reid, G.C. (1969) Associative detachment in the mesosphere and the diurnal variation of polar-cap absorption, Planetary Space Sci. 17:731.

Reid, G.C. (1970) Current problems in polar-cap absorption, Intercorrelated Satellite Observations Related to Solar Events, V. Manno and D.E. Page, Ed., Reidel Publishing Company, p. 319.

Reid, G.C. and Collins, C. (1959) Observations of abnormal vhf radio wave absorption at medium and high latitudes, J. Atmospheric Terrest. Phys. 14:63.

Smart, D.F. and Shea, M.A. (1970) Proposed solar proton event classification system, Intercorrelated Satellite Observations Related to Solar Events, V. Manno and D.E. Page, Ed., Reidel Publishing Company, p. 102.

Van Allen, J.A., Lin, W.C. and Leinbach, H. (1964) On the relationship between absolute solar cosmic ray intensity and riometer absorption, J. Geophys. Res. 69:4481.

Wait, J.R. and Spies, K.P. (1964) Characteristics of the earth-ionosphere waveguide for vlf radio waves, NBS Tech. Note No. 300.

Westerlund, S., Reder, F.H., and Abom, C. (1959) Effects of polar cap absorption events on vlf transmissions, Planetary Space Sci. 17:1329.

Contents

14. Riometers Observations in Antarctica of 2 November 1969 Solar Proton Event

J. Lavergnat, J.J. Berthelier, and M. Pirre*
Groupe de Recherches Ionosphériques
4, avenue de Neptune
94 Saint-Maur-des-Fosses, France

Abstract

Using the method of Hultqvist, which gives the better security, four profiles are derived from the different absorption values obtained during 2 November PCA at Dumont d'Urville. The riometers we have used are centered around frequencies of 13.7, 20.5, 30.1 and 75-MHz, respectively. Calculations are performed for the steady state coefficient from the data of Explorer 41.

14-1 INTRODUCTION

At the French Antarctic base Dumont d'Urville (140° E, -66° S) on the coast of Adelie land, a permanent geophysical observatory has been operated and developed since the IGY. Besides other instrumentation, the Groupe de Recherches Ionosphériques runs a set of four fixed antenna riometers on four different frequencies of 13.7, 20.5, 30.1 and 75-MHz, and also a rotating

* Assistant à la Faculté des Sciences d'Orleans, 45/Orleans, France

antenna riometer on 75 MHz whose line-of-sight is sequentially moved in site and azimuth. We have used the data obtained with the first four riometers during the 2 November solar cosmic ray event to derive electron density profiles in the D region for specially interesting periods, and present hereafter some of these profiles together with the calculated steady state coefficient Ψ.

14-2 OBSERVATIONS

The variations of the absorption with time during the first days of November 1969 are represented in Figure 14-1. According to curves corresponding to 20.5 and 30.1 MHz, the time of onset of the PCA event is 10H48 + 00.01 U. T. This is in a very good agreement with the results from the Thule riometer and seems to indicate that conditions for access of solar protons to polar caps were nearly identical for both hemispheres at this time. Later, and until 03H.00 U. T. on 3 November, the event is fairly irregular with moments of rapidly varying absorption giving sharp maxima near 19.00, 20.00, 22.10 U. T. on 2 November and 02.40 on 3 November. Comparison of these features with particle data from Explorer 41 and Vela reveals a positive correlation for only one peak in absorption at 19.00 on 2 November when the fluxes recorded on Vela show a significant increase. As already stated from previous observations (Reid and Sauer, 1967; Berthelier, 1969), these features imply spatial and/or temporal fast variations of particles fluxes and of their access to polar caps, but these phenomena are beyond the scope of this paper.

More interesting, however, is the fact that in this period of the year the solar zenith angle is greater than 90^{o} for about 7 hr a day thus giving rise to the well known day-to-night effect in absorption. This effect appears nicely during the second day of the event when the solar proton fluxes and spectra are varying smoothly. During this effect the assymmetry between dawn and dusk is emphasized. The absolute value of the slope of the absorption curve is greater for the transition between the day and the night than for the opposite transition.

On the first day, the night-day effect appears also but not so clearly, due in part to the rapid increase of proton fluxes and also perhaps to a large flux of energetic electrons (Lanzerotti and MacLennan, 1971).

Evidently it would have been better to work on the second nighttime period but, unfortunately, radio-interferences on 13.7 and 20.5 MHz prevented us from using the multifrequency analysis and from calculating the electron density profiles. We were thus obliged to work on data pertaining to the first nighttime period and concentrated mainly upon the recovery phase before sunrise.

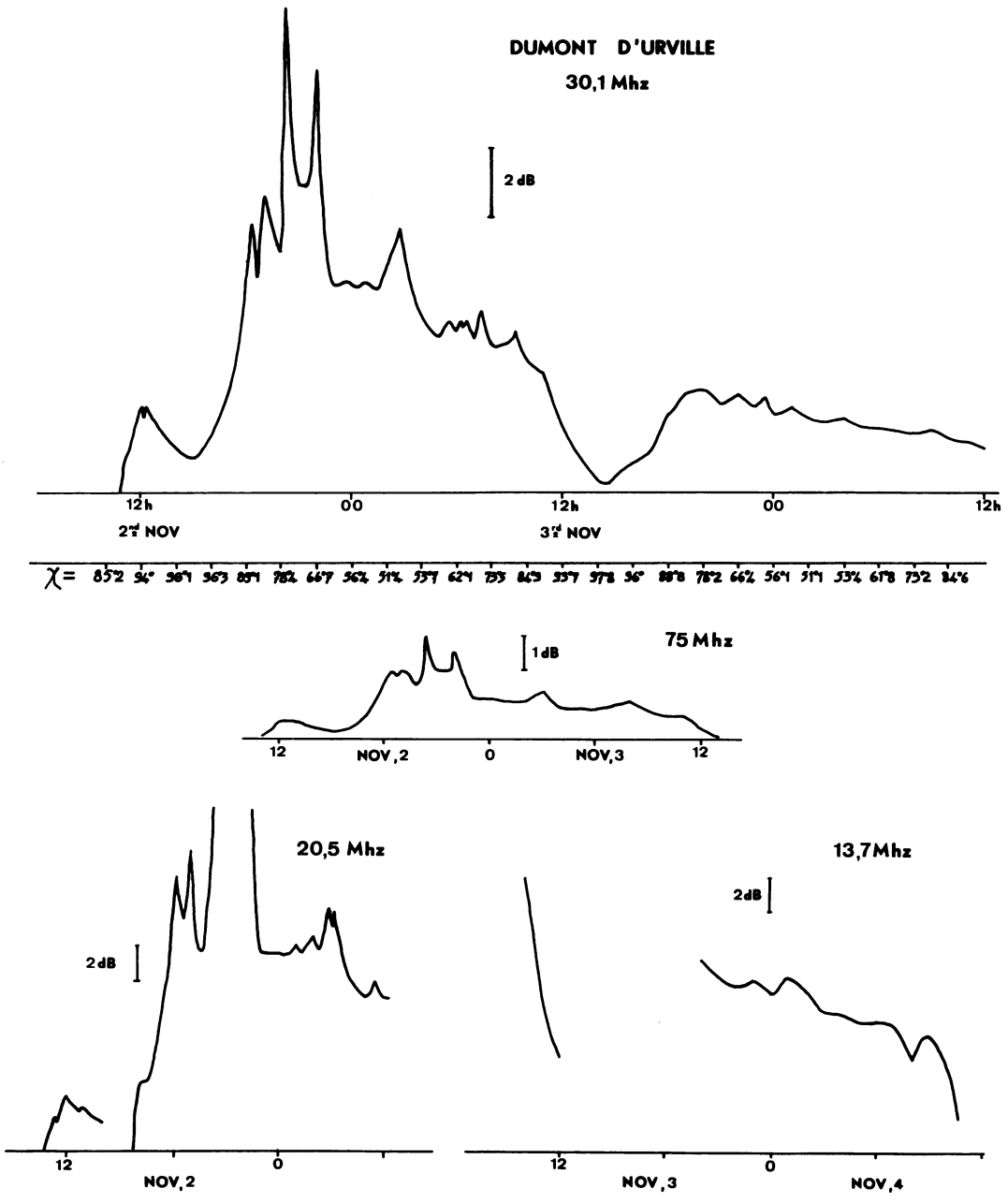

Figure 14-1. Absorption Values for Four Riometers at Frequencies of 13.7, 20.5, 30.1 and 75-MHz During the PCA, 2 November 1969 at Dumont d'Urville

14-3 ANALYSIS OF THE DATA

In order to minimize the errors due to poor estimate of the base curve, we calculated the absorption on the various riometers by using the quiet day curves derived from the intensity of cosmic noise recorded during the ten quietest days before and after the event. We thus know the "abnormal" absorption due to the ionization of the neutral atmosphere by energetic protons with a typical accuracy of ± 0.1. dB on 30.1 and 75 MHz, and between ± 0.1 and ± 0.2 for the lower frequencies.

Prior to describing the method used to obtain the electron density we want to make the following statements which play an important role in this work:

(1) Using the beam geometry actually measured for identical antenna disposition, we have calculated the absorption along a vertical path as a function of the absorption indicated by the riometer (Figure 14-2) and made use of this relationship to correct our data.

(2) According to the Sen and Wyller (1960) generalized theory, we expressed the vertical absorption by

$$A(\omega) = 0.115 \int_{ho}^{h1} \frac{N(h)}{\nu} \; H\left(\frac{\omega}{\nu}\right) \; dh \qquad (14\text{-}1)$$

with

$$H(x) = \frac{1}{\tau\left(\frac{7}{2}\right)} \int_{o}^{\infty} \frac{u^{5/2}\, e^{-u}}{u^2 + x^2} \, du \qquad (14\text{-}2)$$

where A is in dB, N in electrons m^{-3}, ω and ν in Hz, h in km, and ν is the collision frequency for the most probable velocity of electrons

$$\nu = 0.88\ 10^{8} P \qquad \text{(Suchy, 1967)} \qquad (14\text{-}3)$$

where P is in mm of Hg.

In the case of the 13.7, 20.5, 30.1-MHz riomteers, the effect of magnetoionic dissociation of the wave is cancelled by the antenna (Lavergnat, 1970) so that ω is the actual frequency. As for the 75 MHz riometer, the antenna is only sensitive to the extraordinary mode and thus ω must be replaced by $\omega - \omega_B$ in Eq. (14-1) where ω_B is the gyrofrequency.

There exist two general methods to derive the electron density profile in the D region from absorption measurements on several frequencies. The simplest

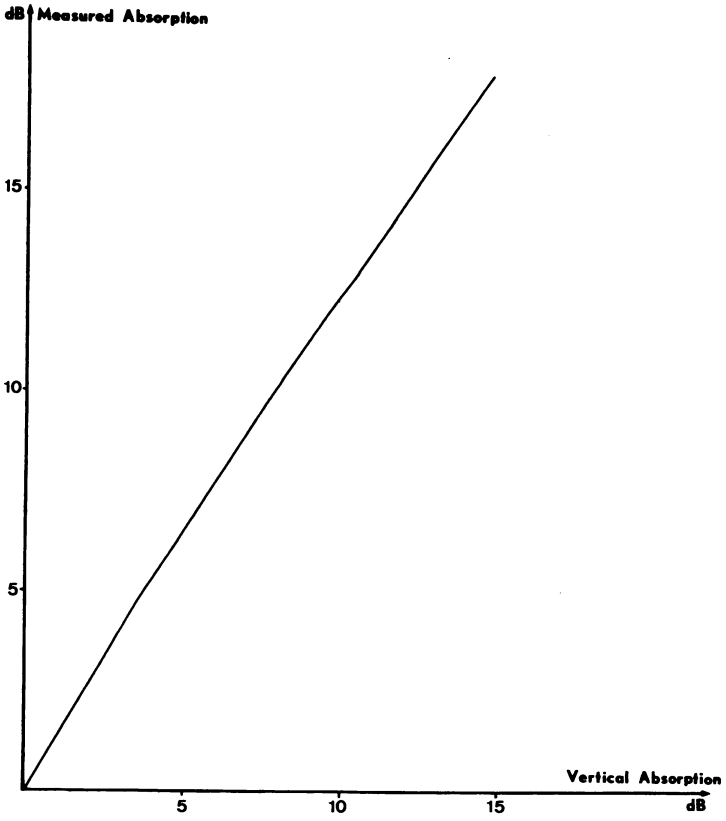

Figure 14-2. Relationship Between Measured Absorption and Vertical Absorption. This relationship is valid for the actual antennas used at Dumont d'Urville for the riometers at frequencies of 13.7, 20.5 and 30.1-MHz

one (Parthasarathy, 1963) consists of writing the electron density under the form of a polynomial in h, the altitude:

$$N(h) = a_1 h + a_2 h^2 + \ldots + a_n h^n \qquad h \geq h_o \ .$$

Theoretically, when there are m frequencies it is possible to calculate an expression of degree m. However, it is well known that there are oscillations in solutions of this type (especially when m is great) particularly when, in practice, the determinant of the matrix giving a_1, $a_2 \ldots a_n$ is small. For this reason, and also because it is not physically sound to look for a very complicated profile, people generally take n = 3 and use a least square fit when $m \geq 3$.

The second method (Hultqvist, 1968) is more complicated with respect to the algebra involved but, as we shall see later, certainly gives a better security and we have used it throughout the course of this work.

Introducing two variables x and y by $\omega = \nu_o \exp(-x)$ and $\nu = \nu_o \exp(-y)$, if it is assumed that $h_o = 0$ and $h_1 = \infty$, then Eq. (14-1) may be written

$$g(x) = \int_{-\infty}^{+\infty} f(y) \cdot k(x-y)\, dy \qquad (14\text{-}4)$$

where

$$f(y) = N(y) \cdot \frac{dh}{dy}$$

$$g(x) = \frac{\nu_o \exp(-x) A(x)}{0.115}$$

$$k(x-y) = \exp(y-x) \cdot H(\exp(y-x)) .$$

Equation (14-4) is a Fredholm's integral equation the solution of which is:

$$f(y) = \frac{5}{\pi}(a_o - 0.7032\, a_1 - 2.4633\, a_2) + \frac{5}{\pi}(a_1 - 1.4064\, a_2)\, y + \frac{5}{\pi} a_2 y^2 \qquad (14\text{-}5)$$

if $$g(x) = a_o + a_1 x + a_2 x^2 . \qquad (14\text{-}6)$$

Choice was made of the expression Eq. (14-6) for g(x) because we generally had only three riometers giving good data at the same time.

With the formulation Eq. (14-4), it is evident that we can start from any height (any ν_o). The solution is independent of ν_o and runs from zero altitude to the infinite. Undoubtedly, it is not physically true.

In order to determine the range of validity of this solution, it is easy to compute the sum of the squares of the differences between the measured and computed absorption on the three different frequencies.

In the range for which this sum is minimal, the density given by the formula

$$N(y) = f(y)\frac{dy}{dh} \qquad (14\text{-}7)$$

may be considered as correct.

If we plot $0.115\, H(\omega/\nu)/\nu$ versus the altitude (Figure 14-3), we can see that the multiriometer technique is very sensitive between 35 and 70 km. But we can

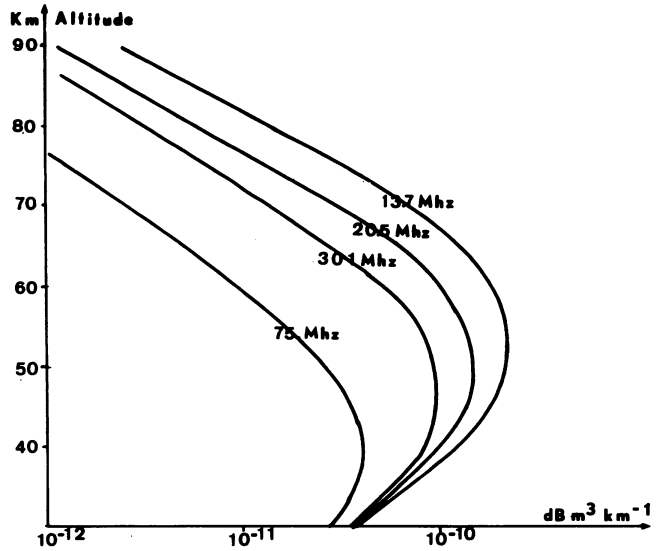

Figure 14-3. Variations of 0.115 H $(\omega/\nu)/\nu$ versus Altitude for Different Frequencies

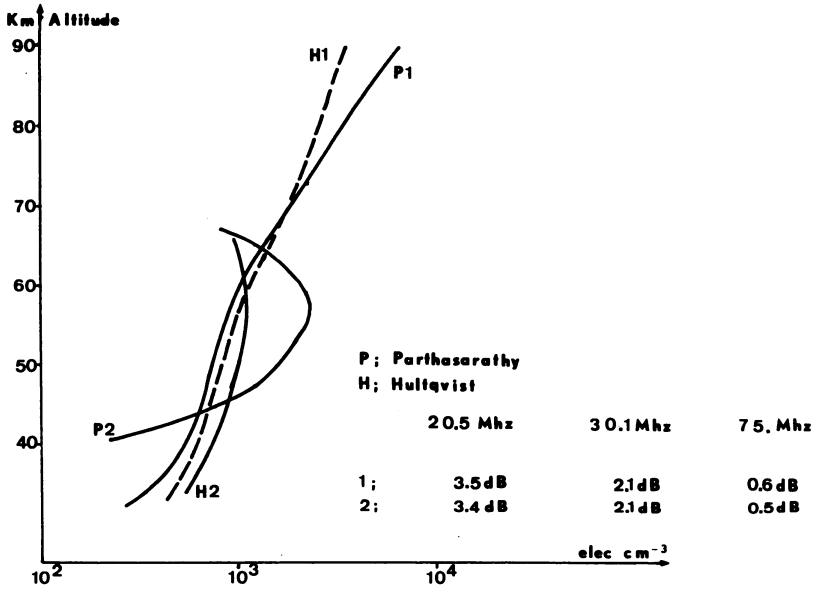

Figure 14-4. Differences Between the Parthasarathy and the Hultqvist Method With Respect to a Small Change in Absorption Values

hope that the regularity of the actual profile extends the range of validity at 80 to 85 km.

A simple test of the respective validity of these two methods is to check the stability of the solutions with respect to small changes in absorption on one or several frequencies; that is, changes of the order of accuracy. Figure 14-4 represents the results obtained for 0.1 dB changes and it is clear that the second method is far better.

14-4 RESULTS

As there are no data relative to the neutral atmosphere for high latitude regions of the Southern hemisphere, we used the profiles given in CIRA for May, the corresponding month in Northern hemisphere. In Table 14-1 are given the neutral pressure between 40 and 90 km, and corresponding electron collision frequencies. The accuracy of these numbers are certainly questionable as the seasonal variation in the upper atmosphere at Dumont d'Urville does not seem to be at all regular. According to a number of results from ionosonde and riometer observations, it seems likely that October represents a rapid change in atmospheric and ionospheric conditions leading without transition to summer time condition. Owing to this fact, we think that it is not reasonable to hope that the neutral pressure is evaluated better than ± 10 percent.

In Table 14-2 are summarized the values of absorption when electron density profiles were calculated.

Essentially, four profiles were obtained during the end of the nighttime period between 16.20 and 19.00 U.T. on 2 November. Indication is given concerning the profile for 12.10 principally because the associated Ψ fits quite well with the other values at $\simeq$ 60 km. At last is given the profile corresponding to a small superimposed proton increase seen on Explorer 41 data on 4 November. All the electron density profiles are drawn on Figure 14-5.

14-4.1 Evaluation of the Production Rate Q

The proton fluxes and spectra we used to calculate the ion-electron pair production rate Q, were derived from the data published in UAG Report 13 and obtained on Explorer 41 by the SP ME. As we had no other data it is evidently the best we could do, but the conditions of access in the magnetosphere often show

Table 14-1. Pressures and Electron Collision Frequencies Adopted for 2 November for the Dumont d'Urville (66°S) Station

Height	Pressure dyn/cm^2	Collision Frequency Hz
40	2.92×10^3	1.92×10^8
45	1.58×10^3	1.04×10^8
50	8.83×10^2	5.82×10^7
55	4.92×10^2	3.25×10^7
60	2.66×10^2	1.75×10^7
65	1.37×10^2	9.04×10^6
70	6.70×10^1	4.42×10^6
75	3.01×10^1	1.98×10^6
80	1.26×10^1	8.31×10^5
85	5.70×10^0	3.76×10^5
90	2.40×10^0	1.58×10^5

Table 14-2. Absorption Values Used for Deriving Electron Density Profile

	Hour U. T	χ	Corrected Absorption dB			
			13.7 MHz	20.5 MHz	30.1 MHz	75 MHz
Nov. 2	12.10	94°6		3.0	2.1	0.5
	16.20	95°4		3.5	2.1	0.6
	16.50	93°9		3.25	1.6	0.6
	17.40	90°5	11.	7.7	3.7	1.2
	19.00	84°1		14.2	6.6	2.
Nov. 4	08.00	73°2	4.		1.4	0.2

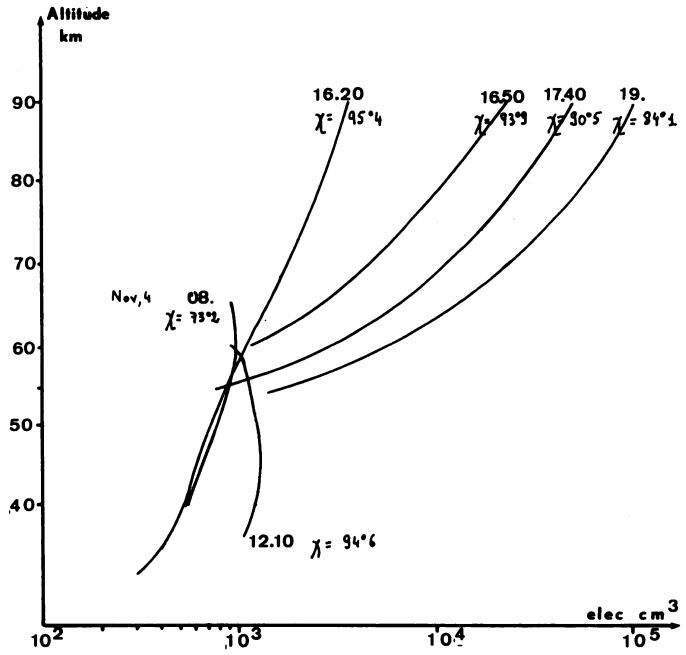

Figure 14-5. Electron Density Profiles at Different Times During the SPE, 2 November 1969

time and space variations and it is necessary to make reservations about the results deduced from these evaluations. To calculate the energy lost by protons, we divided the atmosphere into slabs of varying thickness ΔH according to the neutral scale height (generally $\Delta H = H/10$) and used the specific energy loss tabulated by Williamson (1966). Our earlier remarks regarding pressure data are valid for the neutral densities used in this process. Results are shown in Table 14-3.

14-4.2 Evaluation of the Steady State Coefficient

Assuming the equilibrium conditions to be valid even when the absorption and thus the electron density is increasing relatively fast, we have derived the steady state coefficient $\Psi = Q/N^2$ corresponding to various profiles. The results are represented on Figure 14-6.

Table 14-3 Evaluation of the Production Rate Q in electrons $cm^{-3}\ s^{-1}$

Height km	Hour				
	12.10	16.10	16.50	17.40	19.00
90		33.4	33	32.9	40.
88		45.6	45	44.8	54.4
86		61	60.1	59.8	72.4
84		111	109	108	131
82		148	145	143	173
80		186	181	179	215
78		231	225	221	265
76		276	267	262	312
74		333	320	313	371
72		389	372	362	427
70		441	420	406	477
68		495	467	450	526
66		544	511	489	567
64		582	542	516	594
62		613	567	536	612
60	361	638	584	548	621
58	397	662		559	628
56	424	666		551	613
54	453	665			
52	473	644			
50	492	616			
48	501	573			
46	506	522			
44	519	475			

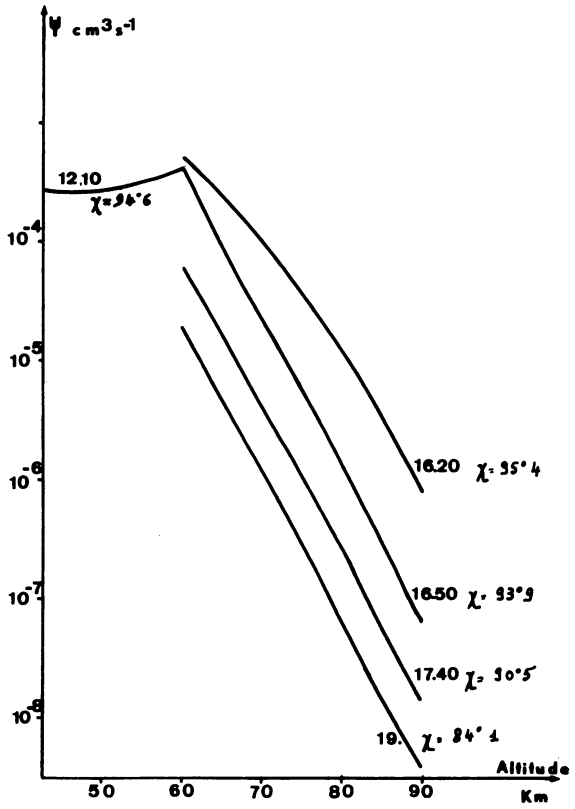

Figure 14-6. Variations of the Steady-state Coefficient as a Function of Altitude. The solar zenithal angle is a parameter

14-5 DISCUSSION AND CONCLUSION

Several comments may be made concerning these results:

(1) Comparison of electron density profiles for $\chi < 90^{o}$ and $\chi > 90^{o}$ shows that during daytime the electron density increase occurs mainly at heights above 65 km thus corresponding to relatively low energy protons. This fact seems to be contradictory to some earlier statements indicating that the daytime lower ionosphere responded primarily to high energy protons.

(2) The steady state coefficient ψ increases steadily with increasing solar angle from $\chi = 84^{o}$ to $\chi \neq 94^{o}$ keeping the same slope versus altitude. Between $\chi = 94^{o}$ and $\chi = 95^{o}4$ conditions at 60 km seems to stay similar but above 60 km

and up to 80 km, after which our calculation lose a great part of sense, the steady state coefficient does not keep the same variation any longer. Accordingly, the value of $\chi = 94^{o} - 95^{o}$ represents certainly a frontier with respect to the night-to-day change in the D region. It is interesting to note the similarity of these results with those of Potemra et al (1969) and Berthelier and Pirre (1971). This fact,however,disagrees with the theoretical results for the two ions model of Adams and Megill (1967).

(3) At 60 km and for $\chi < 94^{o}$ three different profiles give the same value of $\Psi \simeq 5.10^{-4}$ cm^{3}s^{-1} and we think that this measurement is very well confirmed.

The results presented in this paper seem to show some contradiction with some previous statements concerning the D region under PCA conditions. However, in absence of a good knowledge of the precipitation of different species upon the atmosphere and desired ionic composition in the disturbed D region it was difficult to proceed further. With recent results now available concerning particle fluxes and D-region ion composition, we intend now to extend this type of study.

Acknowledgments

This work is a part of the high latitude programme developed by the Groupe de Recherches Ionosphériques. The facilities of the Dumont d'Urville Station are monitored by the Expéditions Polaires Francaises and supported by the Territoire des Terres Australes et Antarctiques Francaises. We are very grateful to B. Morlet who had set up the riometers we have used.

Numerical calculations were made on the C.N.E.S. CDC 6600 computer.

References

Adams, G.W., and Megill, L.R. (1967) A two ion D-region model for polar cap absorption events, Planetary Space Sci. 15:1111.

Berthelier, J.J. (1969) Paper presented at the NATO advanced study Institute Skeikampen, Norway.

Berthelier, J.J., and Pirre, M. (1971) Rocket measurements of Antarctic D-region electron density profiles during the 28 January 1967 PCA event to be presented at the Cospar Symposium on 2 November 1969 Solar Proton Event, Boston.

Bucknam, D. B., and Lincoln, J. V. (1971) Data on the solar proton event of November 2, 1969 through the geomagnetic storm of 8-10 November 1969, U. A. G. Report No. 13.

Cospar International Reference Atmosphere (CIRA).

Hultqvist, B. (1968) On the solution of the integral equation relating height distribution of electron density to radio wave absorption, Planetary Space Sci. 16: 529.

Lanzerotti, L. J. and MacLennan, C. G. (1971) Relative importance of solar electrons, protons and alphas in the November 1969 PCA event. See Chapter of this publication.

Lavergnat, J. (1970) Les mesures d'absorption des ondes H. F. par riomètre dans les calottes polaires. Application à la station Dumont d'Urville. Thèse 3ème Cycle - Faculté des Sciences d'Orsay.

Parthasarathy et al, R. (1963) Derivation of electron-density profiles in the lower ionosphere using radio absorption measurements at multiple frequencies, J. Geophys. Res. 68:3581.

Potemra, T. A. et al, (1969) VLF phase disturbance, hf absorption and solar protons in the events of 28 August and 2 September 1966, J. Geophys. Res. 74: 6444.

Proceedings of Meeting on Operation PCA 69(1970) AFCRL Special Report No. 110, AFCRL-70-0625, James C. Ulwick, Ed.

Reid, G. C., and Sauer, H. H. (1967) Evidence for nonuniformity of solar-proton precipitation over polar caps, J. Geophys. Res. 72:4383.

Sen, H. K., and Wyller, A. A. (1960) On the generalization of the Appleton-Hartree magneto-ionic formulas, J. Geophys. Res. 65:3931.

Suchy, K. (1967) Handbuch der Physik, Geophysik III/2 Springler-Verlag.

Williamson, (1966) Table C. E. A.

15. PCA Behavior as Observed on Riometers

R.J. Cormier
Ionospheric Physics Laboratory
Air Force Cambridge Research Laboratories
Bedford, Massachusetts

Abstract

Riometer data from several stations for the 2 November 1969 Polar Cap Absorption event have been reduced and analyzed. The stations used are Thule and Godhavn, Greenland; Reyjavik (Leirvogur), Iceland; Churchill, Manitoba, Canada; and the Alaskan chain of riometers.

The paper describes in a qualitative manner the morphological development of the event and the relation of the commencement of the Polar Cap Absorption at each station to the local solar zenith angle. Further, the relationship of dB absorption to the solar proton flux of energies ≥ 10 MeV (observed on Explorer 41) is discussed.

Riometer data obtained from several stations were reduced and analyzed to produce dB absorption values versus time to obtain a limited morphological development of the Polar Cap Absorption (PCA) event. Plots for each station are shown. For the first two days of the event, data points are available every 10 min for most stations. For the remaining days of the event, hourly values are available. For the beginning times of the event at each station, two criteria are used - a 0.5 dB and a 1.0 dB decrease in received power.

The frequency used at most stations was 30 MHz; the riometer operating at Reykjavik (Leirvogur), Iceland, was on 27.6 MHz.

Figure 15-1 is a map showing the locations of the stations used in this presentation. The map is a modified version of that from an AFCRL report (Whalen, 1970) which shows the geographic coordinates plotted in corrected geomagnetic coordinates. For clarity, the corrected geomagnetic grid lines are not shown on the map. The shaded portion is the auroral oval as defined by Feldstein and Starkov (1967). This particular oval is for a Q of 2, which is representative of geomagnetically quiet conditions. The position of the oval is set for 1100 hours UT for 2 November 1969. The dashed line represents the day-night line position on the earth's surface for the same universal time.

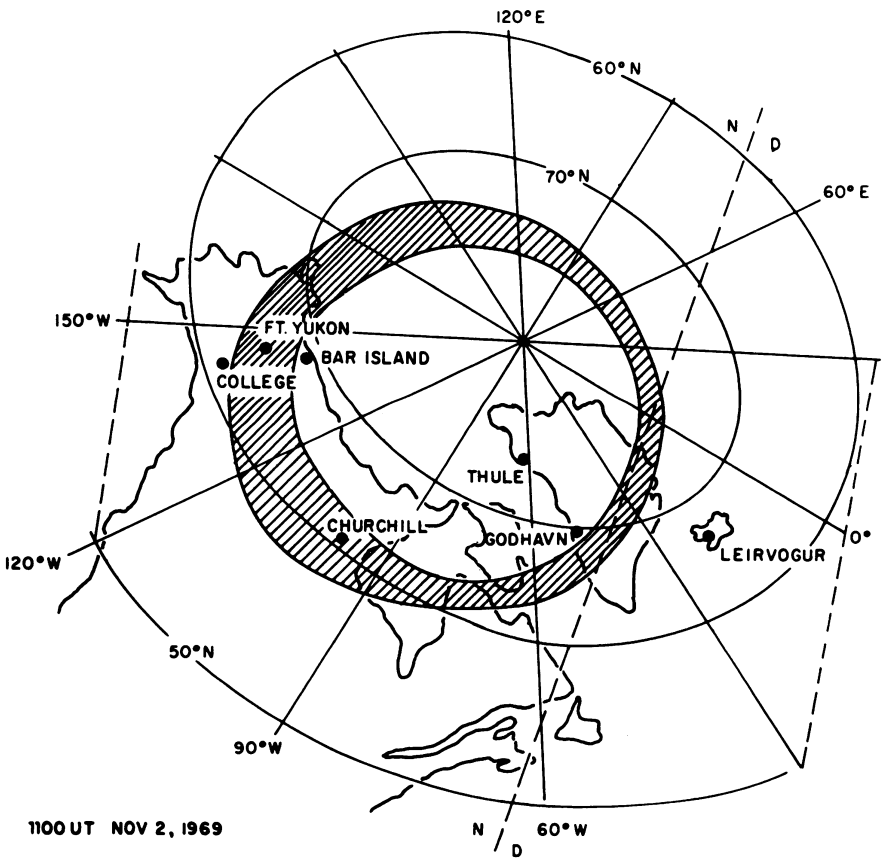

Figure 15-1. Map of Stations Location With Aurora Oval at 1100 UT

The stations used in the investigation are Leirvogur, Iceland; Thule and Godhavn, Greenland; Churchill, Manitoba, Canada; and Fort Yukon, Bar Island and College, Alaska. The geomagnetic coordinates and other detailed information concerning the various stations are found in Table 15-1.

Table 15-1. Stations Used in PCA Investigation

Station	Coordinates		Begin Time UT		Max dB Time in UT
	Geog.	Geom.	0.5dB	1.0dB	
Leirvogur	64°N 21°W	70°N		1100	1300 - 1500
Godhavn	69°N 54°W	80°N	1048	1120	14 - 1700
Thule	76°N 68°W	88°N	1050	1200	1620
Churchill	58°N 94°W	68°N	1210	1245	1500 - 1800
Bar Island	69°N 140°W	70°N	1505	1520	2320
Ft. Yukon	66°N 145°W	66°N	1300	1400	0010
College	64°N 147°W	64°N	1300	1430	2340 - 2350

Figure 15-2 is a plot of dB absorption versus time and a plot of the square root of the proton flux of energies greater than 10 MeV given in number per cm^2/sec/ster as observed by Explorer 41.

The relationship between the slope of the proton flux curve and the slope of the dB absorption curve looks very good; that is, from the standpoint of being able to predict the absorption during a PCA once the maximum has been reached and the ensuing slope determined. (For more information, see Orwen, 1969). However, one must be careful in adjusting the slope of the proton flux curve during particular events, as it is noticed that the slope of the proton flux curve can and often does change during particular events, as it did in this case. Figure 15-3 is a composite showing hourly plots of dB absorption versus time for the stations used in this experiment.

Figure 15-4 is a plot of dB absorption versus time for Thule, Greenland. The Thule riometer data shows 0.5 dB at 1050 UT at a solar zenith angle of 100°, and 1.0 dB at 1200 hr at a solar zenith angle of 99°. The absorption then rapidly increases to a maximum of ≈ 12 dB at 1620 hr UT, then decreases during darkness hours. The maximum absorption was 3 dB the second day and 2 dB the third day. The day-night ratio for the first night, that is, the morning hours of 3 November 1969, was 7; the second day, the ratio was 4.

Figure 15-5 is a plot of dB absorption versus time for Godhavn, Greenland. The Godhavn riometer observed 0.5 dB at 1048 UT at a solar zenith angle of 95°, reached 1 dB by 1120 UT at a solar zenith of 92°, and rapidly increased to 12 dB where the instrument became saturated; the values are, therefore, questionable. The second day showed 1.5 dB absorption maximum, and the subsequent days show no clear-cut PCA behavior, as seen in Figure 15-3B.

Figure 15-6 is a plot of dB absorption versus time for Churchill. The Churchill riometer observed 0.5 dB absorption at 1210 UT and a solar zenith angle of 102°, and reached 1 dB absorption by 1245 UT. The absorption rises rapidly to a maximum of 12 dB by 1500 - 1800 hr UT and decreases to tenths of a dB during the night hours. It seems strange that the absorption value should reach tenths of a dB during that evening. However, it does not have to be caused by natural phenomena. For instance, the reference curves for Churchill were obtained from a limited data sample and the accuracy of the data is between 0.5 and 1.0 dB. The second day at Churchill showed 4 dB absorption, the third day had 2 dB, and the fourth day was rather erratic and no appreciable absorption could be attributed to the PCA, as seen in Figure 15-3C. The data points are erratic due to the auroral contamination which was at times difficult to remove, again due to the limited data base available at AFCRL concerning this station.

Figure 15-7 is a plot of dB absorption versus time for Bar Island, Alaska. The Bar Island riometer observed 0.5 dB at 1505 UT at a solar zenith angle of 105°, and reached 1.0 dB at 1520 UT at a solar zenith angle of 102°. The absorption rapidly increases to 10.6 dB at 2320 hr UT, and then decreases to practically no absorption during the ensuing evening hours. This, again, may be attributed to the limited data base at AFCRL for this station. The maximum absorption observed the third day is 2.7 dB and about 1 dB the fourth day, as observed in Figure 15-3D. This station behaved very similar to that of Godhavn with respect to the amount of absorption on subsequent days following the event start day, which was 2 November 1969.

Figure 15-8 is a plot of dB absorption versus time for the riometer at Fort Yukon, Alaska. The riometer observed 0.5 dB at 1300 hr UT at a solar zenith angle of 118°, and 1.0 dB absorption at 1400 hr UT at a solar zenith angle of 113°. Fort Yukon was detecting a max of 9.0 dB at 0010 UT the 3rd of November, 4 dB the second day, and 1-1/2 dB the third day, as shown in Figure 15-3E. There does occur on 2 Nov. at local noon a decrease in absorption which could be the mid-day recovery mentioned by Leinback (1967). The mid-day recovery is indicative of the southern boundary of the latitudinal growth of PCA events. The decrease, however, does not seem to last long enough - 6 to 8 hours to be consistent with the criteria for a mid-day recovery - as reported by Leinback (1967).

Figure 15-9 is a plot of dB absorption versus time for College, Alaska. The College riometer observed 0.5 dB at 1300 hr at a solar zenith angle of 120^{o}, and 1.0 dB at 1430 UT at a solar zenith angle of 111^{0}. When the solar zenith angle was 100^{o}, College was seeing 1.8 dB. The maximum absorption was observed at 2340 - 2350 hr where the riometer receiver became saturated and was greater than 14 dB. The absorption on 3 November reached a maximum of 2.4 dB and on the third day no absorption was observed which could be attributed to the PCA event, as seen in Figure 15-3F.

Figure 15-10 is an hourly plot of dB absorption versus time for Reykjavik (Leirvogur), Iceland, courtesy of Ernie Oelbermann, formerly of HRB Singer. Greater than 1.0 dB absorption was observed by 1100 on 2 November 1969; the maximum absorption was 12 dB from 1300 - 1500 hr. November 3 data exhibited a great deal of interference, so these data are used only in that they give some insight into the behavior of absorption for that area.

The intent of this paper was to show the PCA behavior as observed at various sites. It was shown that the beginning of the event exhibited solar control in that the eastern stations began sooner than the western stations. However, the Alaskan stations began to show PCA absorption while they were still in darkness, indicating particles other than protons were involved - possibly electrons whose flux was recorded and substantiated during the early part of this event.

The relationship between the proton flux values as observed on satellites and the absorption values observed on 30 MHz riometer data is very good suggesting, as has been stated by many workers, that one can use proton flux data to calculate the expected absorption values on 30 MHz riometers using the relationship from Juday and Adams (1969):

$$J = KA^2$$

where A is absorption, and K a constant that can vary from 8 to 10. Example shown in Figure 15-11.

The relationship, however, is only useful for daytime values of absorption. In order to be usefuly for nighttime values, one must know the proper day-to-night ratio to be used for the particular event.

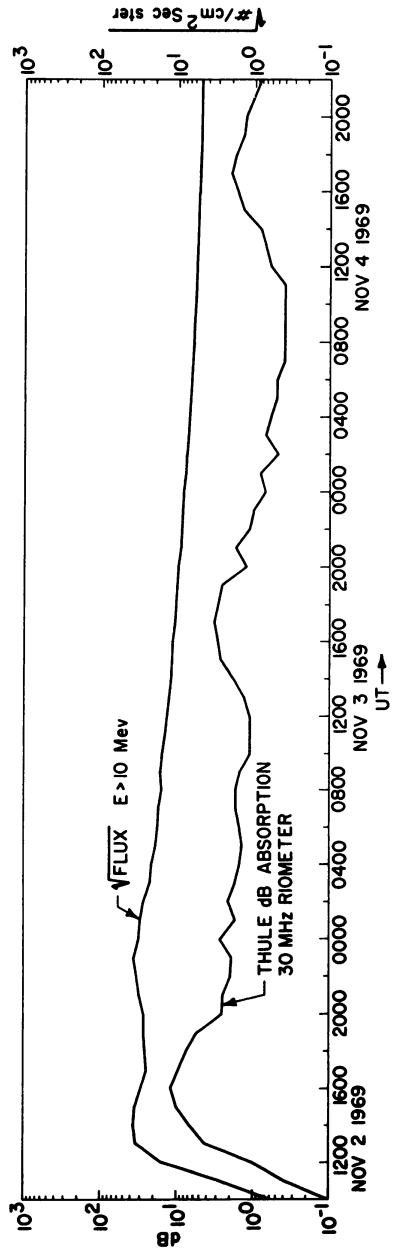

Figure 15-2. Absorption and Proton Flux During the November Event

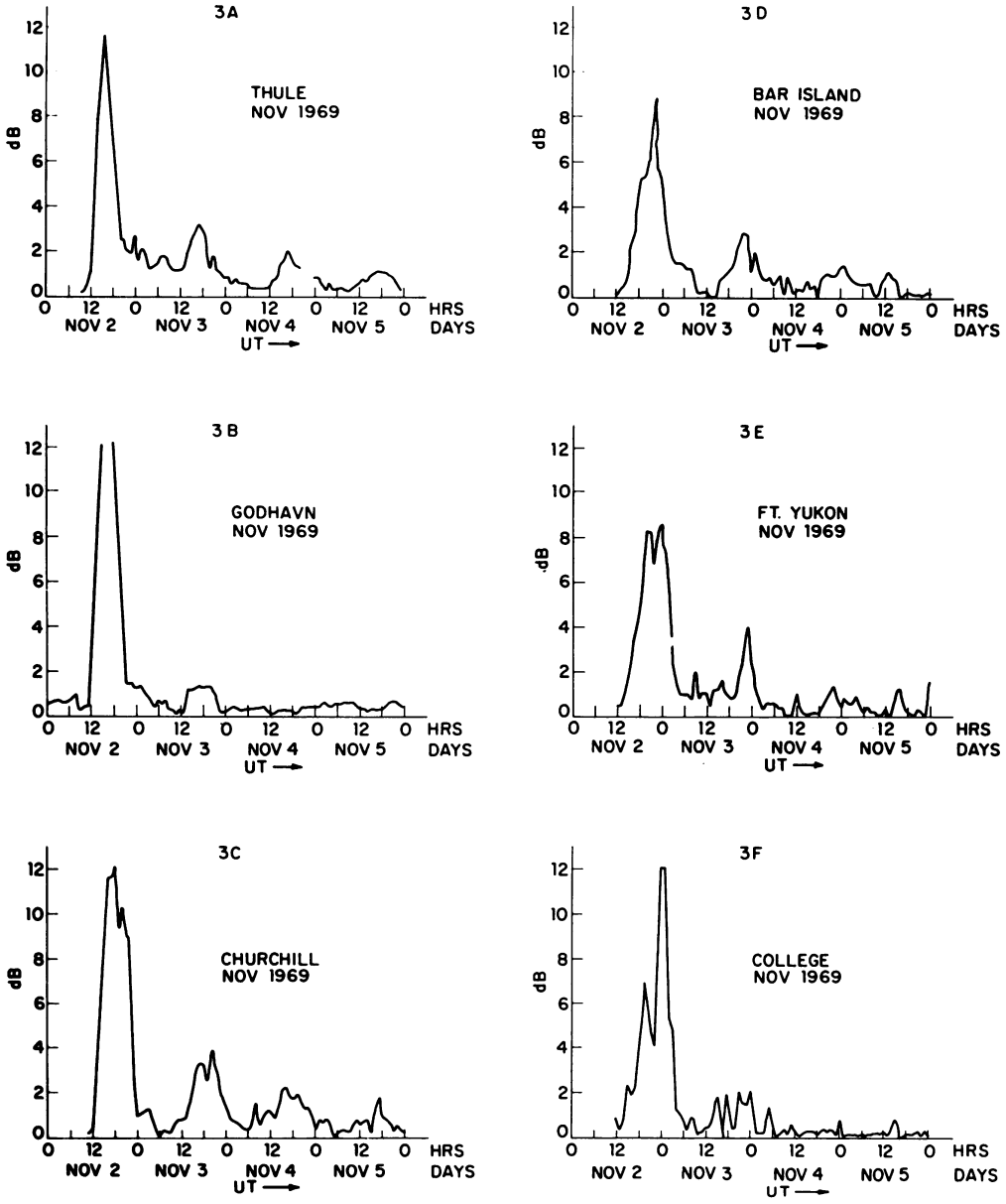

Figure 15-3. Hourly Absorption at Each Station

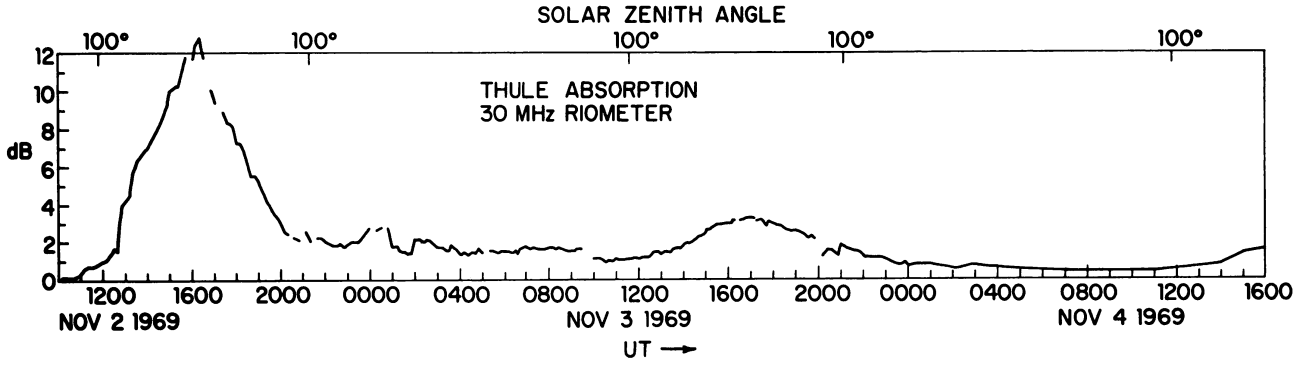

Figure 15.4. Absorption vs Time at Thule

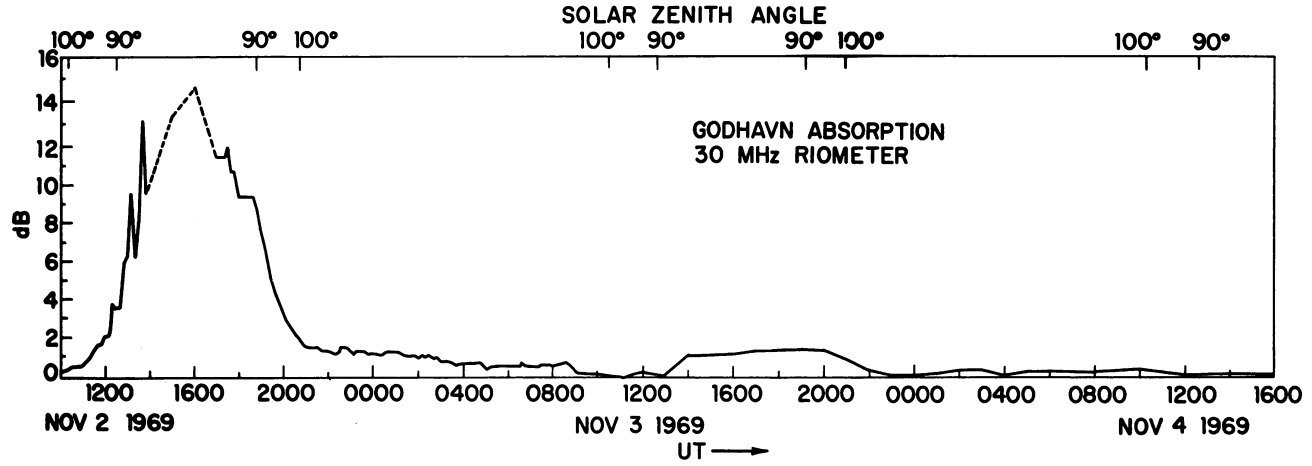

Figure 15-5. Absorption vs Time at Godhavn

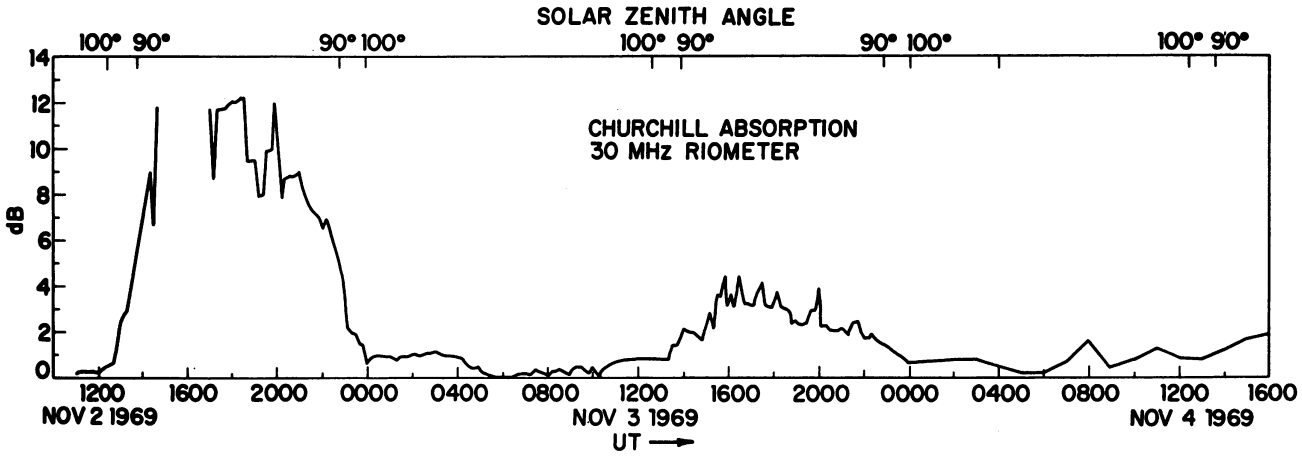

Figure 15.6. Absorption vs Time at Churchill

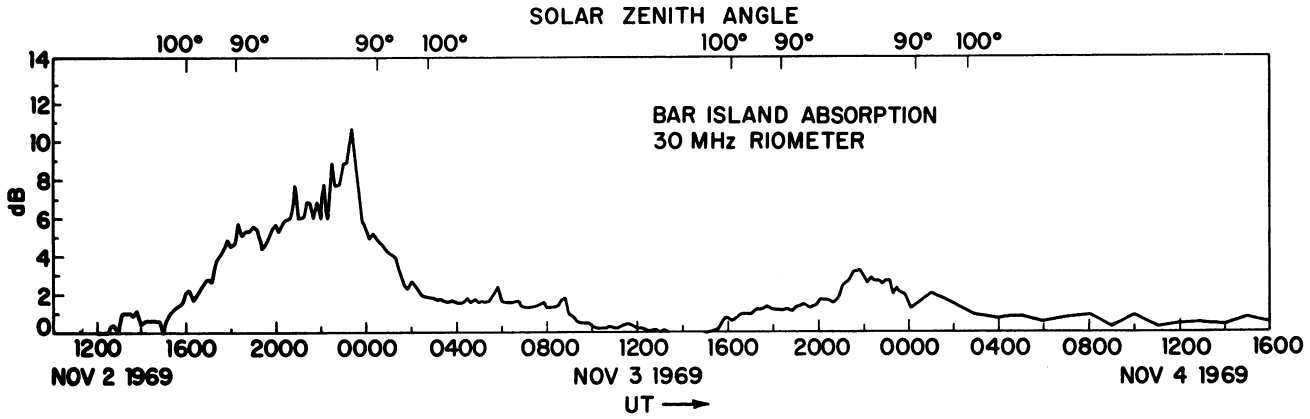

Figure 15-7. Absorption vs Time at Bar Island

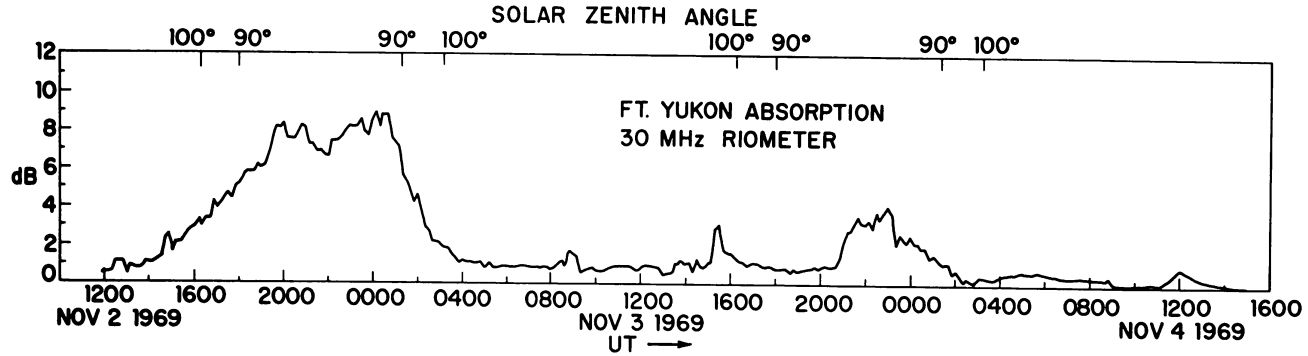

Figure 15-8. Absorption vs Time at Fort Yukon

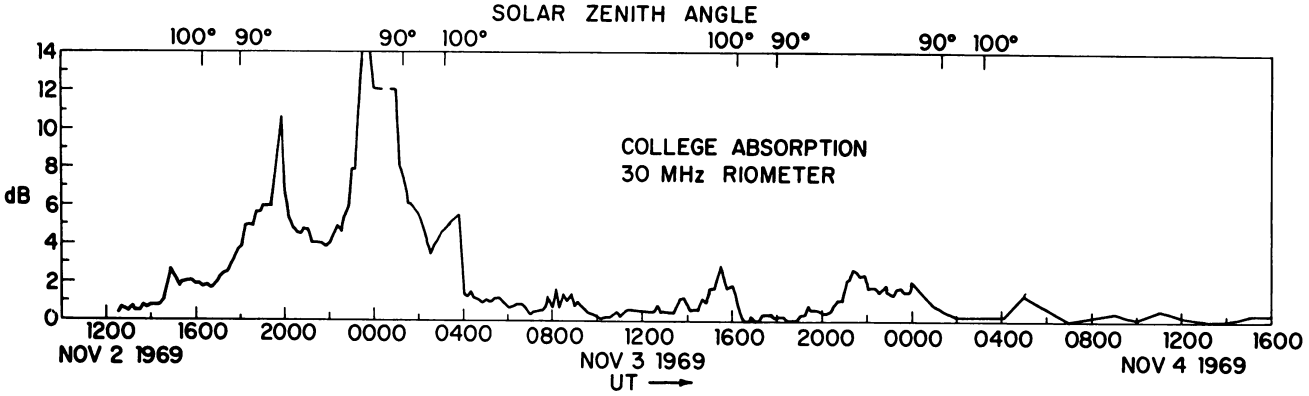

Figure 15-9. Absorption vs Time at College

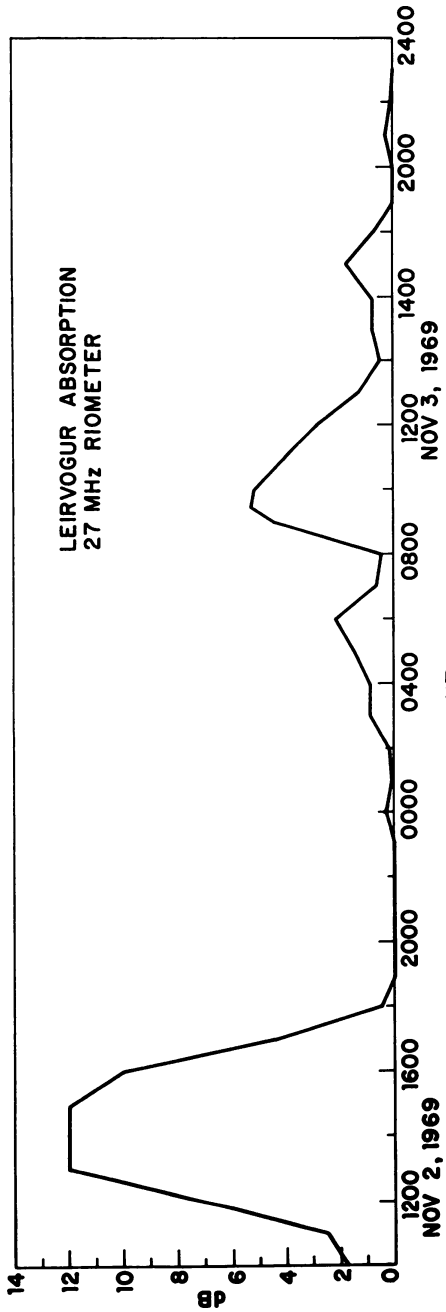

Figure 15-10. Absorption vs Time at Leirvogur

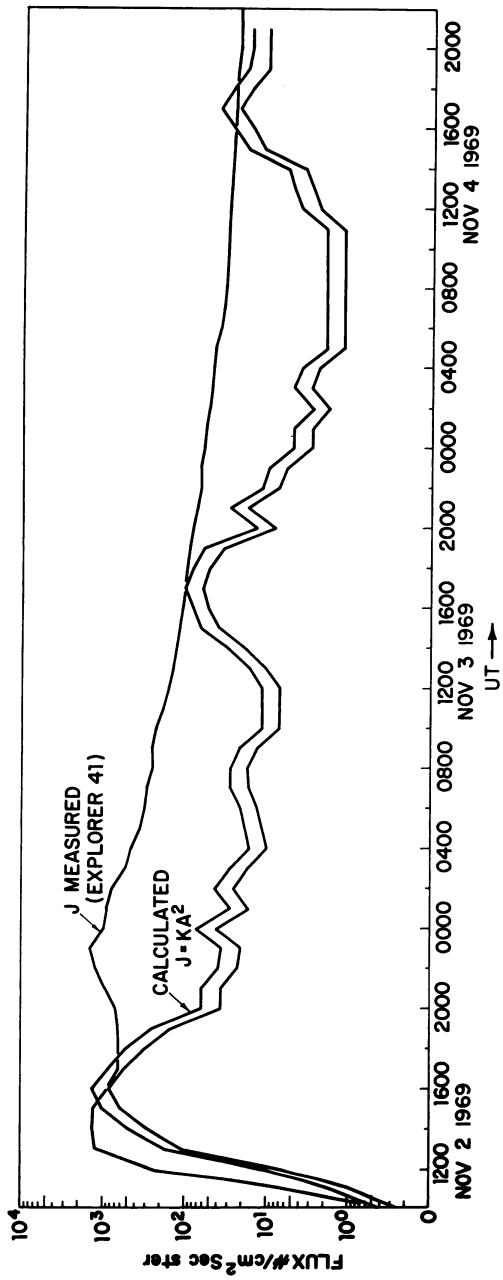

Figure 15-11. Measured vs Calculated Proton Flux

Acknowledgments

The author thanks Dr. Frank Hanes of the Upper Atmosphere Research Section of the National Research Council of Canada for the use of the Churchill zenith riometer data; also, Mr. Ernie Oelberman, formerly of HRB Singer, Inc., College Park, Pennsylvania, for the use of the riometer data from Reykjavik, Iceland.

Thanks also go to the personnel at the Godhavn, Greenland, site for collecting excellent data under an Air Force contract.

Special thanks are given to Dr. S. Silverman and his staff for the operation and maintenance of the riometer equipment at the AFCRL Geopole Station at Thule, Greenland.

Thanks also go to the ESSA World Data Center for providing copies of the Canadian and Alaskan riometer data.

References

Feldstein, Y. I. and Starkov, G. V. (1967) Dynamics of auroral belt and polar geomagnetic disturbances, Planetary Space Sci. 15:209.

Juday, R. W. and Adams, G. W. (1969) Riometer measurements, solar proton intensities, and radiation dose rates, Planetary Space Sci. 17:1313.

Leinback, H. (1967) Midday recoveries of polar cap absorption, J. Geophys. Res. 72:5473.

Orwen, L. (1969) Short-term Prediction on the Course of Polar Cap Absorption, Final Report, AF Contract F19628-68-C-0308.

Whalen, J. A. (1970) Auroral Oval Plotter and Nomograph for Determining Corrected Geomagnetic Local Time, Latitude, and Longitude for High Latitudes in the Northern Hemisphere, AFCRL Report 70-0422.

Contents

16. Ionization Changes in the D Region Associated With the Solar Cosmic Ray (SCR) Event of 2 November 1969

John S. Belrose
Radio Research Directorate
Radio Environment
Communications Research Centre
Department of Communications
Ottawa, Canada

Abstract

The partial-reflection technique uses high-power pulsed mf and hf radio waves on both polarizations to probe the ionosphere from below. The technique is very sensitive to ionization changes in the D region, and measures the electron density distribution if the density increase is not too great.

The SCR event of 2 November 1969 began during the early morning hours over Fort Churchill, at 1038 UT or 0438 CST when the local solar zenith angle χ was 117°. The ionization increase is shown by a rapid decrease, beginning about 10 hr, 40 ± 10 min UT, in the amplitude ratio (A_x/A_o) of the two polarizations, measured at 85 km, and by the decrease in height of the maximum value of the ratio to 48 km during the day.

The associated polar cap absorption (PCA) recorded by the 30 MHz zenith riometer was undetectably small until near sunrise, but became measurable at 1230 UT, when χ was 98.7°, and reached a maximum of 14 1/2 dB at 1500-1700 UT. PCA of about 0.7 dB was observed at Ottawa, indicating an exceptional event, since the magnetic field was undisturbed: A_p = 10, and no magnetic storm followed. The $(A_x/A_o)_{76\ km}$ partial-reflection ratio at Ottawa was decreased during the morning of 2 November, being about 0.3 rather than 1.0 at local noon.

The electron density vs height profiles for Churchill, obtained from the partial-reflection data, show that at 1000 UT on 2 November the D region was undisturbed, and at 1100 and 1200 UT the ionization was increasing due to the SCR event. Later increases are partly due to the rising of the sun. At 1500 UT, the electron density was 5000 cm^{-3} at 49 km. Profiles for following nights indicate excess ionization below 95 km even on 5 November.

16-1 INTRODUCTION

Three methods are employed by CRC to study ionization changes in the D region associated with solar cosmic-ray (SCR) events and other geophysical disturbances. These are: (1) riometer absorption measured at Resolute Bay ($\Lambda = 84.2^{o}$), Churchill ($\Lambda = 70.5^{o}$), Great Whale River ($\Lambda = 68^{o}$), Moosonee ($\Lambda = 64.2^{o}$), Val d'Or ($\Lambda = 61.3^{o}$) and Ottawa ($\Lambda = 58.2^{o}$); (2) long-wave propagation (measurements of phase and amplitude) over a number of paths; and (3) the partial-reflection experiments at Ottawa, Churchill and Resolute Bay. The geographic locations of the experiments are shown in Figure 16-1; magnetic-invariant latitudes Λ are also indicated.

The riometers employ 5-element circularly-polarized, crossed-element yagi antennas directed at the zenith or at the pole star. The extraordinary-mode polarization is received at 30 MHz. Figure 16-1 shows a number of long-wave propagation paths which have been or are being monitored; however, the only path for which observational data were available, for the disturbance to be discussed, was the Ottawa-Churchill link. This circuit employed an operating frequency of 80 kHz; the path length is 1920 km, and the magnetic-invariant latitude of the path midpoint is 65.2^{o}.

The long-wave propagation experiments and the riometer experiments are useful in detecting lower-ionosphere disturbances. They complement each other well since the long-wave propagation method (measurement of phase) is most sensitive in detecting SCR events if they occur during the nighttime and the riometer, which measures the associated polar cap absorption (PCA), is most sensitive during the daytime. Both experiments can be operated, with little difficulty, on a continuous basis.

The partial-reflection experiment, while it is a much more difficult experiment to conduct, is the most valuable of the three techniques since (1) it is the most sensitive of the three methods, and (2) it provides a quantitative measure of the electron density distribution if the increase in ionization density is not too excessive. The experimental installations are described in Table 16-1.

Partial-reflection observations were made continuously at Churchill and Resolute Bay since August 1969 in support of the DASA/AFCRL PCA rocket programme at Churchill, and at Ottawa during the daylight part of the day since the

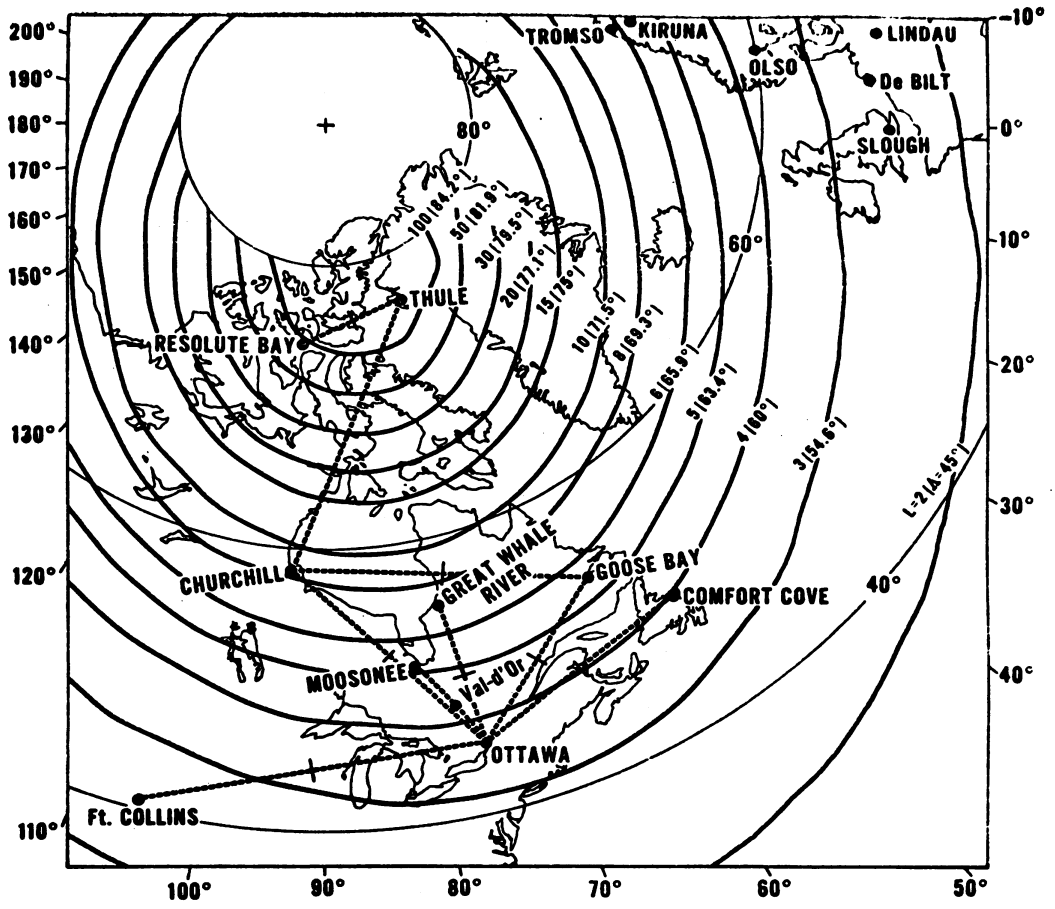

Figure 16-1. Northern Polar Map Showing Various Long-wave Propagation Paths. Locations of riometers and partial-reflection experiments are also marked. Geographic and magnetic-invariant latitudes (at 100 km) are shown

Table 16-1. Partial Reflection Installations

Location	Frequency (MHz)	Transmitter Power (kW)	Antenna Array	Effective Beam Width
Ottawa	2.66	350	40 dipole	28°
Ottawa	6.275	100	128 dipole	14°
Churchill	2.66	100	4 dipole	50°
Churchill	6.275	100	144 dipole	13°
Resolute Bay	2.66	100	4 dipole	50°

beginning of the third week of October 1969. This paper will describe some of the observational results obtained at Ottawa and Churchill during the period 31 October to 6 November 1969. The paper will begin by a brief outline in Section 16-2 of the partial-reflection technique, including the recording methods and method of analysis, and in Section 16-3 the great sensitivity of the technique for detection of SCR events will be illustrated. Section 16-4-16-7 will present the various observational data for the 2 November 1969 event, and Section 16-8 will give electron density-height profiles measured at Churchill for selected periods during this event.

16-2 METHODS OF RECORDING AND ANALYSIS USING THE PARTIAL-REFLECTION TECHNIQUE

The principal features of the partial-reflection experiment have been previously described (Belrose and Burke, 1964; and Belrose, 1970). High-power (100 kW) pulsed mf and hf radio waves are used to probe the ionosphere. Alternate left-hand and right-hand circularly polarized waves (O and X modes) are transmitted in quick succession every second. The weak partial reflections from the D region are received on a circularly-polarized antenna system and amplified by a sensitive receiver. The analogue voltage (amplitude of the echo envelope) at the output of the receiver is converted into digital form, and a value for each 2 km interval of height in a 40-km height range is stored in a computer memory. Both O-mode and X-mode amplitudes (A_o and A_x) are obtained in this way. The information is then stored on an incremental magnetic tape in a format suitable for computer analysis.

The basic experimental parameter is the relative amplitude of the O-mode and X-mode waves, partially reflected from the D region, measured as a function of height. The rate of change of A_x/A_o with height, say in a 2-km interval, is a function of the change in differential absorption of the wave over that height interval, and if the collision frequency is known, the electron density can thus be determined. The collision frequency is determined from a measure of A_x/A_o at heights where differential absorption is negligible, and these values are extrapolated to higher heights employing an assumed scale height for the atmosphere. The A_x/A_o ratio at a particular height is inversely proportional to the integrated differential absorption below that height. Consequently it provides a measure of the total electron content below the height concerned, and is a most useful parameter in the study of diurnal and interdiurnal change.

The ratio at a particular height can be determined, of course, after computer analysis of the data recorded on magnetic tape, but there is also a need to provide a record of this ratio which can be viewed and recorded in real time. Such a record can be used as a guide to inform the operator of the partial reflection

experiment when an ionospheric disturbance is occurring, and also in synoptic studies. Since the prime A_o and A_x data are recorded on magnetic tape, a ratio-meter record is an invaluable aid to the subsequent more detailed analysis by the computer. A digital value for each height interval of 2 km is stored in the memory each second, and so in principle it is possible to obtain the ratios of these values. Since there is considerable scatter in the instantaneous ratio (Belrose et al, 1967), however, these ratios must be averaged in some way. The method developed (Ohno, private communication) involves the averaging of 10 ratios, for which the signal-to-noise ratio is adequate. This average is then converted to an analogue voltage which is applied to a milliampere pen recorder. The pen recorder is held at this level until another 10 good ratios have been recorded. Records obtained in this way at Ottawa are reproduced in Figure 16-2. These data are discussed in Section 16-7.

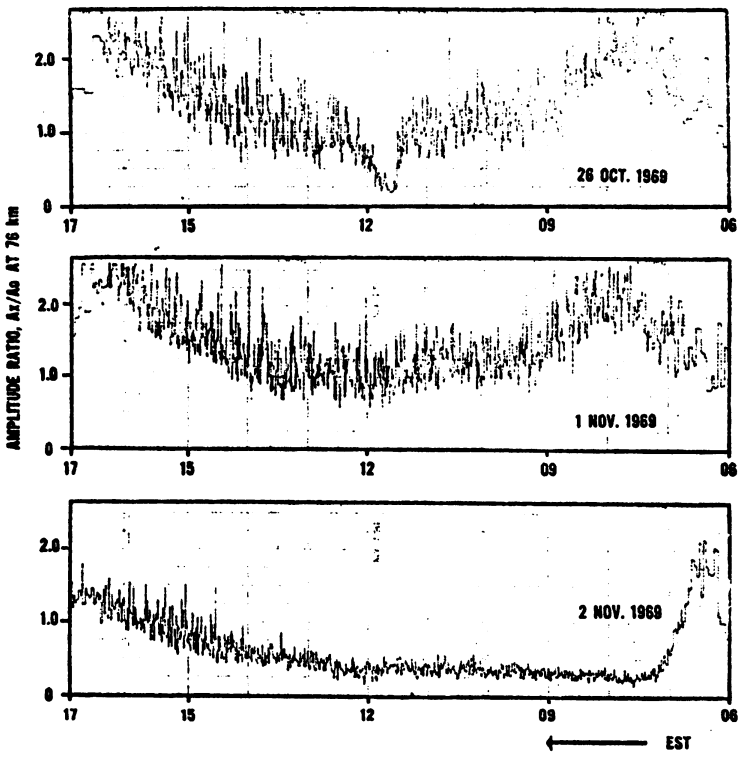

Figure 16-2. Ratio-meter Record (A_x/A_o at 76 km) Recorded at Ottawa for an Undisturbed Day (1 November 1969) and for 2 November 1969 When a Large SCR Event Was in Progress. The short-lived disturbance evident in the record for 26 October 1969 (1130 - 1210 EST) is a solar x-ray flare (SXR) effect

16-3 THE SENSITIVITY OF THE PARTIAL-REFLECTION EXPERIMENT TO SCR EVENTS

The great sensitivity of the partial-reflection experiment for detecting very small SCR events is illustrated in Figure 16-3 which shows results from Resolute Bay in August 1968. The figure shows the change with time of the smoothed A_x/A_o ratio at 84 km. Notice the regular and marked diurnal variation of A_x/A_o even though the sun never sets in August. The bold dots indicate the midnight values that would have been recorded in the absence of a disturbance as judged from long sequences of observations. Decreases in $(A_x/A_o)_{84\ km}$ can be seen for the periods 6-13 August, 14-16 August, and 20-21 August (equipment failure prevented the observation of the decay of this event). All of these decreases, which were identified as SCR events before satellite data became available, were associated with small increases in proton counts observed in the Explorer 34 (IMP-F) satellite data. Even the insignificantly small event of 4 August 1968 was accompanied by a small increase in proton counts (barely above the scatter of the background values). None of these events was detected by other ground-based experiments.

The partial-reflection method is hypersensitive, since in the case of large SCR events the radio-wave pulses are absorbed almost immediately as they travel into the absorbing layer, and useful data for only the very base of the ionosphere are obtained. The experiment at Resolute Bay is more amenable than that at Churchill for detection of small SCR events, since the disturbances associated with

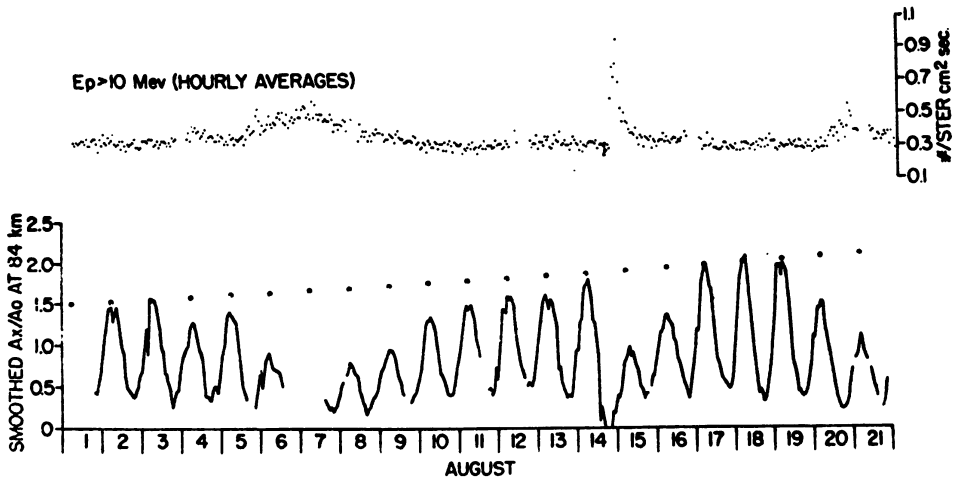

Figure 16-3. Variation of the Amplitude Ratio A_X/A_O at 84 km for the 2.66 MHz Observations at Resolute Bay During 1 - 21 August 1968 Shown With Proton Counting Rate From Explorer 34 (IMP-F). Time is in UT

high-energy particle (HEP) electron precipitation accompanying auroras is seldom observed at Resolute Bay.

16-4 OBSERVATIONAL EFFECTS OF THE SCR EVENT OF 2 NOVEMBER 1959

The various geophysical data are shown in Figure 16-4 for the period 31 October through 6 November 1969. An enlarged portion of this diagram, which shows more clearly the details of the onset of the event, is given in Figure 16-5.

The solar proton data is that measured in Explorer 41. The 4-minute averaged data (kindly provided by D. J. Williams, private communication, 1970) for $E_p > 10$ MeV is plotted in the top parts of Figures 16-4 and 16-5. Two parameters from the partial reflection experiment at Churchill are plotted. The $(A_x/A_o)_{84\ km}$ ratio is plotted for the period 1 - 2 November, as a dashed line, and the height where A_x/A_o is a maximum for the entire period is plotted as a continuous line. The data after 1400 UT on 4 November were contaminated in part by sea echoes; hence the (A_x/A_o) max curve is drawn as a broken line (the parts of the curve that are missing are where reflections from the sea were exceptionally strong). The increase in ionization associated with the SCR event is clearly evident. It is revealed in these data by a rapid decrease of $(A_x/A_o)_{84\ km}$ which became unmeasurably small by 1220 UT on 2 November, and by the large decrease in the height where differential absorption becomes measurable; that is, where A_x/A_o is a maximum. The height of $(A_x/A_o)_{max}$ changes regularly over the day, in the absence of disturbances, from a nighttime height of 85 to 90 km to a daytime height of about 75 km. On 2 November the height of $(A_x/A_o)_{max}$ decreased to 48 km by 15 UT. The nighttime height of $(A_x/A_o)_{max}$ was still less than 84 km on 6 November, although $(A_x/A_o)_{84\ km}$ is not plotted after 1220 UT on 2 November.

Riometer absorption, measured by a 30 MHz zenith riometer at Landing Lake (Churchill), and the phase of an lf 80 kHz transmission from a transmitter at Ottawa and a receiver at Churchill are also plotted in the figures.

16-5 THE ONSET OF THE EVENT

The vertical dashed line at 1038 ±4 minutes in Figure 16-5 has been drawn through the first data point which is above the background fluctuation, and clearly indicates that the event had begun by this time. This onset time is, within the time resolution of the experiments, the same as that determined from the partial reflection experiment; certainly after this time the $(A_x/A_o)_{84\ km}$ continually decreases, becoming unmeasurably small by 1220 UT. Riometer absorption was

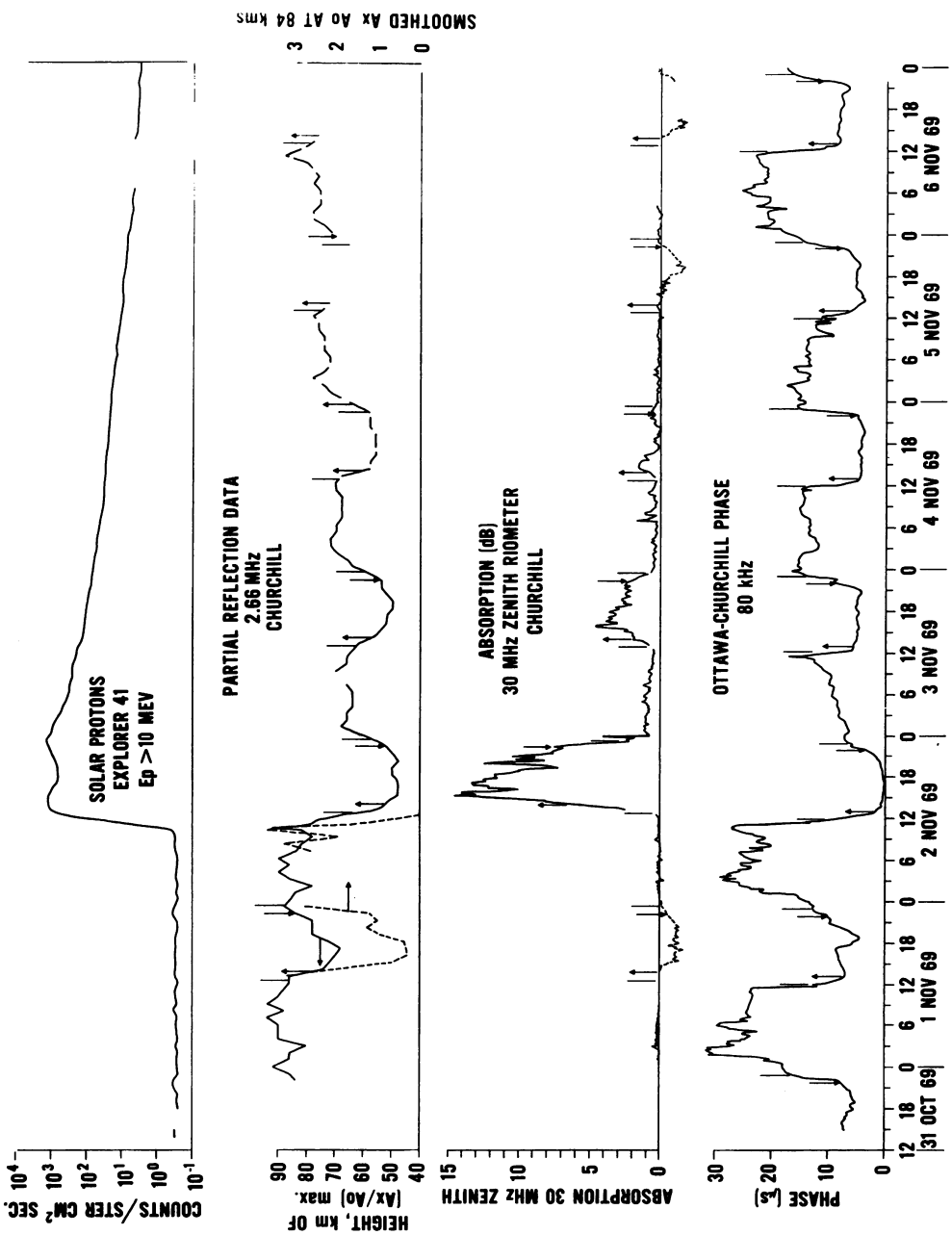

Figure 16-4. Collation of Various Geophysical Data for the Period 31 October to 6 November 1969. Time scale is in UT. The times for solar zenith angles of 98° and 90° are marked as a short vertical line and as an upward (dawn) or downward (dusk) directed arrow (in the case of the long-wave propagation phase data

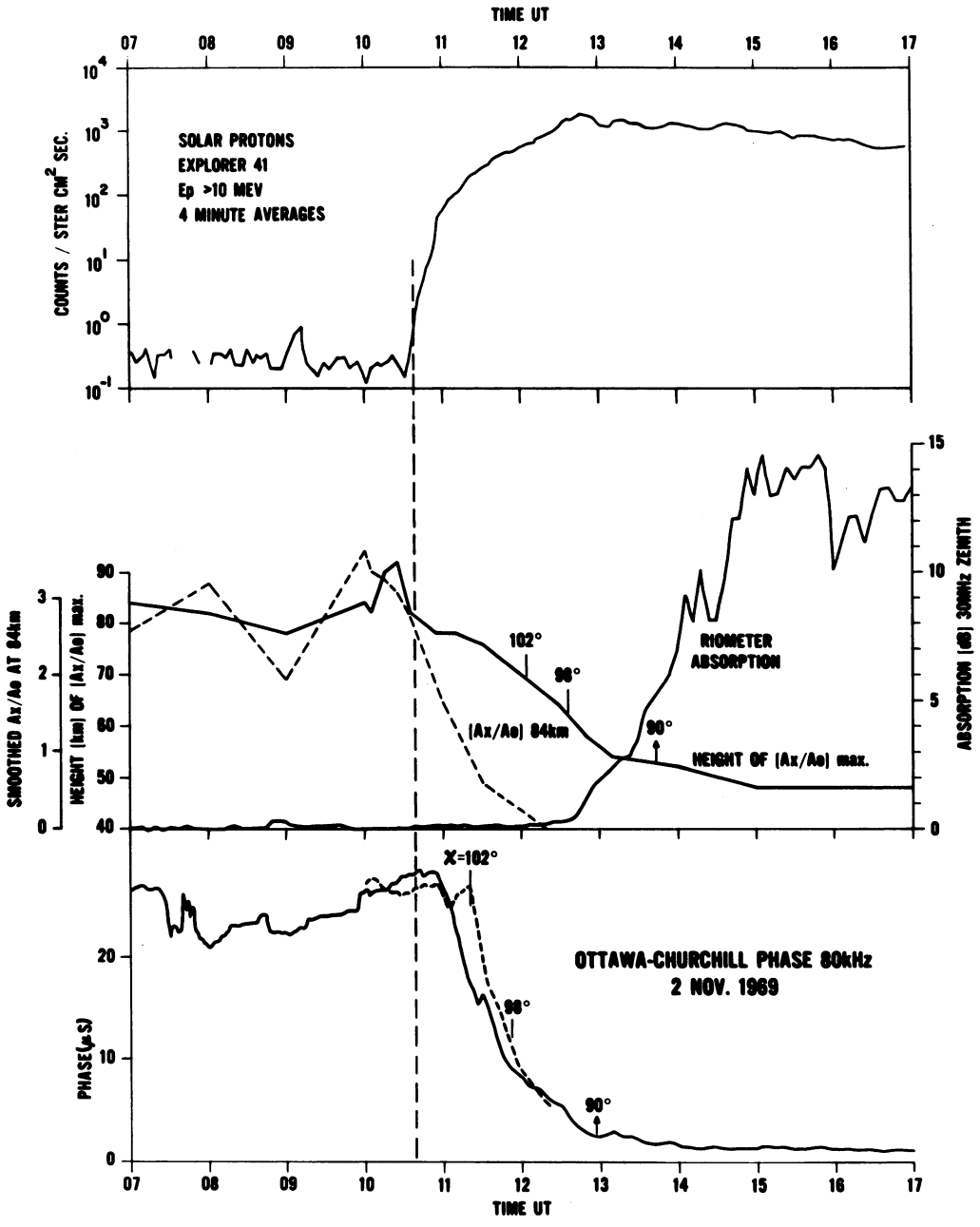

Figure 16-5. Collation of Various Geophysical Data for 2 November 1969

undetectably small until about 1230 UT when the solar zenith angle was about 98.7°. By this time solar proton fluxes in the energy range >10 MeV had reached a plateau value of $\sim 1.1 \times 10^3$ (approximately 4000 times above background). The rapid increase in riometer absorption after this time is almost certainly due to the increase in ionizing radiations from the sun.

The decrease in phase heights of the lf transmission Ottawa - Churchill at 80 kHz was not detected until 1056 UT, even though lf propagation is supposed to be a most sensitive method to detect solar proton events.

16-6 DURATION OF THE EVENT

Solar protons detected in satellites were observed above background levels until at least 7 November 1969, when another event began. The ground-based partial reflection and lf propagation data in Figure 16-4 show that this longevity can be followed until at least 6 November. Riometer absorption became undetectably small by 4 November. The figure shows another interesting feature: the change in day-to-night ratio of absorption, which for the first dawn was unmeasurably large (nighttime absorption could not be detected), was 7:1 at dusk on 2 November and 4 to 5:1 at dawn on 3 November. This same change was observed at dusk on 3 November.

16-7 THE LOW LATITUDE LIMIT

The effect of SCR events is not usually detected at Ottawa ($\Lambda = 58.2°$), unless the PCA is exceptionally strong or unless the earth's magnetic field is disturbed (when disturbed the protons can penetrate to the D region over Ottawa). On 2 November the earth's magnetic field was undisturbed ($A_p < 16$ during the period 31 October to 6 November). However, the PCA was exceptionally strong. The ionization density over Ottawa was clearly enhanced and the diurnal variation distinctly different from normal; this is revealed by the $(A_x/A_o)_{76\ km}$ ratio-meter records shown in Figure 16-2. The record for 1 November 1969 was typical of an undisturbed day. The $(A_x/A_o)_{76\ km}$ ratio decreases to a value of about 1.0, is minimum at midday, and varies regularly with the zenith angle of the sun. The small ratios from 0730 to 1200 EST (1230 - 1700 UT) on 2 November are the result of proton bombardment. The diurnal asymmetry on 2 November is interesting. Riometer absorption on 2 November 1969 was about 0.7 dB.

16-8 ELECTRON DENSITY RESULTS

Electron density height profiles for Ft. Churchill calculated from the 2.66 and 6.275 MHz partial reflection results are given in Figures 16-6 and 16-7. The profiles in Figure 16.6 show the buildup during the early phase of the SCR event. In this figure, profile (1) at 1000 UT ($\chi = 118^{o}$) is prior to the event and is typical of an undisturbed nighttime. The excess ionization evident in nighttime profiles (2) and (3) at 1100 and 1200 UT (where $\chi > 102^{o}$) is associated with the buildup of the intensity of the solar-proton bombardment. The rapid change indicated by profiles (4),(5) and (6), at 1300, 1400 and 1500 UT is due in a large part to the rising of the sun. Notice that the solar proton count for $E_p > 10$ MeV was already ~ 2000 times above background by 1200 UT. The height where the electron density was 10^3 cm^{-3} decreased regularly from a pre-disturbance height of 97.5 km to 90, 82.5, 69, 53 and 48-km for the profiles given. At 1500 UT, when riometer absorption was a maximum (about 14 dB), the electron density was about 5×10^3 cm^{-3} at 49 km.

The profiles in Figure 16-7 indicate the duration of the event insofar as this can be judged by the profiles at local midnight (0600 UT). Profiles (1) and (2) are pre-disturbance profiles. The height where electron density was 10^3 cm^{-3} was about 96 km, and densities were not obtained below 90 km. Profiles (3), (4) and

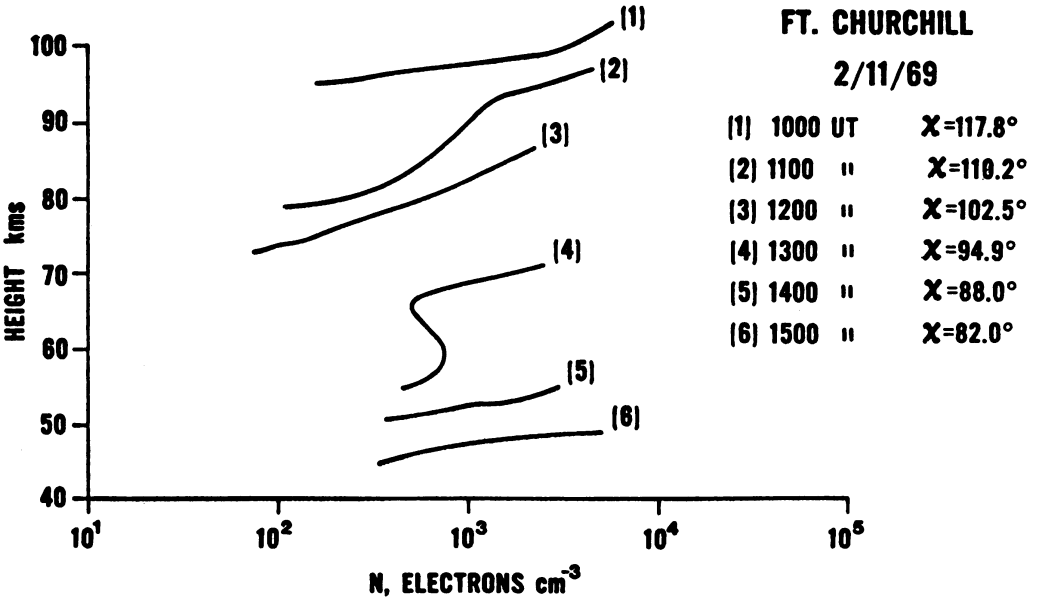

Figure 16-6. Electron Density vs Height Profile Measured by the Partial-reflection Experiment at Churchill for 2 November 1969

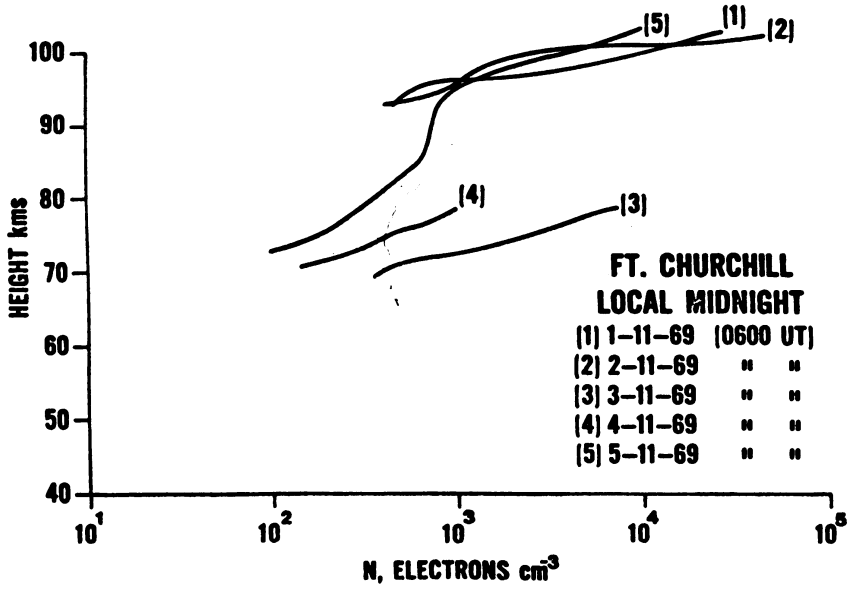

Figure 16-7. Electron Density vs Height Profiles Measured by the Partial-reflection Experiment at Churchill at Local Midnight for the Period 1 November to 5 November 1969

(5) are midnight profiles (0600 UT) on 3, 4 and 5 November. The excess ionization for heights less than 95 km is still evident on 5 November, 1969.

16-9 DISCUSSION

Since solar proton fluxes are measured in satellites the next step in our analysis of this event was to take the integral spectra data counts cm^{-2} sec^{-1} sr^{-1} MeV^{-1} and compute electron production (Q). Since electron density is measured, the effective electron loss rate $\alpha_{eff} = Q/N^2$ can be calculated and a change in α_{eff} (at a particular height) can be studied.

Taking solar proton data at $\Lambda = 70^{o}$ (the magnetic invariant latitude of Churchill) observed in the ISIS I satellite (courtesy of J.R. Burrows) and a method of calculating Q from measured differential proton spectra (by G.C. Reid), we have calculated α_{eff} values for a height of 75 km for nighttime results of 3, 4 and 5 November at 0600 UT (00 LST). Values of 3×10^{-5} for 3 November and 5×10^{-4} cm^3 sec^{-1} for 4 and 5 November were deduced. The early values compare well with those of Ulwick and Sellers (1970) and Megill et al (1970) who deduced values for α_{eff} at 75 km at nighttime of 3×10^{-5} and 1.5×10^{-5} cm^3 sec^{-1} for events on 19 November 1968 and 14 April 1968. The values for 4 and 5 November are more than an order of magnitude more rapid.

The change in the night-to-day ratio of riometer absorption deserves discussion here. Recall that this ratio was unmeasurably large during the first dawn, 7:1 at dusk on 2 November and 4 to 5:1 at dawn on 3 November. A part of this difference is certainly due to a change in the spectra of the precipitating protons, but also the change in the effective electron loss rates must be taken into account.

Acknowledgments

This work is a part of the programme of the Communications Research Centre. I gratefully acknowledge the help of my many colleagues who contributed to the obtaining of these data. In particular, Mr. D. B. Ross provided the long-wave data, Mrs. A. Morrison scaled the riometer data, and Mr. R. Bunker analysed the partial-reflection data. Mr. B. Lisson and Mr. A. P. Maione operated the partial-reflection equipments at Ottawa and Churchill.

References

Belrose, J.S. (1970) Radio wave probing of the ionosphere by the partial reflection of radio waves (from heights below 100 km), J. Atmosphic. Terr. Phys 32 : 567-596.

Belrose, J.S. and Burke, M.J. (1964) Study of the lower ionosphere using partial reflections 1. Experimental technique and method of analysis, J. Geophys. Res. 69:2799-2818.

Belrose, J.S., Bourne, I.A. and Hewitt, L.W. (1967) Review of the Partial Reflection Experiment, in Proc. of Conf. on Ground-Based Radio Wave Propagation Studies of the Lower Ionosphere, Def. Research Board, Ottawa, pp 125-151.

Belrose, J.S., Hewitt, L.W. and Bunker, R. (1970) Regular and Irregular Variations in Electron Number Density in the Lower Ionosphere over Resolute Bay, in The Polar Ionosphere and Magnetospheric Processes, G. Skovli, Ed., Gordon Beach Pub. Co., New York.

Megill, L.R., Adams, G.W., Haslett, J.C. and Whipple, E.C. (1970) Measurement of the Effective Electron Loss Rates in the D region, AFCRL - 70 - 0625, Special Report No. 110, 191 - 200.

Ohno, T., private communication.

Ulwick, J.C. and Sellers, B. (1970) Rocket Measurements of Production and Ionization During 18 November 1968 PCA Event, AFCRL - 70 - 0625, Special Report No. 110, 201 - 207.

Appendix A

Note Added in Proof

We have tried to address the question raised during the symposium as to whether the initial buildup in ionization during the nighttime hours on 2 November for heights below ~95 km was due to solar electrons or protons. The ionization increase occurred coincident, within the timing of the observational data, with the increase in proton fluxes for $E_p > 10$ MeV (Williams, private communication, 1970) beginning at 1038 ± 4 min. UT. This time is somewhat earlier than has been reported elsewhere in these Proceedings; for example, see the paper by Lanzerotti and Maclennan. This paper also reports employing a simplified analysis and empirical relations for calculating riometer absorption, that in these early hours (before 1300 UT on 2 November) solar electrons contribute more significantly than solar protons to the measured absorption (absorption was measured at McMurdo, Antarctica, which was in sunlight). We have tried to improve on this analysis, since electron density profiles were available by our experiments from the onset of the disturbance. In our studies we wish to deduce the effective electron loss rates at a time as late as possible into the event but still in darkness, that is prior to the first dawn, for comparison with nighttime values on the following nights; namely, we require an accurate measure of proton and electron spectra at 1200 UT on 2 November. The changes going on are, however, so rapid at this time, and certainly the proton precipitation is nonuniform over the polar cap, that, even at the time of writing this note added in proof, a best estimate for electron production over Churchill is not available.

The change in α_{eff} nighttime values with time after the onset of the disturbance is most interesting. A similar change has been observed during daytime at times in the decay phase of solar x-ray events (Montbriand and Belrose, 1972).* The α_{eff}-height curves for 3, 4 and 5 November 1969, compared with nighttime values deduced by other researchers during solar proton events, are shown in Figure 16-A1.

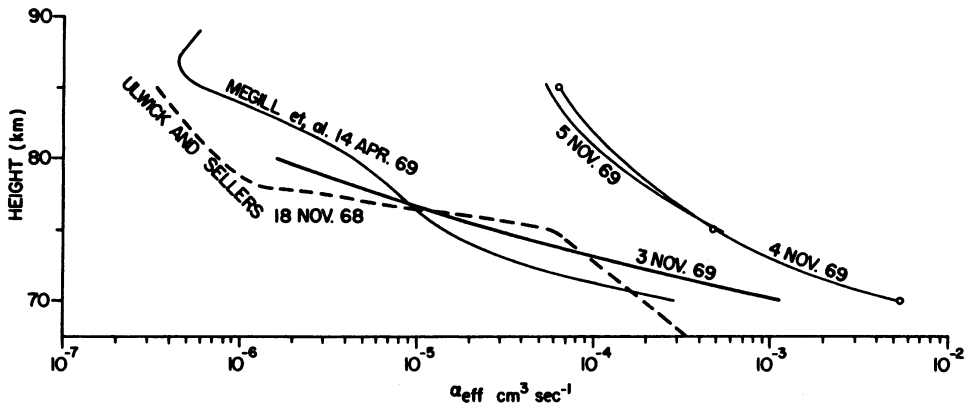

Figure 16-A1

* Montbriand, L.E. and Belrose, J.S. (1972) Effective electron loss rates in the lower D-region during the decay phases of solar x-ray (SXR) events (1972), Radio Science 7:133-142.

Contents

17. Discussion of Polar VLF and Particle Precipitation Data for the 2 November 1969 Solar Particle Event

John P. Turtle
Aeronomy Laboratory
Air Force Cambridge Research Laboratories
Bedford, Massachusetts

Ernest J. Oelbermann, Jr.
Ordnance Research Laboratory
Pennsylvania State University
State College, Pennsylvania

Abstract

The 2 November 1969 solar particle event produced strong vlf amplitude and phase disturbances on the NPM and NPG signals received at Payerne, Switzerland and on NPM, NPG and GBR signals received at the AFCRL Geopole Observatory at Thule, Greenland.

Abrupt amplitude attenuation was recorded on the transpolar paths to Switzerland commencing at 1032 UT, and at Thule the signals were also strongly attenuated. The effects of this attenuation lasted for about nine days. Phase advances were recorded at both Switzerland and Thule reaching a maximum at about 1245 UT approximately the same time as the maximum of the greater than 30 MeV proton precipitation recorded by satellite. The magnitude of the phase and amplitude effects during this solar event indicate that this PCA was one of the strongest recorded on these paths since 1966.

A comparison of VLF and satellite particle data indicates that VLF effects commenced prior to the arrival of protons. Since nighttime conditions existed on the paths, these VLF disturbances were not caused by solar x-rays. Solar electrons were recorded outside the magnetosphere at about 1032 UT. From the VLF disturbances (at 1032 UT); it is evident that these electrons must have been nearly simultaneously present over the north polar cap indicating the possibility of a direct connection of polar cap and interplanetary field lines.

17-1 INTRODUCTION

Very low frequency (VLF) radio wave propagation has been found to be a very sensitive terrestrial means of detecting disturbances of the ionosphere produced by the entry of solar x-rays and particles into the upper atmosphere. It is generally accepted that VLF propagates in a spherical waveguide bounded by the earth's surface and the lower ionosphere, the D region. This propagation can be analyzed in terms of the sum of the waveguide modes in the cavity. Under normal ionospheric conditions, the upper boundary of the waveguide is near 85 to 90 km during the night and near 70 km during the day. During disturbed conditions, however, this upper boundary may be lowered to as low as 50 km due to the increased ionization at low altitudes caused by solar particles. Because of shielding by the earth's magnetic field, the greatest flux of solar particles into the upper atmosphere occurs in the polar cap regions. Thus VLF transmission paths, which cross the polar caps, are the first to be affected by precipitating solar particles. By monitoring these paths, distrubances of solar origin can be detected.

17-2 VLF PATHS MONITORED

During the 2 November 1969 solar particle event, the phase and amplitude of two trans-polar VLF paths were monitored at Payerne, Switzerland: NPM (from Hawaii at 23.4 kHz) and NPG (from Seattle at 18.6 kHz). In addition, three other paths, NPM, NPG, and GBR (from England at 16.0 kHz) were monitored at the AFCRL Geopole Observatory at Thule, Greenland, Three of these paths, the two trans-polar paths to Switzerland and the GBR-Thule path, cross the Greenland ice cap (Figure 17-1). At the time of the solar flare at 0939 UT and the ensuing solar x-ray enhancement at 0945 UT (Bucknam and Lincoln, 1971) the NPM and NPG-Thule paths were in complete darkness, the sun being more than 16^{o} below the horizon over their entire lengths. At Payerne, Switzerland the sun was about 25^{o} above the horizon so that the two trans-polar paths were sunlit only at their eastern end. In November the normal sunrise effects on the two trans-polar paths do not begin until after 1100 UT. Hence, all the paths can be considered to have been under nighttime conditions with the upper boundary of the VLF waveguide at 85 to 90 km. (GBR was down for maintencance at this time.) Because the NPM and NPG-Thule paths were in complete darkness, no sudden phase anomaly (SPA) at the time of the flare was detected. In addition,, the two trans-polar paths showed no disturbance at this time indicating that they were not sufficiently sunlit to be affected by the solar x-rays. A typical SPA flare disturbance, however, was recorded at 0946 ± 0001 UT on the sunlit path from NAA (Culter, Maine, at 17.8 kHz) to Tananarive, Malagasy. (Reder and Westerland, 1971.)

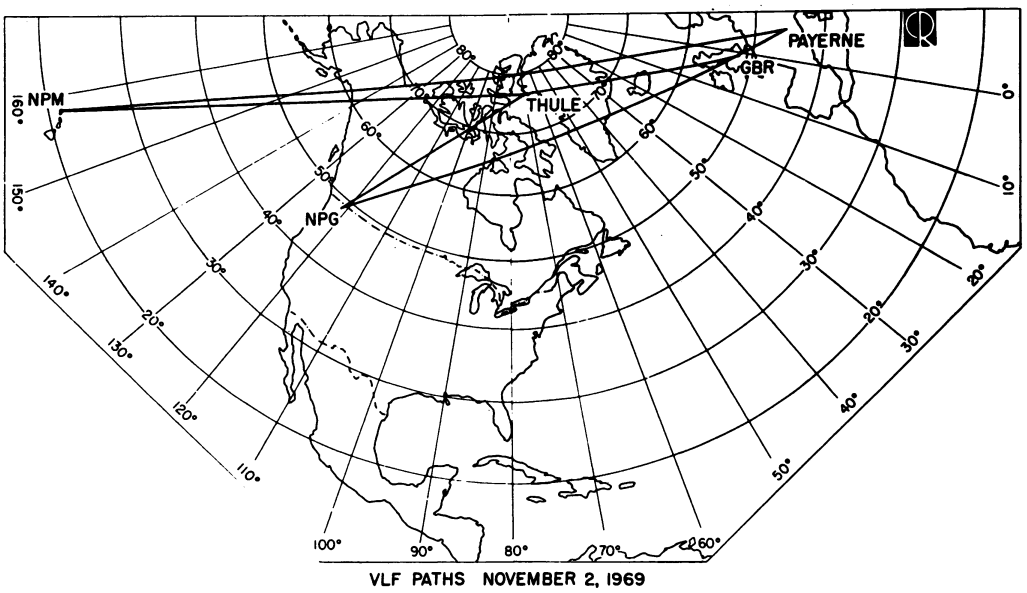

Figure 17-1. VLF Paths Monitored During the 2 November 1969 Solar Particle Event

17-3 DATA

As seen in Figure 17-2, no evidence of a disturbance on the polar VLF paths was detected until 1032:30 ± 30 sec UT. At this time the amplitude of the signal of both NPM and NPG to Switzerland showed abrupt attenuation. This was followed by sharp phase advances at 1034:30 ± 30 sec UT on NPM-Switzerland, at 1035 ± 0001 UT on NPM-Thule, and at 1039 ± 0001 UT on NPG-Switzerland. After the initial onsets, the disturbance effects on both the VLF phase and amplitude continued to increase reaching a maximum at around 1245 UT on 2 November. The gradual recovery of the VLF signal strengths to their normal day-night patterns required about nine days. No phase recovery data are presented because the receivers were referenced to a crystal standard and long term effects would be unreliable due to oscillator drift.

The diurnal amplitude patterns of all the VLF signals were disturbed by the PCA as shown in Figure 17-3. The average attenuation on the two trans-polar paths was calculated using the method of Oelbermann et al (1970) which compares disturbed-day amplitude values to quiet-day values. For the 24 hours following the event, the average attenuation on the NPG-Switzerland path was 19.2 dB and 13.2 dB on the NPM-Switzerland path. The average attenuation on the NPG-Thule path was 13.1 dB. The strongest attenuation during the event was recorded on the GBR-Thule path. This transmitter was off the air at the time of the particle onset; however, from

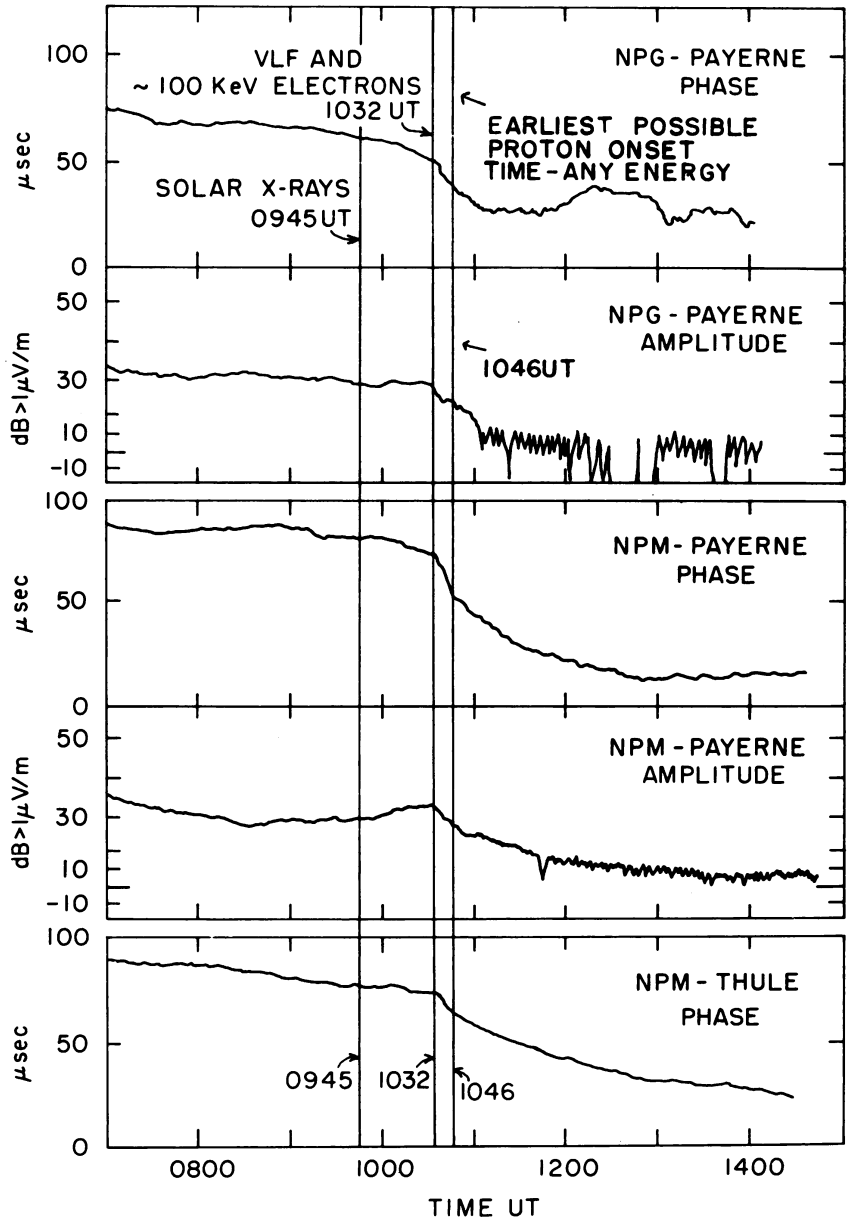

Figure 17-2. Real-time VLF Phase and Amplitude Records With Disturbance and Particle Onset Times

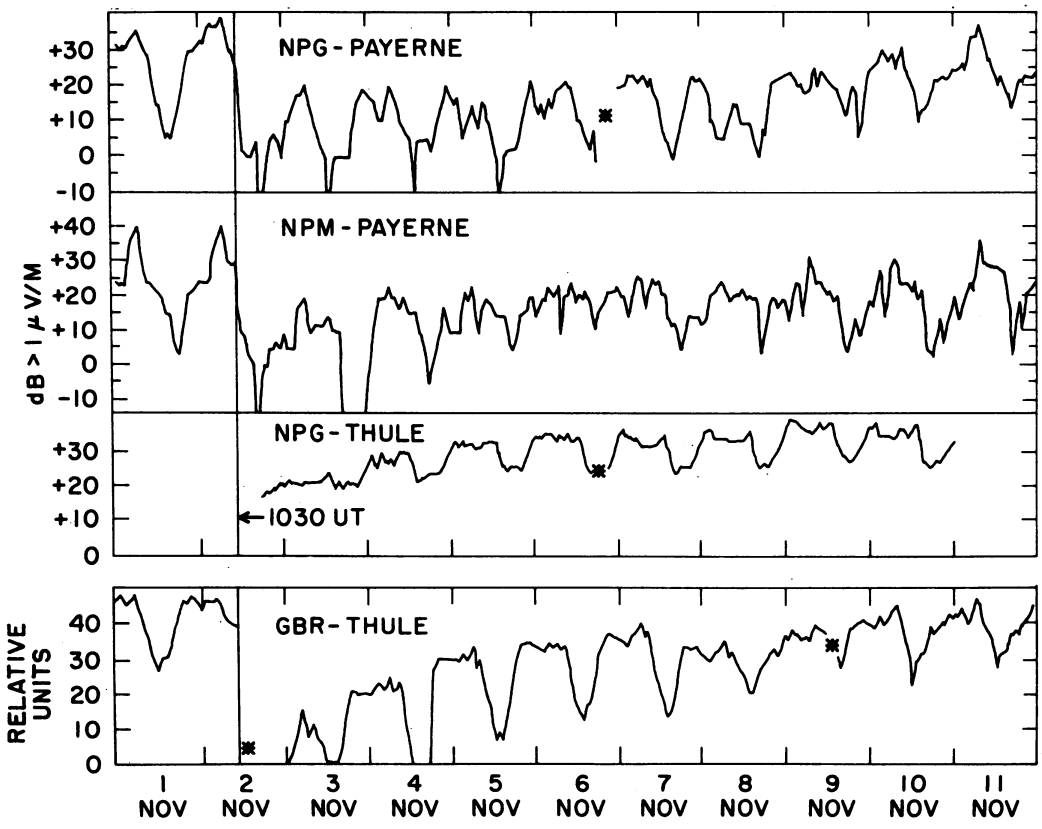

Figure 17-3. VLF Field Strength at Payerne, Switzerland and Thule, Greenland 1 - 11 November 1969. Transmitter maintenance*

the time the transmitter returned to the air at 1400 UT on 2 November until 0200 UT on 3 November, no signal was trackable at Thule. The signal then returned only to be lost again on 4 and 5 November during the usual daytime periods of signal minimum. Unfortunately, no absolute amplitude calibration existed for the GBR receiver so that only a relative value for the attenuation can be given. A reasonable estimate for the attenuation is at least 35 dB. The return of the signal strengths to their typical day-night patterns was about 80 percent complete on 8 November when additional attenuation due to another proton event was detected. Final recovery did not occur until 11 November.

The signal attenuation during the event was accompanied by large phase advances (Figure 17-4). On the NPM-Switzerland path the maximum phase advance was 72 μsec (600°), occurring at about 1300 UT. The maximum phase advance on the NPM-Thule path was about 37 μsec (308°) at 1245 UT. The phase shift on the NPG-Payerne path was complicated by the loss of signal at 1230 UT for about 15 min. At this time the continuity of the phase records was lost so that a comparison of phase

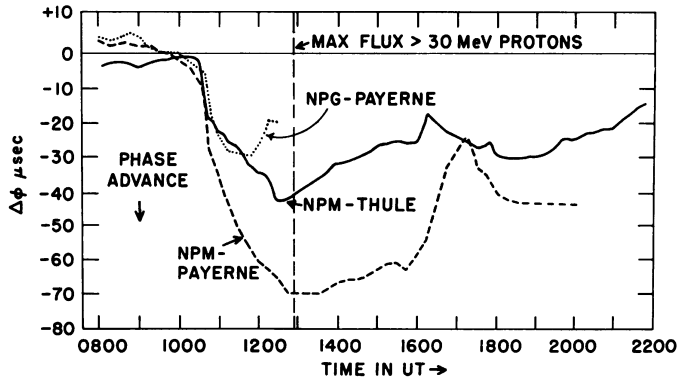

Figure 17-4. VLF Phase Shift (Disturbed-quiet Day) for NPG and NPM to Payerne and NPM to Thule, 2 November 1969

measurements before and after this time would be unreliable. Up to 1230 UT, however, the NPG phase had only advanced about 25 μsec. At the same time, the phase on the NPM-Switzerland path had already advanced 65 μsec. This 25 μsec advance on the NPG-Payerne path seems to be unusually small, considering that the amplitude attenuation on this path was larger than that on the NPM-Switzerland path.

17-4 DISCUSSION

An overall look at both the amplitude and phase records obtained during this PCA indicates that it was one of the most intense events recorded on these paths since 1966. As shown in Table 17-1, the average signal attenuation on the two paths to Switzerland for 20 previous events is 12.8 dB for NPG and 7.6 dB for NPM.

Table 17-1

	November 2, 1969		20 Previous PCA
	Maximum Phase Advance	Average Amplitude Change	Average Amplitude Change
NPM-Switzerland	72 μsec	13.2 dB	7.6 dB
NPG-Switzerland	NA	19.2 dB	12.8 dB
NPM-Thule	37 μsec	NA	2.6 dB
GBR-Thule	NA	35 dB	NA
NPG-Thule	NA	12.1 dB	3.3 dB

The attenuation for the first 24 hours of the 2 November 1969 PCA was 19.3 dB for NPG and 13.1 dB for NPM. Only two stronger events have been recorded on these paths. The attenuation on the NPG-Thule path was 12.1 dB, which is nearly four times greater than the average attenuation recorded on eight previous PCA's.

Westerland et al (1969) and Field et al (1971) have pointed out that paths which cross areas with low ground conductivities such as the Greenland ice cap are more strongly disturbed during PCA's than paths crossing only land, water, or sea-ice. While both the NPM and NPG great circle paths to Switzerland cross the ice cap, the NPM path crosses about two times as much ice as does the NPG path. Thus the NPM attenuation should be greater. During this PCA - as in 85 percent of the events since 1966 - the NPG path was more highly attenuated in spite of crossing less ice (660 km as opposed to 1100 km) and not going as far north as the NPM path. (The ice thickness crossed by both paths is greater than 1 km for most of their over-ice parts.) The GBR-Thule path crosses about 1300 km of the ice cap. In other aspects it is quite similar to the NPG-Thule path; they are both about the same length and since they both terminate close to the geomagnetic pole, their path lengths north of a given geomagnetic latitude are equal. Thus under homogeneous particle precipitation, one could expect similar effects on the two paths. Because 35 percent of the GBR path is over the ice cap, however, the attenuation on this path was about three times greater than that on the NPG-Thule path. This path is a sensitive detector of particle precipitation.

The great circle path from NPM to Switzerland passes fairly close to Thule and is about twice as long as the NPM-Thule path. On this basis one would expect the phase advance on the Switzerland path to be about twice that of the path to Thule. The Switzerland path, however, also crosses about 1100 km of the ice cap which should produce an additional phase advance. During this PCA the maximum advance on the NPM-Switzerland path was 72 μsec and that on the NPM-Thule path was 37 μsec. This is roughly the factor of 2 which would be expected from the differences in the path lengths excluding the over-ice effects. It appears that either there was no large additional advance produced by the over-ice portion of the NPM-Switzerland path, or that the NPM-Thule path was unusally disturbed. The possibility of an unusually strong disturbance in the area covered by the NPM-Thule path has already been mentioned. The amplitude of the NPG-Thule path, which crosses approximately the same area as does the NPM-Thule path, was more strongly attenuated than in previous PCA's.

The connection between the precipitation of solar particles into the polar regions during a PCA and the ensuing VLF phase and amplitude disturbance is well known (Oelbermann, 1970). For the 2 November PCA, the maximum flux of protons greater than 30 MeV as measured by Explorer 41 (Bucknam and Lincoln, 1971) occurred at about 1300 UT. The phase advances recorded on the NPM paths to

Thule and Switzerland showed a maximum within 15 min of the same time. Although VLF phase data during the recovery of the PCA is not reliable, amplitude measurements indicate that the decay in the proton flux was followed by the recovery of the VLF signal strengths. By the time the proton flux greater than 10 MeV had returned to background levels on 11 November, the VLF amplitudes had also returned to their normal levels.

17-5 VLF AND PARTICLE ONSET TIMES

A close look at the onset times of solar particles as measured by satellites and the resulting ionospheric disturbances as detected by VLF is of interest. As was mentioned earlier, no disturbance was recorded on any of the VLF paths in this study from the time of the solar flare at 0939 UT up until about 1032 UT (Figure 17-2). At this time, abrupt VLF amplitude attenuation began on the two transpolar paths. This was followed within a few minutes by phase advances on all paths. Protons can be ruled out as a cause of the disturbances because they were not detected by satellite until after 1046 UT. X-rays also could not have caused the VLF disturbances at this time as low-latitude sunlit paths showed no additional disturbance. In addition, the four paths and particularly the NPM and NPG-Thule paths were not sufficiently sunlit to have been affected by solar x-rays. These disturbances, however, were similar to those normally recorded at the onset of particle precipitation along VLF paths.

Solar electrons were detected by satellite at about the same time as the onset of the VLF disturbances. The Air Force satellite OV5-6 outside the magnetosphere observed the arrival of (45 keV-300 keV) electrons at 1031.5 ± 1 min UT (Yates et al, 1971). Both OV5-6 and Explorer 41 (Lanzerotti and MacLennan, 1971) inside the magnetotail reported 300 keV electrons at about 1034 UT. Since no polar orbiting satellite particle data is available at these onset times, it must be inferred from the VLF disturbances starting at 1032.5 ± 30 sec UT that the electrons detected by satellites were nearly simultaneously present at D-region altitudes over at least the northern polar cap. Since electrons in the 40 to 300 keV range deposit most of their energy in the 70 to 90 km range (Rees, 1963), the electrons detected by the satellites would be easily capable of producing the observed VLF effects.

Hakura's model of a PCA (Hakura, 1967) shows that at the onset, electrons can be precipitated close to the poles. From the VLF data for the November 1969 event, it is possible to estimate the southern extent of electron precipitation in the northern hemisphere at 1045 UT. The great circle path NPG-Switzerland goes to 79° N geomagnetic while the path from the Omega Station at Aldra, Norway (10.2 kHz and 13.6 kHz), to Deal, New Jersey, goes only to 69° N geomagnetic. The NPG path was

strongly disturbed by 1045 UT, while the Aldra path was not affected until about 1100 UT (Reder and Westerland, 1971). It is evident that at 1045 UT, electrons were precipitating from a southern boundary of about 70^{o} N geomagnetic well up towards the pole.

Although particle measurements by satellite have been made outside the magnetosphere and over the polar caps during an event, no data is available from a satellite which was over the polar cap at the onset of an event. A recent article (West and Vampola, 1971), discusses simultaneous satellite measurements in interplanetary regions and over the polar caps during a solar particle event. They show that there can be a close agreement between electron fluxes and spectra measured in the two regions. The data presented here from the onset of the 2 November 1969 solar particle event indicates that the entry of solar electrons into the polar cap can be rapid. From the timing accuracy of the VLF data, the delay for the access of the electrons to the polar cap D region could be no greater than one minute and it could be much less. A rapid access of electrons to the polar cap implies the possibility of an interconnection of interplanetary and polar cap field lines. A more detailed study of this rapid access of electrons to the polar cap will be presented in a forth coming publication (Turtle et al, 1972).

The VLF data presented here indicates that the 2 November 1969 PCA was a very strong event. The overall disturbances produced on the VLF paths were similar to those during other PCA events. The specific effects on several of the paths, however, were not directly consistent with present VLF theory, particularly for the over-the-ice-cap paths. From the comparison of the onset time of the VLF disturbance and the satellite particle onset times, it is apparent that VLF can be a sensitive ground-based detector of ionospheric disturbances produced by the precipitation of solar particles.

References

Bucknam, D. B. and Lincoln, J. V. (Ed.) (1971) University of Iowa Explorer 33 and 35 Data, World Data Center A, Report UAG-13.

Field, E. C., Greifinger, C., Schwartz, K. (1971) Trans-polar Propagation of Long Radio Waves, Rand Report 683, DASA 2621.

Hakura, Y. (1967) Entry of solar cosmic rays into the polar cap atmosphere, J. Geophys. Res. 72:1461.

Lanzerotti, L. and MacLennan, C. G. (1971) Relative importance of solar electrons, protons, and alphas in the November 1969 PCA Event, Proc. Cospar Symp. on November 1969 Solar Particle Event.

Oelbermann, E. J., Jr. (1970) Solar particle effects on polar cap VLF propagation, J. Franklin Inst. 290.

Oelbermann, E. J., Jr., Imhof, G. W., Briggs, M. (1970) Coordinated High-Latitude Experiments for the Sumulation of Nuclear-Burst Effects on VLF Systems. Technical Report 356-F, HRB-Singer, State College, Pennsylvania.

Reder and Westerland (1971) Private communication.

Rees, M. (1963) Auroral ionization and excitation by incident energetic electron, Planetary Space Sci. 11:1209.

Turtle, J. P., Oelbermann, E. J., Jr., Blake, J. B., Lanzerotti, L. J., Vampola, A. L. and Yates, G. K. (1972) Rapid access of solar electrons to the polar cap, J. Geophys. Res. 77:730-735.

West, H. I., Jr., Vampola, A. L. (1971) Simultaneous observations of solar-flare electron spectra in interplanetary space and within earth's magnetosphere, Phys. Rev. Letters 26:458.

Westerland, S., Reder, F. H., Abom, C. (1969) Effects of polar cap absorption events on VLF transmissions, Planetary Space Sci. 17:1329-2374.

Yates, G. K., Katz, L., Blake, J. B., Paulkias, G. A., Vampola, A. L., Sellers, B., Hanser, F. H., (1971) Energetic Particle Measurements Aboard OV5-6 and OV1-19 Satellites, Proc. Cospar Symp. on November 1969 Solar Particle Event.

18. VLF Sounder Measurements During a PCA Event

V.E. Hildebrand, J.R. Hill and J.N. Martin
Electronics Laboratory Center
San Diego, California

Abstract

During the summer of 1970 the NELC vlf-multifrequency sounder was operated at Thule, Greenland; and a multifrequency oblique incidence sounder was operated between Thule and Point Barrow, Alaska. Measurements were obtained during a PCA event on 23-25 July 1970. The oblique sounder simultaneously measures phase and amplitude of the propagated signal at ten frequencies between 8 and 31 kHz. The vertical sounder measurements give phase and amplitude of the reflection coefficients ⊥R⊥ and ⊥R∥ at ten frequencies between 8 and 20 kHz. D-region electron density profiles obtained from an analysis of these data during the July 1970 PCA are presented.

During the summer of 1970, the NELC vlf-multifrequency vertical incidence sounder was operated at Thule, Greenland; and the multifrequency oblique incidence sounder was operated between Thule and Point Barrow, Alaska. The oblique sounder simultaneously measures phase and amplitude of the propagated signal at ten frequencies between 8 kHz and 31 kHz. The vertical sounder measurements give the phase and amplitude of the reflection coefficients ⊥R⊥ and ⊥R∥ also at ten frequencies in the same band. This equipment was operated from June

through August 1970, and data were obtained during two PCA events. The first of these events was caused by a Class X flare on 23 July and the PCA phase lasted through 25 July, with no other important flares occurring during this time. The second event occurred 13 to 15 August and was much more complex. This event was preceded by two Class X flares and for some 30 hr during the PCA, there was a flare of Class M or greater in progress.

Data reduction and analysis have been concentrated on the first of these events, as it appears to be much the simpler of the two. Even this event, however, is complicated by the fact that an increase in low energy proton flux was detected prior to the flare which produced the PCA. Thus, it is probable that the pre-PCA ionosphere was disturbed somewhat from ambient conditions. The time sequence of the flare, proton flux, and observed effects on the vlf sounder and riometer for this event are shown in Table 18-1.

A sample of the steep incidence data during this event is shown in Figure 18-1, which shows the phase and amplitude for the reflection coefficients, $\perp R\perp$ and $\perp R\parallel$, at 9.336 kHz. The flare is seen as approximately 8-dB increase in the reflection coefficient $\perp R\perp$ and 2-dB decrease in the conversion coefficient $\perp R\parallel$. At the time of maximum (30 MHz) riometer absorption the reflection coefficient has increased by

Table 18-1.

Date	Time	Event
23 July	1823	Flare start
	1855	Peak flare effect at VLF
	2100	Protons detected, ATS satellite
	2110	PCA effect begins at VLF
	2240	Thule 30 MHz riometer absorption, 0.9 dB max
24 July	0000	VLF effects continuous next 20 hr, low level
	2200	New phase begins at VLF
	2300-2400	5-21 MeV proton flux peaks at 2000 particles/cm^2/sec
	2340-2350	21-70 MeV proton flux peaks at 40 particles/cm^2/sec
	2350	Sudden commencement begins, magnetometer
25 July	0014	Maximum 30 MHz riometer absorption 7 dB
	0016	Maximum VLF effect

9 dB and the conversion coefficient has decreased by 18 dB. The phase of these signals is retarded 35 to 40 μsec relative to the time preceding the flare. This corresponds to a change in the apparent reflection height of 5 to 6 km. These data were obtained for ten frequencies between 8.299 kHz and 19.708 kHz. Changes in reflection coefficients at all frequencies during the PCA are shown in Figures 18-2 and 18-3. Figure 18-2 compares the pre-event reflection and conversion coefficents with those measured just before the beginning of the second phase of the PCA, and Figure 18-3 compares these values for the pre-event time with the time of peak effect at VLF. Contrary to expectations, the reflection coefficient increased significantly at all frequencies during the PCA event. The behavior of the conversion coefficient was somewhat more complicated, but generally decreased at the lower frequencies and increased at the higher frequencies, with the crossover near 12 kHz.

Figure 18-4 illustrates the phase changes observed at VLF during the flare and PCA. Shown plotted here is the phase change at the time of peak flare effect, a time during the minor phase of the PCA, and at the time of peak PCA effect. The reference was the phase at a time just prior to the beginning of the flare. The phase changes during the minor phase of the PCA are seen to be quite similar in nature and magnitude to those observed during the x-ray flare event; however, the changes at the PCA peak are quite different both in magnitude and frequency dependence. The complex behavior of the phase changes vs frequency are indicative of a complex ionospheric conductivity profile with more than one reflecting region. This hypothesis is further borne out by the occurrence of maxima and minima in the magnitude of the reflection coefficients vs frequency illustrated in Figure 18-5, which shows $|R|$ only for three different times during the progress of the event. The earliest time shown here, 2030Z, is after the ionosphere has essentially recovered from the flare-produced SID and before the arrival of energetic particles; the next time, 2240Z, is shortly after the onset of the proton event; and the latest time, 0300Z the following day, is just after the minor phase of the PCA has reached its maximum. Note the distinct maxima and minima which moves steadily upward in frequency as the PCA progresses. If these are interpreted as interference phenomena due to two distinct reflecting regions, then the separation between the regions must be decreasing after the onset of the PCA. An estimate of the separation distance can be formed by determining a spacing which is equal to an odd multiple of $\lambda/4$ at the frequencies of the minima and an even multiple of $\lambda/4$ at the frequencies of the maxima. This procedure leads to an estimate of reflecting regions with a separation of 20 km at 2030Z, 18 km at 2240Z, and 15 km at 0300Z. These are, of course, only approximate values since steep incidence reflection at VLF is much more complicated than this simple picture of reflection from distinct altitudes. Nevertheless, such an analysis gives valuable clues in the process of determining an electron density profile from vlf data.

As a further example that a complex electron density profile can be inferred from the reflection coefficients, a comparison can be made with calculations based on a simple monotonically increasing electron density (see Figures 18-6 and 18-7). Figure 18-6 is an electron profile measured by Belrose at Resolute Bay, and Figure 18-7 shows the vlf-reflection coefficients calculated from this profile. The calculated reflection coefficients are nearly constant across the entire vlf band, in marked contrast to the measurements made at Thule which are also shown in the figure for comparison. There is, of course, no reason to expect a profile measured at Resolute Bay to be consistent with measurements made at a different time at Thule; the point is simply made that an electron profile which is consistent with the Thule measurements must be of a different nature than the smooth, monotonic profile of Figure 18-6.

The best results to date of the effort to obtain electron density profiles which are consistent with the vlf measurements are illustrated in Figure 18-8. Here are shown a pre-PCA profile, a profile obtained during the minor PCA phase and a profile for the peak PCA. These results were obtained by searching for profiles which minimized the mean square difference between reflection coefficients calculated from the profiles and reflection coefficients actually measured. The profiles shown give good agreement with the experimental data; however, the calculation of reflection coefficients from these profiles did not include any effect of ions. At the low altitudes involved, ions should probably be included in the analysis. The computer program for profile fitting is being modified to account for ions, and future calculations with ions included may change the electron densities somewhat from those presented here.

Very-low-frequency signals measured over the Thule to Point Barrow path are shown in Figure 18-9. Note that during the PCA, propagation was generally enhanced with the degree of enhancement increasing significantly above 24 kHz. No significant changes are noted between the time of minor PCA and the time of peak PCA except at the two highest frequencies.

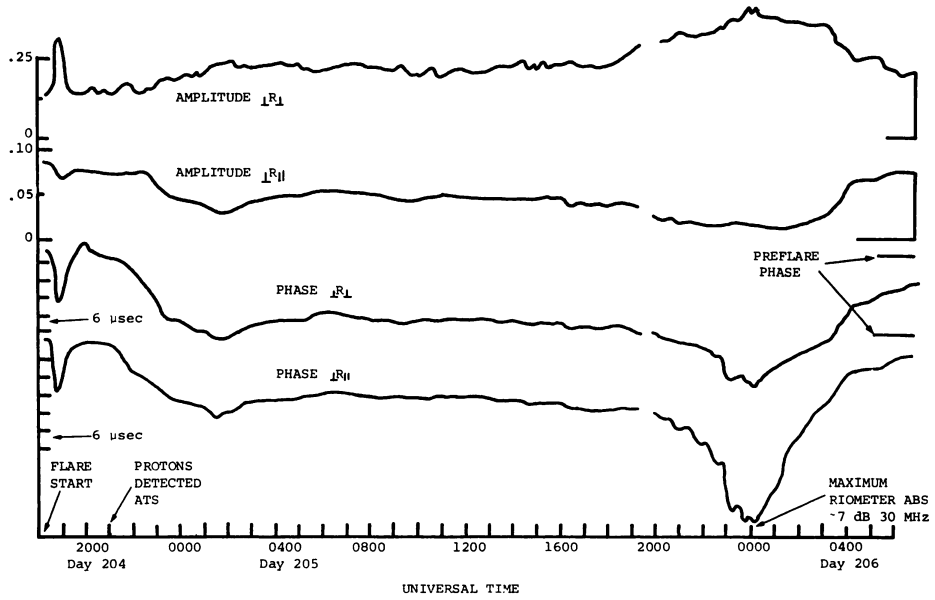

Figure 18-1. Vertical Incidence Reflection Coefficients During July PCA

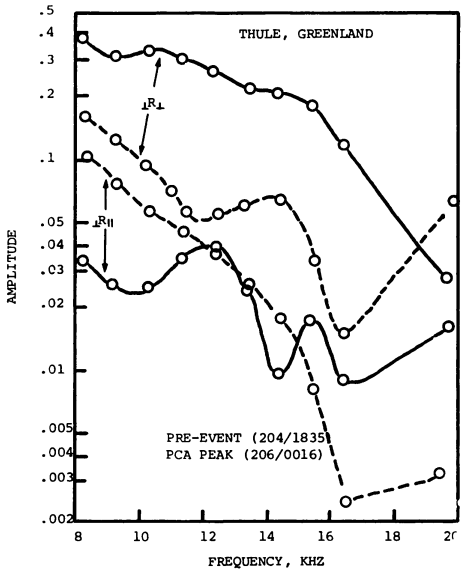

Figure 18-2. Reflection Coefficient Changes During PCA Minor Phase

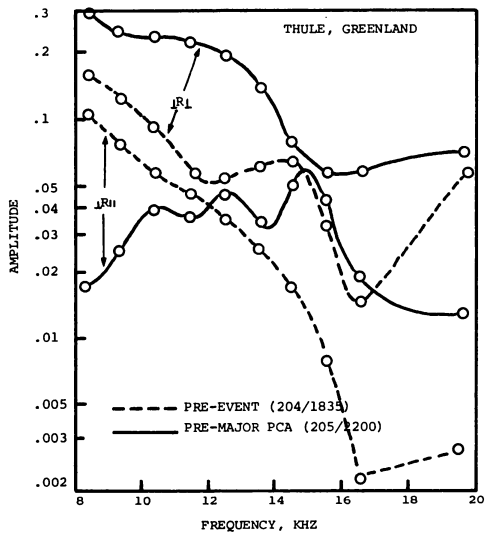

Figure 18-3. Reflection Coefficient Changes at PCA Peak

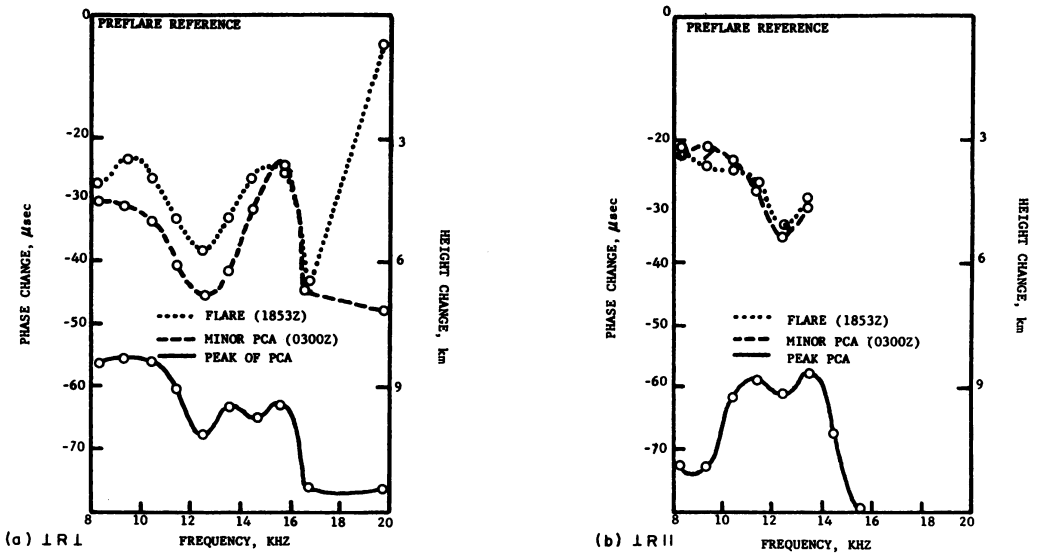

Figure 18-4. Phase Changes During July PCA

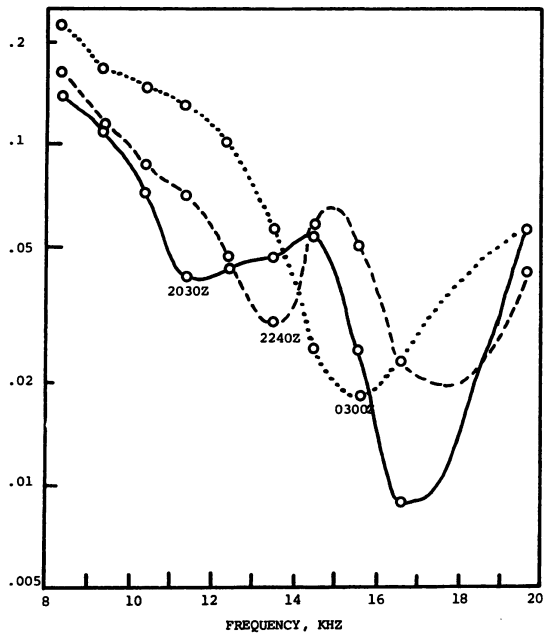

Figure 18-5. Reflection Coefficients, ⊥R⊥, July PCA

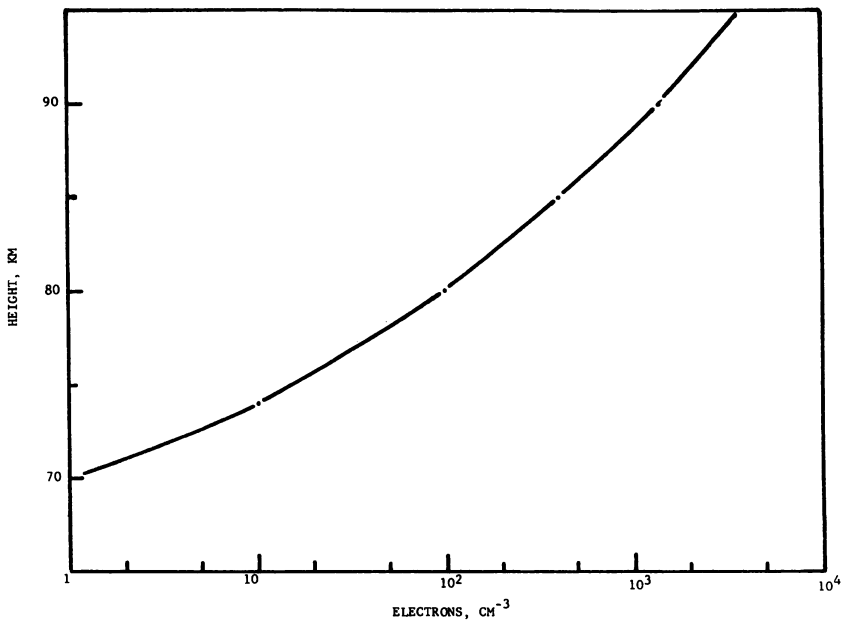

Figure 18-6. Electron Density Profile at Resolute Bay (Belrose)

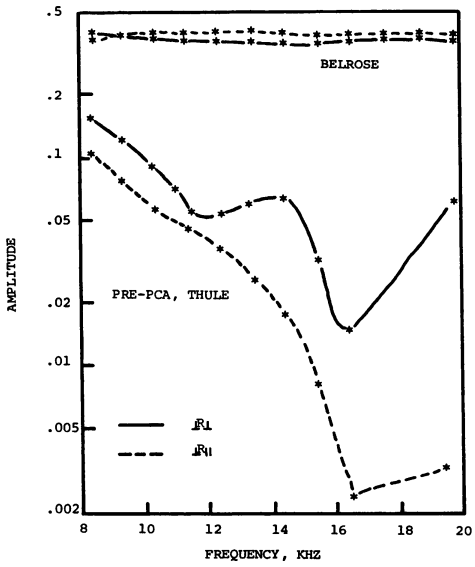

Figure 18-7. Comparison of Measured and Calculated Reflection Coefficients

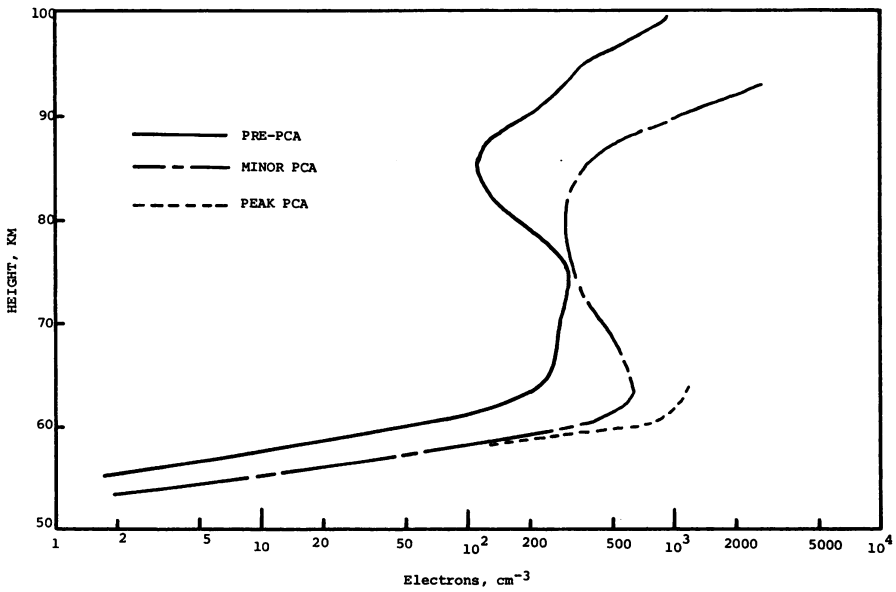

Figure 18-8. Electron Density Profiles, July PCA, Thule

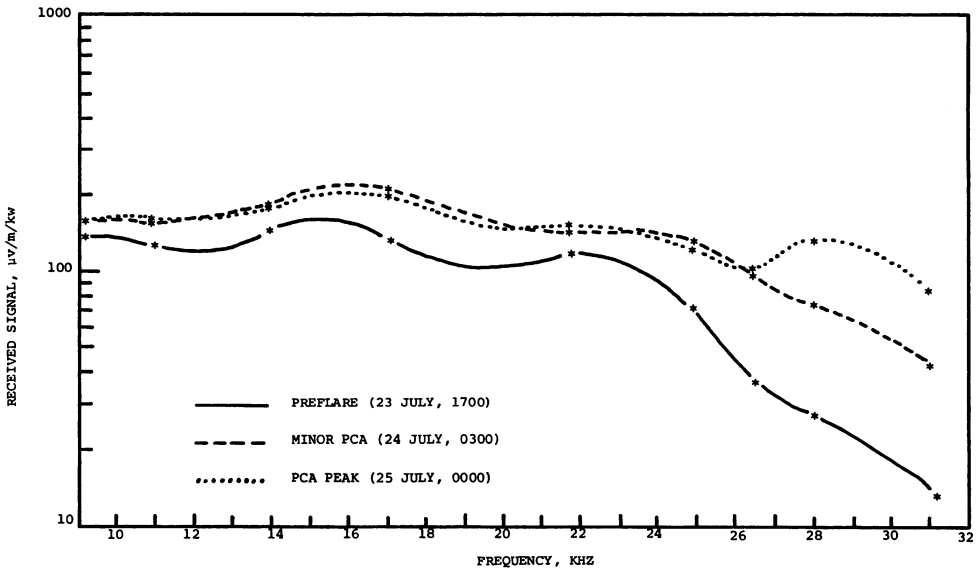

Figure 18-9. Long Path Propagation Changes During July PCA

Contents

19. Rocket Measurements of Antarctic D-Region Electron Density During the 28 January 1967 PCA Event

J.J. Berthelier and M. Pirre*
Groupe de Recherches Ionosphériques
4, avenue de Neptune
94, Saint-Maur-des-Fosses, France

Abstract

During the Southern Hemisphere summer 1966-1967 the Centre National d'Etudes Spatiales organized a campaign in Antarctica, and three Dragon rockets were launched from Dumont d'Urville (+ 140° E - 66.6°S, invariant latitude ~81°) during the solar proton event of 28 January 1967. The scientific payload on board each rocket consisted of particle detectors to measure angular and energy distribution of protons ($E_p \geq 100$ keV) and electrons ($E_e \geq 40$ keV), and electron density and temperature probes. The electron density was an rf-capacitance probe which permitted the measurement of electron density down to 5×10^2 electrons/cm^3. Profiles obtained during the development of the event are presented and discussed in this paper.

19-1 INTRODUCTION

A large increase in solar cosmic-ray intensity was detected on the earth and on polar orbiting or interplanetary satellites on 28 January 1967.

* Assistant à la Faculté des Sciences d'Orléans, 45 Orleans 2, France.

The proton fluxes remained high for several days and produced a significant increase in the absorption of cosmic noise in both polar caps (Masley and Goedeke, 1967). During this event three rockets were launched from the French Antarctic base Dumont d'Urville (140°E-66.6°S), in order to obtain relevant data on the electron density in the lower ionosphere and also on solar particle fluxes.

Dumont d'Urville is located well inside the Southern Polar Cap down on the coast of the Antarctic continent at an invariant latitude of approximately 81° corresponding to a theoretical L value of ~37 (Figure 19-1). This position is therefore particularly well suited for the observation of polar cap phenomena as they are

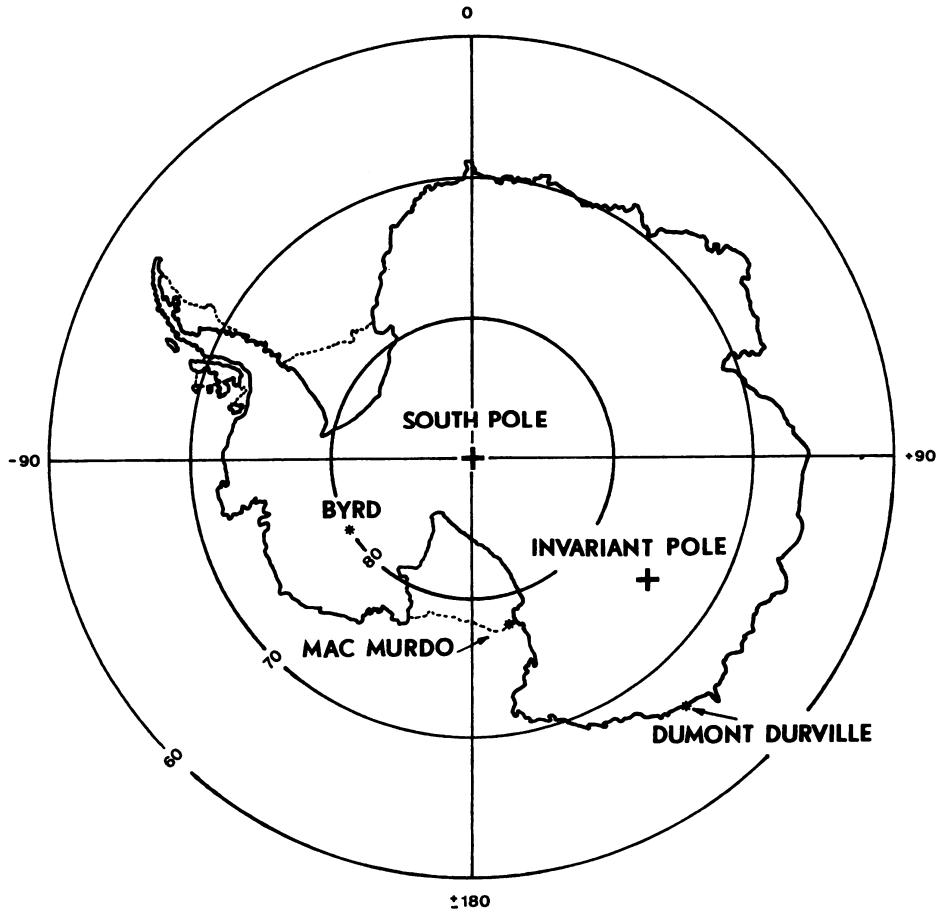

Figure 19-1. Position of Four Important Geophysical Stations in Antarctica

practically free from auroral contamination. In the case of PCA events, the increase of the ionization in the lower ionosphere is then entirely due to solar particles, mainly to protons and, occasionally, to electrons (Lanzerotti and MacLennan, 1971).

The original purpose of the rocket program was to study the diurnal magnetic activity and related ionospheric phenomena (Lebeau, 1965, Mendel, 1966). At the time the program was initiated (early in 1965), the opportunity of launching some rockets during a PCA event was merely disregarded due to the expected low solar activity and the shortness of the campaign only one month long. After having unsuccessfuly waited three weeks for magnetic activity, however, we were lucky enough to fire three rockets during a period of high absorption consecutive to the ejection of energetic particles from the Sun.

19-2 THE SOLAR COSMIC RAY EVENT OF 28 JANUARY 1967

The 28 January 1967 solar cosmic-ray event was one of the largest events of the new solar cycle; it lasted several days and was followed by another smaller event on 2 February. Figure 19-2 shows the increase in neutron monitor counting rates for two stations in the Northern and two stations in the Southern hemispheres (Baird et al, 1967). The time of arrival of the high energy protons ($E \gtrsim 500$ Mev) on the earth as deduced from these records is 08.35 ± 00.05 UT, and a maximum increase of ~17 percent is reached at all the stations at about 11.15 UT. This represents quite a long rise time and is certainly related to the position of the flare and subsequent conditions of propagation in interplanetary space. Data from lower latitude stations (Pic du Midi and Gif-sur-Yvette in France) indicate that the maximum rigidity of the solar protons was of the order of ~ 2 GeV (Labeyrie, private communication).

The riometer observations (Figure 19-3) show a rapid increase in the absorption at approximately the same time as the neutron monitors but the onset of the PCA is not clear, due probably to the arrival of solar protons prior to the beginning of the major event (Masley, 1968; Bukata et al, 1969). In the Southern Polar Cap the stations were all in continuous daylight, except for Dumont d'Urville, and it is possible to distinguish a maximum in the absorption of roughly 8 dB near 22.00 UT.

This event represents an intriguing anomaly as it is not associated, as usual, with a large flare on the western part of the sun. The only reported flare was located in the south eastern quadrant (23^{o}S - 19^{o}E) and was assigned a minor importance 1^{-}. In fact, it seems now to be clearly established that the flare initiating solar protons ejection was ~60^{o} in longitude behind the western limb

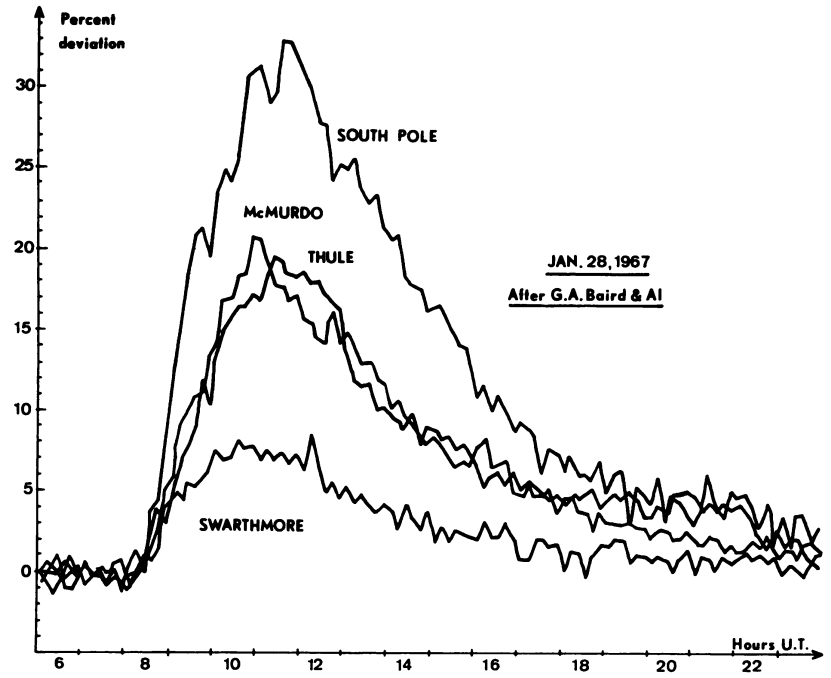

Figure 19-2. Variations in Neutron Monitor Counting Rates During the SPE of 28 January 1967

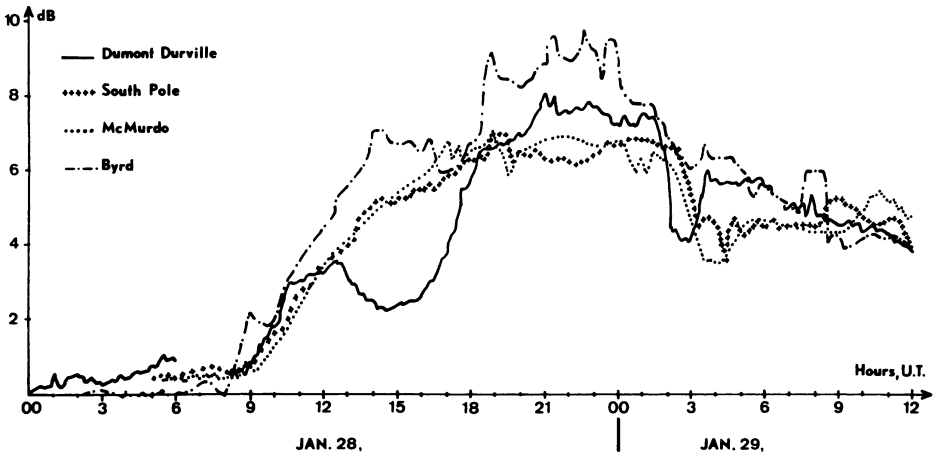

Figure 19-3. 30 MHz Absorption Variations During 28 and 29 January 1967

of the disk (Lockwood, 1968, Bukata et al, 1969), but very abnormal circumstances must have been encountered in order for particles to be brought to the orbit of the earth.

19-3 EXPERIMENT

As previously mentioned, the scientific payload was designed for an experiment on auroral-like phenomena. In addition to the detection of energetic particle fluxes, which may be an effective source of ionization at these high latitudes (Lebeau, 1965), we were also interested in obtaining the electron density and temperature in two regions: (1) E-region—where electric currents responsible for the magnetic activity are thought to circulate (Mendel, 1966), and (2) in the F-region—where still unknown perturbations cause the F1 and/or F2 echoes on the ionograms to disappear quite often near local and magnetic noon in summer (Lebeau, 1965).

In order to reach the F2 layer, choice was made of a two-stage solid propellant DRAGON I rocket which normally culminates at 320 km with a 100 kg payload. Owing to this rather high apogee, the minimum altitude above which significant measurements were made was normally of the order of 70 to 75 km. Fortunately, the rocket did not perform as well on one occasion, and we obtained data down to 55 km.

The scientific instrumentation consisted of an rf probe to measure the electron density, a differential double Langmuir probe to measure the electron temperature, and particle detectors to detect low energy electrons and protons. The payload is represented schematically in Figure 19-4. There are three main parts of the payload:

(1) The upper part contains the plasma probe electronics and booms which are used to put the electrodes approximately one meter apart from the rocket body in order to suppress any sheath effect due to the rocket.

(2) The middle part contains the particle detectors.

(3) The lower part contains the technological package including flight programmer, housekeeping modules and telemetry system.

A three axis magnetometer was located at the top of the payload and was used for attitude determination.

19-3.1 Electron Density Probe

The electron density probe is an rf-capacitance probe developed by Prof. Sayers' group at Birmingham University (U.K.) and has been described in detail elsewhere (McKenzie and Sayers, 1966). Briefly, the principle of the probe

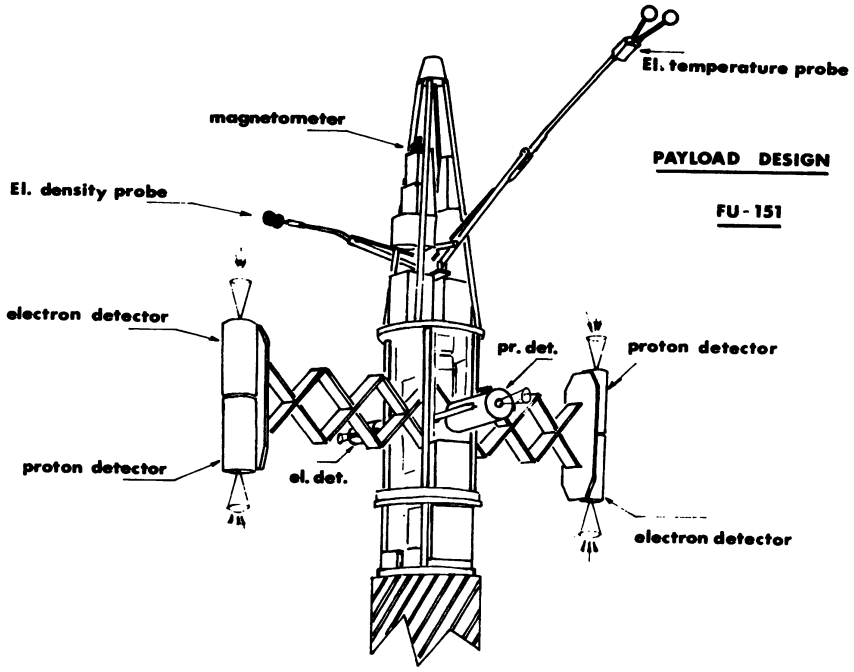

Figure 19-4. Schematic View of the Payload

consists in measuring the impedance of a capacitor, made up of two-plane parallel grids immerged in the plasma at a high frequency of 39 MHz. In the case of the ionosphere above approximately 65 km, both the electron gyrofrequency and collision frequency may be neglected with respect to the high operating frequency. The permittivity of the medium is then equal to:

$$\epsilon = \epsilon_o \left(1 - 80.6 \frac{N_e}{f^2}\right) \qquad (19\text{-}1)$$

where N_e is the electron density in electrons/cm^3, and f is the operating frequency (39 MHz) in kHz.

If Co is the capacitance in vacuum and C the capacitance in the plasma, a straightforward calculation gives

$$N_e = k \Delta C \qquad (19\text{-}2)$$

where

$$\Delta C = |C - Co|$$

$$k = \frac{f^2}{80.6\ Co} \quad .$$

In the lowest part of the D region, under 65 km, it is necessary to take account of the electron-neutral collision frequency, and the exact relationship between N_e and C becomes more complicated. We may then write

$$N_e = k'(h)\ k\ \Delta C \qquad (19\text{-}3)$$

where the altitude dependent correction factor $k'(h)$ is equal to 1 above 66 km and increases with decreasing altitude to reach 1.4 at 55 km.

The measurement rate of the probe is such that the electron density is obtained every 0.25 sec, which corresponds roughly to an altitude resolution of 0.5 km in the D region.

19-3.2 Energetic Particle Detectors

The electron and proton detectors were scintillation counters using plastic scintillators coupled with P.M. tube (Berthelier et al, 1966). A thin -1μ for electrons, 0.2μ for protons—aluminium layer was deposited on the scintillators in order to protect the photomultiplier from sunlight or earth albedo. Energetic particles were counted in three channels corresponding to the following energies:

Electrons: 20 - 50 keV, 50 - 150 keV, > 150 keV

Protons: 90 - 300 keV, 300 - 800 keV, > 800 keV

The counting rate in each of these channels was logarithmically compressed and continuously telemetered. As mentioned previously, the experiment was designed to measure auroral type fluxes of protons and electrons. Consequently, shielding against high energy protons was insufficient, and this led to a high parasitic counting rate, especially during the first flight in the initial phase of the event. A very long and tedious analysis of our data and comparison with satellite or balloon data available for this event (Lanzerotti, private communication; Barcus, private communication) enabled us to get rather good information on the high energy ($\geq$ 50 MeV) protons; data on the low energy particles ($\leq$ 2 MeV) are now being obtained (Pirre, 1971). Proton and electron detectors were identical except for the presence of a broom magnet to deflect electrons of energy E < 400 keV before entering the proton scintillator. On each payload, six of these

detectors were installed; three for protons and three for electrons looking respectively upward, downward, and perpendicularly to the axis of the rocket.

19-4 ELECTRON DENSITY RESULTS

The first rocket (D. 25) was fired at 12. 05 UT in the early phase of the event, nearly 1 hr after the time of maximum arrival of high energy protons, the absorption being equal to 3. 2 dB on 30 MHz. During the propelled phase of the flight, an aerodynamic instability of the rocket resulted in a large tumbling motion and consequently a severe lowering of the whole trajectory. The nose cone was jettisoned at 55 km, and significant data were obtained above 57 km. This enabled us to get a complete electron density profile down to the lowest density measurable by the probe (2×10^2 electrons/cm^2) as shown in Figure 19-5.

The two other flights were made on 29 January respectively at 01. 30 UT (D. 26) and 03. 10 UT (D. 27) under daytime conditions. The absorptions indicated by the 30 MHz riometer were respectively 6. 5 dB and 4. 5 dB, with the second flight corresponding to a serious decrease of the absorption lasting for nearly 2 hr and which has been described earlier (Berthelier, 1969). During these two shots the rockets behaved normally, and the density profiles were obtained only above 72 km for D. 26 and 74 km for D. 27. They are represented on Figure 19-6 which shows a steadily increasing electron density in the case of D. 26 from $\sim 5 \times 10^3$ electrons/cm^3 at 72 km to 7.5×10^4 electrons/cm^3 at 95 km, and a comparable profile for D. 27 with the electron density beginning to decrease more rapidly below 78 km. We are currently working to extend these profiles to the 60 to 70-km zone by means of a multifrequency riometer analysis, and we will not give any more detail on them in the remaining paragraphs.

19-5 DISCUSSION OF THE RESULTS

We will now concentrate the discussion on the electron density profile obtained during the first flight (D. 25). This profile corresponds to sunset conditions as the solar zenith angle was equal to 89.2°. Above 61 km the profile is rather smooth, the electron density increasing from 10^3 electrons/cm^3 at 63 km to 10^4 electrons/cm^3 at 94 km with a gradient weaker above 74 km than below. The most striking feature, however, is the existence of a drastic enhancement of Ne between 55 and 61 km, with two peaks at $\sim$58 km and 60 km corresponding respectively to 8×10^3 electrons/cm^3 and 1.2×10^4 electrons/cm^3. This observation lead us to a careful examination of the data in order to check the electron

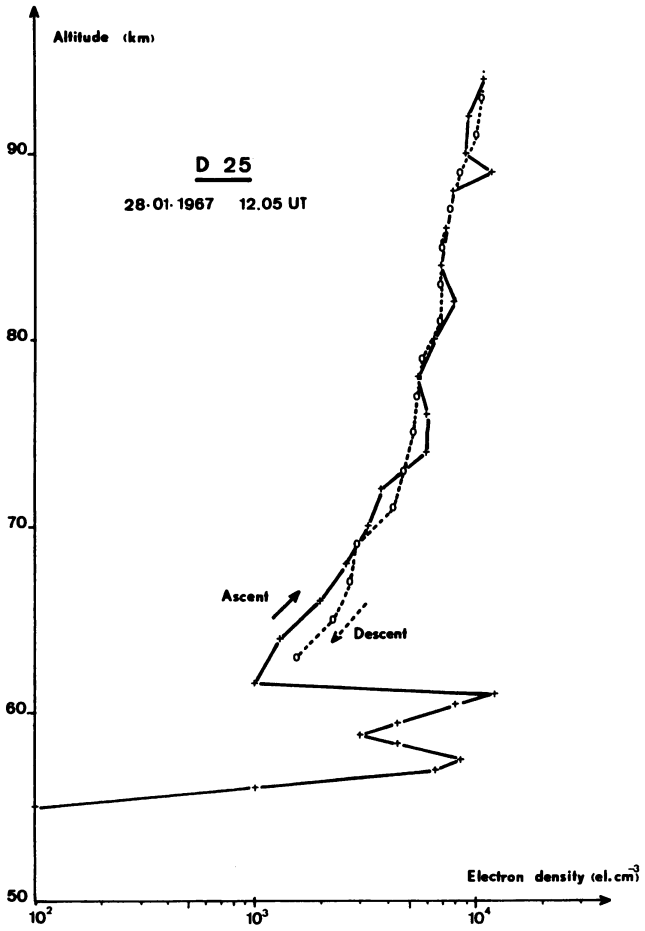

Figure 19-5. D. 25 Electron Density Profile

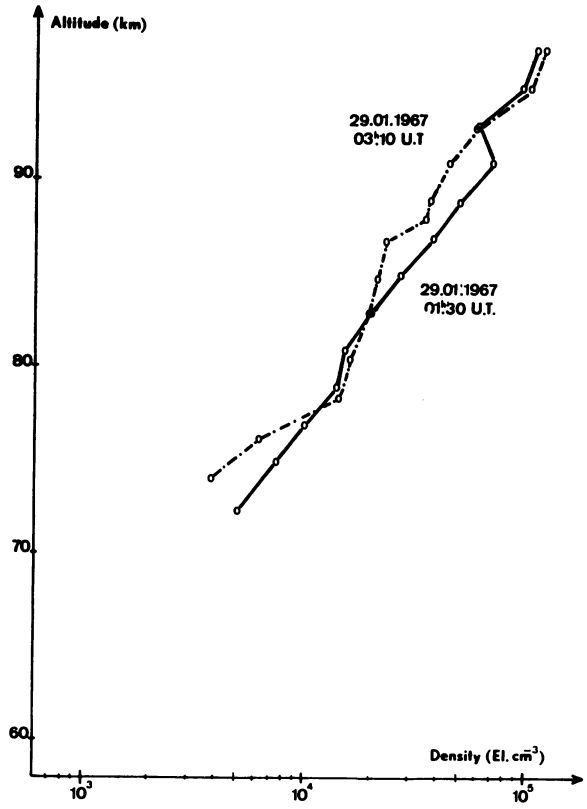

Figure 19-6. D. 26 and D. 27 Electron Density Profiles

density measurements and also the altitude of this layer and its shape. It was primarily intended to calculate the rocket trajectory by use of the data telemetered from an onboard accelerometer, but this method proved completely inadequate. A new method was developed giving an accuracy of ± 1, 5 km in general, but only ± 3 km in the case under study. Checking of the electron density values and altitude determination was made simultaneously by using absorption values of 20 MHz and 30 MHz. It was assumed that the "corrected" electron density was a linear function of the measured one

$$N'_e \text{ (corrected)} = a_N \times \text{Ne (measured)} .$$

Changing the altitude by 1-km steps, we tried to fall in agreement with both the 20 MHz and 30 MHz absorption. The final result was that the trajectory first calculated should be shifted 2. 5 km upward (in good agreement with the ± 3 km estimated error bar), and that the electron density was essentially correct, with a_N being equal to 1. 03 ± 0. 05.

The lower boundary of the peak shows a large gradient, but such steep ledges have been rather frequently observed by rocket borne probes in the quiet D region as well as under disturbed conditions. The upper ledge, however, is far more intriguing.

A detailed examination of the actual telemetered signal from the electron density probe revealed that the electron density dropped abruptly by a factor of ~4 to 5 in roughly 40 ms, which corresponds to a height of ~80 m if we make the hypothesis that the irregularity is horizontally stratified. The hypothesis of any malfunction of the probe was ruled out by examination of the housekeeping measurements and also on the basis that the electron density profile was in good agreement with the absorption measured on 20 and 30 MHz. This latter reason also holds against a possible reduction of Ne above 61 km by gas leakage from the rocket engine. Moreover, several other reasons may be invoked to rule out this possible explanation: the downward leg of the rocket reveals the same value of Ne down to the turnover of the rocket when measurements become wrong and also the outgassing is not efficient when the Mach number is greater than unity. The overall conclusion is that the measurements must certainly be considered as genuine. As far as we know, it is the first time that such a layer of enhanced electron density has been detected in the lower D region by in-situ measurements. The shape and altitude of this layer makes it significantly different from the so-called C-layer (Thomas, 1971). The most widely used ground-based technique for D-region probing—namely, the partial reflection method—is based upon echoes coming from discrete irregularities in the D region (Belrose and Burke, 1964, Austin and Manson, 1969). This provides evidence of existing irregularities in the D region in the range

75 to 90 km with changes ΔN such that $10^{-3} \leq \frac{\Delta N}{N} \leq 10^{-1}$; values as high as $\frac{\Delta N}{N} = 1$ are regarded as unrealistic (Gregory and Manson, 1969). Occasionally, discrete layers have been detected at low altitude between 72 and 82 km (Fraser and Vincent, 1970), and have seemed to be very stable on a time scale in the order of a half hour or more, but the method could not give any information on the exact nature and shape of the irregularity.

Possible causes of such an irregularity are difficult to find at this time. It is quite certain that the variation in the electron density is too great to be due to gravity waves propagating in the D-region; such a mechanism leads to maximum changes of the neutral atmosphere—and consequently of the electron density—in the order of ~10 percent. The only explanation we should like to suggest is the occurrence of a noctulicent cloud or dust layer. It is well known that such layers exist in the ionosphere and are thought to change radically the ion chemistry kinetics. There are rather few in-situ observations of such discrete layers, and their composition and influence on the ambient plasma is far from being understood. We think, however, that they could offer the most plausible explanation for the results reported here.

19-6 DERIVATION OF THE STEADY-STATE COEFFICIENT

In the calculation of production rate Q, we have assumed that ionization due to solar electrons was negligible. In view of the data available, this seems realistic and introduces negligible error under 80 km. Proton fluxes were evaluated by comparison of data from ATS. 1 satellite (Lanzerotti, private communication; Paulikas and Blake, 1969) and from balloon flight (Barcus, private communication) with our own data. A good estimate was obtained between 5 and 200 MeV, but fluxes below 5 MeV may be affected by significant errors. The atmosphere was divided into slabs of varying thickness according to the neutral scale height (0. 5 km below 70 km, 1 km above). Figure 19-7 gives the calculated production rate Q, assuming 36 eV for energy loss per electron-ion pair created. On Figure 19-8 is drawn the Ψ profile which decreases steadily from 10^{-4} cm^3 sr^{-1} at 62 km to 10^{-7} cm^3 sr^{-1} at 90 km. These values are in general agreement with those predicted by Adams and Megill (1968) for a two-ions model with, however, a slope significantly greater in our measurements. Comparison with values given by Reid (1970) indicate a great deal of change in the ion-chemistry between the normal and disturbed D region, as suspected on the basis of preliminary data on ion composition during the November 1969 event (Narcisi et al, 1970); however, in absence of definitive data under PCA condition, the elaboration of a model seems hazardous. Corresponding to the peak in electron density, a large change is observed on Ψ which decreases down to 10^{-6}

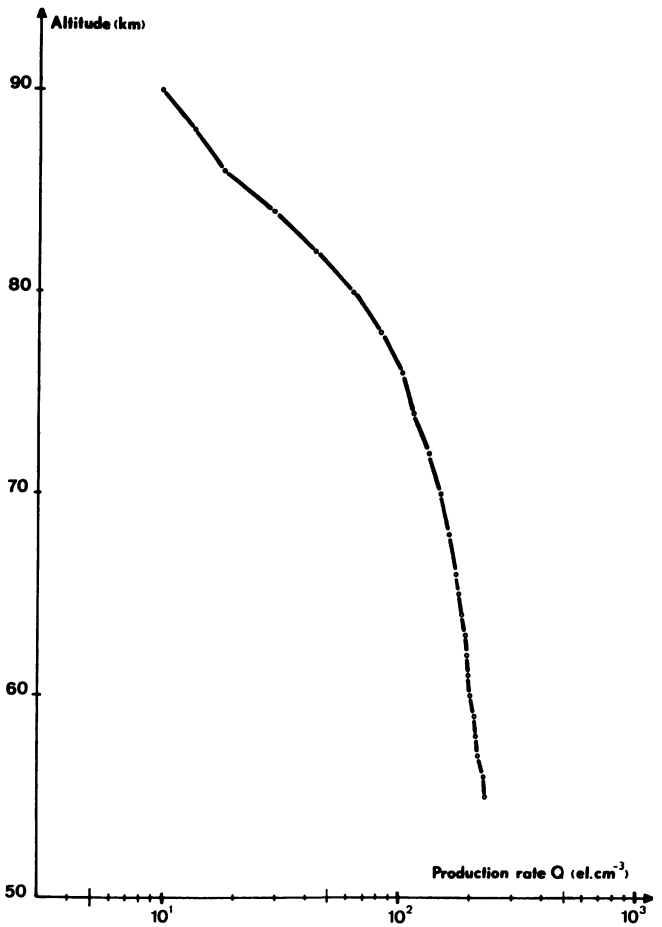

Figure 19-7. Electron-ion Pair Production Rate During D. 25 Flight

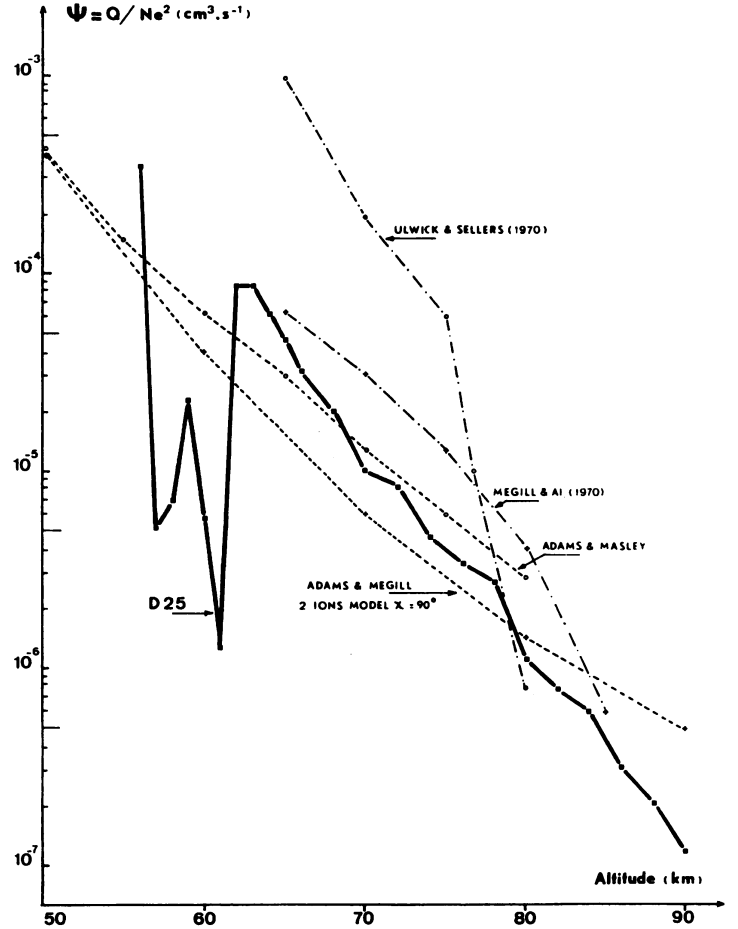

Figure 19-8. Effective Electron Recombination Coefficient Ψ Deduced From D-25 Electron Density Profile. Other experimental or theoretical evaluations are given for comparison

at 61 km and recovers at 56 km—a value in agreement with the one measured above 63 km. A tremendous change in the ion chemistry must prevail at 61 km which leads to a large reduction of the negative ions concentration and/or presence of a very slowly recombining positive ion.

Acknowledgments

The observations reported here could never have been obtained without the skills and dedicated efforts so generously given by many persons often under extremely adverse conditions. A special commendation is due to R. Godard, G. Gogly and J.C. Gillon who so ably and enthusiastically took the largest part in probes and detector construction. It is a pleasure for us to thank MM. Le Fevre and Simon (C.N.E.S.), Marx and Le Gallic (MATRA) for their painstaking efforts during payload design and testing and also all people from C.N.E.S., S.N.I.A.S. and Expeditions Polaires Francaises (Mission P.E. Victor) for having so efficiently prepared and realized the campaign. One of us (J.J. Berthelier) is particularly indebted to Prof. F. Mozer (University of California) for his continuous help and encouragements during design and realization of particle dtectors and we also want to thank Prof. Sayers (University of Birmingham) for his support and kind welcome in his laboratory. The use of unpublished data of Dr. Lanzerotti and Prof. Barcus is gratefully acknowledged. MM. Cazenave and Frichet (C.N.E.S.) offered a continuous help during data processing. This research was supported by C.N.E.S. under the auspices of convention 65.CNES.110 and 66.CNES.036.

References

Adams, G.W. and Megill, L.R. (1968) A two-ion D-region model for polar cap absorption events, Planetary Space Sci. 15:1111.

Austin, G.L. and Manson, A.H. (1969) On the nature of the irregularities that produce partial reflections of radio waves from the lower ionosphere (70-100 km), Radio Sci. 4:35.

Baird, G.A., Bell, G.C., Duggal, S.P., and Pomerantz, M.A. (1967) Neutron monitor observations of high energy solar particles during the new cycle, Solar Phys. 2:491.

Belrose, J.S. and Burke, M.J. (1964) Study of the lower ionosphere using partial reflection, J. Geophys. Res. 69:2799.

Berthelier, J.J. (1969) Rapid variations in the absorption during the 28 January 1967 PCA event, NATO Meeting on Polar Ionosphere, Skeikampen.

Berthelier, J.J., Godard, R., and Gogly, G. (1966) NT/GRI/53.

Bukata, R.P., Gronstal, P.T., Palmeira, R.A., Mackraken, K.G., and Rao, U.R. (1969) Neutron monitor and Pioneer 6 and 7 studies of the 28 January 1967 solar flare event, Solar Phys. 10:198.

Fraser, G.J. and Vincent, R.A. (1970) A study of D-region irregularities, J. Atmospheric Terr. Phys. 32:1591.

Gregory, J.B. and Manson, A.H. (1969) Seasonal variations of electron densities below 100 km at midlatitudes-II. Electron densities and atmospheric circulation, J. Atmospheric Terr. Phys. 31:705.

Lanzerotti, L.S. and MacLennan, C.O. (1971) Relative Importance of Solar Electrons, Protons and Alphas in the 2 November 1969 PCA Event: see these Proceedings.

Lebeau, A.F. (1965) Sur l'activite magnétique dans let calottes polaires, Thèse Université de Paris.

Lockwood, J.A. (1968) Cosmic ray solar flare effect of 28 January 1967 as recorded by neutron monitors. J. Geophys. Res. 73:4247.

McKenzie, E.C. and Sayers, J. (1966) A radio frequency electron density probe for rocket investigation of the ionosphere, Planetary Space Sci. 14:731.

Masley, A.J. (1968) McDonnall-Douglas preprint 5218.

Masley, A.J. and Goedeke, A.D. (1967) The 1966-1967 Increase in Solar Cosmic Ray Activity, McDonnel-Douglas Corp. 4662.

Mendel, A.D. (1966) Courants électriques de l'ionosphère polaire, Thèse de 3ème Cycle, Université de Paris.

Narcisi et al. (1970) Proceedings of Meeting on Operation PCA 69, AFCRL Special report No. 110.

Paulikas, G.A. and Blake, J.B. (1969) Penetration of solar protons to synchronous altitude, J. Geophys. Res. 74:2161.

Pirre, M. (1971) Thèse de 3ème Cycle, Université de Paris, to be published 1971.

Reid, G.C. (1970) Production and loss of electrons in the quiet day time D-region of the ionosphere, J. Geophys. Res. 75:2551.

Thomas, L. (1971) The lower ionosphere, J. Atmospheric Terr. Phys. 33:157.

Contents

20. Electron Density Profiles for the 1969 PCA Event

W.A. Dean
Aeronomy Branch
Concepts Analysis Laboratory
U.S. Army Ballistic Research Laboratories
Aberdeen Proving Ground, Maryland

Abstract

The Ballistic Research Laboratories instrumented seven rockets with a six-frequency propagation beacon, along with other instrumentation, in preparation for a possible PCA event in the fall of 1969 at Fort Churchill, Manitoba, Canada. The six frequencies were nominally 9-, 18-, 36-, 72-, 144-, and 576-MHz. Three of the frequencies employed - 36.4411, 145.7644, and 583.0576 MHz - were intended, primarily, for the measurement of dispersive phase. One rocket, for background information and payload certification, was launched on 5 August 1969, and the remaining six rockets were launched during the 2-4 November 1969 PCA event. All rockets were launched from Fort Churchill, Manitoba, Canada.

Two sets of dispersive phase measurements were made - one between the 36/145-MHz pair of signals and one between the 145/583-MHz pair of signals. Electron density profiles, derived from the dispersive phase measurements, are presented for all seven rocket flights. These profiles show that, relative to the background flight of 5 August 1969, significant amounts of electron production occurred at very low altitudes (as low as 48 km) and that, as time elapsed following the solar flare, the lowest altitude at which significant production of electrons was taking place receded upwards.

Additionally, these rockets were instrumented with a nose tip Langmuir probe for the purpose of measuring electron currents and temperatures. Electron current data, hence electron density data, for the rocket ascent Langmuir probe measurements are presented for comparison with the electron density profiles derived from the dispersive phase measurements.

20-1 INTRODUCTION

Under the Defense Nuclear Agency's (DNA) Mighty Sky Subtask 603, the Ballistic Research Laboratories (BRL) instrumented seven Nike-Javelin sounding rockets in anticipation of a Polar Cap Absorption (PCA) event at Fort Churchill, Manitoba, Canada. Among the instruments carried on the rockets were a six-frequency propagation beacon, photometers, high- and low-energy detectors and, for rocket attitude determinations, magnetometers and solar cells. The photometers, as well as the high- and low-energy detectors were supplied under contract to BRL. The data reduction and analysis from those instruments has also been conducted under contract and the results are to be presented during this meeting by representatives of the contractors.

The signals received from the multifrequency propagation beacon were employed for two primary measurements. One was the measurement of dispersive phase for the determination of electron content and hence electron density, and the other was the measurement of received signal levels for the determination of rf absorption. The absorption results are also the subject of another paper to be presented here. This paper will be addressed to the results obtained from that portion of the propagation beacon employed for dispersive phase measurements and to results obtained from the Langmuir probes.

Three of the six frequencies of the propagation beacon - 36.4411, 145.7644, and 583.0576 MHz - were used for dispersive phase measurements. Although redundant, two dispersive phase measurements were made—one between the 36.4411/145.7644-MHz pair of frequencies and one between the 145.7644/583.0576-MHz pair of frequencies—and, for all rocket flights where the quality of the data warranted, total electron content along the propagation ray path and electron density profiles have been derived.

Electron currents from the Langmuir probe data have been determined for five rocket flights and, after having been converted to electron densities, have been compared to the electron densities derived from the propagation experiment.

As is well known, both the propagation experiment and the Langmuir probe may have significant limitations in the determination of electron densities, under some conditions, when used independently. With the propagation experiment,

although the total electron content along the ray path can be measured with a high degree of accuracy, it is sometimes difficult to discriminate between changes in content occurring at the rocket altitude and changes in content occurring along the propagation ray path anywhere below the rocket altitude. With the Langmuir probe, however, probe currents can be accurately measured but the conversion of current to electron density is not always straightforward. The ratio between current and density, for identical probe configurations, has been observed to vary significantly from one rocket flight to another and apparently varies on a given rocket flight from one altitude regime to another. If treated with the proper caution, however, the Langmuir probe data should yield a good indication of variations in the electron currents and thus a good indication of variations in electron density at the rocket altitude with the possible exception of times when the probe is in the wake of the rocket body during rocket descent; when the rocket is nosing over during reentry; or during transitional periods from one altitude regime to another.

We have attempted to treat these various limitations with the proper caution in the process of reducing the data and presenting the results, and thus believe that the results presented are reliable and valid.

20-2 SCHEDULE OF ROCKET FLIGHTS

The planned BRL participation in the PCA event was for a series of sunrise-sunset rocket measurements during the event. This plan was, to a large extent, fulfilled as two rockets were fired at sunrise on 3 November and two rockets were fired at sunset on 4 November. Of the two other rockets flown during the PCA, one was about noon and one midafternoon. The seventh rocket was launched on 5 August to serve as both a flight to certify the rocket payload and to gather background data preparatory for the PCA. Unfortunately, due to vagaries of range scheduling problems, the 5 August flight was launched at 2136 LST and does not completely fill the need for background data for the sunrise-sunset rockets flown during the PCA. A summary of launch times and other pertinent data for the seven rockets is tabulated in Table 20-1.

20-3 PROPAGATION EXPERIMENT

Seven Nike-Javelin sounding rockets were instrumented with a six-frequency propagation beacon for the dual purpose of making rf absorption measurements and measurements of dispersive phase. Three of the frequencies - 36.4411 MHz, 145.7644 MHz, and 583.0576 MHz - were harmonically related and phase coherent

Table 20-1

BRL Rocket Number	Date	Local Time (hr)	Solar Zenith Angle (degree)	Apogee (km)	Impact Azimuth (degree)	Impact Range (km)
1	1 Aug	2136	-	116	116	54
2	3 Nov	0657	95.5	116	103	62
3	3 Nov	0730	91.6	112	108	29
4	2 Nov	1510	83.2	119	93	63
5	3 Nov	1254	74.7	126	104	57
6	4 Nov	1530	85.7	125	120	80
7	4 Nov	1638	93.2	126	106	63

to facilitate the measurement of dispersive phase in addition to measurements of received signal levels. All of the three frequencies were received with both left- and right-hand polarized ground receiving antennas to insure that, upon properly mixing the left- and right-hand polarized components, rocket spin effects and Faraday rotation effects would be eliminated. Then the spin-free, Faraday-free signals were properly multiplied and differentially mixed to yield the desired dispersive phase data.

Two dispersive phase measurements were made for each rocket flight - one between the 36.4411/145.7644-MHz pair and one between the 145.7644/583.0576 MHz pair. In practice, the required multiplication and differencing of signals is accomplished electronically at the receiving station and the dispersive phase data is recorded directly on paper charts for "quick-look" information as well as on magnetic tape for later data processing and analysis. Letting f_1 = 36.4411 MHz, f_2 = 145.7644 MHz, and f_3 = 583.0576 MHz, the multiplication and differencing of the signals for the two sets of dispersive phase data obtained during the 1969 PCA are described by the expressions

$$\phi_{DD}(f_1/f_2) = 8\phi_1 - 2\phi_2 \tag{20-1}$$

and

$$\phi_{DD}(f_2/f_3) = 2\phi_2 - \tfrac{1}{2}\phi_3 , \tag{20-2}$$

where ϕ_{DD} is the dispersive phase and ϕ_i represents the phase of the received signal for the ith frequency.

The expression $\phi_{DD}(f_1/f_2)$ is considered to be the prime dispersive phase measurement but the redundancy was built into the system to enhance the probability of some data return in the case of a malfunction in some part of the rocketborne or ground-based equipments. (All of the received signals are recorded on magnetic tape so that a third dispersive phase measurement between the 36.4411/583.0576-MHz signal pair can be retrieved if a malfunction occurs in the 145.7644-MHz system.) Additionally, the 36-MHz frequency, in particular, is susceptible to multipath propagation, significant ray bending, or even complete blackout in certain environments. In such a case the other dispersive phase measurement, $\phi_{DD}(f_2, f_3)$, although less sensitive, is used as input for the electron density calculations. Both sets of dispersive phase data were used in computing electron density profiles for four of the seven rocket flights reported here.

The dispersive phase can be simply related to the total electron content along the propagation rath path if electron collisions and magnetoionic effects are neglected. For the two dispersive phase measurements made here, those relationships are

$$\int N_e \, dr = \frac{kcf_1}{80.6(k^2-1)} \phi_{DD}(f_1/f_2) = 3.614 \times 10^{13} \, \phi_{DD}(f_1/f_2) \qquad (20\text{-}3)$$

and

$$\int N_e \, dr = \frac{2k^2cf_1}{40.3(k^2-1)} \phi_{DD}(f_2/f_3) = 5.783 \times 10^{14} \, \phi_{DD}(f_2/f_3) \, , \qquad (20\text{-}4)$$

where

$k = f_2/f_1 = f_3/f_2 = 4$,

c = the velocity of propagation,

and the electron content, $\int N_e \, dr$, is in electrons per square meter column.

For the most part a simple and straightforward technique, which has proven quite satisfactory in the past, was used to compute the electron density profiles. This was accomplished by using appropriate values for cos θ (with θ being the changing zenith angle) for successive rocket positions to convert electron content along the rath path to vertical content. The vertical contents were then numerically differentiated over altitude increments of 1 km yielding an average electron density over the 1-km altitude range. This technique, of course, assumes that all of the change in electron content along the ray path is a result of radial motion of the

rocket; therefore, significant spatial or temporal variations, below the rocket altitude, would introduce errors in the electron density profile. Any gross errors in the electron densities, as a result of this technique, should be readily identifiable by comparison with the Langmuir probe data. A more serious error may be caused by the neglect of collisions, especially at the lower altitudes. Consequently, we used a ray tracing technique employing the generalized Sen and Wyler expression for the index of refraction, and calculated electron densities for all of the rocket flights up to an altitude of 80 km. Without exception, we found that the profiles calculated, taking collisions into account, reproduced the " no-collision " profiles above 65 km in altitude. The results reported here, then, combine these two techniques - "collision" profiles below 65 km and "no-collision" profiles above 65 km.

20-4 LANGMUIR PROBE EXPERIMENT

The Langmuir probe employed for this project had the electrode mounted on the nose tip of the sounding rocket. The applied voltage to the probe was swept from -2.7V to +2.7V with a sweep period of about 1/2 sec. Additionally, the voltage was held constant at both ends of the sweep—at both the -2.7V level and at the +2.7V level—for a period of approximately 1/10 sec. All of the probes were calibrated about 1/2 hr before rocket launch using a stepping 10-point calibrator covering the current range from 10^{-9} to 10^{-4} A. Additionally, a one-step in-flight calibrator, switched into the circuit about every 30 sec, was employed as a check on any drift in the electrometer circuits or in the telemetry system. In general, any such drift noted was well within tolerable limits.

For purposes of this paper, the negative currents associated with the +2.7V applied potential were measured. We made no attempt to convert the Langmuir probe currents to electron densities by the application of probe theory, but did, alternatively, normalize the probe current at one point during rocket ascent to the density derived from the propagation experiment. In general, the normalization factor was derived from data at an altitude of about 90 km. An independent determination of the normalization factor was performed for each rocket flight. Then, using the normalization factors we converted all of the Langmuir probe currents to electron densities for each rocket flight and plotted these densities on the same graphs with the electron density profiles derived from the propagation experiment. Several interesting, although not unique or unusual, features were noted. As has been observed by many other experimenters the probe currents, during rocket descent, were considerably lower than those measured during rocket ascent. During rocket nose-over at reentry there is a significant increase in probe current, and the ascent and descent data agree reasonably well after rocket nose-ove

A significantly different normalization factor from current to density was required for each rocket even though the probe configurations were identical. Additionally, using one normalization factor over the entire rocket altitude regime, a divergence between Langmuir probe data and propagation experiment data occurs below 75 to 80 km. This latter phenomena may be due to several factors including the dependence of probe current on the mobility of charged particles, the electron temperature, the relatively high velocity of the sounding rocket, and the contact potential of either the electrode or the rocket or both.

Because of these several problems, we find it difficult to place complete confidence in the Langmuir probe data as an independent source for electron density determinations. The Langmuir probe data, however, should still be a reliable indicator as to whether variations in density derived from the propagation experiment are actually variations in density occurring at the rocket altitude or at some altitude well below the rocket especially for rocket altitudes above 75 to 80 km and, perhaps, to a lesser degree for lower rocket altitudes.

20-5 RESULTS

The electron density profiles for the propagation experiment derived from the 36/145-MHz dispersive phase data and those derived from the 145/583-MHz dispersive phase data are in excellent agreement for all rocket flights. Since the 145/583-MHz dispersive phase is a less sensitive measurement than the other and, hence, reflects considerably more scatter in the resulting profiles, only the profiles from the 36/145-MHz data are presented here. Because of the problems, mentioned earlier, with the Langmuir probe data only those data from rocket ascent with a single normalization factor for the entire altitude regime are presented.

Figure 20-1 shows the results from Rocket B-1 fired for background information and payload certification at 2136 CST on 5 August 1969. The solid and dashed lines are the electron densities derived from the propagation experiment for rocket ascent and rocket descent, respectively, while the circles are data from the Langmuir probe. In general, the agreement between the various sets of data is excellent with the possible exception of that region around 102 to 106 km. If we had only the propagation experiment data, there would be a strong argument for sporadic E activity. The Langmuir probe shows little if any evidence, however, of density variations at those altitudes. More confidence should, undoubtedly, be placed in the Langmuir probe results during this period. The "apparent" layer, based on the propagation experiment data, is at least a few kilometers in thickness. During this time, the rocket velocity is such that about four sweeps of the Langmuir

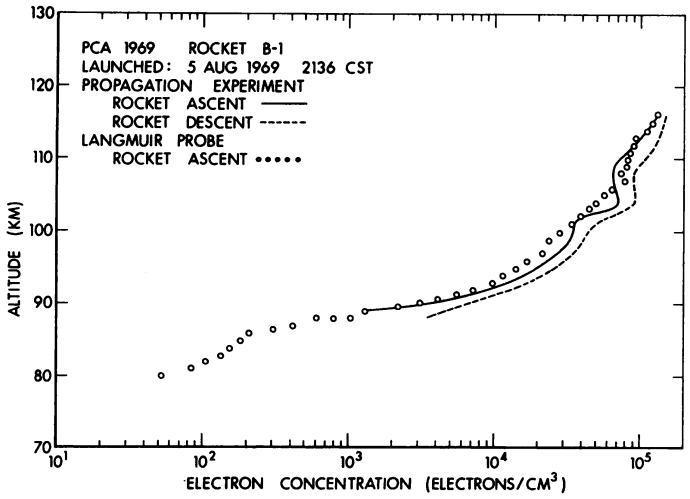

Figure 20-1. Electron Density Profile for BRL Rocket B-1

probe per 1-km change in altitude takes place. There is, then, no chance that the apparent increase in density occurred between times of measurement of the Langmuir probe data. Thus we conclude that some patchy areas of increased density existed below the rocket altitude and that it is only coincidental that this is reflected in the profiles at the same altitude during rocket descent as during rocket ascent.

Figure 20-2 shows the results from Rocket B-2, a sunrise rocket fired at 0657 CST on 3 November 1969. The Langmuir probe failed at rocket launch and did not recover during the flight, so the only data presented are the electron densities derived from the propagation experiment data. Excellent agreement between ascent and descent data exists except below 75 km which suggests no significant temporal or spatial variations below the rocket altitude. I would suggest that the variations in density around 95 to 100 km are real even though they appear very much like the variations seen for Rocket B-1. The disagreement between ascent and descent profiles below 75 km is probably the result of degradation in the resolution of dispersive phase data during rocket descent. The rocket noses-over on reentry at about 75 km. During this period, and until the rocket stabilizes, complete and accurate elimination of spin-induced errors is difficult. Additionally, the angle between the radius vector from the ground station and the longitudinal axis of the rocket is changing rapidly. As a consequence, phase perturbations in the rocketborne antenna phase pattern may introduce significant errors into the dispersive phase data. (An error of ±36 degrees in the dispersive phase data results in an error of approximately 3.6×10^3 electrons/cm^3.) Considerably more

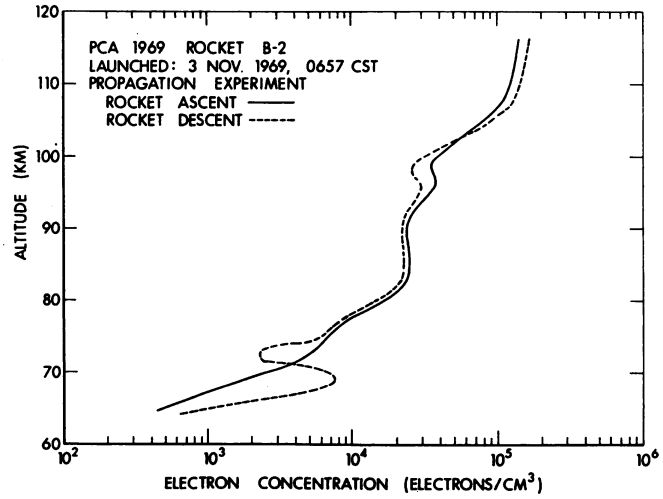

Figure 20-2. Electron Density Profiles for BRL Rocket B-2

confidence, then, should be placed in the propagation experiment results from rocket ascent data, especially at altitudes below 75 to 80 km.

Figure 20-3 shows the results from Rocket B-3, another sunrise rocket launched on 3 November 1969 at 0730 CST. The Langmuir probe preflight calibrator malfunctioned prior to this flight and, although Langmuir probe data were obtained, difficulties in scaling have precluded its use here. Excellent agreement is noted between rocket ascent and rocket descent data with the exception of the region between 90 to 102 km. We suggest that this divergence is due to spatial variations in density at some altitude below the rocket. A considerable horizontal range is swept by the ray path to the rocket during the period that the rocket is descending through the altitude layer from 100 km down to 90 km. For this particular rocket flight the horizontal range swept by the ray path during this period is 3.6 km at the 90-km altitude, 3.2 km at the 80-km altitude, and 2.8 km at the 70-km altitude. The disagreement in densities below 75 km are within the limits of resolution in the determination of phase data for the rocket descent data and, as before, more confidence should be placed in the rocket ascent data because of significantly better phase resolution as a result of more favorable signal-to-noise ratios in the data.

Figure 20-4 shows the results obtained from the flight of Rocket B-4. This was the first BRL rocket launched after the onset of the PCA and was launched at 1510 CST on 2 November 1969. Electron density profiles from the propagation experiment rocket ascent and rocket descent data are shown along with electron

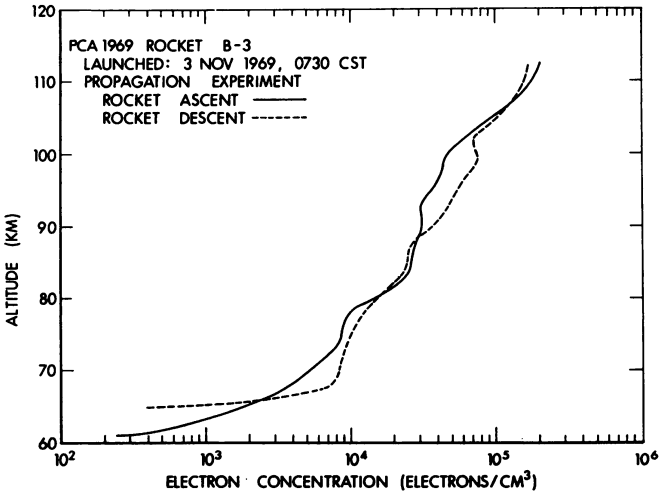

Figure 20-3. Electron Density Profile for BRL Rocket B-3

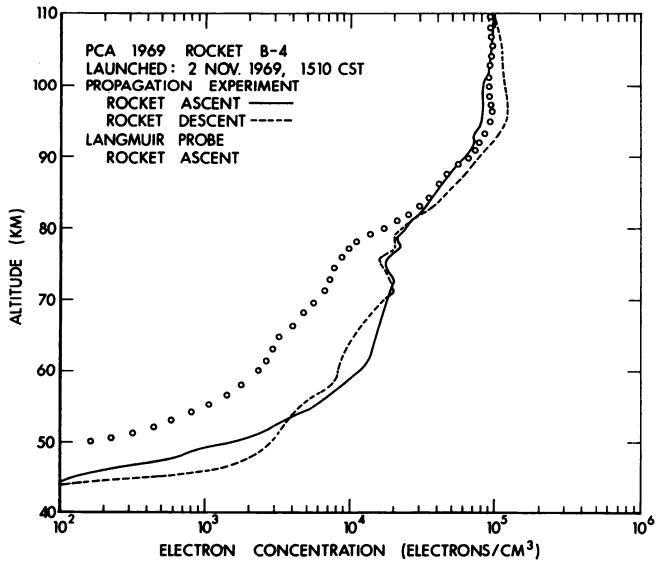

Figure 20-4. Electron Density Profile for BRL Rocket B-4

densities derived from the Langmuir probe rocket ascent data. One single normalization factor was used in converting Langmuir probe currents to electron density for the entire altitude layer traversed by the rocket. In using this technique we have noted, for all rocket flights, consistently lower electron densities from the Langmuir probe data below altitudes of 75 to 80 km. There is no valid reason to expect the ratio between probe current and density to remain constant since probe currents are, in theory, dependent on such parameters as particle mobilities, electron temperatures, and rocket velocity. At any rate, excellent agreement is noted for all data above 80 km and between the propagation experiment results over the entire altitude range. The more significant feature of these data, though, is the definite evidence of electron production in significant amounts at very low altitudes - 10^3 electrons/cm^3 at 49 km. This rocket had an apogee of 119 km. The data above 110 km have not been plotted here in order to maintain a consistent altitude scale and still keep the interesting data at the low altitude on the graph. Very large variations in density were observed in the propagation experiment data above 110 km but were not reflected in the Langmuir probe data. These variations and probable causes are the subject of another paper to be presented here.

Figure 20-5 shows the results from Rocket B-5 launched at 1254 CST on 3 November 1969. Electron densities derived from the propagation experiment rocket

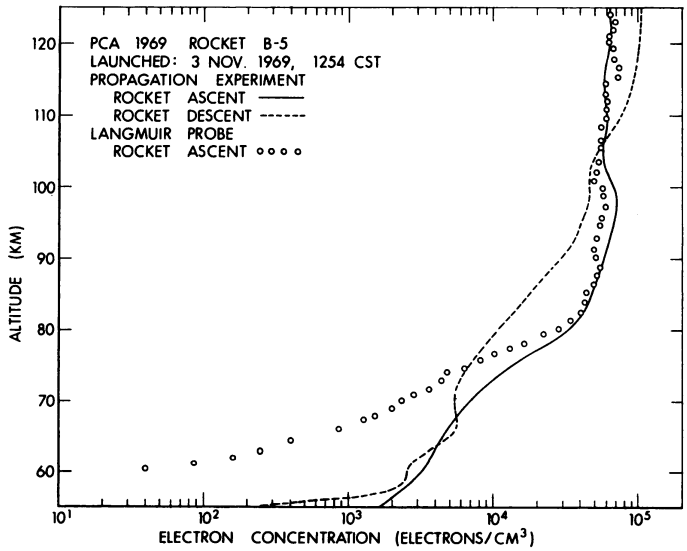

Figure 20-5. Electron Density Profile for BRL Rocket B-5

ascent and rocket descent data are shown along with electron densities derived from the Langmuir probe rocket ascent data. The Langmuir probe current was normalized to the propagation experiment density at about 95 km and this single normalization factor used throughout the flight. The two profiles from the propagation experiment data appear very similar to profiles we have measured in the past where we knew from other instrumentation sources that there were temporal variations. We can only conclude, however, that the disagreement between ascent and descent data is a result of either temporal or spatial variation or both as it can be easily shown that certain spatial variations would be reflected in propagation experiment profiles in exactly the same way as temporal variations. As for other rocket flights reported here, the Langmuir probe data diverges from the propagation experiment profiles below 75 km. As to where to place ones confidence, we would suggest Langmuir probe data above 80 km and propagation experiment rocket ascent data below that altitude.

Figure 20-6 shows the results obtained from the flight of Rocket B-6 which was the first rocket of a sunset pair launched on the afternoon of 4 November 1969. Rocket B-6 was launched at 1530 CST. As for the other rocket flights, propagation

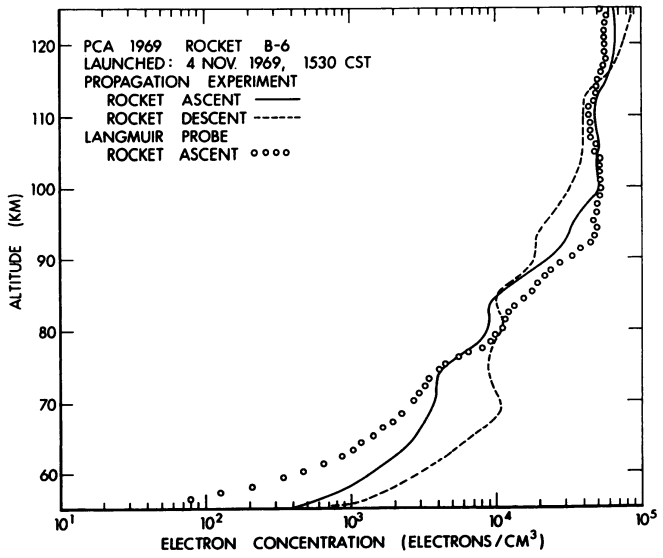

Figure 20-6. Electron Density Profile for BRL Rocket B-6

experiment rocket ascent and rocket descent profiles are shown along with densities derived from the Langmuir probe rocket ascent data. All of the data are in reasonably good agreement except for the usual divergence of the Langmuir probe data below 75 km and, as for previous flights, more confidence should be placed in the ascent data than the descent data below 75 to 80 km.

Figure 20-7 shows the results obtained from the flight of Rocket B-7, the second rocket of the sunset pair on 4 November 1969, launched at 1638 CST. These data exhibit very clearly how patchy areas of increased or decreased ionization below the rocket are reflected in the electron density profiles as determined from the propagation experiment dispersive phase data. Above 105 km, confidence should be placed in the Langmuir probe data. Below 105 km, all data are in excellent agreement except for the usual divergence of the Langmuir probe data below 75 km.

Figure 20-8 is a composite which includes the electron density profiles derived from the propagation experiment dispersive phase data for rocket ascent for all seven BRL rocket flights.

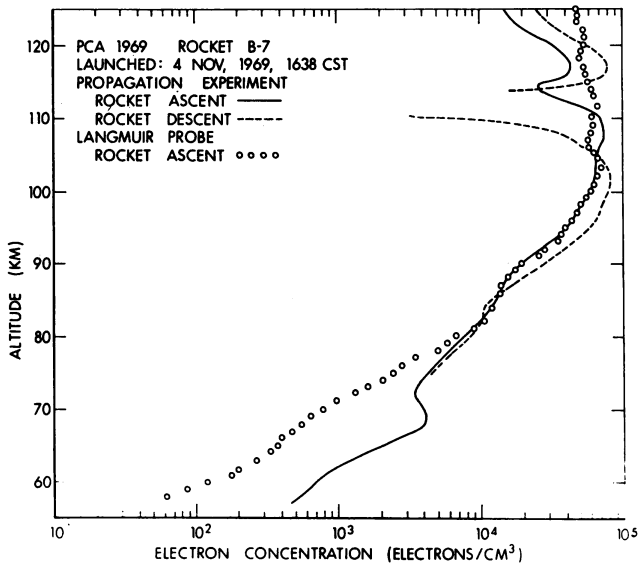

Figure 20-7. Electron Density Profile for BRL Rocket B-7

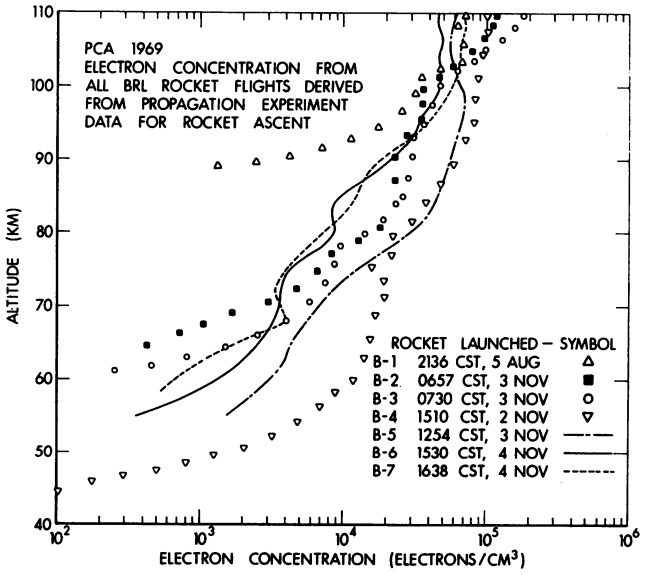

Figure 20-8. Electron Density Profiles for all BRL Rocket Flights

20-6 CONCLUSIONS

The multifrequency propagation beacon operated well for all seven rocket flights and electron density profiles were obtained from the dispersive phase data for all flights. Some degradation of dispersive phase resolution occurred below 75 to 80 km during rocket descent, hence, less confidence should be placed in these data than in rocket ascent data at the lower altitudes.

For two of the rocket flights there was excellent agreement between rocket ascent and rocket descent profiles, indicating the lack of any significant temporal or spatial variations in densities below the rocket altitude. For five of the rocket flights, however, the profiles exhibited varying degrees of disagreement between rocket ascent and rocket descent data. In general, we believe the disagreement to be the result of patchy areas of increased or decreased densities well below the rocket altitude; however, for one flight - Rocket B-5 - the differences between ascent and descent profiles suggest a nearly constant temporal variation or a nearly constant horizontal gradient in electron densities.

The Langmuir probe currents were empirically normalized to densities based on the propagation experiment profiles at one point during rocket ascent - usually at 90 km or above. The ratio between probe current and density, determined in this manner, appear to be invalid for altitudes below 75 to 80 km as, for all

rocket flights, the Langmuir probe data and propagation experiment data diverge below those altitudes. Above 80 km, however, it is felt that the Langmuir probe data can be reliably used to infer errors in the densities derived from the propagation data due to changes in electron content well below the rocket altitude.

It is unfortunate, due to range scheduling vagaries, that the rocket intended for background information was fired at night and, hence, does not give a good basis for comparison with the data obtained from the BRL rockets during the PCA event. Ignoring that, however, it can be seen from the profiles presented here that significant amounts of electron production occurred at very low altitudes (as low as 45 to 50 km) and that, as time elapsed following the solar flare, the lowest altitude at which significant production of electrons was taking place receded upwards.

The compilation and comparison of these data with those of other experimenters in sunrise, daytime, sunset, and night sets should add significantly to the results and conclusions of the overall PCA program.

Contents

21. Multifrequency Polar Cap Absorption Measurements

I.L. Chidsey, Jr.
Aeronomy Branch
Concepts Analysis Laboratory
U.S. Army Ballistic Research Laboratories
Aberdeen Proving Ground, Maryland 21005

Abstract

Received signal levels from the BRL six-frequency propagation experiment were recorded for six-rocket flights during the 2 November 1969 PCA event. Data from a flight at 2100 UT (1510 CST) on 2 November showed absorption beginning at 47-km altitude and increasing to a mean value of 17 dB at 18 MHz when the vehicle was well above the absorbing layer. During the latter period, variations of up to ± 6 dB were noted in the measured absorption at 18 MHz with concordant variations at 36 and 73 MHz, while the 9 MHz signal was too weak to measure. Simultaneous dispersive phase measurements indicate that the electron content was varying as much as $\pm 3.5 \times 10^{14}$ electrons/m^2 about its mean value. Features as short as 3 sec occurred simultaneously on the signal level records at the three frequencies and also on the dispersive phase records.

Similar, but less pronounced effects were noted on later flights. During two flights (one of which was nonevent) refractive effects, probably due to aurorae, were noted.

21-1 INTRODUCTION

The second part of the BRL propagation experiment was an absorption measurement using the received signal levels from the four-frequency beacon. Since the absorption was expected to be moderate at 36 MHz and minimal at the higher frequencies, an additional beacon transmitting at 9.1- and 18.2-MHz was added to give increased sensitivity.

Receiving system channels were available for both right- and left-hand circularly polarized modes at 36-, 145-, and 583-MHz, making it possible to record both ordinary and extraordinary signal levels. At 73 MHz only the ordinary signal was available, and dipole receiving antennas were used at 9- and 18-MHz.

The quantity actually recorded was receiver agc voltage, which can be converted to received signal level by proper calibration. The receiver agc voltages for the four higher frequencies were calibrated using an automatic sequencer which stepped the input signal level from -50 to -150 dBm in 5-dB steps. The two lower frequencies were manually calibrated in 10-dB steps from -40 to -140 dBm. Both preflight and postflight calibrations were made with the antennas connected.

The absolute accuracy of the calibration process was about ± 1 dB at the four higher frequencies and ± 4 dB at the lower two frequencies. The precision of the measurements is, however, considerably better than this. The measurements were conducted in a manner which took advantage of this precision. The absorption data were obtained by differencing the measured signal levels in the absorbing layer from those measured just before the vehicle entered the absorbing layer, effectively eliminating any bias in the measured signal levels or in antenna pattern amplitude measurements. A correction for the difference in space attenuation was also made at this time.

The antenna amplitude pattern may also cause perturbations on the received signal levels. Therefore, both the ground (receiving) and airborne (transmitting) antennas were measured in the BRL antenna facility. This facility has an accuracy of about ± 2 dB at 36 MHz, improving at the higher frequencies. Again, the differencing technique results in considerable improvement in accuracy. The ground antenna look angles, obtained from the trajectories, varied slowly throughout the period when the vehicle was in, or above, the absorbing layer, and were nearly constant for a long period on the upleg. The vehicle aspect angles, obtained through onboard instrumentation, were also well behaved until vehicle turnover commenced at about 80 km on the downleg. Both ground and airborne antennas were designed so that the amplitude patterns would vary slowly over the expected range of look angles, and the vehicle attitude and trajectories were such that, in fact, this expectation was realized. Elevation angles were 79 to 85 deg at 50 km on the upleg, 72 to 83 deg at peak, and 50 to 72 deg just before turnover. The vehicle precession

periods were in the range of 23 to 28 sec with about 10-deg half angles. At the three lower frequencies there was less than 1-dB variation in signal level due to ground antenna amplitude patterns and also less than 1 dB due to airborne antenna patterns.

The airborne antennas consisted of a two-slot array at 583 MHz, a folded dipole at 146 MHz, one-turn loops at 73- and 36-MHz, and two- and three-turn loops at 18- and 9-MHz, respectively. They were so mounted that the amplitude pattern nulls were 90 deg from the rocket tail and were balanced and tuned for minimum interaction with themselves and with the rocket body.

The antenna amplitude patterns were taken in both the E-field and H-field planes, and at the three lower frequencies the measured departure from the theoretical doughnut-shaped pattern was smaller than the expected error in measurement. At 73 MHz the maximum departure from circularity in the E plane was about 1.5 dB. At 146 MHz it was about 2.5 dB, but the variations were less than 1 dB within 60 deg of the rocket tail. Only at 583 MHz was there sufficient departure from the theoretical pattern for the H-plane pattern to show significant gain relative to the E plane within 60 deg of the rocket tail. Since significant absorption data were expected only on the three lower frequencies, and none at all on the two higher frequencies, these results were considered satisfactory.

The antenna patterns for each rocket were normalized at the rocket tail, and at each frequency the greatest relative gain found for each 5-deg point from the tail to the nose, and a table of composite antenna patterns was made for each rocket. During the data processing, the effects of antenna pattern variations due to rocket spin were removed by selecting periodic maxima in the received signal level. These periodic maxima were then corrected for variations in the airborne antenna pattern with aspect angle using the composite antenna pattern tables. In this instance, aspect angle is defined as the angle between the radius vector from receiving station and the longitudinal axis of the rocket.

Theoretical patterns were used for the 9- and 18-MHz ground-based receiving antennas but, since these antennas are simple dipoles and only the variation in amplitude relative to some fixed point on the pattern is used in the pattern correction scheme, any degradation in the final results should be minimal.

The BRL anechoic chamber used for measuring rocket antenna patterns is not large enough to handle a full-scale rocket model for the rockets used during the PCA event. The model used was shortened 25 percent relative to the full-scale rocket. This foreshortening of the rocket model should have an insignificant effect on the pertinent parts of the patterns for the lower frequencies from which the significant absorption data are derived.

The electron density data underwent severe fluctuations during portions of these flights, at time apparently staying negative for up to 20 sec. It is obvious

that a negative electron density has no physical reality, and it arises from a violation of one of the assumptions made in deriving the equations used to obtain electron density from phase data (Dean, 1971). It must be emphasized that the dispersive phase measurement does in fact yield an accurate measurement of the total electron content along the ray path. We obtain the electron density by differentiating the electron content with respect to altitude, and, lacking an independent measure of its variation with respect to time, are forced to assume a linear variation with time over an extended period. If there are erratic variations in the electron density at some altitude below the rocket, these will appear in the output data as erratic variations in the electron density at the altitude of the rocket. If these variations are extensive enough, the local electron density may appear negative. We believe that the assumption that the electron density at a given altitude varied linearly with time was seriously violated during portions of the flights reported here, and so will usually prefix "apparent" to electron density as a reminder.

A cross correlation and power spectrum analysis was performed on that portion of the data which was obtained while the vehicle was above 85 km and, hence, above the greater portion of the absorbing layer. This analysis was used to determine the highest frequency significantly affected by absorption or refraction. At the higher frequencies the relatively slow increase in absorption with altitude becomes indistinguishable from instrumental drift, but the more rapid variations due to temporal or spatial variations in electron density may still be observable; for example, see Rocket 4, 73-MHz signal, after 140 sec.

The cross correlation analysis was also useful in distinguishing between signal level variations due primarily to refractive effects and caused by electron density variations above 85 km, and those due primarily to changes in absorption and caused by electron density variations below 85 km.

We placed in the first, or refractive, category those cases where there was little or no evidence of absorption throughout most of the flight except for a brief strong episode. In both cases, Rockets B-1 and B-2, this episode included a period of actual signal gain, and a period when the apparent absorption was much greater than the average. In both cases the episode occurred earlier at the higher frequencies. In the case of Rocket B-1, this was assumed to be due to simple focussing. In the case of Rocket B-2, where there was a discontinuity in the phase count so that the dispersive phase returned to 5 cycles rather than zero on leaving the ionosphere, we felt there was a true multipath situation.

The remaining cases were placed in the absorption category. These exhibited an average absorption as great as, or greater than, the peak-to-peak variation, gave no evidence that individual episodes did not occur simultaneously, and did not show signs of signal gain before the rocket turned over on reentry.

The power spectrum analysis was used to check the effectiveness of the corrections for vehicle antenna amplitude pattern. Typically, the power density at the precession rate and at its second harmonic were halved by making pattern corrections.

The 9-MHz received signal levels were about 25 dB below expected values for all flights except the certification round, B-1. As a result, signal levels dropped into the noise and became unmeasurable whenever absorption exceeded 10- to 15-dB. Even at greater signal levels, the 9-MHz measurements were degraded because of nonlinearity in the calibration curve for 20 dB above the noise level and also because of shifts in the ambient noise level itself.

21-2 RESULTS FROM ROCKET B-4

The first rocket of the BRL series, after the onset of the event, was launched at 2110 UT (1510 CST) on 2 November and was designated as Rocket B-4. The rf-absorption data for 9-, 18-, and 36-MHz, as derived from received signal levels measured during rocket ascent, are shown in Figure 21-1, with the absorption in dB being plotted as a function of altitude in kilometers. The first measureable absorption for the 18- and 36-MHz frequencies is noted at an altitude of about 48 km, whereas measurable absorption was noted for the 9-MHz frequency at a slightly lower altitude. The 73-MHz frequency suffered no "apparent" absorption. The true absorption at the 73-MHz frequency is believed to be masked by instrumental drift since variations in the 73-MHz received signal levels are significantly correlated with variations at other frequencies, as will be discussed later. The maximum absorption rate occurs between altitudes of 58- and 60-km for the 18- and 36-MHz frequencies. The 9-MHz signal has deteriorated to the receiver noise level by the time these altitudes were reached so no definite determination of maximum absorption rate can be made. The maximum absorption rate for the 18-MHz frequency is 1 dB/km and, for the 36-MHz

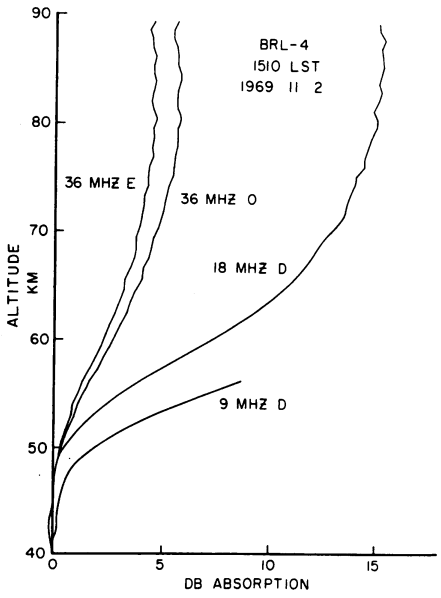

Figure 21-1. Absorption vs Altitude, Rocket B-4

frequency, 1/2 dB/km. At an altitude of 85 km, during rocket ascent, the measured values of absorption were 15 dB for the 18-MHz frequency; 5.5 dB for the 36-MHz frequency extraordinary ray and 4.5 dB for the 36-MHz frequency ordinary ray. Results from rocket descent data were qualitatively compatible with those from rocket ascent data; however, quantitative results were degraded by complicating effects associated with rocket turnover on reentry (the rocket begins to nose-over at an altitude of about 80 km).

An alternate presentation of the data is shown in Figure 21-2 where the independent variable is time after launch rather than altitude. Starting from the bottom of

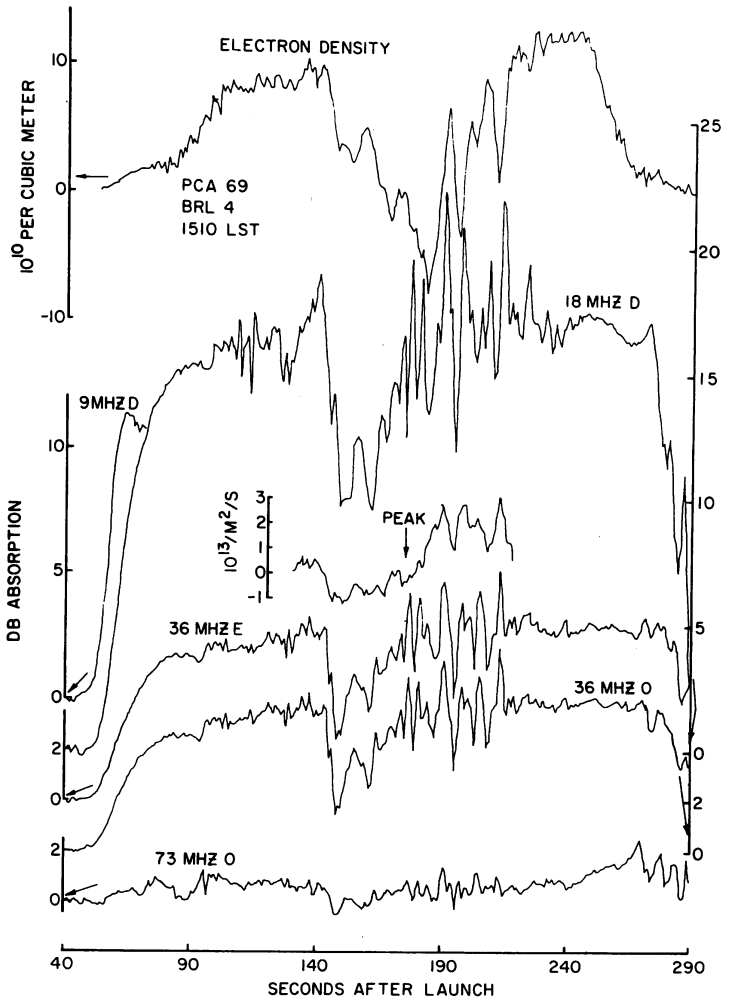

Figure 21-2. Absorption vs Time, Rocket B-4

the graph and working up, the quantities plotted are: absorption on the 73-MHz ordinary channel with dB scale at the left; absorption on the 36-MHz ordinary channel with dB scale at the right; absorption on 36-MHz extraordinary with dB scale at left; a short plot which will be discussed later; absorption on 18 MHz with dB scale at right; absorption on 9 MHz with dB scale at left; and finally, electron density with number density scale at the left.

The data plots in Figure 21-1 were terminated when the rocket was at an altitude of 90 km, 96 sec after rocket launch. At this time the rocket was above the absorbing layer and the plots show that the absorption increased smoothly with altitude through the absorbing layer, and then changed little above it. The time history of the absorption, plotted in Figure 21-2, shows that at 140 sec, when the rocket was at 113 km, the absorption suddenly decreased. The 18-MHz absorption plot reaches a peak of 19 dB at 140 sec, decreases to 10 dB over the next 12 sec, and then recovers to a mean value of 17 dB over the next 30 sec. Even after recovery there is a period of large, short term variations in the measured absorption that finally fade out after 220 sec. The absorption curves for the other frequencies are similar in character, especially at 36 MHz where the two channels are nearly identical and follow the 18-MHz variations at about 1/3 amplitude. At 73 MHz the slow increase in absorption with altitude before 90 sec may still be discerned. During this entire period from 140 sec until 240 sec, the rocket is near apogee and well above the absorbing layer.

During this same period that the absorption was varying so widely, the apparent electron density, which is derived from the dispersive phase measurements, was also greatly affected, as is shown by the top plot on Figure 21-2. It dropped from 10^{11} electrons/m^3 at 140 sec to -0.7×10^{11} electrons/m^3 at 181 sec and was negative for nearly 20 sec. Because the variations in the apparent electron density seemed to reflect certain features which were prominent in the absorption plots, it was felt that these changes in the apparent electron density were actually caused by changes in the electron density which were taking place in the absorbing region far below the rocket, and that the electron density in the vicinity of the rocket was essentially constant over the time period involved. In an attempt to simulate this, the following simple model was used.

The disturbed ionosphere without short term variations was simulated by assuming that the measured electron density was correct up to an altitude of 100 km, and that the electron density remained constant at 10^{11} electrons/m^3 from 100 km to the peak of the trajectory (119 km). The changes in electron content, which would have been measured in the absence of any short term variations, were then computed from this model and then subtracted from the values actually measured sec-by-sec, giving an electron content difference ΔE_t:

$$\Delta E_t = E_{mt} - E_{ct}, \tag{1}$$

where E_{mt} is the measured change in the electron content during the t_{th} sec and E_{ct} is the expected change during the t_{th} sec. These values of E_t were then smoothed using

$$\overline{\Delta E_t} = 0.3\Delta E_t + 0.7\overline{\Delta E}_{t-1}, \tag{2}$$

where $\overline{\Delta E_t}$ is the smoothed difference at time t. The coefficient of 0.3 was selected because it allowed perturbations to decay with a time constant of 3 1/3 sec, which seemed like a reasonable value for the D region. The other coefficient was chosen to give a total of 1.0 so that the algorithm would be self-normalizing.

We will refer to the plot ΔE_t, which appears in the center of Figure 21-2 just above the 36-MHz curve. It can be seen that the curve bears a much greater similarity to the absorption data than does the electron content curve. The major difference from the absorption data, other than a loss of resolution due to the 3 1/3-sec time constant, appears after 180 sec where the absorption recovers to a mean value approximately equal to that just before 140 sec, while the electron difference recovers to a value about 1.5×10^{11} greater than its value just before 140 sec. This apparent zero shift could be caused by an influx of ionizing radiation which did not penetrate to the absorbing region, but which did cause an increase in the electron content below the rocket. In this connection, we might note that the electron density plateau around 240 sec (98.5 km) is much higher than that of 110 sec (99 km).

An additional insight into the magnitude of the perturbations which occurred after 140 sec can be obtained by integrating the values of ΔE_t. Between 140 and 180 sec, we find that a deficit of nearly 3.5×10^{14} electrons was accumulated relative to the electron content which would have been measured if the ionosphere had been time invariant. After 180 sec this deficit is completely recovered and is finally replaced by a surplus of nearly the same number of electrons. This deficit and later surplus were equivalent in magnitude to 10 percent of the total electron measured to peak altitude (119 km), 50 percent of the content below 87 km, and 100 percent of the electron content measured up to 77 km.

Figure 21-3 shows the results of a cross correlation analysis of the absorption data between various pairs of data channels. The zero levels for the successive curves are offset by 0.2 to eliminate the confusion which would occur if the curves crossed. The cross correlation is plotted as a function of lags or 1-sec time displacements between the channels being analyzed. The significance of the cross correlation curves is that lower frequency signals were affected simultaneously and that the variations were well correlated, even including the 73-MHz signal where the

total absorption was so low that it could not be distinguished from instrumental drift and probably amounted to only 1 dB. The 146-MHz channel showed no significant correlation with the lower frequencies. It did show a slight, ill-defined variation at about the precession rate which might be due to incomplete correction for airborne antenna amplitude pattern. A summary of the maximum values of the cross correlations is given later in Table 21-2.

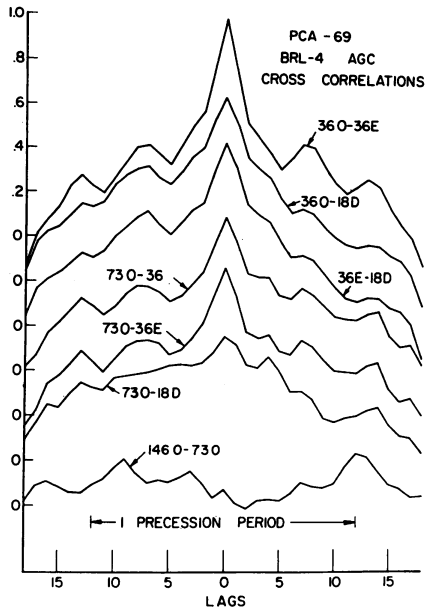

Figure 21-3. Cross Correlation of Absorption Data, Rocket B-4

With reference again to Figure 21-2, several quasi-periodic features or oscillations are in evidence around 180 sec on all of the curves which have a duration in time as short as 3 sec. It is highly unlikely that features of a shorter time duration could be isolated from data taken at a rate of 1 sample/sec. In contrast, the large decrease which appears on all curves at 140 sec has a duration of about 40 sec and the disturbance, as a whole, lasts for about 70 sec. Since 70 sec is relatively long compared to the total time the rocket spends in the ionosphere in reaching apogee, these two limits – 3 and 70 sec – are nearly the extremes in the length of features which can be delimited for rocket flights to altitudes of around 120 km. In an attempt to determine qualitatively whether there were significant variations in the signal level of duration of less than 1 sec, we took advantage of an option in the computer program to analyze 1-sec averages of all the data points gathered rather than analyze 1-sec averages of the local maxima. (The receiver agc voltage was sampled at a rate of 62.5 samples/sec, whereas the local maxima occur at a rate which is twice the rocket spin rate of 7 rps.) As a result of averaging all the data points, we found that relative to averaging only the local maxima, the average signal level decreased about 1 dB and that the standard deviation of the points about the mean increased about 1/2 dB. These figures are consistent with those which were obtained before the vehicle entered the absorbing region based, solely, on the antenna pattern amplitude variations which were reflected in the receiver agc voltage as a result of rocket spin. We conclude, therefore, that there are no significant contributions caused by variations in absorption with periods of less than 1 sec. It should be noted, however, that this test would be quite insensitive to short individual bursts as well as to variations with a very short duty cycle.

Our overall assessment of the data presented here for Rocket B-4 is that a significant perturbation of rather large magnitude occurred at 140 sec and lasted until

210 sec. At 140 sec there was an abrupt decrease in the total absorption accompanied by a decrease in total electron content and apparent electron density. The decrease in absorption and electron content recovered to preperturbation levels by about 190 sec. The quasi-periodic variations in the latter part of the disturbance are reflected in either broad peaks at 6- and 13-lags on the cross correlation plots (Figure 21-3), and may be due to oscillations in the ionosphere or to variations in the incoming ionizing radiation. After 190 sec there is a marked increase in the apparent electron density, as compared to the densities before the disturbance began, with no corresponding change in the absorption data. We would speculate, from these results, that at 140 sec there was a sudden and significant drop in the electron density in the main absorbing region at an altitude well below the rocket altitude since the electron deficit along the ray path is accompanied by a large decrease in absorption. We would further speculate that the surplus obtained from integrating the electron difference curve was the result of an increase in electron density above the main absorbing region since it is not accompanied by a noticeable increase in absorption.

21-3 RESULTS FROM ROCKET B-2

The second BRL rocket of the PCA event was designated as Rocket B-2 and was launched shortly before ground sunrise at 1257 UT (0657 CST) on 3 November. The 9- and 18-MHz portions of the rocket beacon failed at rocket launch and remained inoperative throughout the rocket flight; however, the remaining four frequencies of the beacon operated satisfactorily.

A significant disturbance was noted in the received signal level for Rocket B-2; however, in character, the disturbance contrasted sharply with those from the previous rocket as will be seen in the data presented here. Figure 21-4 has three curves related to the received signal level at 36 MHz. The bottom curve is the received signal level corrected for antenna pattern variations and data points averaged over a 1-sec time interval; the middle curve is excess attenuation (absorption); and the top curve is the standard deviation about the mean of the data points which made up the 1-sec averages. The signal level curve indicates a period of signal enhancement starting at about 128 sec (107 km), followed by a very sharp drop in signal level before returning to normalcy at about 150 sec (114 km). The same disturbance is, of course, reflected in the other two curves in Figure 21-4. The standard deviation about the mean of the data points, which make up the 1-sec averages, varied between 0.1 and 0.2 dB throughout the flight except during the disturbance when it reached a maximum in excess of 4 dB. The excess attenuation, or absorption curve shows measurable absorption at 36-MHz starting at about 66 sec

(62 km) and increasing slowly to about 1 dB at around 100 sec (91 km). After the disturbance, the mean absorption remains at about 1 dB until the data are degraded by the effects of rocket turnover during reentry.

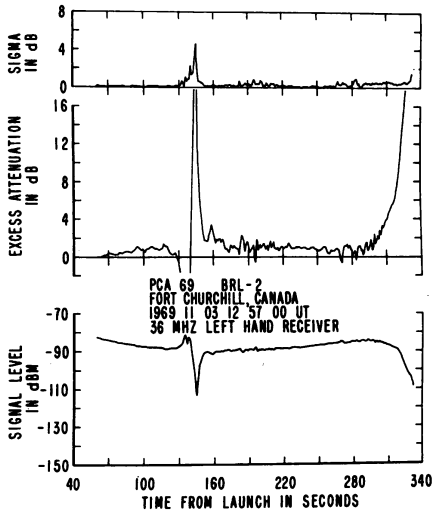

Figure 21-4. Absorption vs Time, Rocket B-2

Figure 21-5 is a plot of the variations from received signal levels expected in the absence of absorption or refraction for the three lower frequencies of the four-frequency beacon. The scales are expanded considerably, as compared to Figure 21-4, to show more clearly the period of time which encompasses the disturbance. Here, negative values indicate periods of signal gain or enhancement. From the curve for the 36-MHz ordinary signal, a period of signal enhancement,— starting at about 125 sec — is noted. The enhancement reaches a maximum gain of about 7 dB at 135 sec, is followed by a brief drop, and then returns to a gain of 6 dB at 138 sec, and then is followed by a precipitous drop to a loss of 25 dB at 145 sec. Following this disturbance the signal level rapidly returns to normal. A similar occurrence, although of lesser magnitude, is noted in the curves for the other frequencies.

Figure 21-6 is a plot of the agc cross correlations with the 36 MHz ordinary-36-MHz extraordinary curve being associated with the top scale on the left; the 73 MHz ordinary-36-MHz ordinary with the top scale on the right; the 146 MHz ordinary-36 MHz ordinary with the bottom scale on the left; and the 583 MHz ordinary-36 MHz ordinary with the bottom scale on the right. As would be expected, regardless of the cause of the disturbance, a strong cross correlation is noted between the two modes of 36 MHz with a maximum value of 0.98. The 73-MHz ordinary signal disturbance also shows a strong cross correlation to the 36-MHz ordinary signal disturbance but, of particular significance, is the fact that the disturbance at 73 MHz occurred about 2 sec earlier than the disturbance at 36 MHz. Likewise, the disturbance at 146 MHz preceded the disturbance at 36 MHz by about 6 sec. The 583-MHz signal cross correlation to the 36-MHz signal shows a slight variation at approximately twice the rocket precession rate. This is interpreted to mean that the 583-MHz signal was not influenced by the disturbing medium and that the variations are probably due to variations in the 583-MHz antenna amplitude pattern.

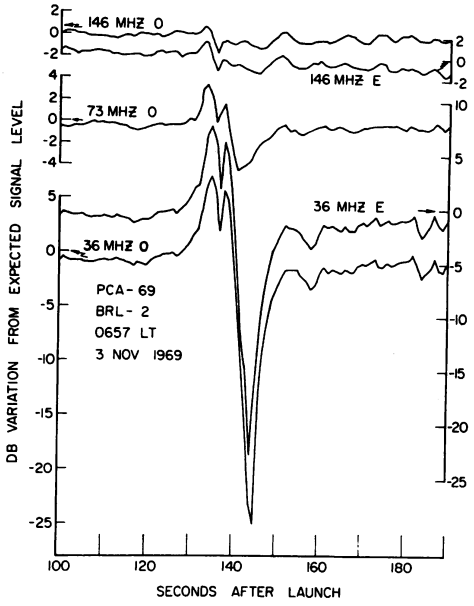

Figure 21-5. Signal Level Variations vs Time, Expanded Scale, Rocket B-2

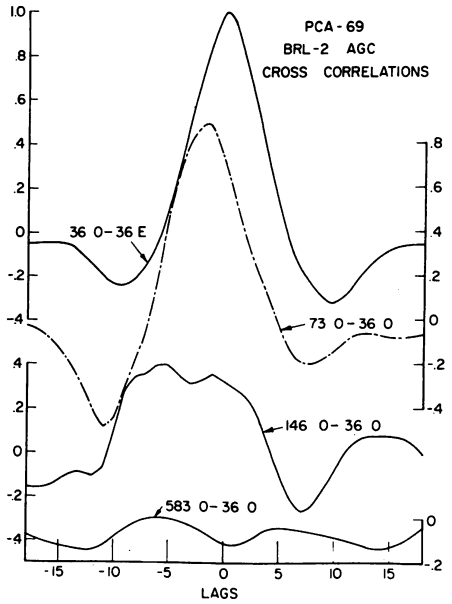

Figure 21-6. Cross Correlation of Absorption Data, Rocket B-2

A highly significant clue to the meaning of these manifestations can be found in the behavior of the dispersive phase data. The dispersive phase measurement between 36/146-MHz pair of frequencies had a discrepancy of 5 cycles of dispersive phase when the rocket descended below the ionosphere, that is, 5 cycles of dispersive phase which were accumulated on the upleg were not removed on the downleg. The 145/583-MHz pair did not show any such discrepancy, and comparison between the two pairs indicated that the discrepancy probably occurred between 140 and 165 sec after launch.

We believe that what happened is as follows: At 125 sec the ray paths approached a small area of enhanced electron density, say a single field aligned striation or a single auroral ray, and since the ray path was subparallel to what we will refer to as the striation, focusing occurred and the signal levels were enhanced. After 140 sec the lower frequencies underwent defocusing. At 36 MHz the refractive effects were severe enough that by 145 sec propagation had become possible along an alternate ray path which was farther from the striation and therefore gave 5 fewer cycles of dispersive phase. At 145 sec the tracking filters in the 36-MHz phase measuring channels lost lock because of the rapid drop in signal level, and when the signal levels recovered and the tracking filter recovered lock, the ray path with the fewer dispersive phase cycles gave the stronger signal.

21-4 RESULTS FROM ROCKET B-3

The third rocket of the BRL series, designated as Rocket B-3, was launched 33 min after Rocket B-2 at 1330 UT (0730 CST) on 3 November, just before local ground sunrise. All six frequencies of the propagation beacon apparently functioned satisfactorily, although the 9-MHz signal dropped into the noise at about 100 sec (90 km) and remained generally below the noise level until the rocket descended below that altitude at 240 sec.

Figure 21-7 is a plot of absorption as a function of altitude for the 9- and 18-MHz signals. There is no significant absorption at either frequency below 60 km, and even at 90 km there was only 2 dB absorption at 18 MHz and 7.5 dB at 9 MHz. At 90 km the 9-MHz signal is rapidly approaching the receiver noise level. At this signal level the calibration curve is quite nonlinear and the 9-MHz measurements are, therefore, somewhat degraded in accuracy.

The lower half of Figure 21-8 is a presentation of the absorption data as a function of time for the 9- and 18-MHz signals and for the two modes of the 36-MHz signal. Additionally, at the top of Figure 21-8 are elctron difference curves similar to those plotted for Rocket B-4. Note that for the absorption curves the dB scales are offset by 1 dB for each successive curve to avoid overlap of the curves. The 36-MHz absorption is difficult to define because of baseline drift.

There are numerous variations in the absorption data which seem to be similar in nature to those observed for Rocket B-4. The magnitudes of both the absorption and of the variations are much smaller, however, than was the case for Rocket B-4. At 18 MHz the magnitudes for Rocket B-3 data are intermediate between those for 36- and 72-MHz data for Rocket B-4, and the Rocket B-3 36-MHz data appears comparable to the Rocket B-4 72-MHz data. The cross correlation data shown in Figure 21-9 indicate very little correlation between the 18-MHz variations and those on the 36-MHz channels. Looking at the 18- and 36-MHz data on Figure 21-8, the eye would note considerable correlation between 150- and 200-sec, but the correlation data indicate that over the full range of the data this similarity is lost in the noise. A cross correlation analysis of data from the time span of 140- to 210-sec after launch indicates, however, that during that restricted period the signal levels at 18-, 36-, and 73-MHz did vary coherently. The maximum values of these cross correlations are listed in Table 21-2 in the discussion section under column 3A, and occurred at zero times lag except for the 146 MHz-73 MHz pair. In agreement with the analysis shown in Figure 21-9, this latter pair showed only precession-induced antenna pattern effects.

Throughout most of the flight the 9-MHz signal was lost in the noise, but Figure 21-8 shows that around 130 sec there were times when a signal was observed. These times do not, however, appear to correlate with periods of low absorption on the higher frequencies.

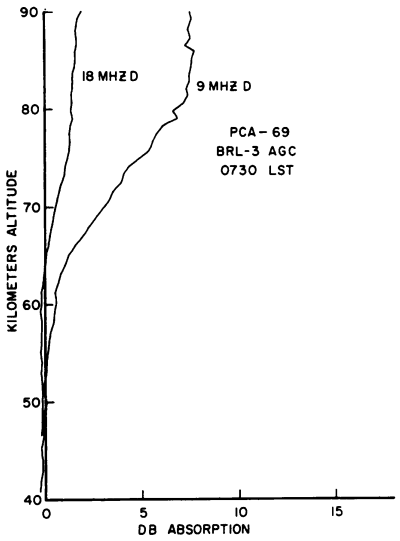

Figure 21-7. Absorption vs Altitude, Rocket BRL-3

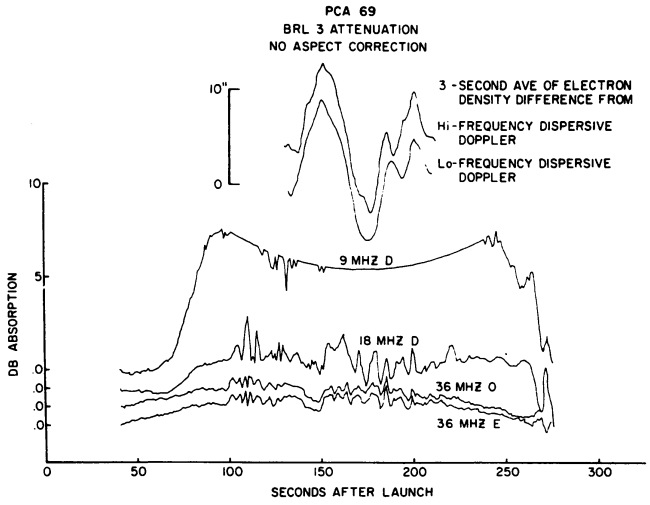

Figure 21-8. Absorption vs Time, Rocket B-3

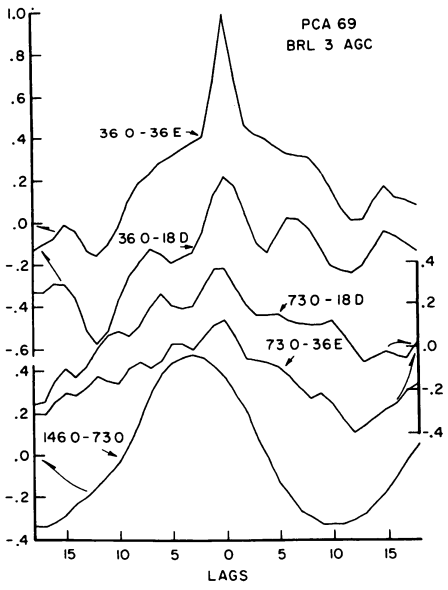

Figure 21-9. Cross Correlation of Absorption Data, Rocket B-3

The upper portion of Figure 21-8 displays plots of electron difference, computed in the same manner as was the electron difference data for Rocket B-4. These electron differences give evidence of considerable variation in electron density below the rocket, but show no correlation with the variations in absorption.

The evidence at hand indicates that there was some variability in the ionosphere below the rocket, but that the measuring system had barely sufficient sensitivity to measure it. The mean absorption may have increased relative to that which existed during the flight of Rocket B-2 33 min earlier, but the failure of the low-frequency beacons on Rocket B-2 prevented any accurate measurement of mean absorption. The variability at 36 MHz seems to have been similar, and the main difference between the two views of the ionosphere is the presence of the "striation" seen by Rocket B-2.

21-5 RESULTS FROM ROCKET B-5

The fourth rocket of the BRL series to be fired during the PCA event was designated as Rocket B-5 and was launched shortly after local noon at 1854 UT (1254 CST) on 3 November.

Figure 21-10 is a plot of the measured absorption as a function of altitude for the 9 MHz, 18 MHz, and both modes of the 36-MHz signals. Absorption first became apparent at about 52-km altitude, which is in reasonably good agreement with the dispersive phase measurements (Dean, 1971). The maximum rates of increase in absorption came at, or slightly below, 60 km, and were 0.1 dB/km at 36 MHz, 0.22 dB/km at 18 MHz, and 0.6 dB/km at 9 MHz. The 9-MHz signal level measurements became unreliable at about 63 km because apparent shifts in the ambient noise level made the lower part of the calibration curve unreliable. The measured values of absorption at 85-km altitude were 5 1/2 dB at 18 MHz, 1 2/3 dB at 36 MHz for the extrordinary mode, and 1 1/3 dB at 36 MHz for the ordinary mode. At 73 MHz about 1 dB of absorption was indicated, with no measurable absorption at 146 MHz.

Figure 21-11 is a plot of absorption as a function of time with the zero's on the vertical (absorption attenuation) scale offset by 1 dB for successive curves to avoid overlap of the curves. For these data, 1-sec averages of local (periodic) maxima were used without making corrections for the rocket antenna amplitude patterns. This was done because the cross correlation and power spectrum analysis indicated there was no measurable variation in signal strength at the precession rate or at its second harmonic, and therefore no variation in signal strength over the total coning angle of 15 deg. In addition, a comparison of the standard deviation about the mean between 1-sec averages of local maxima and 1-sec averages of all data points showed

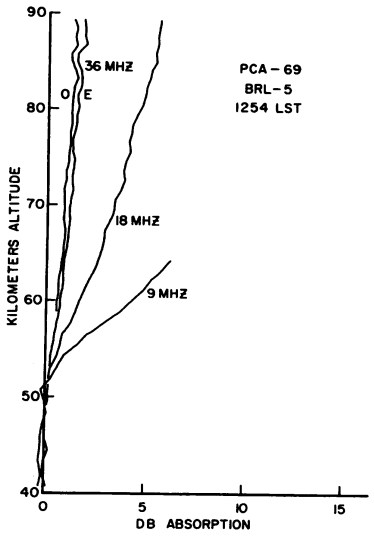

Figure 21-10. Absorption vs Altitude, Rocket B-5

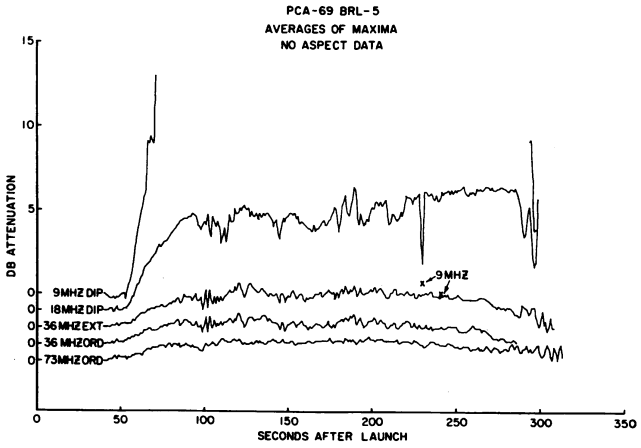

Figure 21-11. Absorption vs Time, Rocket B-5

only a slight increase from 0.2 dB to 0.4 dB indicating no significant effect due to rocket spin.

During the time the rocket was above the absorbing layer, this is, from 100 to 260 sec after launch, Figure 21-11 indicates that there were only moderate variations in the measured absorption data, and little correlation is apparent between the variations at the various frequencies. A possible exception is at about 230 sec where there are two 1-sec bursts of signal at 9 MHz, one of which is coincidentatl with 1 sec of low absorption at 18 MHz. There is, however, no effect at 36- or 73-MHz. This general lack of correlation is confirmed by the results of the cross correlation analysis which are plotted in Figure 21-12, where arrows on the figure indicate which scale and zero level should be used with each curve. Only the two modes of 36 MHz show a significant cross correlation peak, with a maximum value of 0.88. Other cross correlation maxima may be found in Table 21-2 in the summary.

The small change in the standard deviation of the mean alluded to in the discussion of antenna pattern corrections, indicates that there was little variation in the received signal level which occurred with repetition rates greater than 1/sec.

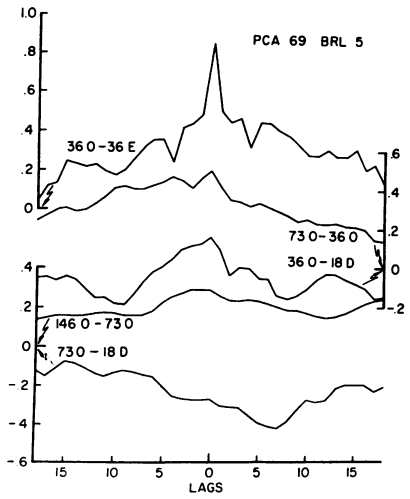

Figure 21-12. Cross Correlation of Absorption Data, Rocket B-5

21-6 RESULTS FROM ROCKET B-6

The fifth BRL rocket of the PCA event was Rocket B-6, which was launched as the first of a sunset pair at 2130 UT (1530 CST) on 4 November. Data from the second rocket of the pair, Rocket B-7, has not as yet been reduced.

Figure 21-13 shows the measured absorption for the 9-, 18-, and 36-MHz signals plotted as a function of altitude. The first observable absorption is noted at about 53 km, an altitude which is in reasonable agreement with the dispersive phase measurement (Dean, 1971). The maximum measured rates of absorption are 0.4 dB/km at 9 MHz, 0.2 dB/km at 18 MHz, and 0.1 dB/km at 36 MHz and occur at an altitude of about 60 km. The measured values of total absorption at 85 km were 1 dB for the 36-MHz ordinary mode, 1 1/3 dB for the 36-MHz extraordinary mode, 2 1/2 dB for the 18-MHz signal and 10 dB for the 9-MHz signal. The value for the 9-MHz signal should be taken with some reserve because of calibration difficulties in the immediate neighborhood of the ambient noise level.

Figure 21-14 presents plots of the absorption data as a function of time after rocket launch. Also shown in the figure is a plot of the temporal variation of the apparent electron density as derived from the dispersive phase measurements. Arrows indicate the scales appropriate to the various curves. There is again a moderate amount of variation when the rocket is well above the main absorbing region, and for this flight the signal levels are such that the 9-MHz signal frequently is measureable. Furthermore, the variations appear to be correlated between the various signal level channels, including the 9-MHz channel when signal levels are appropriate. The electron density variations, however, show no obvious correlation with the absorption variations, although their very existence testifies to the disturbed state of the lower ionosphere.

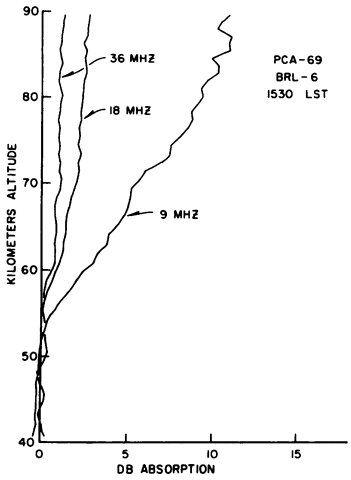

Figure 21-13. Absorption vs Altitude, Rocket B-6

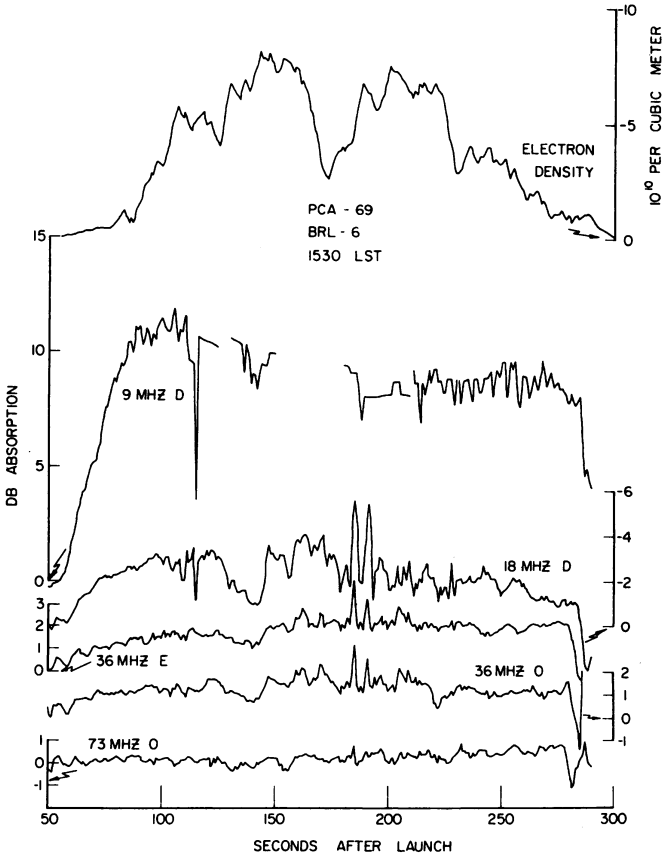

Figure 21-14. Absorption vs Time, Rocket B-6

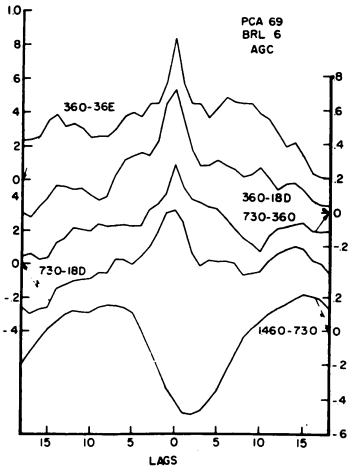

Figure 21-15. Cross Correlation of Absorption Data, Rocket B-6

The results of the cross correlation analysis are shown in Figure 21-15. As might be expected from the data shown in Figure 21-14, significant cross correlation were found between variations in absorption for all of the frequencies below 146 MHz – even for 73 MHz where no net absorption was measured. The 9-MHz data were not included in the cross correlation analysis because much of the time the signal level was below the ambient noise level.

These results for Rocket B-6 show some similarity to those observed for Rocket B-4, although the magnitude of the absorption variations is less and there is no obvious correlation between variations in absorption and variations in electron density. It should be noted, however, that the total absorption is also considerably reduced and that the peak-to-peak variations in absorption are about equal to the mean absorption. The shortest observable features common to all absorption records are again about 3 sec in length.

21-7 RESULTS FROM ROCKET B-1

BRL Rocket B-1 was launched during the evening of 5 August at 2136 CST or 6 August at 0336 UT, as a certification flight for the onboard instrumentation and also to gather background information for use with data obtained during the PCA event. The BRL propagation experiment performed as expected, except that the 9-MHz signal was masked by a very high ambient noise level which appeared just before launch and disappeared shortly after the end of the flight. The 9-MHz signal level was about as expected.

Preliminary absorption data (final data reduction is still in progress) appear to be very similar in nature to data from Rocket B-2, being dominated by a single sharp disturbance during rocket ascent.

Absorption data, plotted as a function of time after launch, are shown in Figure 21-16 where arrows indicate the appropriate scale for each frequency. Immediately above the absorption data in Figure 21-16 is a plot of the apparent electron density as derived from the dispersive phase data. Across the top of the figure is an altitude scale for convenient correlation of time and altitude. The three absorption curves show a significant perturbation shortly after 100 sec which is roughly coincident with an enhancement in the apparent electron density.

These data are replotted in Figure 21-17 with an expanded time scale to better illustrate the variations in the data in the vicinity of the perturbation. The signal level data have been plotted in terms of variation from the expected signal level, inverting the presentation in Figure 21-16; that is, "absorption" is now plotted as a signal decrease and appears as negative in value and signal enhancement appears as positive in value. From the data in Figure 21-17, it would appear that the

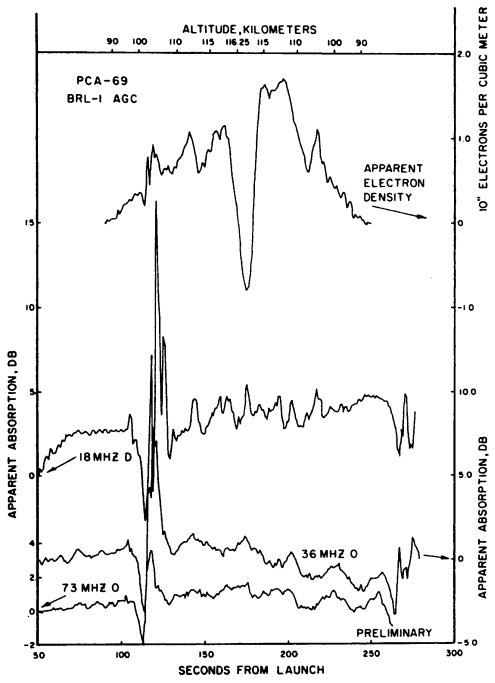

Figure 21-16. Absorption vs Time, Rocket B-1

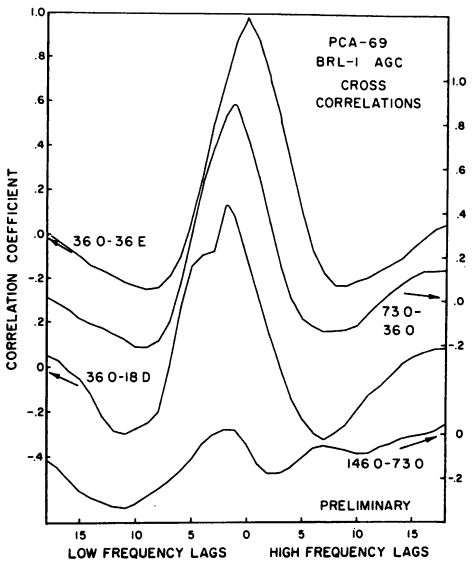

Figure 21-18. Cross Correlation of Absorption Data, Rocket B-1

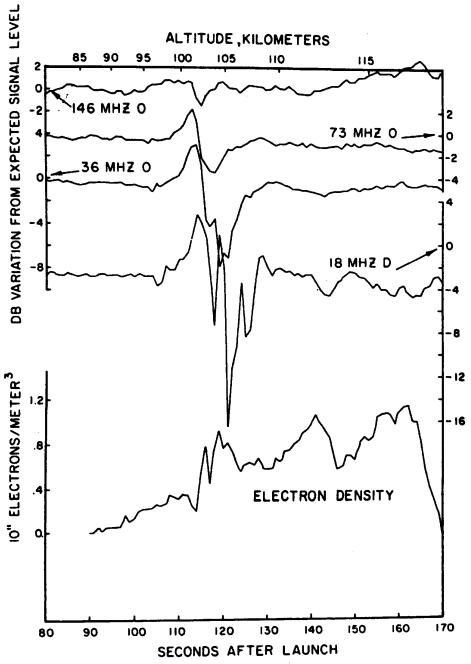

Figure 21-17. Signal Level Variations vs Time, Rocket B-1

rocket traversed a complex region of enhanced electron density at an altitude of 103- to 105-km which significantly affected the received signal levels. No such enhancement in electron density, however, can be observed in the Langmuir probe data (Dean, 1971). From this we deduce that the cause of the perturbations in the data was located below the rocket, but still along the ray path.

A closer examination of Figure 21-17 reveals that the perturbations became more intense, more complex, and reached their maxima later in time at the lower frequencies. At 146 MHz there is only a small dip in the signal level record which is nearly coincident with the onset of the apparent electron density enhancement. At 18 MHz the middle and deepest dip in signal level occurs after the peak of the apparent electron density enhancement.

The results of the cross correlation analysis, shown in Figure 21-18, confirm that there was a significant correlation between the variations in signal level at the various frequencies and that perturbation on the higher frequency channels did indeed lead those on the lower frequency channels.

It would appear, then, that the perturbation seen on the propagation data from Rocket B-1 are similar in nature to those on the data from B-2, and that they therefore have a similar cause. There are, however, certain differences which must be noted. The perturbations on the B-1 data were much less intense at the lower frequencies than those on the B-2 data, and the dispersive phase data did return to zero when Rocket B-1 descended below the ionosphere. From these differences we may infer that B-1 "striation" was also less than the B-2 "striation."

It should also be noted that there were several enhancements in the apparent electron density which were not reflected in changes in the received signal level, and that one of these occurred on the downleg of the trajectory at nearly the same altitude as the upleg enhancement.

21-8 DISCUSSION

The basic absorption experiment was successful, except for the unexpectedly low signal level and dynamic range on the 9-MHz channel and the failure of the low frequency beacons on Rocket B-2. The absorption data obtained are summarized in Table 21-1 and are consistent with the electron density data. Where possible, the product F^2A, where F is the transmitted frequency in MHz and A is the measured absorption in dB, has been added to the table to give an indication of the internal consistency of the data. The data shown here are compatible with the expected accuracies of $\pm$ 4 dB at 9 and 18 MHz and $\pm$ 1 dB at 36- and 73-MHz. The maxima in the absorption rates occurred in the range 65- to 68-km for Rocket B-3, and in the range 58- to 60-km for Rockets B-4, B-5, and B-6.

Table 21-1. Absorption Data

Channel*	Rocket Number				
	B-4	B-2	B-3	B-5	B-6
9 MHz D	>>10	-	7 1/2	>10	10
	>1 1/2	-	0.4	0.6	0.4
	-	-	600	-	800
18 MHz D	15	-	2	5 1/2	2 1/2
	1	-	0.15	0.22	0.2
	5000	-	600	1800	800
36 MHz E	5 1/2	1	1	1 2/3	1 1/3
	1/2	-	-	0.1	0.1
	7000	1300	1300	2000	1700
36 MHz 0	4 1/2	1	1	1 1/3	1
	1/2	-	-	0.1	0.1
	6000	1300	1300	1700	1300
73 MHz 0	≈1	-	-	>1	>1
	-	-	-	-	-
	5000	-	-	-	-
Absorption Starts	47 km	-	61 km	52 km	53 km
Launch Date UT	2.2110	3.1257	3.1330	3.1854	4.2130
and Time CST	2.1510	3.0657	3.0730	3.1254	4.1530

*For each channel the first number is absorption in dB at 85 km, the second is absorption rate in dB/km, and the third is frequency squared times absorption in MHz^2 dB.

Let us now consider the variations in signal level, and begin by recapitulating the distinction between the two categories which were defined in the introduction.

The refractive category included those cases where the variation in signal strength was much greater than the mean measured absorption, the measurements indicated a considerable amount of "gain" above the no absorption signal level, and there was a consistent shift in the time of maximum effect as the signal frequency was changed. In both cases, Rocket B-1 and Rocket B-2, the maximum effect occurred later at the lower frequency. This category may be further subdivided, perhaps artificially, by the magnitude of the effect seen on the dispersive phase measurements.

The data from Rocket B-2 indicate that the effects were severe enough to cause true multipath, that is, the 36-MHz propagation path switched from one ray path to another which differed in phase length by 5 cycles. The data from Rocket B-1 indicate refractive effects, but no actual jump from one ray path to another.

The refractive effects indicate that the electron density variations involved were primarily spatial. A single, field-aligned striation has been suggested as a possible cause (W. W. Berning, personal communications), and exploratory ray tracing has confirmed that such intensity changes can be produced (R. E. Prenatt, personal

communications). The striation may well have been an auroral ray since aurorae are so frequent at Fort Churchill, but we will continue to use the term striation as a caveat that the auroral association, though attractive, is not certain.

The second or absorptive category included those cases where the peak-to-peak variation in abosrption were not significantly larger than the mean absorption, the various features on the signal strength records appeared to occur simultaneously at all frequencies, and there was no apparent signal gain before rocket turnover on reentry.

From the simultaneity of features on the several signal strength records, the great similarity in their shape, allowing for the change in intensity with signal frequency, and satisfactory cross correlations between the various channels (see Table 21-2), we can infer that the several ray paths were essentially the same, that there was little raybending, that horizontal gradients were small, and that the variations were essentially temporal. If the variations were temporal, then the rapidity of these variations would indicate that the interaction was taking place in the lower D region. Spikes only 3-sec wide at their base and appearing on several data channels can be seen in Figures 21-2 and 21-14. These imply that the time constant for change in electron density may be as short as 1 sec. An altitude of 60 km should give the required time constant. If the variations were spatial, the horizontal velocities of 250 m/sec of Rocket B-6 give a half width of about 150 m for the shortest features.

Table 21-2. Cross Correlation Summary

Frequencies	Maximum Cross Correlation Rockets						
	4	2	3	3A	5	6	1
360 - 36E	0.986	0.982	0.922	0.946	0.859	0.829	0.985
360 - 18D	0.856	-	-0.569	0.474	-0.254	0.726	0.728
36E - 18D	0.848	-	-0.572	0.635	-0.283	0.678	0.721
730 - 36O	0.717	0.871	-0.301	0.539	0.493	0.286	0.875
730 - 36E	0.693	0.905	-0.395	0.636	0.570	0.222	0.876
730 - 18D	0.594	-	0.378	0.412	-0.421	0.317	0.554
1460 - 73O	0.293	0.424	0.475	0.824	-0.283	-0.490	-0.331
1460 - 36E	-	0.411	-	-	-	-	-
1460 - 36E	-	0.397	-	-	-	-	-
5830 - 36E	-	-0.131	-	-	-	-	-
5830 - 36O	-	-0.145	-	-	-	-	-
5830 - 73O	-	-0.193	-	-	-	-	-

Whether the variations were spatial or temporal, the electron density can at best follow the changes in the incoming ionizing radiation. Precipitating, or auroral particle fluxes are known to be capable of the required variability (Mozer, 1968), but this capability does not seem to have been demonstrated for solar particle fluxes. Reagan et al (1971) indicate that Fort Churchill was probably within the auroral oval throughout the polar cap event.

Although it might seem attractive to assign the varying component of the absorption an auroral source, reserving the solar particles for the steady-state component, there are problems with this solution. The plots of absorption versus altitude (Figures 21-1, 21-7, 21-10, and 21-13) are more compatible with a unimodal than a bimodal distribution. The height of the centroid of the varying component, obtained from consideration of the time constants involved, is the same as that of the centroid of the sum of the two components, obtained from the absorption versus altitude plots. From the absorption versus time plots (Figures 21-2, 21-8, 21-11, and 21-14), we can see that the peak-to-peak variation is about equal to the mean absorption and that the average value of the varying component must be about equal to the steady-state component. Rather than assume that the polar cap absorption was generally accompanied by auroral absorption of nearly the same intensity at nearly the same altitude, we prefer to account for the variations in absorption and electron density by assuming a variable polar cap absorption resulting from a variable flux of solar particles. This preference applies to the absorptive effects and does not negate the probable auroral cause of the refractive effects seen on data from Rockets B-1 and B-2.

References

Berning, W. W., personal communications.

Dean, W. A. (1971) Electron Density Profiles for the 1969 PCA Event. See Chapter 20 of this publication.

Mozer, F. S. (1968) Rapid variations of Auroral particle fluxes, J. Geophys. Res. 73 (No. 3):99-104.

Niles, F. E., personal communications.

Prenatt, R. E., personal communications.

Reagan, J. B., Imhof, W. L, Johnson, R. G., and Sharp, R. D. (1971) Satellite Data Analysis for Operation PCA-69 Rocket Coordination, Lockheed Missile and Space Co., Palo Alto.

Appendix A

Note Added in Proof

Final reduction of Rocket B-1 data introduced no significant changes from preliminary data reported here. Reduction of data from Rocket B-7 (second of sunset pair with B-7) showed no significant correlations between absorption on different frequency channels in spite of the extensive variations in phase.

The variations observed are evidence of microscale variations in the illumination of the polar cap by solar particles.

Contents

22. Blunt Probe Measurements During a PCA Event

L.C. Hale, J.R. Mentzer, and L.C. Nickell
The Pennsylvania State University
Ionosphere Research Laboratory
University Park, Pennsylvania

Abstract

Data is presented for parachute-borne, blunt-probe, charged-particle conductivity measurements during a PCA, covering a night-sunrise-day sequence of four shots on 3 November 1969 at Ft. Churchill, Manitoba. The measured conductivities show that the effects of the PCA on ionization persists down to about 30 km. The peak positive-ion density and ion production rate was found to be at 48 km, with a peak-ion density of about 8×10^4 cm^{-3}. For an ion-ion recombination rate of 2×10^{-8} cm^3 sec^{-1}, this implies an ion production rate of about 150 cm^{-3}. A daytime electron density of about 300 was found at 48 km, implying a detachment coefficient at that altitude of about 1×10^{-1} sec^{-1}.

22-1 INTRODUCTION

In coordination with other experiments, charged particle conductivity measurements were made at altitudes between 20- and 60-km during the PCA of early November 1969 at Ft. Churchill, Manitoba, Canada. This paper describes the results and some implications of the measurements made on four Arcas

rocket-parachute launches employing the parachute-borne, blunt-probe technique. This is a subsonic system which employs continuum principles to measure polar (positive and negative) charged particle conductivities (Hale et al, 1968). The four rockets were launched during the night-sunrise-day period of 3 November 1969 during the large solar cosmic-ray event which commenced on the previous day.

22-2 CONDUCTIVITY DATA

The polar conductivity results of four Arcas launched blunt-probe experiments during the PCA are shown in Figure 22 -1, along with the results of a similar "certification" or control experiment performed under relatively quiet conditions after sunset on December 1967. The positive and negative conductivities are different for the PCA data, but were essentially indistinguishable on the control data.

It will be noted that the polar conductivities during the PCA are enhanced over those of the control day above 30 km, indicating that the effects of the PCA extended to that altitude. It will also be noted that above 40 km the negative conductivity substantially exceeds the positive conductivity for the two daytime shots

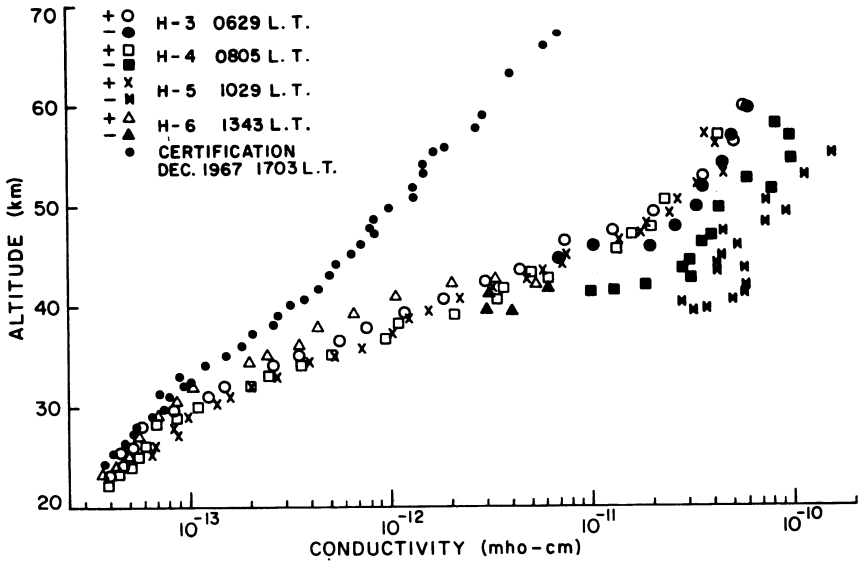

Figure 22-1. Polar Conductivity Data for Fort Churchill, Canada

(H-4 and H-5) for which data is available, but not on the night shot (H-3). The successively greater negative conductivities on H-5 and H-6 shows the build-up of free electrons during the sunrise-day period. The small variation with time in the positive conductivities indicates that the ion production and loss processes did not vary greatly over the period encompassed by the four PCA shots.

The overall accuracy of the conductivity data is about ± 25 percent.

22-3 POSITIVE ION DENSITIES

The basic quantity measured by the blunt probe is electrical conductivity. For many purposes, such as radio-wave propagation studies, this is the most important parameter. For discussion of theoretical models, however, it is useful to convert the measured conductivities to charged particle densities. To make this conversion, it is necessary to make an assumption about the charged particle mobilities.

In Figure 22-2, the conductivity data has been converted to positive-ion densities using the relationship

$$\sigma_+ = N_+ e\mu_+ , \qquad (22\text{-}1)$$

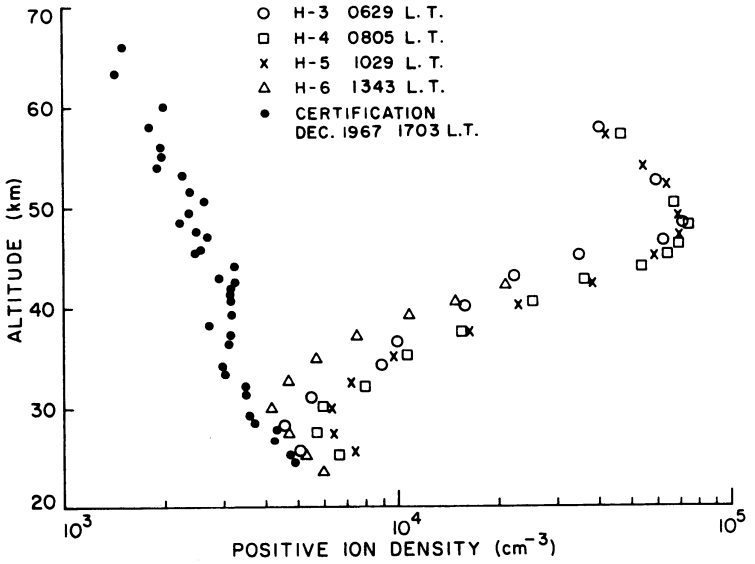

Figure 22-2. Positive-Ion Density Data for Fort Churchill, Canada

where σ_+ is positive conductivity, N_+ is the positive ion density, and e is electronic charge; μ_+ is the charged particle mobility given by

$$\mu_+ = \mu_{o+} \frac{P_o}{P} \frac{T}{T_o} \tag{22-2}$$

where μ_{o+} is the reduced mobility at STP (T_o, P_o) and is taken as 1.7 cm^2 $volt^{-1}$ sec^{-1}, and T and P are taken from the appropriate CIRA 1965 model. This value of μ_{o+} is typical of values used for small ions in dry air. Some recent measurements indicate the possibility that the actual mobilities may be either higher or lower than this value (Conley, 1971; Rose and Widdel, 1972). Because of this uncertainty in mobility, the positive-ion density data is believed to be accurate to a factor of 2.

22-4 POSITIVE-ION LOSS RATE

It is of interest to calculate the ionization production due to solar protons from the data obtained during the PCA. This can be done from the positive-ion data from the simple relationship

$$N^+ \approx N^- \approx \sqrt{Q/\alpha_i} \tag{22-3}$$

where N^+ and N^- are positive- and negative-ion densities, respectively, Q is the ion production rate, and α_i is the ion-ion mutual neutralization coefficient. This equation is valid at night and during the daytime at sufficiently low altitudes that recombination with electrons is not an important process. The coefficient α_i is made up of both three-body (pressure dependent) and two-body (pressure independent) components. The three-body or Thomson coefficient is thought to be fairly well known but the appropriate two-body coefficient was very uncertain. The procedure used was to assume various values of the two-body coefficient to determine which would yield the best fit to the data. Figure 22-3 shows values of the ion-ion recombination coefficient $\alpha_i = \alpha_{i2} + \alpha_{i3}$ plotted assuming Sayers formula (Loeb, 1961) for the Thomson coefficient α_{i3} and assumed values for α_{i2} above and below the commonly assumed value of 2×10^{-7} cm^3 sec^{-1} (McDaniel, 1964).

The recombination coefficient α_{i2} can now be deduced from the control shot positive-ion density data, using Eq. (22-3), by finding which value of α_{i2} yields production rates which most nearly match the galactic cosmic-ray production rates. This is shown in Figure 22-4.

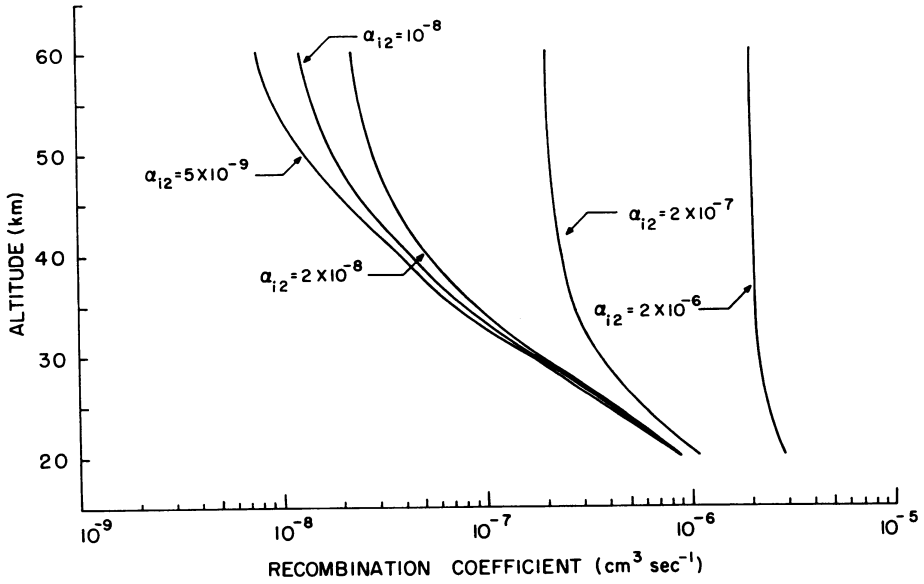

Figure 22-3. Mutual Neutralization Profiles Deduced From Blunt Probe Conductivity Data

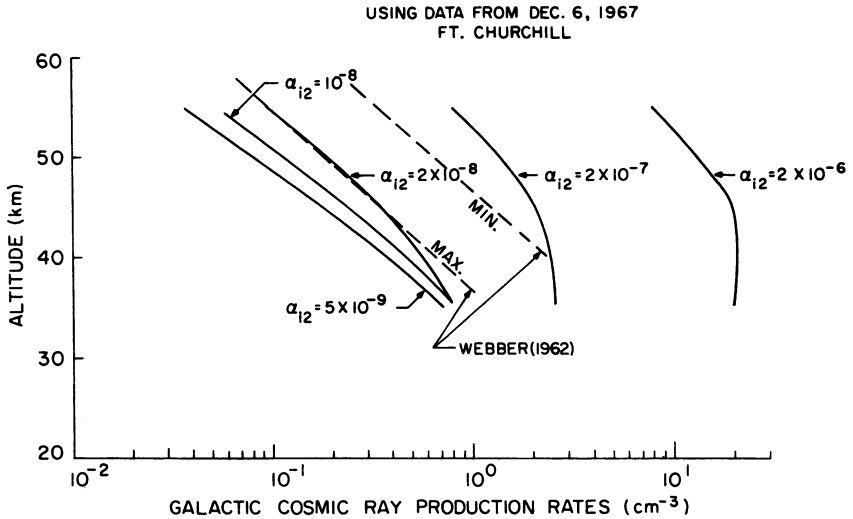

Figure 22-4. Galactic Cosmic-ray Production Rates for Fort Churchill, Canada

The production rates are taken from Webber (1962) and show the range of values appropriate to the magnetic latitude of Ft. Churchill. It will be noted that an α_{i2} of 8×10^{-8} cm^3 sec^{-1} or smaller is necessary to fit this range of ionization production, with a smaller value more likely.

A further but perhaps less strong argument for a small value of α_{i2} can also be made. At higher altitudes where two-body ion-ion recombination must be dominant, the cosmic-rate production rate will be approximately proportional to neutral air density ρ and hence, using Eq. (22-3), positive-ion density will vary as $\rho^{1/2}$. Conversely, if three-body recombination is dominant and is proportional to density (isothermal case), an ion density independent of altitude should result. It will be noted that the ion density on the control data is approximately constant from 33- to 43-km. If the bend in the curve at 43 km is interpreted as the transition from three-body to two-body loss, then $\alpha_{i2} = \alpha_{i3}$ at this altitude. Then, using Sayers three-body relation (Loeb, 1961), α_{i2} is found to be 2×10^{-8} cm^3 sec^{-1}. (The bend in the curve at 33 km would be interpreted as a transition to a non-minimum ionizing regime in cosmic-ray ion production.)

22-5 PRODUCTION RATES

The production rates for the PCA can be calculated from the positive ion data using Eq. (22-3). This is shown in Figure 22-5 for the data from the pre-

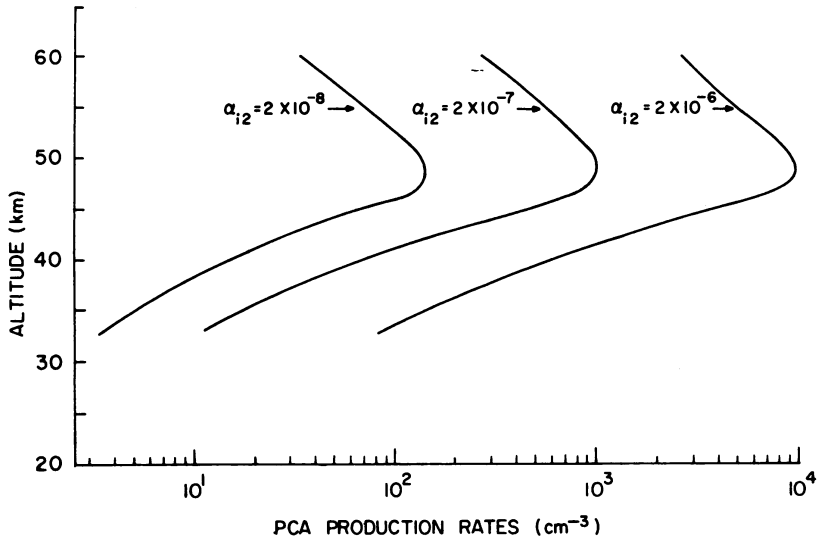

Figure 22-5. PCA Production Rates for Fort Churchill, Canada

sunrise shot (H-3) for various assumed values of α_{i2}. Since the peak ion densities are the same ($\sim 8 \times 10^4$ at 48 km.) for H-3, H-4 and H-5, the peak production rates would also be approximately the same during this period. If the value of 2×10^{-8} cm^3 sec^{-1} were in fact correct for α_{i2}, then the leftmost curve would be the correct one to use. Alternatively, as good calculations of the PCA ion production rates become available, it will be possible to use them in conjunction with Figure 22-5 to deduce the best value of α_{i2} for the PCA.

22-6 ELECTRON DENSITIES

The increase of negative conductivity above 40 km during H-4 and H-5 may be interpreted as a buildup in free electron density during the sunrise-day period. Using available data (McDaniel, 1964) for electron drift velocity v vs E/P (probe electric field over pressure), this excess conductivity may be converted to electron density values as shown in Figure 22-6. Because of the non-linearity in the v vs E/P characteristics, this data is probably good to a factor of 2, and the structure indicated by the curves may not be significant.

In this altitude range, the electron density is related to the positive ion density by the approximate relationship

$$N_e \approx N_+ \frac{D}{A} \qquad (22\text{-}4)$$

where A is the attachment coefficient and D the detachment coefficient.

Since the initial attachment reaction is thought to be well known (three-body attachment to form O_2^-), this relationship may be used to estimate D. For example, at the altitude of peak-ion density—about 48 km— $N^+ \approx 8 \times 10^4$ cm^{-3} and $N_e \approx 300$ for H-5. If A is taken as 30 sec^{-1} at this altitude, D is found to be of order 1×10^{-1} sec^{-1}.

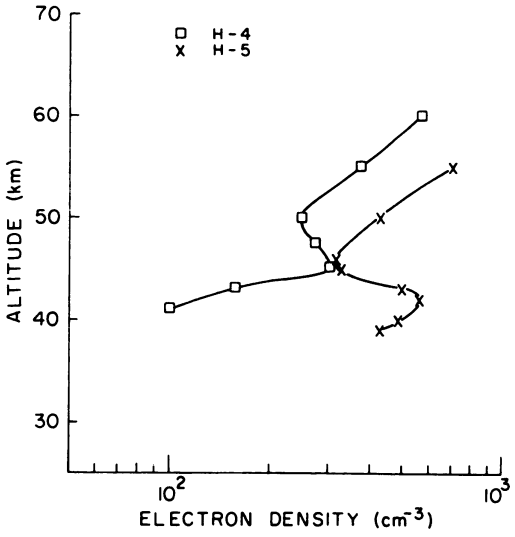

Figure 22-6. Electron Density Profiles for Fort Churchill, Canada

References

Conley, T. (1971). See Chapter 24 of this publication.

Hale, L.C., Hoult, D.P., and Baker, D.C. (1968) Space Research VIII, North Holland, Amsterdam.

Loeb, L.B. (1961) Basic Processes of Gaseous Electronics, University of California Press, Berkeley.

McDaniel, E.W. (1964) Collision Phenomena in Ionized Gases, John Wiley & Sons, New York.

Rose, G. and Widdel, H.U. (1972) Radio Sci. 7(No. 1).

Webber, W. (1962) J. Geophys. Res. 67(No. 13):5091.

Appendix A

Note Added in Proof

A calculation by Klevans and Sum of proton and α-particle ionization for the 3 November 1969 PCA spectrum shows very good agreement with the positive ion data presented here at altitudes below 45 km for an α_{i2} of order 10^{-8} cm^3/sec. Their calculation, however, does not predict a peak in the ion production in the 45 to 50 km range. The observed peak in the ion density, therefore, probably does not correspond to a production peak but is more likely due to a rapid increase in ionization loss rate above 45 km due either to recombination or transport. Although this might be expected due to loss via recombination with free electrons on the sunrise-day shots H-4 and H-5, this possibility is difficult to admit for the pre-sunrise shot H-3 for which the production rate calculations of Figure 22-5 were performed. Thus, the most likely explanations would appear to involve changes in ion mobility or the ion-ion recombination coefficient or upward ionization transport above 45 km.

Contents

23. Positive Ion Densities in a PCA:40 to 100 km

E.N. Richards
Boston College
Chestnut Hill, Massachusetts

23-1 INTRODUCTION

This paper is presented in conjunction with those of Conley (1971), Ulwick (1971), and Sandock (1971); all of these papers deal with charge density measurements during the 2-4 November 1969 PCA event. All of the measurements of the above experimenters were made with instruments flown on the same series of Black Brant rockets. The series of flights and the measurements aboard are summarized in Table 23-1. While this paper is concerned with Langmuir probe ion-density measurements, the other measurements will be referred to often in discussing the ion density results.

Table 23-1 lists the five successful shots in the 2-4 November 1969 series, along with a certification shot in the 18 November 1968 PCA. The last two columns list the charge density measurements that were flown under N_+ for positive ions and N_e for electrons. The Langmuir probe measurements are the subject of the present paper, and the theory and results are presented here. The $Z\theta$ probe is designed to measure electron densities, and these measurements are compared with the Langmuir probe measurements where the two densities may be assumed equal. The Gerdien condenser is designed to measure positive ions

Table 23-1. Summary of PCA Charge Density Measurements From Black Brant Rockets

Rocket No.	Launch Time GMT	Condition	N_+ Measurements	N_e Measurements
17.757	18 Nov 1968 0800	Night	Retarding Potential Probe Langmuir Probe Gerdien Condenser	Langmuir Probe Z θ Probe (2 Freq)
17.602 (U-2)	2 Nov 1969 2020	Day	Langmuir Probe Gerdien Condenser	Langmuir Probe Z θ Probe (2 Freq)
17.758 (U-1)	3 Nov 1969 0605	Night	Langmuir Probe Gerdien Condenser	Langmuir Probe Z θ Probe (2 Freq)
17.616 (U-5)	3 Nov 1969 1352	Sunrise (ψ = 89.5)	Langmuir Probe	Langmuir Probe Z θ Probe (2 Freq)
17.906-1 (U-4)	3 Nov 1969 1711	Day	Retarding Potential Probe Gerdien Condenser	
17.617 (U-6)	4 Nov 1969 2308	Sunset (ψ = 96.8)	Langmuir Probe Gerdien Condenser	Langmuir Probe Z θ Probe (2 Freq)

in the lower D region, below 65 km, and also to provide measurements of charge mobilities which are used in the Langmuir probe calculations. The Gerdien condenser results are compared with corresponding Langmuir probe results.

The Langmuir probe element consists of a hemispherical cap on the forward tip of an rf antenna, which in turn is mounted on the nose of the Black Brant rocket. A short segment of the antenna structure adjacent to the tip is insulated from the tip and from the antenna itself, and serves as a guard electrode for the hemispherical tip, and also houses the Langmuir probe electronics. The antenna and probe are made of stainless steel. A programmed voltage is applied to the probe from launch and the current drawn by the probe is amplified logarithmically. See Figure 23-1.

Figure 23-2 shows the voltage monitor and the current response from a segment of the data from the November 1968 shot. There is an increasing and a decreasing sweep, at 12 V/sec and three "hold" intervals at +3V, -3V, and -9V. The electron and ion currents are shown on separate channels, and appear to respond appropriately to the applied probe potentials. The data used in obtaining the present results are taken from those segments of the sweep pattern which are held at -3V and -9V. In order to interpret these Langmuir probe positive-ion currents, it is necessary to analyze the current collecting properties of a

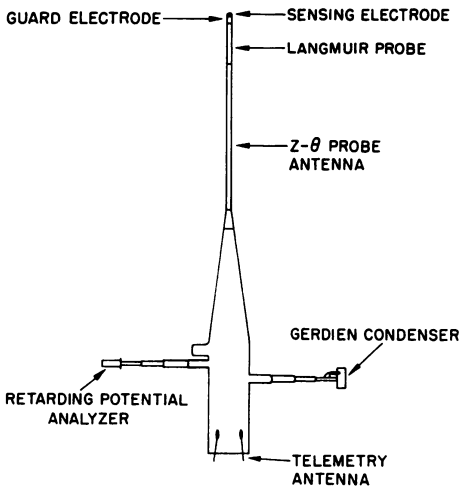

Figure 23-1. Black Brant 17.757 in the Operation Configuration

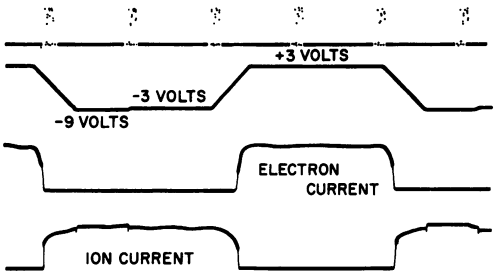

Figure 23-2. Sample of Electron and Ion Current Data

hemispherical electrostatic probe both in the free-molecular flow (collisionless) regime and the collision dominated regime. For the present rocket trajectories, with apogees of about 125 km, density calculations are limited to just over 100 km by approximations employed in the collisionless probe theory. At the low altitudes, the density measurements are limited to around 40 km by the sensitivity of the current amplifier.

The following is a presentation of the results of the Langmuir probe measurements on this series of Black Brant rockets, preceded by an outline of the probe theories used in each of the two altitude regimes. The collisionless probe theory will be outlined more briefly since it is an application of very familiar free-molecular flow concepts to a special hemispherical geometry. The probe theory in the collision-dominated regime will be presented in somewhat more detail since the inherent uncertainties in the theory would require that the basic assumptions and approximations be clear. Further details are published elsewhere (Richards, 1970).

23-2 CURRENT COLLECTION IN THE COLLISIONLESS REGION

In the free-molecular flow region, it is assumed that the probe is moving fast compared to the mean ion velocity. This holds for altitudes to just over

100 km in the case of the Black Brant trajectories involved in these measurements. Thus with a given potential distribution around the probe surface, the net current to the probe is calculated from the particle trajectories in the probe frame of reference, assuming a cold plasma. In the case of the hemispherical probe, however, the traditional calculation of Langmuir and Mott-Smith (1926) and extended by Kanal (1962, 1965) to moving probes, may not be directly applied. This is due to the lack of a complete spherical or cylindrical symmetry in the probe geometry. Instead, it becomes necessary to integrate the particle trajectories explicitly, using a given potential distribution around the probe. With the assumption of a cold plasma (due to a high probe velocity) and a zero angle of attack, the maximum impact parameter is all that is needed to define an effective probe cross section at a given probe velocity and potential. See Figure 23-3.

The trajectory integral is the familiar one for central force motion:

$$\frac{\pi}{2} - \theta_o = \int_{\xi_a}^{\xi_p} \frac{d\xi}{\xi\sqrt{A(\xi)\xi^2\eta^2 - 1}} . \qquad (23\text{-}1)$$

From Figure 23-3, $(\xi_p, \frac{\pi}{2})$ are the coordinates at the probe surface of the trajectory which has the maximum impact parameter. (ξ_a, θ_o) are the coordinates of the trajectory far enough away from the probe so that the potential is negligibly small. The function $A(\xi)$ contains the potential which is assumed to be a function only of the radial parameter ξ. The potential is obtained from a numerical solution of the Poisson equation (Walker, 1965), and is put into analytical form by fitting a function to the numerical solution. This still leaves the above integral analytically intractable, however, so that it was necessary to evaluate it numerically, choosing (ξ_a, θ_o) as the limit of integration. The normalized impact parameter η^{-1} is determined so that this integral equation is satisfied. The current to the probe is then the total charge flux through the cross section determined by this impact parameter.

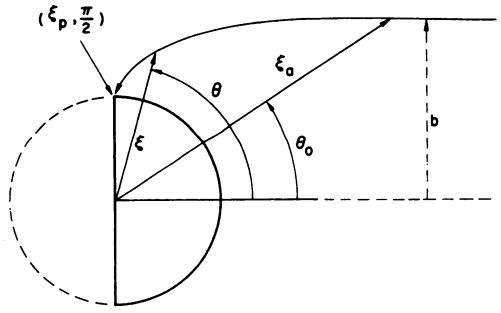

Figure 23-3. Positive Ion Trajectory in Rest Frame of Probe, Showing Coordinates ξ, θ and ξ_a, and the Impact Parameter b

23-3 CURRENT COLLECTION IN THE COLLISION DOMINATED REGION

The problem of interpreting the current collected by a supersonic, hemispherical electric probe in a collision dominated plasma is a basically different one. The plasma is still very dilute, and the charged particles are assumed to collide only with neutral molecules. The condition where charge trajectories are governed by collisions with the neutral molecules (that is, where the mean free path is much smaller than the probe dimension) demands an entirely different approach to calculating the current collection from the one used for the long mean-free-path case.

The ratio of the mean free path to the probe radius (the Knudsen number) has a value of about 0.01 at 60 km, and decreases exponentially below that. The processes governing charge motion under these conditions are the basic transport phenomena in dense gases: mobility and diffusion. In addition these calculations must consider the fact that the probe is moving at a supersonic velocity through the plasma, creating potentially difficult flow problems, and requiring the addition of a convection term to the transport equation. Finally, two charge species must be considered: positive and negative ions. In the altitude region of interest, the collision frequency is sufficiently high so that the number of electrons which do not become attached to neutral molecules, creating negative ions, may be ignored.

Two separate transport equations must, therefore, be considered (a single positive and a single negative species is assumed) along with the Poisson equation. These are:

$$eN\underline{v} - eNK\nabla V - eD\nabla N = \underline{J} \tag{23-2}$$

$$eN_{\_}\underline{v} + eN_{\_}K_{\_}\nabla V - eD_{\_}\nabla N_{\_} = \underline{J}_{\_} \tag{23-3}$$

$$\nabla^2 V = 4\pi e(N - N_{\_}) \tag{23-4}$$

In the above equations the charge density is N, the potential is V, the mobility constant is K, the diffusion coefficient is D, and the current density is $\underline{J}$. When these symbols appear without subscripts they refer to the positive species, and when they appear with negative subscripts they refer to the negative species. The mobility constant and the diffusion coefficient are assumed to be related by the Einstein relation, $K = eD/kT$. The convection term in Eqs. (23-2) and (23-3) involves the flow velocity $\underline{v}$ which must be calculated independently.

The above equations have been applied to a stationary spherical probe ($\underline{v} = 0$) by Su and Lam (1963) and by Cicerone and Bowhill (1967). Su and Lam obtained approximate analytic solutions for the density and potential distributions around

the probe for a small Debye length ($r_p >> h$). Cicerone and Bowhill obtained exact numerical solutions which were limited, because of available computer capacity, to relatively large Debye lengths ($r_p \lesssim h$), but were able to give analytic expressions which closely approximated the numerical results. Using the results of these studies, and assuming charge density values determined from Gerdien condenser measurements, theoretical current values were calculated for the present hemispherical probe assuming it to be stationary. Since the calculated currents were an order of magnitude smaller than the measured currents, it was inferred that in the present measurements convection was the dominant transport process. This appears to be in contrast to the conclusions of Sonin (1967) and Hoult (1965) for a blunt probe, namely, that for comparable probe potentials, the mobility or diffusion processes should dominate.

This is not to say, however, that the probe current may be approximated by simply eliminating the mobility and diffusion terms from the transport equations. An attempt must be made to analyze the neutral gas flow around the probe before the current flow can be analyzed.

23-3.1 Neutral Gas Flow

It is noted first, from the trajectory information, that between 40 and 60 km the probe is moving with a velocity of from 1.2 to 1.1 km/sec, or at a Mach number of just under 4. It is readily ascertained that through this region a detached shock wave should form in front of the probe, with the density, pressure and temperature of the neutral gas behind the shock substantially altered from the ambient values. These are the parameters which influence the transport coefficients in Eqs. (22-1) and (22-2), and may be determined from the ambient values using the Rankine-Hugonoit relations (Owczarek, 1964). It is also possible, using these relations and appropriate gasdynamic information, to estimate in some detail the flow pattern of the neutral gas around the probe.

For this analysis it will be assumed that the gas on both sides of the shock obeys the ideal gas law $P/\rho = RT$, where P is pressure, ρ is the gas density, T is the temperature (^{o}K), and R is the universal gas constant (equal to 8.31×10^{7} ergs/gm-mole-^{o}K). With ambient pressures and temperatures of the order of 0.1 mm Hg and $270^{o}K$, this assumption seems appropriate. Also, a value of $\gamma = 1.4$ will be assumed for the polytrope index since the ambient gas is diatomic. Since the significance of the following gas flow calculations will be more qualitative than quantitative, these assumptions are not critical.

From the Rankine-Hugonoit relations one may immediately compute the quantities shown in Table 23-2. This table shows the density, pressure, temperature and sound speed ratios across the shock, for a free stream Mach number of

Table 23-2. Gas Parameters Across Shock Wave. M = 3.7

Parameter	Normal Incidence	Sonic Line
$\frac{\rho_2}{\rho_1}$	4.4	4.2
$\frac{P_2}{P_1}$	16.1	13.1
$\frac{T_2}{T_1} = \frac{C_2^2}{C_1^2}$	3.64	3.17
M_2	0.44	1.0
$\lvert \underline{V}_2 \rvert$	$0.84C_1$	$1.8C_1$

3.7, at normal incidence and at the sonic point on the shock. This is illustrated in Figure 23-4. Subscripts 1 and 2 refer to the upstream (free stream) and downstream sides of the shock, respectively. The angle of incidence of the upstream flow at a particular point on the shock is $\pi-\xi$. The angle through which the flow is deflected from its incident direction upon crossing the shock (the turning angle) is δ. Table 23-2 and Figure 23-4 both illustrate conditions for a Mach number of 3.7.

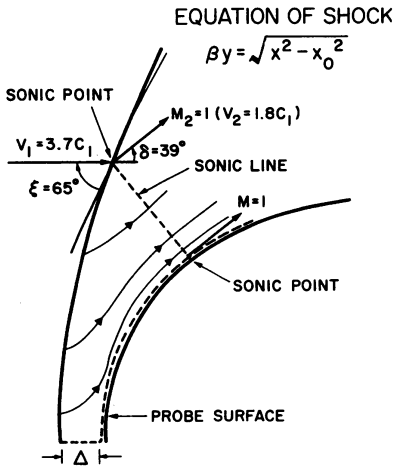

Figure 23-4. Supersonic Flow Past Sphere (M = 3.7), Illustrating Flow Pattern Behind Shock

A straightforward though rather involved technique for constructing an equation to represent the shape of the shock and to estimate the standoff distance Δ is given by Shapiro (1954). This procedure is considerably simplified by an independent estimate of the standoff distance which, under present conditions, is given with sufficient accuracy by $\Delta = 0.41\rho_1\rho_2 D$ (Van Dyke, 1957). Here D is the probe diameter and ρ_1/ρ_2 is the density ratio across the shock at normal incidence. Taking M as the local Mach number, one then fits a hyperbola of the form $\beta y = \sqrt{x^2 - x_0^2}$, where the vertex is at a distance Δ from the probe, $\beta = \sqrt{M^2 - 1}$, and hydrodynamic arguments, bearing on

the similarity of this flow to Laval nozzle flow, are used to give the coordinates of the sonic point ($M_2 = 1$). The angles ξ and δ are also calculated from the Rankine-Hugonoit relations.

To estimate the flow pattern behind the shock, as well as the values of the thermodynamic variables along the probe surface, it will be assumed that adiabatic compressible flow prevails behind the shock. One may write the Bernoulli equation for adiabatic compressible flow as

$$\frac{1}{2}\underline{v}^2 + w = \text{constant} \tag{23-5}$$

for each streamline, where the constant will in general be different for different streamlines (Landau et al, 1959). Here $w = c_v T + P/\rho$ is the heat function per unit mass, or enthalpy, and c_v is the specific heat at constant volume. This equation follows with the assumption that the entropy is constant at each point in the flow; that is, there is no heat transfer due to viscosity or to conduction. Since the boundary layer is very thin ($\sim .06 r_p$), there should be little effect of viscosity in the main flow field behind the shock. Using the following definitions and relations

c $= \sqrt{\gamma RT}$ is the local sonic speed,

γ $= c_p/c_v$ is the polytrope index,

c_p = specific heat at constant pressure,

M $= |\underline{v}|/c$ is the local Mach number,

P/ρ^γ = constant is the adiabatic gas law,

Eq. (23-5) yields the following relation between the pressures P and P' along the same streamline for corresponding Mach numbers M and M':

$$\frac{P'}{P} = \left\{ \frac{1 + (\gamma-1)M^2/2}{1 + (\gamma-1)M'^2/2} \right\}^{\gamma/(\gamma-1)} \tag{23-6}$$

Similar formulae may be derived to relate the density and temperature (and therefore the local sonic velocity) at two points on a streamline. Returning to Figure 23-4, let $P' = P_2$, $\rho' = \rho_2$, and $T' = T_2$, where the subscripts refer to conditions immediately behind the shock at normal incidence. If one now considers a streamline (shown dotted) passing close to the probe surface just outside the boundary layer ($\sim 0.06 r_p$), then conditions where this streamline crosses the sonic line ($M = 1$) may be calculated. These are listed in Table 23-3 and are

Table 23-3. Gas Parameters at Surface of Probe

Parameter	Stagnation Point	Sonic Point
$\frac{\rho}{\rho_1}$	4.8	3.0
$\frac{P}{P_1}$	18.4	9.7
$\frac{T}{T_1} = \frac{C^2}{C_1^2}$	3.8	3.15
M	0	1
$\lvert V \rvert$	0	$1.78C_1$

compared with their corresponding values on the upstream side of the shock to facilitate comparison with Table 23-2. In the same manner, Table 23-3 also lists the ratios of the stagnation point parameters to their free stream values.

These tables are given to indicate the range of variation of the various parameters which define the state of the gas behind the shock. Using numerical results for the pressure variation over a spherical surface as a function of position, given by van Dyke (1957), one may also use the Bernoulli equation to obtain the flow velocity along the probe as a function of position. Figure 23-5 shows the pressure variation for Mach numbers 1.3 and 5.8. The dashed curve was drawn to make the value of the pressure at the sonic point agree with that given by Eq. (23-6). In view of the assumptions behind Eq. (23-6), this discrepancy does not seem too large and this device allows us to see qualitatively how the velocity varies along the probe surface. This is shown in Figure 23-6 where the velocity is expressed in units of the free-stream sonic speed.

The important features to be noted in regard to the flow pattern are the uniformity of the flow velocity across the sonic line from the probe to the shock, and the rapid rise of the velocity profile away from the stagnation point toward the sonic point. The latter means that there is only a relatively small area around the stagnation point where the flow velocity is appreciably less than the free-stream sonic velocity. Finally, numerical solutions of the flow equations show that the streamlines are nearly parallel to the spherical surface behind the shock, except near the stagnation point (Maslen and Moeckel, 1957).

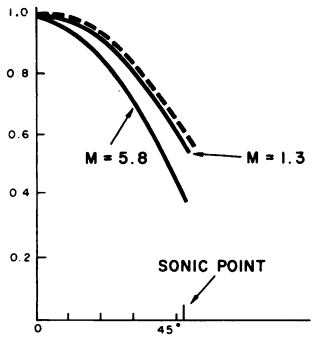

Figure 23-5 Pressure vs Distance From Stagnation Point

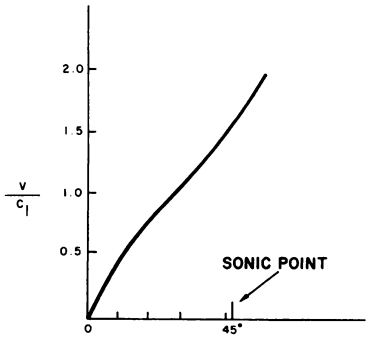

Figure 23-6 Velocity vs Distance From Stagnation Point

23-3.2 The Charge Transport Mechanism

Having established the nature of the bulk flow behind the shock, it is now possible to estimate the effect of the convection term in the transport Eqs. (23-2) and (23-3). Because of the extremely small concentration of charge ($\sim 10^{-10}$), any electrical effects on the bulk flow will be negligible. It will be supposed that the net effect of the convection will be to transport charge in a parallel flow over the surface of the probe along with the mass of neutral gas. This would evidently not contribute directly to the transport of charge to the probe, neglecting the stagnation point region. Superimposed upon this flow of charge will be a radial motion of charge due to the field at the surface of the probe. This may be computed from the mobility term in the transport equation.

To determine this motion, one should know the solution to the Poisson Eq. (23-4) in this region. However, if the drift velocity of the charges is estimated using a zero space charge solution to the Poisson equation, $\bar{v} = KV/r_p$ — using mobility values determined from Gerdien condenser measurements—it is found that for moderate to large probe voltages ($V \sim 10$), the drift velocity is small compared with the flow velocity. Taking, for example, a value for K at 60 km (see Figure 23-7) of $\rho_1/\rho_2 = 10^4$, corrected for the density change across the shock, $\bar{v} = 8 \times 10^3$ cm/sec. This is to be compared with a flow velocity at, say, the sonic line of $|\underline{v}| = 1.8c_1 = 5.7 \times 10^4$ cm/sec. It would then appear to be a plausible assumption that for most of the flow charge, separation does not have time to occur. Consequently, the effective space charge is small, and a free space field should be a good approximation over most of the probe. It also follows that if the charge distribution is not appreciably altered, the effect of diffusion will be negligible. As should be expected, the negative current shows an abrupt

change as the probe voltage is switched between -3V and -9V. Assuming the above flow pattern, with an electric drift considerably smaller than the flow velocity, the current density to the probe should be given essentially by the mobility term in Eq. (23-2): $\underline{J} = N_e K \nabla V$. If $\nabla V = V_p / r_p$, and assuming that these conditions prevail on the average over the whole probe surface, the total current to the probe becomes

$$I = 2\pi r_p N_e K V_p .$$

Here the quantity V_p includes, in addition to the applied probe potential, the potential on the rocket with respect to space, or vehicle potential. This latter quantity is generally uncertain, and use of it may be avoided by writing:

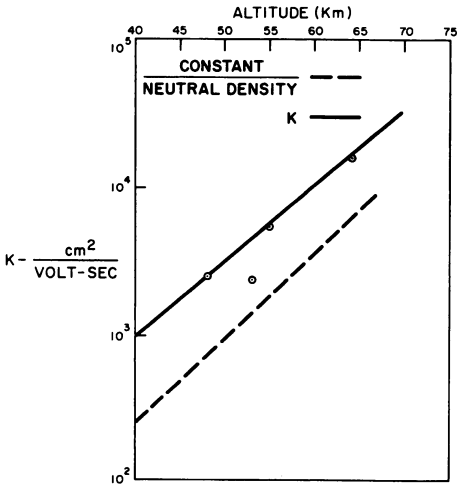

Figure 23-7. Positive Ion Mobility (Gerdien Condenser Measurements) vs Altitude

$$I_9 - I_3 = \Delta I = 2\pi r_p N_e K \Delta V,$$

where I_9 and I_3 refer to currents measured with applied voltages of -9V and -3V, respectively, on the probe. With ΔV = 6V, the final formula for the positive charge density becomes:

$$N = (12\pi r_p e)^{-1} \frac{\Delta I}{K} . \qquad (23\text{-}7)$$

23-4 RESULTS AND DISCUSSION

Positive ion densities calculated from the Langmuir current measurements obtained in the November 1968 PCA are shown in Figure 23-8 as the solid curve. In the upper segment, where the collisionless probe theory was used, the positive-ion densities are shown along with the impedance probe measurements of electron density (dotted curve). The densities from the Langmuir probe are calculated in this way down to 70 km, although the assumption of a long mean free path becomes questionable between 85- and 75-km. This profile represents a quiet nighttime lower E region, as determined from a number of other observations. The lower segments of the curves in this figure are ion density measurements from the

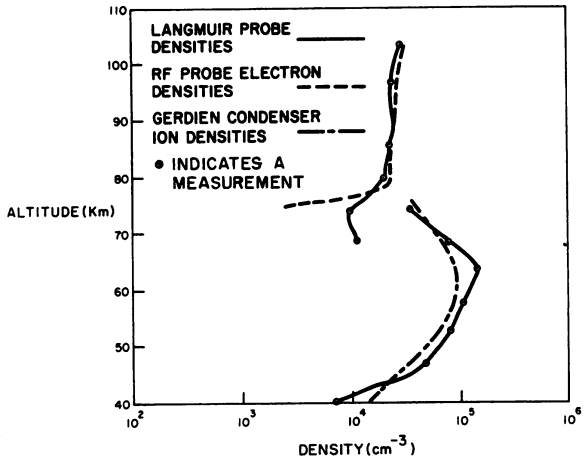

Figure 23-8. Comparison of Charge Density Measurements From Various Probes

Gerdien condenser (dotted curve) (Conley, 1971), and ion density measurements from the same Langmuir probe (solid line), the latter calculated using a probe theory for the collision-dominated region as described above.

The Langmuir probe densities shown here in the upper segment of the profile were obtained from current measurements with -3V applied to the probe. There was also an indicated vehicle potential on the order of -1V, putting a net potential on the probe of -4 V. Densities were also calculated with -9V applied to the probe (-10V net) giving an agreement well within experimental error. The densities which are shown from the Gerdien condenser in the lower segments of the curves were obtained from currents measured in the saturation mode, so that these density measurements are independent of the mobility measurements (Conley, 1971). Thus, while the Langmuir probe densities shown in this segment of the curve used the Gerdien condenser mobility measurements, the two density measurements as shown are independent. The discrepancy between the Langmuir probe measurements and the Gerdien condenser measurements does not seem too large for the present state of lower D-region measurements, and this degree of consistency should indicate an accuracy sufficient for a useful comparison with theoretical models. For these comparisons see Ulwick (1971).

The positive-ion densities calculated from the Langmuir probe currents for the November 1969 PCA are shown in Figures 23-9, 23-10, 23-11, and 23-12. Figure 23-9 shows the ion densities from the 3 November 1969 nighttime shot. As with the November 1968 measurements, these were made around local midnight. There was an aurora in progress, however, which accounts for

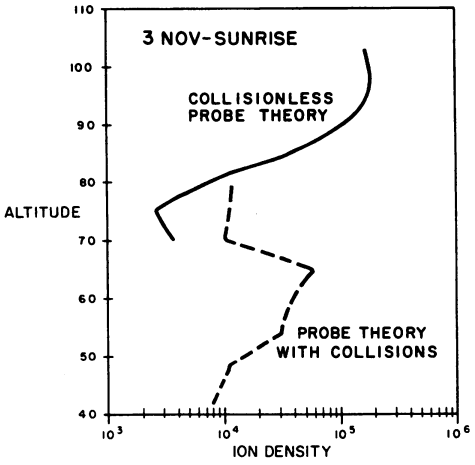

Figure 23-9. Langmuir Probe Ion Density - AJ17.758

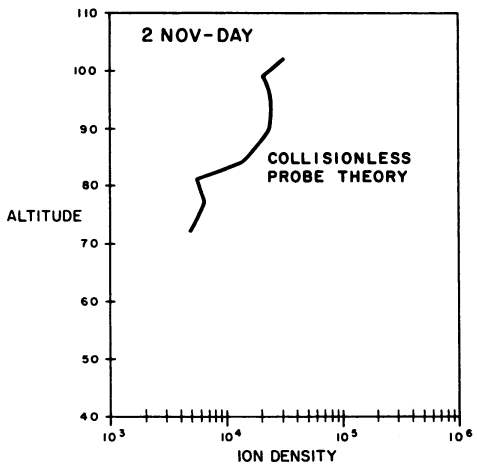

Figure 23-10. Langmuir Probe Ion Density - AJ17.602

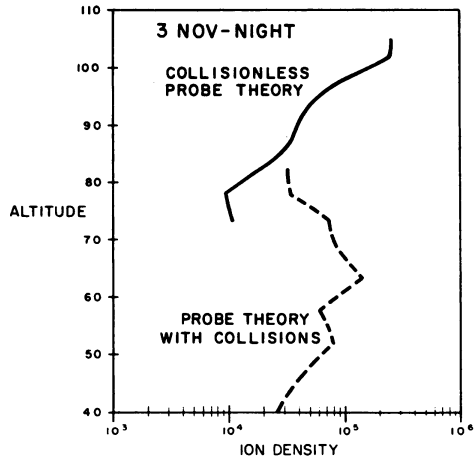

Figure 23-11. Langmuir Probe Ion Density - AJ17.616

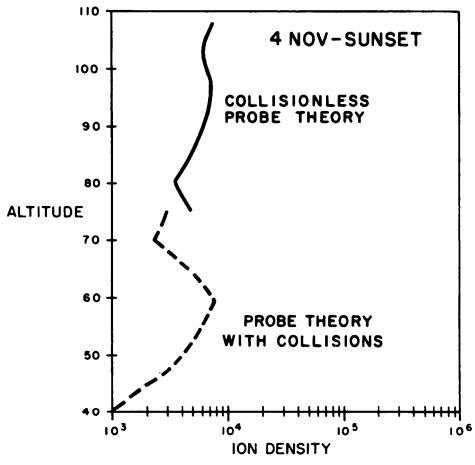

Figure 23-12. Langmuir Probe Ion Density - AJ17.617

the relatively high densities in the 85- to 100-km region which are over an order of magnitude higher than the corresponding November 1968 measurements. The measurements in the lower D region on both of these occasions are similar.

Figures 23-10, 23-11, and 23-12 show density curves from measurements made during full or partial daylight. Figure 23-10 shows just the higher altitude segment of the density curves measured about midday on 2 November 1969. The data from the lower altitudes were not usable. It will just be pointed out now that if these results are compared with simultaneous impedance probe measurements (Ulwick, 1971), they are seen to be lower by about a factor of 2. Figure 23-11 shows densities measured during a sunrise shot on 3 November with a χ angle of 89^{o}. The effect of an ionization buildup is seen at the upper altitudes, relative to the previous daytime densities, but these densities still tend to be substantially lower than the impedance probe results at the upper altitudes. The densities at the lower altitudes show the effect of the PCA flux, but there were no Gerdien condenser measurements available from this shot for comparison. Figure 23-12 shows densities obtained from a sunset shot on 4 November with a χ angle of 97^{o}. Once again a comparison shows that these Langmuir probe measurements are lower than simultaneous impedance probe measurements at higher altitudes by about a factor of 2, while the low-altitude Langmuir probe measurements are lower than simultaneous Gerdien condenser by about the same factor. These comparisons may be found in the paper by Ulwick (1971).

The whole set of Black Brant density measurements are discussed in detail by Ulwick (1971) in terms of their consistency with each other and other measurements, and in terms of other PCA parameters such as particle fluxes. The discussion here will be confined to the Langmuir probe results relative to the assumptions of the probe theory. It should be noted that the overall comparison of the density results involves three independent measurements—the impedance probe, the Gerdien condenser and the Langmuir probe. Looking at the two nighttime shots—November 1968 and 3 November 1969—the Langmuir probe ion densities in the collisionless altitude region show a reasonable quantitative agreement with the impedance probe electron densities. There is a similar quantitative agreement between the Langmuir probe ion-density measurements in the lower D region and the Gerdien condenser measurements. Inasmuch as these density measurements are also generally consistent with theoretical estimates of densities to be expected in the lower D region (for the given particle fluxes and a reasonable recombination coefficient), and with the measured absorptions, the first indication is that these langmuir probe measurements, as well as the other density, are reasonably reliable.

On the other hand, the daytime Langmuir probe density measurements are substantially and consistently lower than both the impedance probe measurements

in the higher altitude region, and the Gerdien condenser measurements in the lower altitude region. This suggests that there may be a difficulty common to this particular set of Langmuir probe measurements (that is, the daytime set), since the impedance probe and Gerdien condenser both give results, in different altitude regions, which are about a factor of 2 higher than the Langmuir probe measurements. It suggests, for example, that the current measurements during the daytime shots are consistently too low. It would at the same time increase the probability that the impedance probe measurements and the Gerdien condenser measurements, being consistent as well as independent, are substantially correct.

It is very difficult at this stage of the probe theory in the collision-dominated region to validate the set of assumptions to within a factor of 2. The results from the two nighttime shots show discrepancies with respect to other measurements of much less than a factor of 2 in this region, as well as in the higher altitude region. On the other hand, a factor of 2 is a very large discrepancy for the higher altitude theory, which agrees very closely with that of Kanal (1962) if it is extended to a spherical geometry (Richards, 1971). An hypothesis to explain this discrepancy would be a contamination of the probe surface combined with the effect of sunlight. Comparison of the present data with some data of Bunting and Heikkila (1970), comparing a contaminated Langmuir probe surface with a clean surface, suggests that surface contamination itself may have a significant effect.

No mechanism is suggested here for a combined effect of surface contamination and sunlight. Efforts have been made thus far, with the help of the results of Bunting and Heikkila, to fit various types of functions to the data in order to represent the electrical resistance which the contaminant presents to the current flow. The nature of the contaminant is not known, and as yet no definite results have been obtained.

In conclusion, the Langmuir probe positive-ion density measurements from this series of Black Brants, taken together with other simultaneous charge density measurements (Ulwick, 1971), give a consistent set of measurements of the charge densities in the two nighttime PCA events. The Langmuir probe measurements in full or partial sunlight, however, are substantially lower than those from the impedance probe and the Gerdien condenser. Much evidence indicates erroneous current measurements with the Langmuir probe, with surface contamination as a possible cause.

References

Bunting, W.D., Heikkila, W.J. (1970) Observations on the effects of surface conditions on Langmuir probes, J. Appl. Phys. 41(No. 5):2263-2284.

Cicerone, R.J. and Bowhill, S.A. (1967) Positive Ion Collection by a Spherical Probe in a Collision-Dominated Plasma, Aeronomy Report No. 21, University of Illinois, Urbana.

Conley, T.D. (1971) Positive Ion Concentrations in the Lower D Region During a PCA Event Measured by a Rocket-Borne Gerdien Condenser. See Chapter 24 of this publication.

Hoult, D.P. (1965) D-region probe theory, J. Geophys. Res. 70:3181.

Kanal, M. (1962) Theory of Current Collection of Moving Spherical Probes, Scientific Report No. JS-5, ORA No. 03484, 03599-9-S, Space Physics Research Lab., University of Michigan.

Kanal, M. (1965) Theory of Current Collection of Moving Cylindrical Probes, Scientific Report No. GS-3, 04304, 03484-11-S, Space Physics Research Lab., University of Michigan.

Langmuir, I. and Mott-Smith, H.M. (1926) The theory of collectors in gaseous discharges, Phys. Rev. 28.

Landau, L.D., and Lifschitz, E.M. (1959) Fluid Mechanics, Addison-Wesley, Reading (Ma.)

Maslen, S.H., and Moeckel, W.E. (1957) Inviscid hypersonic flow past blunt bodies, J. Aeron. Sci. 24.

Owczarek, J.A. (1964) Fundamentals of Gas Dynamics, Scranton.

Richards, E.N. (1970) Positive Ion Densities from a Rocket Borne Hemispherical Langmuir Probe: 40 to 100 Km., Final Report, AFCRL-71-0145.

Sandock, J.A. (1971) Daytime Charged Particle Measurements Made with Rocket-Borne Probes on 3 November 1969. See Chapter 25 of this publication.

Shapiro, A.H. (1954) Dynamics and Thermo-dynamics of Compressible Fluid Flow, Vol. II, New York.

Sonin, A.A. (1967) Theory of ion collection by a supersonic atmosphere sounding rocket, J. Geophys. Res. 72:4547.

Su, C.H. and Lam, S.H. (1963) Continuum theory of spherical electrostatic probes, Phys. Fluids 6:1479.

van Dyke, M.D. (1957) The supersonic blunt-body problem—review and extension, J. Aerospace Sci. 24:683.

Walker, E.H. (1965) Plasma sheath and screening around a stationary charged sphere and a rapidly moving charged body, Interactions of Space Vehicles with an Ionized Atmosphere, S.F. Singer, Ed., Pergamon Press, New York.

Ulwick, J.C. (1971) Comparison of Black Brant Rocket Measurements of Charged Particle Densities During Solar Particle Events. See Chapter of this publication.

Contents

24. Positive Ion Concentrations in the Lower D Region During the November 1969 Solar Particle Event Measured by a Rocket-borne Gerdien Chamber

T.D. Conley
Air Force Cambridge Research Laboratories
Bedford, Massachusetts

24-1 INTRODUCTION

During the PCA of November 1969, Gerdien chambers were flown on all six Black Brant rockets of the Ulwick series. On each rocket, the Gerdien chamber was carried on a boom which was deployed approximately 50 sec after launch. Of the six rockets flown, one lost stability and failed, and another suffered a premature deployment of the boom which, due to the heavy air drag, caused the loss of the boom. Consequently, of the six Ulwick rockets, good quality Gerdien chamber data were obtained on four flights. The results obtained from these four flights are presented in this paper.

The Gerdien chamber is essentially a coaxial cylinder as shown in Figure 24-1 and has been used for many decades to measure ion density and conductivity in the laboratory or at sea level conditions. Ions entering the instrument are collected at a rate proportional to the potential difference between the inner and outer electrode. A typical current-voltage curve is also shown in Figure 24-1. The current saturates when all the ions entering the cylinder are collected.

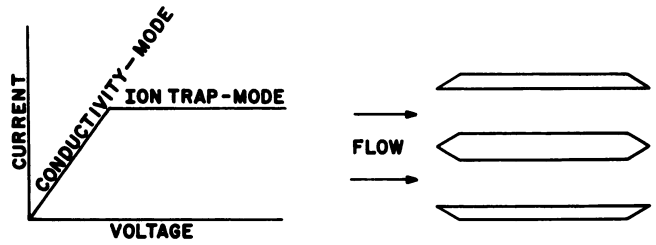

Figure 24-1. The Gerdien Condenser

24-2 MEAN FREE PATH CONSIDERATIONS

When a probe is used for measurements on rockets, a rarefied regime is eventually reached where the sea level operating theory described in Figure 24-1 is no longer appropriate. It is thus instructive to discuss the effects of various flow regimes on a rocket-borne probe. The flow field around a rocket or a rocket-borne probe at supersonic velocities can be divided into free stream, shock front, inviscid flow behind shock front, and boundary layer. Techniques for evaluating the flow characteristics have been found to be applicable only over a certain range of height conditions. Since theoretical and experimental techniques used to evaluate the flow aerodynamically are different for each of these regimes, we would expect similarly that the techniques for evaluating electrical probes to change with each regime. For example, in the free-molecule flow regime, interparticle collisions do not occur, and for stationary probes this case is covered by the original theory of Langmuir. In the slip and transition regimes, the Langmuir current will be modified by collisions between the collected particles. In the continuum regime, particle collection is described by conduction and diffusion. These aerodynamic regimes are separated according to Knudsen number K_n - the ratio of mean free path to a characteristic flow length. If we classify the characteristic length of the Gerdien chamber as the diameter of the outer cylinder (8.9 cm), the flow regime vs altitude become as is shown in Figure 24-2. According to this classification, continuum concepts are applicable only below 70 km,

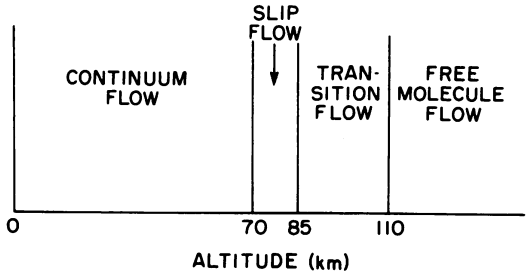

Figure 24-2 Flow Regimes of the Gerdien Condenser

and free molecule flow applies at altitudes above 110 km. In between these altitudes, slip and transition flow prevail.

The classical operation of Gerdien condenser described in Figure 24-1 essentially concerns the use of a probe in the continuum or collision controlled regime.

24-3 PROBE THEORY WITH COLLISIONS

The operation of the Gerdien condenser as shown in Figure 24-1 assumes that particles enter the chamber by convection. The random thermal motion of the particles is thus altered by this convection velocity, and the particles drift toward the end of the tube. The random motion of the charged particles is also altered by the applied radial electric field in such a manner that the charged particles drift towards the collector as well. The drift velocity of the charged particles towards the collector is dependent on their mobility and the strength of the electric field, whereas the drift velocity towards the end of the tube depends of course on the convection velocity. If the electric field is large enough so that all the ions entering the tube reach the collector before the exit is reached, the current saturates. Fundamentally, then, the charge collection in a Gerdien chamber in a collision controlled regime is the result of conduction.

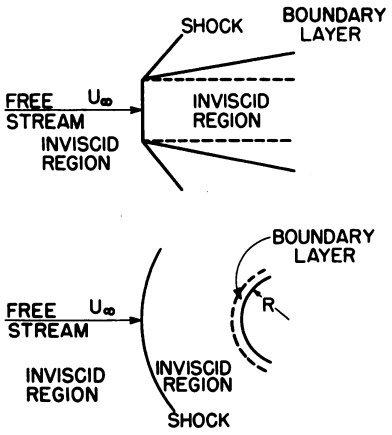

Figure 24-3. Poiseuille and Stagnation Boundary Layer Flow Models

Sonin (1967) and Hoult (1965) showed that the above theory of operation in Poiseuille flow is applicable to a wide class of probes associated with stagnation boundary-layer flows. Consider the flow models shown in Figure 24-3. At large Reynolds numbers, the flow separates into two distinct regions. Electrically, however, there are three distinct regions where different physical mechanisms operate:

(1) Inviscid Region - Convection, diffusion, and conduction all operate in this region. The latter two are unimportant compared with convection. The ambient charge species concentrations and charge neutrality are maintained by convection.

(2) Boundary Layer - Convection, diffusion, conduction operate simultaneously. The effect of convection decreases with distance from the edge of the boundary layer toward the electrode. Charge neutrality is maintained by convection.

(3) Diffusion Layer - As we near the probe surface, convection becomes increasingly negligible. Diffusion and conduction are the main transport mechanisms.

In this analysis it is assumed that the charged particle number density is so small that the space-charge electric field can be neglected, compared with the applied electric field. If the charge density were large, the lines of force emanating from these charges can be comparable in density to those of the imposed electric field of the probe. Thus the electric field is altered, and the potential drop is no longer linear with distance from the electrode. For the cylindrical case, Poisson's equation can be written as:

$$\frac{d^2\phi}{dr^2} + \frac{1}{r}\frac{d\phi}{dr} = \frac{ne}{\epsilon} \qquad (24\text{-}1)$$

where

ϕ = potential

e = electron charge

ϵ = permittivity of free space

Siksna and Lindsay (1959) have shown that the resulting field for a coaxial cylinder is

$$E(r) = \frac{\phi_\rho}{r \ln\frac{b}{a}} - \frac{ne}{2\epsilon}\left(r - \frac{b^2 - a^2}{2r \ln\frac{b}{a}}\right) \qquad (24\text{-}2)$$

where

ϕ_ρ = applied potential on outer cylinder

b = radius of outer cylinder

a = radius of inner cylinder

The electric field produced near the outer electrode by various charge densities is shown in Table 24-1.

Table 24-1

Charge Densities	Space Charge Field
10^6 cm^{-3}	2.5 V/cm
10^5 cm^{-3}	0.25 V/cm
10^4 cm^{-3}	0.025 V/cm
10^3 cm^{-3}	0.0025 V/cm

The extent to which the field is distorted depends of course on the strength of the applied electric field. For an applied potential of 10 V, the applied electric field at outer cylinder is on the order of 2.5 V/cm. This is comparable in magnitude to the space charge field from a charge density of 10^6 cm^{-3} but much larger in magnitude than the field from a charge density of 10^5 cm^{-3}. PCA charge densities reach 10^5 cm^{-3} in the D region. The applied potential is swept from 0 to 50 V. The space charge will therefore have an effect only at the initial portion of the sweep where the field is small.

24-4 THE CURRENT-VOLTAGE CHARACTERISTICS OF THE GERDIEN CONDENSER

The general equation for current collection is:

$$J = -ed\nabla n + Kne\nabla\phi + neU \qquad (24\text{-}3)$$

where

J = current density
D = coefficient of diffusion for the charge specie
K = mobility of charge specie
n = charge particle number density
ϕ = potential
U = convection velocity
e = electrostatic charge

The first term in Eq. (24-3) represents the net contribution of diffusion to the transport of charge to the collector. The second term represents the contribution of mobility or conduction, and the third term represents the contribution of convection.

In the diffusion layer, the convection term disappears and we have

$$J = -eD\nabla n + Kne\nabla\phi \, . \qquad (24\text{-}4)$$

We now make the assumption that the probe potential is large so that the first terms in Eq. (24-4) is negligible compared with the second. Using Einstein's relation for classical diffusion,

$$\frac{D}{K\phi} = \frac{kT}{e\phi} , \tag{24-5}$$

the diffusion term D is smaller than the mobility term by the ratio $\frac{kT}{e}$, provided that the characteristic lengths of the gradients of n and ϕ are the same order of magnitude. In the D region, the value of $\frac{kT}{e} \leq 0.03$ V, so that for probe potentials much greater than this, Eq. (24-4) becomes simply

$$J = Kne\nabla\phi . \tag{24-6}$$

Eq. (24-6) holds for any probe large enough to be in continuum flow in the D region.

For a Gerdien chamber with no space charge, the potential gradient $\nabla\phi$ can be obtained easily from the Laplacian.

$$\frac{d^2\phi}{dr^2} + \frac{1}{r}\frac{d\phi}{dr} = 0 \tag{24-7}$$

whose general solution is

$$\phi = A \ln r + B . \tag{24-8}$$

The constant A is determined in terms of the charge density per unit length σ_L giving:

$$\phi = -2\sigma_L \ln r + B . \tag{24-9}$$

The potential on the inner electrode a is

$$\phi_a = 2\sigma_L \ln(a) + B . \tag{24-10}$$

The potential on the outer electrode b is

$$\phi_b = 2\sigma_L \ln(b) + B . \tag{24-11}$$

The potential difference between the two cylinders is

$$\phi_b - \phi_a = 2\sigma_L \ell n(b/a) \tag{24-12}$$

and

$$\frac{d\phi}{dr} = \frac{2\sigma_L}{r} .$$

Let $\phi_b - \phi_a = \phi$; then,

$$2\sigma_L = \phi/\ell n(b/a) , \tag{24-13}$$

and

$$\frac{d\phi}{dr} = \frac{\phi}{r\, \ell n(b/a)} . \tag{24-14}$$

The drift velocity v_d of the charged species to the collector depends on the mobility and the potential gradient

$$v_d = K\frac{d\phi}{dr} = K\frac{\phi}{r\, \ell n(b/a)} . \tag{24-15}$$

The current density to the collector can therefore be written as

$$J = nev_d$$

or

$$J = ne\frac{dr}{dt} . \tag{24-16}$$

If air flows into the cylinder with a velocity U, and x is the coordinate along the axis of the cylinder, then

$$\frac{dx}{dt} = U \text{ and } dt = \frac{dx}{U} = \frac{\ell n(b/a) r dr}{K\phi} \tag{24-17}$$

so that

$$Ur\, dr = \frac{K\phi dx}{\ell n(b/a)} . \tag{24-18}$$

When all the ions, moving radially from b to a are collected along the length of the electrode,

$$\pi U \int_a^b r\, dr = \frac{\pi K \phi_s L}{\ell n(b/a)} \tag{24-19}$$

where

ϕ_s = saturation potential.

If ϕ is less than saturation, the ions reaching the electrode come from a smaller area of the cross section and the number is integrated from a→ y:

$$\pi U \int_a^y r dr = \frac{\pi K \phi L}{\ell n(b/a)}. \tag{24-20}$$

Integrating Eq. (24-19), we find

$$\pi U (b^2 - a^2) = \frac{2\pi K \phi_s L}{\ell n(b/a)}. \tag{24-21}$$

If n is the number density of ions flowing into the chamber, the rate of supply of charge Q is

$$Q = neAU \tag{24-22}$$

where

A = inlet area A.

In terms of the radii b and a, the inlet area is

$$A = \pi(b^2 - a^2) \tag{24-23}$$

and

$$Q = ne\pi (b^2 - a^2) U . \tag{24-24}$$

When $\phi \geq \phi_s$ all the ions are collected and the current I is

$$I = ne\pi(b^2 - a^2) U = \frac{2\pi neK\phi_s L}{\ell n(b/a)} \tag{24-25}$$

Eq. (24-27) can be simplified by considering the capacitance. The capacitance of a coaxial cylinder in electrostatic units is

$$C = \frac{L}{2\ell n(b/a)} . \tag{24-26}$$

In terms of the capacitance, in cgs units,

$$I = 4\pi\, neKC\phi_s . \tag{24-27}$$

Or in the mks system,

$$I = \frac{neKC\phi_s}{\epsilon} . \tag{24-28}$$

The instrument operates in a similar manner if the electric field is reversed and negative charged particles are collected. The saturated current I_s is then proportional to $U(N_e + N^-)$. Electrons having an extremely high mobility will be collected at a small electric field. In the PCA series, however, only positive ions were measured.

A sample current voltage characteristic is shown in Figure 24-4(a). The characteristic is indicative of two types of positive ions of different mobilities. As shown in Figure 24-4(b) the saturation current is proportional to $(n_1^+ + n_2^+)$ U. The slope of the current-voltage characteristic is proportional to $(n_1^+ K_1 + n_2^+ K_2)$ for $\phi < \phi_1$ and proportional to $n_2^+ K_2$ for $\phi_1 < \phi < _2$. In order to obtain information about the charge particle density, either K or U must be known. If K is known and U unknown, the slope of the current-voltage characteristic can be used to determine n. If K is unknown and U known, the saturated current can be used to determine n and the slope of the characteristic used to determine K. In Figure 24-4, the relative charge concentrations can be obtained from I_1, I_2 and U. The average mobility can be obtained from the voltage at point M. In order to obtain the characteristic shown in Figure 24-4, the driving electrode was swept with a sawtooth waveform that varied from 0 - 50V in 1 sec as shown in Figure 24-4(c).

At altitudes above 70 km, the current is no longer proportional to applied voltage. Experimental data seems to verify this. Figure 24-5 shows a plot of saturation voltage vs altitude obtained from an earlier rocket flight. The rocket was launched on 6 December 1967 1015 CST from Churchill Research Range during an auroral absorption event. The figure shows the expected exponential relation between altitude and the voltage required for saturation until an altitude of 68 km is reached. Above 68 km, the current saturates at a constant low

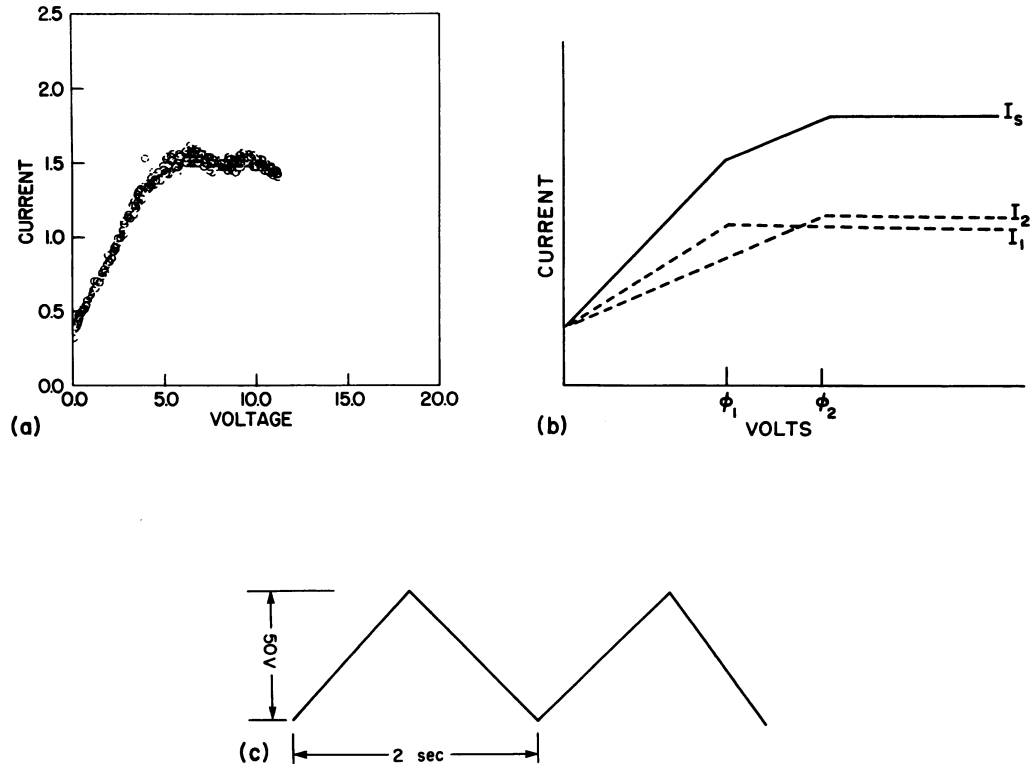

Figure 24-4. Current-Voltage Characteristic. (a) Experimental, (b) theoretical, and (c) driving voltage sweep

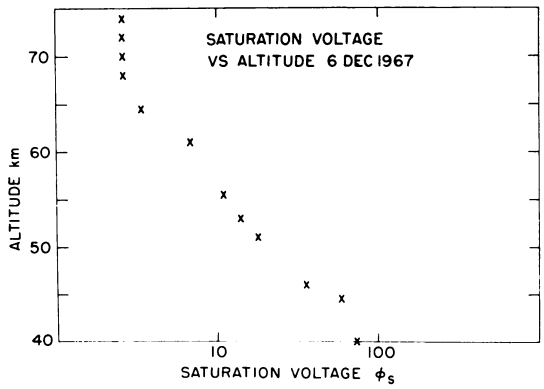

Figure 24-5. Saturation Voltage vs Altitude

applied voltage. The instrument functions only in the ion trap mode above 68 km.

24-5 SUPERSONIC FLOW CONSIDERATIONS

As discussed in the previous section, one of the fundamental problems in operating the Gerdien chamber is to calculate the volume rate of flow through the condenser so that one can calculate the ion density from the saturation current. The problem is similar to that of the intake to a jet engine. Consider the flow through a simple ram intake at supersonic velocities. Let the inlet area be A; the flow rate at subsonic velocities would then be

$$Q = \rho AU \tag{24-29}$$

where

ρ = mass density.

In the supersonic case, the flow enters the intake in a manner similar to that shown in Figure 24-6(a). If the flow is less than ρAU, then from continuity considerations, it is necessary for the excess flow to be deflected around the leading edge of the intake. This requires the bow shock to be detached from the leading edge so that the flow can be deflected as shown in Figure 24-6(b). The bow shock occurs ahead of the intake no matter what the internal configuration is, provided $Q < \rho AU$. The criteria for determining whether the bow shock is detached, attached or swallowed depends on the Mach number and the boundary layer thickness. The growth of the boundary layer reduces the cross-section area available

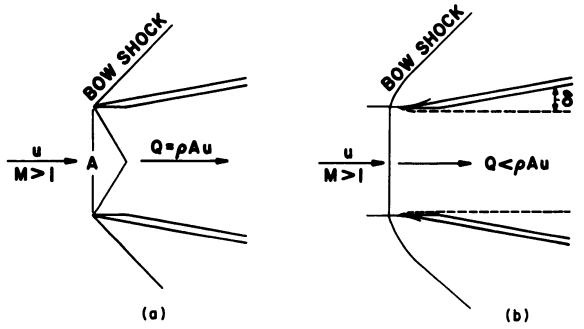

Figure 24-6. Bow Shock on the Inlet. (a) Attached shock, and (b) detached shock

for the core flow. The diameter reduction is proportional to the layer thickness δ:

$$\delta \simeq 5 \frac{L}{\sqrt{Re_L}} \tag{24-30}$$

where

L = distance from inlet and

Re_L = length Reynolds No.

The minimum area reduction in the Gerdien condenser allowed without changing the effective flow capture is determined by the swallowing function $Q(M) = A_{th}/A$, where A_{th} = cross-section area of throat.

The swallowing function depends on the Mach number and the ratio of specific heats

$$Q(M) = \left(\frac{\gamma-1}{\gamma+1}\right)^{1/2}\left(\frac{2\gamma}{\gamma+1}\right)^{\frac{1}{\gamma-1}}\left(1+\frac{2}{\gamma-1}\frac{1}{M^2}\right)^{1/2}\left(1-\frac{\gamma-1}{2\gamma}\frac{1}{M^2}\right)^{\frac{1}{\gamma-1}}. \tag{24-31}$$

This formula, however, depends upon assumptions which are not valid at the lower Reynolds numbers which occur at higher altitudes because the boundary layer will merge within the probe. It was therefore necessary to determine experimentally the mass flow efficiency of the instrument in a wind tunnel. This was accomplished by performing pressure measurements at various simulated altitudes and Mach numbers.

The instrument is shown in the wind tunnel in Figure 24-7. The figure shows the instrument with pressure orifices attached in front of a Mach 3 nozzle. The rf loop in front of the nozzle was used to illuminate the flow about the inlet. The figure shows the location of the detached bow shock at a simulated altitude of 86 km. The effect of altitude on the position of a Mach 3 bow shock is shown in Figure 24-8. The ratio of the most forward static pressure orifice P_1 and the ambient pressure P_∞ is the ordinate. The ratio remained constant with decreasing altitude until an altitude of 72 km where the ratio decreased rapidly, indicating the shock became attached and swallowed by the inlet. For a Mach 2 flow, the shock did not become attached until an altitude of 56 km.

A typical Mach profile for the Black Brant with an Ulwick payload is shown in Figure 24-9. In the altitude regime between 40 and 80 km, the Mach number is in the Mach 3 range and in this region approximates the wind tunnel test conditions

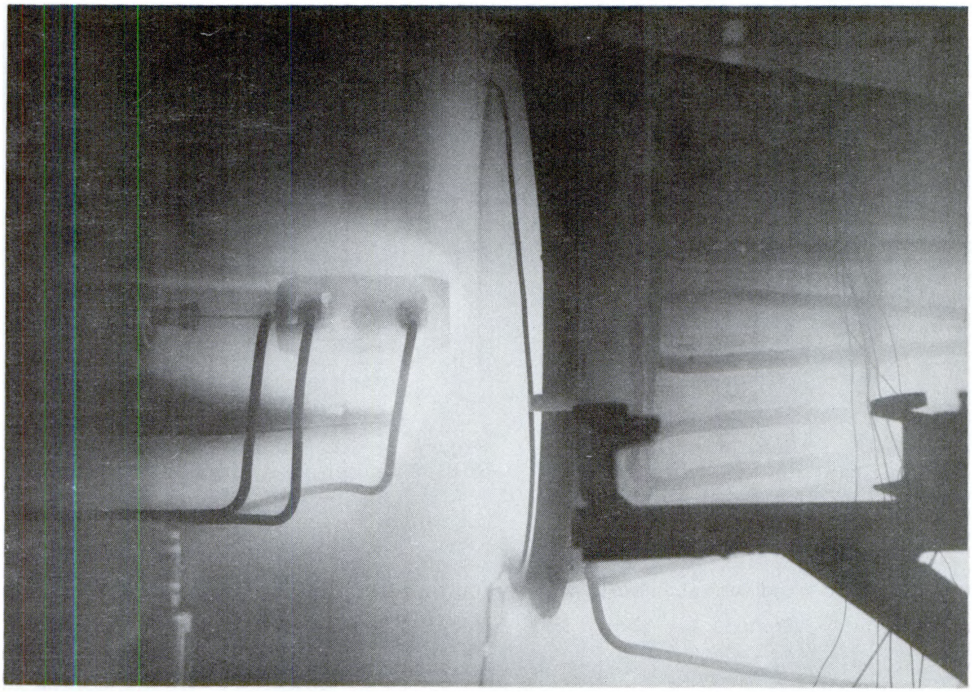

Figure 24-7. The Gerdien During Wind Tunnel Calibrations

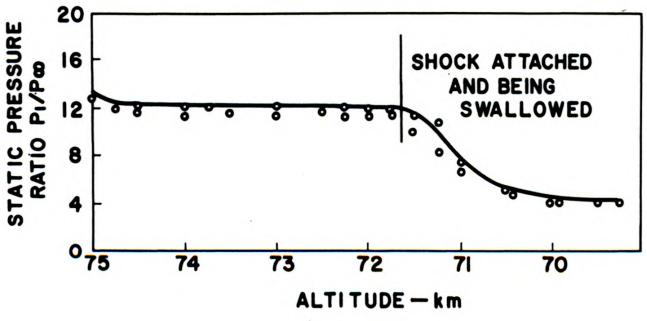

Figure 24-8. The Effect of Altitude on the Bow Shock at Mach 3

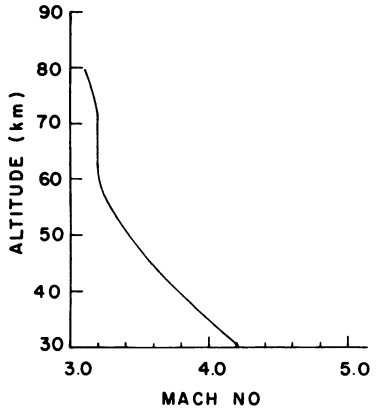

Figure 24-9. Typical Mach Profile of a Black Brant Rocket with Ulwick Payload

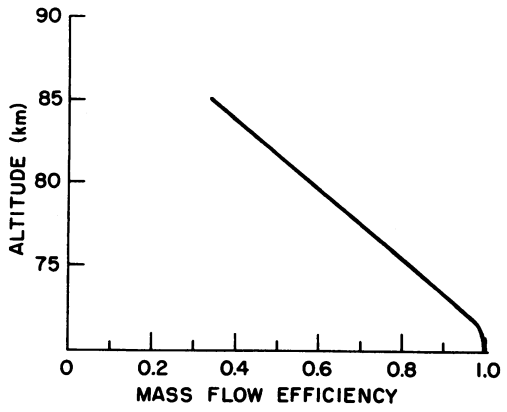

Figure 24-10. Mass Flow Efficiency of the Gerdien vs Altitude at Mach 3

very well. The wind tunnel results were used to determine the mass flow efficiency versus altitude. Results are shown in Figure 24-10.

24-6 ROCKET FLIGHT RESULTS

24-6.1 Positive Ion Mobility

In the analysis of the data, the saturated current can be used to determine the positive ion concentration. The slope of the voltage—current characteristic can be used to investigate the mobility of the ions. As shown in Figure 24-4, the voltage-current characteristic tends to indicate that two types of positive ions of different mobility are present. It was not possible, however, to determine the mobility of each ion because the slope of the characteristic varied with the direction of the sweep of the driving voltage. The cause of this behaviour is not known. Perhaps it is due in part to the effects of a space charge field discussed earlier, or a surface contamination on the wall of the Gerdien chamber causing a sort of hysteresis effect. The mean slope, however, remained stable from increasing to decreasing sweep of the driving voltage. It was consequently feasible to determine the mean mobility of the ion distribution. The mobility of the ions varies directly with altitude according to the relation

$$\rho_o K_q (T) = \rho_\infty K_\infty (T) \qquad (24\text{-}32)$$

where

$K_o(T)$ = mobility at STP

ρ_o = density at STP

It was difficult to determine the mobility using the slope method on descent because the rocket was tumbling and the aspect angle was continually changing. Consequently, the saturation voltage was used to determine the mobility on descent. The two techniques are compared in Figure 24-11 using data from two earlier measurements (December 1967, November 1968). The slope method was used on the ascent data of November 1968. This flight occurred during a PCA event. The saturation voltage was used on both ascent and descent data of 6 December 1967. This flight occurred during an auroral absorption event. Close agreement exists between the two techniques, considering the errors involved in reading the data. Also shown in the figure is a theoretical calculated profile using a CIRA mean atmosphere and a representative value of reduced mobility K_o of 1.8 $cm^2\ V^{-1}\ S^{-1}$. From the data it appears that the mean ion mobility is approximately a factor of 1.5 larger than the small ion mobilities measured in the laboratory.

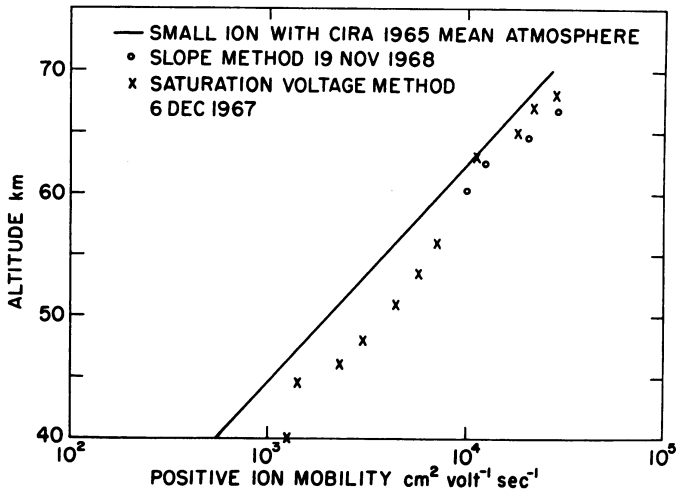

Figure 24-11. Positive Ion Mobility vs Altitude

24-7 POSITIVE ION CONCENTRATIONS

As indicated in the introduction (Section 24-1), the Gerdien condenser was carried on a boom which was deployed approximately 50 sec after launch. Consequently, on ascent, measurements were not made until an altitude of 57 to 60-km was reached. On descent, data was continually obtained until the increasing drag tore the boom off at an altitude usually below 40 km. In this series of measurements, however, saturation current was generally not obtained below 45 km due to limited range of driving voltage (50V).

At an altitude of 40 km, for example, a driving voltage of 80V would have been necessary to saturate the current. Since the saturation current is the most reliable indication of change particle concentration, the data below 45 km is ignored for the purposes of this paper.

The data from four flights during the PCA are presented in this paper. The launchings were made on the following dates:

Date	Time	Solar Zenith Angle
2 Nov 1969	1420 CST	79^{o}
3 Nov 1969	0005 CST	136.2^{o}
3 Nov 1969	1111 CST	74.5^{o}
4 Nov 1969	1708 CST	96.8^{o}

The data from the first flight is shown in Figure 24-12. This represents the ion profile approximately 8 hr after the onset of the event. The ascent data (solid curve) is drawn from 57 to 85 km. The descent data (dashed curve) is portrayed from 45 to 85 km with a hiatus in the region 67 to 74 km. The data in this region was not shown because it was noisy and difficult to interpret.

Good agreement exists between ascent and descent. Variations are attributed to measurement errors due to rapidly changing aspect of the Gerdien aperture with the velocity vector which occurs only on descent. This applies to all four rocket flights. The profile shows a minimum in the 70 km region and a maximum near 50 km, decaying rather rapidly below 50 km.

The second flight occurred approximately 18 hr after the onset of the event. The positive ion profile is shown in Figure 24-13. This is the only nighttime flight among the four launchings. Ascent data begins at about 59 km on this flight. Descent data was available to about 46 km. Good agreement is obtained between ascent and descent. The variation is attributed to aspect sensitivity on decent as noted in the first flight.

The third rocket was launched approximately 29 hr after the onset of the event. The positive ion profile is shown in Figure 24-14. Ascent data was obtained

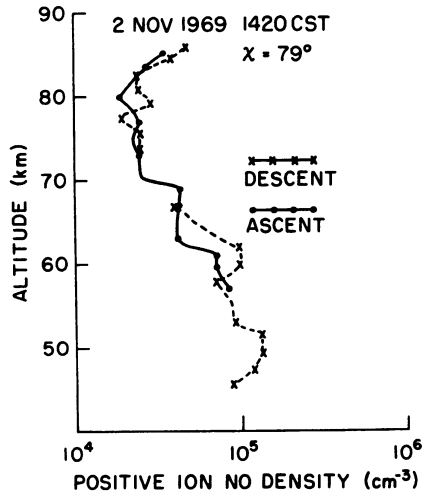

Figure 24-12. Positive Ion Profile on 2 November 1969 1420 CST

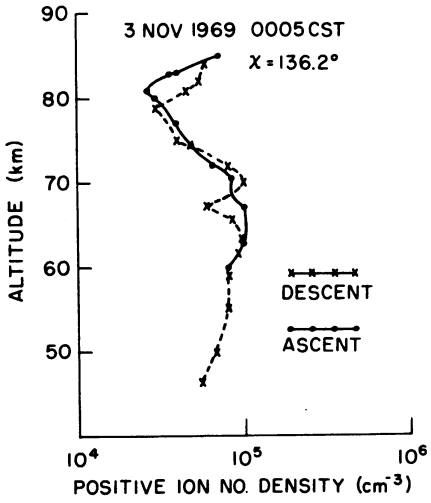

Figure 24-13. Positive Ion Profile on 3 November 1969 0005 CST

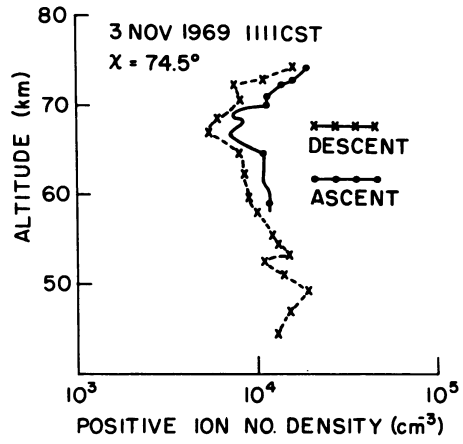

Figure 24-14. Positive Ion Profile on 3 November 1969 1111 CST

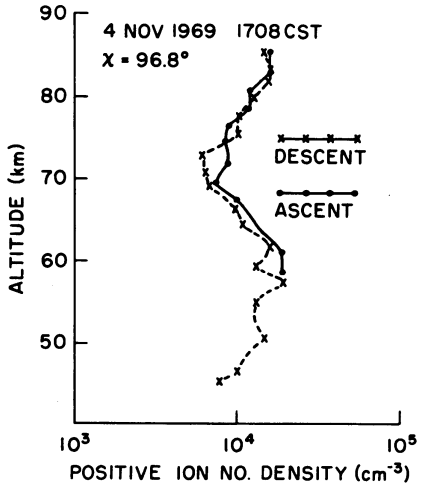

Figure 24-15. Positive Ion Profile on 4 November 1969 1708 CST

beginning at 58 km. Data on this flight was limited to an altitude of 75 km. Ion saturation-current data above this altitude was not usable. The electrode arrangement for this flight was changed. The inner electrode was used as both the collector and driving electrode to determine the change in the edge effect. The electric field lines in this arrangement are different from the arrangement where the external electrode is used as the driving electrode. The field lines in the former case influence the ions which are not originally in the measured volume of air, making the effective area for ion collection larger with increasing electric field. Thus, saturation is not cleanly reached for charged particles of large mobility such as the positive ions above 75 km. For charged particles of lower mobility, such as positive ions below 75 km, the electric field outside the chamber is sufficiently weak that it has little influence on the ions outside the chamber. Consequently, saturation is cleanly reached. Descent data was obtained to nearly 44 km. Good agreement is obtained between ascent and descent.

The fourth rocket was launched approximately 59 hr after the beginning of the solar cosmic event during sunset conditions. The positive ion profile at this time is shown in Figure 24-15. Again, ascent data is shown as the solid curve beginning near 58 km. Close agreement exists between ascent and descent.

24-8 CONCLUSIONS

The rocket-borne Gerdien condenser has been developed into an extremely useful instrument to measure positive ions in the D region. The instrument has been calibrated in the wind tunnel under supersonic conditions. Data obtained from two electrode arrangements indicate that using the outer electrode as the driving electrode with a guard electrode at each end and the inner electrode as the collector will give the cleanest saturation current. Data above 85 km has not been used because the effective aperture of the cylinder has not been calibrated.

References

Hoult, D. P. (1965) D-region probe theory, J. Geophys. Res. 70:3183 - 3187.

Siksna, R. and Lindsay, R. (1959) Air ions produced by a trituim - ion generator II measurements of ions in a room - mobility, Arkiv Geofysik 3(No. 9).

Sonin, A. A. (1967) Theory of ion collection by a supersonic atmospheric sounding rocket, J. Geophys. Res. 72:4547 - 4557.

Contents

25. Ion Measurements Made by Collapsing the Space Charge Sheath on a Spherical Rocket Probe

J.A. Sandock
Ionospheric Physics Laboratory
Air Force Cambridge Research Laboratories
Bedford, Massachusetts

Abstract

On 3 November 1969, a Black Brant rocket carrying a spherical retarding potential analyzer was launched at 11:00 local time when the solar zenith was 74.1 deg. The aperture voltage of the analyzer was varied by 0.25 V in seven steps, in an effort to collapse the space charge sheath during one of the steps. The results produced a family of curves which, when compared with the theoretical results of Kanal for the sheath radius, are consistent with the measurements at low accelerating voltages of 0.25, 0.50, and 0.75 V. At a high accelerating voltage (-9 V), the current to the probe has increased by a factor of 10 as compared to the current at space potential. Kanal's "Theory of Current Collection of Moving Spherical Probes" has been applied to explain this factor. Analysis of the data at space potential shows that the ion density reached a value of 3×10^5 ions/cm^3 at 95 km.

25-1 INSTRUMENTATION

Kanal (1962) in his theory of a moving probe extended the Langmuir and Mott-Smith (1926) theory to a spherical probe moving in the free molecular flow

regime of the ionosphere. The shape of the positive ion sheath was assumed to be spherical and the size of the sheath clearly defined.

A semiempirical approach was taken in the design of a spherical retarding potential analyzer, which would at some time during its programmed cycle, collapse the ion sheath by placing the aperture grid at space potential. By eliminating the problem of the ion sheath, a more accurate ion density and temperature would be obtained from the probe.

After the positive ion density profile was determined, further study of the data in the accelerating region was undertaken. The experimental results from the probe were compared to the theoretical predictions of Kanal.

25-2 INSTRUMENTATION

The spherical retarding potential analyzer shown in Figure 25-1 is comprised of an aperture grid, a retarding grid, an auxiliary grid, and a cathode. These grids are made of tungsten and are gold plated. Each grid has a transparency factor of 80 percent.

The output of the log amplifier (Io), the retarding grid (VR) and the aperture voltage (VA) is shown in Figure 25-2. The aperture potential (VA) was programmed in 8 steps of 0.2 sec for one complete cycle of operation. In each step the retarding grid (VR) is swept according to the formula VR = VA ± 2.4 V. During the first step, the aperture grid is placed at -10.0 V in order to attract

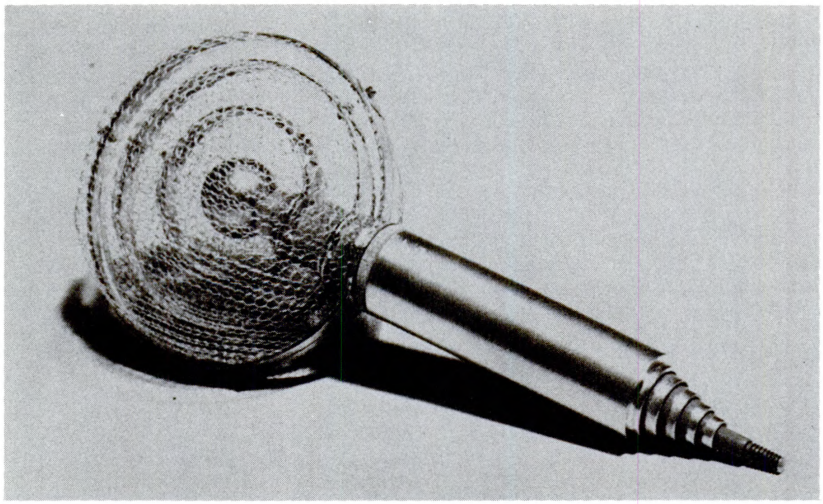

Figure 25-1. Spherical Probe

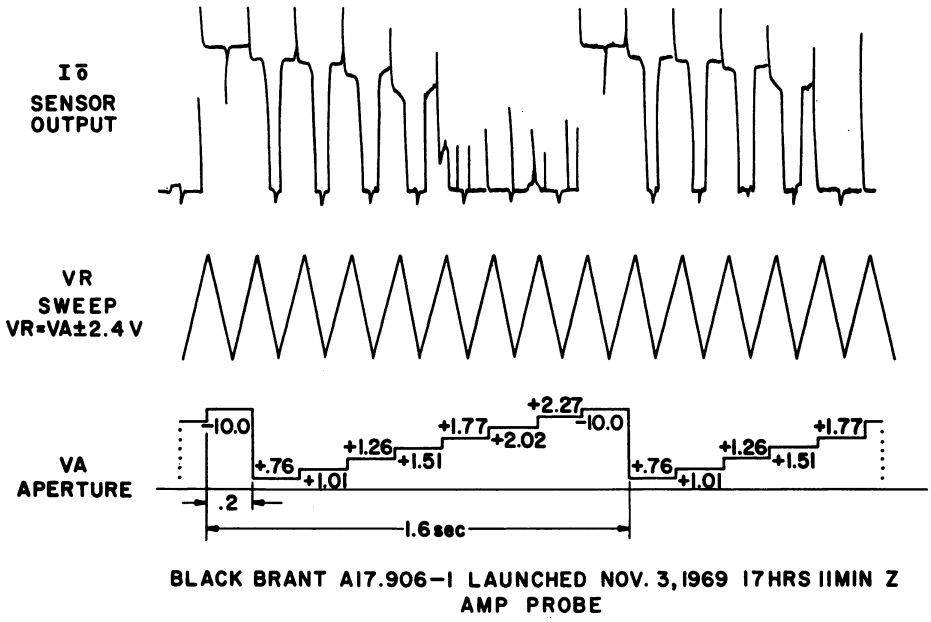

Figure 25-2. Telemetry and Output During Typical 1.6 sec Cycle

as many ions as possible. The next step placed the aperture grid (VA) at -0.76 V with succeeding steps incrementing the aperture voltage by 0.25 V.

In selecting the current at space potential (Io), the following criteria was used: It is the last saturated current before an order of magnitude drop in the saturated current is observed. In the above example, the -1.5 V step was taken as the saturated current at space potential (Io).

25-3 POSITIVE ION DENSITY

The objective of collapsing the space charge sheath was to approach the condition by which the sheath thickness $t = a - r \ll r$, where a = sheath radius, and r = probe radius. The current to the probe in this case is given by:

$$I_i = N_i A e V \left\{ \left(\frac{1+\alpha_i^2}{2V_r^2} \right) \operatorname{erf} \frac{V_r}{\alpha_i} + \frac{\alpha_i}{V_r \sqrt{\pi}} \exp \left[-(V_r/\alpha_i)^2 \right] \right\} \qquad (25\text{-}1)$$

where

A = effective area of the probe

N_i = positive ion density

e = electron charge

V_r = rocket velocity

α_i = most probable ion thermal velocity

The current to the probe at zero probe potential (Io) is shown in Figure 25-3 together with the ion Mach number (λ_i). These measurements were used in the above equation to calculate the positive ion density shown in Figure 25-4 labeled (AP). The results show a peak density of 3×10^5 ions/cm^3 at 95 km. In the altitude regime 90 to 120 km where free molecular flow exists, the density is fairly constant to within a factor of 2. Also shown on this figure are the results of the Gerdien detector of Conley (1971) which were flown on the same rocket as the spherical retarding potential analyzer.

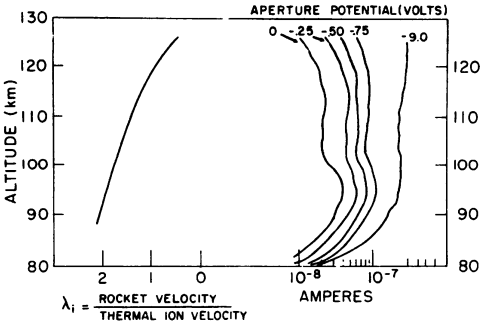

Figure 25-3. Currents at Various Accelerating Potentials and the Ion Mach Number as a Function of Altitude

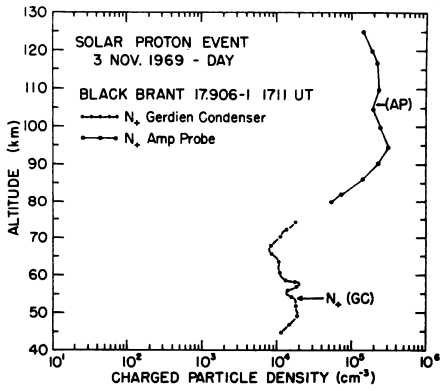

Figure 25-4. Positive Ion Density as a Function of Altitude

25-4 DATA ANALYSIS

With the current to a moving spherical probe from an undisturbed plasma measured experimentally, one can now compare how the theoretical technique of Kanal compare with the experimental results at various accelerating voltages. The normalized general ion current (Ini) is defined by Kanal in which he assumes a spherical sheath:

$$Ini = \frac{a^2}{r^2}\ \Lambda(\lambda_i) - \left(\frac{a^2-r^2}{r^2}\right) H\left(\gamma\sqrt{\bar{V}}, \lambda_i\right)$$

where

$$\Lambda(\lambda_i) = \frac{\sqrt{\pi}}{2}\left(\lambda_i + \frac{1}{2\lambda_i}\right) \operatorname{erf} \lambda_i + \frac{1}{2} e^{-\lambda_i^2} \quad \text{letting } x = \gamma\sqrt{\bar{V}}$$

$$H(x, \lambda_i) = \frac{\sqrt{\pi}}{4\lambda_i}\left(\lambda_i^2 + \frac{1}{2} - x^2\right)\left[\operatorname{erf}(x+\lambda_i) - \operatorname{erf}(x-\lambda_i)\right]$$

$$+ \frac{x+\lambda_i}{4\lambda_i} e^{-(x-\lambda_i)^2} - \frac{x-\lambda_i}{4\lambda_i} e^{-(x+\lambda_i)^2}$$

In the above expressions, $\bar{V}$ = normalized probe potential = $\frac{eV}{kT_i}$, where

V = accelerating potential

T_i = ion temperature

$\gamma^2 = \frac{1}{a^2/r^2 - 1}$

$\lambda_i = V_r/\alpha_i$

When we are at space potential $\bar{V} = 0$, $H(\gamma\bar{V}, \lambda_i)$ is zero and $\Lambda(\lambda_i)$ defines the current to a collapsed sheath and is equivalent to Eq. (25-1). The function $H(\gamma\bar{V}, \lambda_i)$ describes the additional contribution to the normalized current due to the larger sheath area caused by an applied potential (V). The normalized general ion current (Ini) has been plotted by Kanal as a function of $\bar{V}$ with a/r as a parameter and a set of graphs computed for various ion Mach numbers (λ_i). A typical graph is shown in Figure 25-5.

$Ini = f(\bar{V}, a/r, \lambda_i)$ where the sheath radius (a) is a function of $\bar{V}$. In order to solve his equation, Kanal introduced Poisson's space charge equation (Langmuir and Mott-Smith, 1926):

$$Ii = \frac{4}{9}\left(\frac{2e}{mi}\right)^{1/2} \frac{V^{3/2}}{(-\beta^2)}$$

where $(-\beta^2)$ is a transcendental function of (a/r) which is expressed as a power series:

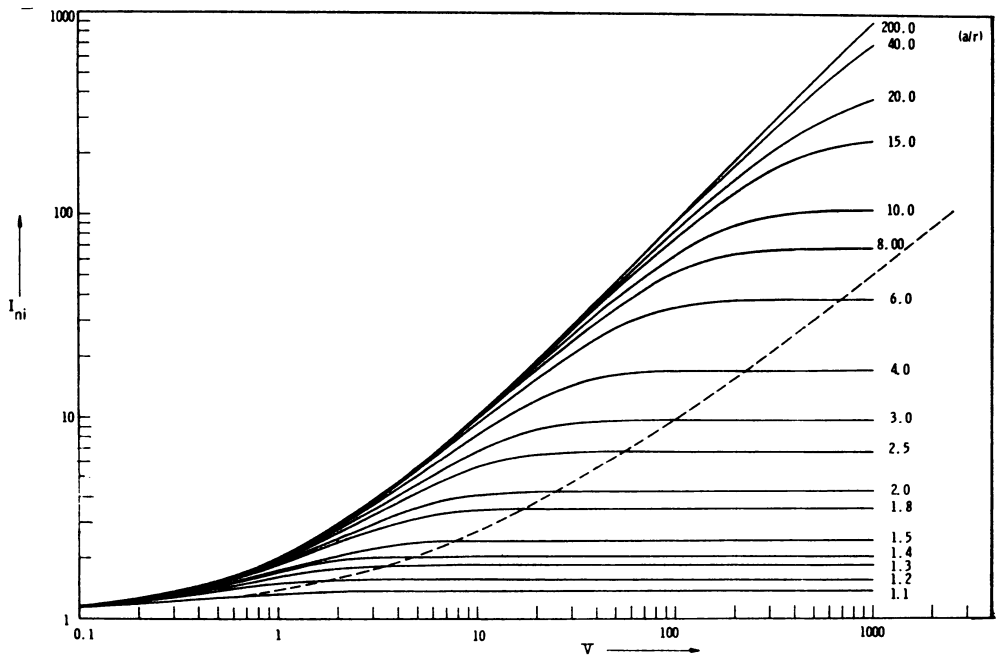

Figure 25-5. Sample of Kanal Curves of the Normalized General-ion Current Function for $\lambda_i = 0.5$ Case

$$\beta = \Delta - 0.3\Delta^2 + 0.075\,\Delta^3 - 0.01432\Delta^4 + 0.00216\Delta^5 \ldots\ldots$$

where $\Delta = \ell n(r/a)$.

Upon normalizing

$$Ini = \frac{P(\bar{V})^{3/2}}{(-\beta^2)} \qquad (25\text{-}2)$$

where $P \simeq 7.5 \times 10^3\, T_i/N_i r^2$ and corresponds to the ratio of Debye length to probe radius. Poisson's space-charge equation was derived for: a probe at rest, and that ions enter the sheath with zero initial velocity. This is not what physically happens, of course, but it is a good approximation for our case where the ion Mach number (λ_i) never exceeds 2.

With these limitations in mind, Kanal solved graphically the two independent ion current equations and arrives at the current-voltage characteristic curve shown in Figure 25-5. A brief description of the technique used to derive the current-voltage curve shown in the Figure 25-5 may be helpful. The space charge Eq. (25-2) is plotted for a number of values of a/r (1.4, 1.5, 1.8, 2.0, etc.) simultaneously

with Kanal normalized current (Ini) for various a/r on log paper. The solutions of the space charge equation are straight lines with a 3/2 slope. The x intercept on the $\bar{V}$ axis is given by:

$$\bar{V}x = \frac{(-\beta^2)^{2/3}}{P} .$$

The intersection of equivalent a/r from the solutions of Poisson's space-charge equation and Kanal's curves produce the current-voltage solution for a particular ion Mach number (λ_i).

In Figure 25-6, the experimental data for an ion Mach number $\lambda_i = 2$ are normalized to the current at space potential (Io) at four accelerating voltages (0.25, 0.50, 0.75 and 9.0 V). These values are plotted on the graph as normalized current (⊙'s). The theoretical current (Ini) is now normalized to the current at space potential ($\bar{V} = 0$) and plotted as (x) on the same graph. At the higher Mach number ($\lambda_i = 2$), there is agreement between the theoretical results and experimental results within a factor of 2 at the low accelerating potentials. At the higher accelerating potential (9 V case), the current to the probe is much lower than theory predicts.

As the rocket approaches apogee, the ion Mach number becomes small ($\lambda_i \approx 0.5$). The rocket has slowed down and approaches the case of the spherical

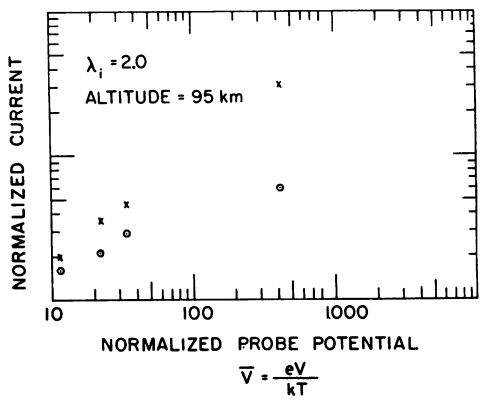

Figure 25-6. Comparison of Theoretical and Experimental Results at an Ion Mach Number $\lambda_i = 2$. X Theoretical results; ⊙ experimental results

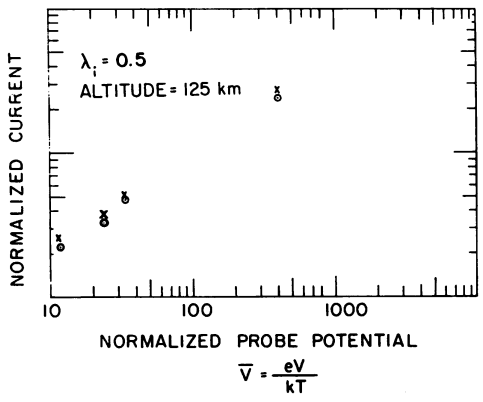

Figure 25-7. Comparison of Theoretical and Experimental Results at an Ion Mach Number $\lambda_i = 0.5$. X Theoretical results; ⊙ experimental results

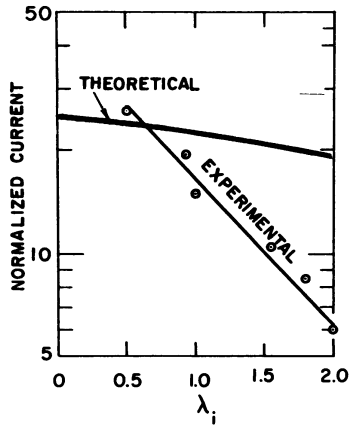

Figure 25-8. Comparison of Theoretical and Experimental Results for the 9 V Accelerating Case vs Ion Mach Number λ_i

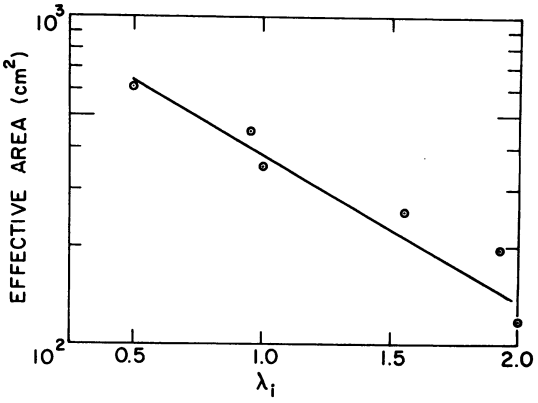

Figure 25-9. Effective Area of the Probe vs Ion Mach Number (λ_i) for the 9 V Accelerating Case

probe at rest. The agreement between the experimental and theoretical results are shown in Figure 25-7 and is excellent.

Figure 25-8 shows the normalized current plotted against the ion Mach number for the 9 V accelerating case. The discrepancy between the experimental and theoretical results improve as the ion Mach number decreases.

Figure 25-9 shows how the effective area changes for the 9 V accelerating case plotted versus the ion Mach number. It appears that effective area decreases exponentially with ion Mach number.

25-5 CONCLUSION

At high accelerating potential -9 V, the current to the probe is too low at high Mach numbers but approaches the correct current when the vehicle approaches the thermal velocity of the ions. It appears at high vehicle velocities, ions that should be collected are not fast enough to enter the sheath as it passes quickly by.

With regard to the low accelerating potential, there is an agreement within a factor of 2 between the experimental results and the theoretical calculation and this agreement improves with decreasing ion Mach number.

References

Conley, T. D. (1971) Positive Ion Concentrations in the Lower D-Region During a PCA Event Measured by a Rocket-Borne Gerdien Condenser. See Chapter 24 of this publication.

Kanal, M. (1962) Theory of Current Collection of Moving Spherical Probes, Scientific Report Number JS-5 ORA No. 03484, 03599-9-S, Space Physics Research Lab., University of Michigan.

Langmuir, I. and Mott-Smith, H. M. (1926) The theory of collectors in gaseous discharges, Phys. Rev. 28.

Contents

26. Rocket Measurements of Electron Precipitation During the November 1969 PCA Event

E.R. Hegblom
Boston College
Chestnut Hill, Massachusetts

L.C. Howlett
Utah State University
Logan, Utah

Abstract

Measurements of electron precipitation were made during the November 1969 Polar Cap Absorption (PCA) Event on three Black Brant rockets. Four Geiger counters with various window thicknesses were flown on two rockets. One rocket, launched during a Class II aurora at 00:05 local time on 3 November 1969, measured appreciable electron fluxes and the other rocket launched at sunset 17:08 local time on 4 November, did not measure any electron precipitation.

A scintillator was flown on a third rocket launched at 14:20 local time on 2 November 1969 and measured a peak energy flux (for electrons with energies greater than approximately 4 keV and protons greater than 60 keV) which was predominantly due to electrons of 5×10^{-2} ergs/cm^2-sec-sr.

26-1 INTRODUCTION

During the PCA 1969 program conducted at Fort Churchill, Canada, particle detectors were included in the payloads of three Black Brant rockets (Numbers 17.602, 17.758 and 17.617) to provide information on the precipitation of electrons into the upper atmosphere during the PCA event.

26-2 INSTRUMENTATION

A scintillator was flown on Rocket 17.602, and a set of four Geiger counters with various window thicknesses were flown on Rockets 17.758 and 17.617.

The scintillator was composed of a scintillation phosphor (Pilot B plastic) about 0.1-cm thick, which was viewed by an RCA 4441 photomultiplier. The output of the photomultiplier was logarithmically amplified and telemetered to ground. A thin coating ($\sim$2200 Å) of aluminum covered the face of the crystal to reduce the sensitivity of the instrument to light. This window thickness corresponds to a threshhold energy (50 percent transmission) of approximately 5 keV for electrons and 60 keV for protons. The half-angle of the field of view was approximately 22° (0.45 sr solid angle) and the geometric factor was 0.56 cm^2-sr. The instrument was capable of measuring energy fluxes from 10^{-3} to 20 ergs/cm^2-sec-sr, and was calibrated with a Ni^{63} source. The center of the field of view was at 90° to the rocket axis.

The Geiger counters measured electrons with energies greater than 17, 26, 42 and 90 keV, protons with energies greater than 180, 350, 600 keV and 2 MeV and was also sensitive to x-rays in the energy range from 1 to 10 keV. The field of view of the counters was approximately 11° half-angle and the counters were mounted at an angle of 80° with respect to the rocket axis. The geometric factor for the 17 and 26 keV counters was 5×10^{-3} cm^2-sr, and for the 42 and 90 keV counters was 7×10^{-2} cm^2-sr. The output of the counters was integrated (0.05-sec time constant) and an output that was proportional to the logarithm of the input count rate was obtained. These voltages were placed on an 8 segment, 30 frames/sec commutator and telemetered to ground.

26-3 RESULTS

26-3.1 Rocket 17.602

The output of the scintillator (converted to energy flux) as a function of time is shown in Figure 26-1. The data appears to be divided into two bands (dark and light regions in the figure) but the upper band is produced by solar radiation (visible light, x-rays, Lyman α and Lyman β) and occurs only for the short period of time that the scintillator is pointed at the sun. The aspect system flown on the rocket was used to determine the times the instrument was viewing the sun. The lower band represents the actual particle energy flux measurement, and the width of the band is due to variations in the flux with pitch angle for pitch angles greater than 90°.

The response of the Pilot B scintillator to protons is about a factor of 3 less than its response to electrons (Birks, 1964), and the proton energy flux (Reagan et al, 1972; Sellers and Hanser, 1972) that was deposited in the scintillator is about a factor of 3 to 4 less than the maximum measured energy flux. Therefore, the

contribution of protons to the output of the scintillator is about 10 percent, and the scintillator is responding primarily to electrons over most of the flight.

Figure 26-2 is an expanded section of Figure 26-1 showing the narrow pulse that occurs when the instrument was viewing the sun superimposed on the pitch angle variation of the energy flux. The pitch angle variation of the flux is shown in Figure 26-3 at an altitude of approximately 120 km, but it is typical of the pitch angle distribution observed throughout the flight. The measured distribution is essentially isotropic for pitch angles less than $\sim 80^{o}$, and decreases sharply with increasing pitch angle beyond 90^{o}.

The absorption by the atmosphere of the electron energy flux can be used to obtain an estimate of the differential energy spectrum (McIlwain, 1960). The average energy lost per electron in an electron beam traversing an absorber is approximately equal to the energy E_o of an electron with an end-point range equal to the absorber thickness (Young, 1956).

The electron energy flux transmitted through the atmosphere as a function of the end-point range energy corresponding to the atmospheric depth (after accounting for the increased effective atmospheric depth for electrons with pitch angles near 70^{o}) at which the measurement was made is plotted in Figure 26-4. If a power law spectral shape is assumed for the incident differential spectrum ($dN/dE = AE^{-\gamma}$), then the energy flux transmitted through an absorber is given by $\frac{A}{(\gamma-2)(\gamma-1)}E_o^{-\gamma+2}$ where E_o is the electron end-point range energy. From Figure 26-4 it is found that $\gamma = 3$ and $A = 3 \times 10^{8}$ $(keV)^2/cm^2$-sec-sr. The ion-pair production rate has been calculated from this spectrum using the technique described by Rees (1963) and is shown in Figure 26-5 The production rates calculated from two electron density measurements ($q = \alpha_{eff} N_e^2$) with an α_{eff} of 2×10^{-7} cm^3 sec^{-1} are shown for comparison. The electron density was measured by the $Z(\theta)$ probe on the same rocket (17.602) as the scintillator, while the density determined from the BRL propagation experiment was measured 50 minutes later. The agreement is within the uncertainties resulting from the technique employed.

26-3.2 Rocket 17.758

The results from two Geiger counters for rocket 17.758 are shown in Figure 26-6. This rocket was launched at 0605 UT on 3 November during a visible aurora. The 5577 Å line measured by the Auroral Observatory at Churchill was about 5 KR (Class II Aurora).

The correction for the dead time of the counters was negligible except for the greater than 42 keV counter which was saturated for most of the flight and is not shown in this paper. The integral spectrum measured near apogee is shown in Figure 26-7. The spectral form can be represented by $dJ/dE = Ae^{-E/E_o}$ where

E_o = 26 keV and A = 6×10^3 for energies greater than 17 keV. The ion-pair production rate calculated from this spectrum is shown in Figure 26-8. The production rate calculated from the electron density ($q = \alpha_{eff} N_e^2$) with $\alpha_{eff} = 2 \times 10^{-7}$ cm^3 sec^{-1} is in good agreement with these results from 80 to 90 km. Above 95 km, lower energy electrons which were not measured and which were producing the observed Class II aurora are significant and this implies that the spectrum below 17 keV increases steeply with decreasing energy. Below 80 km, the PCA event protons are the most important ionization source, and the production rate due to precipitating electrons is negligible.

26-3.3 Rocket 17.617

The Geiger counters on Rocket 17.617 launched at 2308 UT on 4 November did not measure any electrons above the background noise level. This result sets an upper limit to the integral flux with energies greater than 17 keV of approximately 10^3 electrons/cm^2-sec-sr.

References

Birks, J.B. (1964) The Theory and Practice of Scintillation Counting, Pergamon Press, New York.

McIlwain, C.E. (1960) Direct measurement of particles producing visible auroras, J. Geophys. Res. 65:2727-2747.

Reagan, J.B., Imhof, W.L., Gaines, E.E. (1972) Satellite Measurements of Energetic Solar Protons, Alpha Particles, Electrons and Auroral Particles During the 2 November 1969 PCA Event. See Chapter 10 of this publication.

Rees, M.H. (1963) Auroral ionization and excitation by incident energetic electrons, Planetary Space Sci. 11:1209-1218.

Sellers, B. and Hanser, F.A. (1972) Heavy Particle Ionization Rates. See Chapter 12 of this publication.

Young, J.R. (1956) Penetration of electrons and ions in aluminum, J. Appl. Phys., 27:1-4.

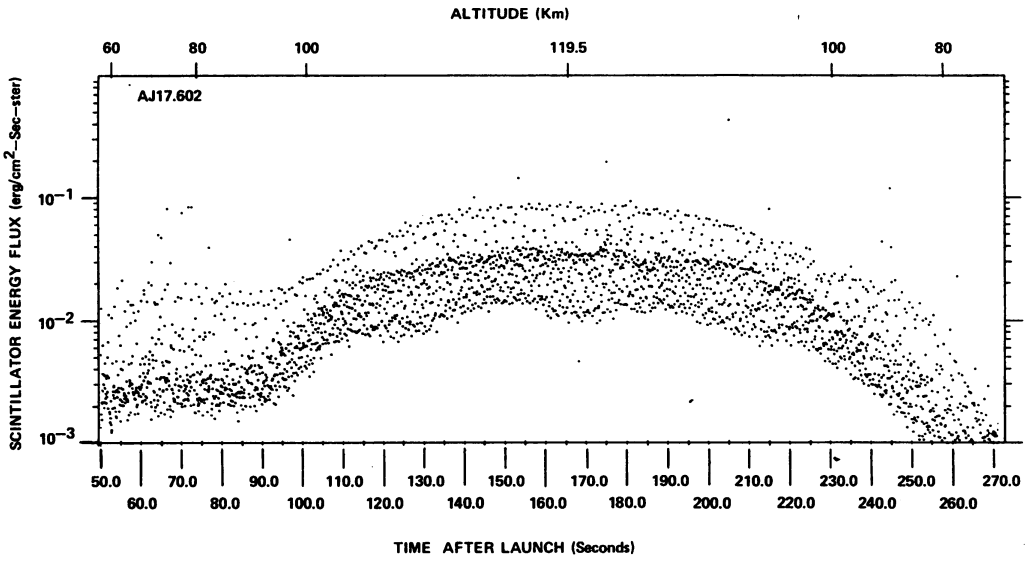

Figure 26-1. Energy Flux Measured by Scintillator on Rocket 17.602. The dark band is the scintillator output due to the particle flux, while the light band above it is due to solar radiation.

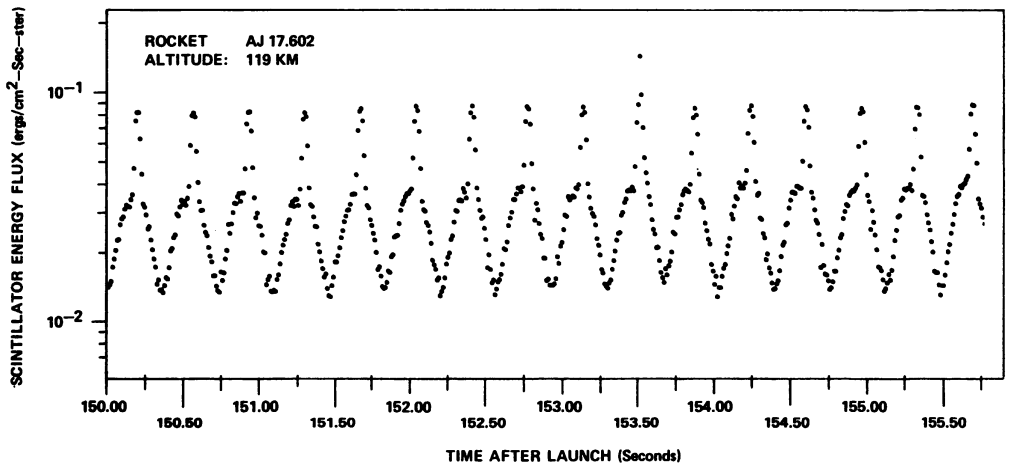

Figure 26-2. Energy Flux Measured by Scintillator on Rocket 17.602 Plotted Over a Five-sec Interval to Show the Short Pulse Due to Solar Radiation When Viewing the Sun and Particle Flux Variation as the Pitch Angle Changes

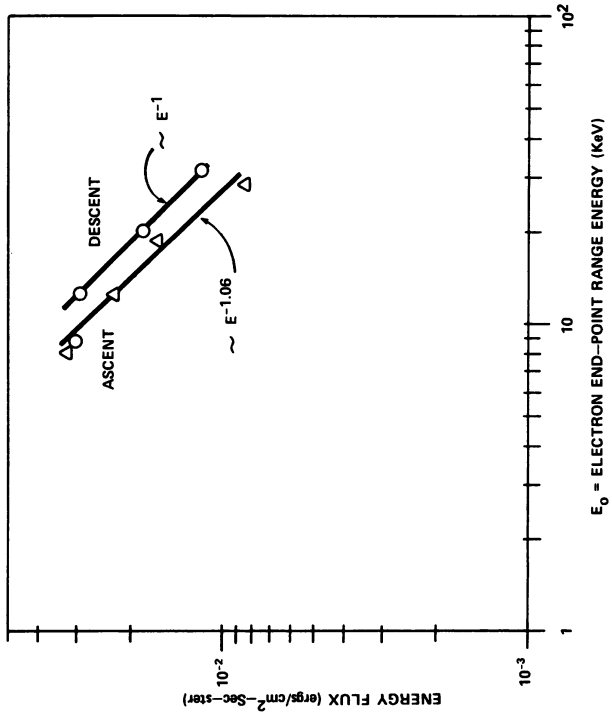

Figure 26-4. Particle Energy Flux Measured by Scintillator on Rocket 17.602 at Various Altitudes Plotted as a Function of the Energy of an Electron Having a Range Corresponding to the Atmospheric Depth at the Same Altitude

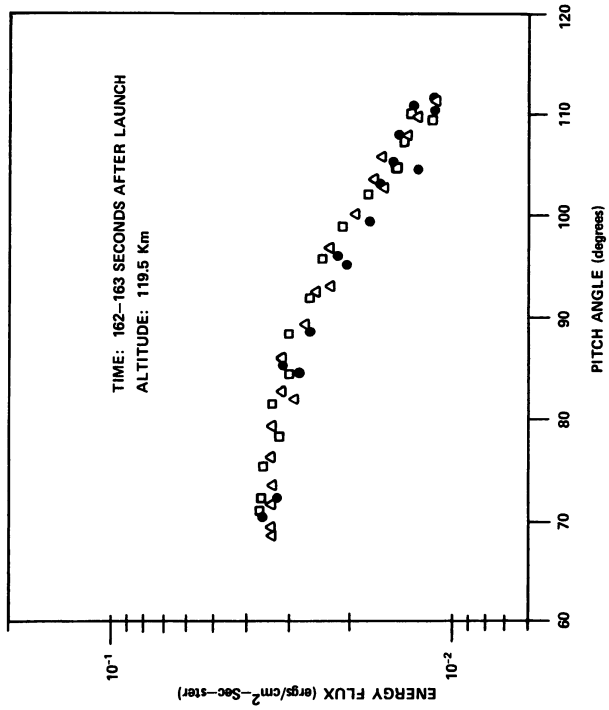

Figure 26-3. Particle Energy Flux Variation With Pitch Angle, as Measured by Scintillator on Rocket 17.602

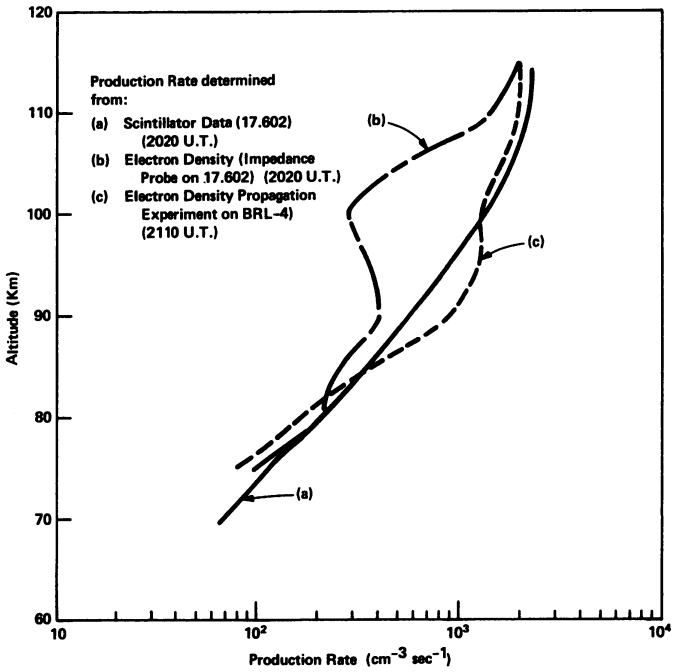

Figure 26-5. Comparison of Production Rate Determined From Electron Spectrum With That Calculated From Measured Electron Density Profiles Using an Effective Recombination Rate of 2×10^{-7} cm^3 sec^{-1}

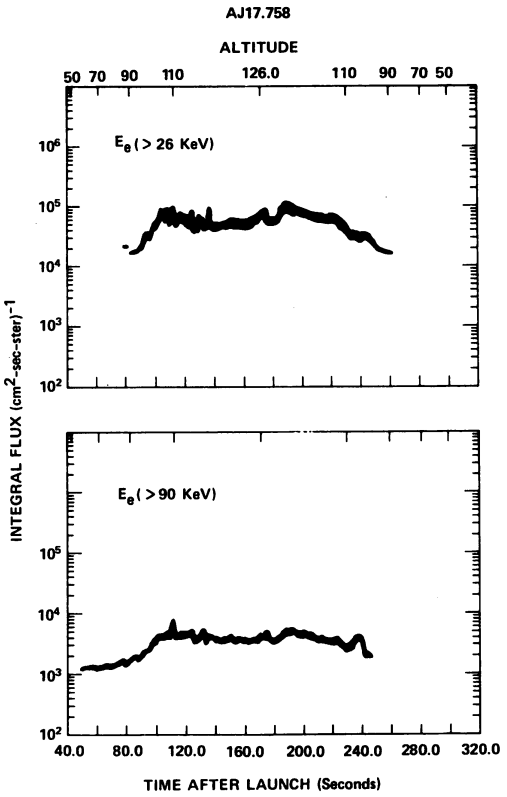

Figure 26-6. Integral Particle Flux (Primarily Electrons) Measured by Two Geiger Counters on Rocket 17.758

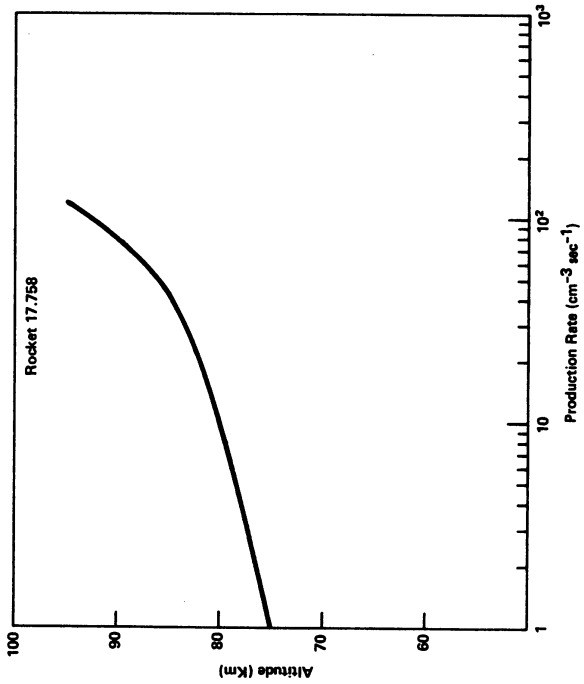

Figure 26-8. Production Rate Due to Electron Flux Measured on Rocket 17.758

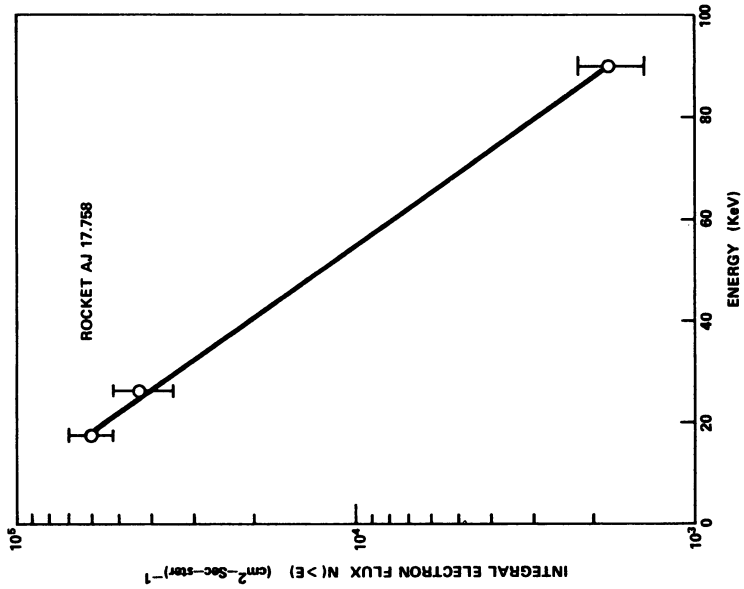

Figure 26-7. Integral Electron Flux Spectrum Determined From Geiger Counter Data on Rocket 17.758 at 150 sec After Launch at an Altitude of 124 km

Contents

27. Comparison of Black Brant Rocket Measurements of Charged Particle Densities During Solar Particle Events

James C. Ulwick
Air Force Cambridge Research Laboratories
L.G. Hanscom Field
Bedford, Massachusetts

Abstract

Impedance (Z-θ) probe measurements were made on five of the seven Black Brant rocket flights flown during Operation PCA 69. The antenna impedance changes are determined from the telemetered antenna voltages, currents and phase angles, and derived from these are electron densities. Profiles were obtained at daytime, nighttime, sunrise and sunset during the 2 November 1969 event and at night by the certification rocket launched during the 18 November 1968 event. The results are compared with measured electron currents from Langmuir probes and ion density profiles from Gerdien condensers, retarding potential analyzer and Langmuir probes flown on the same rockets. Profiles are compared to BRL rocket results and are used to compute absorption at 30 MHz to compare with riometer measurements.

27-1 INTRODUCTION

The probes for the measurement of electron and ion densities that were flown on the Black Brant rockets during Operation PCA 69 have been summarized (Richards, these proceedings). Six of the rockets were flown during the 2 November 1969 solar particle event and one other during the 18 November 1968 event to certify the payloads and to obtain background measurements. Impedance (Z-θ) probe measurements for the determination of electron density profiles were successfully made on four of the six Black Brants during the 2 November 1969 event and on the certification rocket. The results are shown and compared to other results from Langmuir probes, Gerdien Condensors, and retarding potential analyzers which were also flown on some of these rockets. Where possible the Black Brant probe results will be compared to the propagation results (Dean, these proceedings) from Nike Javelin rocket flights. This paper then is concerned with establishing the best electron and ion density profiles from the measurements. Another paper (Ulwick, these proceedings) discusses the implication of the data.

27-2 Z-θ PROBE

The Z-θ probe is used to measure the local electron density of a plasma in which the instrument's antenna is immersed. This is accomplished by measuring the RF impedance of the antenna at frequencies of 3.0 and 7.2 MHz. Changes in antenna impedance are not measured directly, but may be determined from the Z-θ probe system outputs; voltage applied to the antenna, resulting antenna current, and phase angle between the antenna voltage and current. The electron density can be determined from the changes in the antenna impedance.

A block diagram of the Z-θ probe system is shown in Figure 27-1. Indications of antenna current and voltage are taken at points A and B respectively, and are fed to the phase detector to provide a measurement of the phase relationship of antenna voltage to current. The voltage at point C is also monitored and sent to the commutator as an indication of the dc antenna potential. Finally antenna current, antenna current times ten (amplified for greater sensitivity), phase angle, and antenna ac and dc voltages are fed to the commutator and subsequently become, according to the commutator format, the Z-θ probe telemetry record.

Figure 27-2 shows the Z-θ probe frequency application and commutator sweep formats. As shown, the sequence of rf voltages applied to the cylindrical antenna through the matching network is as follows:

a. One commutator frame with no rf voltage applied,

b. Seven frames at 7.2 MHz,

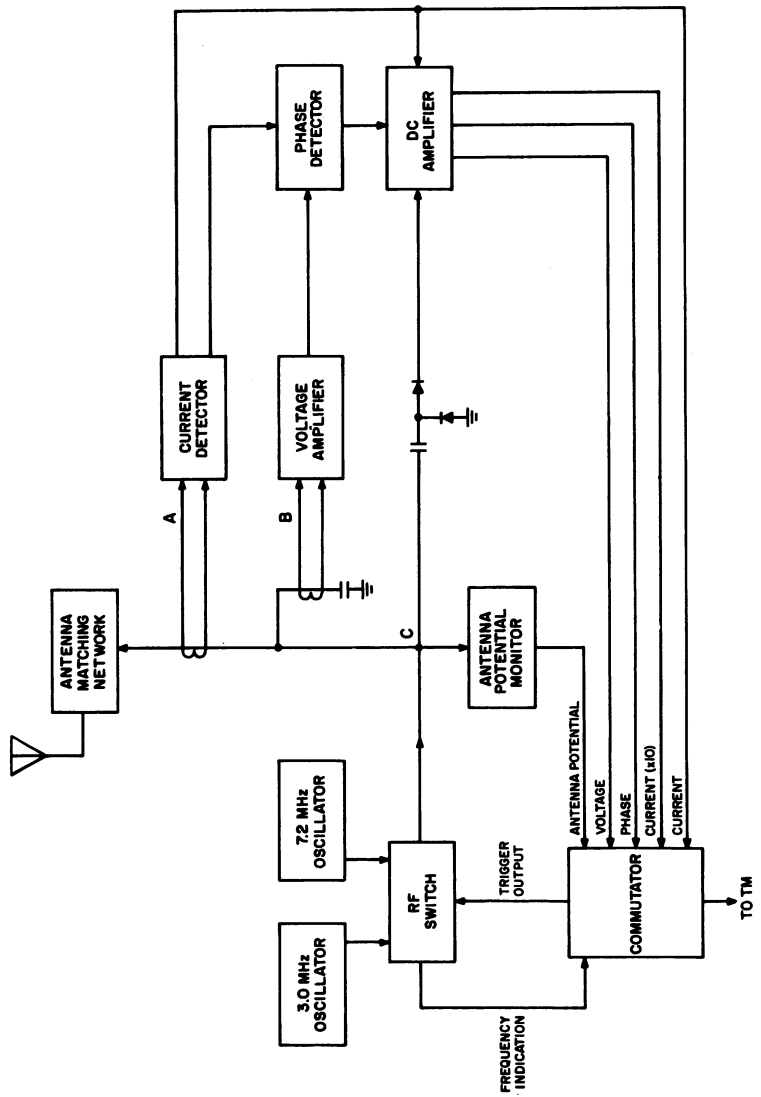

Figure 27-1. Probe System

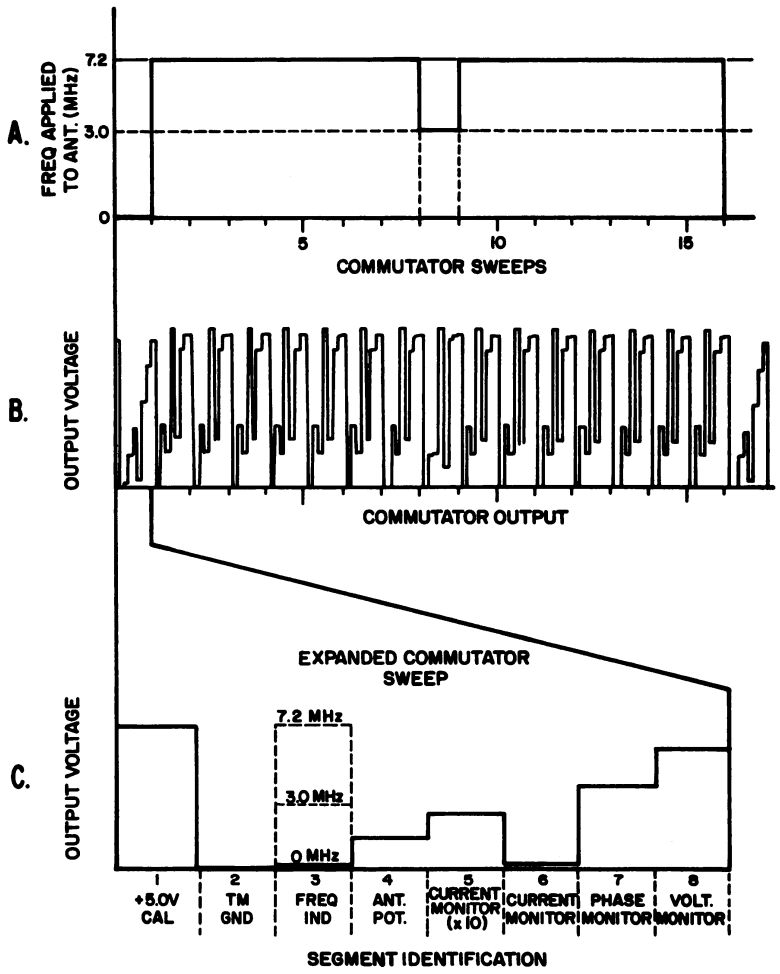

Figure 27-2. Frequency Application and Commutator Sweep Formats

c. One frame at 3.0 MHz,

d. Seven frames at 7.2 MHz.

Complete schematic diagrams for the Z-θ probes are given by Baker et al (1970). During instrument calibration, the antenna is replaced by a known impedance value. The instrument outputs of voltage, current, and phase angle are recorded for that impedance value; and this process is repeated for many known impedances. Calibration curves are then plotted for each output. These curves, frequency matching network information, antenna potential monitor calibration and rf oscillator frequency outputs are also given by Baker et al (1970).

27-3 Z-θ PROBE DATA REDUCTION

The basic output data of the Z-θ probe consists of the readings (in volts) of antenna current, antenna voltage and antenna phase angle. The auxiliary frequency monitor is utilized to separate the data from each commutator sweep into the appropriate frequency. The readings of dc voltage on the antenna with respect to the rocket skin are obtained by applying the antenna potential monitor calibration curve to the voltage values measured by the antenna potential monitor.

The antenna current, voltage, and phase angle are determined by applying the appropriate calibration curves to measured telemetry values. The measured impedance is then found by:

$$Z = \frac{V}{I}\theta = R + jX \tag{27-1}$$

where

V is the antenna voltage in volts,

I is the antenna current in amperes,

and

θ is the measured phase angle of the antenna voltage with respect to the antenna current.

The impedance determined from the readings of the Z-θ probe will be at the output of the rf head. This impedance must be transformed to take into account the cable connecting the rf head to the matching network. The basic equation relating the impedance Z_L at the end of a transmission line to that at a point of a distance L up the line (Z_{in}) according to Westman (1956) is:

$$Z_L = Z_o \frac{Z_{in} \cosh \gamma L - Z_o \sinh \gamma L}{Z_o \cosh \gamma L - Z_{in} \sinh \gamma L} \tag{27-2}$$

where

Z_o = the characteristic impedance of the line,

γ = $\alpha + j\beta$,

α = line attenuation constant,

and

β = $2\pi/\lambda$ = line phase shift constant.

For the case of small loss here, this can be approximated by:

$$Z_L = Z_o \frac{Z_{in} \cos 2\pi L\lambda - jZ_o \sin 2\pi L\lambda}{Z_o \cos 2\pi L\lambda - jZ_{in} \sin 2\pi L\lambda} \qquad (27\text{-}3)$$

where

L_λ = L/λ, the line length in wavelengths
= $.0061\lambda$ at 7.2 MHz
= $.0025\lambda$ at 3.0 MHz.

Z_L is the impedance at the input of the matching network. To calculate the actual antenna impedance, the equivalent series impedance of the network must be subtracted from Z_L and the effect of the capacitance shunting the antenna taken into account. Once the antenna impedance is known, it can be compared to the free space values, and application of a valid antenna theory yields the desired plasma parameters.

When the operating frequency is greater than about twice the gyro frequency and is large compared to the collision frequency, the electron density can be calculated from the antenna reactive charge (ΔX) by:

$$N_e = \frac{f^2(\text{MHz})}{80.6} \cdot \frac{C_o}{C_2} \times \frac{\Delta X}{\Delta X + 1/\omega C_o} \times 10^6 \text{ electrons/cm}^3 \qquad (27\text{-}4)$$

where

f = operating frequency in MHz
C_o = $C_1 + C_2$
C_1 = shunt capacity of antenna mounting
C_2 = free space capacity of the antenna

and

ω = angular operating frequency ($2\pi f$).

For the 7.2 MHz data, this formula is used over the range of sensitivity of the instrument ($\sim 10^4$ to 10^6 electrons/cm^3) corresponding in general to measurements above 75 km. For the 3.0 MHz data, the more complicated analysis, including the effects of the earth's magnetic field and collision frequency, must be used below 75 km. Despain (1965) considers the plasma as a warm electron fluid media. The antenna impedance he derives includes electron density, electron collision, electron temperature and magnetic field effects for the case where the antenna is parallel to the magnetic field. This expression was programmed for a range of electron densities and temperatures at one kilometer intervals and using a model total particle density from Faire and Murphy (these proceedings) corresponding to approximate Black Brant rocket flight times. The real and reactive part of the

antenna impedance was computed for the 3.0 MHz operating frequency and the Black Brant antenna configuration. Using the resulting tables and the measured antenna impedance we can find the electron density down to the limit of sensitivity for the 3.0 MHz operating frequency (~3 x 10^2 electrons/cm^3).

Figure 27-3 is an example of the results for both frequencies. Each measurement at 7.2 MHz (which was 14 times more often than the 3.0 MHz measurement, see Figure 27-2) is shown above 80 km. As can be seen, there is little scatter in the 7.2 MHz results and since there is at least one measurement every 0.1 km, subsequent figures will show the Z-θ probe results as continuous curves for comparison with other data. The 3.0 MHz results overlap the 7.2 MHz results on both rocket ascent and rocket descent from about 2 x 10^4 to 9 x 10^4 electrons/cm^3. In subsequent figures the results below approximately 10^4 electrons/cm^3 will be from the 3.0 MHz data. Rocket ascent data will also be used in all figures. The difference between the rocket ascent and descent data above about 98 km in Figure 27-3 (ascent values are the higher ones) are attributed to outgassing effects (Pfister and Ulwick, 1965). This was a persistent feature in all five results (for example, the nighttime 1968 PCA results, Ulwick and Sellers, 1971).

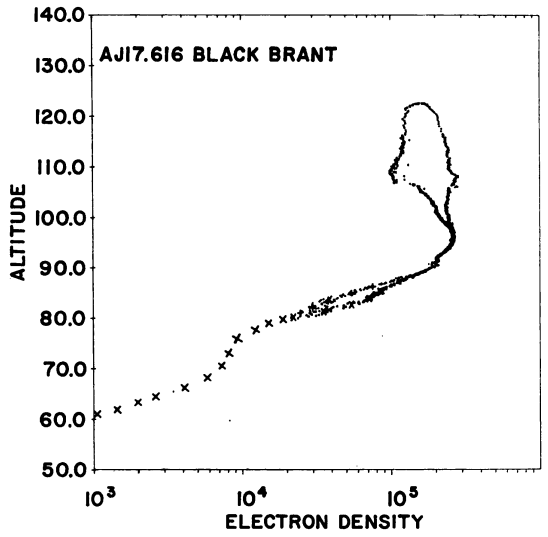

Figure 27-3. Typical Electron Density Measurements at 3 and 7.2 MHz

27-4 RESULTS

27-4.1 2 November 1969 (Daytime)

The schedule of rocket launchings for PCA 69 did not originally include any measurements during the early part of an event. The emphasis was on the latter part of the event when the ionizing flux would be more stable. However, since the 2 November 1969 event was on the limb, it was decided to launch rockets as early as possible to achieve measurements the first day in case the event was short lived.

Consequently Black Brant 17.602 was launched at 2020 UT (1420 L.T.) on 2 November 1969 and Nike Javelin BRL-4 at 2110 UT (1510 L.T.). Figure 27-4 shows the electron densities from the Z-θ probe, Ne(Z-θ), and Langmuir probe, Ne(LP), and the ion densities from the Gerdien condenser, N_+ (GC), and Langmuir probe, N_+ (LP), from the Black Brant rocket 17.602. The Ballistic Research Laboratories (BRL) electron density results, N_e (PROP), from the propagation experiment flown on a Nike Javelin rocket is also shown. To avoid continuous reference to these results, all positive ion densities from Gerdien Condenser measurements are from Conley, all positive ion densities from Langmuir probes are from Richards, all electron densities from BRL propagation experiments are from Dean, and their results are in these proceedings.

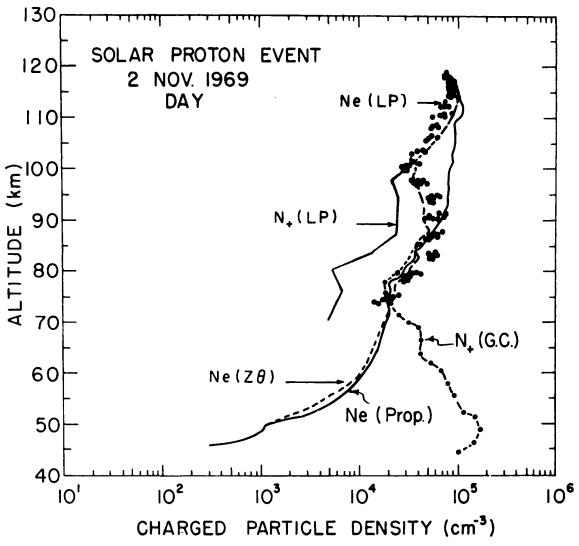

Figure 27-4. Electron and Positive Ion Measurements, Daytime 2 Nov 1969

There is good agreement comparing first the Black Brant electron density measurements from the Z-θ probe and the Langmuir probe. The Langmuir probe results were from the measured negative currents, and a scaling factor determined on previous measurements was used to convert to electron densities. Below 90 km the Black Brant results compare very well with the propagation results from the BRL rocket flown about 50 minutes later. The very high electron densities compared to undisturbed conditions are due to the solar particles. The effect of auroral energetic electrons can be seen in the higher electron density results of the propagation experiment in the altitude region from 90 to 110 km. Satellite measurements showed that during the 3 days of the event, energetic electrons were an additional ionizing source at various times (Regan et al, these proceedings). Also, Hegblom (these proceedings) discusses the energetic electron flux measurements made on the Black Brant rockets. The positive ion densities from the Gerdien Condenser are essentially the same as the Z-θ and propagation electron densities in the altitude range 72 to 85 km. Below 72 km, negative ions are the dominant

negatively-charged particles. The positive ions reach a peak at about 50 km at a value of approximately 1.5×10^5 ions/cm^3, and the electrons are at about 10^3 electrons/cm^3. Both results show the intensity of the event, being at least two orders of magnitude greater than ambient. Langmuir probe measurements of positive ion densities are lower than the other results in the altitude range of measurements by a factor of about 2.5. No Langmuir probe measurements were reliable below 70 km because the vehicle potential in this region was changing, with the highest values approximately 3 volts negative. Above 70 km, however, the vehicle potential was almost constant at a value of about 1 volt negative.

27-4.2 3 November 1969 (0005 L.T.—Nighttime Conditions)

Figure 27-5 shows the Black Brant results from the Z-θ probe, Langmuir probe, and Gerdien condenser for 3 November 0605 UT (0005 L.T.). Immediately obvious in this figure is the excellent agreement with the positive ion densities from the Langmuir probe data with the rest of the data in contrast to the previous figure. Below 80 km the positive ion densities from the Gerdien condenser and the Langmuir probe measurements show good agreement, and above 80 km the positive ion and electron densities are in good agreement. The 18 November 1968 Black Brant nighttime results also show the same good agreement between all the probes (Richards, these proceedings). Subsequent figures will show that, like the daytime results in Figure 27-4, the LP sunset and sunrise positive ion densities above 75 km are lower by about a factor of two compared with the other probe results in contrast to the good agreement obtained in both night flights. The electron densities from the Z-θ probe and the Langmuir probe show good agreement above 75 km. During this flight an aurora was in progress at Churchill, and the high electron density results above 90 km indicates the rocket was in a bright region.

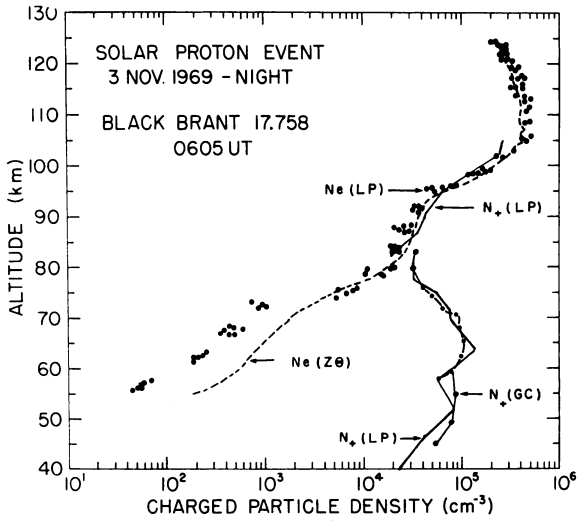

Figure 27-5. Electron and Positive Ion Measurements, Nighttime 3 Nov 1969

Hegblom (these proceedings) discusses the energetic electron measurements and these auroral data. Note here that the negative ions begin to appear at about 80 km in contrast to the daytime result of about 70 km. The ratio of negative ions to electrons (λ) are shown for all Black Brant results (Ulwick, these proceedings).

27-4.3 3 November (Sunrise)

This is the only Black Brant rocket flight where we do not have Gerdien Condenser measurements of the positive ion densities. As in the 2 November daytime results, the LP ion densities (shown in Figure 27-6) are down about a factor of two in the altitude range 80 to 105 km. The different ion densities in the 70 to 80 km range using the same Langmuir probe ion currents is due to two different analysis of the data. One analysis is used from 40 to 80 km and the other from 70 to 105 km, and these have been discussed by Richards (these proceedings). The ion densities from 40 to 70 km, compared with the nighttime results, show the same shape with a peak near 65 km but down by a factor of about three. The electron densities show an unusual sharp increase beginning at 80 km to a peak value of 3×10^5 electrons/cm^3 at 90 to 95 km. This is discussed and compared to the other sunrise results from BRL rockets in Section 27-5.

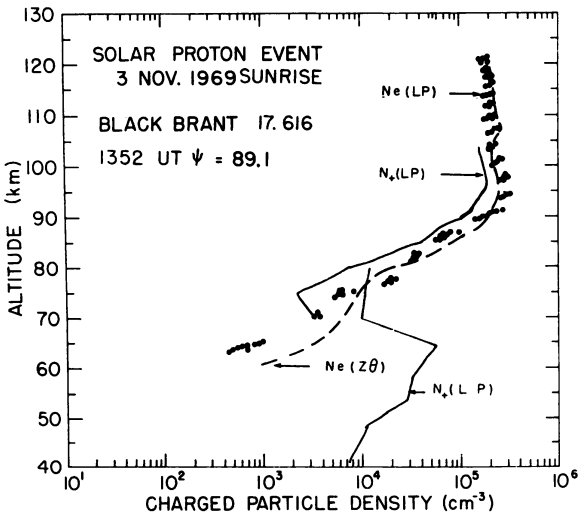

Figure 27-6. Electron and Positive Ion Measurements, Sunrise 3 Nov 1969

27-4.4 3 November (Daytime)

The electron and ion densities from three different rocket flights flown near local noon are shown in Figure 27-7. Ion density results from Gerdien Condenser (GC) and retarding potential analyzer (RPA) measurements (Sandock, these proceedings) are from Black Brant rocket 17.906 flown at 1711 UT. There is a gap in the data between the last GC result at 75 km and the first RPA result at 80 km but the general agreement is good. Electron densities from Langmuir probe

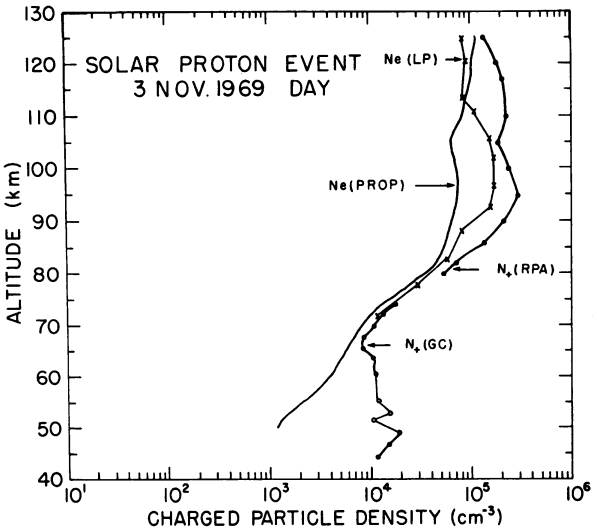

Figure 27-7. Electron and Positive Ion Measurements, Daytime 3 Nov 1969

measurements (NIROS 7.886, 1730 UT) and propagation measurements (Nike Javelin, 1854 UT) are shown for comparison. From about 70 km to 80 km all three results are about the same, and below 70 km negative ions appear to be the dominant negative-charged particle. Above about 80 km the three results are quite different, showing a marked charged-particle decrease between the rocket flights flown at 1711, 1730 and 1854 UT, respectively. Comparing the positive ion densities from the RPA results to the electron densities from the Z-θ probe (see Figure 27-6) on Black Brant 17.616 flown at sunrise (1352 UT), there is excellent agreement from about 80 km to 125 km. This would indicate that the production source that produced the high ionization during this period of time was fairly constant and then decreased during the firings of the NIRO and Nike Javelin rocket. The charged particle profile from the Z-θ probe and the RPA are very similar to results obtained from auroral absorption measurements (Ulwick et al, 1968).

27-4.5 4 November (Sunset)

The charged density measurements from Black Brant 17.617 flown at 2308 UT on 4 November are shown in Figure 27-8. As in the other figures, the Langmuir probe and the Z-θ probe electron density results compare fairly well, and the positive ion densities from the Langmuir probe measurements are down by a factor of about two. The positive ion densities from the Gerdien Condenser agree with the electron densities within about 25 percent in the altitude range 85 to 75 km and show the significance of negative ion densities below this altitude. The lack of agreement between the positive ion densities from the Langmuir probe and the Gerdien Condenser below 70 km is again apparent as in Figure 27-4. The agreement of the Gerdien Condenser results with the Z-θ and Langmuir probe results above 75 km would seem to indicate that the Langmuir probe ion densities are too low. The sunset results have been compared to those from BRL propagation experiments in the next section.

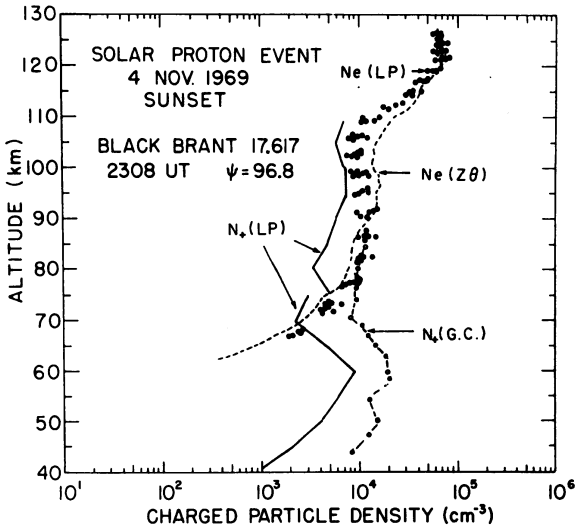

Figure 27-8. Electron and Positive Ion Measurements, Sunset 4 Nov 1969

27-5 DISCUSSION

Cormier (these proceedings) gives the absorption as measured by 30 MHz riometers for a number of locations including Churchill, Canada, during the 2 November event. Using our measured electron density profiles, we calculate the absorption one would expect on a 30 MHz riometer to compare with the ground observations. The method described by Pfister (1965) is used, but instead of using the ARDC Model atmosphere density values we used the ones measured by Faire and Murphy (these proceedings) to calculate the electron collisional frequency. The absorption calculated using the profile in Figure 27-4 is 6.6 db and assuming the commonly used correction factor for antenna beam width of 1.4, our absorption value is 9.2 db. This compares favorably to the measured value by Cormier of about 8.8 db at the time this rocket was launched. On the BRL rockets the differential absorption as a function of altitude was measured for a number of frequencies (Chidsey, these proceedings). We calculated the differential absorption at 18 MHz using our profile and compare this to the measured BRL values in Figure 27-9. The agreement is quite good. The collisional frequency as a function of altitude we used is also included in the figure.

The variation of the electron density from night, through sunrise, to day conditions using the results of Figures 27-5, -6, and -7 and the BRL results (Dean, these proceedings) is shown in Figure 27-10. What is immediately apparent is the

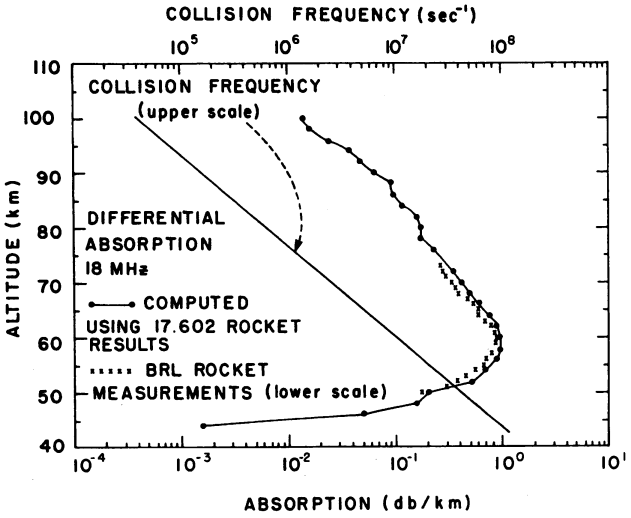

Figure 27-9. Calculated and Measured Differential Absorption

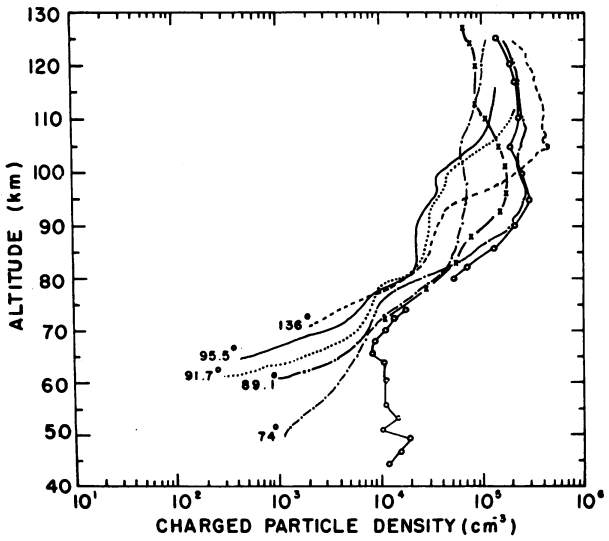

Figure 27-10. Variation of Electron Density With Solar Zenith Angle (o—o Positive Ion Densities X = 74.5°)

complex and variable structure above 80 km compared to the smooth increase of electron density from night to day conditions below 80 km. With respect to the latter, note that this increase exhibits the so-called "twilight anomaly" effect (Reid and Collins, 1959) whereby the electron density increases gradually with decreasing

solar angle and not when the visible light first illuminates the region. Above 80 km there is a sudden increase in electron density of over an order of magnitude between the times of the BRL rocket (X = 91.7) and Black Brant (X = 89.1°) rocket launches (approximately 30 minutes). As mentioned, a similar profile to the X = 89.1° results (Figure 27-10) was obtained previously during an auroral absorption event at Churchill. Satellite observations showed the presence of energetic electrons in addition to the protons during this event. In addition, the nighttime results obtained about 8 hours previously and the magnetometer and riometer ground measurements showed auroral activity over Churchill. However, different in this case, compared to the auroral absorption event results obtained previously, is the fact that there is no corresponding increase in the 30 MHz riometer located near the launch site. Using the profile for X = 89.1°, we calculate an absorption of about 3.7 db for a 30 MHz riometer, whereas the measured value was about 2.0 db. This perhaps could be due to the fact that the antenna of the riometer is vertically pointed, whereas the rocket results are for the region about 20 km southeast of the launch site. If we calculate the absorption for profiles X = 95.5^{o} and 91.7^{o}, we get 0.84 and 1.65 db, respectively, which compares quite well to the riometer values of about 0.98 and 1.5 db.

Since most auroral absorption events are short lived, it is unusual that the ion density measurements from the Black Brant (X = 74.5^{o}), fired about three hours later (1711 UT), show almost identical results (Figure 27-10) above 80 km compared to the X = 89.1^{o} results. The Langmuir probe results from a Nike Iroquis rocket carrying a mass spectrometer fired about 90 minutes after the X = 74.5^{o} rocket shows a decreasing electron density above 80 km. A further decrease above 80 km is noted in the BRL results (X = 74^{o}) approximately 15 minutes later. Note, however, that for these three results there is good agreement in the 70 to 80 km range. If we calculate the absorption for a 30 MHz riometer using the BRL (X = 74^{o}) electron densities below 80 km and the Black Brant X = 74.5 ion densities) above 80 km, we calculate about 5.6 db. The 30 MHz riometer in this time period is generally above about 3.0 db with peaks going slightly over 4.0 db at various times, showing indications of auroral absorption in addition to the absorption due to the proton event.

A composite of the sunset results for 4 November is shown in Figure 27-11. The two BRL propagation results for (X = 85.7^{o} and 93.2^{o}) and the Z-θ probe Black Brant results (X = 96.8^{o}) are compared. Included also is the total ion density from the mass spectrometer measurements of Narcisi et al (these proceedings). With respect to the latter, the mass spectrometer results compare quite well with the Z-θ probe results obtained about 18 minutes later. These results show a substantial decrease in electron density in the 80 km to 110 km region

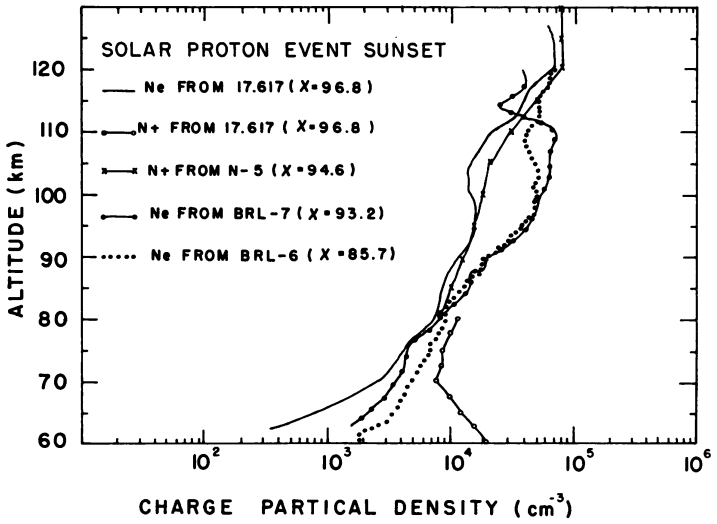

Figure 27-11. Composite of Sunset Measurements on 4 Nov 1969

compared to the propagation results (X = 93.2°) about 12 minutes earlier. The decrease took place within that time since the propagation results made to establish daylight conditions, about one hour earlier (X = 85.7), agree quite well above 80 km with the X = 93.2 propagation results. Below 80 km the electron density decreases with increasing solar zenith angle (X = 85.7°, 93.2° and 96.8°) and, like the sunrise results, show the "twilight anomaly" effect.

References

Baker, K., Burt, D., Howlett, C., and Allard, G. (1970) AFCRL 70-0251, Air Force Cambridge Research Laboratories, Contract No. F19628-67-C-0275, Univ. of Utah.

Despain, A. M. (1966) AFCRL 66-412, Air Force Cambridge Research Laboratories, Contract No. AF19(628)-4995, Univ. of Utah.

Pfister, W. (1965) Handbook of Geophysics and Space Environments, McGraw-Hill Book Co., Inc.

Pfister, W., and Ulwick, J. C. (1965) Radio Science 69D(No. 9).

Reid, G. C., and Collins, C. (1959) J. Atmos. and Tenest. Phys. 14.

Ulwick, J. C., Pfister, W., and Baker, K. D. (1968) Space Research VIII, North Holland Publishing Co.

Ulwick, J. C., and Sellers, B. (1971) Space Research XI, North Holland Publishing Co.

Westman, H. P. (1956) Ed., Reference Data for Radio Engineers, 4th ed., International Tel. & Tel. Corp., New York.

Contents

28. Negative Ion Composition of the D and E Regions During a PCA

R.S. Narcisi, C. Sherman, C.R. Philbrick,
D.M. Thomas, A.D. Bailey, L.E. Wlodyka,
R.A. Wlodyka, D. Baker and G. Federico
Air Force Cambridge Research Laboratories
L.G. Hanscom Field
Bedford, Massachusetts

Abstract

Rocket-borne, cryopumped, quadrupole mass spectrometers were used to measure the negative ions in the lower ionosphere during the November 1969 PCA event. Measurements were made near midday (1147 LT) and midnight 0029 LT) on 3 November. The PCA day flight showed very large concentrations of ions of 32 amu, probably O_2^-, between 72 and 94 km. In two earlier flights into nighttime quiescent conditions, O_2^- was either undetectable or in extremely small concentrations over this altitude range. The PCA night flight also showed O_2^- present below 80 km but ions of mass 16 amu, probably O^-, were generally the predominant ions between 74 and 94 km. In contrast, O^- ions were found only in very small concentrations in the flights during quiet conditions. (The mass range of the PCA day spectrometer did not include 16 amu.) In both PCA flights, heavy negative ions, similar to those measured previously and normally found predominant, were found below 85 km. These ions have been tentatively identified as $NO_3^-(H_2O)_n$, n = 0 to 5, with some possible admixture of $CO_3^-(H_2O)_n$, n = 0 to 5. Ions of mass 76 amu, perhaps CO_4^-, were present below 78 km. In the E-region, Cl^-(35 amu) and NO_2^-(46 amu) ions were measured, but these species may have resulted from contamination.

28-1 INTRODUCTION

This paper reports the negative ion composition measurements obtained in the lower ionosphere during the PCA project. Data were obtained from four rocket flights; two were launched at night prior to the PCA event and the other two were launched near midday and midnight during the event. A general view of the types and altitude distributions of negative ions found in the lower ionosphere under both disturbed and quiescent conditions is presented here.

The measurements were performed with cryopumped, quadrupole mass spectrometers employing a pulse-counting ion detection system. Figure 28-1 shows a schematic of the instrument in the rocket sampling configuration. The electron

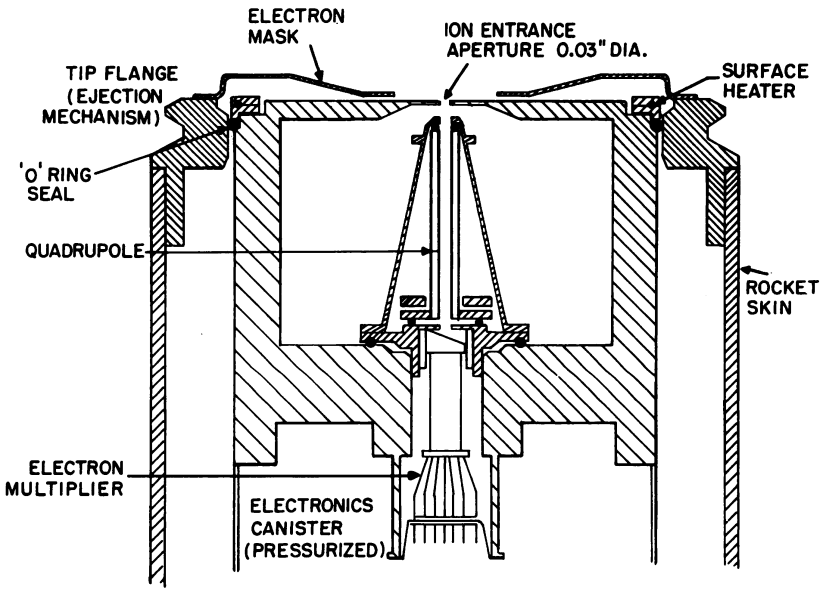

Figure 28-1. Schematic Outline of the Quadrupole Mass Spectrometer in the Rocket Sampling Configuration Showing the Electron Mask Which Reduces the Collection Area for Negative Particles

mask shown is electrically connected to the vehicle skin and serves to reduce the collecting area for negatively-charged particles (especially electrons) to about one-1000th that for positively-charged particles so that the vehicle skin will not be driven overly negative and repel negative ions. Through several rocket experiments, it was found that about +10 volts on the entrance aperture plate will efficiently gather negative ions above 90 km in the E region, but an increasingly larger

potential with decreasing altitude was found necessary to draw-in negative ions in the D region. There are still many details concerning the sampling of negative ions that are not understood, and studies of the nature and effects of the electric field are continuing (Narcisi et al, 1971; Sherman and Parker, 1971). Because of these and other complications, the measurements are presented without conversion into ambient concentrations.

28-2 FLIGHTS OF AUGUST AND OCTOBER 1969

Nighttime measurements of the negative ion composition in the D and E regions were performed on two rocket flights from Ft. Churchill, Canada during quiescent conditions. Both instruments were programmed to study the dependence of the negative ion signal on both the draw-in potential and configuration of the electric field. More details concerning these two flights may be found in Narcisi et al, (1971).

Figure 28-2 shows the voltage programming of the quadrupole and the sampling plate for the two flights. In the August flight, the mass spectrum was swept from

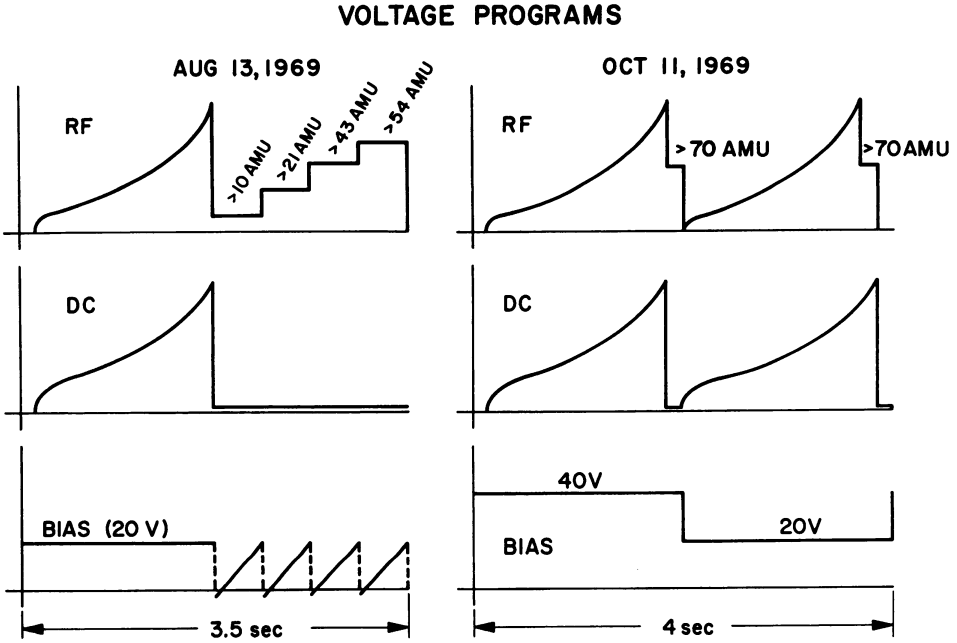

Figure 28-2. Instrument Voltage Programs. Included are the DC and RF quadrupole voltages and also the voltages applied to the sampling plate

12-79 amu, and the total ion transmission mode was stepped so that all negative ions >10, >21, >43 and >54 amu were measured. The sampling plate bias was fixed at 20 volts during the mass scan, but during the total ion steps the plate bias was swept from about 0 to +20 volts. Additionally, the electron mask was switched at apogee and connected to the sampling plate potential throughout descent.

The October flight instrument was adjusted to scan the mass range 12-162 amu because the results of the August flight indicated the presence of heavier mass ions. The sampling plate was alternately biased at 40 and 20 volts, the former because it was found that 20 volts was insufficient for drawing in negative ions efficiently, and the latter for comparison with the August flight results.

Figure 28-3 shows the more striking results of the August flight. Plotted in this figure are the measurements for two of the total ion steps: >10 amu >54 amu. Since the count rate in both steps is about equivalent below 90 km, this indicated that the majority of the ions was heavier than 54 amu. Since the ion count rates measuring up to 79 amu in the mass scan were insufficient to account for the large total ion count rates, this meant that the more abundant negative ions were >79 amu. Mass peaks at 32, 35, 37, 61 $\pm$ 1, 63 $\pm$ 1, 76 $\pm$ 1, 78 (?) amu were measured between 78 and 90 km (Narcisi et al, 1971).

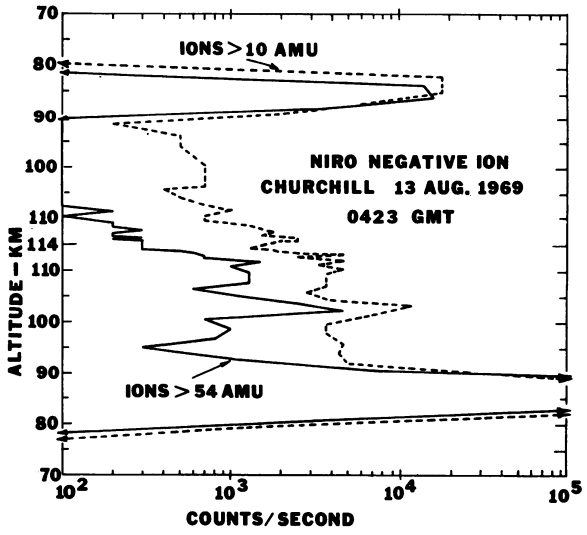

Figure 28-3. Counts/Sec vs Altitude for Ions >10 amu and for Ions > 54 amu for the Flight of 13 Aug 1969. The cutoff below 80 km is due to insufficient draw-in potential and is not real. On ascent, the vehicle angle of attack between 70 and 103 km was less than 10^o and increased to 90^o near apogee. On descent, the angle of attack attained a maximum of 137^o at 100 km and decreased uniformly to 82^o at 83 km

The precipitous decrease in the negative ion concentrations between 90 and 92 km is apparent on both ascent and descent in Figure 28-3. The total ion steps separate in the E region, indicating that most of the ions have masses between 10 and 54 amu, and indeed the only negative ions measured were 16(O^-), 35/37(Cl^-), and 46(NO_2^-). The Cl^- and NO_2^- probably arise from contaminants, and O^- may result from the reaction $e + O_2 \rightarrow O^- + O$ which becomes energetically possible when the electrons gain kinetic energy in the attractive electric field. In any case, the negative ion concentrations in the E region are relatively small.

Based on the August results, an instrument was adjusted to scan up to 162 amu to mass analyze the heavy ions, and launched at night at 0200 GMT on 11 Oct 1969. Figure 28-4 is a photograph of the telemetry data in the D region on upleg. Shown are the RF sweep monitor and three spectrum outputs corresponding to 15, 127 and 1025 counts full scale. A digital-to-analog converter in the instrument samples and reads out the counter every 10 msec. Therefore, to obtain counts/sec the counts in the spectra must be multiplied by 100. It is seen that a group of heavy negative ions are present with masses near 62, 80, 98, 116, 134 and 152 amu. Because the mass resolution is low, there are uncertainties concerning the absolute values of these mass numbers, but they do appear to be 18 amu apart, suggesting a multiple hydration of some basic ion. These ions were tentatively identified as $NO_3^-(H_2O)_n$, n = 0 - 5, but possible admixtures of $CO_3^-(H_2O)_n$ cannot be ruled out since multiple peaks may be present within the large peak widths. There is also evidence of a 76 amu peak, perhaps CO_4^-, at lower altitudes. The signal intensity with the 40 volt bias is clearly larger than that for the 20 volt bias. Furthermore, mass 134 appears only at the 40 volt bias, indicating that the draw-in potential affects both the absolute and relative intensities. The 134 amu ion may result from collisional fragmentation of a larger cluster ion after it acquires the dissociation energy in the draw-in field.

Figure 28-5 shows the descent spectra obtained in the D region from the October flight. It is seen that the measurements are essentially identical to those on upleg in Figure 28-4.

28-3 PCA MEASUREMENTS

During the 2-4 November 1969 PCA event at Ft. Churchill, Canada, D and E region negative ion composition measurements were performed near midday and midnight. Figure 28-6 presents the results from the night flight (0029 CST, $\chi = 136^{o}$). The mass 16 amu peak is clearly enhanced during the PCA; only very small peaks at 16 amu are seen in Figures 28-4 and 28-5 during quiescent conditions. Unfortunately, the signal intensity was diminished on upleg because of the slow

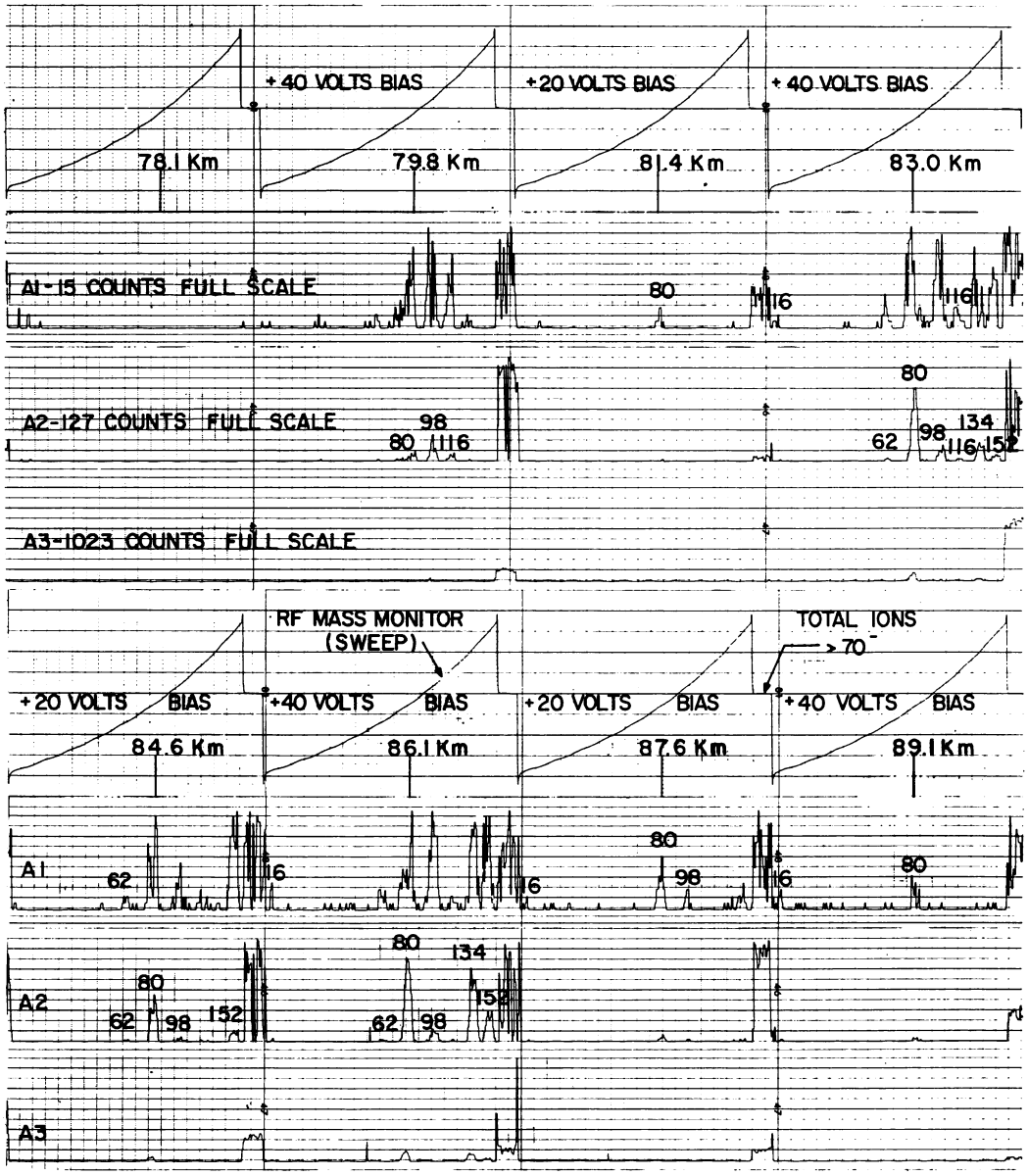

Figure 28-4. Strip Chart Record of Ascent Data Between 77 and 90 km for the Flight of 11 Oct 1969. The vehicle angle of attack was between 15° and 21° over the 77–90 km range

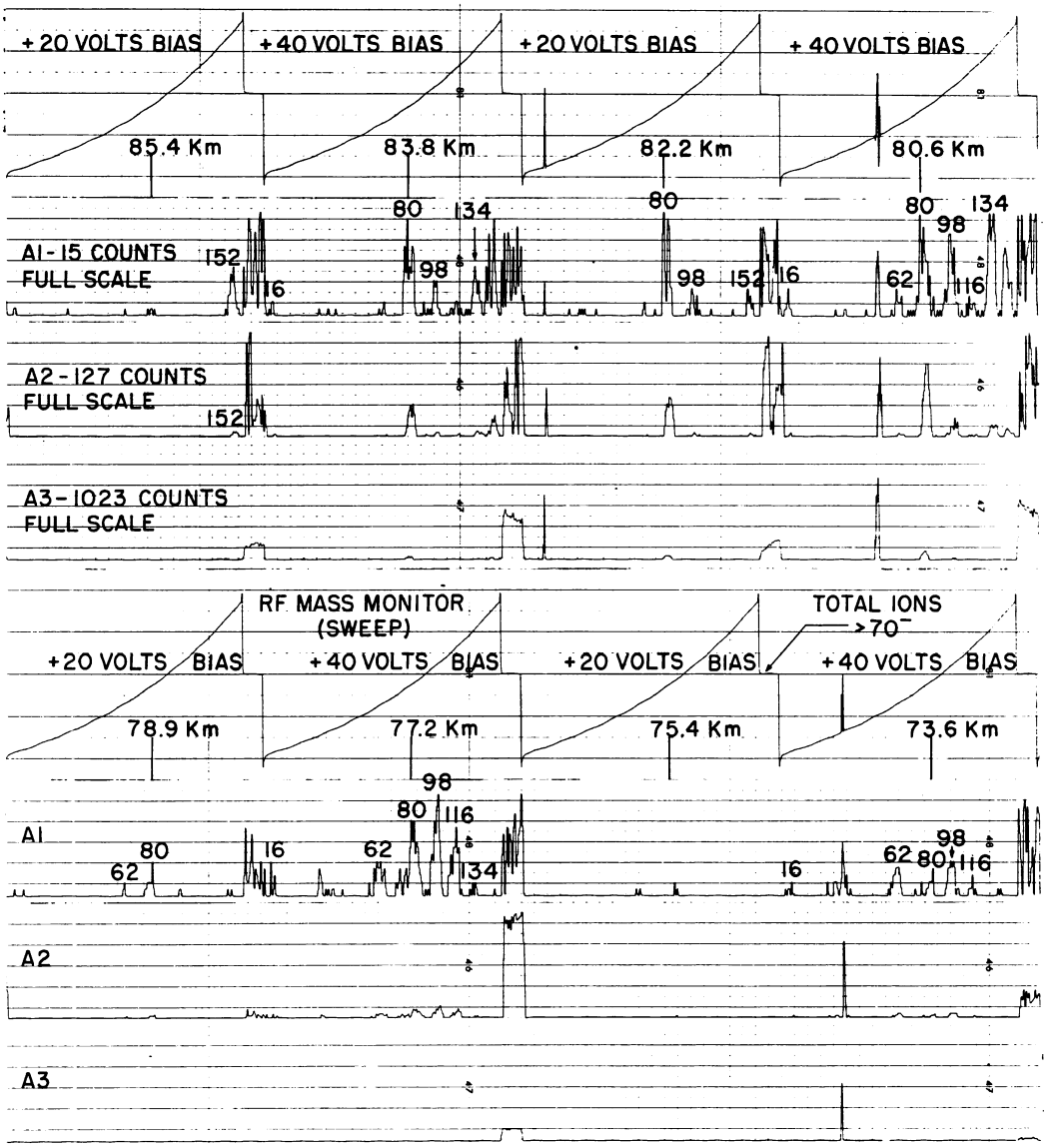

Figure 28-5. Strip Chart Record of Descent Data Between 86 and 73 km for the Flight of 11 Oct 1969. The vehicle angle of attack decreased monotonically from 82° to 11° from 86 to 74 km

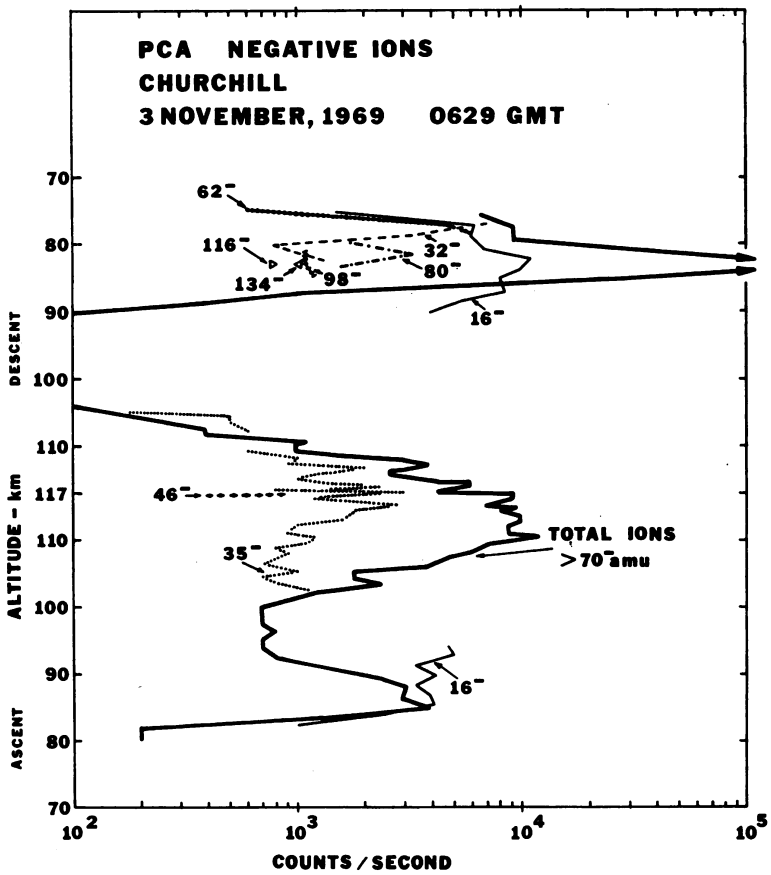

Figure 28-6. Nighttime Negative Ion Composition Measurements in the D and E Regions During a PCA

pump recovery following the pressure burst on nose cone ejection. Collisional loss in the instrument accounts for the absence of the heavy ions in the mass scans on upleg. As the vehicle went over apogee, the pump recovered and the heavy ions appeared in the mass scans on downleg. Heavy ions greater than 70 amu were measured in the more sensitive total transmission mode of the quadrupole and are shown in Figure 28-6. The signal intensity for the ions >70 amu was about equivalent to that for mass 16 on upleg, but on downleg, when the instrument pressure was lower, the signal was off scale (>102,500 counts/sec). Signal cutoff below 77 km on descent is due to increasing pressure in the quadrupole.

On downleg, the mass 32 amu (O_2^-) concentration becomes larger than the 16(O^-) concentration below 76 km, in contrast to quiescent conditions when O_2^- is present in relatively small concentrations. The E region ions are Cl^- and NO_2^-, which again are probably contaminants.

The daytime (1147 CST, $\chi = 73.9^{o}$) PCA measurements are shown in Figure 28-7. Unfortunately, the instrument did not scan down to mass 16, so the profile of O^- is unknown. Clearly the 32 amu ion, identified as O_2^-, is a dominant daytime ion above 76 km to 94 km. The heavy cluster ions are still present along with CO_4^-(76 amu) below 77 km. The downleg measurements, although affected by vehicle aspect, appear to agree qualitatively with the upleg measurements.

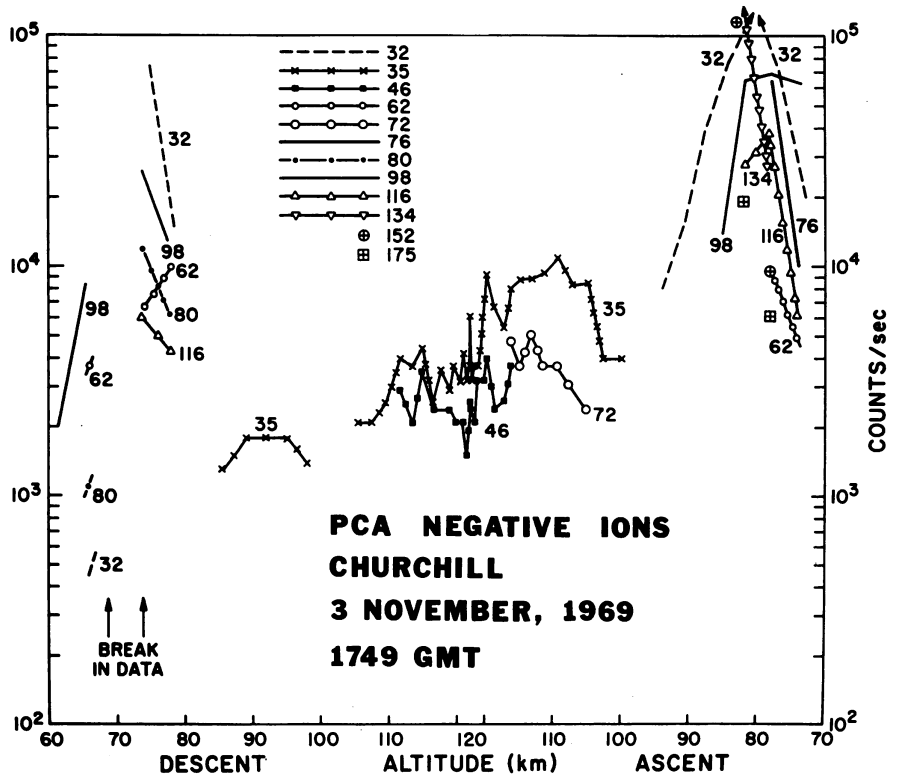

Figure 28-7. Daytime Negative Ion Composition Measurements in the D and E Regions During a PCA

The aeronomical implications of these measurements are discussed by Narcisi (these proceedings).

Acknowledgments

This research was supported in part by the Defense Nuclear Agency.

References

Narcisi, R.S., Bailey, A.D., Della Lucca, L., Sherman, C., and Thomas, D.M. (1971) Mass spectrometric measurements of negative ions in the D- and lower E- regions, J. Atmosph. Terr. Phys. 33:1147.

Narcisi, R.S. (1972) Aeronomical Implications from Ion Composition Measurements during a PCA, these proceedings.

Sherman, C., and Parker, L.W. (1971) Potential due to a circular double disk, J. Appl. Phys. 42:870.

Contents

29. Positive Ion Composition of the D and E Regions During a PCA

R.S. Narcisi, C.R. Philbrick, D.M. Thomas,
A.D. Bailey, L.E. Wlodyka, D. Baker,
G. Federico, R. Wlodyka and M.E. Gardner
Air Force Cambridge Research Laboratories
L.G. Hanscom Field
Bedford, Massachusetts

Abstract

Positive ion composition measurements were obtained from three rocket flights in the D and E regions over Ft. Churchill, Canada during the 2-4 Nov 1969 PCA event. The rockets were launched at 0130 CST (0.4 dB) and 1130 CST (3 dB) [30 MHz riometer absorptions in parentheses] on 3 November and at 1650 CST (0.7 dB) on 4 November. Results from the nighttime measurements between 62 and 139 km showed that water cluster ions were predominant below 77 km and that NO^+ and O_2^+ were the major ions from 77 to 139 km. A class II^+ aurora was also in progress during the night flight as evidenced by the total ion density, which attained a maximum of 8×10^5 ions/cm^3 at 122 km and exceeded 10^5 ions/cm^3 between 105 and 127 km. Daytime and sunset measurements were made between 73 and 144 km and between 78 and 144 km, respectively. NO^+ and O_2^+ were dominant ions down to the lower altitude measurement limits of both flights. The persistent broad meteoric ion layer centered near 95 km, and submerged thin layers of meteoric species at higher altitudes were measured in all flights. Previous measurements obtained under more quiescent conditions are compared to the PCA measurements.

29-1 INTRODUCTION

During the 2-4 November 1969 PCA event at Ft. Churchill, Canada, three rocket measurements of the D and E region positive ion composition were performed with cryopumped, quadrupole mass spectrometers. Each rocket payload contained a mass spectrometer, a cylindrical Langmuir probe, a gyro aspect system, radar beacon and FM/FM telemetry. The first mass spectrometer was launched on November 3 at 0130 CST, the second was fired 10 hours later at 1130 CST, and the third was launched at sunset at 1650 CST on November 4. Table 29-1 gives other pertinent flight details. The results of the mass spectrometer measurements are presented and are compared with previous measurements obtained over Ft. Churchill and at mid-latitudes during more quiescent conditions.

Table 29-1.

Rocket	Launch Time Date	Solar Zenith Angle	Zenith Riometer Absorption (dB)*	Mass Range (amu)	Total Ion Step(s)	Mass Scan Time (Sec)
AG7.882	0730Z 3 Nov 69	133°	0.4	13.5 - 108.5	>34 amu >50 amu	2.6
AH7.886	1730Z 3 Nov 69	74°	3.0	9.5 - 71.5	41.5 amu	2.0
AH7.893	2250Z 4 Nov 69	94.6°	0.7	12.5 - 67.0	42 amu	1.5

*R. Cormier, these proceedings.

29-2 EXPERIMENTAL METHOD

The cryopumped positive ion mass spectrometer has been described elsewhere (Narcisi and Bailey, 1965; Bailey and Narcisi, 1966). Table 29-1 also lists the mass ranges, total ion transmission steps, and the mass scan times for the three instruments flown. The mass range was periodically swept and followed by the total ions step(s) in the times noted. The mass spectrometer on AG7.882 had two total ion steps. Figure 29-1 shows this feature and gives examples of D and E region flight spectra. In each step the draw-in potential imposed on the surface containing the ion entrance aperture was varied from +4 volts to -19 volts in order to examine the fragmentation of cluster ions caused by the sampling electric field (Narcisi, 1970). In all other cases the draw-in potential was fixed at about -10 volts. A vacuum cap seal was ejected with the nose cone in the vicinity of

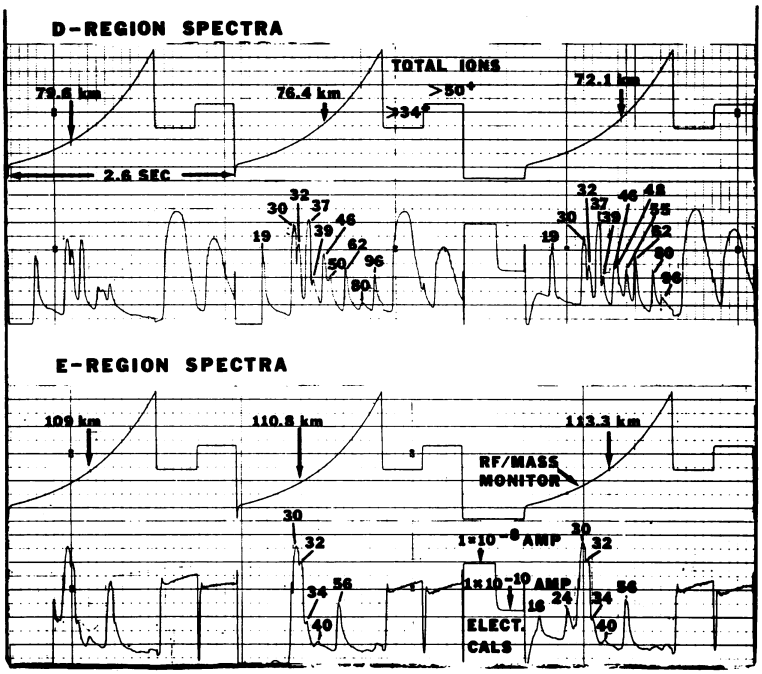

Figure 29-1. Flight Mass Spectra Obtained in the D and E Regions on Rocket AG7.882

72 km on vehicle ascent to expose the 0.030 in. diameter mass spectrometer sampling orifice.

29-3 DATA AND ANALYSIS

The measured mass peak ion currents for each species were plotted as a function of altitude, and straight lines were drawn to connect adjacent data points. These profiles were then normalized for vehicle speed and vehicle attitude by the method outlined by Narcisi (1971). The normalized currents of all species were summed at each altitude and the resulting profile was multiplied by a constant factor to obtain profiles of ion density vs altitude. This constant factor was derived from electron density measurements with Langmuir probes, 3-frequency beacons, and ion mass spectrometer sensitivities. Other details and uncertainties in this method may be found in Narcisi (1971). Generally, except where indicated otherwise, the error in the absolute concentrations is less than or about $\pm$ 30 percent. The altitude error is probably less than 0.2 km.

The positive ion mass numbers and identifications of species measured in the D and E regions are listed here for future reference: 16(O^+), 19(H_3O)$^+$,

24(Mg^+), 27(Al^+), 28(N_2^+ or Si^+), 30(NO^+), 32(O_2^+), 34($^{16}O\ ^{18}O^+$), 37($H_5O_2^+$), 39($H_5{}^{16}O^{18}O^+$), 40(Ca^+), 46(NO_2^+), 48($NO^+ \cdot H_2O$), 50($O_2^+ \cdot H_2O$), 55($H_7O_3^+$), 56(Fe^+), 62 ± 1 (?), 72($Fe\ O^+$), 80 ± 1 (?), 96 ± 1 (?). The unidentified mass numbers, 62 and 80, are separated by 18 amu, possibly suggesting a hydrated species.

29-4 RESULTS

29-4.1 AG7.882

Figure 29-2 gives the ascent results obtained between 72 and 139 km from the night flight of rocket AG7.882. The zenith riometer absorption was 0.4 dB.

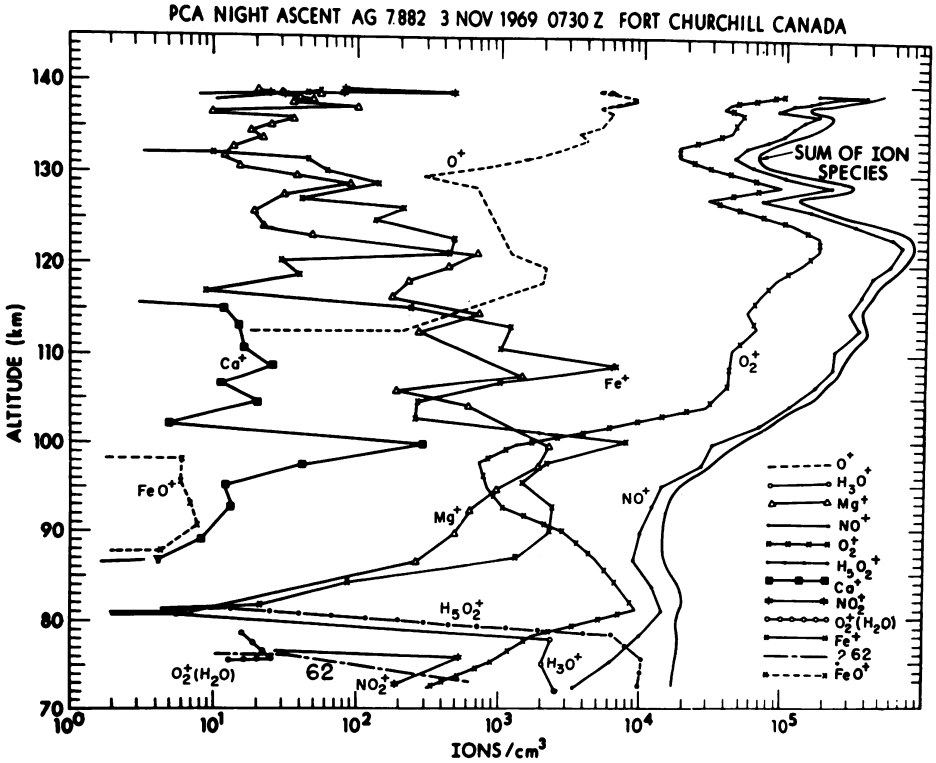

Figure 29-2. The Positive Ion Composition in the Nighttime D and E Regions During a Simultaneous PCA Event and Auroral Event

The ion concentrations in both the D and E regions were greatly enhanced. Below 90 km, the ion concentrations were increased by more than 100 times normal

due to proton ionization. The most striking of the results in the D region was the significant change in the water-cluster ion distribution. Water-cluster ions normally dominate the nighttime D region below 86 km (Narcisi, 1971; Narcisi et al, 1972). But Figure 29-1 shows that under these disturbed conditions water-cluster ions are predominant only below 77 km and that NO^+ and O_2^+ are the major ions above this altitude.

The results between 90 and 100 km which include the main meteoric layer are typical of measurements obtained during more quiescent conditions at Ft. Churchill (Narcisi, 1971). Submerged sporadic E-like layers of meteoric species were present up to apogee. Above 100 km, the ion concentrations were again significantly increased and attained a maximum of 8×10^5 per cm^3 at 122 km. This ion density is indicative of an IBC class II^+ aurora which was most likely produced by energetic electrons. Overcast skies prevented ground-based optical observations of auroral activity.

Energetic electrons and increased charged-particle concentrations in the E region were measured by a Black Brant rocket payload fired 1 hr 25 min earlier (Ulwick, 1972). No such measurements were available for the time of this rocket flight. Unfortunately, the Langmuir probe failed so that no other charged-particle profile was available for comparison. The Ft. Churchill ionosonde, however, indicated that strong auroral activity was present. Figure 29-3 shows three ionograms taken during the flight of this rocket. Typical of a PCA event, the lower frequency radiation is absorbed, but in the vicinity of 120 km strong auroral pulsations were observed with returns up to and exceeding 16 MHz. It is, however, not possible to obtain reliable quantitative values from these ionograms to apply to the flight results.

Measurements were obtained on downleg to 62 km on rocket AG7.882. Figure 29-4 gives the uncorrected currents for the various species vs altitude on descent, and the figure demonstrates the complexity of the D region. The identifications listed previously apply for the mass numbers shown. The rocket was backing into the atmosphere, and as the rocket's speed increased on descent the currents were increasingly reduced. The rocket began turning over at 82 km and by 78 km the instrument was pointed into the direction of motion and the currents increased markedly.

There are several difficulties associated with the D region measurements that are worthy of discussion. The true relative abundance of the ion species in the D region is distorted by the rocket sampling method which causes a breakup of the cluster ions. Because the ion clusters, and especially the larger ones, are weakly bound, they can be torn apart by collisions in the shock-heated gas and/or by collisional fragmentation after the ion gains sufficient energy in the sampling electric field (Narcisi, 1970; Narcisi and Roth, 1970). Typically, water molecules are

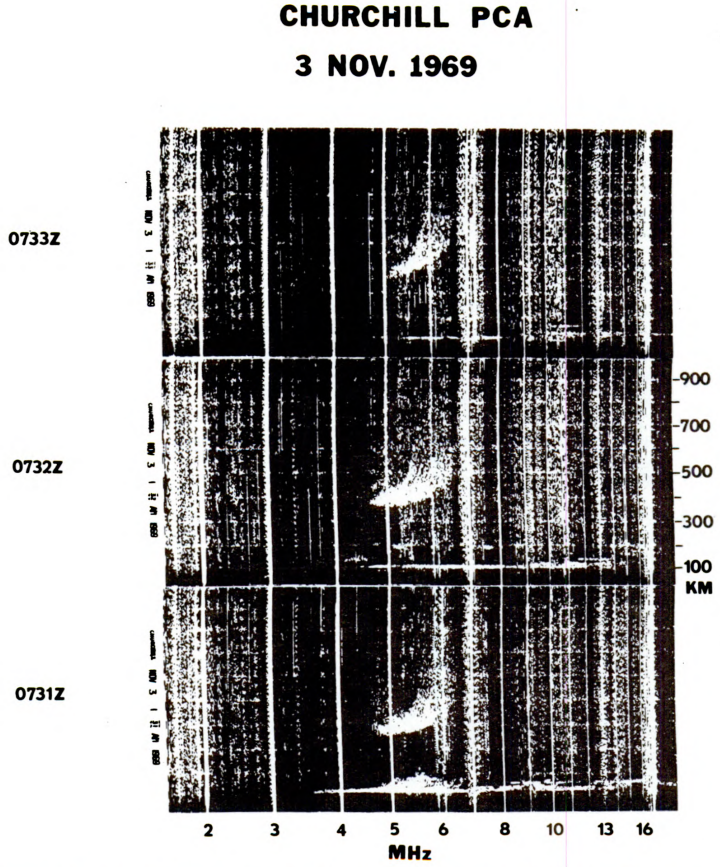

Figure 29-3. Ionograms Indicating Auroral Activity During the Flight of Rocket AG7.882

broken off the cluster ion in these processes. The decrease in ion species currents below about 72 km, as seen in Figure 29-4, was due to increasing pressure in the mass spectrometer and collisional loss of ions from the ion beam. The heavier ions with the larger collisional cross sections, were affected most. The measured lighter mass ions below 70 km were most likely the fragments of heavier ones.

29-4.2 AH7.886

Figure 29-5 presents the ascent results obtained between 73 and 144 km from the daytime flight during which the zenith riometer absorption was 3 dB. There are two peculiarities in the results shown in Figure 29-5. First, the decrease in concentrations below 80 km is not actual, but was due to high pressure in the quadrupole resulting from the slow pump recovery after the pressure burst on nose-cone

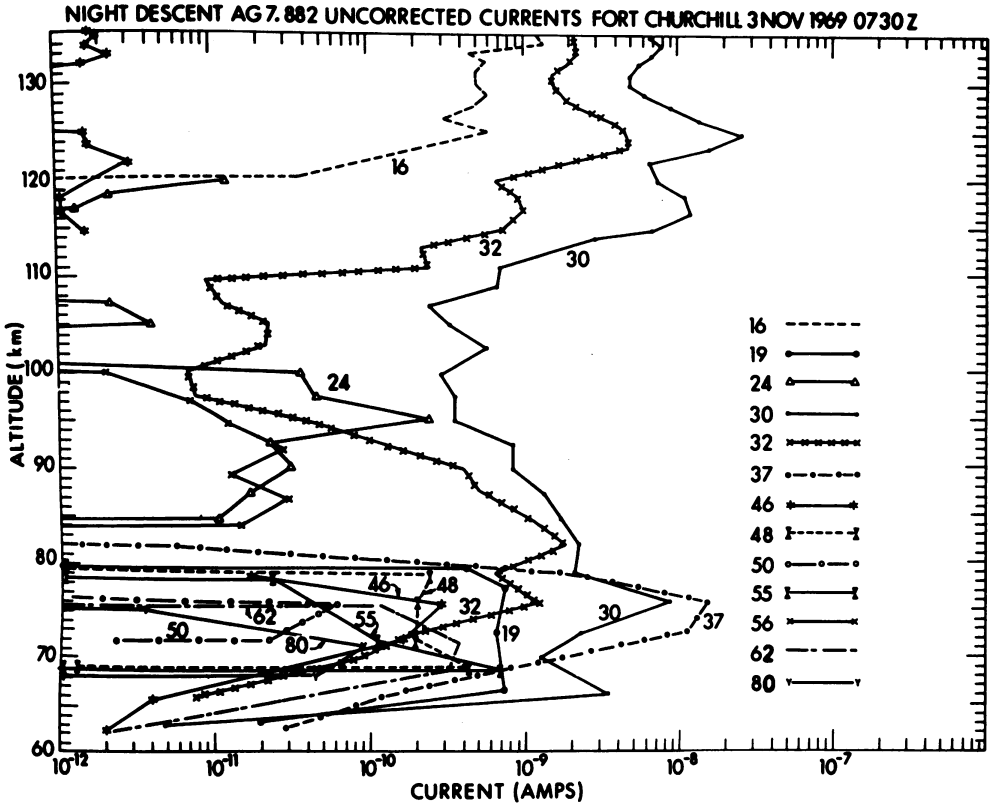

Figure 29-4. D and E Region Positive Ion Composition Measurements Obtained on Downleg of Rocket AG7.882 During a PCA

ejection. Secondly, the modulations in the data were produced by the spin of the vehicle and azimuthal variations in ion transmission of the quadrupole, especially at large angles of attack. This is difficult to correct. Although not performed here, smooth profiles may be determined by utilizing the relative composition which is considerably less modulated and then normalizing the relative abundances to the total density profile determined from the Langmuir probe measurements. The altitude profile of the NO^+/O_2^+ ratio for this flight generally exhibits less than a 20 percent modulation. On the other hand, mean profiles could simply be drawn through the modulated ones in Figure 29-5, and the results generally would not deviate by more than a factor of two from these mean curves.

There are several interesting features in the daytime flight results. NO^+ and O_2^+ were the major ions over the entire altitude range with O_2^+ dominating only between 78 and 90 km. During normal daytime conditions at mid-latitudes, water-cluster ions predominate below about 82 km (Narcisi et al, 1972). The concentrations

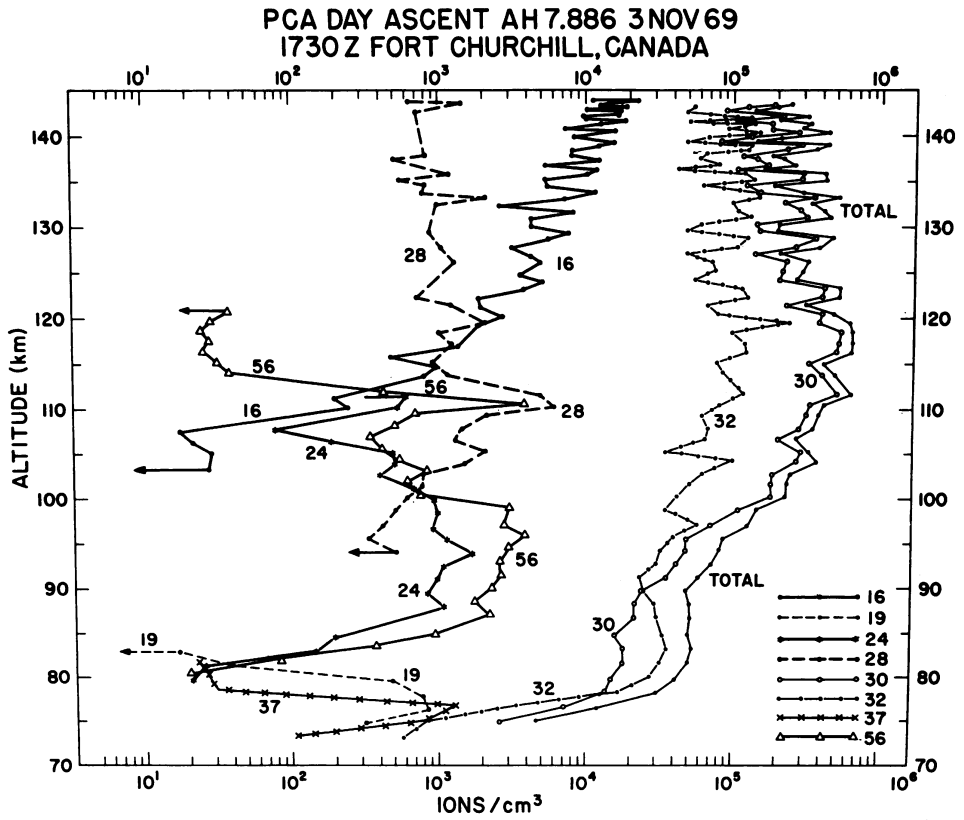

Figure 29-5. Daytime Positive Ion Composition of the D and E Regions During a PCA

of H_3O^+ and $H_5O_2^+$ in the day flight are similar to those during quiescent midday and mid-latitude conditions, but their concentrations are considerably smaller than the previous night flight values (compare Figures 29-2 and 29-5).

The iron and magnesium ions in the main meteoric band around 95 km were in about the same concentrations as in the nighttime flight; aluminum and calcium ions were also measured but are not plotted in Figure 29-5. An upper layer of meteoric species was located at 109 km at night; another one was measured at 110.5 km 10 hours later. Also note that the major ion in the daytime layer was silicon (28^+). Mass 28 above and below the layer was most likely N_2^+.

The diurnal model of the E region of Keneshea et al (1970) predicts ion densities somewhat less than 10^5 cm^{-3} above 95 km for the normal solar flux at the solar zenith angle for this flight (74^o). In the PCA daytime flight the ion densities were greater than 10^5 cm^{-3} above 96 km and as high as $5\text{-}6 \times 10^5$ cm^{-3}. Even applying the factor of two error reduction in density does not reduce the

concentrations sufficiently; therefore, it is believed that energetic electrons created most of the E region ionization during the daytime flight.

29-4.3 AH7.893

Figure 29-6 presents the ascent results between 78 and 144 km from the rocket flown near sunset on November 4 when the zenith riometer absorption was 0.7 dB. The results showed considerable variations above 112 km; however, again the NO^+/O_2^+ ratio was not as seriously modulated. Only a trailing off of the water-cluster ion ledge was seen between 78 and 86 km. NO^+ and O_2^+ were generally the dominant ions over the D and E regions with meteoric ions also present in significant concentrations between 90 and 104 km. O^+ was less than 2-3 percent of the total density.

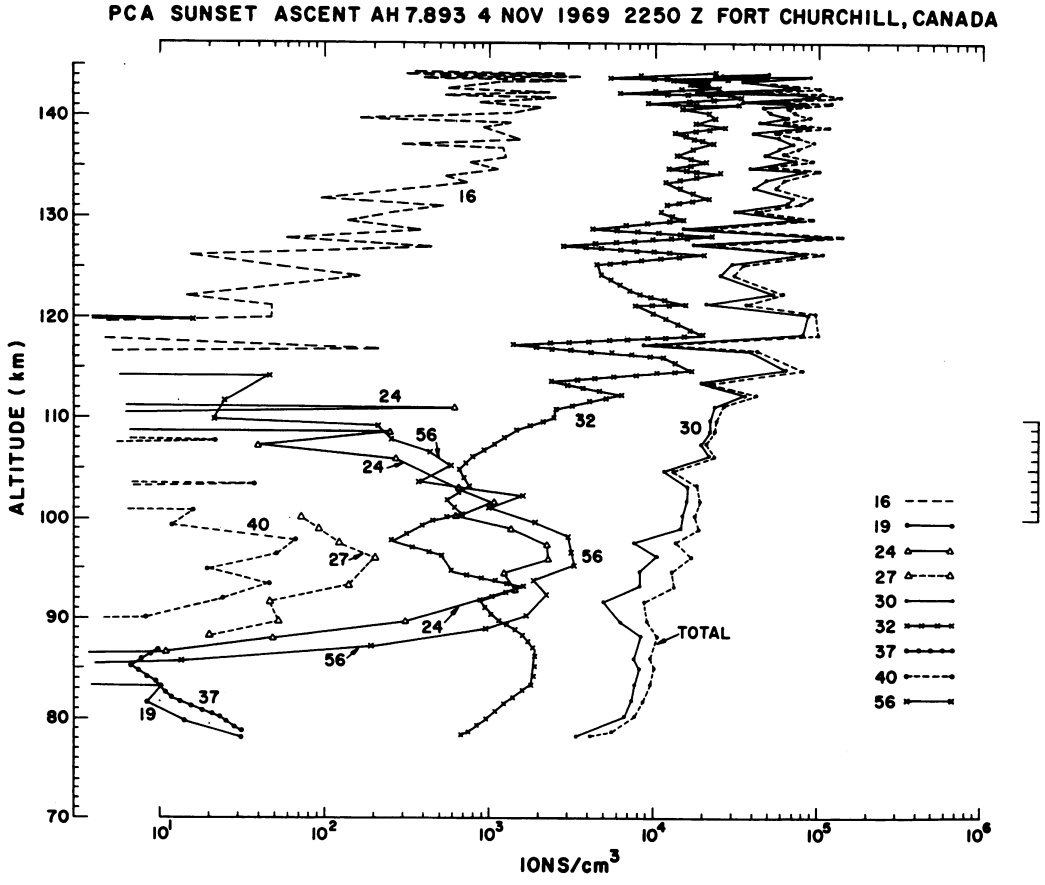

Figure 29-6. Sunset Positive Ion Composition of the D and E Regions During a PCA

A comparison of the results from this rocket flight launched at 94.6° solar zenith angle with the results from a sunset flight launched at 96.4° on 4 Dec 1967 from Ft. Churchill during more quiescent conditions is quite interesting. The 1967 results above 85 km (Narcisi, 1971, Figure 15) are essentially identical to those in Figure 29-6, considering the errors in absolute densities. However, below 86 km, the 1967 measurements (Narcisi, 1971, Figure 14) indicated that water-cluster ions ($H_5O_2^+$) were the dominant ions up to 86 km. In the PCA sunset flight, water cluster ions were present in extremely small concentrations down to 78 km. It is possible that the water-cluster ion concentrations could have increased steeply to become predominant by 76 or 75 km. In any case, the water cluster ions were suppressed at least over the 9 km range between 77 and 86 km.

The aeronomical implications of these measurements are discussed by Narcisi (these proceedings).

Acknowledgments

This research was supported in part by the Defense Nuclear Agency.

References

Bailey, A.D., Narcisi, R.S. (1966) Miniature Mass Spectrometers for Upper Atmosphere Composition Measurements, Instr. Paper No. 95, AFCRL 66-148.

Keneshea, T.J., Narcisi, R.S., and Swider, W. (1970) Diurnal model of the E region, J. Geophys. Res. 75:845.

Narcisi, R.S., and Bailey, A.D. (1965) Mass spectrometric measurements of positive ions at altitudes from 64 to 112 km, J. Geophys. Res. 70:3687.

Narcisi, R.S. (1970) Shock wave and electric field effects in D region water cluster ion measurements, Trans. Amer. Geophys. Union 51:366.

Narcisi, R.S., and Roth, W. (1970) The formation of cluster ions in laboratory sources and in the ionosphere, Adv. Electronics Electron Phys. 29:79.

Narcisi, R.S. (1971) Composition studies of the lower ionosphere, chapter in Upper Atmos. Phys. F. Verniani, ed., Casa Editrice Compositori, p. 12-59.

Narcisi, R.S., Bailey, A.D., Wlodyka, L.E., and Philbrick, C.R. (1972) Ion composition measurements in the lower ionosphere during the November 1966 and March 1970 solar eclipses, J. Atmos. Terr. Phys. 32:663.

Narcisi, R.S. (1972) Aeronomical implications from ion composition measurements during a PCA (these proceedings).

Ulwick, J.C. (1972) Comparison of Black Brant rocket measurements of charged particle densities during solar particle events (these proceedings).

Contents

30. Ozone Measurements in the Mesosphere During the Solar Proton Event of 2 November 1969

L.H. Weeks, R.S. CuiKay*, and J.R. Corbin
Air Force Cambridge Research Laboratories
L.G. Hanscom Field
Bedford, Massachusetts

Abstract

Two Sidewinder-H.V. Arcas rockets were instrumented to measure the ozone distribution during the initial and final phases of a solar proton event. The measurements were obtained by the technique of solar absorption spectroscopy and covered the altitude range 51-80 km. The ozone distribution on 4 November 1969 is significantly less than typical mid-latitude data but lies generally within the range of other high-latitude observations. Current photochemical-transport models are found to overestimate ozone but approach agreement with the data at higher altitudes. During the initial phase of the disturbance on 2 November 1969, the ozone concentration is found to be significantly less at all altitudes. The change amounts to a factor of 2 at 54 km, 3 at 60 km, and 4 at 67 km. The pronounced decrease in ozone is believed to result from the particle precipitation.

*Now at Raytheon Co., Norwood, Mass. 02062

30-1 INTRODUCTION

Two Sidewinder-H.V. Arcas payloads were instrumented with UV photometers for measuring the ozone distribution in the mesosphere. The rockets were launched from Ft. Churchill, Manitoba, in conjunction with the PCA 69 program, a coordinated series of D-region measurements during a solar proton event. The first rocket was fired into the initial phase of the event on 2 November 1969, and the second rocket was fired during quieter conditions on 4 November 1969. Rocket flight information and zenith riometer levels at Ft. Churchill are summarized in Table 30-1. Both observations were conducted at sunset, to take advantage of the increased sensitivity resulting from the long solar radiation absorption path in the atmosphere, permitting measurements of ozone to 80 km.

Table 30-1. Circumstances for Ozone Measurements

Rocket	A30.900-2	A30.900-3
Date	2 Nov 1969	4 Nov 1969
Launch	2211 U.T.	2206 U.T.
Solar Zenith Angle (65 km, ascent)	89.75°	89.77°
Zenith Angle Variation (50-80 km, ascent)	0.13°	0.13°
30 MHz Absorption (Riometer)	7 db	1.3 db

The primary objective of the measurements was to determine what effect, if any, the solar proton event has on the high-altitude ozone distribution. A secondary objective was to obtain badly needed information on the ozone distribution at high latitudes. So that possible diurnal variations in ozone did not compromise the primary objective, both rockets were launched as close to the same zenith angle as possible.

30-2 DESCRIPTION OF EXPERIMENT

The measuring technique is based on solar absorption spectroscopy. For wavelengths above approximately 2400Å, in the region of the Hartley absorption bands, ozone is the only significant absorber of solar radiation. Analysis of the absorption profile at selected wavelength bands can then be used to determine the altitude distribution of the absorber. It is convenient to choose wavelength bands of about 40Å

half width, centered between 2550 and 2600Å, where the absorption cross section of ozone has reached a maximum and is nearly constant. Consequently the absorption profile is obtained at higher altitudes and a constant absorption cross section can be used in the analysis over a wider range of altitudes than would be the case at higher wavelengths or for wider spectral bands.

Figure 30-1 illustrates the absorption cross section of ozone on an expanded scale in the vicinity of the peak of the Hartley bands. The agreement between the data of Inn and Tanaka (1953) and Vigroux (1969) is very good. An effective cross section value of 11×10^{-18} cm^2 is seen to be applicable to a bandpass defined by a typical interference filter, even for an angular shift of 20° (which could result from rocket precession). Filters with rather low transmission are found to be adequate in combination with a photodiode to provide sufficiently high current levels and have the advantage of narrower bandpasses than are frequently used for ozone measurements.

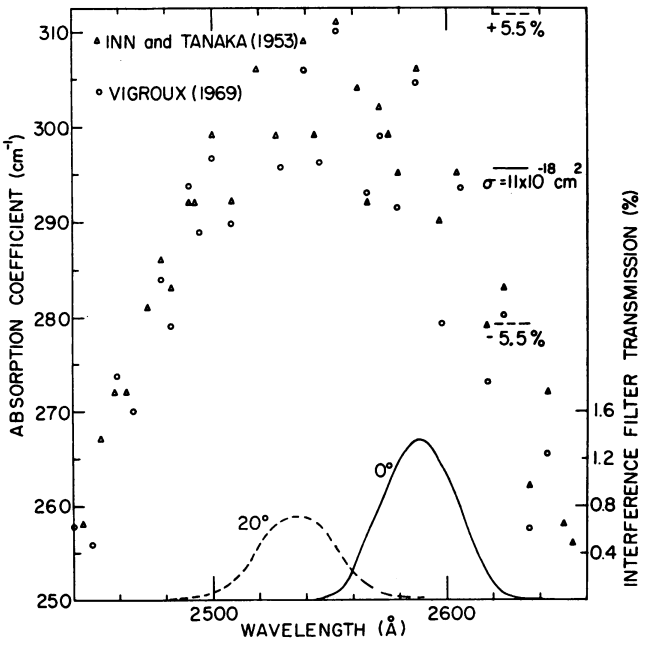

Figure 30-1. Absorption Coefficients of Ozone and Typical Interference Filter Response

For solar zenith angles less than 90°, the number density is determined from the relation

$$n(z) = \frac{1}{\sigma F(H,\chi)} \frac{1}{I(z)} \frac{dI(z)}{dz} \qquad (30\text{-}1)$$

where n is number density, z is rocket altitude, I is the photometer current (or solar flux), σ is the effective absorption cross section, H is the density scale height, and χ is the solar zenith angle. The quantity F is the optical depth factor, and is given by

$$F(H,\chi) = \frac{100.4}{H^{1/2}} \left[1 - \operatorname{erf}\frac{90-\chi}{H^{1/2}}\right] \exp\left[\frac{(90-\chi)^2}{H}\right]. \qquad (30\text{-}2)$$

A more complete discussion of these relationships is given in Weeks and Smith (1968).

The data accuracy (see Appendix A-30) is estimated from the maximum differences in calculations based on computer fits spanning different height intervals and hand calculations. The computer runs are based on constant scale height fits over the given interval. Good resolution is obtained with six to nine data points/km interval. Lower accuracy is obtained at the higher altitudes from uncertainties in calculating the derivatives when they are small. The major error at the lowest altitudes is from the uncertainty in the baseline correction term for filter "leak" radiation. This becomes important in the vicinity of 3 to 4 optical depths for these photometers and restricts the low altitude limit to approximately 4 optical depths. An additional systematic error of ± 6 percent is obtained from uncertainties in trajectory (± 5.5 percent), telemetry ($\pm$ 1-2 percent), and effective cross section (± 1 percent).

30-3 RESULTS

Two photometers were used in the payloads to provide backup. Their orientations with respect to the longitudinal axis were skewed in order to lessen the dependence of data quality on rocket precession. In both flights all data were obtained at aspect angles less than 20° so that there was no significant change in effective absorption cross section for the photometers. Solar aspect was also obtained so that the data could be corrected for variations in sensitivity resulting from rocket precession. During ascent, the positions of the two rockets with respect to the sun differed by less than 0.02° (see Table 30-1).

The measurement on 4 November 1969 is considered first. It is shown in Figure 30-2 together with high latitude winter data of Hilsenrath (1971). Our results are well fitted by a scale height of 3.6 km from 52 to about 66 km and by a

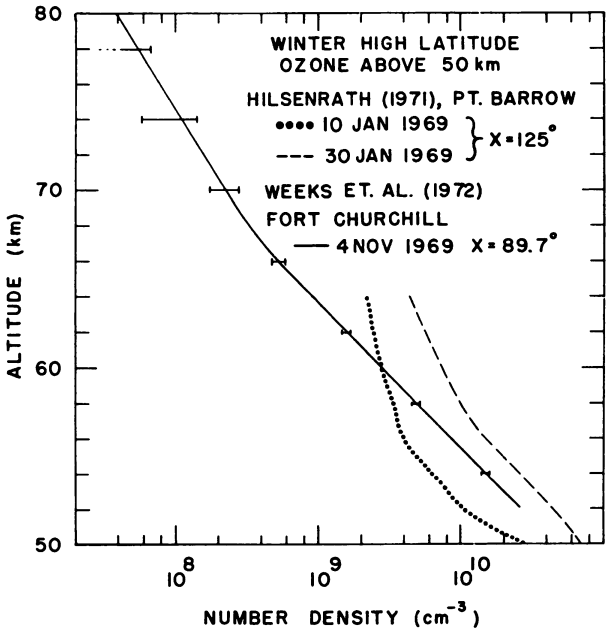

Figure 30-2. Sunset Ft. Churchill Data of 4 Nov 1969 Compared With Nighttime Pt. Barrow Data

scale height of 5.2 km from about 70 to 80 km. The scale height below 66 km and the densities are significantly less than typical mid-latitude observations; for example, the densities are 60 to 70 percent less than the data of Johnson et al (1952), the only other sunset data in the literature (see Appendix A-30). Our data lies within Hilsenrath's profiles up to 60 km but shows a significantly different trend from 58 to 64 km.

Atmospheric ozone is formed by the three-body reaction

$$O + O_2 + M \xrightarrow{k_1} O_3 + M \qquad (30\text{-}3)$$

The major loss processes in the mesosphere are dissociation by solar radiation and reactions with the minor species O, H, and NO. For the most part, these minor species have not yet been measured over the same altitudes as the ozone, and their concentrations and variability are not estimated by models to better than an order of magnitude. The quantities O_2 and M in Eq. (30-3) cause a strong dependence of ozone concentration on the total neutral density. The neutral atmosphere at high latitudes shows considerable variability and generally low densities. Thus we would expect that the high latitude ozone will also tend to be lower and

more variable than at mid-latitudes. The minor species may significantly modify these trends, and more information is needed on them.

The lower ozone densities we observed compared to Johnson et al (1952) may be due to a latitudinal and seasonal effect on the total density. Total density measurements by Faire and Murphy (1972) near the time of our data were typical of the 60°N Jan. model of the U.S. Standard Atmosphere Supplements (1966). It is probable that the mesosphere above White Sands during Johnson's measurements is close to a 30°N summer from these supplements, so that about two-thirds of the difference in ozone density could result from neutral density changes alone.

Hilsenrath (1971) has interpreted the Pt. Barrow data as showing that the ozone is governed by a dry photochemistry, and the large temperature differences measured by Smith et al (1971) were believed to be the controlling factor in changing the ozone distribution. Loss of ozone to HO_2 and OH were believed to be temperature insensitive, and since Eq. (30-3) and the two body recombination reaction with O have a known temperature dependence, this temperature dependence was assumed to cause the ozone variability. We estimate that the large changes in total neutral density measured at that time by Smith et al (1971) were much more significant than temperature effects and that this probably had the dominant influence on the observed ozone variations. Further, the loss of ozone to HO_2 is now considered negligible (Nicolet, 1970).

Comparison is made between the 4 November data and two recent photochemical-transport models in Figure 30-3. The ozone concentration is seen to be overestimated, especially at the lower altitudes, by both the George et al (1972) [designated GZK] and Shimazaki and Laird (1972) [designated SL] models. In the vicinity of 80 km the agreement is close. The GZK model is based on a mean winter 60°N from the supplements, while the SL model is based on larger neutral densities which contribute toward greater ozone production. The differences in the shape of the ozone density distributions are primarily the result of quite different eddy diffusion coefficient profiles. An adequate comparison of these two models would require consideration of many different features including eddy diffusion coefficients, water vapor mixing ratios, and boundary conditions, which is beyond the scope of this paper.

Even for the GZK model, which generates an ozone production close to the conditions during our observations, somewhat greater losses are needed. The inclusion of nitric oxide into their code might provide better agreement with the data. As noted earlier, there are large uncertainties associated with all the loss terms, thus a unique explanation for the differences from the data cannot be made.

The ozone profile on 2 November 1969, during highly disturbed conditions, is shown in Figure 30-4 with the 4 November 1969 data. The error bars here

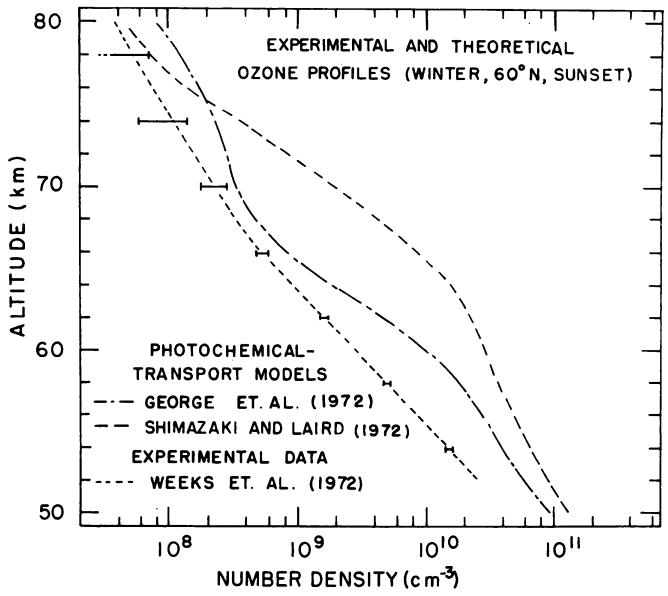

Figure 30-3. Ozone Data of 4 Nov 1969 Compared With Theoretical Profiles for Winter Sunset, 60°N

represent relative uncertainty rather than total uncertainty as in Figures 30-2 and 30-3. The ozone density during the more disturbed conditions is significantly less at all altitudes. This decrease is a factor of 2 at 54 km, 3 at 60 km, and 4 at 67 km. Lower accuracy data at higher altitudes (see Appendix A-30) continues this trend. From 51 to 70 km, the scale height is well represented by a value of 2.9 km, considerably less than observed on 4 November 1969.

As noted earlier, the neutral atmosphere structure measured by Faire and Murphy (1972) was close to a mean winter model for this latitude. These measurements actually spanned a 16 hour interval on 3 November 1969 and are believed to be representative of the mesosphere during the time of our measurements. In any event, the deviations required in total density to account for the ozone change through Eq. (30-3) would be somewhat more than a cold winter 60°N model on 2 November 1969 to a warm winter 60°N model on 4 November 1969. The possibility of such an effect appears to be ruled out by Faire's data, which shows no such trends. It is believed that differences in the ozone density distributions result from effects associated with the particle precipitation.

The measured change in ozone is opposite to the increase predicted by Maeda and Aiken (1968) and Maeda (1968) during hard spectrum auroras. Their scheme, which excludes ion chemistry and reactions with nitric oxide, provides this increase from the additional molecular oxygen dissociation by energetic electrons.

A decrease in ozone during auroral activity resulting from nitric oxide enhancements has been predicted by Sekihara (1969). The basis for this enhancement was the reaction of O_2^+ with N_2 to form nitric oxide and its ion with a rate coefficient of 10^{-15} cm^{-3} sec^{-1}. This reaction is probably a negligible source of nitric oxide, as this coefficient is at least one order of magnitude less (Shahin, 1967).

It is more likely that if nitric oxide is built up during a proton event, it is due to increases in atomic nitrogen, followed by atom molecule interchange with molecular oxygen. A possible enhancement of atomic nitrogen could occur from dissociation of molecular nitrogen by energetic protons. Strobel (1972) has discussed other sources of atomic nitrogen which also need to be considered as possible sources for enhanced nitric oxide.

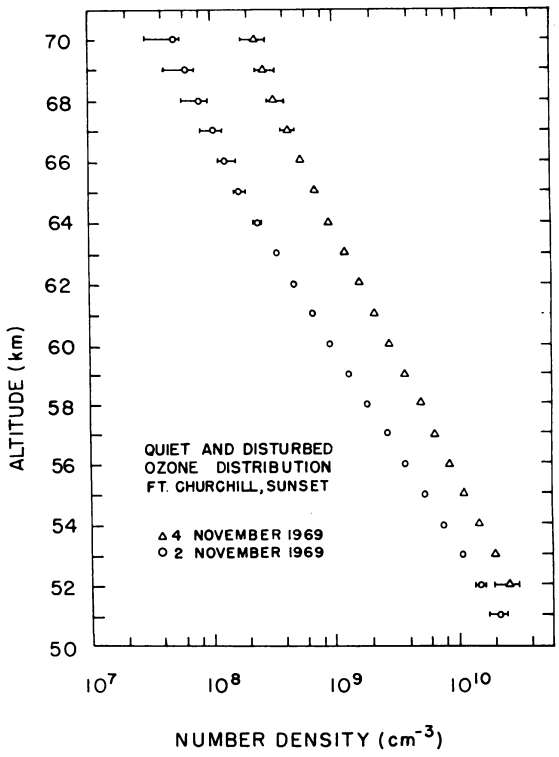

Figure 30-4. Comparison of Disturbed (2 Nov 1969) and Quieter (4 Nov 1969) Ozone Distributions

30-4 SUMMARY

The ozone densities measured during the initial phase of a solar proton event were found to be considerably reduced relative to quieter conditions two days later. It is not believed that these differences reflected changes in total neutral density but that they are the result of effects associated with the particle precipitation. Various models that have been developed appear to be incomplete to give a satisfactory answer. A possible mechanism for decreased ozone during the highly disturbed conditions is through the effects of enhanced nitric oxide or other minor species. Agreement with photochemical-transport models is rather good in the vicinity of 80 km during less disturbed conditions, but greater losses and/or lessened production are needed at lower altitudes.

Acknowledgments

Technical assistance was given by Mr. C. Doiron and Mr. J. P. Mammola. Mr. P. L. Orswell was responsible for payload integration. Ms. M. E. Gardner provided computer calculations. Riometer data were supplied by Mr. R. J. Cormier.

References

Faire, A. C., and Murphy, E. A. (1972) These proceedings.

George, J. D., Zimmerman, S. P., and Keneshea, T. J. (1972) The latitudinal variation of major and minor neutral species in the upper atmosphere, Space Research XII, Akademie-Verlag, Berlin.

Hilsenrath, E. (1971) Ozone measurements in the mesosphere and stratosphere during two significant geophysical events, J. Atmos. Sci. 28:295.

Inn, E. C. Y., and Tanaka, Y. (1953) Absorption coefficient of ozone in the ultraviolet and visible regions, J. Opt. Soc. Am. 43:870.

Johnson, F. S., Purcell, J. D., Tousey, P., and Watanabe, K. (1952) Direct measurements of the vertical distribution of atmospheric ozone to 70 km altitude, J. G. R. 57:157.

Maeda, K. (1968) The auroral O_2 dissociation and the infrared OH* emission, Ann. Geophys. 24:173.

Maeda, K., and Aiken, A. C. (1968) Variations of polar mesospheric oxygen and ozone during auroral events, Planet. Space Sci. 16:371.

Nicolet, M. (1970) Ozone and hydrogen reactions, Ann. Geophys. 26:531.

Sekihara, K. (1969) Auroral X-ray and atmospheric ozone: â preliminary consideration, Ann. Geophys. 25:269.

References

Shahin, M. M. (1967) Use of corona discharges for the study of ion-molecule reactions, J. Chem. Phys. 47:4392.

Shimazaki, T., and Laird, A. R. (1972) Seasonal effects on distributions of minor neutral constituents in the mesosphere and lower thermosphere, Radio Science 7:23. [Their results as shown in Figure 30-3 are taken from private communication, 1971, based on the same model referenced above.]

Smith, W. S., Theon, J. S., Casey, J. F., and Horvath, J. J. (1971) Temperature, Pressure, Density, and Wind Measurements in the Stratosphere and Mesosphere, 1969. NASA Tech. Rpt TR R-360.

Strobel, D. F. (1972) Minor neutral constituents in the mesosphere and lower thermosphere, Radio Science 7:1.

Vigroux, E. (1969) Coefficients d'absorption de l'ozone dans la bande de Hartley. Ann. Geophys. 25:169.

Weeks, L. H., and Smith, L. G. (1968) Molecular oxygen concentrations in the upper atmosphere by absorption spectroscopy, J. G. R. 73:4835.

Appendix A

Tabular Ozone Densities

h(km)	2 November 1969†	4 November 1969†	Johnson et al (1952)‡
50			6.45×10^{10}
51	2.18×10^{10} (±.38)		
52	1.52 (±.13)	2.60×10^{10} (±.60)	3.77
53	1.07 (±.05)	1.97 (±.06)	
54	7.54×10^{9} (±.26)	1.49 (±.03)	2.14
55	5.32 (±.13)	1.13 (±.02)	
56	3.74 (±.09)	8.57×10^{9} (±.15)	1.48
57	2.64 (±.06)	6.49 (±.12)	
58	1.86 (±.04)	4.91 (±.09)	1.04
59	1.31 (±.03)	3.72 (±.07)	
60	9.15×10^{8} (±.30)	2.82 (±.05)	8.68×10^{9}
61	6.66 (±.30)	2.13 (±.04)	
62	4.73 (±.28)	1.61 (±.03)	5.49
63	3.36 (±.20)	1.22 (±.04)	

h(km)	2 November 1969†		4 November 1969†		Johnson et al (1952)‡
64	2.38	(±.16)	9.24×10^{8}	(±.42)	3.48
65	1.69	(+.21, -.13)	7.00	(±.42)	
66	1.37	(±.23)	5.30	(+.51, -.40)	1.88
67	1.03	(±.21)	4.15	(+.65, -.38)	
68	8.00×10^{7}	(+1.5, -2.3)	3.25	(+.75, -.35)	1.10
69	6.20	(+1.3, -2.2)	2.75	(+.60, -.44)	
70	4.90	(+.7, -2.0)	2.25	(+.55, -.50)	7.2×10^{8}
71	3.68	(+.61, -1.68)	1.90	(+.44, -.57)	
72	2.76	(+.56, -1.36)	1.57	(+.39, -.57)	
73	2.03	(+.48, -1.04)	1.30	(+.34, -.54)	
74	1.52	(+.41, -.82)	1.09	(+.28, -.51)	
75	1.14	(+.34, -.65)	9.20×10^{7}	(+2.3, -4.85)	
76	8.55×10^{6}	(+2.85, -5.10)	7.60	(+2.0, -4.3)	
77			6.45	(+1.55, -3.95)	
78			5.30	(+1.4, -3.4)	
79			4.50	(+1.1, -3.07)	
80			3.80	(+.9, -2.72)	

† Relative errors are given. Total uncertainty includes an additional ±6% systematic error.

‡ Original data has been increased by 7.5% to correct for improved values of ozone absorption cross section.

Contents

31. Neutral Density and Temperature Measurements

A.C. Faire and E.A. Murphy
Air Force Cambridge Research Laboratories
L.G. Hanscom Field
Bedford, Massachusetts

Abstract

Results from neutral density and temperature measurements made at Churchill Research Range, Canada, are presented for a summer day in 1969 and for the solar particle event of 2-4 November 1969. The summer measurements were obtained on 6 August 1969 at 2236 hours CST to serve the twofold purpose of providing a certification round and background data during relatively quiet atmospheric conditions. Three measurements were made during the event on 3 November at 0042, 0632, and 1708 hours CST. Data were obtained with rocketborne 7-in. falling sphere payloads instrumented with omnidirectional accelerometers. Below 90 km the August data are within 0 to 15 percent of the 60°N summer model from the US Standard Atmosphere Supplements, 1966 (USSAS-66). Above 90 km the sphere densities become greater than model values until a maximum density departure from the summer model of 100 percent is attained at 106 km. Three density measurements, made the day following peak absorption, exhibit no large-scale perturbations below 85 km. Above 85 km, density excursions relative to USSAS-66 were observed to be as great as 70 percent. Temperature profiles deduced from the density results show small fluctuations below 75 km with a wavelike structure developing around 45 km and expanding progressively with height. Above 75 km, all sphere data obtained during the event show enhanced temperatures relative to the models. The temperatures deduced from density data were a maximum on the first round launched at 0042 hours CST, approximately 15 hours after peak absorption at Churchill. The two following rounds, with successively decreasing temperatures, indicate a trend toward recovery from the proton absorption event. Significant density-temperature perturbations observed following this event occurred in the upper mesosphere and lower thermosphere regions.

31-1 INTRODUCTION

Neutral density and temperature results are presented which have been determined from four rocketborne AFCRL 7-in. falling sphere payloads launched from Churchill Research Range, Canada, in support of the solar particle event of 2-4 November 1969. A certification (or background) round was launched on 6 August 1969. The remaining payloads were launched on 3 November during the progress of the event. Chemical release payloads were also flown on the falling sphere rockets. The results of the chemical release experiments will be presented elsewhere in these proceedings. The density-temperature observations are discussed, with special attention directed toward the unusual features of the measurements. A summary is given in Table 31-1 of falling sphere launches and the altitude range of the data obtained. This paper contains an appendix of tabular results of density and temperature measurements for the convenience of investigators who may require the use of the data for further computational work.

31-2 EXPERIMENTAL METHOD

The AFCRL 7-in. rigid falling sphere, instrumented with an omnidirectional accelerometer and telemetry, is deployed from an appropriate rocket vehicle during ascent. Measurements are obtained of atmospheric drag on the free-falling sphere during both the ascending and descending portions of the sphere trajectory. This technique affords increased credibility of the observations by providing two discrete measurements with a temporal separation of 3 to 5 minutes and a spatial separation of 70 to 80 km. Atmospheric density is obtained from drag acceleration results in the nominal altitude range 35 to 120 km, the upper limit being determined by the threshold sensitivity of the accelerometer employed. Temperature results are computed from the density data. For more details on the experimental technique and data reduction, reference is made to publications by Faire (1970, 1964), Faire and Champion (1965, 1966), and Westlund et al (1967).

31-3 DENSITY RESULTS

Density results obtained during the progress of the solar particle event and the certification round are presented as percent departures from the US Standard Atmosphere (COESA, 1962). In order to provide a more meaningful comparison with results obtained during the highly disturbed conditions of the PCA event and seasonal norms, three winter models are included from the US Standard Atmosphere Supplements (COESA, 1966). These models represent a normal, warm and cold

Table 31-1. Launch Summary of Falling Sphere/Chemical Release Payloads

Rocket No.	Vehicle No.	Launch Date and Time	Payload Description	Rocket Peak Time (sec)	Rocket Peak Altitude (km)	Range of Sphere Data (km)
1	AT 7.197	6 Aug 69 2236 hrs CDT	Sphere/Barium	221	195.0	40 - 110
2	AT 7.396	3 Nov 69 0042 hrs CST	Sphere/TMA	221	196.0	38 - 98
3	AT 7.397	3 Nov 69 0632 hrs CST	Sphere/TMA	220	191.0	56 - 106
4	AT 7.398	3 Nov 69 1708 hrs CST	Sphere/TMA	220	191.1	42 - 106

January for 60°N latitude. The 60°N July model is plotted in another figure for comparison with data acquired from the August certification round. When available, metrock data are also included to provide comparison with sphere results in the altitude range 40 to 60 km where the data overlap. The density results obtained on 3 November at 0042 hours CST are presented in Figure 31-1 as a density height profile in order to show the pronounced oscillations present in the data above 60 km.

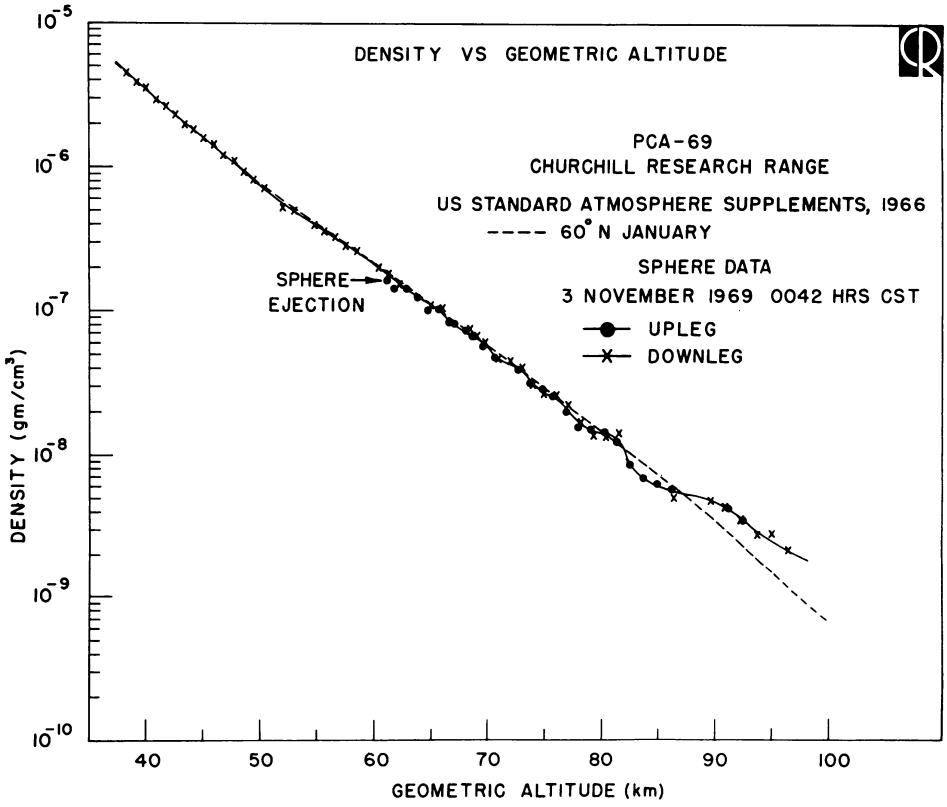

Figure 31-1. Density vs Geometric Altitude 3 November 1969, 0042 Hrs CST

Density oscillations during enhanced geomagnetic activity have been reported by Marcos and Champion (1972) from OV 1-15 satellite density data obtained 6-8 August 1968. Also oscillations in density data obtained by the LOGACS satellite in May 1967, following one of the most intense solar proton events ever recorded, have been reported by Bruce (1971). These waves were observed to be traveling in a north-south direction, and it was concluded that they were gravity waves which

have a high probability of occurrence during a PCA event. To the best of our knowledge, this is the first time large amplitude density oscillations have been observed in data obtained from rocket measurements during this type of atmospheric disturbance. Since the highly distinctive oscillations occur only in the first set of data obtained following peak particle precipitation, there is a strong suggestion that they may have been induced by the solar particle event.

Three sets of density data acquired during the PCA event are shown in Figure 31-2 as density departures from USSA-62. Below 80 km, density departures relative to USSA-62 for the normal and cold January models lie within 8 to 17 percent

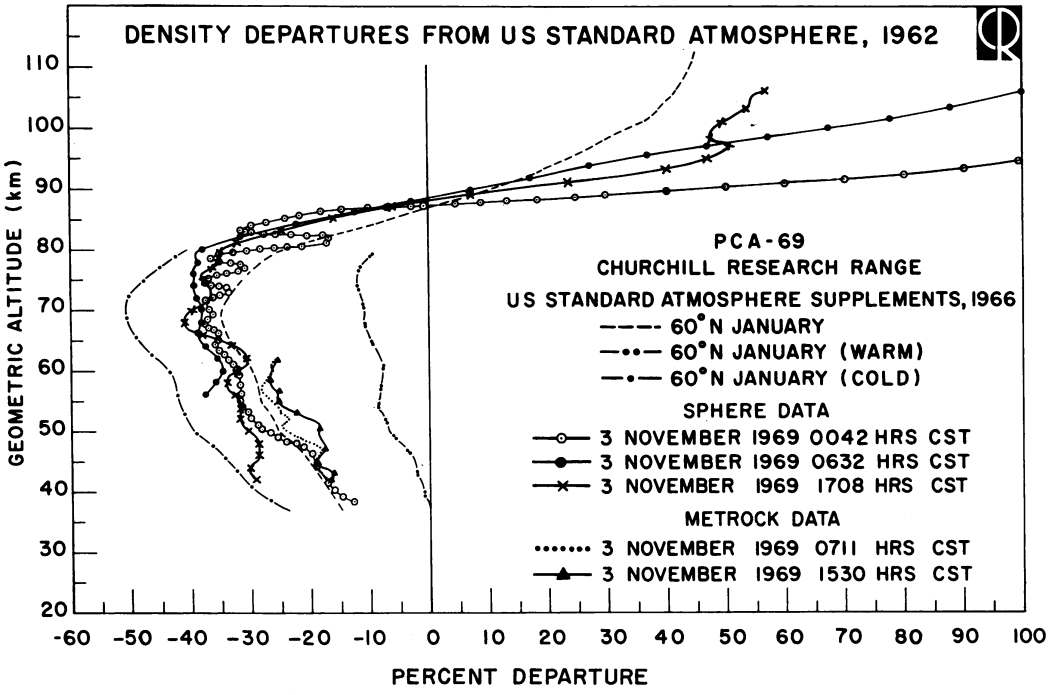

Figure 31-2. Density Departures From USSA-62, 3 November 1969 0042, 0632 and 1708 Hrs CST

of one another. The sphere densities fall between the cold and normal January models, tending to be in more satisfactory agreement with the normal January than the cold January model values. Above 85 km, densities obtained at 0042 hours and 0632 hours CST are characterized by large positive going departures relative to USSA-62. Unfortunately, the maximum amplitude of these perturbations cannot be determined because the altitude range of the data was limited due to the added

weight of the chemical payloads. However, at 1708 hours CST, it is apparent that the perturbations are decreasing in magnitude and are within 20 percent of the normal January model at the highest altitude of the measurement. This point is brought out more clearly with the aid of Figure 31-3.

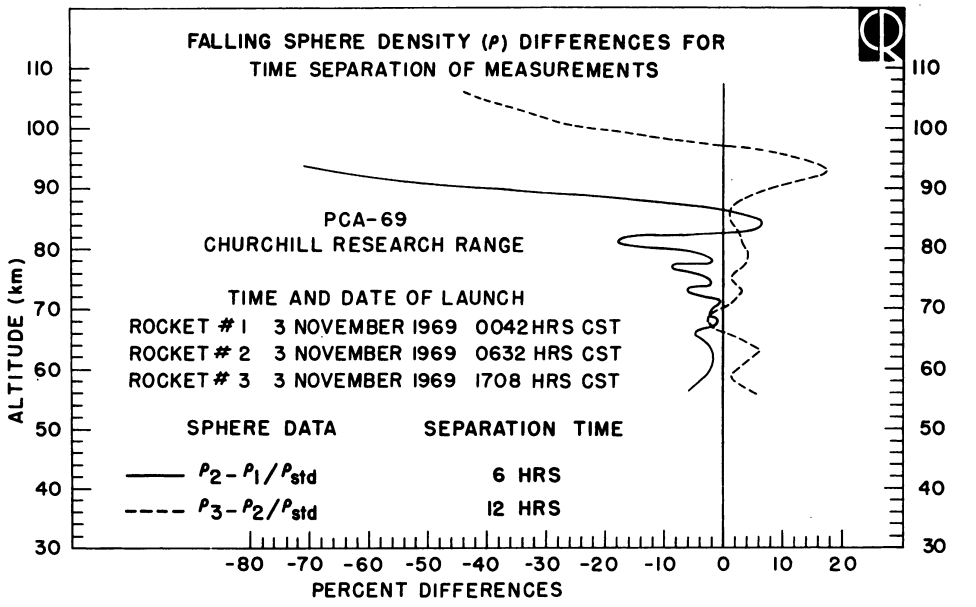

Figure 31-3. Sphere Density Differences for Time Separation of Measurements

Density differences for time separation of measurements are shown in Figure 31-3. The curves illustrate the percent changes in absolute density as a function of altitude that occur between measurements separated in time by approximately 6 to 12 hours (actually 10-1/2 hours). Below 80 km, both curves show complex wave structure which could be due to interactions between two or more modes of oscillations. Above 80 km, however, large amplitude wavelike motions replace the small scale structure found at the lower altitudes. It is also interesting to observe that in the curve representing the 12-hour separation ($\rho_3 - \rho_2 / \rho_{std}$), the major perturbations have shifted to a higher altitude than were observed to occur during the 6 hour separation results which were obtained closer to peak absorption. The data indicate either a secular variation with a decaying amplitude and/or a time-dependent variation in the neutral atmosphere with a 6-hour component. This component would have a lower boundary or reflection point somewhere near the 60 to 70 km altitude level.

Density departures relative to the USSA-62 are plotted in Figure 31-4 for the 6 August certification round launched at 2236 hours CDT and the last round of the PCA launched at 1708 hours CST. Although there was no visible aurora and both the local and planetary geomagnetic indices were quite low up to a few days prior to launch time, the summer data above 80 km show departures relative to the USSA-62 and the summer model values that vary between 0 and 100 percent.

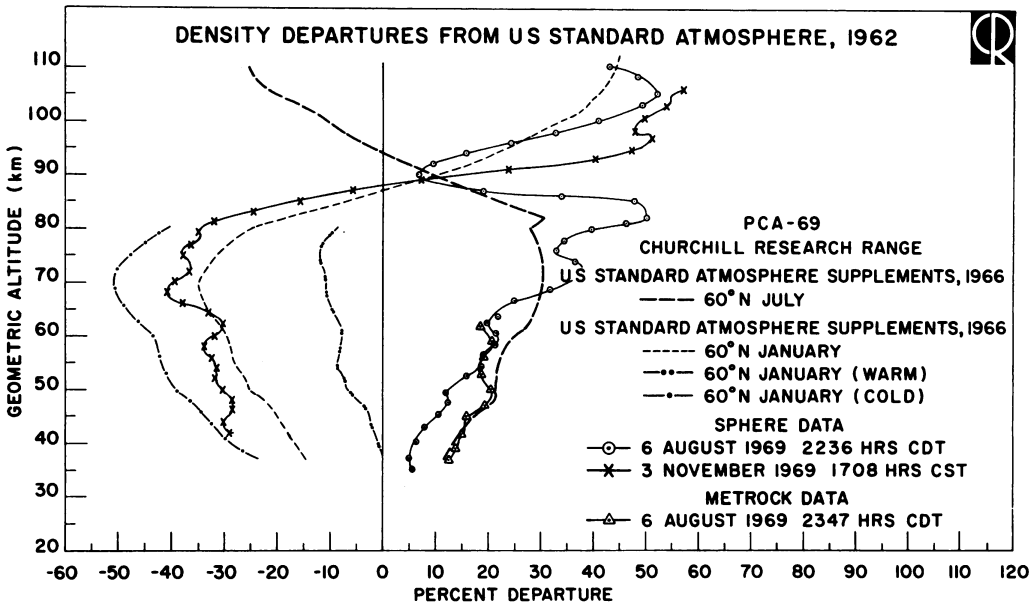

Figure 31-4. Density Departures From USSAS-62 6 August 1969, 2236 Hours CDT; 3 November 1969, 1708 Hours CST

The 1708 hours data were obtained during the recovery portion of a highly disturbed atmosphere. However, in this case the maximum variation of the experimental data from the normal January model values is about 20 percent. A comparison and analysis of these results certainly raises the question as to what criteria should be used to define a quiet summer day or a typical summer day at high latitudes. These results also imply that caution should be exercised when assuming a density or temperature value above 70 km to be used in critical computations of processes or mechanisms where neutral density or temperature are considered to be significant parameters.

31-4 TEMPERATURE RESULTS

The validity of the temperature values obtained by integration over the density height profiles depend on the time history of the density variations. Density measurements during PCA 69 indicate that a disturbance was present which lasted for at least two days. Considering the duration of the disturbance, the temperatures obtained from the density measurements are fairly good approximations of the actual temperatures. There is little doubt that considerable enhancement of temperature occurs in the disturbed atmosphere, especially in the upper mesosphere and lower thermosphere. It can then be inferred by inspection of Figure 31-5 that from the time of peak absorption at 1000 CST on 2 November, it took approximately 35 to 40 hours for the neutral atmosphere to recover. The trend toward recovery by 1708 hours CST on 3 November is suggested by the close agreement of the temperature minimum with the model mesopause value.

Below 60 km it is not possible to distinguish between any effects from the PCA that may have occurred and those synoptic scale meteorological disturbances

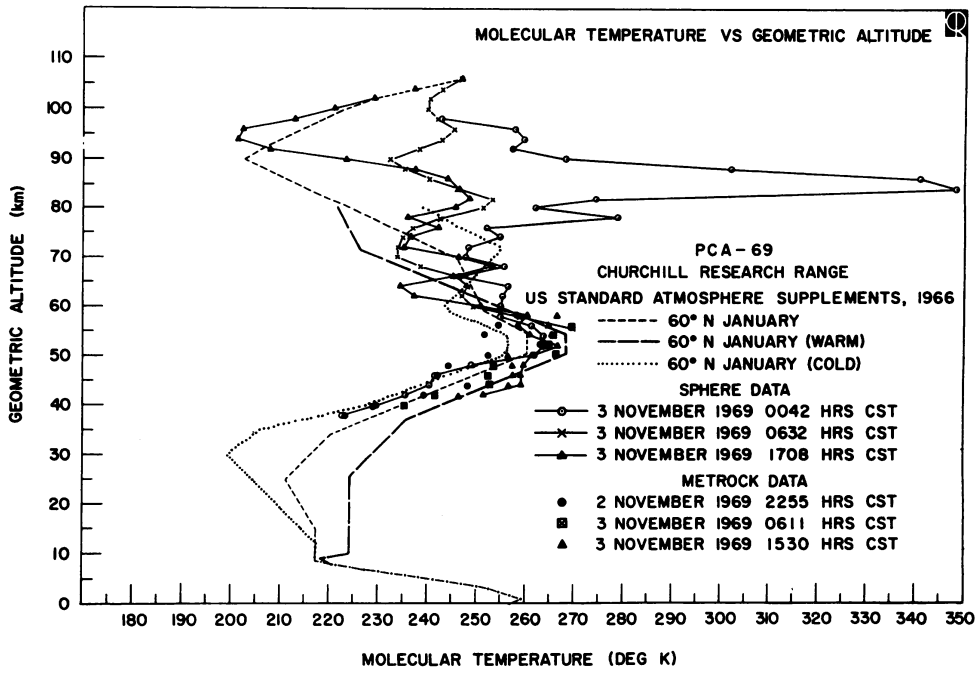

Figure 31-5. Molecular Temperature vs Geometric Altitude: 3 Nov 1969, 0042 Hrs CST; 3 Nov 1969, 0632 Hrs CST; 3 Nov 1969, 1708 Hrs CST

that are common in the wintertime at high latitudes. This is true since the variations that occurred in meteorological data during the PCA on 3 November 1969 were approximately the same magnitude as those that occurred before and several days after the PCA event [10, 11]. The temperature height profile deduced from the PCA certification round launched at 2236 CST on 6 August 1969 is plotted in Figure 31-6. The maximum difference between sphere and metrock temperatures is approximately 15°K near the stratopause. This difference is not significant considering the time between measurements and the variations that are known to occur at stratospheric heights. Below and above the stratopause, the lapse rates for both experimental results are in fairly good agreement with that of the model. The enhanced temperatures above 85 km in the August data cannot be explained without the aid of additional supporting evidence such as transport. Geomagnetic and solar activity were low near the time the data were acquired.

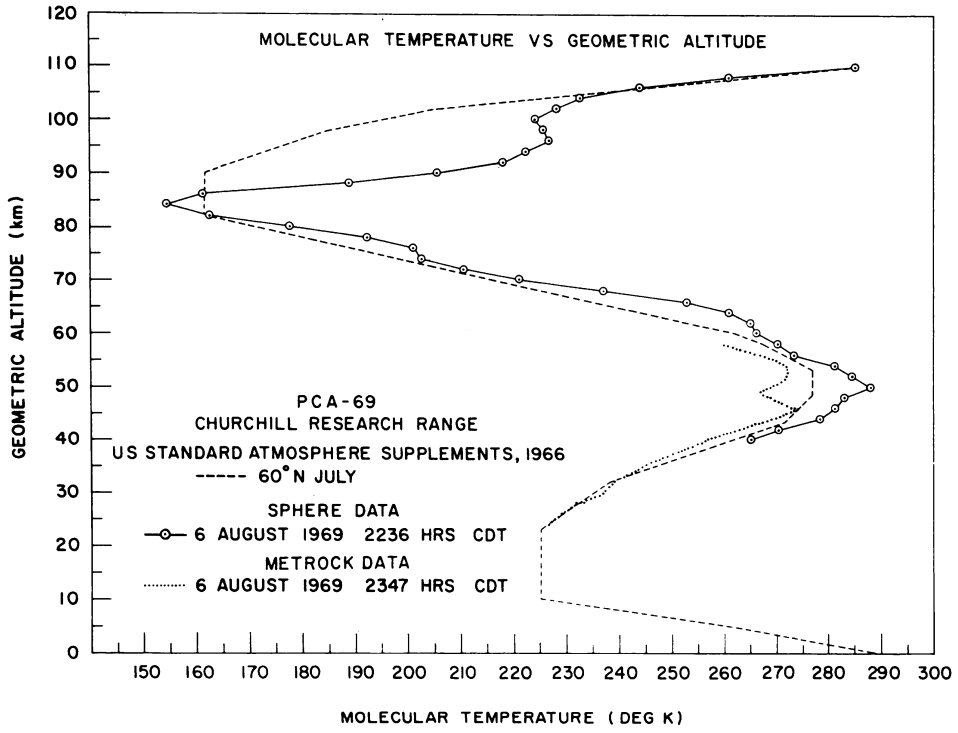

Figure 31-6. Molecular Temperature vs Geometric Altitude
6 August 1969, 2236 Hours CDT

31-5 SUMMARY AND CONCLUSIONS

The data presented in this paper tend to support the following conclusions:

(1) The most significant density variations occurred above 75 km, with a maximum enhancement obtained with data from the first sphere launched 15 hours after peak absorption. Data obtained from two following sphere launches indicate considerable dissipation of the disturbance over a 17-hour period. Based on the three sets of sphere measurements, 40 to 50 hours is a good approximation of the recovery time of the disturbed neutral atmosphere above Churchill following the onset of the 3 November 1969 PCA which had a maximum absorption level of 12 db.

(2) The temperatures presented must be considered as approximate rather than absolute. Temperature data above 75 km indicate the degree of heating at the time of the measurement closest to peak absorption and the trend toward more normal temperatures as observed in data from the two successive measurements. The heating had nearly subsided by 1708 hours CST on 3 November, the time of the last neutral measurement.

(3) There is evidence which suggests that the particle influx resulted in heating and oscillations in the atmosphere with a lower boundary in the altitude level between 60 and 70 km. Inspection of meteorological temperature measurements for altitudes below 60 km and for times before and several days after the PCA onset revealed variations that were of the same magnitude as those temperature variations observed at these altitudes during the PCA.

Acknowledgments

The authors wish to acknowledge their indebtedness to Dr. K. S. W. Champion (AFCRL) for valuable discussions, G. Stromberg, P. Mundis, and M. Baratz at Wentworth Institute, Boston, Mass. for invaluable technical assistance. We wish also to thank the entire staff of Churchill Research Range for technical and logistical support.

References

Bruce, R. W. (1971) Upper Atmosphere Density Determined from LOGACS; presented at Fourteenth COSPAR Meeting, Seattle.

Faire, A. C. (1964) AFCRL rigid falling sphere program, IQSY Instruction Manual No. 9, IQSY Secretariat, London, p. 40.

Faire, A. C. (1970) New Falling Sphere Instrumentation for Aerospace Density Determination, Proc. National Telemetry Conf., p. 70, Boston, Mass.

Faire, A. C. and Champion, K. S. W. (1965) Space Research V, p. 1039, North-Holland, Amsterdam.

Faire, A. C., and Champion, K. S. W. (1966) Space Research VI, Spartan Books, Washington, D. C.

Marcos, F. A., and Champion, K. S. W. (1972) Space Research XII, Akademie, Verlag-Berlin.

U. S. Standard Atmosphere, 1962 (COESA) Government Printing Office, Washington, D. C.

U. S. Standard Atmosphere Supplement, 1966 (COESA) Government Printing Office, Washington, D. C.

Westlund, C. D., Haycock, O. C., Smith, R. S., and Allred, G. D. (1967) Instrumentation for Air Density Measurements, AFCRL-67-0532; Upper Air Research Laboratory, Univ. of Utah.

World Data Center A, Meteorology (1969) Data Report, High Altitude Meteorological Data VI(No. 10).

World Data Center A, Meteorology (1969) Data Report, High Altitude Meteorological Data VI(No. 11).

Appendix A

Tabular Data — Density and Molecular-Scale Temperature Vs Geometric Altitude

Table A-1. 3 November 1969, 0042 Hours CST

PCA-69 3 NOV 69 0042 HRS CST

INPUT DATA FOR THIS RUN

ALTITUDE	98.000	KM
MOLECULAR TEMPERATURE	243.000	DEG K
VALUE OF Q	3483.280	
LENGTH OF INTERVAL	2.000	KM
LENGTH OF SUBINTERVAL	.500	KM

COMPUTATION OF MOLECULAR TEMPERATURE SIMPSONS RULE (7-INCH FALLING SPHERE)

ALTITUDE KM	MOLECULAR TEMPERATURE DEG K	DENSITY GM/CC
96.0	257.946	.2270E-08
94.0	265.413	.2840E-08
92.0	259.368	.3750E-08
90.0	267.193	.4700E-08
88.0	301.785	.5270E-08
86.0	340.855	.5740E-08
84.0	351.211	.6770E-08
82.0	262.770	.1110E-07
80.0	264.830	.1440E-07
78.0	283.236	.1710E-07
76.0	252.108	.2480E-07
74.0	258.464	.3130E-07
72.0	249.891	.4250E-07
70.0	247.504	.5570E-07
68.0	254.369	.7100E-07
66.0	245.458	.9620E-07
64.0	255.698	.1210E-06
62.0	254.808	.1580E-06
60.0	254.586	.2060E-06
58.0	254.677	.2680E-06
56.0	261.235	.3390E-06
54.0	263.602	.4340E-06
52.0	263.481	.5600E-06
50.0	261.748	.7300E-06
48.0	249.151	.1000E-05
46.0	241.537	.1360E-05
44.0	240.414	.1810E-05
42.0	235.551	.2460E-05
40.0	229.894	.3370E-05
38.0	222.824	.4680E-05

Table A-2. 3 November 1969, 0632 Hours CST

PCA-69 3 NOVEMBER 1969 0632 HRS CST

INPUT DATA FOR THIS RUN

ALTITUDE	106.000	KM
MOLECULAR TEMPERATURE	246.820	DEG K
VALUE OF Q	3483.280	
LENGTH OF INTERVAL	2.000	KM
LENGTH OF SUBINTERVAL	.500	KM

COMPUTATION OF MOLECULAR TEMPERATURE SIMPSONS RULE (7-INCH FALLING SPHERE)

ALTITUDE KM	MOLECULAR TEMPERATURE DEG K	DENSITY GM/CC
104.0	243.040	.475OE-09
102.0	240.023	.6330E-09
100.0	240.006	.835OE-09
98.0	242.075	.1090E-08
96.0	245.756	.1416E-08
94.0	242.970	.1870E-08
92.0	238.264	.2510E-08
90.0	232.985	.3410E-08
88.0	236.175	.4470E-08
86.0	240.642	.5800E-08
84.0	246.535	.7450E-08
82.0	253.710	.9450E-08
80.0	251.573	.1240E-07
78.0	242.842	.1680E-07
76.0	237.183	.2270E-07
74.0	234.953	.3040E-07
72.0	234.079	.4060E-07
70.0	233.862	.5410E-07
68.0	238.636	.7040E-07
66.0	246.094	.9000E-07
64.0	248.264	.1170E-06
62.0	247.032	.1540E-06
60.0	249.460	.2000E-06
58.0	259.013	.2510E-06
56.0	270.123	.3100E-06

Table A-3. 3 November 1969, 1708 Hours CST

PCA-69 3 NOVEMBER 1969 1708 HRS CST

INPUT DATA FOR THIS RUN

ALTITUDE	106.000	KM
MOLECULAR TEMPERATURE	246.820	DEG K
VALUE OF Q	3483.280	
LENGTH OF INTERVAL	2.000	KM
LENGTH OF SUBINTERVAL	.500	KM

COMPUTATION OF MOLECULAR TEMPERATURE SIMPSONS RULE (7-INCH FALLING SPHERE)

ALTITUDE KM	MOLECULAR TEMPERATURE DEG K	DENSITY GM/CC
104.0	237.280	.3850E-09
102.0	229.076	.5300E-09
100.0	220.936	.7380E-09
98.0	212.878	.1040E-08
96.0	202.345	.1510E-08
94.0	201.214	.2110E-08
92.0	207.881	.2830E-08
90.0	223.257	.3650E-08
88.0	237.393	.4580E-08
86.0	244.910	.5850E-08
84.0	246.634	.7620E-08
82.0	248.653	.9900E-08
80.0	245.635	.1310E-07
78.0	236.039	.1800E-07
76.0	242.257	.2320E-07
74.0	236.398	.3140E-07
72.0	235.153	.4200E-07
70.0	246.518	.5300E-07
68.0	253.316	.6740E-07
66.0	245.082	.9100E-07
64.0	234.520	.1260E-06
62.0	237.220	.1660E-06
60.0	251.018	.2070E-06
58.0	260.448	.2590E-06
56.0	258.807	.3370E-06
54.0	260.946	.4330E-06
52.0	266.544	.5470E-06
50.0	261.461	.7190E-06
48.0	259.738	.9380E-06
46.0	259.104	.1220E-05
44.0	259.282	.1580E-05
42.0	251.462	.2120E-05

Table A-4. 6 August 1969, 2236 Hours CST

PCA-69 (CERTIFICATION ROUND) 6 AUGUST 1969 2236 HRS CSDT

INPUT DATA FOR THIS RUN

ALTITUDE	110.000	KM
MOLECULAR TEMPERATURE	285.550	DEG K
VALUE OF Q	3483.280	
LENGTH OF INTERVAL	2.000	KM
LENGTH OF SUBINTERVAL	.500	KM

COMPUTATION OF MOLECULAR TEMPERATURE SIMPSONS RULE (7-INCH FALLING SPHERE)

ALTITUDE KM	MOLECULAR TEMPERATURE DEG K	DENSITY GM/CC
198.0	261.119	.1950E-09
196.0	244.184	.2710E-09
194.0	232.917	.3750E-09
192.0	228.358	.5100E-09
190.0	224.103	.6980E-09
98.0	225.901	.9300E-09
96.0	226.937	.1240E-08
94.0	222.582	.1700E-08
92.0	218.376	.2340E-08
90.0	206.611	.3380E-08
88.0	188.886	.5160E-08
86.0	161.080	.8830E-08
84.0	154.299	.1420E-07
82.0	162.519	.2060E-07
80.0	177.667	.2780E-07
78.0	192.207	.3680E-07
76.0	200.777	.4950E-07
74.0	202.682	.6830E-07
72.0	209.851	.9130E-07
70.0	221.169	.1180E-06
68.0	237.482	.1470E-06
66.0	253.094	.1810E-06
64.0	260.742	.2280E-06
62.0	265.080	.2890E-06
60.0	266.578	.3700E-06
58.0	270.238	.4690E-06
56.0	273.617	.5930E-06
54.0	281.289	.7350E-06
52.0	284.441	.9220E-06
50.0	288.130	.1150E-05
48.0	283.037	.1480E-05
46.0	281.365	.1890E-05
44.0	278.581	.2430E-05
42.0	270.673	.3200E-05
40.0	265.337	.4200E-05

Contents

32. Results From the PCA 69 Chemical Release Experiments

F.A. Marcos and C.F. Bloemker*
Air Force Cambridge Research Laboratories
L.G. Hanscom Field
Bedford, Massachusetts

J.F. Bedinger and E. Constantinides
GCA Corporation
Bedford, Massachusetts

Abstract

Four rockets carrying chemical payloads were launched during the PCA 69 program. These consisted of a barium certification launch and three trimethyl aluminum (TMA) launches during the event. Barium is injected into the atmosphere at twilight as a point release and forms both a neutral and ionized cloud. The barium cloud was photographed from the three camera sites established at the CRR. The velocity of the neutral and of the ionized cloud was measured. An estimate of the earth's electric field vector has also been derived from the barium data. The TMA releases occurred during the night, morning twilight, and evening twilight after the PCA event. In spite of unfavorable visibility due to weather conditions, the morning twilight release was photographed. The resulting wind profile has been reduced and analyzed. The aeronomical significance of this measurement will be described.

*Present address – North Carolina State University

32-1 INTRODUCTION

Experiments with chemicals released from rockets were conducted during PCA 69 to measure upper atmosphere winds. This transport process is calculated from photographs of the artificial chemical clouds taken at ground camera sites. The chemicals utilized in this program were barium for the certification round and trimethyl aluminum (TMA) for the event. Barium is injected into the atmosphere at twilight as a point release and forms both a neutral and ionized cloud. Neutral wind speed at the altitude of the release is determined from the motion of the neutral barium cloud. The ionized cloud moves primarily along the lines of force of the earth's magnetic field. From the drift of this cloud perpendicular to the magnetic field, the earth's electric field can be measured. TMA is released as a trail which is visible both at night (by chemi-luminescence) and at twilight (by fluorescence).

During the summer and early fall of 1969, photographic observing sites were established and maintained at the Churchill Research Range (CRR) for the purpose of recording the chemical releases during the time of the PCA project.

Three camera sites were established at the CRR: (1) Belcher, 88 km south and 21 km west of launch; (2) Twin Lakes, 13 km south; and (3) at the Auroral Observatory, 10 km west of the launch site. At each site were two K-24 cameras (5 in. × 5 in. format, 178 mm f/2.5 lens) and a 70 mm night camera (85 mm f/1.5 lens). Interference filters of approximately 100Å bandwidth and centered at 4554Å and at 5535Å were available for the K-24 cameras. Roll film, Kodak 2475 with Estar base, was used in all cameras.

Although the observing sites were operated during the entire period, cloud cover at the sites allowed data to be obtained from only one barium release and one TMA release. The results of these observations are discussed independently.

32-2 BARIUM RELEASE OF 6 AUGUST 1969

At 2136 Central Standard Time on 6 August 1969, a Nike Iroquois rocket was launched at CRR. This was one of a series of rockets launched during the certification phase of PCA 69. The payload consisted of a falling sphere and a barium chemical release. The barium point release occurred at T + 225 sec at apogee (approximately 196 km). The cloud was photographed from the three camera sites, and the separation of the neutral and ionized particles is clearly shown in Figure 32-1.

There were three prominent sources of resonance radiation observed in the release, neutral barium (Ba I) at 5535Å, ionized barium (Ba II) at 4554Å, and neutral strontium (Sr I) at 4607Å. The strontium is an impurity in the barium payload,

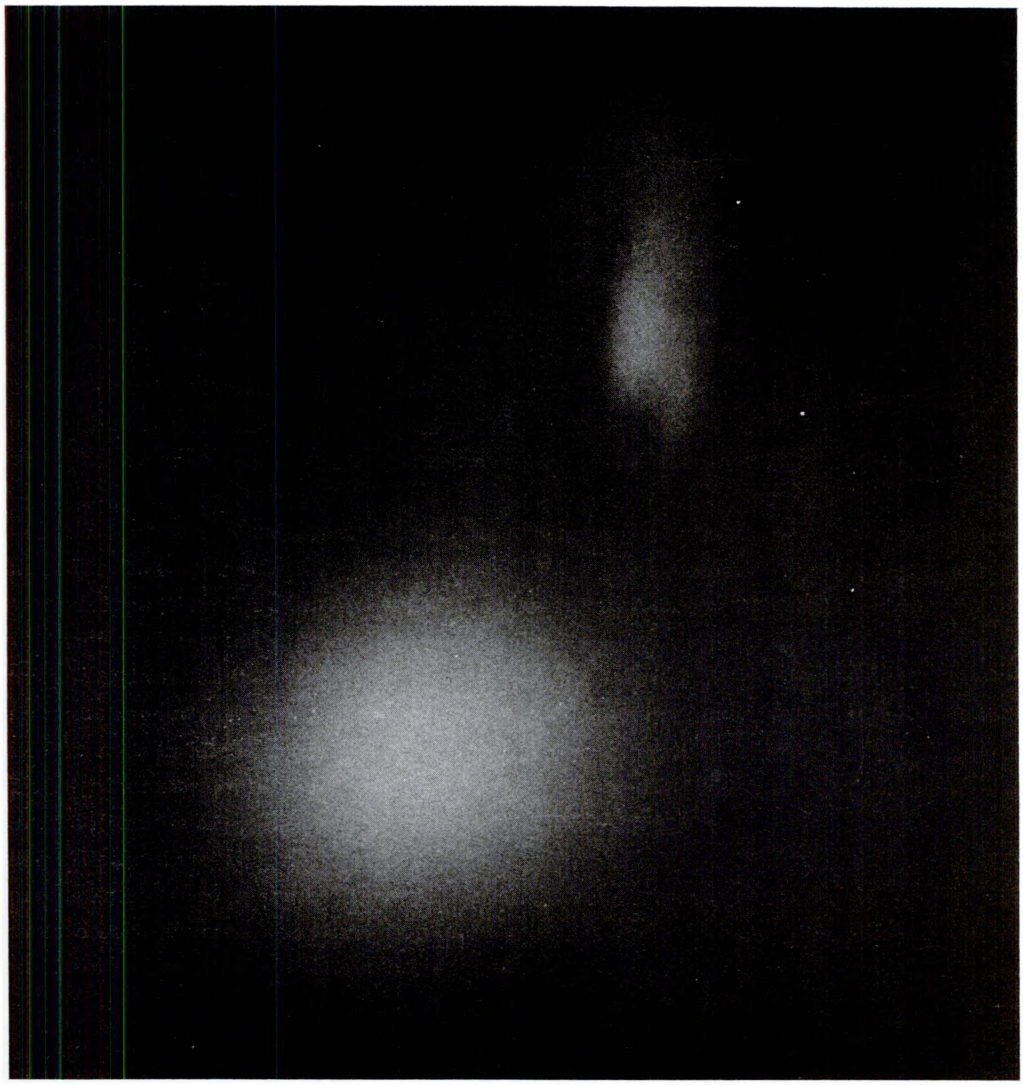

Figure 32-1. Barium Clouds at 196 Km After Release From a Nike Iroquois Rocket Launched From Ft. Churchill at 2136 CST on 6 Aug 1969

but because of a good evaporation efficiency the Sr I is seen as part of the neutral cloud. The 4554Å filter has sufficient transmission at 4607Å to allow observation on the same photograph of the neutral Sr I and ionized Ba II. The 5535Å filter allows observations of only the neutral barium cloud.

Examination of the photographs of this release shows an initial rapid expansion of the Ba I/Sr I cloud to equilibrium with the atmosphere and then a slower

expansion due to diffusion. A cigar-shaped Ba II cloud separated from the neutral cloud and aligned itself along the earth magnetic field lines in a northerly direction. The ionized cloud then moved rapidly in that direction, passing out of the field of view of the camera. The neutral Ba I/Sr I cloud moved due to atmospheric winds in the same general direction. An interesting feature in the ionized cloud was the development of fine structure of striations along the field lines.

The position and motion of the clouds were determined by triangulation from the photographic data. It was found that the neutral Ba I/Sr I cloud and ionized Ba II were moving in the same direction on an azimuth of 280°. The neutral cloud was moving at a speed of approximately 200 m/sec and the ionized cloud at 350 m/sec. Neutral winds of this magnitude (with a maximum of 300 m/sec) moving in a westerly direction have been previously measured at CRR (Bedinger, 1966).

The motion of the ionized and neutral clouds was analyzed to determine the value of the electric field. The transverse electric field was calculated on the basis of the following expression, derived by Haerendel and his co-workers (Haerendel et al, 1967):

$$\vec{E}_1 = \frac{(1+\lambda)}{2} \frac{B}{C} \left\{ \hat{b} \times \vec{V} + \frac{(\lambda - 1)}{(\lambda + 1)} \vec{V} \times \hat{b} + \frac{1}{K} [\vec{V} - \vec{U} - b \cdot (\vec{V} - \vec{U})] \right\} \qquad (32\text{-}1)$$

where

$\vec{V}$ = ion cloud velocity
$\vec{U}$ = neutral cloud velocity
B = magnitude of geomagnetic field
$\hat{b}$ = unit vector in the direction of geomagnetic field
C = speed of light
λ = σ_p/σ_o
σ_p = height-integrated Pedersen conductivity in the presence of the ionized cloud
σ_o = height-integrated Pedersen conductivity in the absence of the ionized cloud
K = ratio of gyrofrequency to collision frequency for the barium ions.

Table 32-1 lists the values of the various parameters pertinent to the calculation. The value of λ is unknown. However, even for the largest barium release, the value of λ was less than 1.5 (Haerdendel et al, 1967). Accordingly, in calculating the electric field we have performed the calculation for three different values of λ. Finally the contribution of the unknown vertical motion to the electric field is small, since the magnitude of vertical motions is dwarfed by the magnitude of horizontal motions.

Table 32-1. Data Pertaining to the Calculation of the Electric Field

Time of Barium Release	2136 CST
Height of Barium Release	196 km
Value of K at 196 km	~100
Magnitude of Geomagnetic Field	0.55 gauss
Dip Angle	82°
Magnetic Declination	8.25°W
Speed of Ionized Cloud	350 ± 15 m/s
Speed of Neutral Cloud	200 ± 15 m/s
Direction of Motion of Ionized Cloud*	297.7° ± 3°
Direction of Motion of Neutral Cloud*	282° ± 3

*Measured east of geographic north.

The results of the calculations are shown in Table 32-2 in three columns, one for each value of λ used. It can be seen that the values deduced for $\lambda = 2$ vary by less than 20 percent from the values for $\lambda = 1$. The insensitivity of the results to the precise value of λ is a direct consequence of the fact that the directions of motion of the ionized and neutral clouds were nearly identical. This fortuitous circumstance allows the accurate determination of the electric field without a precise knowledge of the value of λ.

Table 32-2. Electric Fields Inferred From the Motion of the Neutral and Ionized Barium

Value of λ	1	1.5	2.0
Eastboard Component*	3.1 ± 1.0	3.3 ± 1.2	3.6 ± 1.5
Northboard Component*	18.8 ± 1.0	20.8 ± 1.1	22.8 ± 1.3
Upward Component*	2.6 ± 0.1	2.8 ± 0.2	3.1 ± 0.2
Horizontal Field	19.0 ± 1.2	21.1 ± 1.3	23.1 ± 1.5
Total Field	19.2 ± 1.2	21.2 ± 1.3	23.3 ± 1.5

*Directions are geographic. All values are in millivolts/meter.

The value of 21 mv/m for the total electric field is in the range of values obtained previously at high altitudes (Haerendel et al, 1969; Wescott et al, 1969).

32-3 TMA RELEASE OF 3 NOVEMBER 1969

A night start series of 3 launches containing TMA releases was initiated at 0042:00 CST, 3 November 1969. All three camera sites were completely overcast and no visual sighting of a TMA release was reported. During the morning twilight release (0632:30 CST) the Auroral Observatory and Twin Lakes sites were completely overcast and the Belcher site mostly overcast. A visual sighting of the TMA release was made by the operator at Belcher although no stars were visible before or during the release. No sightings were made from the other two sites. All sites were again completely overcast for the evening twilight shot (1703:00 CST) and no visual observations of a release were made.

In spite of the unfavorable weather conditions, photographs were taken from each site of each planned release. Subsequent processing of the film revealed that the Belcher site had photographed the morning twilight TMA trail for a period of 120 seconds. No stars were recorded and no rocket trajectory was available. However, due to the fact that much data was obtained from other phases of the PCA program, it was decided to attempt to obtain wind data from the Belcher photographs. The data reduction proceeded as follows.

The trail image appeared in the expected location on the photograph, which confirmed that the predicted rocket trajectory was followed in flight. The slant range and bearing of trail points with respect to the Belcher site were then determined.

The heights of identifiable features were determined by comparison with other trails. TMA down trails in twilight have been photographed from the Belcher site previously in October 1965 and September 1966. Heights in the lower part of the trail were determined from the extent of the bright chemi-luminescent region. Heights on the upper parts of the trail were determined from relative trail diameters.

Utilizing identifiable frame boundaries as fiducial marks, successive photographs were superimposed and the displacement of the selected points were recorded. Using the known quantities, the focal length of the camera lens, the magnification of the measured reproduction, and the slant range from Belcher, these displacements were converted to two actual horizontal cloud displacements, one perpendicular to and one parallel to the bearing from the Belcher site. Division by the appropriate time intervals yielded wind components along those axes. Finally, the known bearing of the points from Belcher were used to compute eastward and northward wind components. These wind values are tabulated in Table 32-3 and a hodograph of the winds is shown in Figure 32-2.

Table 32-3. Estimated Winds Deduced From the Belcher Site Photographs

Altitude (km)	Winds to the East (m/sec)	Winds to the North (m/sec)
90	76	-13
96	-17	40
103	-67	57
106	47	23
112	50	-92
120	15	-130
130	-7	-115
145	-18	-67
160	-43	-90

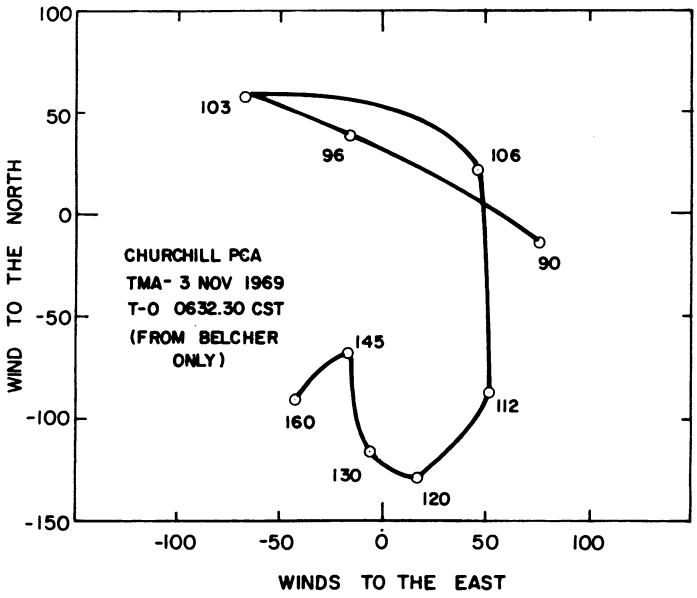

Figure 32-2. Hodograph of Winds From TMA Trail of 3 November 1969

It must be noted that the wind speeds in Table 32-3 were obtained from limited observations from one site and the reduction process involved several areas of uncertainty. These factors should be realistically considered when use is made

of these data. Certainly, little confidence could be assigned to detailed analyses involving other measurements. However, comparison to other wind measurements at Churchill (GCA-TR-67-11-N), and (Bedinger, 1966) show that the data from 3 November are very similar to winds observed at other times. Thus, it appears that the winds in the morning twilight were not dramatically different during the PCA.

32-4 SUMMARY

Four rockets carrying chemical payloads were launched during the PCA 69 program. Results from the barium certification round showed that the neutral and ionized clouds moved in approximately the same direction (within 10^{o}) on an azimuth of 280^{o} with speeds of about 200 m/sec and 350 m/sec, respectively. A value of 21 mv/m for the total electric field was obtained. Due to poor weather conditions, it was possible to photograph only one of three TMA releases during the PCA event. Results of this measurement indicate that the winds in the morning twilight were not significantly different during the PCA event.

References

Bedinger, J. F. (1966) Compendium of Wind Data From the Vapor Trail Technique, GCA Technical Rpt No. TR-66-7-N, NASA Contract No. NASW-1083.

GCA (1967) Technical Rpt TR-67-11-N, Final Rpt on Contract No. NASW-1083.

Haerendel, G., Lust, R., and Rieger, E. (1967) Planet. Space Sci. 15:1.

Haerendel, G., Lust, R., and Rieger, E. (1969) Atmospheric Emissions, pp. 293-303, Van Nostrand-Reinhold, N. Y.

Wescott, E. M., Stolarik, J. D., and Heppner, J. P. (1969) J. Geophys. Res. 74:3469.

Contents

33. Airborne Optical Measurements of Auroral Effects During Polar Cap Absorption Events

W.P. Boquist and R.W. Deuel
Technology International Corp.
Bedford, Massachusetts

Abstract

Photographic and spectrographic instrumentation were prepared and installed on two AFCRL KC-135 research aircraft to perform optical measurements of polar glow aurora and discrete auroral effects during a polar cap absorption event. During the operational phase of the PCA program which began in August 1969, periodic auroral flight missions were made to the vicinity of 80°N latitude as part of an integrated PCA-Auroral program conducted by AFCRL. Auroral background data was obtained on each of these flights in order to aid in the interpretation of solar-induced auroral effects which might occur during the operational program. On 2 November 1969 a polar cap absorption event occurred and AFCRL KC-135 aircraft No. 53120 was flown to 76°N latitude on this date. All of the DASA optical instrumentation on A/C 53120 operated satisfactorily and both photographic and spectrographic records were obtained for most of the flight profile. Subsequent to the PCA flight mission an additional auroral background flight was made.

Analysis of the optical data has resulted in spectroscopic identification of auroral and polar glow emissions as well as the radiance history and spatial extent of these features. An analysis of the photographic records of the polar glow aurora has provided a qualitative description of the intensity structure. In addition, representative photographic records describing the discrete auroral activity occurring at the times of the rocket experiments are also presented.

33-1 INTRODUCTION

The optical measurements program performed by Technology International Corporation was designed to obtain measurements of the visible photon emissions of the polar glow aurora related to the PCA and, in addition, to obtain background coverage of natural discrete aurora which might occur during the period of observation of PCA events. The specific objectives of the research program were to prepare, flight test, and operate optical instrumentation on board AFCRL KC-135 aircraft to obtain such optical data. These measurements were to be performed from AFCRL KC-135 aircraft nos. 53120 and 53131.

Phase I of this effort consisted of optical equipment preparation, engineering design and stress analysis for the aircraft instrumentation mounts, installation of the equipment on the KC-135 aircraft, and test procedures to insure operational readiness of the equipment. Photographic instrumentation, optical interference filters, mounts, and electrical control systems were checked out both in the laboratory and on the aircraft during ground checks and test flights. As part of Phase I, a mount was designed for the Huet Auroral Spectrograph to permit its installation on AFCRL aircraft 53120.

Subsequent to engineering approval and installation of the optical instrumentation, the equipment was tested during airborne observations of natural auroral activity. The data thus obtained were processed and studied in order to provide background emission data for the evaluation of the PCA measurements during the Phase II operational program. These data included optical sky background of natural discrete auroral forms, essential to the interpretation of the polar glow aurora and correlation with other experiments conducted during Operation PCA-69.

Phase II of this research program consisted of operating the optical instrumentation on the PCA mission flown by the AFCRL aircraft during the field period of the operation. In addition, post-flight processing and quick-look examination of the data were performed as soon as possible after the mission with the results reported to the PCA Technical Director.

The Phase III effort entailed the examination, documentation, and analysis of the data records obtained during the PCA operation. The objectives of the data analysis were:

(1) spectral characteristics, radiance history, spatial extent, and structure of the polar glow aurora associated with the PCA;

(2) documentation of the visual discrete aurora as background information during the period of observation of the PCA event.

This paper describes all of the data analysis performed in connection with the objectives stated above and summarizes the conclusions derived therefrom.

33-2 DATA SUMMARY

33-2.1 Data Flights

The DASA optical instrumentation systems were manned and operated during the PCA flight of 2 November 1969 which was the only PCA data flight of the field phase of this research program. The systems were also manned and operated durint other flights both before and after the PCA event for the purposes of flight testing the instrumentation and for the acquisition of auroral and airglow background data. A list of these flights is presented in Table 33-1 indicating the dates of observations, the aircraft flown, and the mission status. In all, data were obtained on 10 flights into the auroral region primarily on latitudinal traverses at longitude 78°W and extending to 76°N (see Figure 33-1).

Table 33-1. Summary of Flights for Operation PCA 1969

Date	Aircraft	Remarks
10- 6-69	53120	First operational check
10- 9-69	53120	
10- 9-69	53131	Abort, no data
10-10-69	53131	
10-13-69	53120	
10-16-69	53120	
10-20-69	53120	Abort, no data
10-30-69	53120	
11- 2-69	53120	PCA Alert Flight
11- 6-69	53120	
11-13-69	53120	
11-17-69	53120	

33-2.2 Records Obtained

Examination of the film records from the PCA flight of 2 November 1969 indicates that considerable photographic and spectrographic data was obtained throughout the latitudinal traverse. Details of the data records for each optical instrument are listed in Table 33-2.

Film exposure times for the pulse cameras were obtained by operating the control unit in an open-to-open mode and allowing shutter action to be accomplished simultaneously with the film transport. Exposure duration is thus the time between pulses from the control unit's intervalometer which ranged from 5 sec to 100 sec.

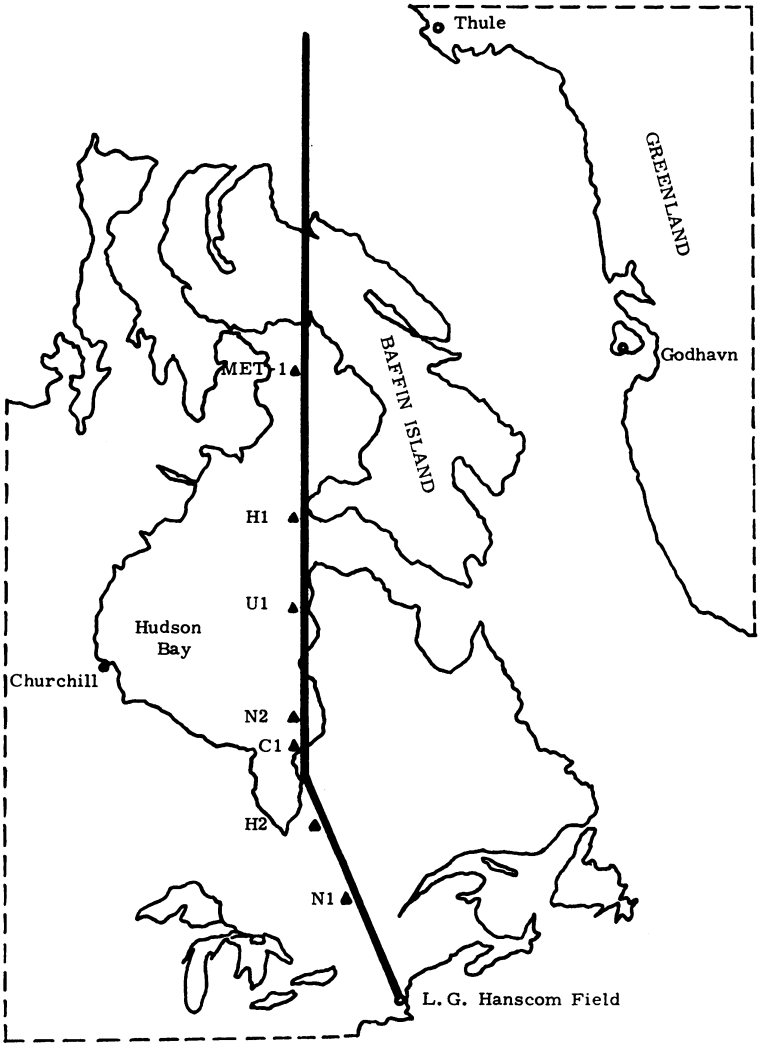

Figure 33-1. Flight Route of Aircraft 53120

Spectrographic exposures were manually controlled to provide short durations for the region of bright discrete aurora and long exposures of more than one hour to integrate the weak radiation of the polar glow region.

The backup Canon camera was used with the same 50 mm f/0.95 lens employed on the pulse cameras performing the filter photography. The same filter holder could thus be used with the backup camera permitting the interchange of interference filters to record the selected emission intensities in any direction accessible

Table 33-2. PCA Optical Data Summary

Record No.		
82624	B/W Record; DXN Emulsion	Approx. 50' of film with exposures
82633	B/W Record; 2484 Emulsion 5577 A Interference Filter	Approx. 70' of film with exposures
82634	Spectrogram; I-F Emulsion	4 moderate exposures 3 faint exposures
82636	B/W Record; 2484 Emulsion 3914 A Interference Filter	Approx. 70' of film with exposures
82635	B/W Record; 2484 Emulsion 3914 A and 5577 A Filters Manual Camera used on Port Side of Aircraft	Approx. 18 exposures
82637	Color Record; EH Emulsion No filters used. Manual Camera used on Port Side of Aircraft for qualitative coverage only	Approx. 6 exposures

to the hand camera. This proved of particular advantage both for PCA and background missions when data was taken directly forward from the flight deck, as well as out the port side of the aircraft. This additional coverage extends the spatial and temporal base of the data by providing information for regions not viewed by the fixed instrumentation at a given time.

33-3 DATA CALIBRATION AND PROCESSING PROCEDURES

The determination of the radiance of an optical source recorded photographically requires a detailed accounting of a number of factors; these include the attenuation effect of the radiation path, the transmission characteristics of optical windows, fore filters and objective optics employed for imaging and bandwidth limiting; the effect of the duration of the exposure, the etendue or throughput of the optical instruments, and the calibrated relation between irradiance at the film plane and the resulting photographic density. All of these parameters can significantly affect the derivation of source radiance and must be considered in the data analysis program.

33-3.1 Atmospheric Transmission

Atmospheric characteristics for the optical geometry encountered at the time of measurement can be reasonably accounted for by attenuation data relevant to the

intervening air mass. For an observational altitude of 40,000 ft, the residual air mass in a vertical direction is 15 percent; from Allen (1955) values for the continuous atmospheric absorption are derived for the aircraft altitude which give a transmission of 93 percent at 3914 A and 97 percent at 5577 A. These results are a practical lower limit inasmuch as direct proportions of sea level conditions used include water vapor and dust which are non-constant mixing ratio components of the atmosphere. Neglect of these constituents in the calculation results in an increase in transmission of about one percent. This non-critical dependence for the conditions of the PCA experiment will permit appropriate corrections to be readily made to the observed intensities.

33-3.2 Instrument Calibration and Operation

Filter transmission characteristics were generally known for the previously used filter set although when such filters were employed accurate calibration required re-measurement due to the inherent aging degradation of dielectric films. The new filters were made to the same design specifications as the existing set and calibration data were provided from the manufacturer for transmission vs wavelength.

Transmission characteristics for the lenses on the cameras and spectrograph are also required in the determination of source intensity. The fast Canon lens used on the Flight Research cameras for filter photography has been calibrated for transmission vs wavelength. This data is shown in Figure 33-2. The characteristics of the other lenses employed were similarly determined. The optical transmission of the lens used on the Huet spectrograph is included in the overall transfer function of this instrument which is described later.

Temporal calibrations for the photographic records required a determination of the exposure duration and the time at which the exposure occurred. Duration was generally known from the interval setting of the camera's electronic control; in addition, a timing check of the exposure interval was performed during data acquisition by using a stopwatch. Exposure time is determined from the recording of the data clock in the IV-E camera and synchronization of the multiple cameras using coded single-frame exposures. The times of these synchronization exposures were separately recorded as a check on the data clock.

The various camera mount platforms were calibrated in elevation angle prior to flight for the cases where incremental adjustment is employed. During flight any changes to the variable elevation adaptors were measured with a precision inclinometer. Elevations were changed infrequently but as required to optimize the field of view with respect to the major visible activity. Verification of pointing angle is provided in part by long duration exposures and identification of the star field recorded on such exposures.

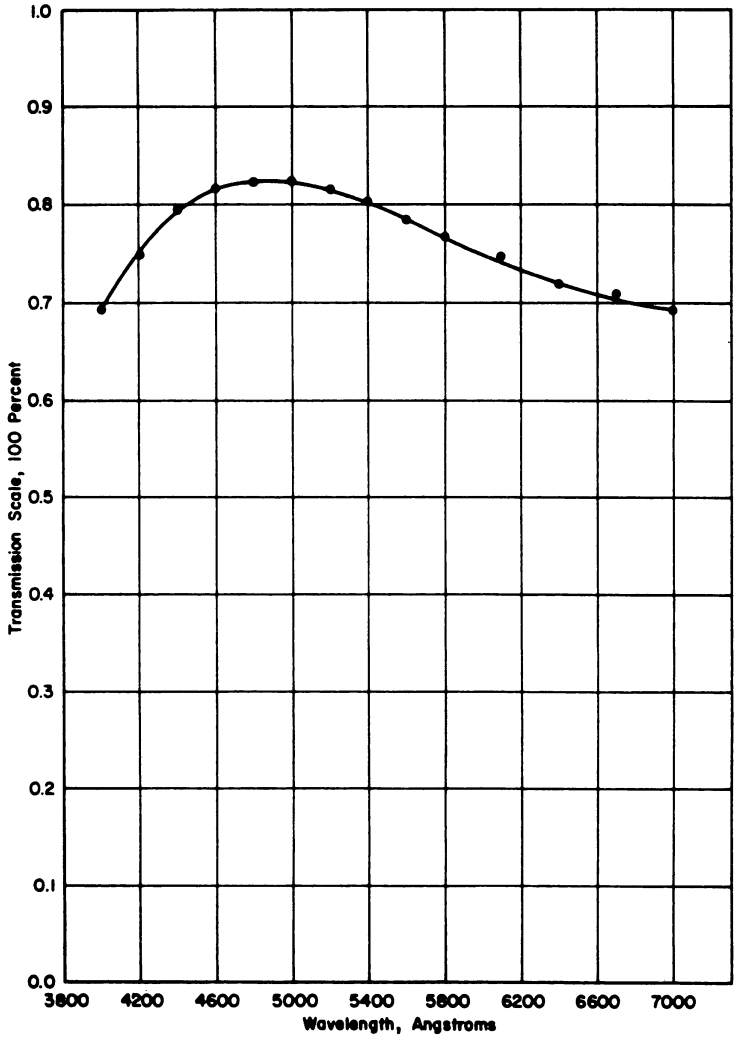

Figure 33-2. Transmission Calibration: DASA 50 mm f/0.95 Canon Lens S/N 27004

33-3.3 Radiometry of Photographic Data

The radiance of an object (N) which has been photographically recorded is related to the energy density of exposure (E) by the following equation:

$$E\ (\text{ergs/cm}^2) = N\ (\text{ergs/cm}^2/\text{sec/ster})\ \tau\ t\ (\text{sec})\ \Omega \qquad (33\text{-}1)$$

where τ is the total optical transmission ($\tau = \tau_{atmos} \times \tau_{lens} \times \tau_{filter} \cdots$)

(t) is the exposure duration, and Ω is the solid angle of acceptance of the optical instrument ($\Omega = \pi/4 \times 1/(f/n)^2$, f/n = f-number of the optics). The relation between the energy density of exposure and the resulting photographic density is the sensitometric data generally shown as the characteristic curve. For a given film emulsion, this is a single-valued function which is parametrically defined by the conditions of processing.

In order to determine the characteristic curve for the types of emulsion used during data acquisition, each emulsion is exposed to a calibrated neutral density step wedge using a sensitometer. The sensitometer calibration provides the source radiance that produced the known density increments. When the exposed scale is processed with data films of the same emulsion, the characteristic curve resulting from density measurement of the calibrated scale provides absolute source radiance vs photographic density. Because the characteristic curve is a function of wavelength, it is desirable to produce the scale with the same wavelength light that is recorded on the data film. This is readily performed using the narrow band interference filters that were similarly employed during data acquisition.

From the sensitometric calibration procedure, one can relate the source radiance, energy density of exposure, and photographic density on an absolute scale. Subsequent densitometry of data records can then be correlated by photographic density to derive the absolute energy density of exposure. Eq. (33-1) may then be solved for the source radiance:

$$N_s = (1/t_s) \times E_s \times (1/\tau_{atmos}) \times (1/\tau_{lens}) \times (1/\tau_{filter}) \times 4(f/n)^2/\pi. \quad (33\text{-}2)$$

For most auroral and airglow observations, the source intensity is expressed as a photon emission rate in Rayleighs. The conversion is thus:

$$I(\text{Rayleighs}) = N_s \ (\text{watts/cm}^2\text{/ster}) \times \lambda \times 0.632 \times 10^{10}. \quad (33\text{-}3)$$

The densitometry of the data records and their appropriate step wedge scales is discussed in a following section.

33-3.4 Radiometry of Spectrographic Data

In contrast to the photographic data, radiometric measurements of spectrographic data is somewhat more complex. As previously discussed, the conversion of photographic density to the energy density of exposure requires a characteristic curve of the emulsion for the wavelength observed. Since the spectrograph observes all wavelengths in the visible region simultaneously, it is in general necessary to obtain data for the emulsion characteristic as a function of wavelength.

A straightforward procedure to accomplish this involves the exposure of the step wedge scale with the spectrograph illuminated by a continuum light source. Density scales as a function of wavelength are thus obtained which may be correlated with sensitometrically exposed scales for several discrete wavelengths throughout the visible region. This comparison to the known light source of the sensitometer provides the absolute calibration of the spectrographically obtained data. Furthermore, the use of the spectrograph in the same configuration (field lens and auxiliary optics) as employed for the acquisition of data provides coincidental determination of the instrument's transmission function vs wavelength.

Failure of the reciprocity law must be considered in applying calibration data to the PCA exposures which cover a range of exposure intervals from 2 to 100 minutes. A series of sensitometric scale exposures covering this range were made on the same I-F emulsion that was used for the acquisition of auroral data. The measured density for each scale was then used to calculate the 'effective length of exposure' which would have produced the same density in the absence of reciprocity failure when compared to a reference time interval. These results, normalized for an exposure of 10 minutes duration, are shown in Figure 33-3. The effective

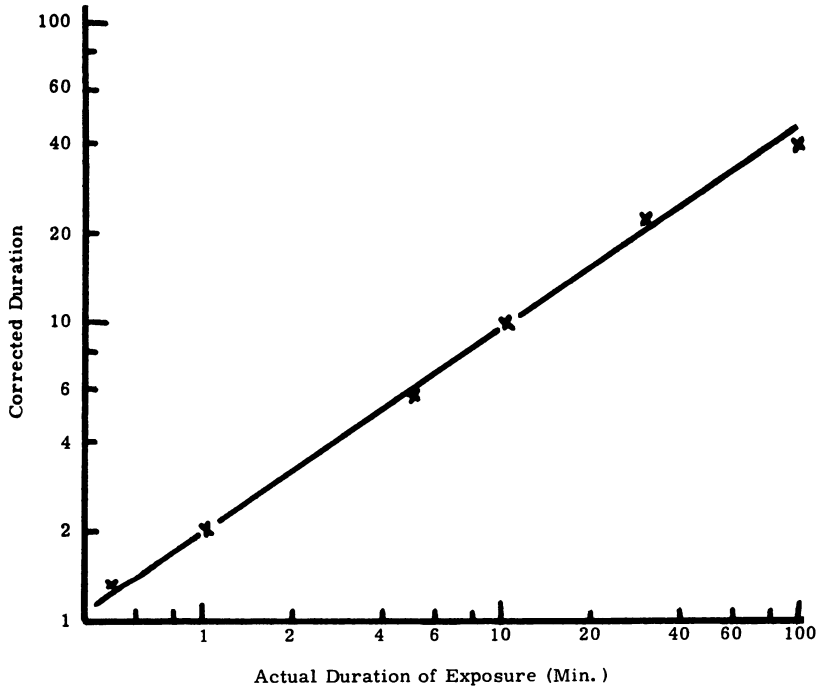

Figure 33-3. Correction for Reciprocity Failure of I-F Spectrographic Plates

exposure time for each spectrogram was then reduced from this relation and used in the calculation of source radiance.

The determination of emission line intensities from the spectrographic record is similar to that described for the photographic data with the following form of the radiance equation:

$$E = N \tau t A_{slit} \Omega_{collimator} \times (1/h_s m) \times (d\lambda/dx) \quad (33\text{-}4)$$

where $(A\Omega)$ refers to the area of the entrance slit and the solid angle of the collimator lens, (h_s) is the slit height, (m) is the magnification of the spectrograph optics, and $(d\lambda/dx)$ is the dispersion of the instrument in the focal plane. From the calibration experiments, this equation can be solved and combined with a similar equation for the line source as follows:

$$N_L = (E_L/E_c) \times (\tau_c/t_L) \times \Delta\lambda_L \times N_c \quad (33\text{-}5)$$

where $\Delta\lambda_L$ is the halfwidth of the desired line. As before, the conversion for photographic density to energy density of exposure is made from the characteristic curve. In the present experiment, the sensitometrically exposed step wedges for the spectrographic data were produced directly on the I-F emulsion without using the spectrograph. The photographic density obtained is thus the combined effect of all wavelengths emitted by the light source in the sensitometer to which the emulsion is sensitive. The corresponding calculation of the energy density of exposure involved the convolution of the energy vs wavelength of the source and the sensitivity vs wavelength of the emulsion. The resultant 'characteristic curve', expressed as relative energy density of exposure vs transmission of the emulsion is presented in Figure 33-4. In this calculation, sensitivity was normalized to the maximum value which occurred at 4000 A. As part of the transformation from photographic density to source intensity, the energy density of exposure derived from the data in Figure 33-4 was corrected for film sensitivity and spectrograph instrument function. The results presented in the next section are corrected radiance values for each wavelength at the entrance to the spectrograph. An additional consideration with the spectrographic data is the integration of the line intensity as a function of wavelength. In view of the non-linear film characteristic, the integration was performed after density vs wavelength was transformed into intensity vs wavelength.

33-3.5 Processing Controls

All photographic and spectrographic records obtained on black and white film emulsion were processed using calibrated sensitometric procedures in order that

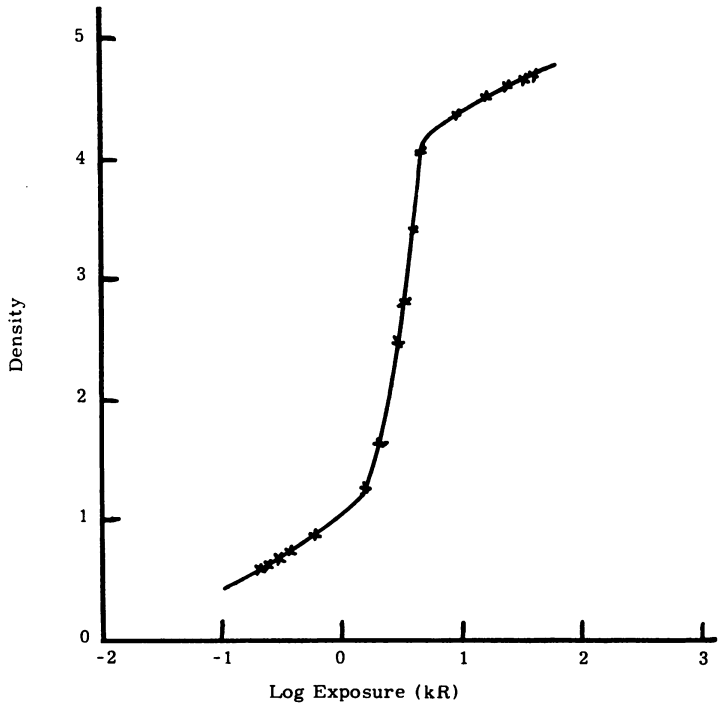

Figure 33-4. I-F Emulsion-Characteristic Curve

subsequent densitometric analysis could be used to determine the absolute brightness of the observed phenomena. The primary sensitometric scales were processed with the PCA data as the absolute brightness reference and all records incorporated calibrated neutral density wedges as processing controls. These controls permit the determination of variability in the processing of different data sets and the corresponding correction in the transformation from photographic density to intensity.

33-4 POLAR GLOW AURORA

33-4.1 Morphology

The polar glow aurora is described (Sandford, 1967) as the optical emission generated by the protons and alpha particles which cause polar cap absorption (PCA). It generally consists of a rather uniform glow covering the whole of the polar cap region without the small scale structure of discrete aurora. For large PCA events, it is generally considered that the protons are precipitated over the entire polar cap region with a considerable degree of uniformity which gives rise

to the polar glow aurora. Near the low latitude boundary, as far as 60° geomagnetic latitude for larbe events, significant fluctuation structure has been observed, particularly after sudden commencements and during magnetic storms. For smaller PCA events, structure may be seen throughout the polar cap region.

Variation in riometer absorption data indicates greater structure in the precipitation pattern than is observed optically although other emission and absorption sources may account for this discrepancy. Argemi (1964) reported details of structure in polar glow aurora observed from Antarctica during events in 1957 which were interpreted as a broad arc of 3914 A emission lying at a geomagnetic latitude of 78°. Furthermore, the arc appeared to be oriented normal to the sun-earth line. Discrete auroral forms at high latitudes, commonly called polar cap aurora at latitudes greater than 70° geomagnetic, are often observed as poleward movements of aurorae from the normal auroral zone. This movement occurs as an expansion of the auroral zone during the development of magnetic storms and should thus be differentiable from structure associated with the polar glow aurora.

Although at times the intensity of the polar glow aurora may exceed the threshold for visual perception, the lack of contrast prevents visual recognition and it is generally classified as sub-visual. The lack of twilight enhancement for solar illumination above 100 km altitude indicates that nearly all the emission occurs below that altitude. The maximum excitation apparently occurs at about 60 km with significant emission from altitudes as low as 20 km.

The onset of polar glow aurora following a solar proton flare is gradual, rising to a peak in a day or so, and then decaying in a uniform manner over a period of days. The emission features observed in other types of aurora and a primary concern in these investigations is the discrimination against interfering types of optical radiation. Visual and sub-visual discrete aurorae are readily detected photographically and their absence presents the opportunity to study the polar glow even in the region of the auroral oval. The proton excited aurora is recognized by bright H_α emission on the low latitude side of the discrete visual aurora. The mantle aurora described by Sandford (1967) is an extensive, all-sky glow occurring in a band centered on geomagnetic latitude 70° throughout the day. It is described as the primary source of high latitude optical emission with an integrated output exceeding that of the discrete visual aurora. The best way to avoid contamination effects from the mantle aurora is to limit observations to latitudes higher than 75° geomagnetic. The only other contribution is from the fairly stable normal airglow which can be subtracted from measurements of the polar glow.

33-4.2 Excitation

The excitation mechanisms for the polar glow aurora are described by Sandford (1963), Brown (1964), and Dalgarno (19) with the most prominent visible spectral feature due to the first negative bands of nitrogen excited as follows:

$$p + N_2 \; X^1\Sigma_g^+ \rightarrow p + N_2^+ \; B^2\Sigma_u^+ + e$$

$$\alpha + N_2 \; X^1\Sigma_g^+ \rightarrow \alpha \; N_2^+ \; B^2\Sigma_u + e .$$

The brightest radiation from this band is the 0-0 transition at 3914 A whose intensity is directly proportional to the total energy of the particles incident on the atmosphere. The relation between 3914 A intensity and incident energy is given as:

$$E \text{ (ergs/cm}^2\text{sec)} = 1.2 \times I \text{ (kiloRayleighs–kR)} .$$

Another feature of the polar glow aurora is the atomic oxygen line 5577 A which is primarily derived from the dissociative recombination of molecular oxygen ions:

$$O_2^+ + e \rightarrow O(^1S) + O^* .$$

33-4.3 Intensity Levels

The reported intensity ratio of 5577 A/3914 A is 0.2 with the nitrogen emission intensity ranging from airglow levels to about 10 kR at the peak of a PCA event. Excitation of hydrogen is considered to be very inefficient for the proton energies involved in polar cap absorption and the resulting intensity is calculated at only a few Rayleighs. A charge exchange reaction with the alpha particles gives rise to helium emission which has been observed in the infrared. All other emissions observed in discrete aurora are present to some extent in the polar glow aurora but they have not been examined in detail.

33-4.4 Spectrographic Measurements

Spectrographic data was obtained during eight data flights of A/C 53120 as part of the PCA research program, including the one PCA event of 2 November 1969. Positive reproductions of the spectrographic plates for the PCA event of 2 November and the adjacent background flights of 30 October and 6 November are shown in Figures 33-5 and 33-6. Identification data for each of the spectrograms

Figure 33-5. Spectrographic Data of Auroral and Airglow Emissions From PCA Flight of 2 November 1969

taken on these flights is listed in Table 33-3 indicating the times of exposure, the duration, and the position of the aircraft during the time of exposure. Since the majority of the flights were latitudinal traverses at constant longitude, the position data is given only in geographic latitude for a specified longitude. It is noted that

Figure 33-6. Spectrographic Data of Auroral and Airglow Emissions From Background Flight of 6 November 1969

for these data the spectrograph was supported in a fixed mount pointing normal in azimuth to the aircraft axis and 30° in elevation above the horizon.

In terms of the phenomenology of the auroral emissions, it is desirable to relate the data to geomagnetic coordinates. Table 33-4 indicates that the spectrographic data can be arbitrarily categorized into six groups representing different

Table 33-3. Spectrographic Exposure Data

Plate Position	Relative Brightness	Exposure Time (Local) Start	Stop	Duration (Min.)	Position Latitude	Latitude Group
Record 82634 — 2 November 1969 — Longitude 78°W						
2		08:22	08:24	2	58°N	-
4		08:58	09:21:30	23-1/2	64-82°	
6		09:23	10:01	38	69-64°	-
8	6	10:01	10:49	48	74-69°	6
10	5	11:03	12:11	68	68-76°	6
12	2	12:22	12:45	23	63-66°	5
14	3	12:45	12:58	13	61-63°	4
16	4	01:00	01:02	2	61°	4
18	1	01:15	02:28:30	73-1/2	50-59°	2
Record 82734 — 6 November 1969 — Longitude 78°W						
4		07:05	08:40	75	63.5-75°	6
6		08:50	10:05	75	75.5-67°	6
8		10:30	11:00	30	64-60°	4
10		11:02	11:09	7	59.5-59°	3
12		11:09	12:15	66	59-50.5°	-
14		12:15	12:45	30	50.5-47°	1

Table 33-4. Geographic Latitude Vs Geomagnetic Latitude

Group	Geographic Latitude Range Total	Average	Geomagnetic Latitude Average
1	46 - 53°	47 - 51°	62°
2	50 - 59°	51 - 58°	62 - 70°
3	57 - 60°	58 - 59°	70 - 71°
4	58 - 64°	60 - 63°	71 - 74°
5	65 - 66°	63 - 66°	74 - 77°
6	63 - 76°	66 - 76°	77 - 87°

ranges in geomagnetic latitude. The corresponding group for each spectrogram is identified in the tables concerning the spectrographic exposures and the group identification will be used later for correlation of the occurrence of specific auroral features.

The mercury calibration spectra placed on each spectrographic plate is used to derive the wavelength scale for the auroral data. The wavelength calibration data of 2 November 1969 is shown in Figure 33-7. Density measurements were made of each spectrogram including the mercury calibration lines in order to accurately identify each observed feature with respect to wavelength and also to provide the means for determining relative intensities of the emission lines. Typical densitometer tracings for the auroral data are shown in Figures 33-8 and 33-9 which indicate the line identification and the relative photographic density.

In order to derive the intensities of the spectral features recorded on the spectrograms, it was necessary to convert the photographic density measured by the

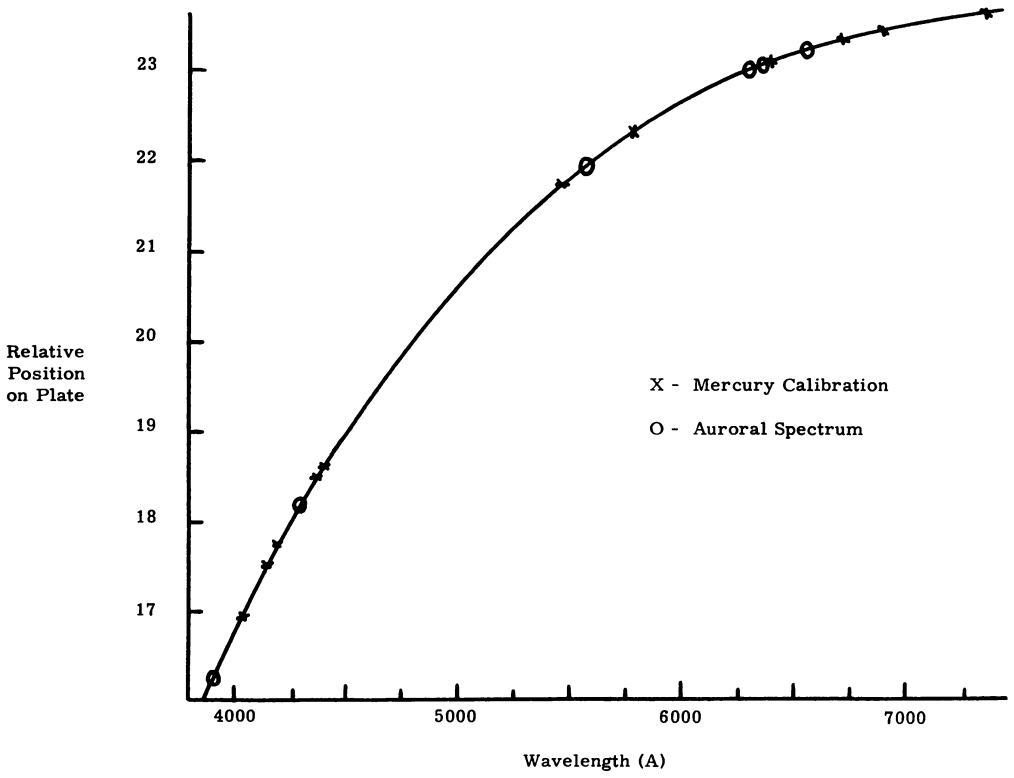

Figure 33-7. Wavelength Calibration for Huet Spectrograph (Data from 2 Nov 1969)

Figure 33-8. Densitometer Tracing of Record 82634-16: 2 Nov 1969; Latitude 61°N

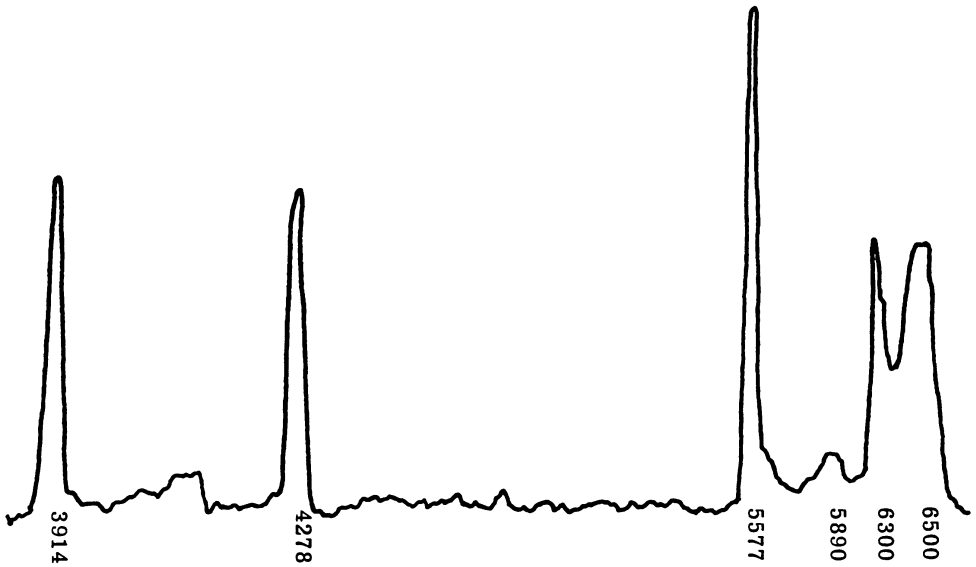

Figure 33-9. Densitometer Tracing of Record 82634-18: 2 Nov 1969; Latitude 59°N - 50°N

densitometer to energy density of exposure using the characteristic curve for the plate emulsion (Figure 33-7). This transformation was then corrected for the wavelength response of the film emulsion and the spectrograph. The resulting intensity vs wavelength curve for each spectrogram was then integrated to obtain the total intensity for each spectral feature. In addition to the corrections previously discussed, final calibration was achieved by comparison of the photographic results with photometric measurements made from the aircraft. In making the comparison, a correction is made for the variation in pointing between the zenith-viewing photometer and the spectrograph which was pointed 30° above the horizon.

The 'van Rhijn calculation' (Chamberlain, 1961) and the consideration of a thick uniform layer of emission results in an increase of 2.5 over the zenith intensity. The photometric data (Kofsky, 1971; Sandford, 1971) was selected for the time periods of photographic measurement with greater emphasis given to intervals of fairly constant intensities.

As an approximation to this detailed procedure, a linear transformation was used for emission features with a peak density less than that of the first inflection point of the characteristic curve. This approximation corresponds to the observed initial linear relation between photographic density and the energy density of exposure (at minimum density or maximum transmission) and thus gives equal weight to each level of density in the integration procedure. The source radiance values derived for strong and weak lines by the respective methods described above are presented in Table 33-5 for the PCA observations of 2 November 1969 and for background observations on 30 October and 6 November. To facilitate interpretation, the results are arranged in groups according to the geomagnetic latitude range covered during data acquisition.

Examination of the total light record from the PCA flight of 2 November indicated discrete auroral activity throughout a region from approximately 50°N to 65°N geographic latitude corresponding to 60° - 75°N geomagnetic latitude. Therefore, discrete auroral forms are possibly present in the data for geomagnetic latitudes less than 75°N with a high probability in the region between 62° - 70°N. The relative intensities of 3914 A, 5577 A, and 6300 A emissions for the latter data agree with Chamberlain's (1961) IBC III aurora. At high geomagnetic latitudes where the polar glow aurora should be uncontaminated with other forms (77° - 87°), the PCA related data shows measurable emission from the N_2^+ band at 3914 A in comparison to the background records where this emission is less than the detection level even in cases where the atomic oxygen emissions are brighter. There is thus the expected enhancement of nitrogen emission with respect to atomic oxygen emission during the PCA event.

Because the background level of 3914 A emission in the absence of PCA is below the detection level of the spectrographic measurements, an accurate determination of the increase due to the particle precipitation related to the PCA is not possible. The peak 3914 A intensity observed (0300-0400 UT) is about 120 R above the detection level which corresponds to a zenith intensity of 50 R.

Relating the zenith intensity to the total energy of the incident particles gives:

$$E \text{ (ergs/cm}^2\text{/sec)} = 1.2 \times 0.05 \text{ (kR)}$$
$$E = 0.06 \text{ ergs/cm}^2\text{/sec}$$

Table 33-5. Intensities of Observed Auroral Emission
(Arranged by Geomagnetic Latitude)

Wavelength (A)	3914	4278	5577	5890	6300	6500
Record	N_2^+	N_2^+	OI	NaI	OI	$OH+N_2$
			87^o — 6 — 77^o			
PCA 11-2/8	0.2		0.9	0.3		
/10	0.1		1.0			
BG 10-30/3			1.4	0.3		
11-6/4			2.1	0.8	0.6	0.5
/6			2.5	1.1	0.4	0.5
			77^o — 5 — 74^o			
PCA 11-2/12			4.8		0.4	
			74^o — 4 — 71^o			
PCA 11-2/14			5.4		0.7	
/16			17.0			
BG 10-30/11			5.3		0.6	
11-6/8	0.6	1.2	10.5	0.7	1.8	0.5
			71^o — 3 — 70^o			
BG 11-6/10			17.1		3.0	3.0
			70^o — 2 — 62^o			
PCA 11-2/18	0.8	0.7	4.6	0.9	0.5	0.5
BG 11-6/12	0.7	0.7	4.3	0.3	1.2	1.0
			$< 62^o$			
BG 10-30/12			1.0	1.6		3.0

All intensities in KiloRayleighs (kR)
BG = Background

33-4.5 Photographic Measurements

The objectives of the airborne photographic measurements of the polar glow aurora were to measure the intensity of the aurora and to determine whether any measureable spatial structure was present. The photographic records obtained from the Flight Research cameras for the PCA event of 2 November 1969 were also examined for the presence of discrete auroral forms and the results are presented in the succeeding section. In the regions where discrete aurorae were not apparent, images were selected from each record corresponding to total light and filtered photographs for wavelengths 3914 A and 5577 A. Due to the low levels of intensity encountered during that period of observation, the relatively short exposure times (about 50 seconds) achieved with normal pulse operation produced photographic densities only slightly above fog level on the filtered records. Therefore, additional frames were selected corresponding to a much longer exposure duration—essentially covering the northernmost portion of the data flight (69° - 71.5°N).

The selected data frames were measured with a two-dimension scanning densitometer resulting in a family of isodensity traces for each frame. Using the calibration procedure previously discussed, density levels for each frame were converted to intensity values of the radiation entering the measuring instrument. The isodensity/isointensity contour map and corresponding photograph for the filter record at 5577 A are presented in Figures 33-10 and 33-11.

The more sharply defined areas within the photograph are produced by star images and the relative motion of the aircraft during the exposure interval. The remaining apparent structure is a rather uniform intensity exhibiting radial symmetry. Analysis of the isointensity contour map corresponding to this photograph substantiates the general radial symmetry plus an increase in intensity from the top toward the bottom of the frame.

If the radiant source is considered to be fairly uniform, it should appear to be symmetric about a vertical axis with increasing intensity from the zenith to the horizon due to the increasing emitting volume.

The observed intensity distribution for this filter photographic record could be explained by the off-angle transmission characteristics of interference type filters assuming a constant volumetric source radiance. Typically, thin film interference filters show a downward shift in wavelength for the transmission peak as the incident angle of radiation increases from the normal. Additional effects include a decrease in peak transmission and an effective broadening of the half-width.

Therefore, the observed structure on the iso-intensity contour maps cannot be definitively related to any structure in the source other than an increasing intensity from the zenith towards the horizon.

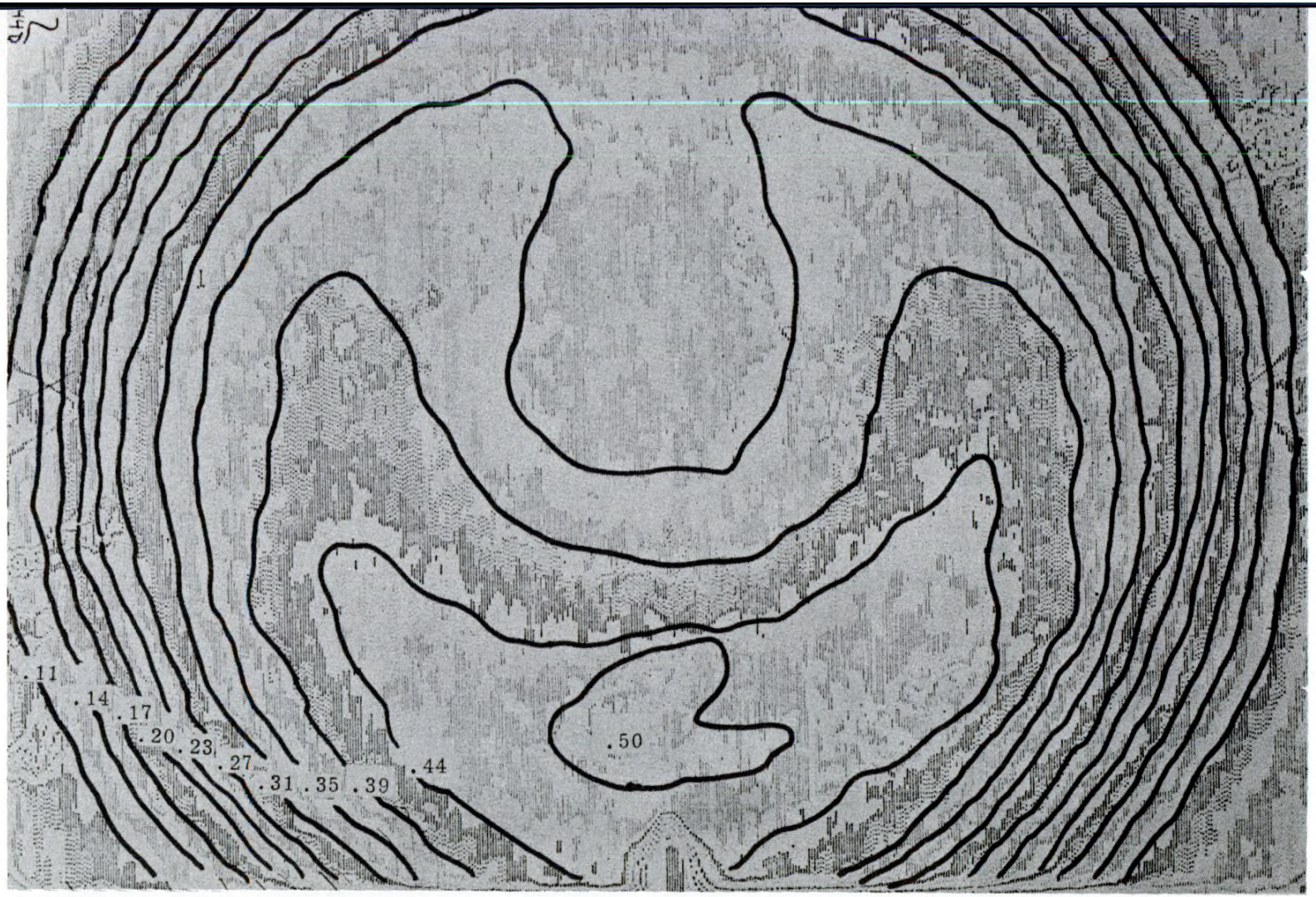

Figure 33-11. Isodensity Trace of Record/Figure 33-10 (Isointensity Contours in kR) 5577A, 0300/0322 UT

33-5 VISUAL DISCRETE AURORA

33-5.1 Rocket Launches

The in situ measurements of atmospheric parameters during the course of a PCA event were accomplished by rocket probes launched from Fort Churchill, Canada. Inasmuch as an objective of Project 8.4 was to provide documentation of visual discrete auroral activity during PCA observations, photographic data acquired from A/C 53120 on 2 November 1969 were correlated to the times of the rocket launches. Data was acquired throughout the flight from 2305 ZT, 2 November to 0855 ZT, 3 November. During this period of observations from the aircraft, seven rocket experiments were conducted from Fort Churchill as listed in Table 33-6.

Table 33-6. Rocket Launches During Photographic Observations

Time	Project	Photo Data	
		Launch	+2-3 Minutes
† 0455	MET	8298	---
0535	6.3A	8545	8559
0605	6.4.1	8617	8622
† 0629	6.4.2	8785	---
0642	9.1	8862	8869
0700	6.3A	8914*	8926
† 0730	6.4.2	8999	---

† No visual discrete aurora present at time of launches or within 5 minutes afterward.

* With filters.

Consideration of the geometry of the aircraft flight path and the optical field-of-view (see Figure 33-12) permits calculation of the atmospheric volume observed at any time. And although in general, this volume recorded photographically does not correspond to that encompassing the rocket trajectory, these results may be of some benefit to the other PCA experiments requiring a knowledge of visual auroral activity.

33-5.2 Visual Discrete Aurora

Analysis of the total light photographic record from 2 November 1969 enabled a determination of the regions and times of observation of visual discrete auroral

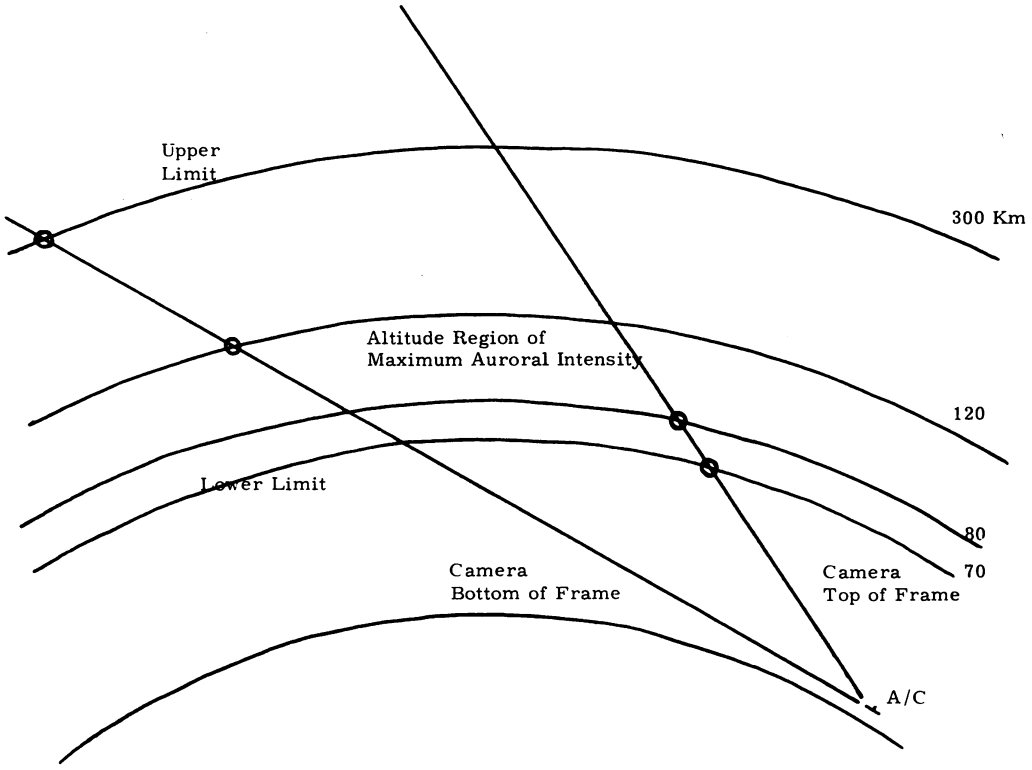

Figure 33-12. Atmospheric Volume Observed by A/C Cameras

emissions. A summary of this information is presented in Table 33-7 which indicates the presence of discrete auroral activity throughout a region from approximately 50°N to 65°N geographic latitude (corresponding to 60°N to 75°N geomagnetic latitude).

The brightest auroral forms during the times of rocket launches occurred at 0700 ZT and are illustrated in Figure 33-13.

Correlation of this data with other experiments must consider the moving aircraft platform from which the data was acquired. For the 29° square field of the total light camera, calculations were made to define the atmospheric volume observed. The results of these calculations are presented in Figure 33-14 for each of seven data sets corresponding to the rocket launch times. The near field limit is determined by the intersection of the projected upper frame line with the lower altitude boundary of auroral emission; limits are shown for 70 and 80 km. The far field limit is defined by the intersection of the lower frame line with the higher altitude boundary of the aurora; limits are shown here for 120 and 300 km.

Table 33-7. Summary of Discrete Auroral Forms
Observed 2 November 1969

Record No.	Time Z	Intensity†	Form‡	Latitude	Camera Field of View	
					Position*	Extent
8308	045910	F	D		L	1/3
8468	052626	F	R		L	1/5
8535	053545	M	R-B	64-1/2	L	1/3
8566	054254	M	R-B		L	1/2
8574	054444	S	B	62-1/2	C	1/2
8582	054826	M	B		L	1/2
8599	055741	S	B	61	C	1/2
8614	060409	F	B		L	1/2
8630	061027	S	B	60	L	1/5
8660	061345	F	B-D		L	1/3
8717	061733	M	B	58-1/2	C	1/4
8771	062518	F	D		L-C	1/2
8830	063228	VF	D	56-1/2	L	1/2
8869	064444	M	R-B	55	L	1/2
8902	065513	M	R-B	53	L-C	2/3
8937	070720	M	B	52-1/2		1
8982	072424	F	D	50	R	1/2
9085	075734	VF	D		L	1/4

† Faint, Moderate, Strong
‡ Diffuse, Rays, Bands
* Left, Center, Right

The variation in range evident on the figure is merely due to the exaggerated linear effect of the Mercator Map projection.

It is noted that additional photographic data exists for both total light and filtered records covering most of the duration of the aircraft flight. Records corresponding to specific times (and therefore to specific locations of the aircraft) can be provided as required.

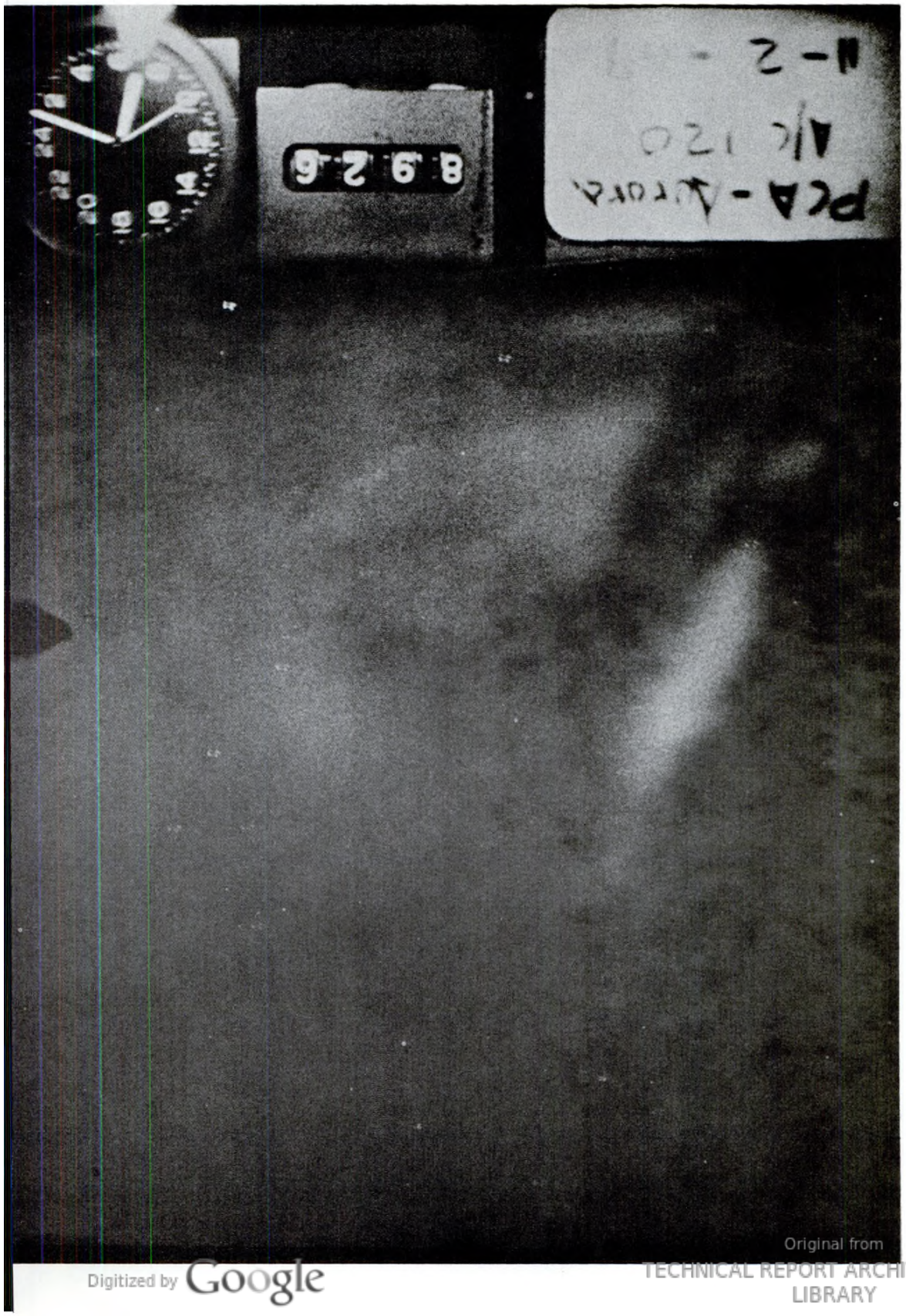

Figure 33-13. Total Light Record - 0703 UT (Related Rocket Project - 6.3A) 8926

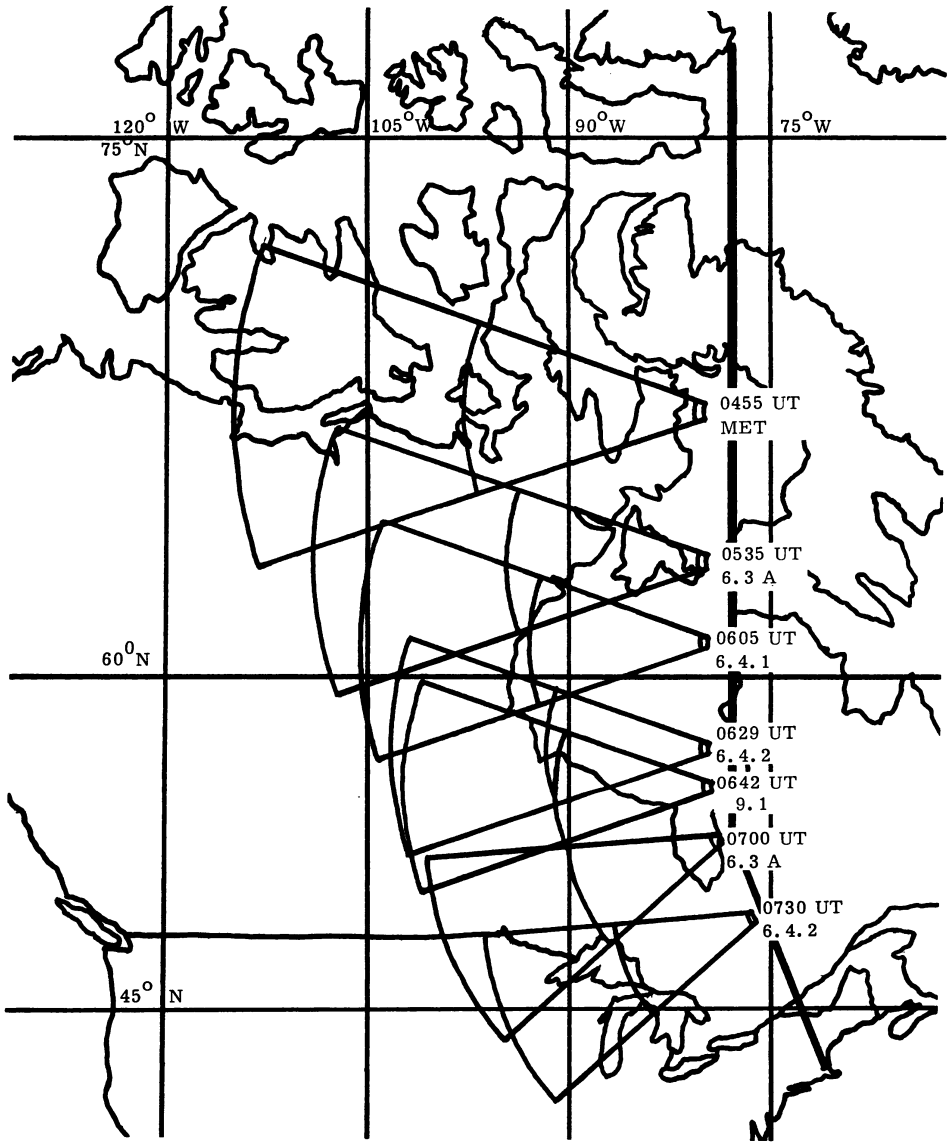

Figure 33-14. Field-of-View for Discrete Auroral Observations

33-6 CONCLUSIONS

The general performance objectives of Project 8.4 PCA were achieved by the successful flight operation of the DASA instrumentation on board the AFCRL KC-135 aircraft during the field period of Operation PCA. Photographic and spectrographic data on aurora and airglow phenomena were obtained on 10 flights into the polar region including the PCA event of 2 November 1969.

The results of the analysis of the spectrographic data obtained of the polar glow aurora indicate the anticipated enhancement of the N_2^+ emission at 3914 A throughout a region from 67° to 76°N geographic latitude. The average intensity of this emission decreased by a factor of two between 0300-0400 UT and 0400-0500 UT during which intervals the aircraft traversed the same latitude range. The observed spectral characteristics of the polar glow aurora are presented in comparison with related background observations in Table 33-5.

The photographic measurements of the polar glow aurora do not reveal detailed structure in the radiant source during the period of observations. Interpretation of the records indicates a broad uniform source which increases in intensity from the zenith towards the horizon.

Typical photographic data has also been presented as documentation of the degree of visual discrete auroral activity occurring at the times of rocket-borne experiments. It should be noted that a significant amount of additional photographic data in total light and filtered records at 3914 A and 5577 A is available should further requirements be developed by other PCA experimenters.

References

Allen, C.W. (1955) Astrophysical Quantities, 122, The Athlone Press, London.

Argemi, L.H. (1964) Ann. Geophys. 20:273.

Brown, R.R. (1964) Planet. Space Sci. 12:665.

Chamberlain, J.W. (1961) Physics of the Aurora and Airglow, 197, Academic Press, N.Y.

Dalgarno, H. (19) Space Research VII, North-Holland, Amsterdam.

Kofsky, I.L. (1971) Private communication.

Pollack, S.A. (1966) Applied Optics 5(No. 11).

Sandford, B.P. (1963) Planet. Space Sci. 10:195.

Sandford, B.P. (19) Polar Glow Aurora, Space Research VII, North-Holland, Amsterdam.

Sandford, B.P. (1971) Private communication.

Contents

34. Optical Airborne Measurements During 2—3 November 1969

B.P. Sandford
Air Force Cambridge Research Laboratories
L.G. Hanscom Field
Bedford, Massachusetts

Abstract

On 2-3 November 1969, aircraft KC-135, Serial No. 53150, flew from Massachusetts to Thule, Greenland and returned to Massachusetts. Measurements of the 1.65 μm OH, .6300 μm and .5577 μm (O) and .4278 μm N_2^+ emissions and auroral all-sky photographs were recorded in the polar cap and in the auroral oval. The only enhancement observed as directly attributable to solar particles was the N_2^+ first negative emission. All other emissions observed remained at typical levels. In the auroral belt, unusual active and bright pulsating aurorae were observed in the morning hours.

34-1 INTRODUCTION

During the Solar Particle Event (SPE), which began on 2 November 1969, the Air Force Cambridge Research Laboratories' KC-135 aircraft, Serial No. 53120, made optical measurements in the polar regions. The aircraft flew north from a point near Boston to 55N, 78W, then along 78W to 76N near Thule, Greenland, and then returned along the same track as illustrated in Figure 34-1. Visible and

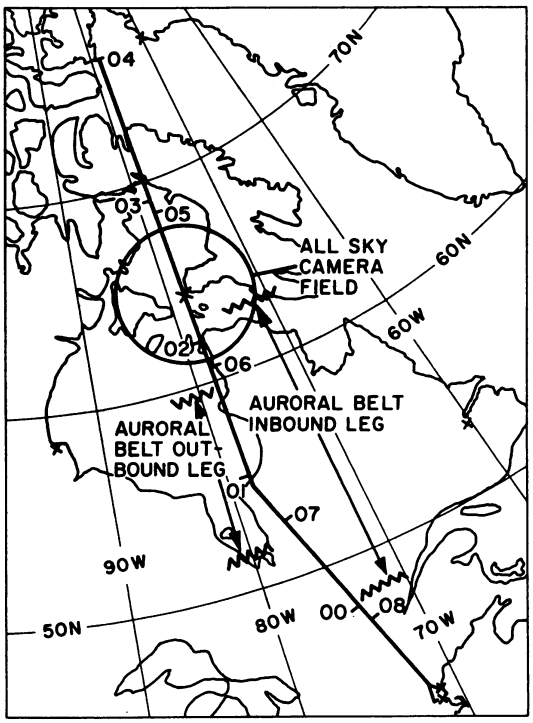

Figure 34-1. Track of the KC-135 Aircraft S/N 53120 on 2-3 November 1969. The field of view of the all-sky camera for a 110-km altitude is shown by the circle. Universal Time in hours is shown along the track

near infrared emissions at .5577 and .6300 μm (OI), .4278 μm 0-1 first negative band of N_2^+ and 1.65 μm 5-3 band of OH, and all-sky camera records are reported here. The zenith intensities of these features are illustrated in Figure 34-2.

The observations can be divided into two major groups, one while the aircraft was in the polar cap, and the other while the aircraft crossed the auroral oval. A third region showing some weak auroral contamination at the beginning and end of the flight is more typical of mid-latitude airglows and will not be discussed.

34-2 OBSERVATIONS IN THE POLAR CAP

The aircraft was in the polar cap from 0130 to 0530 UT on 3 November 1969. At this time the 1.65 μm and .6300 μm emissions are typical of levels that were normally observed on other flights in October and November 1969. The .5577 μm intensity was greater than the .6300 μm intensity which was not normally the case

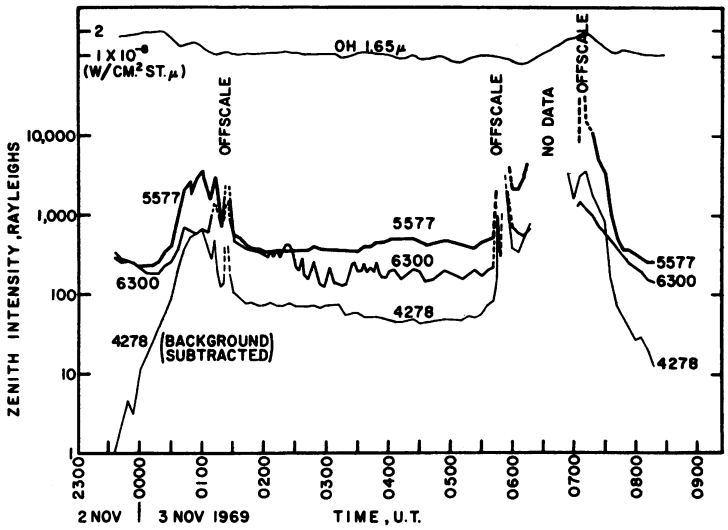

Figure 34-2. The Zenith Intensity of Emissions at .4278, .5577, .6300 and 1.65 μm During the Aircraft Flight

on other flights in October and November 1969. However, there is no reason to believe that this high intensity of the green line is associated with the solar particle event.

The emission observed at .4278 μm is considerably more intense than normal and is caused by the precipitating solar particles. The intensity of this emission for the complete 0-1 band system of N_2^+, with continuum background signals such as starlight subtracted, is given in Figure 34-3 for the period 0140 to 0536 UT, 3 November. Careful comparison with the other emissions and with the all-sky camera films indicate that all the N_2^+ radiation arises from the solar particle event, except for the sharp rise after 0530 UT. This rise is probably due to auroral emission as the aircraft approaches the auroral oval. The intensity of the 0-1 band is one-third the intensity of the 0-0 band at .3914 μm.

The observed intensity of the 0-1 band between 83 and 42 Rayleighs corresponds to a total precipitating energy in the range of .3 to .5 erg cm^{-2} sec^{-1} (Sandford, 1967). The general trend of decreasing intensity from 0140 until 0500 UT is in agreement with measurements of the .4278 μm intensity at Thule, Greenland, reported by Hall (these proceedings), riometer absorption measurements at Thule and Godhavn, Greenland and Churchill, Canada reported by Cormier (these proceedings) and with

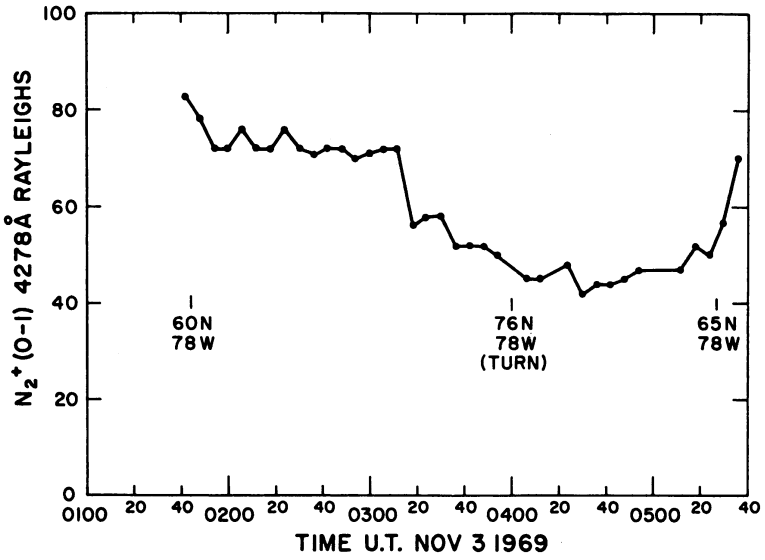

Figure 34-3. The Zenith Intensity of the 0-1 Band of N_2^+ (.4278 μm) in the Polar Cap on 3 November 1969

Explorer 41 deep space proton fluxes reported by Potemra, et al (these proceedings). Detailed changes on a small time scale do not show an exact correspondence. From these observations it appears that a fairly uniform particle precipitation pattern occurred over northeast Canada and Greenland during the early hours of 3 November 1969.

In the polar cap no visual auroral forms were seen, except for one short-lived ray bundle at 0430 UT.

34-3 OBSERVATIONS IN THE AURORAL OVAL

The aircraft crossed the auroral oval on the eastern edge of the Churchill Rocket Range. As the Range was cloud covered, auroral observations are reported as an aid to interpreting rocket data, even though there is no reason to identify the auroral activity with solar particle precipitation. The instantaneous field of view of the all-sky camera at a typical auroral altitude of 110 km is indicated by the circle on Figure 34-1. The all-sky photographs were taken every minute with a 1-minute exposure and are presented in Figure 34-4. for the northward crossing and in Figure 34-5 for the southward crossing of the auroral oval. Each row of photographs covers the 10-minute intervals starting with the indicated time. The camera orientation is indicated on each figure for the periods before and after the aircraft turns at 0055 and 0644 UT. In Figure 34-5 the bright image at the bottom

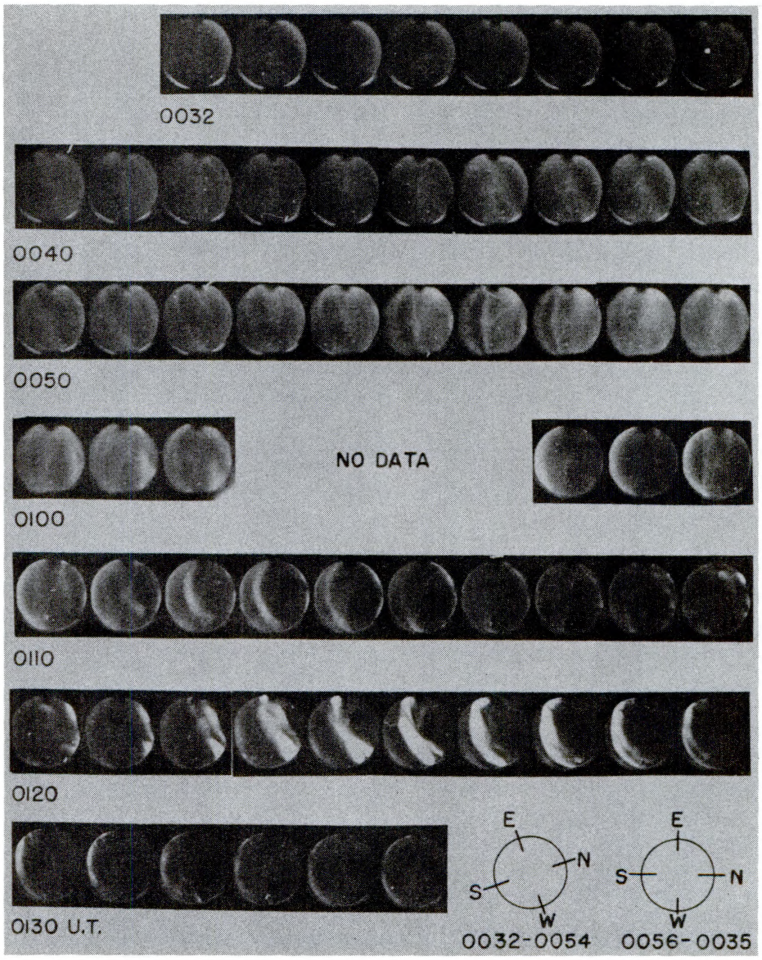

Figure 34-4. All Sky Camera Photographs for Each Minute From 0032 to 0135 UT and Camera Orientation on 3 Nov 1969. See Figure 34-1 for aircraft position and field of view. The Milky Way runs near E-W across each photograph

of each all-sky photograph is the moon, which also produces a ghost image in the upper part of each photograph. The zenith intensity of the N_2^+ and (O) emissions for these crossings is shown in Figure 34-2.

The visual auroral oval lay between geographic latitudes of 52°N and 59°N at 78°W around 0030 to 0140 UT on 3 November. The aurora consisted of a broad glow between 52° and 57°N. In the region of the glow were discrete arc forms, which also occurred with brighter intensity north of the glows to 59°N (Figure 34-4).

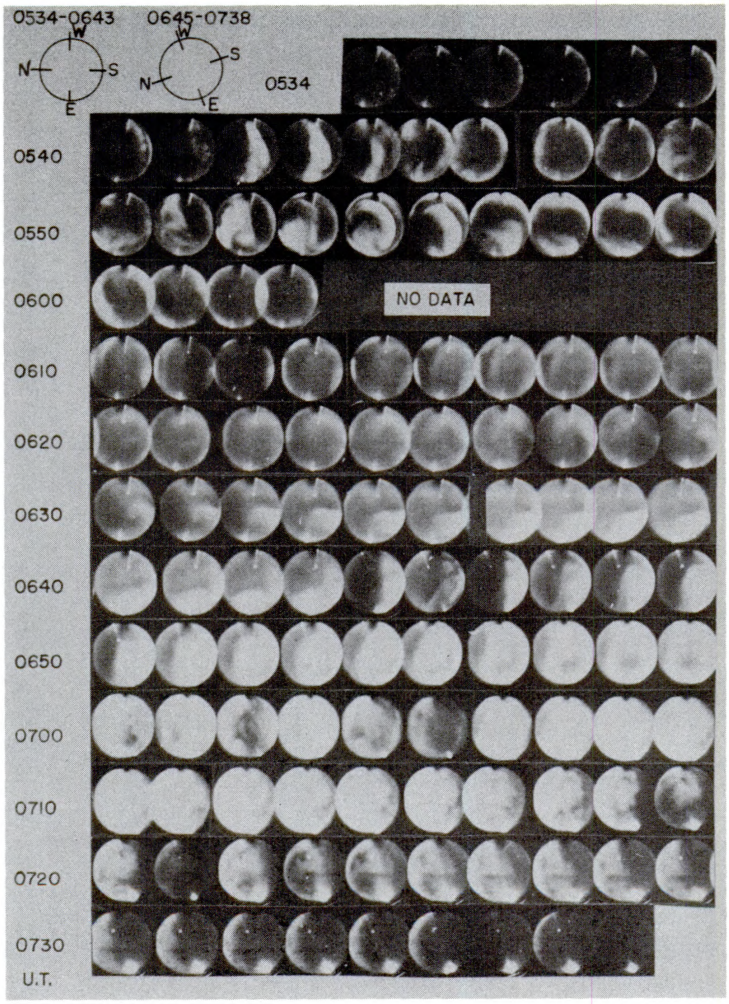

Figure 34-5. All-Sky Camera Photographs for Each Minute From 0534 to 0738 UT and Camera Orientation on 3 Nov 1969. See Figure 34-1 for aircraft position and field of view. The bright image at the bottom and the ghost above arise from the moon

The visual auroral oval was very broad and lay between geographic latitudes of 63°N and 48°N at 78°W around 0540 to 0740 UT. Discrete and active bands lay between 63°N and 59°N. From 59°N to 50°N extensive and bright patch aurora was observed which exhibited unusual, active pulsation activity with east-west bands of light running from south to north through the patches in a jerky and flickering motion.

The 5-3 band of OH showed a typical nighttime behavior in this region, with an enhancement of about a factor of two south of the auroral oval at 0000 UT. On the return crossing of the oval around 0700 UT, an enhancement was again observed which was coincident with the region of the patch aurora. Such behavior has been observed on other occasions and is not considered to be influenced by the solar particle event.

This work is part of the DASA sponsored research of Optical Physics Laboratory, Air Force Cambridge Research Laboratories. The visible region photometric measurements were made and reduced by PhotoMetrics, Inc. and the OH measurements were made and reduced by the Stewart Radiance Laboratory of Utah State University.

References

Cormier, R. J. PCA Behavior as Observed on Riometers, these proceedings.

Hall, W. N. Polar Cap Optical Intensities During the 2 November 69 Solar Particle Event, these proceedings.

Potemra, T. A., Zmuda, A. J., and Haave, C. R. The Connection of Solar Proton Fluxes to Airglow, VLF and HF, these proceedings.

Sandford, B. P. (1967) Polar-Glow Aurora, Space Research VII, ed. Smith-Rose, North Holland Publishing Co., Amsterdam, P. 836.

Contents

35. Photometric Measurements From PCA 69 Black Brant Rockets

K.D. Baker, D.A. Burt and D.J. Baker
Center for Research in Aeronomy
Utah State University
Logan, Utah 84321

Abstract

The six Black Brant rockets flown during the November 1969 PCA Event each contained a complex array of instruments, including a large number which made photometric measurements. These measurements had two primary objectives: (1) the ascernment of ionization rates in the D region due to various sources, and (2) the measurement of the concentrations of minor constituents important to the lower ionospheric processes. Measurements in the first category are emission from N_2^+ and Lyman-α and X-ray fluxes. The ionization rates due to energetic particles are obtained directly from the N_2^+ (3914 A) emission rate profile deduced from the photometer data. The Lyman-α and X-ray flux measurements are used to assess the importance of these sources to the total ion production rate during this event. The results of the minor constituent measurements are also presented.

35-1 PAYLOAD INSTRUMENTATION

The six Black Brant rockets flown during the 2 November 1969 solar proton event (PCA 69) included instruments for measurements of photon fluxes of various wavelengths. The objectives of these measurements were twofold: (1) To assess

the importance of various ionization sources in the D region during energetic solar particle bombardment, and (2) to determine the concentration of minor constituents important in chemical processes controlling the D-region ionization during a PCA event and in the quiet D region.

The Black Brant payloads were of three different configurations containing photon-measuring devices as illustrated in Figure 35-1 (Baker et al, 1970). The three Type A payloads (Rocket Nos. 17.602, 17.611, 17.616) each contained a Lyman-α ionization chamber, an X-ray proportional counter, and a filter-wheel photometer. The ionization chamber provided a measure of both solar and extended non-solar Lyman-α fluxes to make possible the ascernment of ion production rates due to these sources. The X-ray counter (1-20 keV) gave relative indications of the degree of energetic electron bombardment through measurement of bremsstrahlung X-ray fluxes and, secondly, allowed assessment of the possible contribution of hard solar X-rays to D-region ionization. The filter wheel photometer measured emissions near the zenith in five colors: (1) 3914 A (N_2^+) for ion production rates; (2) 5577 A from atomic oxygen; (3) 4861 A (H_β) for information on proton fluxes; (4) 5775 A (NO_2 continuum) for information on NO processes; and (5) 4050 A background light. The first Type A payload (17.602) was launched during the day of 2 November (χ = 79°); the other two payloads were launched at sunrise and sunset on 3 November.

The two Type B payloads (17.758, 17.617) included Lyman-α and X-ray instruments identical with those of the A payloads and, in addition, a 3914 A photometer for determination of ion production rates and a 1.27-μ radiometer for determination of the metastable $O_2(^1\Delta_g)$ concentration. The Type B payloads were flown at night on 3 November (χ = 136°) and at sunset on 4 November (χ = 97°).

The Type D payload (17.906-1) was specially designed to emphasize photometric measurements of minor atmospheric constituents during daytime PCA conditions. Ionization source measurements included 1-20 keV X-rays, 44-60 A X-rays, Lyman-α flux, and N_2^+ emission (3914 A). Minor constituent measurements were obtained by photometers at 5577A for 0, 7620 A for $O_2(^1\Sigma_g)$, 5775 A for NO_2, 7300 A for OH, 2155 A for NO from γ-band resonance scattering, 2590 A for O_3 from solar ultraviolet absorption, and 1.27 μ for $O_2(^1\Delta_g)$. This payload was flown near local noon (χ = 74°) on 3 November.

35-2 EXPERIMENTAL RESULTS

The results of the $O_2(^1\Delta_g)$ measurements are of special significance and are described by Bishop et al (1971) in these proceedings. The results of the other successful measurements will be discussed here.

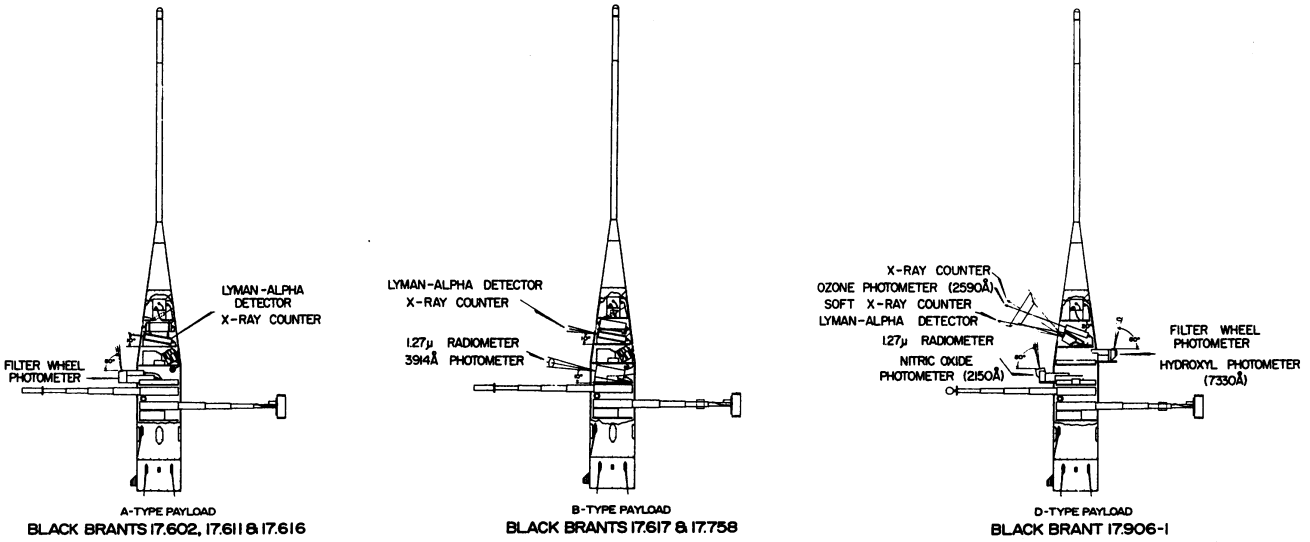

Figure 35-1. Outline of Black Brant PCA Payloads Showing Instruments for Photon Measurements

Since these measurements were conducted during a Polar Cap Absorption Event of fairly large magnitude, sources of ionization other than energetic solar particles might be expected to be unimportant. Accordingly, many of these results are negative in nature in that they were used to verify the validity of using only the primary energetic particle source in ion production rate calculations.

During the daylight hours the solar Lyman-α flux was measured to be about 5 ergs cm^{-2} sec^{-1}. If nitric oxide concentrations similar to those reported by Meira (1971) are assumed, the NO ionization rate by this Lyman-α flux for noontime conditions ($\chi = 75°$) would range from about 10 cm^{-3} sec^{-1} at 90 km to about 0.5 cm^{-3} sec^{-1} at 70 km. Lower solar zenith angles would produce correspondingly lower ionization. The work of Huffman et al (1971) shows that ionization of $O_2(^1\Delta_g)$ can be neglected compared with the NO ionization. The Lyman-α measurements indicated a glow of a few kilorayleighs in non-sunlit regions. Integrating this flux with an assumed NO concentration as before gives ionization rates less than 0.1 cm^{-3} sec^{-1} in the D region. The ionization resulting from Lyman-α can thus be neglected compared with that produced by the solar particles except in the last phases of the event during the day (from 4 November on).

The X-ray counter results show that the hard component of the solar X-ray flux was not significantly enhanced during the phases of the event studied by the rocket probes and hence can be ignored when significant protons were bombarding the D region. The bremsstrahlung X-ray flux, although not important as an ionization source itself, is a useful indicator of the importance of auroral electron precipitation to the upper part of the D and lower E region. The night flight on 3 November (17.758) showed a relatively large X-ray flux. This indicates that a high degree of auroral activity was prevalent during this period. As a result the region at about 90 km would be expected to show greatly enhanced ionization due to these auroral electrons. Significant but considerably less auroral activity was indicated during both day flights 17.602 and 17.906-1 (2020 NT 2 November, and 1711 3 November, respectively). The evening flight on 4 November (17.617) showed very little electron precipitation.

These miscellaneous ionization source studies reveal that X-ray and Lyman-α ionization can be ignored during the event except during the daytime on 4 November or later. The electron fluxes definitely need to be taken into account in the upper regions during the midnight period of 3 November and could be significant at the higher altitudes at other times.

The results of the measurement of 3914-A emission attributable to excited N_2^+ by the side-viewing photometer are shown in Figure 35-2. Since the rocket was spinning at about three revolutions per second, complete azimuthal data scans were available at this same rate. The data were sorted on the basis of elevation of the

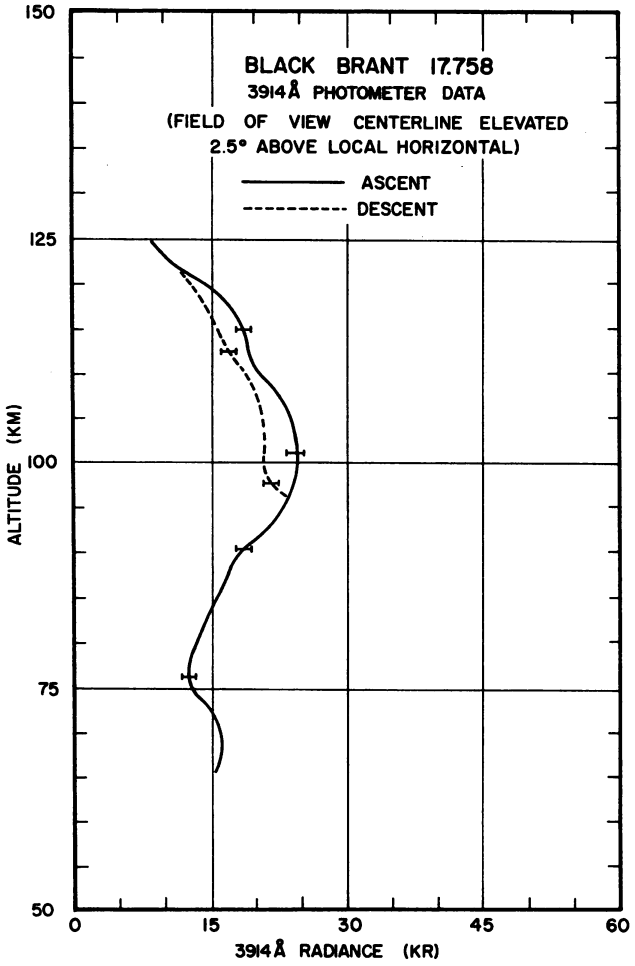

Figure 35-2. Intensity of N_2^+ (3914 A) Measured by the Side-Viewing Photometer (17.758) the Night of 3 November During the Solar Proton Event

center of the 10° (full angle) field of view of the photometer with respect to the local horizontal. The data shown in Figure 35-2 are for an elevation angle of 2.5°. Two maxima are seen in these data, one of 15 kR at about 70 km, and a second of 25 kR at about 100 km.

To be really meaningful, such profiles measured along the nearly horizontal field of view should be converted to vertical emission rate profiles. An attempt to approximate the emission rate profiles responsible for the measured values was carried out by assuming the profile to be adequately represented by two Gaussian-shaped layers. Values for the height, width, and maximum intensity of the layers

were assumed, and then the predicted values along the actual field of view were calculated on the computer. The comparison of this computation with the actual measurements guided the next approximation until adequate agreement was achieved.

Data from rocket ascent and descent and for several elevation angles were used to deduce the emission rate profile shown in Figure 35-3 for the night data illustrated earlier in Figure 35-2. The layer at about 68 km with a peak emission of about 300 cm^{-3} Sec^{-1} is associated with ionization due to the energetic protons, whereas the higher layer at 110 km is due to the electron-induced auroral activity.

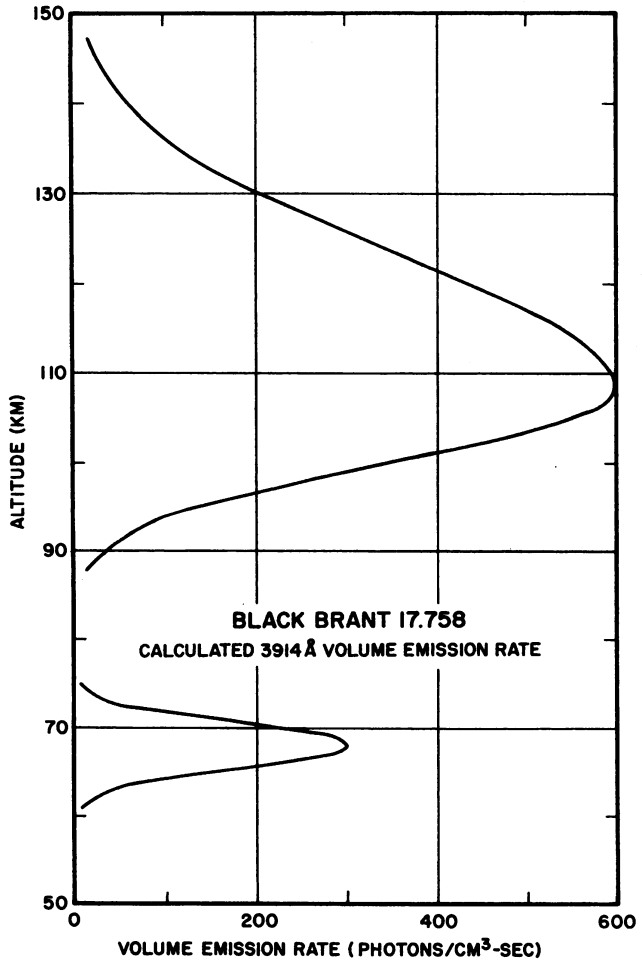

Figure 35-3. N_2^+ Volume Emission Rate Derived From Side-Looking Photometer Data From Black Brant 17.758

It must be pointed out that due to the relatively wide photometer field of view and discrepancies in the measured values, this fitting technique has large uncertainties associated with it. The intensities are uncertain to about a factor of two, and the layer heights have about a 10-km uncertainty. The other photometer flights were made during sunlit conditions, so it is extremely difficult, if not impossible, to extract N_2^+ emission light from the background of Rayleigh and resonance scattered light.

The ozone concentration was measured on rocket 17.758 near local noon (χ = 74°) on 3 November by the standard solar ultraviolet absorption technique (Tohmatsu, 1969). The results of this measurement are shown in Figure 35-4. The O_3 measurement range extends from about 2×10^{10} cm^{-3} at 52 km to about 3×10^{7} cm^{-3} at 80 km with nearly a constant scale height of about 4 km. These results are compared in Figure 35-5 with measurements made at Wallops Island by Weeks and Smith (1968) and with those of Nagata et al (1971) in Japan and with a calculated model of George et al (1971) for noon conditions at the latitude of Churchill, Canada. The measurements reported here for PCA conditions at the relatively high latitude of Churchill (59°N) are not greatly different from the other

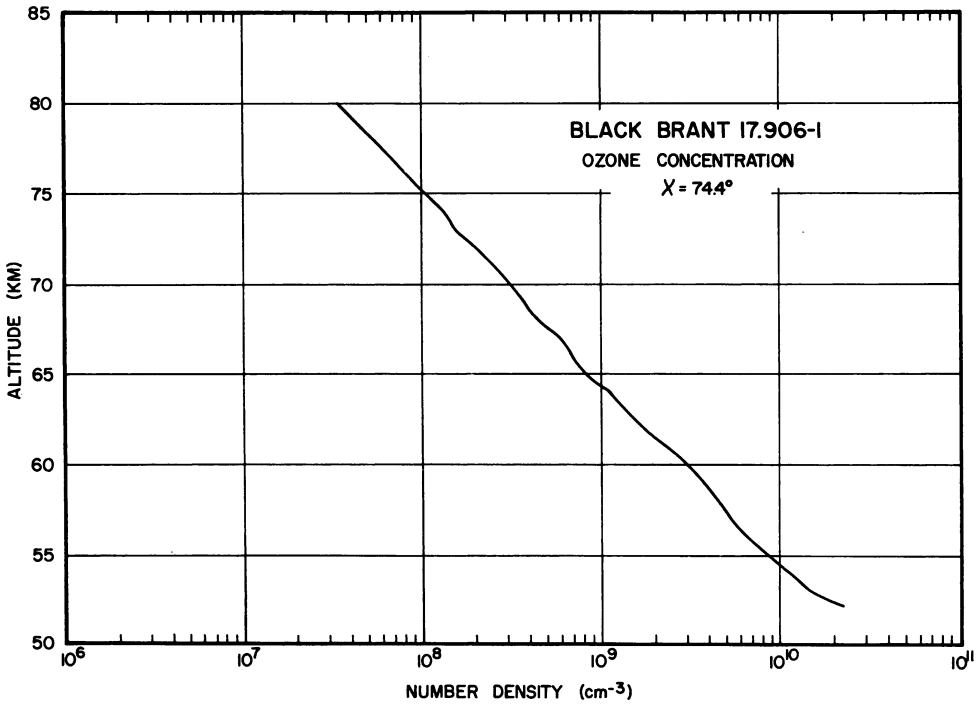

Figure 35-4. Ozone Concentration Measured by Black Brant 17.906-1 Near Noon (χ = 74°) on 3 November

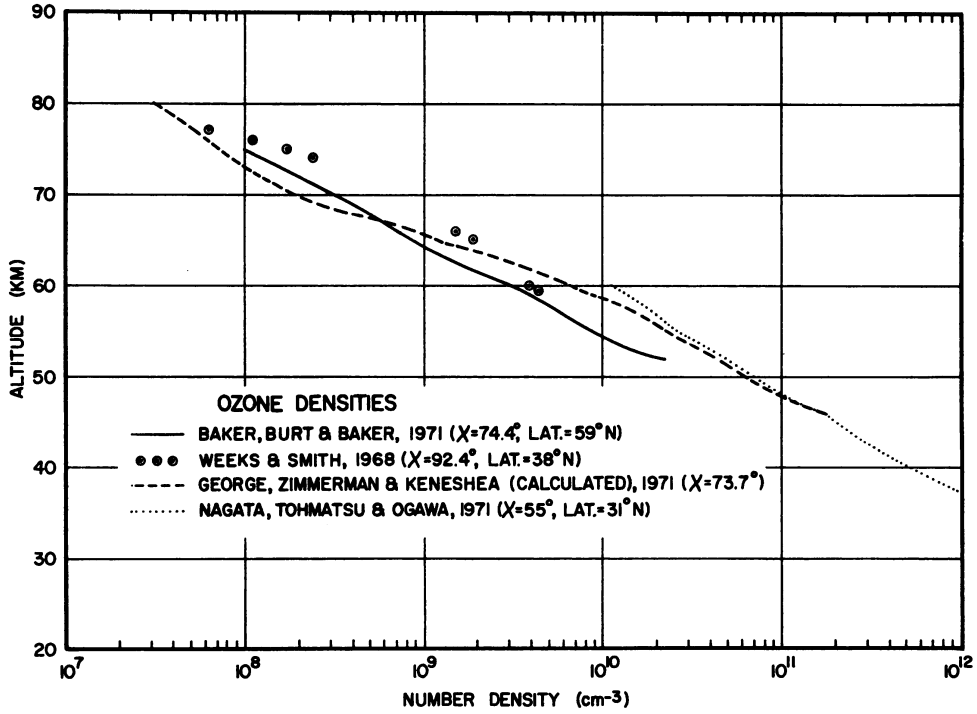

Figure 35-5. Comparison of Ozone Concentrations Measured on Black Brant 17.906-1 (Baker, Burt and Baker, 1971) to Values Measured at Wallops Island (Weeks and Smith, 1963) and Japan (Nagata, Tohmatsu and Ogawa, 1971) and Also to a Calculated Model (George Zimmerman and Keneshea, 1971)

mid-latitude results. The greatest discrepancy exists at about 60 km where the PCA results are a factor of three lower than the Japanese results. Below 65 km the high latitude measurements are about a factor of two lower than the calculated densities; above this altitude the agreement is better with the measurements showing larger densities than the model above 68 km.

The agreement between all these results is considered remarkable under the widely differing atmospheric conditions, latitudes and solar zenith angles. The results of this measurement are in quite good agreement with the O_3 density values given by Weeks (1968) elsewhere in this report for a sunset measurement (χ = 89.5°) on 4 November at the late phase of the event. They are, however, about a factor of two higher than Weeks' measurement at sunset (χ = 89.5°) on 2 November earlier in the event.

References

Baker, K.D., Burt, D.A., Howlett, L.C., and Allred, G.D. (1970) Rocket instrumentation for the study of a Polar Cap Absorption Event–PCA-69, UARL Final Report, AFCRL 70-0251, 270 pp, Contract F19628-67-C-0275, Upper Air Research Laboratory, University of Utah, Salt Lake City.

George, J.D., Zimmerman, S.P., and Keneshea, T.J.J. (1971) The Latitudinal Variation of Major and Minor Neutral Species in the Upper Atmosphere, Space Research XII.

Huffman, R.E., Paulsen, D.E., Larrabee, J.C., and Cairns, R.B. (1971) Decrease in D-region $O_2(^1\Delta_g)$ photo-ionization rates resulting from CO_2 absorption, J. Geophys. Res. 76:1028.

Meira, L.G. (1971) Rocket measurements of upper atmospheric nitric oxide and their consequences to the lower ionosphere, J. Geophys. Res. 76:202.

Nagata, T., Tohmatsu, T, and Ogawa, T. (1971) Sounding rocket measurement of atmospheric ozone density, 1965-70, Space Res. 11.

Tohmatsu, T. (1969) Solar radiation detector system for meso-turbosphere ozone density measurement, in Small Rocket Instrumentation Techniques, ed. K.I. Maeda, North-Holland Publishing Co., Amsterdam.

Weeks, L.H., and Smith, L.G. (1968) A rocket measurement of ozone near sunrise, Planet. Space Sci. 16:1189.

Contents

36. Observations of $O_2(^1\Delta_g)$ in the D and Lower E Region During PCA 69

R.H. Bishop, K.D. Baker, and R.Y. Han
Center for Research in Aeronomy
Utah State University
Logan, Utah

Abstract

Payloads on three Black Brant rockets launched during the November 1969 Polar Cap Absorption Event included a radiometer designed to measure the emission from $O_2(^1\Delta_g)$ at 1.27μ in the upper atmosphere. Irradiance data are presented for a sunset flight (χ = 97°) and a night flight (χ = 136°) from side-looking radiometers. Rocket spin and precession caused the instruments to have changing elevation and azimuth angles in the local horizontal frame of reference. In this frame, data were sorted according to selected elevation angles and then analyzed separately. A volume emission profile was fit to the data at a particular elevation angle and once determined, the profile was verified by comparison with data at other elevation angles. The $O_2(^1\Delta_g)$ concentration profiles were deduced from these emission rates. The $O_2(^1\Delta_g)$ profiles for each of the above flights are presented and the implications of these results on the understanding of D-region processes will be discussed.

36-1 INTRODUCTION

The concentration of metastable oxygen molecules are important to the understanding of D-region processes. The $O_2(^1\Delta_g)$ state is particularly interesting

because its long lifetime (nearly an hour) makes its excitation energy of approximately 1 ev available in interactions of many types. Hunten and McElroy (1968) pointed out that this excited state can be ionized by ultraviolet radiation in the wavelength band 1027-1118Å, parts of which can penetrate below 70 km, and therefore is an important source of daytime ions. Although the importance of this mechanism appears to be diminished by the work of Huffman, et al (1971) which included absorption by CO_2, it should still be considered for overall D-region ionization processes. More important to the D-region processes during a Polar Cap Absorption (PCA) Event is the ability of the $O_2(^1\Delta_g)$ molecules to detach loosely-bound negative ions as discussed by Megill and Hasted (1965). Since the daytime production of $O_2(^1\Delta_g)$ is primarily by photolysis of ozone, the correspondence of the increased radiowave absorption to ultraviolet sunrise instead of visible sunrise (the so-called absorption hysterisis effect) might be explained in this manner. Several other mechanisms involving excited $O_2(^1\Delta_g)$ molecules could be important to D-region chemistry, for example the possible short-circuiting of the chain of reactions resulting in the hydration of ions. In an attempt to help answer the questions associated with D-region processes in which $O_2(^1\Delta_g)$ may be playing a part, infrared radiometers were included in the payloads of three of the Black Brant rockets flown during the 2 November 1969 PCA Event.

36-2 MEASUREMENTS

The radiometers carried aboard Black Brant rockets 17.758, 17.906-1, and 17.617 to measure the $O_2(^1\Delta_g)$ emission at 1.27μ utilized a 300Å interference filter, blocking filter, honeycomb baffle, tuning fork chopper, and a lead sulphide detector. The field of view was approximately square with about a 10° field of view (full angle). The radiometer on the night flight (Black Brant 17.758) had a logarithmic output with a dynamic range of 5×10^5 to 10^8 Rayleighs. The other instruments had linear outputs with a range from 10^7 to 3×10^8 Rayleighs. In addition to this difference it should be pointed out that on Black Brants 17.758 and 17.617, the night and sunset flights respectively, the axis of the acceptance cone was inclined 80° with respect to the longitudinal axis of the rocket. The radiometer on Black Brant 17.906-1 (the day flight) incorporated a mirror arrangement which inclined its acceptance cone axis at 10° with respect to the rocket axis. Meaningful measurements were obtained only on the night and sunset flights and the remainder of this paper will discuss those results.

The general rocket motion for both flights was a roll rate of about 3 rev/sec about an axis that was slowly precessing about the local vertical. This general motion leads to instrument elevation angles changing much more slowly than their

azimuth angles. The flight data were sampled 250 times/sec or approximately one point every 4° of azimuth.

The philosophy used in the reduction of data was to select a given radiometer elevation angle and then to collect all data at this particular elevation angle throughout the flight, allowing the azimuth angles to fall where they may. It should be mentioned that no azimuthal dependence was observed with the exception of that due to sunlight on the instrument (on the sunset flight) and that data in this region was deleted from the analysis. Several elevation angles were selected and studied on each flight. The data were then interpolated with respect to time and smoothed.

Figure 36-1 shows the 1.27μ radiance observed on the night flight (17.758) when the radiometer was inclined 2.5° above the local horizontal plane. Observations on both ascent and descent are presented on this plot. Figure 36-2 is similar to Figure 36-1 but here the radiometer was inclined at an angle of 10°.

The data for an elevation angle of 2.5° (Figure 36-1) show a rather broad maximum of about 2 MR from about 70 to 95 km with the intensity dropping off rather rapidly above and below this region. These data suggest the existence of a single emitting layer somewhere between 75 and 100 km.

The 10° data shown in Figure 36-2 exhibit the same general behavior except that the peak magnitude is down and the altitude of maximum signal is lower. Both these effects are to be expected because of the higher elevation angle of the instrument.

36-3 CALCULATED PROFILES

It is important that the measured data be interpreted in terms of the height profile of the $O_2(^1\Delta_g)$ concentration. Because of the relatively wide field of view of the radiometers, the determination of the concentration profile producing the measured data must be a rather rough approximation. A Gaussian-shaped height distribution was chosen as a first approximation to the actual distribution since this shape seems reasonable to most layering phenomena and it is analytically easy to deal with. The calculated profiles then amounted to the proper choice of the height of the layer, its width to the first standard deviation (an altitude), and the peak concentration to fit the measured data. The actual method used to determine the appropriate profile was that of "cut and try" technique. A particular layer was assumed and the resulting radiance profile which the rocket would have observed was calculated. Based on the amount of agreement with the actual measured data, a better estimate of the $O_2(^1\Delta_g)$ height profile was then assumed and the process repeated until satisfactory agreement was achieved. This computation involves a triple integration of the number density (after changing its functional dependence from height

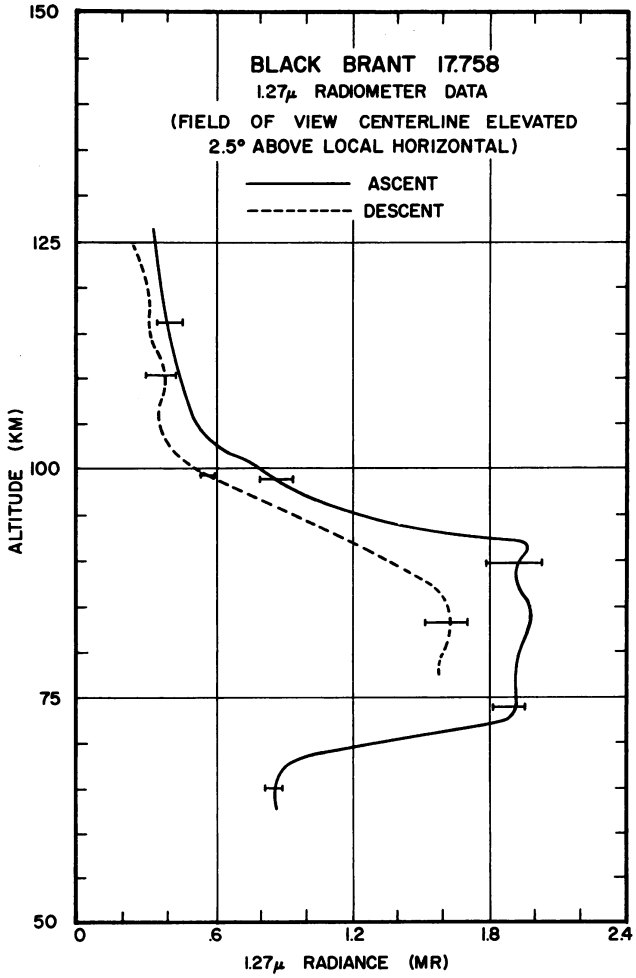

Figure 36-1. Inflight Data, Taken by Black Brant 17.758, of the 1.27μ Irradiance in MegaRayleighs as a Function of Altitude for an Instrument Elevation Angle of 2.5°

to radial distance from the instrument) and due to its complexity was carried out on a Univac 1108 computer.

The $O_2(^1\Delta_g)$ concentration profile determined for the night data (Figures 36-1 and 36-2) is shown in Figure 36-3. The layer maximum has a value of about 2.1 $\times 10^8$ cm^{-3} at an altitude of about 92 km. The width of the layer to first standard deviation is 12.5 km. Due to the wide radiometer field of view and the best fit nature of the technique, this profile has rather large uncertainties. The density is uncertain to about a factor of two and the height of the center of the layer has an uncertainty of 7.5 km. The width of the layer is uncertain by ±3.0 km.

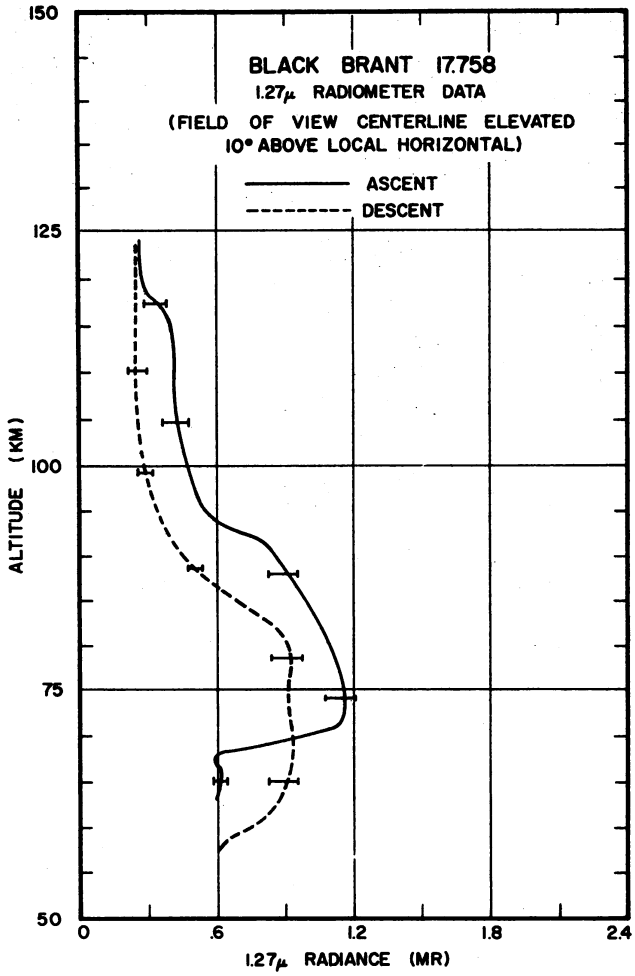

Figure 36-2. $O_2(^1\Delta_g)$ Irradiance in MegaRayleighs Plotted vs Altitude, as Obtained From Black Brant 17.758, for a Selected Instrument Elevation Angle of 10.0°

The measured $O_2(^1\Delta_g)$ intensities on the sunset flight (17.617) (χ 97°) are shown in Figure 36-4 for an elevation angle of 1°. The intensities are about an order of magnitude higher than observed on the night flight and there is a definite indication of a second higher layer. Figure 36-5 shows the $O_2(^1\Delta_g)$ intensities observed on the same flight, but here the elevation angle is 5°. Here again definite indications of a higher layer were recorded. Applying the same technique as for the earlier flight except utilizing two Gaussian layers results in the profile shown in Figure 36-6. In this case the data is best fit by two layers of about equal

concentration of 3.5×10^9 cm^{-3} at about 95 and 120 km with layer widths of 5.0 km to the point of first standard deviation. The uncertainties again are about a factor of two in concentration, ±7.5 im in altitude, and ±3.0 km in width.

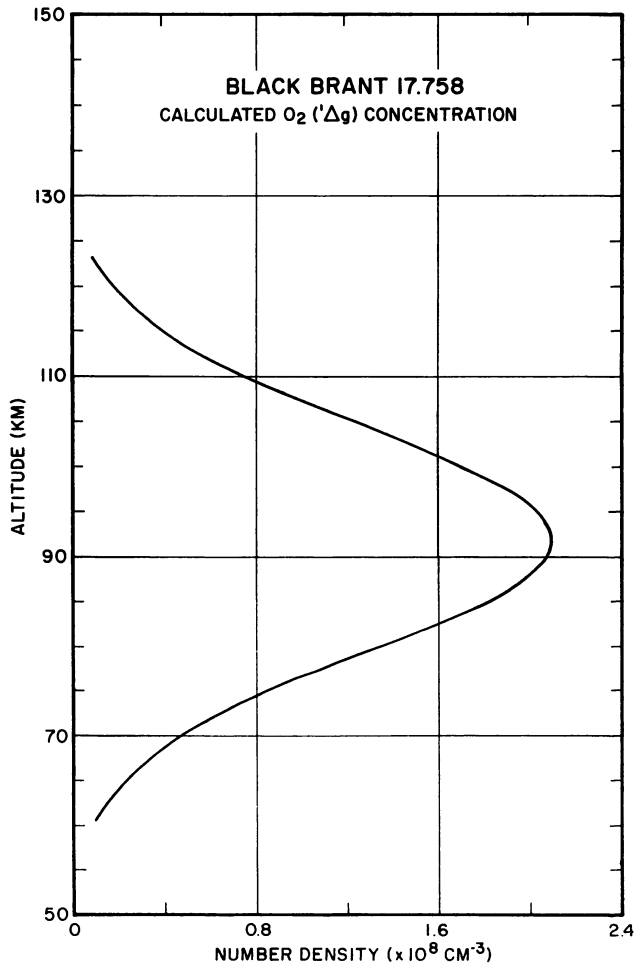

Figure 36-3. Calculated $O_2(^1\Delta_g)$ Concentration as a Function of Altitude. The concentration profile was obtained by a "cut and try" technique to best fit the data presented in Figures 36-1 and 36-2

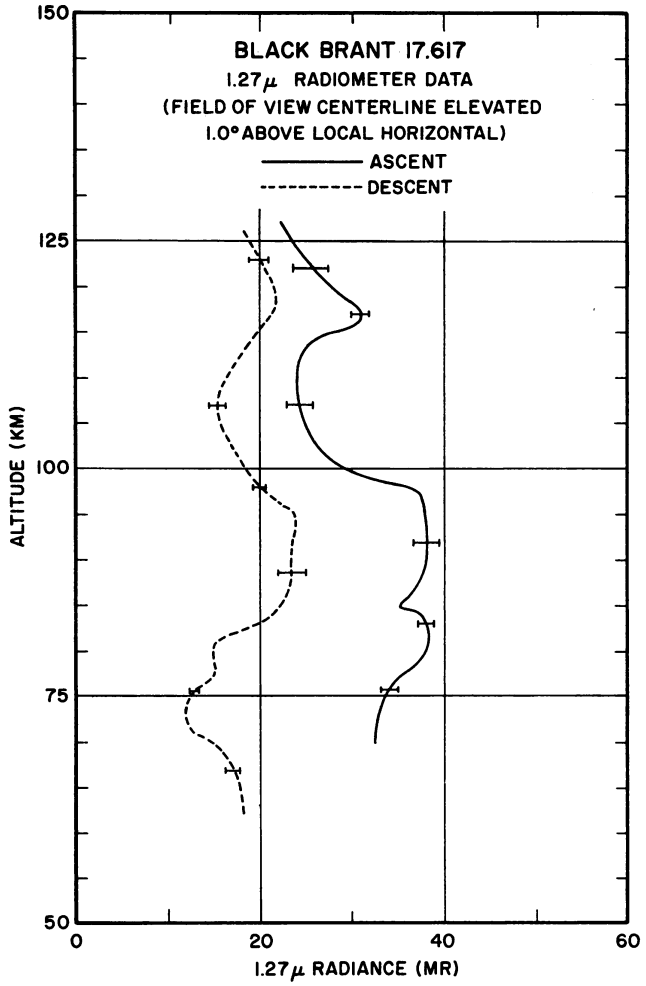

Figure 36-4. Inflight Data, as Observed by Black Brant 17.617, of $O_2(^1\Delta_g)$ Irradiance in MegaRayleighs vs Altitude for an Instrument Elevation Angle of 1.0^o

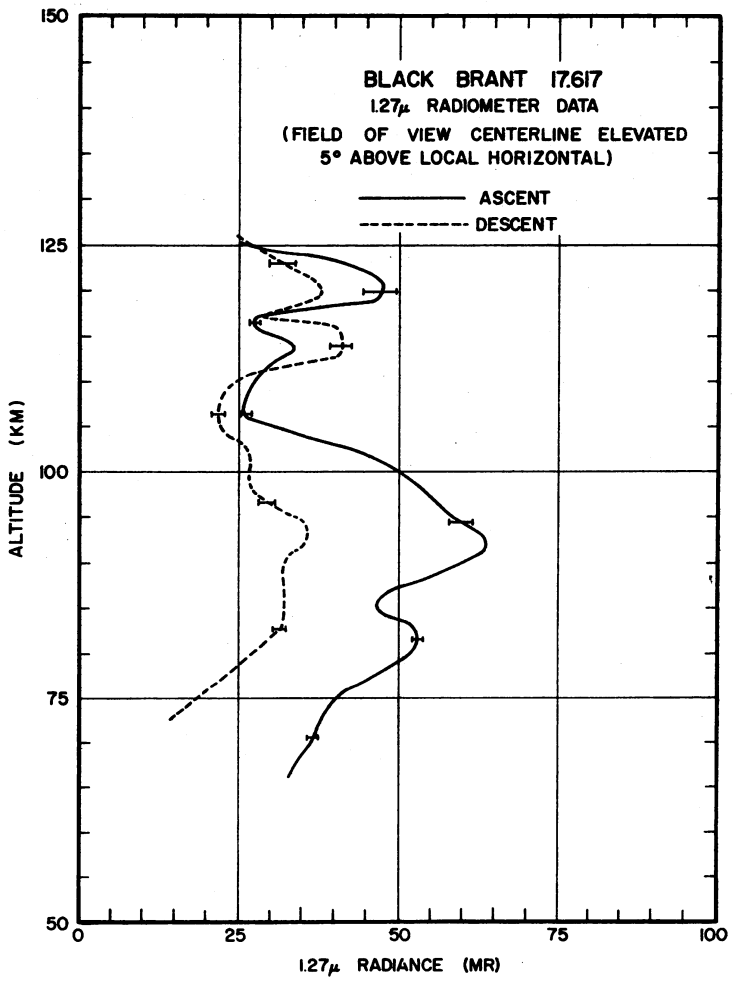

Figure 36-5. 1.27μ Irradiance in MegaRayleighs as a Function of Altitude, as Taken by Black Brant 17.617, for an Instrument Elevation Angle of 5.0°

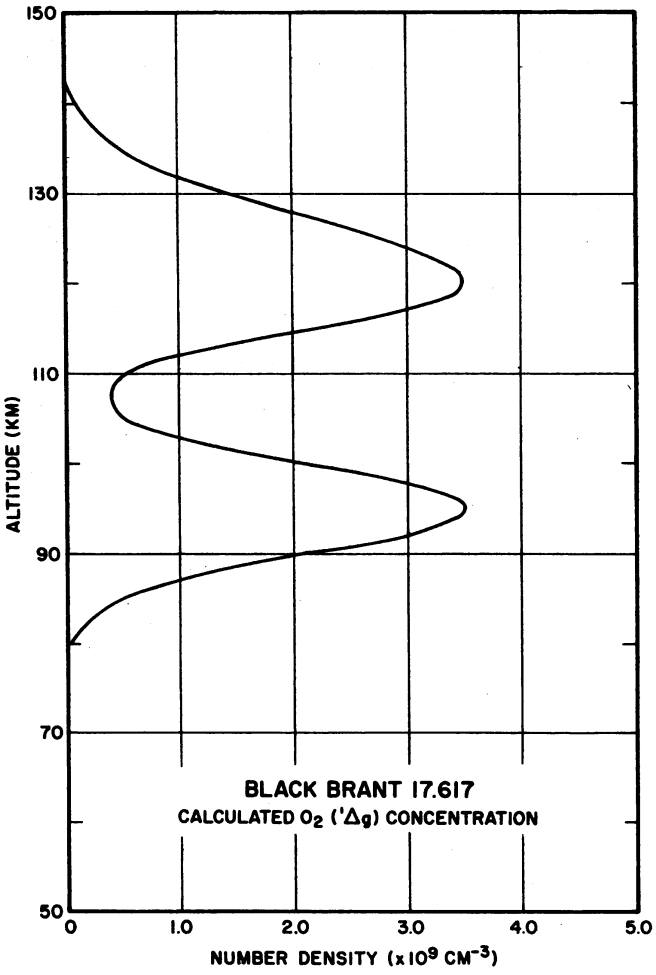

Figure 36-6. Calculated $O_2(^1\Delta_g)$ Number Density as a Function of Altitude. This profile was obtained by a "cut and try" technique to best fit the data presented in Figures 36-4 and 36-5

36-4 DISCUSSION OF DATA

A somewhat limited investigation of possible sources of the high altitude $O_2(^1\Delta_g)$ concentrations observed was undertaken. The following reactions were investigated:

$$O(^3P) + O(^3P) + M \xrightarrow{k_1} O_2(^1\Delta_g) + M$$

$$k_1 = 2.7 \times 10^{-33} \text{ cm}^6 \text{ sec}^{-1}$$

$$OH + O(^3P) \xrightarrow{k_2} O_2(^1\Delta_g) + H$$

$$k_2 = 5 \times 10^{-11} \text{ cm}^3 \text{ sec}^{-1}$$

$$O_3 + h\nu \xrightarrow{k_3} O_2(^1\Delta_g) + O$$

$$k_3 = 9.5 \times 10^{-3} \text{ sec}^{-1}.$$

Although this list of reactions is not by any means complete, it is felt that production of $O_2(^1\Delta_g)$ by these processes is important. More reactions will be investigated in future work. In order to determine a profile of $O_2(^1\Delta_g)$ from these reactions, models of the concentrations of $O(^3P)$, OH, and O_3 are necessary. The models used in these calculations are shown in Figure 36-7. The O and OH data were taken from Hunt (1966). It should be pointed out that the OH concentration model has been modified such as only to include vibrational states in which $\nu \geq 2$ This is necessary since the reaction will not occur, at least at the rate constant given, when $\nu < 2$. The lower altitude concentrations of O_3 were measured by Black Brant 17.906-1 during the PCA event. The upper O_3 concentrations are extrapolated from the data taken up to 80 km assuming a constant scale height above this altitude.

If one assumes (however unlikely) that each reaction results in a $O_2(^1\Delta_g)$ molecule then one can compare the production profiles with the computed profiles of Figures 36-3 and 36-6. This has been done and is presented in Figures 36-8 and 36-9 for Black Brant 17.758 and 17.617 respectively. About the only conclusion which one can definitely state from such information is that the observed

maximum occurs at approximately the same altitude as the maximum of the production curves.

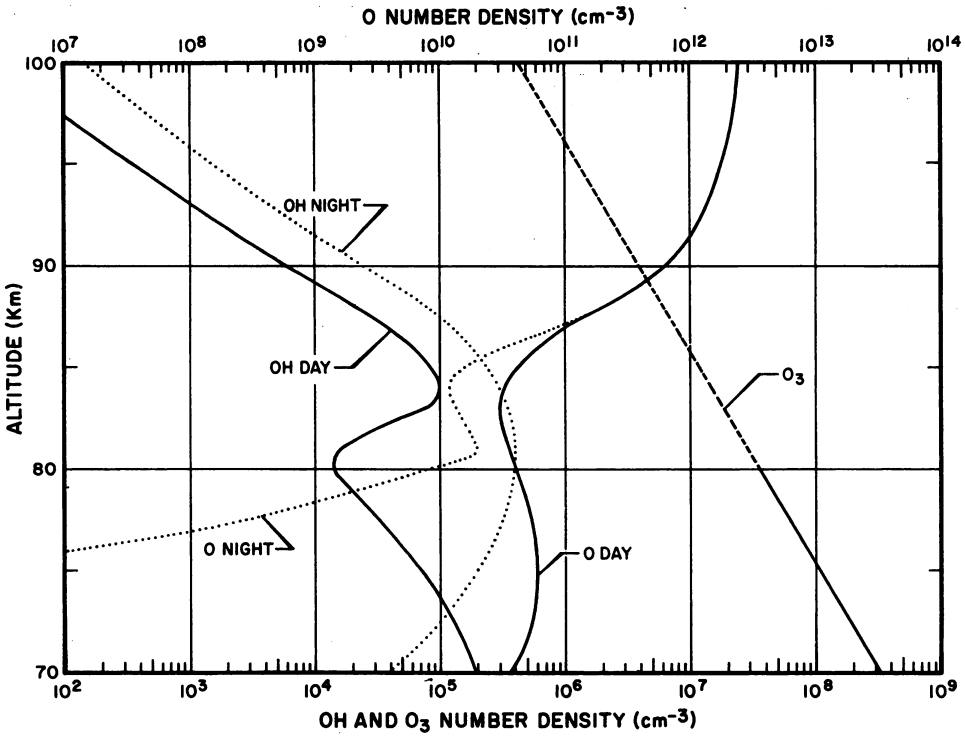

Figure 36-7. Height Profiles for O, OH, and O_3. O and OH were obtained from Hunt (1966) with OH being modified such as to consist only of OH in vibrational states $\nu \geq 2$. O_3 was obtained from Black Brant 17.906-1 during the 2 November 1969 PCA. Note that the uppermost scale is for the O number densities whereas the lower-most scale is for OH and O_3 number densities

36-5 CONCLUSIONS

Data from Black Brant flights 17.758,and 17.617 have confirmed the suggested layer by Evans, et al (1968). The night layer was broader and of less maximum number density than that observed during the sunset flight. The integrated radiance due to the calculated nighttime layer is 183 kilorayleighs, in reasonable agreement with the nighttime balloon observations by Evans, et al (1969). In addition to this layer, careful examination of the data from the sunset flight strongly indicates the possibility of an even higher $O_2(^1\Delta_g)$ layer.

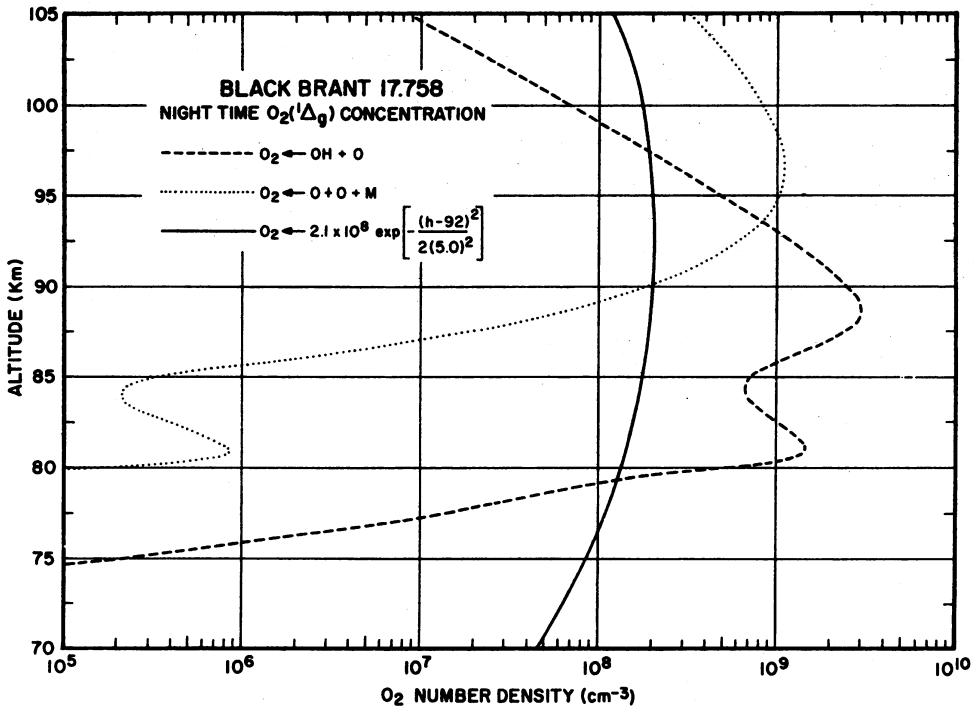

Figure 36-8. A Comparison of the Calculated $O_2(^1\Delta_g)$ Height Profile at Night With Production of $O_2(^1\Delta_g)$ by the Reactions O + OH and O + O + M. This comparison assumes 100 percent branching into the excited $^1\Delta_g$ state

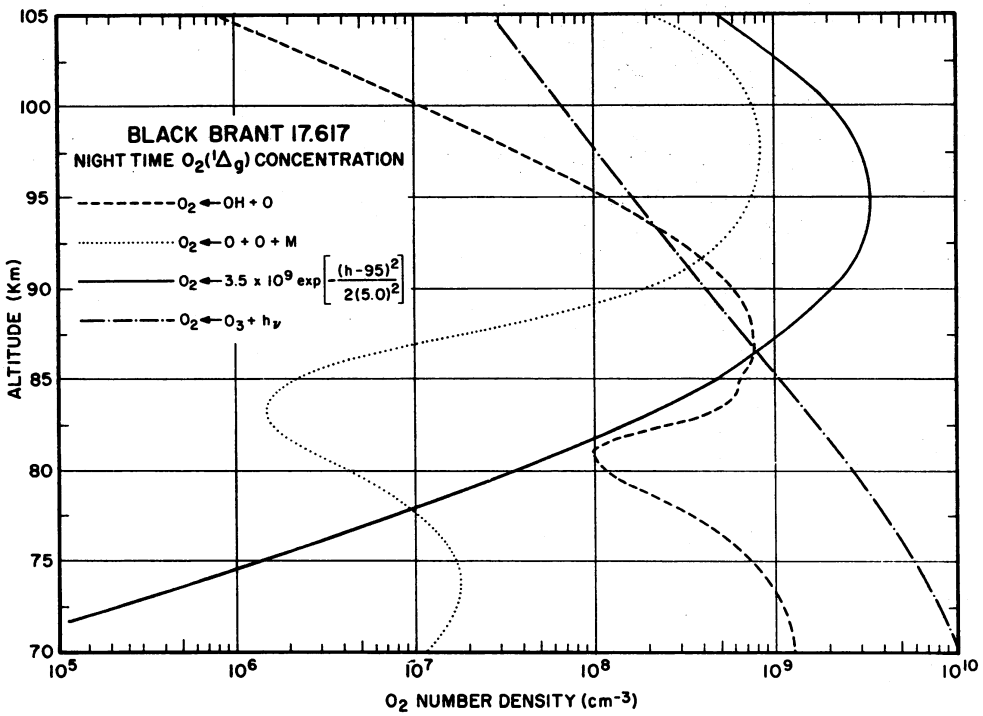

Figure 36-9. A Comparison of the Calculated $O_2(^1\Delta_g)$ Height Profile During Sunset With Production of $O_2(^1\Delta_g)$ by the Reactions O + OH, O + O + M and $O_3 + h\nu$. This comparison assumes 100 percent branching into the excited $^1\Delta_g$ state

References

Evans, W. F. J., Hunten, D. M., Llewellyn, E. J., and Vallance Jones, A. (1968) Altitude profile of the infrared atmospheric system of oxygen in the dayglow, J. Geophys. Res. 73:2885.

Evans, W. F. J., Llewellyn, E. J., and Vallance Jones, A. (1969) Balloon observations of the temporal variation of the infrared atmospheric oxygen bands in the airglow, Planet. Space Sci. 17:933.

Huffman, R. E., Paulson, D. E., Larabee, J. C., and Cairns, R. B. (1971) Decrease in D-Region $O_2(^1\Delta_g)$ photoionization rates resulting from CO_2 absorption, J. Geophys. Res. 76:1028.

Hunt, B. G. (1966) Photochemistry of ozone in a moist atmosphere, J. Geophys. Res. 71:1385.

Hunten, D. M., and McElroy, M. B. (1968) Metastable $O_2(^1\Delta_g)$ as a major source of ions in the D-region, J. Geophys. Res. 73:2421.

Megill, L. R., and Hasted, J. B. (1965) Free electron balance during polar cap absorption events, Planet. Space Sci. 13:339.

Contents

37. Polar Cap Optical Intensities During the 2 November 1969 Solar Particle Event

William N. Hall and John W. F. Lloyd
Aeronomy Laboratory
Air Force Cambridge Research Laboratories
L.G. Hanscom Field
Bedford, Massachusetts

Abstract

The intensities of the ionized molecular nitrogen 4278A first negative band and the 5577A and 6300A atomic oxygen spectral lines were measured at Thule, Greenland from 2-5 November 1969 during a solar particle event. The 4278A nitrogen emission was enhanced and incident energy calculated from the optical emission agrees within 5-30 percent with integral energy calculated from satellite measurements of particle fluxes in the northern polar cap. The 6300 A intensity did not show enhancement during this time period. The 5577A intensity was higher than usual but had been enhanced for two days prior to the solar particle event. Ground based measurements of the ionized nitrogen first negative band at 4278A are shown to be a good indicator of the total energy of the particle flux in the polar cap during night time.

37-1 INTRODUCTION

Measurements were made from 2 to 5 November 1969 during the solar particle event which began on November 2 of atmosphere optical emissions as part of the routine observations at AFCRL Geopole Observatory located at Thule in northern Greenland, geomagnetic latitude 88 degrees. Observations were made with an Ebert-Fastie spectrometer scanning from 3500A to 7000A, with an IGY Patrol Spectrograph and with an IGY all sky camera. All sky camera films showed that weather conditions were favorable for ground level observations with clear skies during much of this time. No discrete auroras were photographed by the all sky camera throughout this period.

The night time intensities of the ionized molecular nitrogen first negative band at 4278A and the atomic oxygen spectral lines at 5577A and 6300A are shown in Figure 37-1.

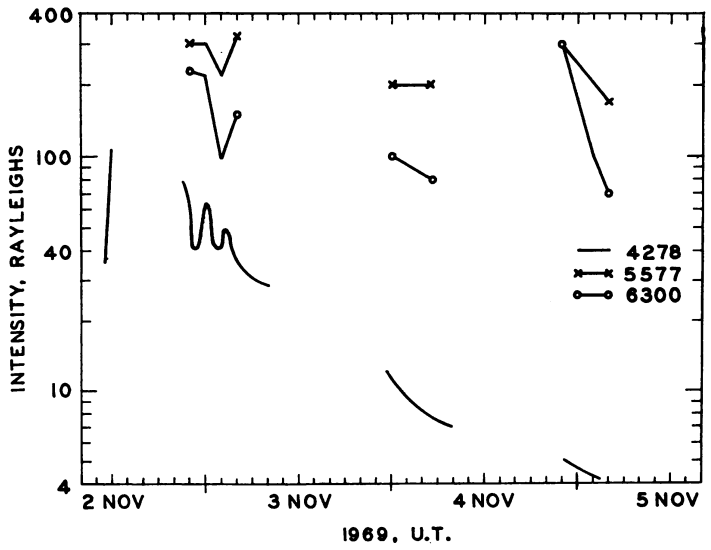

Figure 37-1. Night Time Intensities of 4278A, 5577A, and 6300A at Thule following the 2 November 1969 Solar Particle Event

The intensity of the atomic oxygen emission at 6300A was consistent with twilight enhancements and with diurnal variations recently reported (Stromman, et al 1971). The 5577A atomic oxygen green line was more intense than would be expected from an enhancement of the expected value due to the solar particle flux. The solar particle flux is estimated to produce a 5577A intensity 60 percent that of 4278A (Sandford, 1967, Vallance Jones, 1971). The average 5577A intensity at the magnetic pole has been recently reported to be 70 rayleighs (Eather, 1969). However, during the period 31 October to 5 November the intensity was unusually high, 500-700 rayleighs on the night of 31 October-1 November and 400-500 rayleighs on 1-2 November. On the same nights the 6300A oxygen red line was approximately the same as on 3, 4, and 5 November. The 5577A emission was therefore 4-7 times more intense than the 6300A emission on 31 October-2 November, an unusual result (Sandford, 1970, Eather, 1969). The contribution to the 5577A intensity due to the solar particle flux could not be readily identified because of these as yet unexplained high 5577A intensities before and after the solar particle event.

The 4278A nitrogen emission was first detected on the 11 minute patrol spectograph exposure which ended at 1104 U.T. on November 2. The presence of this emission is evidence of energy deposition by means of particle fluxes, although the particles may be electrons, protons or alpha particles. The intensity increased rapidly, reaching 106 rayleighs at 1146 U.T. and appeared to be still increasing after this time when twilight conditions interfered with the optical measurements. The 4278A intensity presumably reached a maximum during the daylight hours. By the time optical intensity measurements began again at 2100 U.T. on 2 November, a general trend of diminishing intensity was established. Superimposed on this trend were several distinct oscillations in intensity, exhibiting minima at 2250 and 0130 U.T. and maxima at 2400 and 0230 U.T. Thereafter the intensity decreased uniformly, reaching the limit of detectivity of the instrumentation at 0300 U.T. on 5 November. This behavior of the ionized nitrogen first negative band is in agreement with previous studies of polar glow aurora (Sandford, 1967 and references cited therein), although the rise in intensity was more abrupt than in many other events.

It has been shown (Sandford, 1967) that the intensity of the ionized molecular nitrogen first negative band emission is proportional to the total energy of the particles incident upon the atmosphere in the polar glow aurora associated with solar particle events. Using the air fluorescence measurements of O'Neil and Davidson (1969) and the relative band intensities of the ionized molecular nitrogen first negative bands of Vallance Jones (1971) a ratio of 282 R of 4278A total band intensity per erg cm^{-2} sec^{-1} of particle energy incident upon the top of the atmosphere was calculated. O'Neil and Davidson found that 0.4 percent of the energy of the incident electrons was converted into optical emission in the 3914A ionized molecular

nitrogen first negative band. Vallance Jones calculated that in an IBC III aurora the intensities of the 3914A and 4278A bands would be 50 kR and 16.3 respectively. The ratio of 282 rayleighs per erg cm^{-2} sec^{-1} is consistent with calculations by Dalgarno, et al (1965) and with similar ratios recently used by Eather (1969) and Whalen, et al (1971).

Figure 37-2 shows the energy in ergs cm^{-2} sec^{-1} incident upon the top of the atmosphere calculated from the ionized molecular nitrogen first negative band intensities. The values designated as measured (Reagan, et al 1971) are integral energy values calculated from differential particle spectra measured in the northern polar cap. The agreement between the integral incident energies calculated from optical measurements and from integrating differential particle fluxes is excellent, within 5-11 percent after 1000 U.T. on 3 November.

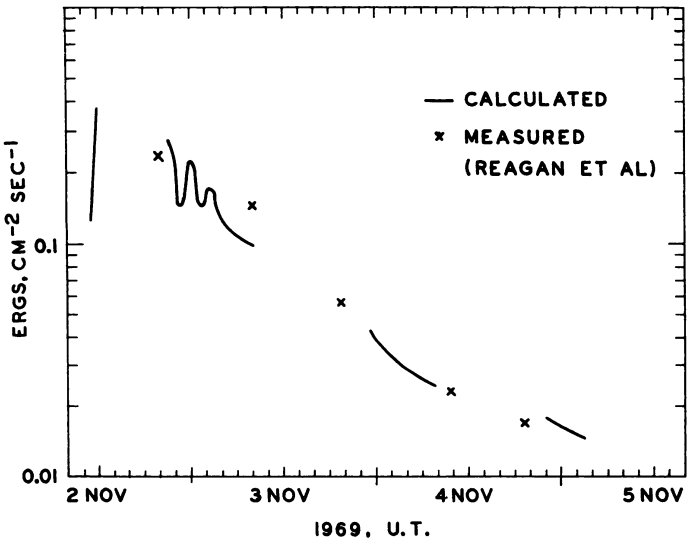

Figure 37-2. Comparison of Integral Incident Energy on Top of the Atmosphere Calculated From Ground Based Observations of 4278A Intensity and From Satellite Measurements of Particle Fluxes in the Polar Cap

Riometer absorption has been shown (Bailey, 1964; Potemra, et al 1970) to be a good indicator of incident particle energy flux during daylight hours. During night time the relationship between riometer absorption and particle flux changes because of differences in atmospheric chemistry and riometer absorption and particle flux do not show as close agreement (Potemra, et al 1970). The results

reported here show that measurements of ionized molecular nitrogen first negative band emissions can be used during night time as an accurate indicator of integral particle energy flux. The optical measurements have an additional advantage in that the energy is integrated over all heights and over protons, electrons and alpha particles whereas the riometer absorption is due to electrons, protons greater than 7-10 Mev and alpha particles greater than 30-40 Mev (Potemra, et al 1970).

In previous comparisons of 3914A intensity and particle fluxes, model exponential rigidity particle spectra were fitted to particle measurements from balloon observations (Sandford, 1967). The results showed disagreements by factors of 4 to 7. The close agreement reported here using satellite measurements of differential particle fluxes of electrons, alpha particles and 1-46 Mev protons suggests that the use of model exponential rigidity particle spectra based on balloon observations does not give an accurate representation of solar particle fluxes.

References

Bailey, D.K. (1964) Polar cap absorption, Planet. Space Sci. 12:495-541.

Dalgarno, A., Latimer, I.D., and McConkey, J.W. (1965) Corpuscular bombardment and N_2^+ radiation, Planet. Space Sci. 13:1008-1009.

Eather, R.H. (1969) Latitudinal distribution of auroral and airglow emissions, The soft auroral zone, J. Geophys. Res. 74:153-158.

O'Neil, R., and Davidson, G. (1969) Luminous efficiency of electron induced emission in nitrogen, in Atmospheric Emissions 477-483; Ed., B.M. McCormac and A. Omholt, New York, Van Nostrand.

Potemra, T.A., Zmuda, A.J., Shaw, B.W., and Haave, C.R. (1970) VLF phase disturbances, HF absorption and solar protons in the PCA events of 1967, Radio Science 5:1137-1145.

Reagan, J.B., Inhof, W.L., Johnson, R.G., and Sharp, R.D. (1971) Satellite Data Analysis for Operation PCA 69 Rocket Coordination, Lockheed Missiles and Space Co. reports LMSC/N-HE-71-1 and Proceedings of Symposium on November 1969 Solar Particle Event.

Sandford, B.P. (1967) Polar glow aurora, in Space Research VII 836-843; Ed., R.L. Smith-Rose, S.A. Bowhill and J.W. King, Amsterdam, North Holland.

Sandford, B.P. (1970) Optical emission over the polar cap, in The Polar Ionosphere and Magnetospheric Processes 299-321; Ed., G. Skovli, New York, Gordon and Breach.

Stromman, J.R., Maehlum, B.N., and Olesen, J.K. (1971) Storm time variations in the high latitude fluxes of low energy electrons inferred from OI (6300A) observations, Planet. Space Sci. 19:540-543.

Vallance, Jones, A. (1971) Auroral spectroscopy, Space Science Review 11:776-826.

Whalen, J.A., Buchau, J., and Wagner, R.A. (1971) Airborne ionospheric and optical measurements of noontime aurora, J. Atmos. Terrestr. Phys. 33:661-678.

Contents

38. Atmospheric Ionization by Precipitating Protons and Alpha Particles

W. Swider and M. E. Gardner
Air Force Cambridge Research Laboratories
L.G. Hanscom Field
Bedford, Massachusetts

Abstract

Calculations of the ionization generated by precipitating protons and alpha-particles may differ by about a factor of two, depending upon the various input parameters adopted. The energy deposited by these energetic particles in the D-region is small compared to the thermal kinetic energy of the atmosphere at these altitudes. Production of atomic oxygen and O_2 ($^1\Delta$) as a result of these precipitating particles does not appear to be significant. Production of atomic nitrogen, especially in the more intense PCA events may lead to some enhancement in the level of nitric oxide in the D-region.

38-1 INTRODUCTION

Energetic protons and alpha-particles generated during solar disturbances produce enhanced ionization rates in the D-region if the trajectory of these particles intercepts the earth. Calculations of the ionization produced in the D-region have been performed by a number of researchers (for example, Freier and Webber, 1963; Adams and Masley, 1965; Velinov, 1970; Swider and Gardner, 1971). The emphasis of this paper is on the relative accuracy of these computations. The heat deposited by the absorption of energetic particles in the atmosphere and the possible changes induced in some important minor neutral gas concentrations are also considered.

38-2 PARTICLE RANGE AND IONIZATION RATES

Figure 38-1 depicts the lowest altitude reached by a proton or an alpha-particle of the indicated kinetic energy. For PCA events, as related to 30 MHz absorption, the deposition of energetic particles between 40-85 km is important. Thus protons with kinetic energy, T, exceeding 1 Mev (~5 Mev for alpha-particles) contribute to PCA events, protons with T $\gtrsim$50 Mev ($\gtrsim$200 Mev for alpha-particles) being much less important. It appears that most of the 30 MHz absorption occurs between 75 and 50 km by day (2-20 Mev protons, 10-100 Mev alpha-particles) and at about 85-70 km at night (1-5 Mev protons, 3-20 Mev alpha-particles) (Reid, 1970).

Our ionization rate calculations (Swider and Gardner, 1971) are compared in Figure 38-2 to those of Freier and Webber (1963) for an integral proton flux of $10^3\ e^{-P/50MV}\ cm^{-2}\ sec^{-1}\ ster^{-1}$ with a negligible cutoff, where P represents the rigidity, the momentum per unit charge. We have also calculated an ionization rate resulting from an integral proton flux of $10^9\ T^{-4}\ cm^{-2}\ sec^{-1}\ ster^{-1}$ with a 20 Mev cutoff for comparison with Velinov (1970) in Figure 38-2. The symbol T represents the kinetic energy of the particle. Both fluxes were considered to be isotropic over the upper hemisphere, that is, multiplication by π yields the effective vertical fluxes, $cm^{-2}\ sec^{-1}$. Differences between the curves apparently result from the adoption of somewhat different loss functions for particle attenuation. Application of different atmospheric models and the method by which the angular distribution of the particles is treated are presumably less significant points.

It may be that any spectrum is rarely, if ever, of a pure exponential rigidity form, e^{-P/P_o}, or power law form, T^{-n}. Adams and Masley (1965) found it necessary to describe several proton distributions by a composite of three partial exponential rigidity distributions. Freier and Webber's (1963) initial work describing exponential rigidity spectrums was based on balloon data, that is, they observed

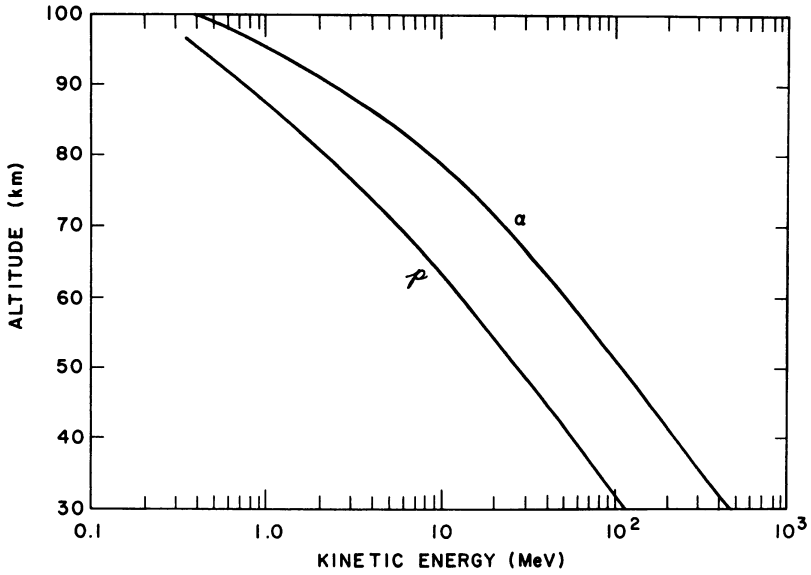

Figure 38-1. Range of Vertically Incident Protons and Alpha Particles (From Swider and Gardner, 1971)

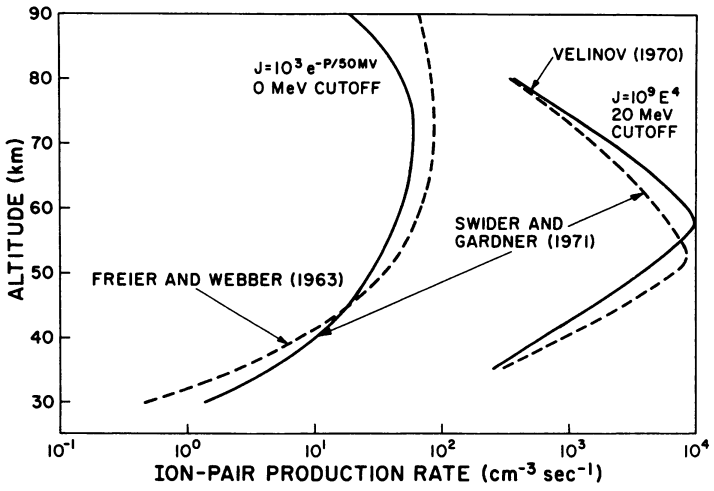

Figure 38-2. Ionization Rate Comparisons for Selected Proton Distributions

only the harder portions of the spectra. Our calculations of ionization rates generated by protons and alpha-particles with integral fluxes of $10^3\ e^{-P/P_o}\ cm^{-2}\ sec^{-1}$ are shown elsewhere (Swider and Gardner, 1971) for five values of P_o and five different geomagnetic cutoffs. Ionization rates resulting from protons and alpha-particles with integral fluxes $10^6 T^{-n}$ are shown in Figures 38-3 and 38-4, respectively. Negligible geomagnetic cutoffs are assumed.

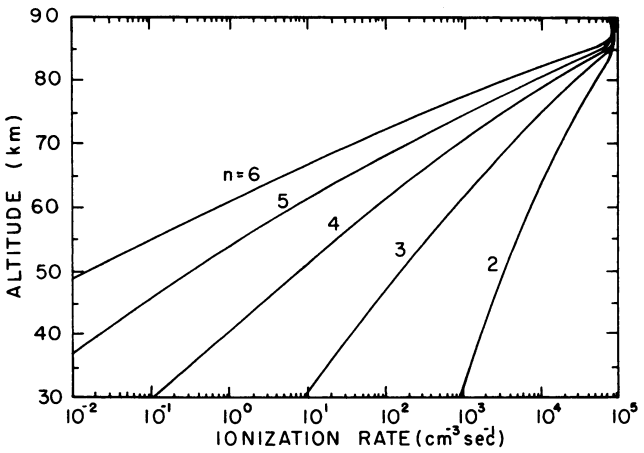

Figure 38-3. Electron-ion Pair Production Rates Resulting From the Absorption of Isotropically Incident Protons With $J = 10^6 T^{-n}\ cm^{-2}\ sec^{-1}\ ster^{-1}$ Integral Spectrum and a Geomagnetic Cutoff of 0.3 MeV

38-3 ENERGY DEPOSITION

The energy content of the atmosphere is compared in Figure 38-5 to the ionization rate required to increase the kinetic temperature of the atmosphere by 10 percent providing this rate is maintained for 24 hours and there is no loss of heat. (The maximum heat deposited is 35ev times the ionization rate.) Production rates exceeding $10^4\ cm^{-3}\ sec^{-1}$ below 85 km are probably rare. Even at 85 km, a production rate of $10^4\ cm^{-3}\ sec^{-1}$ for ten days is required in order to increase the local temperature by 10 percent. Strong auroras are another matter. Production rates near 120 km can reach $10^6\ cm^{-3}\ sec^{-1}$ or more perhaps. This can be significant even if the lifetime of the aurora is much shorter than that of PCA events. Perturbations of the neutral atmosphere by auroral heating have been considered theoretically by Volland and Mayr (1971).

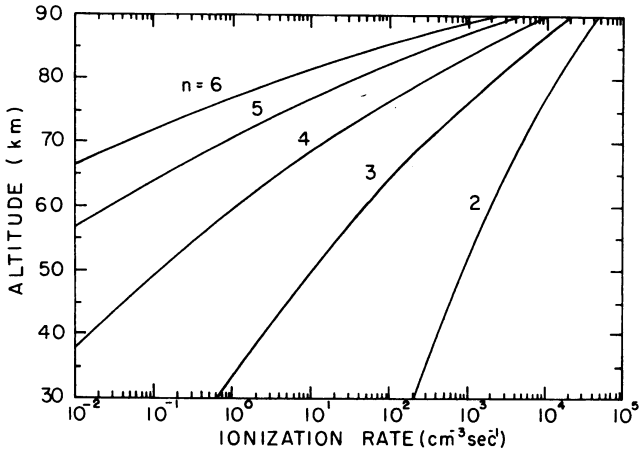

Figure 38-4. Electron-ion Pair Production Rates Resulting From the Absorption of Isotropically Incident Alpha-particles With $J = 10^6 T^{-n}$ cm^{-2} sec^{-1} ster^{-1} Integral Spectrum and a Geomagnetic Cutoff of 1 MeV

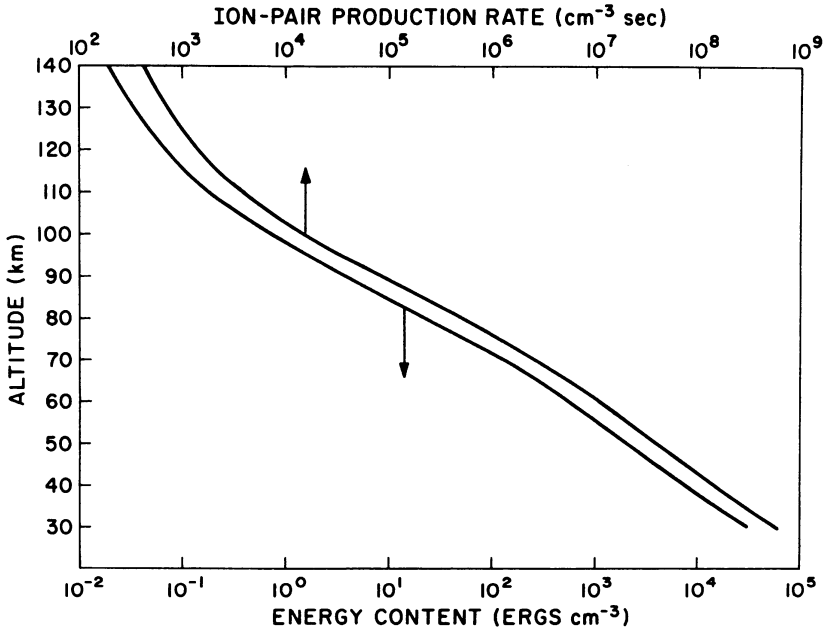

Figure 38-5. Atmospheric Kinetic Energy Compared With the Energetic Particle Ionization Rate That Must be Maintained for 24 Hours in Order to Increase the Atmospheric Temperature by 10 Percent, Providing There is no Heat Loss

38-4 PRODUCTION OF IMPORTANT NEUTRAL SPECIES IN A PCA EVENT

Ionization by energetic particles leads to some production of atomic species, regardless of the nature of the energetic particles. Thus for x-rays the total ionization rate, q, is approximately distributed (Swider, 1969) as 0.62: 0.17: 0.14: 0.07: for $q(N_2^+)$: $q(O_2^+)$: $q(N^+)$: $q(O^+)$. This implies a production of atoms $q(N) = q(N^+)$, $q(O) = q(O^+)$. Processes like $O^+ + O_2 \rightarrow O_2^+ + O$ also yield atomic neutral species. If we estimate about one O_2 dissociation and 10 $O_2(^1\Delta)$ are generated per ion-pair formed [35 ev = 1 ion-electron pair (20 ev), including some excitation, plus 1 O_2 dissociation (5 ev) plus 10 $O_2(^1\Delta)$ excitations (10 ev)], we obtain the equilibrium distribution shown in Table 38-1 using the normal loss processes for O and $O_2(^1\Delta)$ at these altitudes.

Table 38-1. Estimated Upper Limits For Atomic Oxygen and Electronically Excited Molecular Oxygen Production For the Indicated Total Ionization Rate and the Resultant Steady-state Concentration Profiles Obtained Using the Known Loss Processes for These Species

IONIZATION RATE = 10^3 CM^{-3} SEC^{-1} $q(O) = 10^3$ CM^{-3} SEC^{-1}, $q(O_2{}^1\Delta) = 10^4$ CM^{-3} SEC^{-1}		
Z(KM)	[O] CM^{-3}	[$O_2{}^1\Delta$] CM^{-3}
80	1.8×10^8	2.4×10^7
70	1.3×10^7	9.9×10^6
60	1.2×10^6	3.2×10^6
50	1.6×10^5	1.0×10^6

We believe these numbers are generous upper limits for the production of $O_2(^1\Delta)$ through the sum total of all possible excitation processes which can occur. Likewise for atomic oxygen, except that where O_2^+ and NO^+ are major ions, the dissociative recombination of these species are important sources of atomic oxygen. The rate of atomic oxygen production due to dissociative recombination alone could be as great as 2q if O_2^+ is the only important ion (q, if NO^+ is the only major ion).

In any case, the concentrations listed in Table 38-1 are negligible in comparison to those generated by day as a result of the photodissociation of ozone. Thus, at 80 km, photoproduction rates for these species are $\geq 10^6$ cm^{-3} sec^{-1}. The photoproduction rates for $O_2(^1\Delta)$ and O are about $2\text{-}3 \times 10^6$ cm^{-3} sec^{-1} at 70 km. We do not believe that the concentrations shown in Table 38-1 are significant at

night either. Above about 75 km atomic oxygen is always a major species anyway and at 70 km these atomic oxygen levels lead to detachment rates for O_2^- about two orders of magnitude below the daytime levels, $O_2(^1\Delta)$ being even less important. It is important to point out that Weeks, et al (1971) have observed a depletion in ozone during a PCA event rather than an augmentation. Swider and Keneshea (1971) also note a decline in ozone (and atomic oxygen) with increasing PCA ionization rates in their photochemical computations. This appears to be a result (Swider and Keneshea, 1971) of increased H generated by the dissociative recombination of oxonium ions.

The production of atomic nitrogen may be more significant since in the mesosphere, compounds of nitrogen other than N_2 are much less plentiful than oxygen compounds. Estimating (as an upper limit) that the dissociation of N_2 by fast particles equals the dissociative ionization rate, $q(N) = \frac{q}{4}$ may be possible at some altitudes. This would lead to an increase in the NO level of the D-region at these altitudes during a PCA event. A production rate $q = 10^3$ cm^{-3} sec^{-1} at 80 km, for example, would result in 2×10^7 NO in the course of a 24 hour day if all N reacts with O_2 to form NO and there is no depletion by transport. The normal concentration at this altitude is about 2×10^7 cm^{-3} (Meira, 1971) probably within a factor of two.

38-5 CONCLUSIONS

Differences of as much as a factor of two occur between various calculations for ionization rates generated by precipitating protons and alpha-particles in the D-region. These differences appear to be mainly a result of the application of different energy loss functions. The absolute error of such calculations is more difficult to establish; it probably is about a factor of two on the average.

The energy deposited in the atmosphere during a PCA has been seen to be negligible. The enhancement in atomic oxygen and ozone does not appear to be great. In fact we have cited some reports claiming a slight depletion may occur. There may be some increase in the NO content of the D-region.

References

Adams, G.W. and Masley, A.J. (1965) Production rates and electron densities in the lower ionosphere due to solar cosmic rays, J. Atmos. Terr. Phys., 27:289-298.

Freier, P.S. and Webber, W.R. (1963) Exponential rigidity spectrums for solar-flare cosmic rays, J. Geophys. Res., 68:1605-1629.

Reid, G.C. (1969) Associative detachment in the mesosphere and the diurnal variation of polar-cap absorption, Planet, Space Sci., 17:731-736.

Swider, W. (1969) Ionization rates due to the attenuation of 1-100Å nonflare solar x-rays in the terrestrial atmosphere, Rev. Geophys., 7:573-594.

Swider, W. and Gardner, M.E. (1971) Ionization rates due to the absorption of solar protons and alpha-particles in the upper atmosphere, AFCRL-71-0059.

Swider, W. and Keneshea, T.F. (1971) These Proceedings.

Velinov, P. (1970) Solar cosmic ray ionization in the low ionosphere, J. Atmos Terr. Phys., 32:139-147.

Volland, H. and Mayr, H.G. (1971) Response of the thermospheric density to auroral heating during geomagnetic disturbances, J. Geophys. Res., 76:3764-3776.

Weeks, L.H., Cuikay, R.S., and Corbin, J.R. (1971) These Proceedings.

Contents

39. Calculation of Ionization Produced by Solar Protons During a PCA Event*

Edward H. Klevans
Ionosphere Research Laboratory
and Nuclear Engineering Department

Edwin Sum
Ionosphere Research Laboratory
The Pennsylvania State University
University Park, Pennsylvania

39-1 INTRODUCTION

Calculations of the ionization produced by solar protons during a PCA event have been performed by numerous authors.[1-6] The model which is adopted is the following: A proton flux, isotropic in pitch angle over the upper hemisphere, is incident on the ionosphere at altitude H. (See Figure 39-1.) We adopt a coordinate system with x = 0 at H, and x increasing as we come toward the ground. Letting Q = 36 ev be the energy needed to produce an ion pair, the ion production rate q(x) can be written

*The research reported in this paper has been sponsored by the Department of the Army ARO Durham under contract no. DAH-CO4-68-C0034

$$q(x) = \frac{1}{Q} \int_{n \cdot \Omega \geq o} d\Omega \int_{E_{min}}^{\infty} dE \left[\frac{dJ\,(E,x,\theta)}{dE}\right] \left[-\frac{dE}{dx}\right] \qquad (39\text{-}1)$$

where $(-dE/dx)$ = rate of energy loss in air in ev/cm and (dJ/dE) = particle flux differential energy spectrum. The quantity E_{min} will be discussed later.

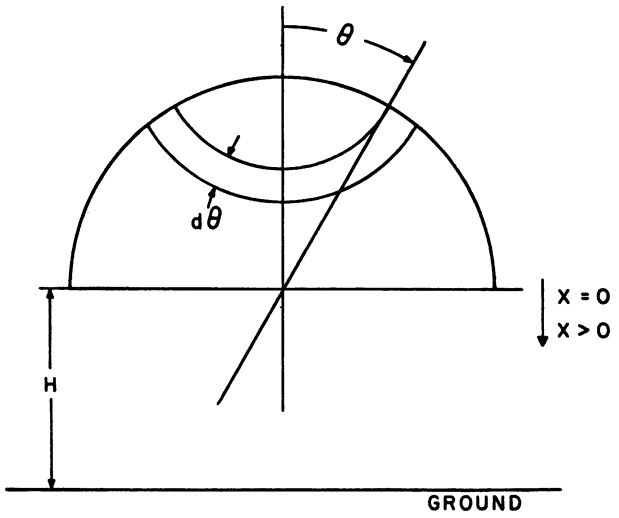

Figure 39-1. Geometry for Model

To perform this integral we use the analytically manageable energy loss function of Green and Peterson[7] and eliminate the need for range-energy data. The expression appropriate for this problem is

$$-\frac{dE}{d\ell} = -\mu \frac{dE}{dx} = a\, n(x)\, L(E) \qquad (39\text{-}2)$$

where $\mu = \cos\theta$, $\ell = x/\mu$, $a = 10^{-21}$ Mev-cm^2 and

$$L(E) = \left(\frac{E_a}{E}\right)^{\Omega} \frac{E^k}{E_b{}^k + E^k} \qquad E \text{ in Mev} \qquad (39\text{-}3)$$

For air $\mathcal{Q} = 0.75$, $E_b = 0.082$ Mev, $k = 1.35$ and $E_a = 22.0$ Mev.*

The flux at position x can be related to that at $x = 0$ by assuming a continuous slowing down model. Then

$$\frac{dJ(E,x,\theta)}{dE} = \frac{dJ(E_o,o)}{dE_o} \left(\frac{dE_o}{dE}\right)$$

where E_o is the energy at $x = 0$ and $dJ(E_o)/dE_o$ is independent of angle. Actually, for many PCA events, Freier and Webber[5] have shown that flux data at the top of the atmosphere can be fitted to an exponential in rigidity space, that is,

$$\frac{dJ}{dP} = \frac{J_o}{P_o} \exp\left[-P/P_o\right] \qquad P > P_1 \tag{39-4}$$

where $P = [2m_p c^2 E_o]^{1/2}$ (with P in Mv, E_o in Mev, and $m_p c^2 = 938$ Mev), J_o = integrated flux, and P_1 is a cutoff value. For a comparison with earlier work,[4-6] we choose $J_o = 10^3$ protons/cm^2-sec and $P_o = 50$ Mv. Different values of P_1 will be chosen. If one uses Eq. (39-4) it is more convenient to perform the integrals in rigidity space than in energy space.[5] The ion production formula can then be written

$$q(x) = \frac{2\pi a n(x)}{Q} \frac{J_o}{P_o} \int_o^1 \frac{d\mu}{\mu} \int_{P_{min.}}^{\infty} dP e^{-P/P_o} L(E(P,x,\mu)) \tag{39-5}$$

To complete the specification of the problem we need $E(P,x,\mu)$ and P_{min}. The former can be obtained by integration of Eq. (39-2). Adopting an exponential model for the density we obtain

*Green and Peterson[7] give $E_a = 25.0$ Mev in their paper. This does not yield a correct fit to the range-energy data or stopping power data.

$$\int_{E}^{E_o} \frac{dE'}{n_o a L(E')} = \frac{1}{n_o} \int_{o}^{\frac{x}{\mu}} d\ell \; n(\ell)$$

$$= \frac{\kappa T}{Mg\mu} \left(\exp\left(\frac{Mgx}{\kappa T}\right) - 1 \right) \tag{39-6}$$

where $Mg/\kappa T = 1.38 \times 10^{-4}/m$.
To a good approximation this yields

$$E(P,x,\mu) = \frac{P^2}{2m_p c^2} \left[1 - \left(\frac{A(x)}{P}\right)^{7/2} \frac{1}{\mu}\right]^{4/7} \tag{39-7}$$

where

$$A(x) = \left\{ \frac{7}{4} \frac{(2m_p c^2)^{7/4} \kappa T n_o a E_a^{0.75}}{Mg} (\exp \frac{Mgx}{\kappa T} - 1) \right\}^{2/7}$$

$$= 4.66 \times 10^{-3} [n(x) - n_o]^{2/7}$$

The value of P_{min} is either the cutoff value P_1 or the value needed for the particle to reach (x, μ) (that is, the value for which $E = 0$) whichever of these values is larger. Using Eq. (39-7) in Eq. (39-3), defining

$$B = (2m_p c^2 E_b)^{1.35} = 0.895 \times 10^3$$

$$D(x) = \frac{2\pi a}{Q} \left(\frac{J_o}{P_o}\right) (2m_p c^2 E_a)^{0.75} n(x) = 1.014 \times 10^{-11} n(x)$$

and interchanging the order of integration, we obtain

$$q(x) = D(x) \int_{\mathrm{Max}[P_1,\ A]}^{\infty} dP\ P^{1.2} \exp\left[-\frac{P}{P_o}\right] \int_{\left(\frac{A}{P}\right)^{7/2}}^{1} \frac{d\mu}{\mu}$$

$$\cdot \frac{\left\{1 - \frac{A}{P}^{7/2}\ \frac{1}{\mu}\right\}^{0.343}}{\left\{B + P^{2.7}\ \ 1 - \left(\frac{A}{P}\right)^{7/2}\ \frac{1}{\mu}\right\}^{0.771}} \qquad (39\text{-}8)$$

A comparison of the results of this method with that of Freier and Webber[5] is shown in Figure 39-2 for $P_o = 50$, and, in Figure 39-3, for $P_o = 100$. It is seen that the results are in substantial agreement although our numbers for q are slightly higher.

The method we have presented is simple, inexpensive to calculate, and, we believe, accurate. Various checks are now being conducted on our approximations to test the accuracy. Calculations associated with the PCA event of November 1970 are in progress.

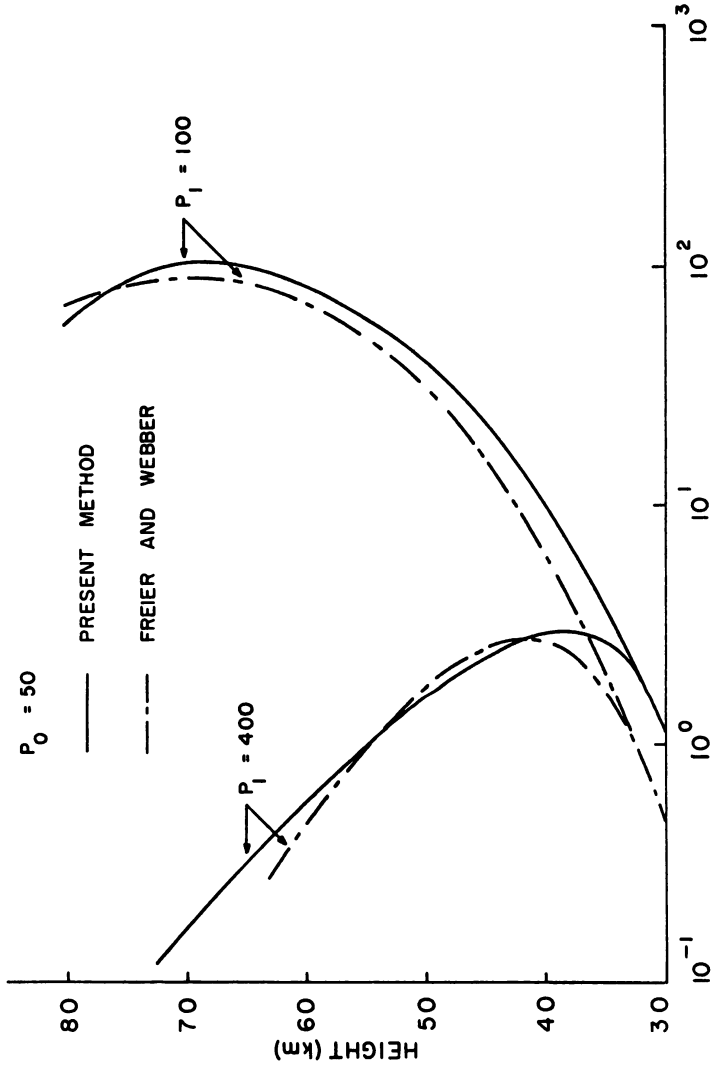

Figure 39-2. Ion Pair Production Rate as a Function of Height in the Atmosphere for Solar Protons; P_o = 50, J_o = 10^3

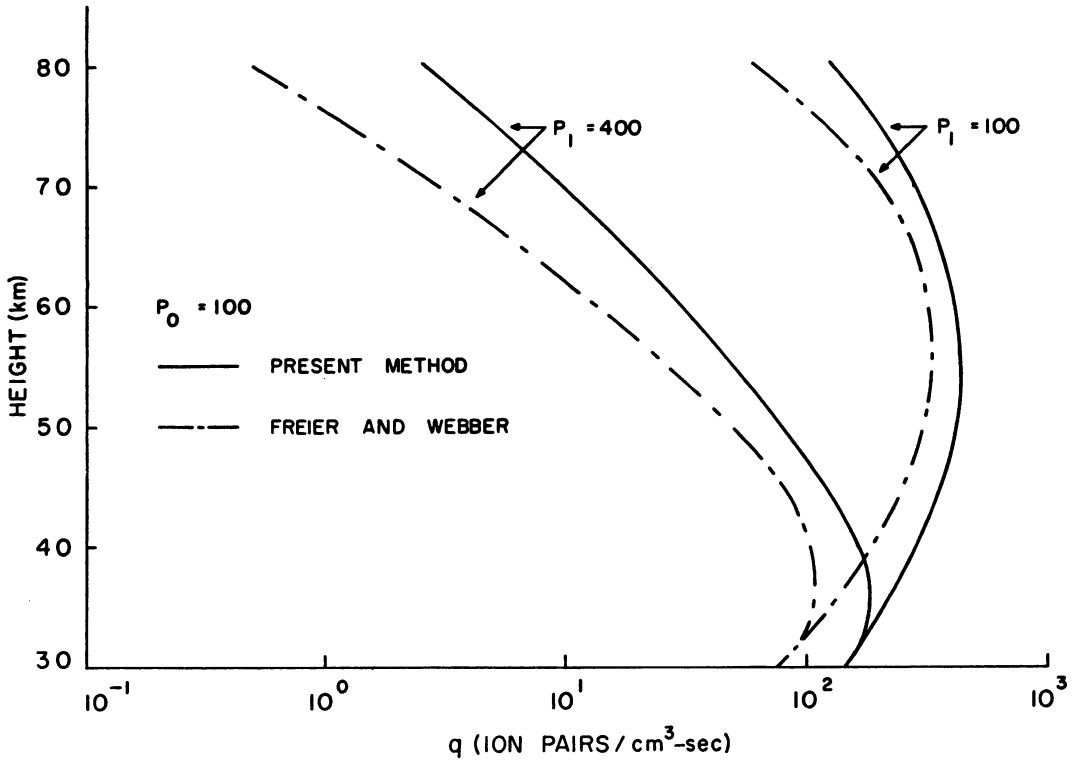

Figure 39-3. Ion Pair Production Rate as a Function Height in the Atmosphere for Solar Protons; P_o = 100, J_o = 10^3

Acknowledgments

We wish to thank Professors John Mentzer and Les Hale for helpful discussions.

References

Bailey, D.K. (1959) Proc. IRE 47:255.
Hultquist, B. and Ortner, J. (1959) Planetary Space Sci. 1:193.
Reid, G.C. (1961) J. Geophys. Res. 66:4071.
Webber, W.R. (1962) J. Geophys. Res. 67:5091.
Freir, P.S. and Webber, W.R. (1963) J. Geophys. Res. 68:1605.
Weir, R.A. and Brown, R.R. (1964) J. Geophys. Res. 69:2193.
Green, A.E.S. and Peterson, L.R. (1968) J. Geophys. Res. 73:233.

Contents

40. Aeronomical Implications From Ion Composition Measurements During a PCA

R. S. Narcisi
Air Force Cambridge Research Laboratories
L.G. Hanscom Field
Bedford, Massachusetts

Abstract

Positive and negative ion composition measurements in the D and E regions during a PCA disturbance have aided in clarifying several aeronomical processes but also have generated several problem areas as well. Analysis of the positive ion measurements have (1) revealed the ionospheric chemistry of O_2^+ and its importance as a source of water-cluster ions; (2) permitted a calculation of day, night and sunset nitric-oxide concentrations in the mesosphere; (3) permitted a determination of the enhancement of nitric-oxide in the E region during an intense aurora; and (4) demonstrated that the duration of the ionization in the upper D region is increased during disturbed conditions by virtue of changes in the ion composition and a lowered effective electron-ion recombination rate. Analysis of the negative ion composition measurements have pointed out several problem areas. The predominance of O^- at night and O_2^- during the day between 75 and 94 km is inexplicable with presently known processes, (this is also true for the heavy negative ions for both quiet and disturbed conditions). The difficulties of maintaining large concentrations of O^- and O_2^- above 75 km are discussed. The implications of the negative ion measurements in terms of the twilight riometer variations in a PCA are considered.

40-1 INTRODUCTION

The prime objective of the ion composition experiments in the PCA 69 program was to obtain data from which the detailed physical chemical processes of the disturbed D region could be determined. A specific goal of the positive ion composition measurements was to examine the O_2^+ reaction sequence for water cluster ion production (Fehsenfeld and Ferguson, 1969; Good et al, 1970). It was realized that this chemical scheme applied most directly to the disturbed rather than the quiet D region for which it was originally proposed (Narcisi and Roth, 1970). It apparently does not explain the undisturbed D region, especially since the ionization rate of $O_2(^1\Delta)$ has been shown to have been greatly overestimated (Huffman et al, 1971). Negative ion composition measurements were also performed with the hope of interpreting the twilight riometer variations during a PCA (Reid, 1970).

In this paper, it is shown that the PCA positive ion composition measurements have (a) clarified the positive ion chemistry of the disturbed D region to a considerable extent; (b) allowed a determination of day, night and sunset nitric-oxide concentrations in the mesosphere; (c) permitted a calculation of the enhancement of nitric-oxide concentrations during an intense aurora; (d) demonstrated that by virtue of changes in the ion composition in the upper D region during disturbed conditions a significantly lower electron-ion recombination rate results. The PCA negative ion composition measurements are considered in terms of the known negative-ion chemistry and the problem areas generated by the measurements are discussed. The observed twilight riometer variations during a PCA are considered in view of the negative ion composition measurements.

40-2 PROTON IONIZATION AND SUBSEQUENT ION CHEMISTRY

Figure 40-1 presents the ion products created by energetic particles in the D region. Protons, alpha particles, energetic electrons and x-rays react with air to produce about 62 percent N_2^+, 17 percent O_2^+, 14 percent N^+ and 7 percent O^+, the latter two ions are created in dissociative ionization reactions (Swider, 1969). Below 90 km, in times of milliseconds, these primary ions are converted to about 90 percent O_2^+ and 10 percent NO^+ through such well-known reactions as $N_2^+ + O_2 \rightarrow O_2^+ + N_2$, $N_2^+ + O \rightarrow NO^+ + N$, $N^+ + O_2 \rightarrow O_2^+ + N$, or $NO^+ + O$, $O^+ + O_2 \rightarrow O_2^+ + O$, and $O^+ + N_2 \rightarrow NO^+ + N$. The O_2^+ ions were expected to convert immediately to water-cluster ions by the reaction sequence shown in Figure 40-2 (Fehsenfeld and Ferguson, 1969; Good et al, 1970). Omitting the reaction in brackets in Figure 40-2, and with only 1 ppm of H_2O, O_2^+ can be quickly converted to water-cluster ions. However, during the PCA, instead of the expected predominance of

water-cluster ions, the positive ion composition in the upper D region was composed almost entirely of NO^+ and O_2^+ (Narcisi et al, I). Water-cluster ions became predominant below 77 km at night, somewhere below 73 km during the day, and somewhere below 77 km at sunset; the latter two altitudes represent the lowest altitudes where measurements were obtained. The fact that the water-cluster conversion did not occur in the upper D region meant that the clustering chain had to be short circuited in such a manner to regenerate O_2^+. NO^+ would then become a major ion by O_2^+ charge transfer with NO. These results precipitated further laboratory work and subsequently the reaction $O_4^+ + O \rightarrow O_2^+ + O_3$, shown in brackets in Figure 40-2, was found to proceed with a rate constant of 3×10^{-10} cm^3 sec^{-1} (Ferguson, 1971). The reaction $O_4^+ + O_2(^1\Delta) \rightarrow O_2^+ + 2O_2$ may also be operative, but its rate constant has not been measured. Thus, sufficient quantities of oxygen atoms can preclude water-cluster ion production and regenerate O_2^+ ions in the D region.

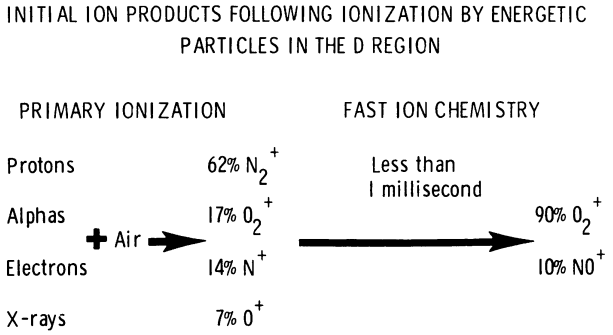

Figure 40-1. D Region Ionization by Energetic Particles

CLUSTERING REACTIONS

$$O_2^+ + O_2 + M \rightarrow O_4^+ + M$$

$$\left[O_4^+ + O \rightarrow O_2^+ + O_3\right]$$

$$O_4^+ + H_2O \rightarrow O_2^+(H_2O) + O_2$$

$$O_2^+(H_2O) + H_2O \rightarrow H_3O^+ + OH + O_2$$

$$\rightarrow H_3O^+ \cdot OH + O_2$$

$$H_3O^+ \cdot OH + H_2O \rightarrow H^+(H_2O)_2 + OH$$

$$H^+(H_2O)_2 + H_2O + M \rightarrow H^+(H_2O)_3 + M$$

Figure 40-2. Reactions That Lead to the Conversion of O_2^+ to Water-cluster Ions. M equals O_2 or N_2

Figure 40-3 shows model calculations of atomic oxygen concentrations for 60° north latitude in winter (Keneshea et al, 1972). This model includes turbulent transport with the turbopause assumed to be at 102 km. The model conditions are chosen to match the conditions for the PCA measurements at Ft. Churchill, Canada. It is seen that at midnight (χ = 136.3°) the atomic oxygen concentration decreases rapidly below 80 km while at noon (χ = 73.7°) the atomic oxygen concentration is greater than 10^{10} cm^{-3} down to 60 km. The PCA ion composition results apparently reflect this diurnal variation of atomic oxygen in the mesosphere as can be seen by considering the O_2^+ chemistry.

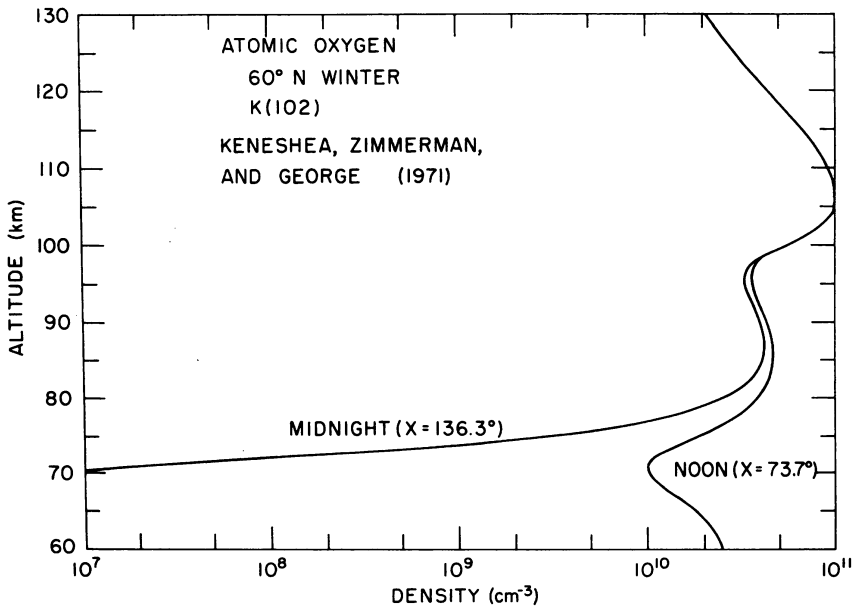

Figure 40-3. Model Calculations of Atomic Oxygen Concentrations in the Mesosphere and Lower Thermosphere. The calculation includes both chemistry and turbulent transport

The calculations for the O_2^+ chemistry shown in Figure 40-4 were made utilizing the atomic oxygen concentrations in Figure 40-3, with 2 ppm of mesospheric H_2O, Meira's (1971) NO concentrations, typical daytime electron densities in the undisturbed D region and mean CIRA O_2 concentrations. Once O_4^+ is formed, by the second reaction in Figure 40-4, it can either react with H_2O and produce $O_2^+(H_2O)$ or react with atomic oxygen and regenerate the O_2^+. The $O_2^+(H_2O)$ can

then go on to create $H^+(H_2O)_n$. The rate, $K_4[O]$, at which O_4^+ is converted to O_2^+ exceeds the rate, $K_3[H_2O]$, of O_4^+ reacting with H_2O above 72 km in the daytime and above 76 km at night. Above these altitudes atomic oxygen prevents O_4^+ from forming significant quantities of water-cluster ions. It is realized that this statement depends upon the actual water vapor and atomic oxygen concentrations and if, for example, the water vapor concentration exceeds 10 ppm, water-cluster ions should appear in significant abundance up to 80-85 km. However, the PCA measurements indicate that the situation seems to be close to that presented in Figure 40-4.

If O_2^+ is continually regenerated in the upper D region it can react further by charge transferring with NO or by recombining with electrons. The electron recombination rate (sec^{-1}) appears to be smaller than the charge transfer rate, not only for normal daytime electron densities as shown in Figure 40-4, but also for D region electron concentrations less than or about 3×10^4 cm^{-3}.

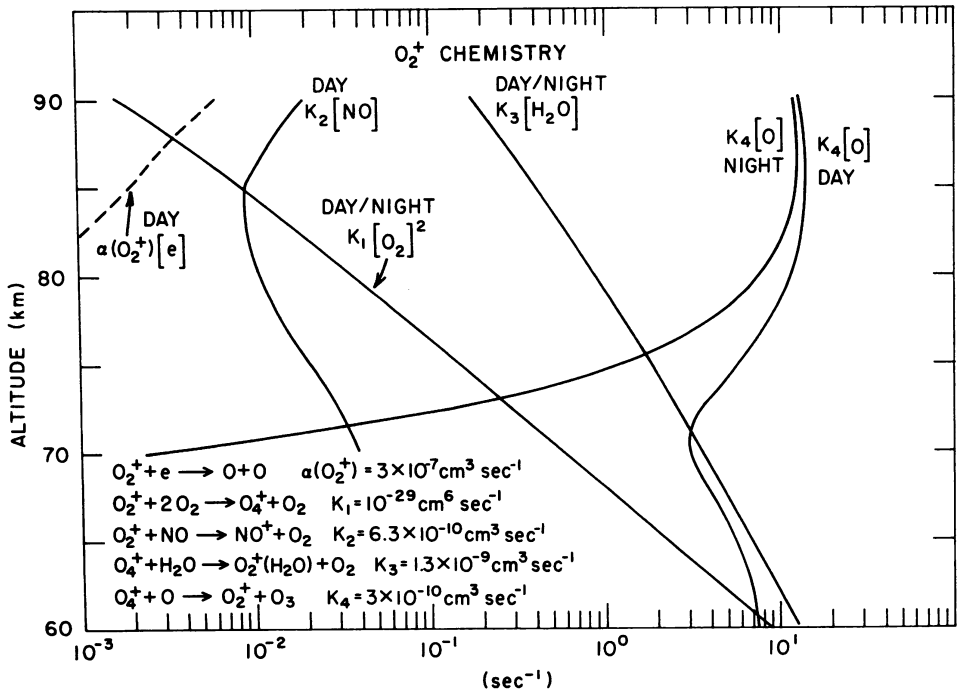

Figure 40-4. The Ionospheric Chemistry of O_2^+. The rate constants K_1 and K_3 are from Good et al (1970), K_2 is from Dunkin et al, J. Chem. Phys., 54:3817, 1971, K_4 is from Ferguson (1971) and $\alpha(O_2^+)$ is from Biondi (1969)

The PCA measurements indicate that during moderately disturbed conditions, the ion composition changes from mainly water cluster ions to mostly NO^+ and O_2^+ in the upper D region so that the effective electron-ion recombination rate is decreased significantly. This, in effect, increases the amount and the duration of the D region ionization (compare $\alpha\,(H_5O_2^+) = 2.7 \times 10^{-6}$ cm^3 sec^{-1} at 415 K with $\alpha\,(NO^+) = 6 \times 10^{-7}$ cm^3 sec^{-1} and $\alpha(O_2^+) = 3 \times 10^{-7}$ cm^3 sec^{-1} both at D region temperatures (Biondi et al, 1971; Biondi, 1969). The effects occurring in the D region during a PCA are most likely quite similar to those produced during SID and auroral absorption since O_2^+ is the major initial ion that is produced following ionization by protons, x-rays or energetic electrons.

Swider and Keneshea (these proceedings) have calculated the diurnal variation of positive ion concentrations in the D region during PCA events. The calculations were performed with 195 reactions in the Keneshea code. Figure 40-5 shows an example of the noontime species profiles obtained with 5 ppm H_2O and Meira's (1971) concentrations; the atomic oxygen concentrations are generated in the code except from 80–90 km where constant values were used. The agreement between the model calculation and the noontime measurements (Figure 40-5, Narcisi et al, I) is qualitatively quite good considering the errors involved. The proton ionization production rates shown in Figure 40-5 are two to five times larger than those for midday 3 November 1969, but there may also have been additional ionization created by energetic electrons on 3 November. In the future, it is planned to calculate the mesospheric water vapor concentrations required to fit the PCA ion composition results. At the present time, it appears that 5 ppm H_2O is too high and that 1-2 ppm H_2O seems to provide a better fit.

The disturbed D region now appears to be much better understood than the undisturbed D region! The problem associated with the quiescent D region is the need for an efficient reaction mechanism which converts NO^+ to water-cluster ions. Figure 40-6 exhibits the presently known situation wherein the NO^+ production rate considerably exceeds the O_2^+ production rate below 90 km for normal conditions. Although there are reactions which can convert NO^+ to water-cluster ions, they are too slow to be significant in the D region (Narcisi and Roth, 1970). However, the mass spectrometer measurements consistently show the dominance of water-cluster ions below 86 km at twilight and at night and below 82 km during the day. Evidence for the existence of a fast ionospheric reaction which converts NO^+ to water-cluster ions was apparent from eclipse measurements, although the actual reaction could not be determined (Narcisi et al, 1972a).

Since the production rate of O_2^+ is small and atomic oxygen short circuits the O_2^+ to water-cluster ion conversion chemistry, it appears that O_2^+ is never a significant source of water-cluster ions above 70 km during quiet conditions. Below

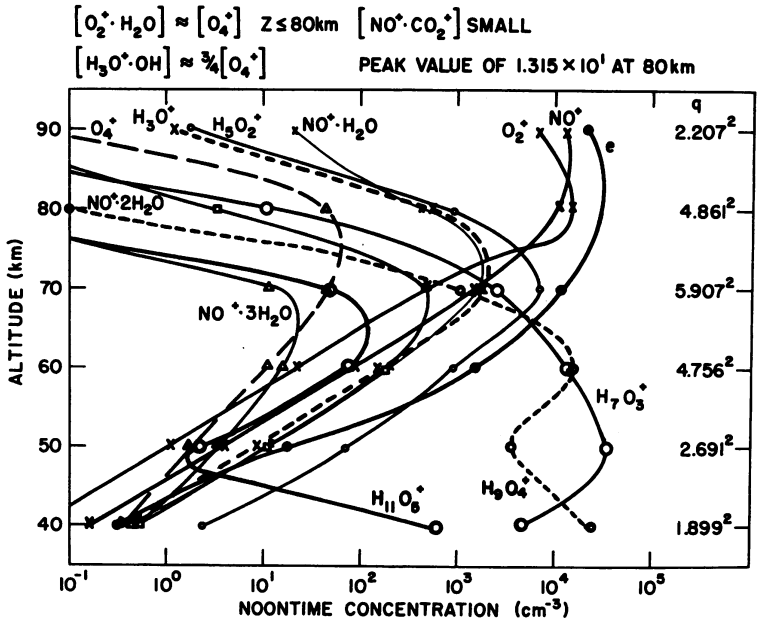

Figure 40-5. D Region Model Calculations Showing the Noontime Distributions of the Positive Ion Species During a PCA. The proton ionization rate, q (cm^{-3} sec^{-1}) is listed

70-65 km cosmic rays become the important ionizing source so that O_2^+ is the major initial ion produced. By comparing the relative rates in Figure 40-4, it is seen that the O_2^+ conversion chemistry should proceed rapidly to produce water-cluster ions below 70 km.

40-3 MESOSPHERIC NITRIC-OXIDE CONCENTRATIONS DURING THE PCA

Day, night and sunset NO concentrations have been derived between 77 and 88 km by utilizing the rocket measurements of the positive ion composition and charged-particle densities obtained during operation PCA 69 (Narcisi et al, 1972b). Since this work has been published, only the results will be summarized here.

Figure 40-7 presents the NO concentration derived from the PCA measurements compared with those of Keneshea et al (1970), Barth (1966) and Meira (1971). The derived PCA NO concentrations are within a factor of 2 of 3×10^7 cm^{-3} between

77 and 88 km and generally lie between the values obtained by Barth and Meira at mid-latitudes. All of the profiles shown in Figure 40-7 have errors of factors of 2 to 3. The three PCA profiles exhibit minimums near 84 $\pm$ 1 km, which are similar to the minimums of the profiles of Meira. There does not appear to be a significant temporal variation in NO concentrations during the PCA.

40-4 ENHANCEMENT OF NITRIC-OXIDE CONCENTRATIONS IN AURORA

Zipf et al, (1970) reported an extremely great and presently unaccountable increase in NO concentrations in an auroral arc. They found an NO concentration of 3.8×10^{10} cm^{-3} at 120 km, more than the O_2 concentration and more than 400 times larger than Meira's values. Consistent with their large NO concentrations, Zipf, et al, found no O_2^+ ions because of the very large charge transfer rate with NO.

During operation PCA 69, the night flight results (Figure 29-2, Narcisi et al, I) indicate a near similar total ion density as obtained in the flight of Zipf et al, at least near 122 km. But instead of the absence of O_2^+ ions, an O_2^+/NO^+ ratio of about 0.25 was found. Utilizing the measurements in Figure 29-2, the CIRA 1965 neutral species concentrations with [N] $\leqq 10^8$ cm^{-3}, and the known ion chemistry, it is straightforward to derive the following equilibrium expression for the NO concentration:

$$[NO] = 6.6 \times 10^2 \left[\frac{NO^+}{O_2^+}\right][e] - 0.25 \left[\frac{N_2^+}{O_2^+}\right][O] - 0.35\,[N]$$

$$- 2 \times 10^3 \left[\frac{O^+}{O_2^+}\right][N_2] - 0.5 \left[\frac{N^+}{O_2^+}\right][O_2]$$

where the various species concentrations are in cm^{-3}. Other details in this calculation and results from other auroral measurements will be published elsewhere. For the PCA night flight the above expression yields [NO] = 1.5×10^9 cm^{-3} at 122 km. Nitric-oxide concentrations do appear to be considerably enhanced in aurora, however, there seems to be a considerable disparity as to the amount of the enhancement.

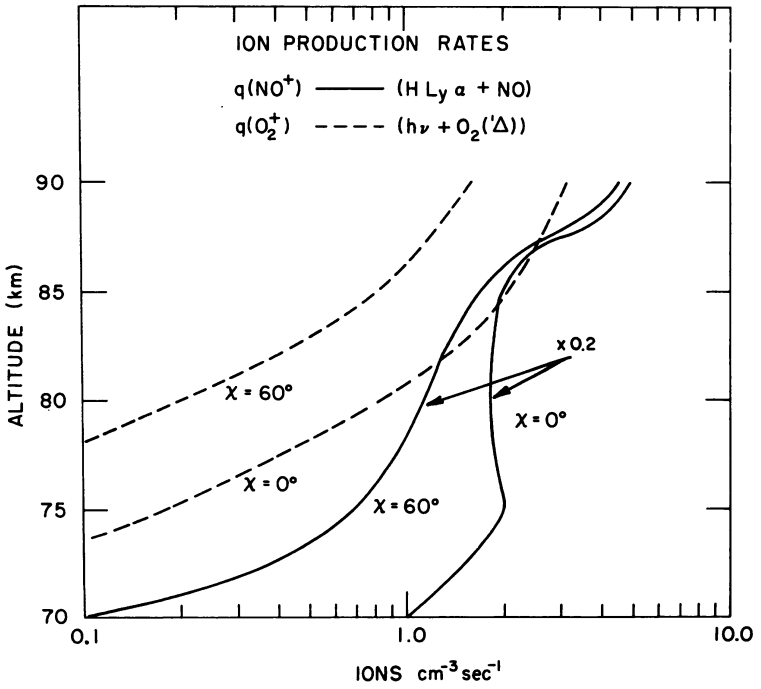

Figure 40-6. Photoionization Production Rates for NO^+ and O_2^+ for Two Solar Zenith Angles. The O_2^+ production rates are from Huffman et al, (1971). The NO^+ production rates were calculated utilizing Meira's (1971) NO concentrations

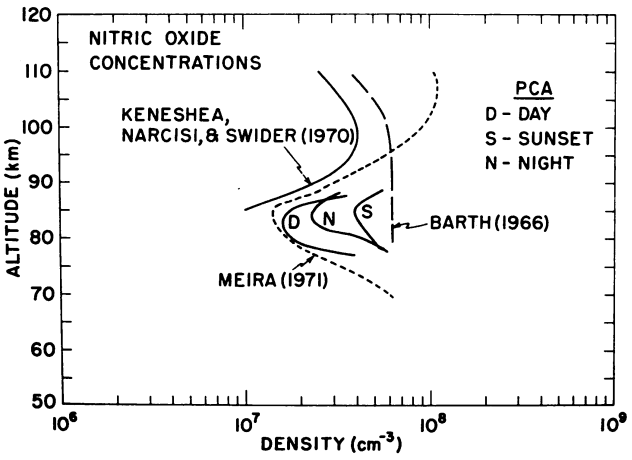

Figure 40-7. Nitric-oxide Concentrations Derived From PCA Measurements Compared With Other Measurements and Determinations

40-5 NEGATIVE ION PROCESSES IN THE DISTURBED D-REGION

Reid (1970) has summarized the twilight riometer measurements during a PCA. The transition between the two steady-state conditions (day and night) is observed to begin at a solar zenith angle close to 90^{o} at sunset while the sunrise transition, although not so clear or consistent, is found to start at about 99^{o}. Two possible explanations for the sunset variation have been proposed. Either associative-detachment reactions such as $O_2^- + O \rightarrow O_3 + e$ (Fehsenfeld et al, 1967) are of dominating importance and the reactions are slow below 75 km after atomic oxygen recombines, or ultraviolet photodetachment is required. The suddenness of the sunrise transition suggests that the top of the negative-ion region is sharply bounded and that near 75-80 km there are negative ions with low election affinities which can be destroyed by visible light while near 30-40 km the negative ions are tightly bound requiring ultraviolet radiation for photodetachment.

Measurements of negative ion composition near midday and midnight during operation PCA 69 were performed to shed some light on this situation (Narcisi et al, II). (Instrument vacuum problems precluded an attempt for negative ion measurements at sunset.) Rather than resolve the situation, the negative ion measurements have appeared to heighten the confusion. In the nighttime measurements, the dominance of O^- and its relatively large concentrations above 75-80 km are difficult to explain. In the daytime measurements, although D region model calculations indicate O_2^- is the major ion above about 73 km, the O_2^- does not decrease steeply above 75 km as predicted by the calculations. Associative detachment reactions with atomic oxygen (Fehsenfeld et al, 1967) are apparently so fast that it is not possible to have negative ions above 80 km. This situation is exemplified in the PCA model calculations of Swider and Keneshea (these proceedings) as shown in Figure 40-8. Negative-ion reactions with water vapor were not included since the rate constants have generally not been measured; other conditions for the model calculations have been discussed previously. If the mass spectrometer results are correct, either new mechanisms are required for producing O^- and O_2^- at much faster rates, or the associative detachment rate constants must be lowered considerably. (Recall that the distribution of O^- during the day is unknown because the mass spectrometer did not scan over 16 amu (Narcisi et al II). Thus, the twilight riometer behavior remains unresolved, although the 'right' species are present, their concentrations do not decrease steeply above 75-80 km as required. Along the same lines, we have shown that at night, during a PCA, the electrons are irretrievably lost below about 75 km by means of three-body attachment processes producing O_2^- ions (Swider et al, 1971).

In addition to the above difficulties there is no adequate explanation for the layer of very large negative-ion clusters that extends over the cold temperature

region of the mesopause where noctilucent clouds are observed. During quiescent periods, these large negative ion clusters are the major D region ions (Narcisi et al, 1971). Because it is difficult to conceive how gas-phase reactions could produce such large molecules, we have suggested the possibility that mesospheric agglomerates might be responsible for the formation of the cluster ions (Narcisi et al, 1972a).

Clearly, more laboratory work and rocket measurements are required to resolve the negative ion situation in the D region.

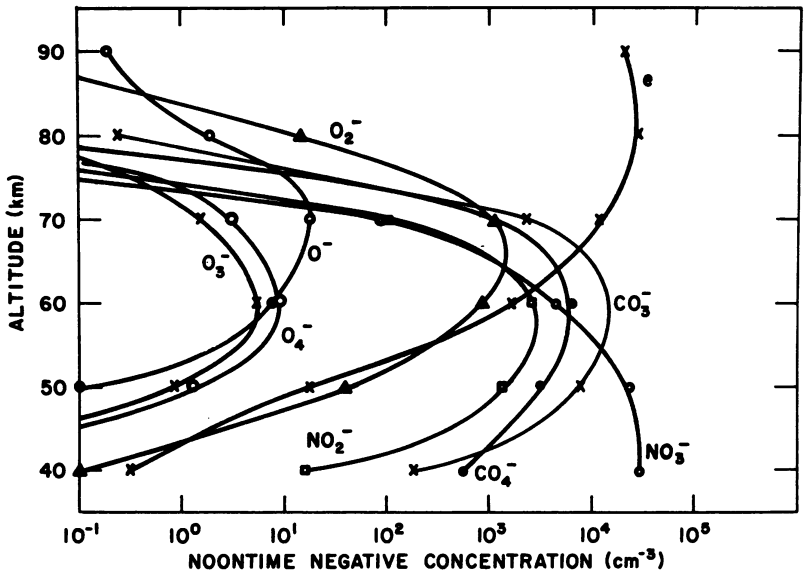

Figure 40-8. D Region Model Calculations Showing the Noontime Distributions of the Negative Ion Species During a PCA

Acknowledgments

This research was supported in part by the Defense Nuclear Agency.

References

Barth, C.A. (1966) Nitric oxide in the upper atmosphere, Ann. Geophys. 22:198.

Biondi, M.A. (1969) Electron recombination and ion recombination, Can. J. Chem. 47:1711.

Biondi, M.A., Leu, M.T., and Johnsen, R. (1971) Recombination of electrons with positive ions of the $H_3O^+ \cdot (H_2O)_n$ series, paper presented at Symposium on D and E region ion chemistry, COSPAR, Urbana, Illinois

Fehsenfeld, F.C., Schmeltekopf, A.L., Schiff, H.I., and Ferguson, E.E. (1967) Laboratory measurements of negative ion reactions of atmospheric interest, Planet. Space Sci. 15:373.

Fehsenfeld, F.C., and Ferguson, E.E. (1969) Origin of water-cluster ions in the D region, J. Geophys. Res. 74:2217.

Ferguson, E.E. (1971) D region ion chemistry, Rev. Geophys. 9:997.

Good, A., Durden, D.A., and Kebarle, P. (1970) Mechanism and rate constants of ion-molecule reactions leading to formations of $H^+(H_2O)_n$ in moist oxygen and air, J. Chem. Phys. 52:222.

Huffman, R.E., Paulsen, D.E., Larrabee, J.C., and Cairns, R.B. (1971) Decrease in D region $O_2(^1\Delta)$ photoionization rates resulting from CO_2 absorption, J. Geophys. Res. 76:1028.

References

Keneshea, T. J., Narcisi, R. S., and Swider, W. (1970) Diurnal model of the E region, J. Geophys. Res. 75:845.

Keneshea, T. J., Zimmerman, S. P., and George, J. D. (1972) The latitudinal variation of major and minor neutral species in the upper atmosphere, Space Research XII, in press.

Meira, L. G. (1971) Rocket measurements of upper atmosphere nitric-oxide concentrations and their consequences to the lower ionosphere, J. Geophys. Res. 76:202.

Narcisi, R. S., and Roth, W. (1970) The formation of cluster ions in laboratory sources and in the ionosphere, Advan. in Electron. and Electron Phys. 29:79.

Narcisi, R. S., Bailey, A. D., Della Lucca, L., Sherman, C., and Thomas, D. M. (1971) Mass spectrometric measurements of negative ions in the D and lower E regions, J. Atmosph. Terr. Phys. 33:1147.

Narcisi, R. S., Bailey, A. D., Wlodyka, L. E., and Philbrick, C. R. (1972a) Ion composition measurements in the lower ionosphere during the November 1966 and March 1970 solar eclipses, J. Atmosph. Terr. Phys. 34:647.

Narcisi, R. S., Philbrick, C. R., Ulwick, J. C., and Gardner, M. E. (1972b) Mesospheric nitric-oxide concentrations during a PCA, J. Geophys. Res. 77:1332.

Narcisi, R. S., Philbrick, C. R., Thomas, D. M., Bailey, A. D., Wlodyka, L., Baker, D., Federico, G., Wlodyka, R., and Gardner, M. E. Positive Ion Composition of the D and E Regions During a PCA, I, these proceedings.

Narcisi, R. S., Sherman, C., Philbrick, C. R., Thomas, D. M., Bailey, A. D., Wlodyka, L. E., Wlodyka, R. A., Baker, D., and Federico, G. Negative Ion Composition of the D and E Regions During a PCA, II, these proceedings.

Reid, G. C. (1970) Current problems in polar-cap absorption, Intercorrelated Satellite Observations Related to Solar Events, V. Manno and D. E. Page (Eds.) D. Reidel Publishing Company, Dordrecht-Holland, pp 319-334.

Swider, W. (1969) Ionization rates due to the attenuation of 1-100A nonflare solar x-rays in the terrestrial atmosphere, Rev. Geophys. Space Phys. 7:573.

Swider, W., Narcisi, R. S., Keneshea, T. J., and Ulwick, J. C. (1971) Electron loss during a nighttime PCA event, J. Geophys. Res. 76:4691.

Swider, W., and Keneshea, T. J. Diurnal variations in the D region during PCA events, these proceedings.

Zipf, E. C., Borst, W. L., and Donahue, T. M. (1970) A mass spectrometer observation of NO in auroral arc, J. Geophys. Res. 75:6371.

Contents

41. Effective Recombination Coefficients and Lumped Parameters in the D Region During Solar Particle Events

James C. Ulwick
Air Force Cambridge Research Laboratories
L.G. Hanscom Field
Bedford, Massachusetts

Abstract

Rocket and satellite measurements were made during the 2 November 1969 solar particle event of the proton spectra, for the determination of the rate of ion production, and of the altitude profiles of electron and ion concentrations. The effective recombination coefficient and the effective positive ion recombination coefficient, determined from the measurements for nighttime and daytime conditions are compared and discussed. The daytime effective recombination coefficients obtained over the three day period, where the ion production rate changed by almost 2 orders of magnitude, differ by less than a factor of two. Variations of the coefficients with solar zenith angle for both sunrise and sunset are shown. Lumped parameters are derived and compared to parameters derived from the output of the Keneshea code which preserves the detailed chemistry.

41-1 INTRODUCTION

The problem of computing particle densities in the D-region is very difficult due to the complex chemistry of the region. Computer codes that solve the differtial equations (that is, Keneshea, 1967) are limited by the poor information on many

of the required reaction rates. Investigations of the undisturbed region to provide input data for code development are difficult because it is a weakly ionized region and at the same time the neutral density is most dense. Various natural ionospheric phenomena, however, provide unique opportunities whereby ionization is substantially increased due to a measurable production source. Solar particle events (commonly referred to as polar cap absorption – PCA – events) are particularly important because of the long, slowly decaying production source, the intense ionization of the lower ionosphere and the production of high concentration of negative ions at low altitudes. The coordinated rocket, ground, aircraft and satellite program known as PCA 69 was implemented to utilize this phenomena to provide data on atmospheric perturbation and recovery mechanisms for computer code development. This paper is concerned with utilization of these data, as a first approach, in the development of an approximation code which neglects the detailed chemistry and thereby reduce the considerable and sometimes prohibitive computer time necessary for codes that preserve the physics. The approximation is known as the lumped parameter method.

In this approximation the de-ionization model consists of three species: electrons, positive ions and negative ions (the neutrals are considered as unchanged). The reactions which are considered to occur are as follows:

1. Attachment of electrons to neutral species.
2. Recombination of electrons to positive ions.
3. Mutual neutralization of negative and positive ions.
4. Detachment of electrons from negative ions.

From this limited set of species and reactions, the well known differential equations describing the system is as follows:

$$d N_e/dt = q - \alpha_D N_e N_+ - A N_e + D N_-$$

$$d N_+/dt = q - \alpha_i N_+ N_- - \alpha_D N_e N_+$$

$$d N_-/dt = A N_e - D N_- - \alpha_i N_+ N_-$$

where

N_e = electron density (cm^{-3})

N_- = negative ion density (cm^{-3})

N_+ = positive ion density (cm^{-3})

q = rate of ion production (cm^{-3} sec^{-1})

α_i = ion-ion recombination coefficient (cm^3 sec^{-1})

α_D = ion-electron recombination coefficient (cm^3 sec^{-1})

A = attachment rate coefficient (sec^{-1})

D = detachment rate coefficient (sec^{-1})

Since charge neutrality must be preserved ($N_+ = N_- + N_e$), there are only two independent equations.

Rocket and satellite measurements (Sellers, these proceedings; Reagan et al, these proceedings) have been made at various times during the 2 November 1969 PCA event of the proton spectra for the determination of the rate of ion production (q). Simultaneous rocket measurements were made of the altitude profiles of electron [N_e] (Ulwick, these proceedings; Dean, these proceedings) and ion [N_+] (Conley, these proceedings; Richards, these proceedings) concentrations. The effective recombination coefficient (α_{eff}) and the effective positive ion coefficient ($\alpha_{i\,eff}$) are determined from the measurements for nighttime and daytime conditions, compared and discussed. Variations of the coefficients with solar zenith angle for both sunrise and sunset are shown. The ratio of the negative ions to electrons (λ) is shown for night, day and sunset conditions. Lumped parameters under certain assumptions are derived from the experimental data and compared to lumped parameters derived from the output of the Keneshea code which preserves the detailed chemistry and uses the same rates of ion production (Swider and Keneshea). Electron and ion densities computed from these calculations are compared to the measured results.

41-2 EFFECTIVE RECOMBINATION COEFFICIENTS

From the differential equations the relationship between the rate of ionization and the electron density can be expressed under quasi-equilibrium conditions, as in a PCA event, by

$$q = \alpha_{eff} N_e^2 \qquad (41\text{-}1)$$

where

$$\alpha_{eff} = (1 + \lambda)\ (\alpha_D + \lambda \alpha_i)$$

and λ is the ratio of the negative ion density to the electron density. α_{eff} has been designated the effective recombination coefficient by some authors (see, for example, Webber, 1962; Whitten et al, 1965) and the steady state coefficient by others (Adams and Megill, 1967). Since α_D, α_i and λ all may be functions of q, α_{eff} is not necessarily characteristic of the lower ionosphere under all conditions. In fact Ulwick and Sellers (1971) pointed out the large differences between three different nighttime α_{eff} profiles derived from experimental observations with three distinct ionization sources of auroral electrons (McDiarmid and Budzinski, 1964), β particles (Whitten et al, 1965) and protons (Ulwick and Sellers, 1971). For daytime conditions Adams and Masely (1965) show experimental results during PCA events that suggest α_{eff} is only a function of altitude. During the 2-5 November 1969 PCA event the ion production rate as a function of altitude (Swider, Private Communication) was determined from four rocket measurements of the proton flux (Sellers and Hanser, these proceedings) and electron flux (Hegblom, these proceedings) and is shown in Figure 41-1. From these measurements and nearly simultaneous electron density measurements (Ulwick, these proceedings; Dean, these proceedings), the α_{eff} profiles shown in Figure 41-2 were derived for daytime conditions on 2, 3 and 4 November. The results are in agreement within a factor of about two at all altitudes. The factor of two difference is within the experimental error (40 percent) of our electron density measurements at the lower (below 65 km) altitudes. This means that even though the production rate changed by over two orders of magnitude in the three day period, the α_{eff} profile is essentially constant and α_{eff} is only a function of altitude. Thus the electron density profile can be computed ($N_e = \sqrt{q/\alpha_{eff}}$) for daytime PCA events if the production rate (that is, the proton spectrum) is known. It should be pointed out that the value of α_{eff} at the lowest altitude (the highest value of α_{eff}) in each case is the value with the greatest error since the electron density is lowest and therefore derived from measurements near the limit of instrumentation sensitivity. Therefore, at 55 km the α_{eff} derived from the 2 November measurements ($N_e = 5.5 \times 10^3$ cm^3/sec) is less in error than the α_{eff} for 3 November ($N_e = 1.5 \times 10^3$ cm^3/sec) and 4 November ($N_e = 4 \times 10^2$ cm^3/sec). Comparing these results with other experimentally derived α_{eff} values under PCA conditions, there is excellent agreement with Potemra et al (1969) but different from Megill et al (1971) values by almost an order of magnitude at some altitudes.

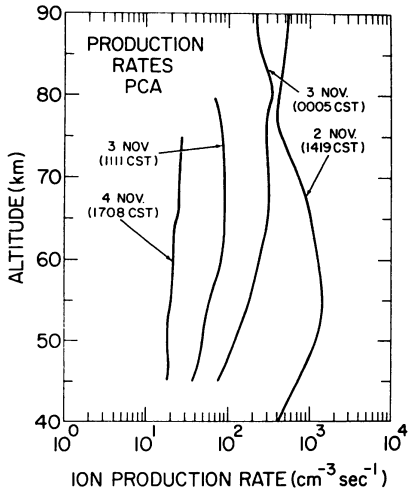

Figure 41-1. Ion Production Rate as a Function of Altitude During 2 November 1969 PCA Event From Rocket Proton and Electron Flux Measurements

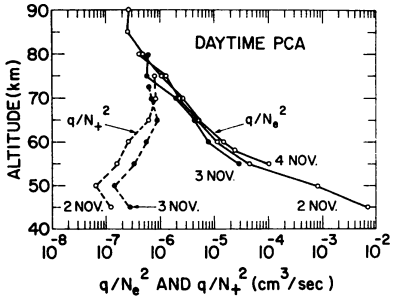

Figure 41-2. Effective Electron Recombination Coefficients ($\alpha_{eff} = q/N_e^2$ From 2 November 1969 PCA Daytime Results

From the differential equations the relationship between the rate of ionization and the ion density can be expressed under quasi-equilibrium conditions by:

$$q = \alpha_{i\,\mathrm{eff}}\, N_+^2$$

where

$$\alpha_{i\,\mathrm{eff}} = \frac{1}{1+\lambda}\,(\alpha_D + \lambda\,\alpha_i) \qquad (41\text{-}2)$$

and the $\alpha_{i\,\mathrm{eff}}$ is the effective position ion recombination coefficient. From the ion production rates (Figure 41-1) and positive ion density measurements from rocketborne Gerdien condensers (Conley, these proceedings) the $\alpha_{i\,\mathrm{eff}}$ for 2 and 3 November were calculated and are shown in Figure 41-2. These two curves show similar shape

and magnitude irrespective of the ion production rate decrease by over an order of magnitude in the two days and the altitude of maximum production changing from 55 km on 2 November to 65 to 75 km on 3 November as shown in Figure 41-1. The q/N_+^2 curves differ by about a factor of two below 65 km while the q/N_e^2 for the same two days is somewhat less. It can also be seen that no adjustment of the ion production rate, q, can decrease the difference between the 2 and 3 November q/N_+^2 results and simultaneously the 2 and 3 November q/N_e^2 results indicating the difference is a result of the N_e and N_+ measurements. The relationship between the two coefficients is

$$\alpha_{i\ eff}\ (1+\lambda)^2 = \alpha_{eff} \qquad (41\text{-}3)$$

Thus when $\lambda \rightarrow 0$ the two coefficients are equal, the positive ion density is equal to the electron density, and α_{eff} is the ion-electron recombination coefficient (α_D). In the same figure this is at approximately 75 km altitude.

Figure 41-3 shows the variation of λ as a function of altitude calculated from the positive ion and electron densities measurements for the daytime, sunset and nighttime rocket flights. The nighttime values were from two different PCA events. Rocket 17.757 was launched during the 18 November 1968 PCA while 17.758 and the other results are from the 2 November event. The ion production rates at the time of the two nighttime launches were quite similar. Using the 17.757 results, Swider et al (1971) gave a simple expression for λ for night showing the dependence on the production rate. In daytime, λ, to a first approximation, is regarded as a characteristic parameter of the atmosphere and independent of the production rate and the electron density. The daytime λ values in Figure 41-3 show agreement at least within a factor of two even though the production rate changes by over an order of magnitude. The change from nighttime, sunset transition, and daytime is evident with $\lambda = 1$ at approximately 80 km, 72 km and 68 km respectively.

Figure 41-4 shows the 2 November 1969 daytime (17.602) α_{eff} values compared to the 3 November 1965 (17.758) and 19 November 1968 nighttime values. Both nighttime results are quite similar reflecting the similarity of the ion production rates for the two events which were within about 30 percent. Differences, such as the sharper gradient between 79 and 80 km on the 19 November 1968 results, are essentially due then to different electron density concentrations. For nighttime, the parameter α_{eff} can only be used below about 75 km associated with a specific production rate as mentioned. Swider et al, (1971) using the 19 November 1968 rocket results were able to develop instead, a simple expression to determine the electron concentration where the electron loss rate above 75 km is due

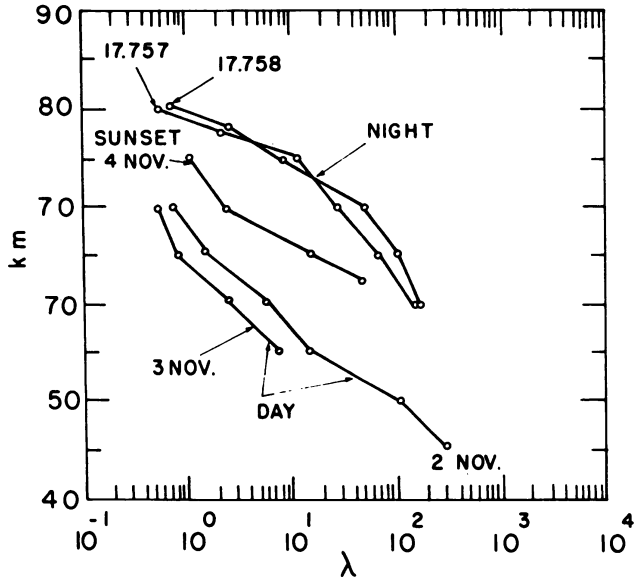

Figure 41-3. The Variation of the Ratio of Negative Ions to Electrons (λ) for Daytime, Nighttime and Sunset Conditions During 2 November 1969 PCA Event

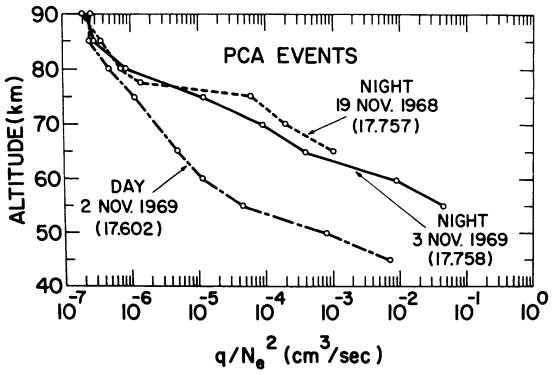

Figure 41-4. Comparison of Nighttime and Daytime α_{eff} (a/N_e^2) Values. The nighttime results are for two different PCA events

to dissociate recombination and below this by means of three body attachments to produce O_2^- with no detachment processes significant. They point out, however, that detachment by the process $O_2^- + O \rightarrow O_3 + e$ may be operative in the vicinity of 80 km since there is a sharp decrease in the electron density at this altitude (reflected in Figure 41-4 as the sharp decrease in α_{eff} near 80 km) that appears to be comparable with the steep gradient in atomic oxygen calculated by Shimazaki

and Laird (1970) between 80 and 75 km. In the figure, above about 78 km, the three α_{eff} values are about the same indicating that photodetachment processes are not significant, α_{eff} is not a function of the production rate and α_{eff} is the ion-electron recombination coefficient.

Figures 41-5 and 41-6 show the q/N_e^2 variation for sunrise and sunset on 3 and 4 November respectively. Electron densities were from rockets launched at the designated solar zenith angles noted on the figures (Ulwick, these proceedings; Dean, these proceedings). The ion production rates shown in Figure 41-1 were used for the corresponding days and were considered unchanged during the time interval of rocket launching. In both figures the variation with solar zenith angle is clear. At each altitude where increase in α_{eff} is significant, the α_{eff} is always largest for the largest solar zenith angle and all approach the daytime values as a limit at different altitudes dependent upon the solar zenith angle. Both figures exhibit the so-called "twilight anomaly" effect (Reid and Collins, 1959; Bailey, 1964); that is, the day/night and night/day transitions take place when the shadow of the solid earth is traversing the altitude range 0 to 50 km and not when the visible light is removed from the ionized altitudes. Chivers and Hargreaves (1965) using riometer data showed the pronounced asymmetry between the changes in absorption during the sunset and sunrise due to the time lag in the absorption increase during sunrise was due to a time effect and also was not a function of the spectrum of the solar flux. Comparing Figures 41-5 and 41-6, the asymmetry in the α_{eff} values during the runrise and sunset is apparent with the runrise (3 November) lagging the sunset (4 November) values.

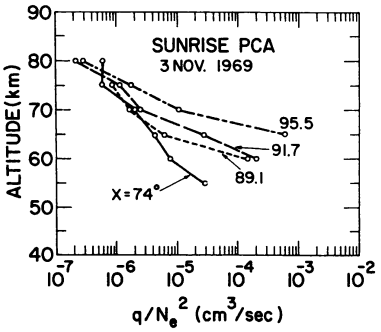

Figure 41-5. The Variation of $\alpha_{eff}(q/N_e^2)$ With Solar Zenith Angle (χ) From Rocket Results During Sunrise

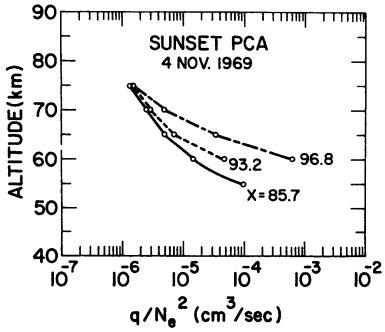

Figure 41-6. The Variation of α_{eff} (q/N_e^2) With Solar Zenith Angle (χ) From Rocket Results During Sunset

41-3 LUMPED PARAMETERS

To use the PCA data to find profiles of the lumped parameters of detachment, ion-ion recombination and ion-electron recombination, certain assumptions have to be made. This is necessary since there are only two independent differential equations (Eqs. 41-1 and 41-2) with four unknown parameters. The first assumption is that three body attachment to form O_2 is the only important attachment mechanism and it can be calculated from the following equation:

$$A = 1.4 \times 10^{-29} \left(^{300}/_{T}\right) e^{-600/T} \left[O_2\right]^2 + 10^{-31} \left[O_2\right] \left[N_2\right] \quad (41\text{-}4)$$

where A is in sec^{-1} and $\left[O_2\right]$ and $\left[N_2\right]$ in cm^{-3}. Another assumption is that detachment at nighttime is negligible below 75 km. Finally the equations can be simplified in certain altitude regions where λ, the ratio of negative ions to electrons, is very large or very small. The lumped parameters are derived from the data and are compared to parameters calculated from the Keneshea code.

41-3.1 Ion-Ion Recombination Coefficient (α_i)

The first parameter we derive from the data is the ion-ion recombination coefficient (α_i) which, from the differential equations, is given by:

$$\alpha_i = \frac{A}{N_+ \lambda} - \frac{D}{N_+}$$

and for nighttime we assume no detachment (D = O) and α_i is given by:

$$\alpha_i = \frac{A}{N_+ \lambda} \quad (41\text{-}5)$$

The α_i profile can be found for the two nighttime rocket flights 17.757 (November 1968 event) and 17.758 (November 1969 event) using the λ values in Figure 41-3, the ion density (N_+) values from Conley (these proceedings) and the attachment (A) values calculated from Eq. (41-4) using the 60^o north latitude, November CIRA models. The results are shown in Figure 41-7. The lower altitude limit is 60 km because no λ values are available (see Figure 41-3) since the electron density is below the sensitivity of our probes (10^2 electrons/cm^3).

The ion-ion recombination coefficient is also given by:

$$\alpha_i = \frac{q}{N_+^2} + \frac{q}{N_+^2 \lambda} - \frac{\alpha_D}{\lambda}$$

and for sufficiently large values of λ, the approximation is:

$$\alpha_i \simeq \frac{q}{N_+^2} \qquad (41\text{-}6)$$

The q/N_+^2 values for PCA conditions of day (rocket 17.602), night (rockets 17.758 and 17.757) and sunset (rocket 17.617) are shown in Figure 41-7. It is obvious that when λ is less than about 10^2, the q/N_+^2 values become quite large in all four cases and this occurs at progressively higher altitudes going from day to sunset to nighttime conditions. The α_i values from Eq. (41-6), when λ is greater than about 10^2, compare within a factor of about 1.5 in all four results and also with the α_i values from expression Eq. (41-5). At 60 km the nighttime α_i's from Eq. (41-5) are about a factor of two higher than the nighttime α_i's from Eq. (41-6). We think the α_i's from Eq. (41-5) are the least accurate since our electron density probe was near the limit of sensitivity at this altitude. Note the good agreement of the sunset results with the nighttime results from expression Eq (41-6) at this altitude. Also note that the α_i values at 65 km from expressions Eqs. (41-5) and (41-6) are consistent for each nighttime rocket flight. The average α_i at 5 km intervals from these results is shown in Figure 41-8. No error bars are placed on the values but considering the uncertainty in the probe measurements, it is estimated that the values are within about a factor of two. The results in the 50 to 75 km altitude range can be approximated by a value of $6.5\ (\pm 1.5) \times 10^{-8}$ cm^3 sec^{-1}. This value compared to laboratory data for α_i which range from 10^{-7} to 10^{-8} cm^3 sec^{-1} (Biondi, 1969)

41-3.2 Ion-Electron Recombination Coefficient (α_D)

The ion-electron recombination coefficient α_D can be expressed from Eq. (41-2) as follows:

$$\alpha_D = \frac{(1+\lambda)q}{N_+^2} - \lambda\alpha_i \qquad (41\text{-}7)$$

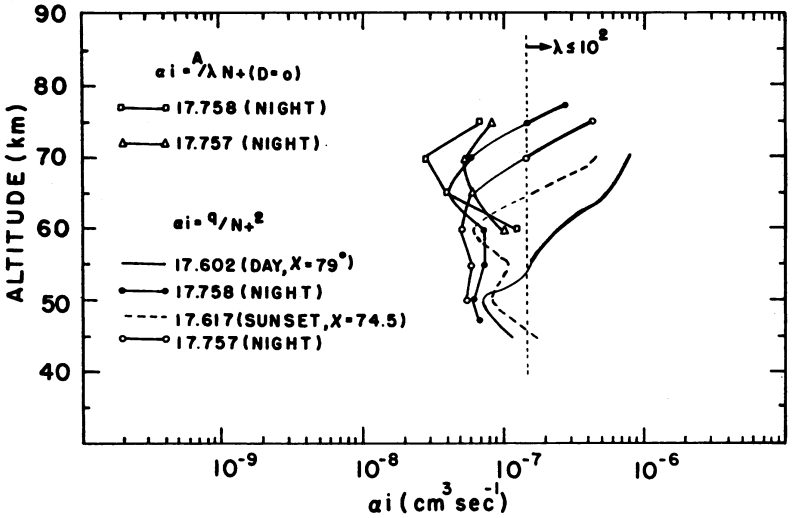

Figure 41-7. Ion-ion Recombination Coefficient (α_i) From Rocket Measurements During 2 November 1969 PCA Event

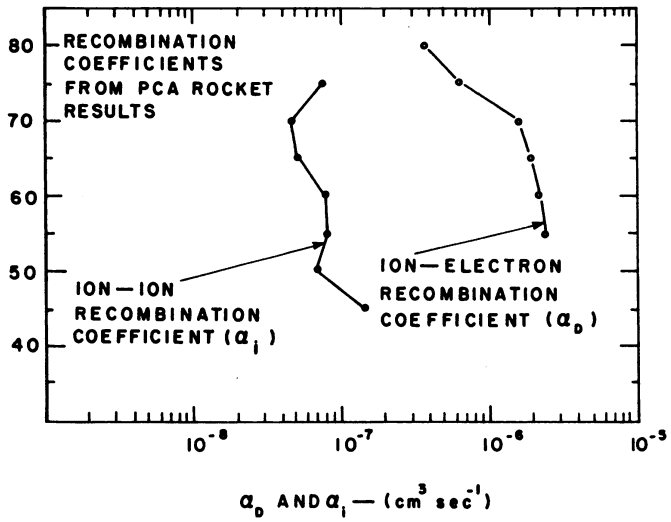

Figure 41-8. Average Recombination Coefficient α_i (ion-ion) and α_D (ion-electron) From Rocket PCA Results (Figures 41-7 and 41-9)

Using the α_i values in Figure 41-8 and the rocket measurements of the other parameters, the α_D values shown in Figure 41-9 were calculated for the solar particle event. Profiles are shown for the two daytime rockets (17.602, 2 November launch and 17.906-1, 3 November launch) and for the twilight rocket (17.617, X = 96.8°, 4 November launch). During this time between the 17.602 and 17.617 launches, the production rate changed by about two orders of magnitude but the α_D values for the three flights shown in Figure 41-9 were within a factor of two at each altitude. The average α_D values at each 5 km interval are shown in Figure 41-8. From 80 km down to 75 km, the α_D values are between 3.8×10^{-7} cm^3 sec^{-1} and 6.5×10^{-7} cm^3 sec^{-1} and were determined principally by the term q/N_+^2 in Eq. (41-7) because the λ values were quite small in this altitude range. These values are consistent with published values for O_2^+ and NO^+ (Biondi, 1969) which were predominant positive ions above 73 km during daytime in this event (Narcisi et al, these proceedings). Below about 73 km, Narcisi et al (these proceedings) showed that the water cluster ions were predominate. Recent laboratory measurements by Biondi et al (these proceedings) of coefficients of recombination of electrons with water ions give values (normalized to 300°K) as follows:

$$\alpha(19^+) = (1.3 \pm 0.6) \times 10^{-6},\ \alpha(37^+) = (2.7 \pm 1 \times 10^{-6}),\ \text{and}$$

$$\alpha(55^+) = (4.6 \pm 1) \times 10^{-6}\ cm^3\ sec^{-1}.$$

The α_D values below 70 km shown in Figure 41-8 range between about 1.4×10^{-6} to 2.5×10^{-6} cm^3 sec^{-1} which are within the values for $\alpha(19^+)$ and $\alpha(3.7^+)$. As in the α_i values, the α_D values are considered to be good within about a factor of two.

41-3.2 Ion-Electron Recombination Coefficient (α_D)

The detachment rate coefficient (D) is given from Eq. (41-3) as follows:

$$D = \frac{A}{\lambda} - \alpha_i N_+$$

From the PCA rocket measurements of the ratio of negative ions to electrons (λ), the positive ion density (N_+), the ion-ion recombination coefficients of Figure 41-8, and the attachment rate coefficients (A) from Eq. (41-4), the detachment rate coefficients were determined for the two daytime PCA rocket flights (17.602 and 17-609-1) and for the sunset rocket flight (17.617). The assumption in

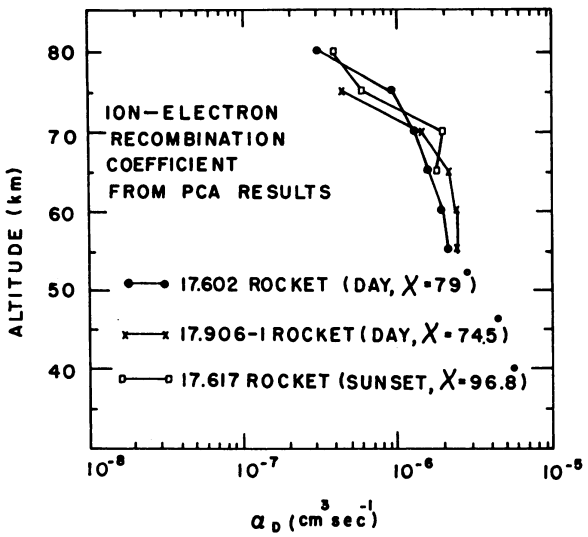

Figure 41-9. Ion-electron Recombination Coefficient (α_D) From Rocket Measurements During 2 November 1969 PCA Event

the calculations of the lumped parameters was that there was no detachment at night (D = o). The sunset results compared to the daytime results in Figure 41-10 show the sharp decrease in the detachment as nighttime conditions are approached. The data show the "twilight anomonly" effect mentioned previously. The detachment values are determined mainly from the ratio of A/λ in Eq. (41-8) since the term $\alpha_i N_+$ is comparatively small. The difference then in the two daytime results are a result of the difference in the λ values in Figure 41-3. The detachment values from the 17.602 rocket results are considered to be the most accurate. This is because of the good agreement between the propagation probe and the $Z\theta$ impedance probe results of the electron density (Ne) measurements whereas the 17.906-1 results depend on just the propagation measurements (Ulwick, these proceedings). Also positive ion and electron densities measured on 2 November (17.602) were substantially higher than on 3 November (17.906-1) which makes probe measurements more accurate.

41-3.3 Detachment Rate Coefficient (D)

The photochemical code of Kenechea (1967) has been used to compute the electron and positive ion densities using the rocket measured production rates to compare with rocket measurements of positive ion and electron densities. Swider

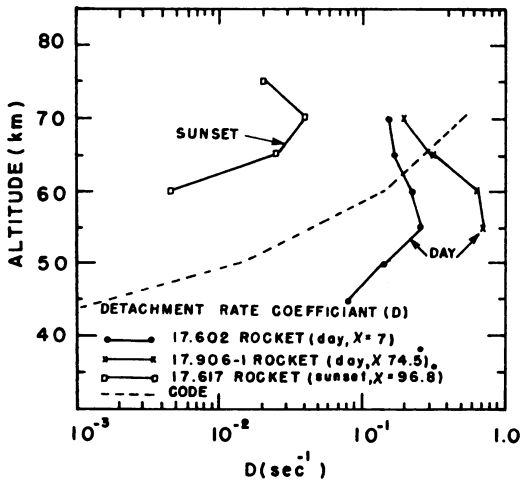

Figure 41-10. Detachment Rate Coefficient (D) From Rocket Measurements During 2 November 1969 PCA Event and From Keneshea Code

et al, (1971) have discussed the nighttime PCA measurements. The electron and positive ion densities from the code, Ne(comp) and N_+(comp), are compared to the rocket results in Figure 41-11. The comparison between the positive ion densities is quite good but the computed electron densities are substantially lower than the measured results. If we calculate the absorption that would be measured by a riometer operating at 30 MHz using the rocket electron densities (Ulwick, these proceedings), we get a value of 9.2 dB, which compares well with the 30 MHz riometer measurement during the rocket flight of about 8.8 dB. Using the same technique to calculate the 30 MHz absorption for the computed electron densities, we get a value of 4.5 dB which is almost half the measured value. Comparing the 3 November daytime computed and measured values gave similar results. The ion densities compared well; the computed electron densities were substantially lower than the measured ones; and the computed absorption, using the rocket measured electron densities, compared well with the 30 MHz riometer measurements while that from the computer electron densities were almost half the measured riometer absorption. Using the 2 November computer results, lumped parameters were calculated to compare with the rocket results. The α_D and α_i values were within a factor of two with the big difference in the detachment rate coefficients as shown in Figure 41-10. This is because the λ values one gets from the computed electron and negative ion ($N_+ - N_e$) densities are a great deal larger than the rocket values (because of the small computed electron densities) and as pointed out, the λ values determine the detachment rate coefficients from Eq. (41-8). Future work using the PCA rocket results will concentrate on development of the negative ion chemistry in the Keneshea Code.

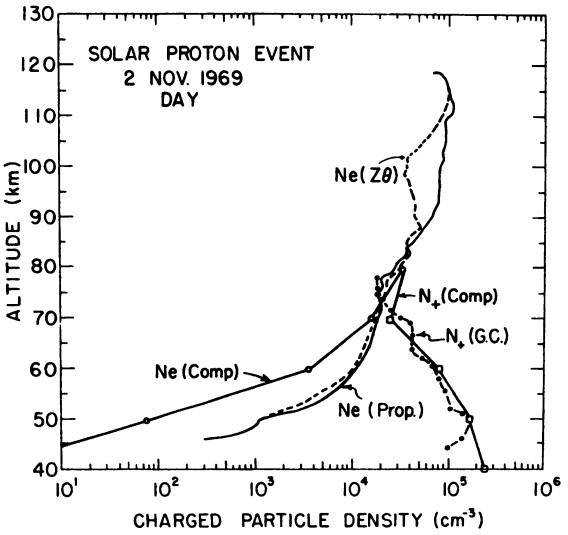

Figure 41-11. Electron and Ion Densities Measurements on 2 November 1969 During PCA Event Compared With Computed Values From Keneshea Code

References

Adams, G.W., and Masley, A.J. (1966) Planet. Space Sci. 14.

Bailey, D.K. (1966) Planet. Space Sci. 12.

Biondi, M.A. (1969) Can. J. Chem. 47.

Biondi, M.A., Len, M.T., and Johnsen, R. (these proceedings) COSPAR Symposium on D- and E-Region Ion Chemistry, Univ. of Illinois.

Chivers, H.J.A., and Hargreaves, J.K. (1965) Planet. Space Sci. 13.

Conley, T. (these proceedings) COSPAR Symposium on 2 November 1969 Solar Particle Event.

Dean, W. (these proceedings) COSPAR Symposium on 2 November 1969 Solar Particle Event.

Hegblom, R. (these proceedings) COSPAR Symposium on 2 November 1969 Solar Particle Event.

Keneshea, T.J. (1967) Sci. Res. Report, AFCRL-67-0221.

McDiarmid, I.B., and Budzinski, E.E. (1964) Can. J. Phys.

Megill, L.R., Adams, G.W., Haslett, J.C., and Whipple, E.C. (1971) J. Geophys. Res. 76.

Narcisi, R.W., Philbrick, C.R., Thomas, D.M., Bailey, A.D., Wlodyka, L., Baker, D., Federico, G., Wlodyka, R., and Gardner, M.E. (these proceedings) COSPAR Symposium on 2 November 1969 Solar Particle Event.

Potemra, T.A., Zmuda, A.J., Haave, C.R., and Shaw, B.W.J. (1969) J. Geophys. Res. 74.

Reagan, J.B., Imhof, W.L., and Gaines, E.E. (these proceedings) COSPAR Symposium on 2 November 1969 Solar Particle Event.

Reid, G.C., and Collins, C.J. (1959) J. Atmos. and Terrest. Phys. 14.

Richards, E. (these proceedings) COSPAR Symposium on 2 November 1969 Solar Particle Event.

References

Sellers, B., and Hanser, F.W. (these proceedings) COSPAR Symposium on 2 November 1969 Solar Particle Event.

Shimazaki, T., and Laird, A.R.J. (1970) J.Geophys.Res. 75.

Swider, W., Narcisi, R., Keneshea, T., and Ulwick, J.C. (1971) J.Geophys. Res. 76.

Ulwick, J.C., and Sellers, B. (1971) Space Research XI.

Ulwick, J.C. (these proceedings) COSPAR Symposium on 2 November 1969 Solar Particle Event.

Webber, W. (1962) J.Geophys.Res. 67.

Whitten, R., Poppoff, I.G., Edmonds, R.S., and Berning, W.W. (1965) J.Geophys.Res. 70.

Contents

42. Diurnal Variations in the D Region During PCA Events

W. Swider and T.J. Keneshea
Air Force Cambridge Research Laboratories
L.G. Hanscom Field
Bedford, Massachusetts

Abstract

Extensive computations have been performed in order to simulate the diurnal behavior of the D region during PCA events. Computations using 98 reactions with only NO^+ and O_2^+ as positive ions apparently yield too much 30 MHz riometer absorption. Nevertheless, we further substantiate the argument of Swider et al (1971) that this simple positive ion chemistry is sufficient regarding the deduction of the nighttime electron concentration profile. Expansion of the computer code to 195 reactions, including species like $H_3O^+ \cdot (H_2O)_n$ provides more reasonable results as far as the positive ion chemistry is concerned since such ions are known to exist in the D region. However, too few electrons appear to be generated in the 50-65 km region, which we believe is indicative of insufficient knowledge of the negative ion chemistry. Thus, for example, the process $CO_4^- + h\nu \rightarrow CO_2 + O_2 + e$ is suggested as one process, the inclusion of which may increase the calculated electron population in this region. From 60 km down to 40 km, our lower altitude limit, we find that the dominant positive ions, $H_7O_3^+$ and $H_9O_4^+$, are in thermodynamic equilibrium. We also note that the dissociative recombination of the $H_3O^+ \cdot (H_2O)_n$ ion population, which is enhanced during a PCA event as compared to quiet conditions, leads to an increase in HO_2 and OH and a subsequent depletion of ozone. This may explain ozone observations by Weeks during the November 1969 PCA event, which appear to indicate that ozone declined above 50 km, the decrease increasing with altitude.

42-1 INTRODUCTION

The chemistry of the D region is far more complex than any other portion of the ionosphere because it is the only ionospheric section where three-body processes are important. The formation of negative ions in the ionosphere originates with the processes $e + O_2 + O_2(N_2) \rightarrow O_2^- + O_2(N_2)$, and only at D-region altitudes are neutral concentrations large enough to provide for significant O_2^- formation. Radiative processes like $e + O_2 \rightarrow O_2^- + h\nu$ are too slow.

During a PCA event, the ionization production rate changes slowly in comparison to the behavior of the electron distribution in the D region near twilight. (The day and night distributions are steady, but different.) Reid (1961) was the first to demonstrate that simple negative ion chemistry would not suffice, and Narcisi and Bailey (1963) were the first to determine that $H_3O^+ \cdot (H_2O)_n$ ions are the dominant D-region species. Furthermore, minor neutral species are apparently important (Reid, 1967).

In this paper we present the most elaborate computations made to date concerning PCA events. In a sense, we extend the work of Adams and Megill (1967) who considered a simple model: the negative ions O_2^- and X^-, some unknown composite ion, speculating about the nature of X^- by concluding their paper with a six-negative ion model. Here, we commence our work with a computation considering these same negative ions (O^-, O_2^-, O_3^-, CO_3^-, NO_2^-, NO_3^-) plus electrons, NO^+ and O_2^+ ions. Further computations will also be presented with these species plus O_4^-, CO_4^- and $H_3O^+ \cdot (H_2O)_n$, (n = 0 - 4) and $NO^+ \cdot (H_2O)_n$, (n = 1 - 3) ions. This final set of computations, utilizing 195 reactions, is perhaps still inadequate, but we shall attempt to indicate those processes which are unaccounted for and which may contribute to the discrepancies between experiment and theory.

Calculations were performed at decade intervals, from 40 to 90 km. Transport is not considered and consequently, for those neutral species which are of particular importance in the study, an alternate approach was provided as described in the text. Neutral atmospheric densities and temperatures were taken from CIRA 1965. Computations were performed for a latitude of 60° and a solar declination of zero.

42-2 COMPUTATIONS INCLUDING NO^+, O_2^+, e, O^-, O_2^-, O_3^-, CO_3^-, NO_2^- AND NO_3^- AS THE ONLY CHARGED PARTICLES

Reactions 1 - 100, excluding 97 and 98 (see Appendix 42-A) were considered. Ionization production rates generated by integral proton spectrums described by $10^3\ e^{-P/P_o}$ protons $cm^{-2}\,sec^{-1}\,ster^{-1}$ with P_o, the rigidity or particle momentum

per unit charge, having values of 25, 50, 100, and 200 MV were adopted as calculated by Swider and Gardner (1971) for negligible geomagnetic cutoffs. The greater the value of P_o, the harder the spectrum and the greater the total vertical ionization production rate, $cm^{-2} sec^{-1}$. The electron concentrations generated at noon and midnight are depicted in Figures 42-1 and 42-2.

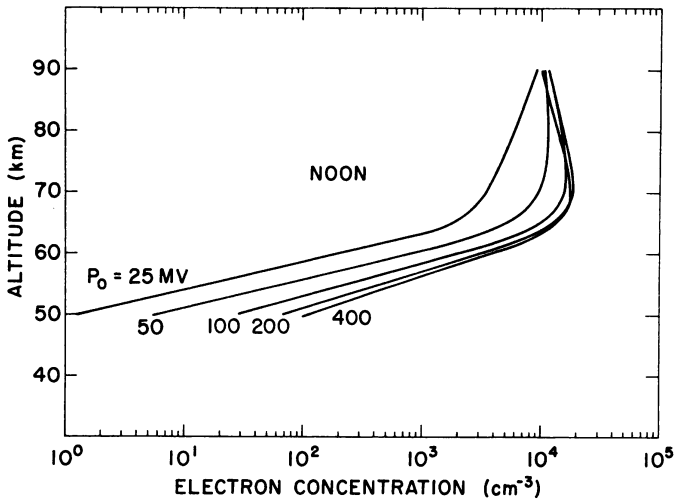

Figure 42-1. Distribution of Noontime Electron Concentrations for Proton Fluxes $10^3 e^{-P/P_o} cm^{-2} sec^{-1} ster^{-1}$

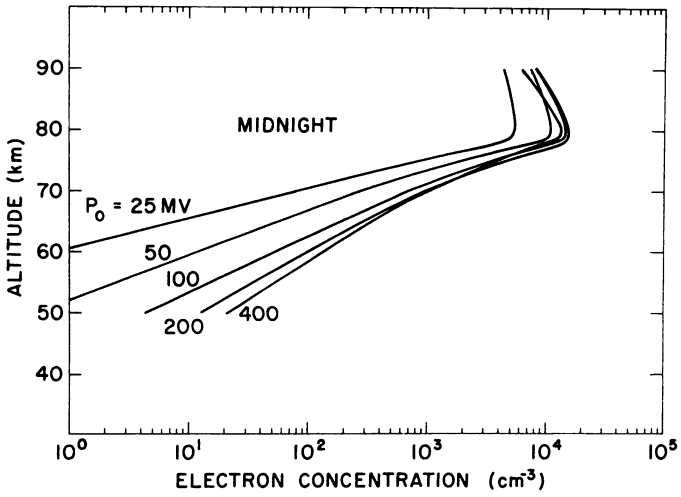

Figure 42-2. Distribution of Midnight Electron Concentrations for Proton Fluxes $10^3 e^{-P/P_o} cm^{-2} sec^{-1} ster^{-1}$

The 30 MHz absorption has been determined for each of the electron density profiles depicted in Figures 42-1 and 42-2 using the electron-neutral collision frequency, ν_m, of Thrane and Piggott (1966). The variation of the effective collision frequency from $2.5\nu_m$ to $1.5\nu_m$ was accounted for through use of Deek's (1966) Figure 1. The resultant numerical values by which [e] is multiplied in order to yield dB/km are 5.02×10^{-7}, 2.99×10^{-6}, 1.56×10^{-5}, 6.02×10^{-5}, 1.20×10^{-4} and 8.22×10^{-5} for altitudes of 90 - 40 km in decade units, respectively.

The calculated differential absorption curves for noon and midnight, depicted in Figure 42-3 show a peak effect near 80 km at night and near 65 km by day.

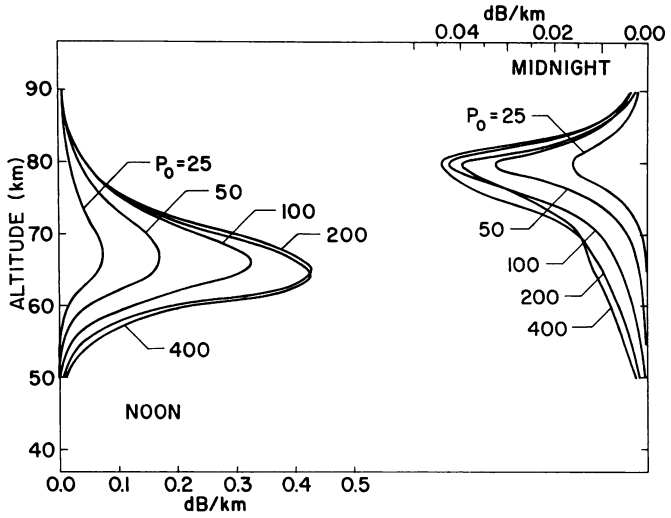

Figure 42-3. Differential Absorption at 30 MHz for the Electron Distributions of Figures 42-1 and 42-2

Since about 2 MeV protons stop at 80 km, the significance of a negligible geomagnetic cutoff can be appreciated. Thus in the important early work of Bailey (1959), a fairly high geomagnetic cutoff was adopted which contributed to the conclusion that some detachment process was operative at night. The cutoff is often negligible, especially at night (Reid and Sauer, 1967) when fairly soft protons appear to be responsible for the observed ionization (Reid, 1970). This stresses the need for good measurements of the soft proton flux (1 - 10 MeV). In addition, the precise amount of nighttime radio absorption may be lower than indicated by riometer measurements (Heisler and Hower, 1970), implying that fewer electrons are needed to explain the measured absorption and therefore diminishing the need to invoke detachment processes. Crain (1960) doubted the existence of a nighttime detachment mechanism,

and analysis of a 1962 nuclear explosion at night (Whitten et al, 1965; Adams and Megill, 1967) required no detachment process to explain the measured electron distribution. The electron profile measured in a nighttime PCA event (Ulwick et al, 1970; Ulwick and Sellers, 1971) was satisfactorily explained (Swider et al, 1971) without invoking detachment processes other than perhaps $O_2^- + O \rightarrow O_3 + e$ near 80 km. This process is not effective at night below about 75 km since atomic oxygen declines precipitously below this altitude (Shimazaki and Laird, 1970; George et al, 1971). In addition, as shown later, O_2^- is a minor ion at night. The electron affinities of the major negative ions present exceeded 1 eV, which means collisional detachment will be neglibible. The species $O_2(^1\Delta)$ and O are not important below 75 km at night.

Our peak daytime absorption occurs near 65 km (Figure 42-3), which may be too high an altitude since this is the stopping altitude for about 10 MeV protons whereas daytime riometer absorption correlates best with the integral flux of protons above 10 MeV. The implication is that the dB/km peak occurs at a somewhat lower altitude. The relationship between absorption and the proton intensity can be understood physically in a rough way (Bailey, 1964). Juday and Adams (1969) estimate that $J = 47A_\nu^2$ where J is the integral proton flux $cm^{-2}\,sec^{-1}\,ster^{-1}$ above 11 MeV and A_ν is the 30 MHz vertical absorption. Riometers normally do not have pencil-like beams and hence J is approximately equal to $24\,A_r^2$ for a riometer with a 60° half power response, since $A_r \simeq 1.4\,A_\nu$ (Freier and Webber, 1963). Table 42-1 compares the computed total absorption by night and day, the ratio, and the daytime absorption given by $J = 47\,A_\nu^2$ based on the proton fluxes used. The results presented here apparently generate too much absorption. This is largely because of the omission of $H_3O^+ \cdot (H_2O)_n$ ions, as they combine much faster with

Table 42-1. Correlation Between the Calculated 30 MHz Vertical Absorption and the Integral Proton Flux

30 MHz Absorption Relationships					
Rigidity (P_o)	J(≥10 MeV)	A_D/A_N	A_N	A_D	$(J/47)^{1/2}$
25MV	4	4.7	0.19	0.89	0.30
50	64	5.9	0.40	2.4	1.2
100	253	6.9	0.61	4.2	2.3
200	503	7.7	0.70	5.4	3.3

Note: J indicates the integral proton flux $cm^{-2}\,sec^{-1}\,ster^{-1}$ above 10 MeV for a spectrum of the form $J = 10^3 e^{-P/P_o}$. Computed vertical absorption values are A_D(day) and A_N (night). The last column is an empirical daytime relation deduced by Juday and Adams (1969).

electrons than NO^+ and O_2^+ ions. The nighttime calculated absorption, A_N, appears to be somewhat low. However, as already noted, there may be some problems concerning nighttime riometer measurements (Heisler and Hower, 1970). The day to night ratio, A_D/A_N, is probably within the range of the data since the spread appears to be large (Fichtel et al, 1963).

Figures 42-4 and 42-5 illustrate the behavior of $\lambda = \sum$ Neg ions/[e] and $\alpha_{EFF} = q/[e]^2$ respectively. The shadowing of the curves relates to the fact that each curve is composed of four different curves corresponding to the four different

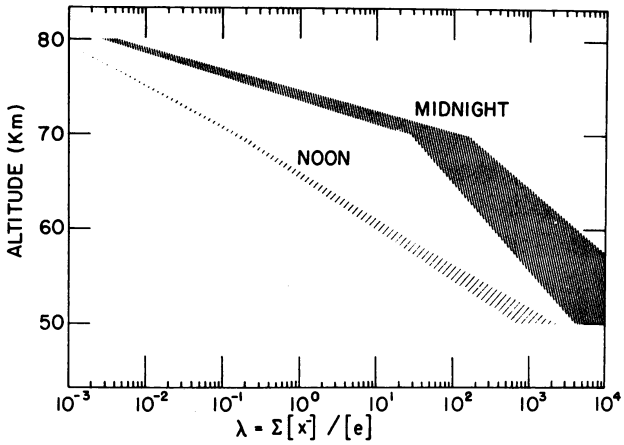

Figure 42-4. The Variation With Altitude of the Ratio of Negative Ions to Electrons

production rates used. The parameters λ and α_{EFF} become smaller as q, the production rate, increases. Of special note is the greater breadth of λ and α_{EFF} at night, which may be clarified by considering a specific example. Figure 42-6 compares a measured nighttime electron concentration with a calculation based on the particular proton flux measured. Swider et al (1971) interpret these results as indicative of the fact that electrons are irretrievably lost by the processes $e + O_2 + O_2(N_2) \rightarrow O_2^- + O_2(N_2)$ below 75 km. The dominant negative ions are not O_2^- ions, which further strengthens their argument that detachment processes are not occurring below this altitude. Therefore, the effective electron loss coefficient is simply given by $\alpha_{EFF} = L(A)^2/q$ below 75 km since $[e] = q/L(A)$, where L(A) is the electron loss (attachment) rate, sec^{-1}. Thus, α_{EFF} is a strong function of the production rate, being inversely proportional to it. Similarly, where the electron concentration is small ($\lambda \gtrsim 10$), $\sum$ Neg ions $\simeq (q/\alpha_i)^{1/2}$, the relationship

$\lambda = (q/\alpha_i)^{1/2}/[e]$ becomes $\lambda = L(A)/\sqrt{q\alpha_i}$ where α_i represents the ion-ion recombination coefficient. The formula shows that λ is inversely proportional to the square root of the production rate.

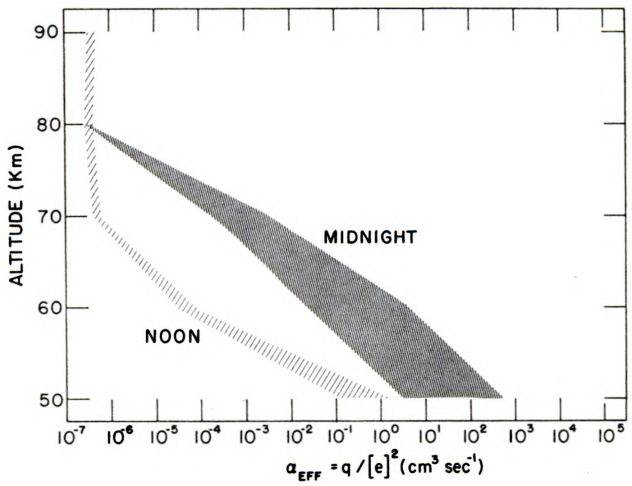

Figure 42-5. The Variation With Altitude of the Effective Electron Loss Rate, $\alpha_{EFF} = q/[e]^2$

In the daytime λ and α_{EFF} have a much weaker dependence on the production rate, but the dependence increases with decreasing altitude and finally, at 40 km, day and night results for [e] are almost identical, the above relationships being applicable. The connection between these parameters and the production rate can be understood in simple terms. As q becomes large, the loss of electrons through recombination with positive ions grows at the expense of the term L(A), which is a constant at each altitude, so that the effective recombination coefficient approaches the dissociative recombination coefficient as a lower bound. Simultaneously, the formation of negative ions is lessened because the electrons are relatively more likely to react with positive ions than with neutrals, causing λ to decrease.

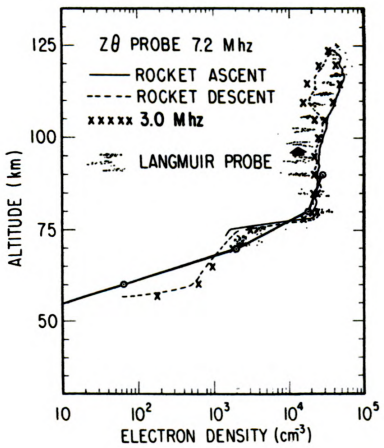

Figure 42-6. Nighttime Electron Concentrations Measured During a PCA by Ulwick and Sellers (1971) as Compared to Computations (Circles) by Swider et al (1971)

The chemistry of certain minor neutrals is of especial importance. Transport processes were not considered in this code, but their effect was included in a simple way. Ozone was set at constant values of $10^8\,cm^{-3}$ at 80 km, and $2 \times 10^7\,cm^{-3}$ at 90 km (cf. Shimazaki and Laird, 1970). This is not important in the sense that O_3 at these altitudes does not interact appreciably with the charged-particle chemistry. Photoequilibrium solutions were obtained for O_3 at the lower altitudes, which appears to be reasonable. They did not change significantly with P_o. The computed $O_2(^1\Delta)$ distribution also appears to be satisfactory. The noontime 1.27μ emission from $O_2(^1\Delta)$ is approximately 28 MR. This is in good agreement with the experimental data (Evans and Llewllyn, 1970; Haslett et al, 1969).

Atomic oxygen was set at $5 \times 10^{10}\,cm^{-3}$ at 80 km, and $5 \times 10^{11}\,cm^{-3}$ at 90 km (Shimazaki and Laird, 1970). At 90 km this is certainly reasonable and more than enough to inhibit negative ion formation via the destruction (reactions 5 and 9) of the few O_2^- and O^- ions produced through processes 10-14 (cf Fehsenfeld et al, 1967). The situation is more delicate at 80 km where O_2^- formation is much greater. However, it appears that even $[O] = 10^9\,cm^{-3}$ at 80 km would be sufficient to strongly inhibit negative ion formation; that is, $O_2^- + O \rightarrow O_3 + e$ would be the major O_2^- loss process as compared to $O_2^- + O_3 \rightarrow O_3^- + O_2$ and $O_2^- + O_2 + M \rightarrow O_4^- + M$, processes 9, 34, and 122, respectively. The photochemical values of [O] generated at the lower altitudes are comparable to similar calculations by others, unfortunately, there are no measurements. Like O_3, values for O appeared to be unaffected by the flux used. (Diurnal variations of O, O_3 and $O_2(^1\Delta)$ shall be provided later.)

We adopted $[NO] = [NO_2] = 10^{-7}[O_2]$ in these first set of computations for $z \leq 80$ km, using $2 \times 10^7\,cm^{-3}$ at 90 km. This appears to be reasonable for [NO] but too high for $[NO_2]$ in the daytime (Nicolet, 1965). Changes were made in later studies with $H_3O^+ \cdot (H_2O)_n$ chemistry. This high NO_2 concentration helped reduce daytime 30 MHz absorption results by providing for faster conversion of low affinity ions to higher affinity ions (reaction 33, for example. This artificial approach, however, cannot be supported by a physical argument. It was necessary to hold nitric oxide constant because otherwise the code's chemistry increased NO to the point where it was decreasing O_3 significantly (reaction 61) at the lower altitudes, in contradiction to the experimental information concerning ozone. Nitric oxide is not very important in these computations since it only provides for $O_2^+ + NO \rightarrow NO^+ + O_2$, NO^+ recombining with electrons about twice as fast as O_2^+. Nitric oxide does help convert CO_3^- to the more stable negative ion NO_3^- by means of reaction 45.

42-3 COMPUTATIONS INCLUDING O_2^+, O_4^+, $H_3O^+ \cdot (H_2O)_n$, n = 0-4, $NO^+ \cdot (H_2O)_n$, n = 0-3, e, O^-, O_2^-, O_3^-, O_4^-, CO_3^-, CO_4^-, NO_2^-, NO_3^- AS CHARGED SPECIES

Inclusion of 97 additional reactions and 11 new charged species was straightforward. However, while some results could be anticipated, there were a few surprises. It should be noted that for these computations a more acceptable arrangement (see Table 42-2) was adopted for NO and NO_2 (cf Nicolet, 1965; Shimazaki and Laird, 1970). The integral proton fluxes were increased by a factor of 10 in comparison to fluxes used in the work of the previous section. This was done to provide better agreement with the proton fluxes measured during the November, 1969 PCA event which roughly, from very preliminary data, seemed to suggest

Table 42-2. Distribution of NO and NO_2 Used in the Computations

Z(km)	NO		NO_2	
	day	night	day	night
90	3(7)cm^{-3}		1(0)cm^{-3}	
80	1.9(7)		1(1)	
70	6.6(7)		1(3)	5(6)
60	3.2(8)	1.0(6)	1(5)	3.2(8)
50	1.0(9)	1.0(1)	1(6)	1.0(9)
40	4.2(9)	1.0(0)	4.2(9)	4.2(9)

Notes: Read 3(7), for example, as 3×10^7.
NO(day) = $5 \times 10^{-8} \times$ [M] is based on Meira's (1971) measurements for Z ≤ 80 km.

something like (T < 20 MeV) $10^4 e^{-P/P_o}$ with $P_o \approx 50$ MV for the early, but not the initial stages of the event (see Figure 1 of Imhof et al, 1971). Besides considering a proton integral flux of $10^4 e^{-P/P_o}$ (P_o = 50 MV) protons $cm^{-2} sec^{-1} ster^{-1}$, we were able to complete computations for a case where P_o = 200 MV prior to this conference. In Appendix 42-B, detailed results are displayed for the P_o = 50 MV computation.

Values of α_{EFF} obtained for the two proton flux distributions are compared in Figure 42-7 with the values obtained previously (Figure 42-3) and a relationship deduced by Adams and Masley (1965). (Their original curve has been multiplied by 2.225 [Megill et al, 1971]). All our points join at 80 km since negative ions are unimportant at this altitude in our work, NO^+ and O_2^+ ions being the only

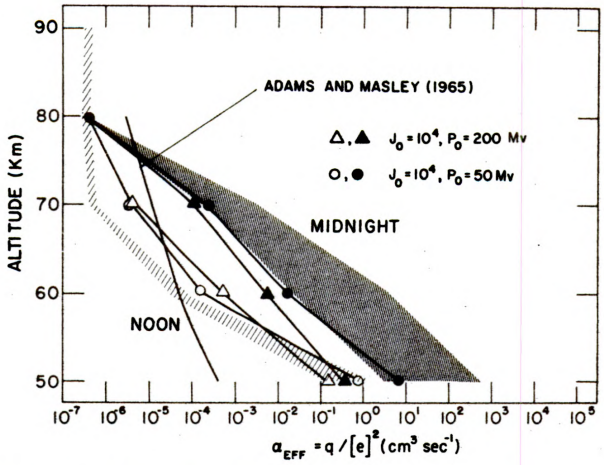

Figure 42-7. The Effective Loss Rate, $\alpha_{EFF} = q/[e]^2$ for Computations Including Oxonium Ions as Compared to Previous Computations (Figure 42-5) Without Them

important positive ions, in agreement with experiment (Narcisi et al, 1971). At night, we see the harder flux (higher production rate) has a lower value of α_{EFF}, as expected on the basis of our earlier remarks (also Swider et al, 1971). In the daytime, the fact that α_{EFF} is slightly lower is surprising. This may be attributable to a depletion of the neutral atomic oxygen concentration, which will be discussed.

Agreement with the relationship of Adams and Masley (1965) is fair except below 60 km. The somewhat high value they obtained at 80 km, about 3×10^{-6} cm^{-3} sec^{-1}, appears to be questionable, as well as newer results by Megill et al (1971). The mass-spectrometer data (Narcisi et al, 1971) indicate that only NO^+ and O_2^+ are important ions at 80 km during a PCA event. Therefore, at 80 km the bounds $\alpha(O_2^+) \leq \alpha_{EFF} \leq \alpha(NO^+)$ must hold. Note that $\alpha(O_2^+) \simeq 3 \times 10^{-7}$ cm^3 sec^{-1} and $\alpha(NO^+) \simeq 7 \times 10^{-7}$ cm^3 sec^{-1} near 200°K (Biondi, 1969).

The ratio of negative ions to electrons is depicted in Figure 42-8 along with the ratios previously obtained (Figure 42-4). Again, as expected, we find λ ($z \leq$ 75 km, at night) decreases as production increases. In the daytime, the slight reversal, an increase of λ with the production rate, apparently may be related to a decline in atomic oxygen.

The change in ozone and atomic oxygen for these PCA calculations is illustrated in Figure 42-9. The change appears to have been induced by the recombination of $H_3O^+ \cdot (H_2O)_n$ ions with electrons and the subsequent increase in HO_2 and OH. The increase in these latter two species varied from less than a factor of 2 to 4.

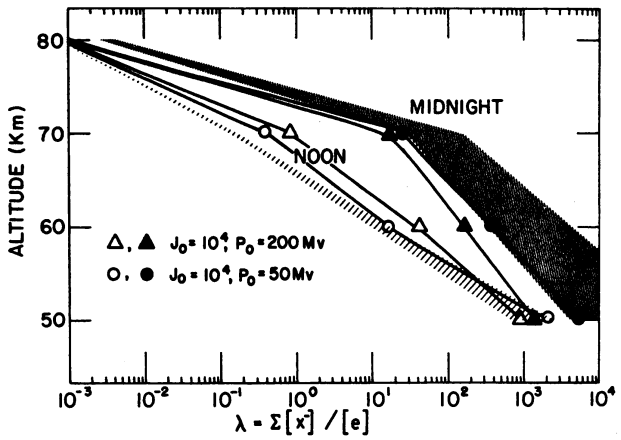

Figure 42-8. The Ratio of Negative Ions to Electrons for Computations Including Oxonium Ions as Compared to Previous Computations (Figure 42-4) Without Them

Both act to deplete O. A reduction in O forces a reduction in O_3 since the source of O_3 at these altitudes is mainly reaction 51. It is interesting that Weeks et al (1971) report a decrease in O_3 for the PCA event over quiet conditions. (Quiet conditions in Figure 42-9 represent a computation performed with only the normal quiet D-region ionization sources.) It should be noted that in this code

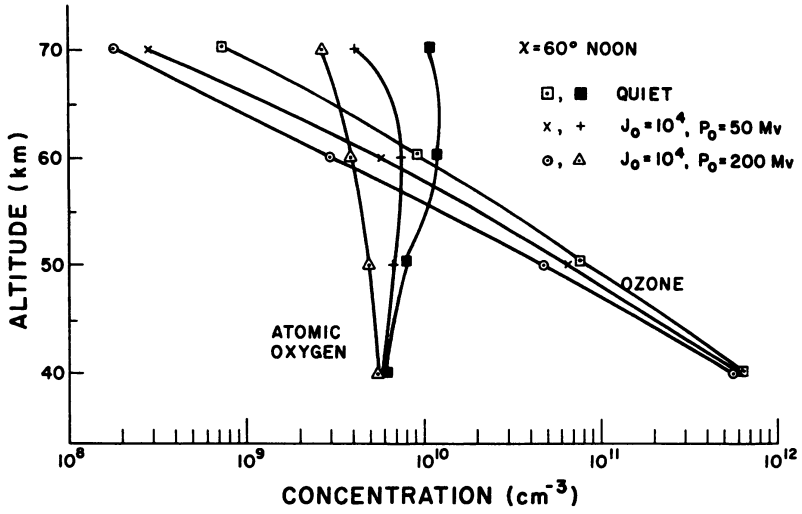

Figure 42-9. The Computed Noontime Distributions of Atomic Oxygen and Ozone for Two PCA Events as Compared to Quiet Conditions

we have used an upper limit for the reaction rate for $OH + O_3 \rightarrow HO_2 + O_2$ (reaction 70). The rate coefficient may be a factor of 10^3 less (Langley and McGrath, 1971). Without new calculations, we hesitate to estimate what would happen if a lower rate coefficient is used. In any case, it is clear that an enhancement of $H_3O^+ \cdot (H_2O)_n$ ions will increase the production rate of H atoms via the dissociative recombination processes (reactions 117-121). No change in O_3 or O of any consequence was observed for the earlier computations which did not include oxonium ions.

The role of photo-detachment and atomic oxygen is illustrated in Figure 42-10. The sudden jump in the electron concentration near $\chi = 98°$ is a detachment effect primarily as a result of reaction 1, $O_2^- + h\nu \rightarrow O_2 + e$. Detailed computations show that at $\chi = 97.45°$, the rate at which electrons are being produced by this process is 2.39×10^2 cm^{-3} sec^{-1} with reaction 9, $O_2^- + O \rightarrow O_3 + e$, yielding 1.26×10^1 electrons cm^3 sec^{-1} as the second most productive electron source, not including the ionization production rate, 1.56×10^3 cm^{-3} sec^{-1}. At $\chi = 89.78°$, the next time detailed computations are available, the electron yield of processes 1 and 9 are about equal, 8.47×10^2 cm^{-3} sec^{-1} and 8.72×10^2 cm^{-3} sec^{-1}, respectively. According to the rate coefficients used (Appendix 42-A), the yields of these reactions will be equal when $[O] = 1.1 \times 10^9$ cm^{-3}. The initial rise in electrons thus appears to be a result of photo-detachment, associative detachment becoming important (Figure 42-10) near about $\chi = 93°$ when sufficient O is present. However, atomic oxygen also acts to reduce the more complicated ions to simpler species; for example, $O + CO_3^- \rightarrow O_2^- + CO_2$, which are subject to detachment processes. The initial rise of atomic oxygen is a result of the photo-dissociation of O_3 by visible light. Photo-dissociation of O_3 in

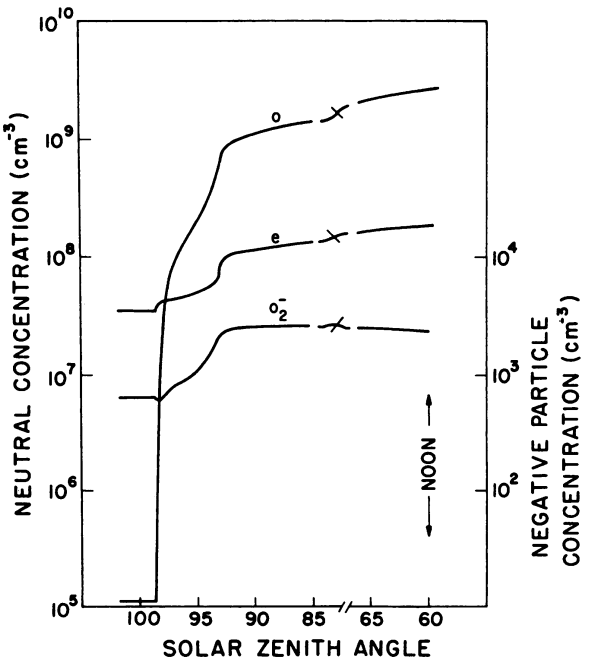

Figure 42-10. The Computed Variation in the Electron, O_2^- and O Concentrations at Sunrise for a PCA Event

the UV becomes more important for $\chi \leq 94°$. At sunset, the finite lifetime of atomic oxygen, about 20 min at 70 km, will contribute to [e] being somewhat larger, for the same χ, at sunset than at sunrise (see also Adams and Megill, 1967), contributing to a sort of hysteresis loop for [e] vs χ.

Figures 42-11 - 42-14 illustrate the relative distribution of the major positive and negative species at noon and midnight for the case $J = 10^4 e^{-P/50MV}$ protons $cm^{-2} sec^{-1} ster^{-1}$. Comparison of Figures 42-11 and 42-12 leads to the conclusion

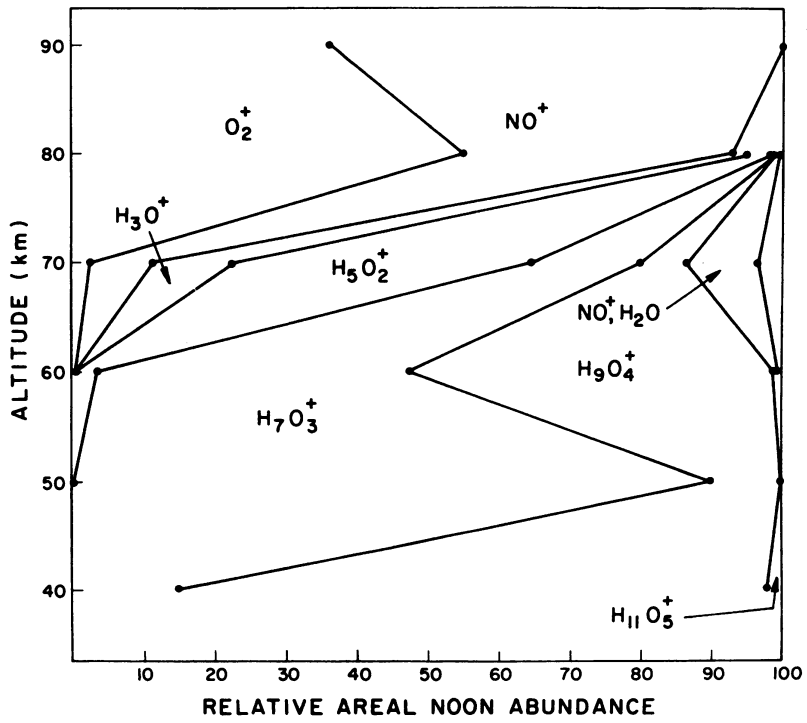

Figure 42-11. Relative Distribution of Positive Ions for Daytime PCA Conditions

that in this work the positive ions are in thermodynamic equilibrium below about 60 km since there is no substantial change between day and night. The change in the negative ion populations between day and night (Figures 42-13 and 42-14) may be linked to changes in O, NO and NO_2.

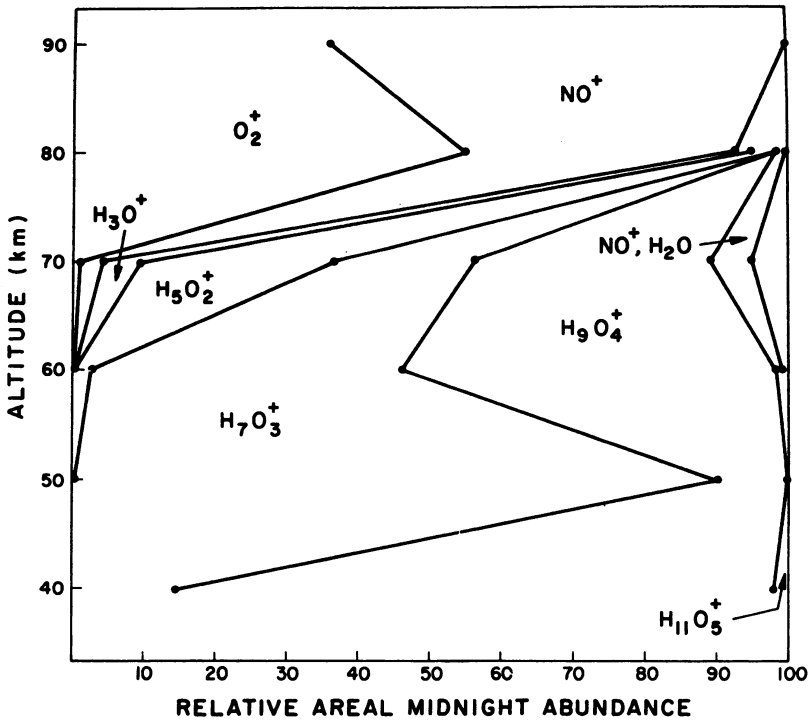

Figure 42-12. Relative Distribution of Positive Ions for Nighttime PCA Conditions

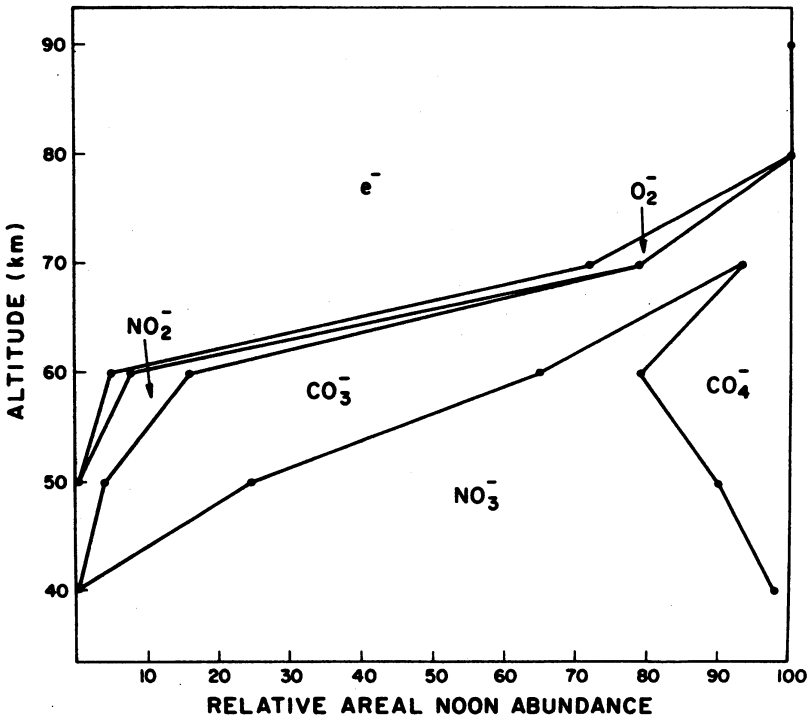

Figure 42-13. Relative Distribution of Negative Particles for Daytime PCA Conditions

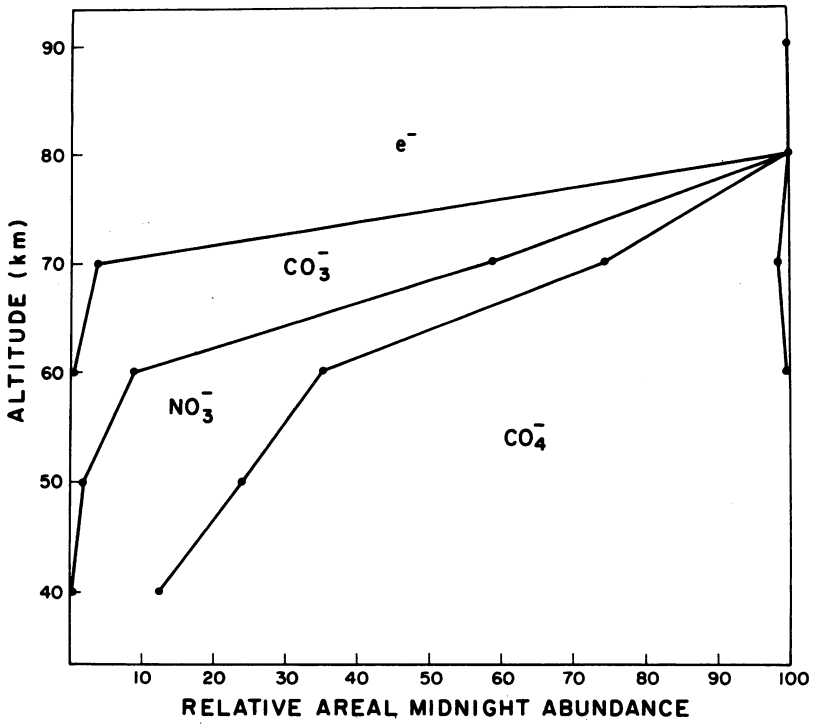

Figure 42-14. Relative Distribution of Negative Particles for Nighttime PCA Conditions

42-4 DISCUSSION AND CONCLUSIONS

We have seen that calculations which consider only NO^+ and O_2^+ as major positive ions result in electron density profiles which yield too much 30 MHz absorption by day as compared to the experimental results. On the other hand, such a computation yields fairly good results at night (Swider et al, 1971) because electron loss is primarily by attachment below 75 km and above this altitude NO^+ and O_2^+ are the dominant ions (Narcisi et al, 1971). Inclusion of $H_3O^+ \cdot (H_2O)_n$ (oxonium) ions leads to fewer electrons per unit ionization production rate since electrons combine more rapidly with oxonium ions than with O_2^+ and NO^+ ions (Biondi, 1971). The vertical 30 MHz absorption generated by the two computations performed with oxonium ions yielded noontime values of about 3.9 dB(P_o = 50 MV) and 5.6 dB(P_o = 200 MV). The proton fluxes above 10 MV were 640 (P_o = 50 MV) and 5030 (P_o = 200 MV) protons $cm^{-2}\,sec^{-1}\,ster^{-1}$ since $J = 10^4\, e^{-P/P_o}$ (see Table 42-1). The calculated absorption appears to agree well with the Juday and Adams (1969) relation for P_o = 50 but not for P_o = 200 where the calculated result is about a factor of two too low. The empirical α_{EFF} curve of Adams and Megill (1967) suggests that our electron loss is somewhat greater near 50 km (see Figure 42-7) than it should be. The experimental data (Ulwick et al, 1971) also appears to suggest that we have too few electrons near 50 km.

One possible explanation may be that further photo-detachment coefficients are needed. The present code considers photo-detachment of only O^-, O_2^-, O_3^- and NO_2^-. However, the major daytime negative ions in this work near 50 km (see Figure 42-13) are CO_3^-, NO_3^-, and CO_4^-. Only 1.22 eV is required to break CO_4^- into $e + O_2 + CO_2$ (Pack and Phelps, 1966); that is, wavelengths less than 10,200 Å, which includes the entire visible spectrum. The ions CO_3^- and more likely NO_3^- require more energy, but photo-detachment could still play some role. The problem is further complicated by the fact that some hydrates of these ions may exist and be quite important. In addition, other ions may exist. Arnold et al (1971) report an ion of 61 amu, possible HCO_3^-. This species might be created by the reaction $CO_4^- + OH \rightarrow HCO_3^- + O_2$, if exothermic.

One surprise of this work has been that the increased number of oxonium ions in the PCA leads to an increase in H as produced in the dissociative recombination processes. This excess hydrogen results in a depletion of O_3 and O. This may be the explanation for the O_3 profile measured by Weeks et al (1971) during the PCA event.

In conclusion, we believe that the distribution of electrons at night in a PCA is a function of a rather simplified chemistry. In the daytime, our results appear to suffer from fewer electrons in the 50-55 km region than indicated by the

experimental results. This may be a result of our lack of knowledge of the negative ion chemistry, particularly such information as photo-detachment rates for CO_4^-, CO_3^- and NO_3^-.

References

Adams, G.W., and Masley, A.J. (1965) Production rates and electron densities in the lower ionosphere due to solar cosmic rays, J. Atmos. Terr. Phys. 27:289-298.

Adams, G.W., and Megill, L.R. (1967) A two-ion D-region model for polar cap absorption events, Planet. Space Sci. 15:1111-1130.

Arnold, F., Kissel, J., Krankowsky, D., Wieder, H., and Zahringer, J. (1971) Negative ions in the lower ionosphere: A mass-spectrometric measurement, J. Atmos. Terr. Phys. 33:1169-1175.

Bailey, D.K. (1959) Abnormal ionization in the lower ionosphere associated with cosmic-ray flux enhancements, Proc. Inst. Radio Engrs 47:255-266.

Bailey, D.K. (1964) Polar-cap absorption, Planet. Space Sci. 12:495-541.

Biondi, M.A. (1969) Electron recombination and ion recombination, Canad. J. Chem. 47:1711-1719.

CIRA (1965) COSPAR International Reference Atmosphere 1965, N. Holland Pub. Co.

Crain, C.M. (1961) Ionization loss rates below 90 km, J. Geophys. Res. 66:1117-1126.

Deeks, D.G. (1966) Generalized full wave theory for energy-dependent collision frequencies, J. Atmos. Terr. Phys. 28:839-846.

Evans, W.F.J., and Llewellyn, E.J. (1970) Molecular oxygen emissions in the airglow, Ann. Geophys. 26:167-178.

Fehsenfeld, F.C., Schmeltekopf, A.L., Schiff, H.I., and Ferguson, E.E. (1967) Laboratory measurements of negative ion reactions of atmospheric interest, Planet. Space Sci. 15:373-379.

Fichtel, C.E., Guss, D.E., Malitson, H.H., McCracken, K.G., Ogilvie, K.W., and Webber, W.R. (1963) Solar Proton Manual NASA TR R-169.

Freier, P.S., and Webber, W.R. (1963) Exponential rigidity spectrums for solar-flare cosmic rays, J. Geophys. Res. 68:1605-1629.

References

George, J.D., Zimmerman, S.P., and Keneshea, T.J. (1972) The latitudinal variation of major and minor neutral species in the upper atmosphere, Space Res. 12:695-709.

Haslett, J.C., Megill, L.R., and Schiff, H.I. (1969) Rocket measurements of $O_2(^1\Delta g)$, Canad. J. Phys. 47:2351-2354.

Heisler, R., and Hower, G.L. (1970) Comparisons between calculated ionospheric absorption and riometer measurements, J. Atmos. Terr. Phys. 32:1755-1764.

Juday, R.D., and Adams, G.W. (1969) Riometer measurements, solar proton intensities and radiation dose rates, Planet. Space Sci. 17:1313-1319.

Langley, K.F., and McGrath, W.D. (1971) The ultra-violet photolysis of ozone in the presence of water vapor, Planet. Space Sci. 19:413-416.

Megill, L.R., Adams, G.W., Haslett, J.C., and Whipple, E.C. (1971) Measurement of the effective electron loss rates in the D region during polar cap absorption events, J. Geophys. Res. 76:4587-4595.

Meira, L.G. (1971) Rocket measurements of upper atmospheric nitric oxide and their consequences to the lower ionosphere, J. Geophys. Res. 76:202-212.

Narcisi, R.S., and Bailey, A.D. (1965) Mass spectrometric measurements of positive ions at altitudes from 64 to 112 kilometers, J. Geophys. Res. 70:3687-3700.

Narcisi, R.S., Philbrick, C.R., Thomas, D.M., Bailey, A.D., Wlodyka, L.E., Wlodyka, R.A., Baker, D., Federico, G., and Gardner, M.E. (1972) These proceedings.

Nicolet, M. (1965) Nitrogen oxides in the chemosphere, J. Geophys. Res. 70:679-689.

Reid, G.C. (1961) A study of the enhanced ionization produced by solar protons during a polar cap absorption event, J. Geophys. Res. 66:4071-4085.

Reid, G.C. (1967) Ionospheric implications of minor mesospheric constituents, Space Res. 7:197-211.

Reid, G.C. (1969) Associative detachment in the mesosphere and the diurnal variation of polar-cap absorption, Planet. Space Sci. 17:731-736.

Reid, G.C., and Sauer, H.H. (1967) The influence of the geomagnetic tail on low-energy cosmic-ray cutoffs, J. Geophys. Res. 72:197-208.

Shimazaki, T., and Laird, A.R. (1970) A model calculation of the diurnal variation in minor neutral constituents in the mesosphere and lower thermosphere including transport effects, J. Geophys. Res. 75:3221-3235.

Swider, W., and Gardner, M.E. (1971) Ionization rates due to the absorption of solar protons and alpha particles in the upper atmosphere, AFCRL-71-0059.

Swider, W., Narcisi, R.S., Keneshea, T.J., and Ulwick, J.C. (1971) Electron loss during a nighttime PCA event, J. Geophys. Res. 76:4691-4694.

Thrane, E.V., and Piggott, W.R. (1966) The collision frequency in the E- and D-regions of the ionosphere, J. Atmos. Terr. Phys. 28:721-737.

Ulwick, J.C., Baker, K.D., and Sellers, B. (1970) Rocket measurements in a PCA event, Space Res. 10:825-830.

Ulwick, J.C., and Sellers, B. (1971) Rocket measurements of production and ionization during a PCA event, Space Res. 11:1173-1179.

References

Weeks, L.H., Cuikay, R.S., and Corbin, J.R. (1972) Ozone measurements in the mesosphere during the solar event of 2 November 1969, these proceedings.

Whitten, R.C., Poppoff, I.G., Edmonds, R.S., and Berning, W.W. (1965) Effective recombination coefficients in the lower atmosphere, J. Geophys. Res. 70:1737-1742.

Appendix A

Reactions and Rate Coefficients Adopted in This Work

The reactions and rate coefficients used in this work are listed below, followed by the references cited. The letters D and ES represent two major reference sources (see below). The other letters represent comments:

PC - private communication

U - upper limit

L - lower limit

NA - not applicable because one of the reactants is not considered. In particular, N and $O(^1D)$ concentrations are zero in this code at all times. The atomic oxygen generated in all processes is considered to be in the ground state.

E - estimate; this symbol immediately indicates a reaction of interest not yet measured in the laboratory, at least not published up through about June 1970. Note that reference D may actually be an estimate, especially in the case of ion-ion recombination rate coefficients.

We are uncertain in regard to some of the reaction products; for example, for reaction 145, HNO_3 may be a product rather than $OH + NO_2$ and for reaction 148, HNO_2 may be a product rather than $H + NO_2$. This is not a trivial point since such processes may be important in the fixation of nitrogen in lightning discharges and following nuclear weapons test, in addition to the processes suggested by Ferguson and Libby (1971). Some products are written for convenience; for example, in reaction 172 the products $2NO_2 + H_2O$ may rather be $NO + NO_3 + H_2O$. But, NO_3

is not included in the computations as a species. Certain reactions have been omitted because they are of minor importance; for example, $NO^+ \cdot H_2O + CO_4^- \rightarrow$?. The process is not a major one for either species.

Three-body reactions are in units of $cm^6\ sec^{-1}$; $cm^3\ sec^{-1}$ for two-body processes. Photon processes 1-4, 83-92, 96 and 106 are in units of sec^{-1}. Specific rates for reactions 83-92 cannot be given because they are complicated functions (see Keneshea, 1969). Read (-x) as 10^{-x}.

Reaction	Rate/Rate Coefficient	References/ Comments
1. $O_2^- + h\nu \rightarrow O_2 + e$	0.33	D
2. $O^- + h\nu \rightarrow O + e$	1.4	D
3. $NO_2^- + h\nu \rightarrow NO_2 + e$	4(-2)	D
4. $O_3^- + h\nu \rightarrow O_3 + e$	6(-2)	D
5. $O^- + O \rightarrow O_2 + e$	1.4(-10)	D
6. $O^- + N \rightarrow NO + e$	1.6(-10)	NA
7. $O^- + NO \rightarrow NO_2 + e$	2.0(-10)	D
8. $O_2^- + N \rightarrow NO_2 + e$	3.0(-10)	NA
9. $O_2^- + O \rightarrow O_3 + e$	2.5(-10)	D
10. $O + e \rightarrow O^- + h\nu$	1.3(-15)	D
11. $O_2 + e \rightarrow O_2^- + h\nu$	2.0(-19)	D
12. $O_3 + e \rightarrow O^- + O_2$	3.0(-12)	D
13. $O_2 + O_2 + e \rightarrow O_2^- + O_2$	$1.4(-29)(300/T)e^{-600/T}$	D
14. $O_2 + e + N_2 \rightarrow O_2^- + N_2$	1.0(-31)	D
15. $O_2^+ + e \rightarrow O + O$	2.0(-7)(300/T)	Biondi (1969)
16. $NO^+ + e \rightarrow N + O$	4.0(-7)(300/T)	Biondi (1969)
17. $N_2^+ e \rightarrow N + N$	3.0(-7)	Biondi (1969)
18. $O^- + NO^+ \rightarrow O + NO$	2.0(-7)(300/T)	D
19. $O_2^- + NO^+ \rightarrow O_2 + NO$	2.0(-7)(300/T)	D
20. $O_3^- + NO^+ \rightarrow O_3 + NO$	2.0(-7)(300/T)	D
21. $NO_2^- + NO^+ \rightarrow NO_2 + NO$	2.0(-7)(300/T)	D
22. $NO_3^- + NO^+ \rightarrow NO_2 + NO_2$	2.0(-7)(300/T)	E
23. $CO_3^- + NO^+ \rightarrow CO_2 + NO_2$	2.0(-7)(300/T)	E

Reaction	Rate/Rate Coefficient	References/ Comments
24. $O^+ + O_2 \rightarrow O + O_2^+$	$2(-11)(300/T)^{0.5}$	Smith and Fouracre (1968)
25. $O^+ + NO \rightarrow O + NO^+$	2.4(-11)	D
26. $O_2^+ + NO \rightarrow O_2 + NO^+$	6(-10)	Fehsenfeld et al (1970)
27. $N_2^+ + O \rightarrow N_2 + O^+$	1(-12)	D
28. $N_2^+ + O_2 \rightarrow N_2 + O_2^+$	5(-11)(300/T)	Dunkin et al (1968)
29. $N_2^+ + NO \rightarrow N_2 + NO^+$	5(-10)	D
30. $O^- + NO_2 \rightarrow O + NO_2^-$	1.2(-9)	D
31. $O^- + O_3 \rightarrow O + O_3^-$	5.3(-10)	D
32. $O_2^- + O \rightarrow O_2 + O^-$	1.0(-11)	D
33. $O_2^- + NO_2 \rightarrow O_2 + NO_2^-$	8.0(-10)	ES
34. $O_2^- + O_3 \rightarrow O_2 + O_3^-$	4.0(-10)	D
35. $O_3^- + NO_2 \rightarrow NO_3^- + O_2$	2.0(-10)	ES (products uncertain)
36. $O^+ + N_2 \rightarrow NO^+ + N$	$1.2(-12)(300/T)^{0.5}$	Dunkin et al, (1968)
37. $O^+ + NO \rightarrow O_2^+ + N$	3(-12)	D
38. $O_2^+ + N \rightarrow NO^+ + O$	1.8(-10)	NA
39. $O_2^+ + N_2 \rightarrow NO^+ + NO$	1(-19)	E
40. $O_2^+ + NO_2 \rightarrow NO^+ + O_3$	1(-11)	D
41. $N_2^+ + O \rightarrow NO^+ + N$	1.5(-10)	Fehsenfeld et al (1970)
42. $O_3^- + O \rightarrow O_2^- + O_2$	1(-10)	D, E
43. $O_3^- + CO_2 \rightarrow CO_3^- + O_2$	4(-10)	D
44. $CO_3^- + O \rightarrow O_2^- + CO_2$	8(-11)	D
45. $CO_3^- + NO \rightarrow NO_2^- + CO_2$	9(-12)	D
46. $O_3^- + NO \rightarrow NO_3^- + O$	1(-11)	D
47. $NO_3^- + O \rightarrow NO_2^- + O_2$	1(-11)	D, U
48. $N + O_3 \rightarrow O_2 + NO$	5.7(-13)	Schofield (1967)
49. $O + NO \rightarrow NO_2 + h\nu$	6.2(-17)	D
50. $O + O + M \rightarrow O_2 + M$	$3(-33)(300/T)^{2.9}$	D
51. $O + O_2 + M \rightarrow O_3 + M$	$5.5(-34)(300/T)^{2.6}$	D

Reaction	Rate/Rate Coefficient	References/ Comments
52. $N + O + M \rightarrow NO + M$	$1.1(-32)(300/T)^{0.5}$	D
53. $O + NO + M \rightarrow NO_2 + M$	$3.8(-33)e^{935/T}$	HTRRD No. 5
54. $O + NO_2 \rightarrow NO + O_2$	$3.2(-11)e^{-530/T}$	Schofield (1968)
55. $O + O_3 \rightarrow O_2 + O_2$	$1.2(-11)e^{-2000/T}$	Schiff (1969)
56. $N + O_2 \rightarrow NO + O$	$1.3(-12)(T/300)^{1.5}e^{-2842/T}$	NA
57. $N + NO \rightarrow N_2 + O$	$5.1(-11)e^{-167/T}$	NA
58. $N + NO_2 \rightarrow NO + NO$	$3(-12)$	NA
59. $N + NO_2 \rightarrow N_2 + O_2$	$1.5(-11)$	NA
60. $N + NO_2 \rightarrow N_2O + O$	$1.5(-13)$	NA
61. $NO + O_3 \rightarrow NO_2 + O_2$	$1.7(-12)e^{-1310/T}$	Schofield (1967)
62. $H + O_2 + M \rightarrow NO_2 + M$	$5(-32)(300/T)^2$	Kaufman (1969)
63. $H + OH + M \rightarrow H_2O + M$	$2.5(-31)$	Kaufman (1969)
64. $H + H + M \rightarrow H_2 + M$	$2.6(-32)$	Larkin-Thrush (1964)
65. $O + OH + M \rightarrow HO_2 + M$	$1.4(-31)$	Petersen and Kretschmer (1960)
66. $O(^1D) + O_3 \rightarrow O_2 + O_2$	$7(-12)$	NA
67. $O(^1D) + M \rightarrow O(^3P) + M$	$5(-11)$	NA
68. $H + O_3 \rightarrow OH + O_2$	$2.6(-11)$	Kaufman (1969)
69. $OH + O \rightarrow H + O_2$	$5(-11)$	Kaufman (1969)
70. $OH + O_3 \rightarrow HO_2 + O_2$	$5(-13)$	Kaufman (1969), U
71. $OH + OH \rightarrow H_2O + O$	$2(-12)$	Westenberg et al (1965)
72. $OH + HO_2 \rightarrow H_2O + O_2$	$1(-11)$	Kaufman (1969), L
73. $H + HO_2 \rightarrow H_2 + O_2$	$3(-12)$	Kaufman (1969), L
74. $H + HO_2 \rightarrow OH + OH$	$1(-11)$	Kaufman (1969), L
75. $O + HO_2 \rightarrow OH + O_2$	$1(-11)$	Kaufman (1969), L
76. $HO_2 + HO_2 \rightarrow H_2O_2 + O_2$	$3(-12)$	Kaufman (1969), L
77. $OH + H_2O_2 \rightarrow H_2O + HO_2$	$1.7(-11)e^{-900/T}$	HTRRD No. 3
78. $O + H_2O_2 \rightarrow OH + HO_2$	$4(-15)$	Foner and Hudson (1962)
79. $H + H_2O_2 \rightarrow H_2 + HO_2$	$3.9(-11)e^{-4600/T}$	HTRRD No. 3

Reaction	Rate/Rate Coefficient	References/ Comments
80. $O(^1D) + H_2 \rightarrow H + OH$	1(-11)	NA
81. $O(^1D) + H_2O \rightarrow OH + OH$	1(-11)	NA
82. $HO_2 + O_3 \rightarrow OH + O_2 + O_2$	1(-14)	E
83. $O_2 + h\nu \rightarrow O + O$	$1750 < \lambda < 2424$ Å	
84. $O_2 + h\nu \rightarrow O_2 + O(^1D)$	$\lambda < 1750$	
85. $O_3 + h\nu \rightarrow O_2 + O$	$3100 < \lambda < 11,800$ Å	
86. $O_3 + h\nu \rightarrow O_2(^1\Delta) + O(^1D)$	$\lambda < 3100$ Å	
87. $NO + h\nu \rightarrow N + O$	6(-8)	
88. $NO_2 + h\nu \rightarrow NO + O$	3(-3)	
89. $N_2O + h\nu \rightarrow N_2 + O$	4.08(-7)	
90. $N_2O + h\nu \rightarrow N + NO$	5.58(-8)	
91. $H_2O + h\nu \rightarrow OH + O$	$\lambda < 2390$ Å	
92. $H_2O_2 + h\nu \rightarrow OH + OH$	$\lambda < 5650$ Å	
93. $NO_2^- + O_3 \rightarrow NO_3^- + O_2$	1.8(-11)	D
94. $O_3 + O_2(^1\Delta) \rightarrow O_3 + O_2$	3(-15)	Crutzen et al (1971)
95. $M + O_2(^1\Delta) \rightarrow O_2 + M$	4.4(-19)	Crutzen et al (1971)
96. $O_2(^1\Delta) \rightarrow O_2 + h\nu$	2.58(-4)	Badger et al (1965)
97. $O_2^+ + O_2 + M \rightarrow O_4^+ + M$	2.4(-30)	Good et al (1971)
98. $O_4^+ + O_2(^1\Delta) \rightarrow O_2^+ + O_2 + O_2$	1(-10)	E
99. $O_2^- + O_2(^1\Delta) \rightarrow O_2 + O_2 + e$	2(-10)	Fehsenfeld et al (1969a)
100. $O^- + O_2(^1\Delta) \rightarrow O_3 + e$	3(-10)	Fehsenfeld et al (1969a)
101. $O_4^+ + O \rightarrow O_2^+ + O_3$	~5(-10)	E - Ferguson
102. $O_2^+ + H_2O + M \rightarrow O_2^+ \cdot H_2O + M$	1(-27)	E
103. $CO_3^- + NO_2 \rightarrow NO_3^- + CO_2$	8(-11)	D
104. $H_9O_4^+ + CO_4^- \rightarrow 4H_2O + CO_2 + HO_2$	2(-7)	E
105. $H_{11}O_4^+ + CO_4^- \rightarrow 5H_2O + CO_2 + HO_2$	2(-7)	E
106. $HO_2 + h\nu \rightarrow OH + O$	1.2(-4)	E - Hunt (1966)
107. $O_4^+ + H_2O \rightarrow O_2^+ \cdot H_2O + O_2$	1.3(-9)	Good et al (1970b)

Reaction	Rate/Rate Coefficient	References/ Comments
108. $O_2^+ \cdot H_2O + H_2O \rightarrow H_3O^+ \cdot OH + O_2$	9(-10)	Good et al (1970b)
109. $O_2^+ \cdot H_2O + H_2O \rightarrow H_3O^+ + OH + O_2$	3(-10)	Good et al (1970b)
110. $H_3O^+ \cdot OH + H_2O \rightarrow H_5O_2^+ + OH$	1.2(-9)	Good et al (1970b)
111. $H_3O^+ + H_2O + M \rightarrow H_5O_2^+ + M$	3.5(-27)	Good et al (1970a, b)
112. $H_5O_2^+ + H_2O + M \rightarrow H_7O_3^+ + M$	2.2(-27)	Good et al (1970a, b)
113. $H_7O_3^+ + H_2O + M \rightarrow H_9O_4^+ + M$	2.3(-27)	Good et al (1970a, b)
114. $H_9O_4^+ + M \rightarrow H_7O_3^+ + H_2O + M$	$5(-2)e^{-8358/T}$	E from Kebarle et al (1967)
115. $H_9O_4^+ + H_2O + M \rightarrow H_{11}O_5^+ + M$	1(-27)	Good et al (1970a, b)
116. $H_{11}O_5^+ + M \rightarrow H_9O_4^+ + H_2O + M$	$4(-1)e^{-7668/T}$	E from Kebarle et al (1967)
117. $H_3O^+ + e \rightarrow H_2O + H$	~1.5(-6)	PC Biondi (1970)
118. $H_5O_2^+ + e \rightarrow 2H_2O + H$	~3(-6)	PC Biondi (1970)
119. $H_7O_3^+ + e \rightarrow 3H_2O + H$	~4.5(-6)	PC Biondi (1970)
120. $H_9O_4^+ + e \rightarrow 4H_2O + H$	6(-6)	E
121. $H_{11}O_4^+ + e \rightarrow 5H_2O + H$	7.5(-6)	E
122. $O_2^- + O_2 + M \rightarrow O_4^- + M$	1(-30)	E Ferguson (1970)
123. $O_4^- + O \rightarrow O_3^- + O_2$	3(-10)	Fehsenfeld et al (1969a)
124. $O_4^- + O \rightarrow O^- + O_2 + O_2$	1(-10)	E
125. $O_4^- + CO_2 \rightarrow CO_4^- + O_2$	4.3(-10)	Fehsenfeld et al (1969a)
126. $CO_4^- + NO \rightarrow NO_3^- + CO_2$	4.8(-11)	Fehsenfeld et al (1969a)
127. $CO_4^- + O \rightarrow CO_3^- + O_2$	~1(-10)	PC Ferguson (1971)
128. $CO_4^- + O \rightarrow O_3^- + CO_2$	~5(-11)	PC Ferguson (1971)
129. $H_3O^+ + O_2^- \rightarrow H_2O + HO_2$	2(-7)	E
130. $H_3O^+ + NO_2^- \rightarrow H_2O + H + NO_2$	2(-7)	E
131. $H_3O^+ + O^- \rightarrow H_2O + OH$	2(-7)	E
132. $H_3O^+ + O_3^- \rightarrow H_2O + OH + O_2$	2(-7)	E
133. $H_3O^+ + NO_3^- \rightarrow H_2O + OH + NO_2$	2(-7)	E
134. $H_3O^+ + CO_3^- \rightarrow H_2O + OH + CO_2$	2(-7)	E
135. $H_5O_2^+ + O_2^- \rightarrow 2H_2O + HO_2$	2(-7)	E

Reaction	Rate/Rate Coefficient	References/ Comments
136. $H_5O_2^+ + NO_2^- \rightarrow 2H_2O + H + NO_2$	2(-7)	E
137. $H_5O_2^+ + O^- \rightarrow 2H_2O + OH$	2(-7)	E
138. $H_5O_2^+ + O_3^- \rightarrow 2H_2O + OH + O_2$	2(-7)	E
139. $H_5O_2^+ + NO_3^- \rightarrow 2H_2O + OH + NO_2$	2(-7)	E
140. $H_5O_2^+ + CO_3^- \rightarrow 2H_2O + OH + CO_2$	2(-7)	E
141. $H_7O_3^+ + O_2^- \rightarrow 3H_2O + HO_2$	2(-7)	E
142. $H_7O_3^+ + NO_2^- \rightarrow 3H_2O + H + NO_2$	2(-7)	E
143. $H_7O_3^+ + O^- \rightarrow 3H_2O + OH$	2(-7)	E
144. $H_7O_3^+ + O_3^- \rightarrow 3H_2O + OH + O_2$	2(-7)	E
145. $H_7O_3^+ + NO_3^- \rightarrow 3H_2O + OH + NO_2$	2(-7)	E
146. $H_7O_3^+ + CO_3^- \rightarrow 3H_2O + OH + CO_2$	2(-7)	E
147. $H_9O_4^+ + O_2^- \rightarrow 4H_2O + HO_2$	2(-7)	E
148. $H_9O_4^+ + NO_2^- \rightarrow 4H_2O + H + NO_2$	2(-7)	E
149. $H_9O_4^+ + O^- \rightarrow 4H_2O + OH$	2(-7)	E
150. $H_9O_4^+ + O_3^- \rightarrow 4H_2O + OH + O_2$	2(-7)	E
151. $H_9O_4^+ + NO_3^- \rightarrow 4H_2O + OH + NO_2$	2(-7)	E
152. $H_9O_4^+ + CO_3^- \rightarrow 4H_2O + OH + CO_2$	2(-7)	E
153. $H_{11}O_5^+ + O_2^- \rightarrow 5H_2O + HO_2$	2(-7)	E
154. $H_{11}O_5^+ + NO_2^- \rightarrow 5H_2O + H + NO_2$	2(-7)	E
155. $H_{11}O_5^+ + O^- \rightarrow 5H_2O + OH$	2(-7)	E
156. $H_{11}O_5^+ + O_3^- \rightarrow 5H_2O + OH + O_2$	2(-7)	E
157. $H_{11}O_5^+ + NO_3^- \rightarrow 5H_2O + OH + NO_2$	2(-7)	E
158. $H_{11}O_5^+ + CO_3^- \rightarrow 5H_2O + OH + CO_2$	2(-7)	E
159. $NO^+ + CO_2 + M \rightarrow NO^+ \cdot CO_2 + M$	2.5(-29)	Dunkin et al (1971)
160. $NO^+ \cdot CO_2 + H_2O \rightarrow NO^+ \cdot H_2O + CO_2$	~5(-10)	Dunkin et al (1971)
161. $NO^+ + H_2O + M \rightarrow NO^+ \cdot H_2O + M$	1(-27)	E
162. $NO^+ \cdot H_2O + H_2O + M \rightarrow NO^+ \cdot (H_2O)_2 + M$	~1(-27)	Puckett and Teague (1971)
163. $NO^+ \cdot (H_2O)_2 + H_2O + M \rightarrow NO^+ \cdot (H_2O)_3 + M$	~1(-27)	Puckett and Teague (1971)

Reaction	Rate/Rate Coefficient	References/ Comments
164. $NO^+ \cdot (H_2O)_3 + H_2O \rightarrow H_7O_3^+ + HNO_2$	7(-11)	Puckett and Teague (1971)
165. $NO^+ \cdot (H_2O) + e \rightarrow NO + H_2O$	1.5(-6)	E
166. $NO^+ \cdot (H_2O) + e \rightarrow NO + 2H_2O$	3(-6)	E
167. $NO^+ \cdot (H_2O)_3 + e \rightarrow NO + 3H_2O$	4.5(-6)	E
168. $NO^+ \cdot H_2O + O_2^- \rightarrow NO + H_2O + O_2$	2(-7)	E
169. $NO^+ \cdot H_2O + O^- \rightarrow NO + H_2O + O$	2(-7)	E
170. $NO^+ \cdot H_2O + O_3^- \rightarrow NO + H_2O + O_3$	2(-7)	E
171. $NO^+ \cdot H_2O + NO_2^- \rightarrow NO + H_2O_2 + NO_2$	2(-7)	E
172. $NO^+ \cdot H_2O + NO_3^- \rightarrow NO_2 + H_2O + NO_2$	2(-7)	E
173. $NO^+ \cdot H_2O + CO_3^- \rightarrow NO_2 + H_2O + CO_2$	2(-7)	E
174. $NO^+ \cdot (H_2O)_2 + O_2^- \rightarrow NO + 2H_2O + O_2$	2(-7)	E
175. $NO^+ \cdot (H_2O)_2 + O^- \rightarrow NO + 2H_2O + O$	2(-7)	E
176. $NO^+ \cdot (H_2O)_2 + O_3^- \rightarrow NO + 2H_2O + O_3$	2(-7)	E
177. $NO^+ \cdot (H_2O)_2 + NO_2^- \rightarrow NO + 2H_2O + NO_2$	2(-7)	
178. $NO^+ \cdot (H_2O)_2 + NO_3^- \rightarrow NO_2 + 2H_2O + NO_2$	2(-7)	E
179. $NO^+ \cdot (H_2O)_2 + CO_3^- \rightarrow NO_2 + 2H_2O + CO_2$	2(-7)	E
180. $NO^+ \cdot (H_2O)_3 + O_2^- \rightarrow NO + 3H_2O + O_2$	2(-7)	E
181. $NO^+ \cdot (H_2O)_3 + O^- \rightarrow NO + 3H_2O + O$	2(-7)	E
182. $NO^+ \cdot (H_2O)_3 + O_3^- \rightarrow NO + 3H_2O + O_3$	2(-7)	E
183. $NO^+ \cdot (H_2O)_3 + NO_2^- \rightarrow NO + 3H_2O + NO_2$	2(-7)	E
184. $NO^+ \cdot (H_2O)_3 + NO_3^- \rightarrow NO_2 + 3H_2O + NO_2$	2(-7)	E
185. $NO^+ \cdot (H_2O)_3 + CO_3^- \rightarrow NO_2 + 3H_2O + CO_2$	2(-7)	E
186. $H_3O^+ + CO_4^- \rightarrow H_2O + CO_2 + HO_2$	2(-7)	E
187. $H_5O_2^+ + CO_4^- \rightarrow 2H_2O + CO_2 + HO_2$	2(-7)	E
188. $H_7O_2^+ + CO_4^- \rightarrow 3H_2O + CO_2 + HO_2$	2(-7)	E
189. $H_7O_3^+ + M \rightarrow H_5O_2^+ + H_2O + M$	$5.5(-2)e^{-10,960/T}$	E from Kebarle et al (1967)
190. $O + H_2 \rightarrow OH + H$	$7(-11)e^{-5100/T}$	Wong and Potter (1965)
191. $H + H_2O_2 \rightarrow H_2O + OH$	$5.3(-10)e^{-4500/T}$	HTRRD No. 3

Reaction	Rate/Rate Coefficient	References/ Comments
192. $O_4^+ + e \rightarrow O_2 + O_2$	2.3(-6)	Kasner and Biondi (1968)
193. $O^- + O_2 + O_2 \rightarrow O_3^- + O_2$	9.0(-31)	Burch and Geballe (1957)
194. $O_4^- + NO \rightarrow NO_3^- + O_2$	2.5(-10)	Fehsenfeld et al (1969b)
195. $O_2^- + CO_2 + O_2 \rightarrow CO_4^- + O_2$	2.0(-29)	PC Ferguson (1971)

References

Badger, R. M., Wright, A. C., and Whitlock, R. F. (1965) J. Chem. Phys. 43:4345.

Biondi, M. A. (1969) Canad. J. Chem. 47:1711.

Burch, D. S., and Geballe, R. (1957) Phys. Rev. 106:183.

Crutzen, P. J., Jones, I. T. N., and Wayne, R. P. (1971) J. Geophys. Res. 76:1490.

D-DASA (1967) Reaction Rate Handbook.

Dunkin, D. B., Fehsenfeld, F. C., Schmeltekopf, A. L., and Ferguson, E. E. (1968) J. Chem. Phys. 49:1365.

Dunkin, D. B., Fehsenfeld, F. C., Schmeltekopf, A. L., and Ferguson, E. E. (1971) J. Chem. Phys. 54:3817.

ES-ESSA, Fehsenfeld, F. C., Schmeltekopf, A. L., Dunkin, D. B., and Ferguson, E. E. (1969) Tech. Rpt ERL 135-AL 3.

Fehsenfeld, F. C., Abritton, D. L., Burt, J. A., and Schiff, H. I. (1969a) Canad. J. Chem. 47:1793.

Fehsenfeld, F. C., Ferguson, E. E., and Bohme, D. K. (1969b) Planet. Space Sci. 17:1759.

Fehsenfeld, F. C., Dunkin, D. B., and Ferguson, E. E. (1970) Planet. Space Sci. 18:1267.

Ferguson, E. E. (1970) Ann. Geophys. 26:589.

Ferguson, E. E., and Libby, W. F. (1971) Nature 229:37.

Foner, S. N., and Hudson, R. L. (1962) J. Chem. Phys. 36:2681.

Good, A., Durden, D. A., and Kebarle, P. (1970a) J. Chem. Phys. 52:212.

Good, A., Durden, D. A., and Kebarle, P. (1970b) J. Chem. Phys. 52:222.

HTRRD, High Temperature Reaction Rate Data, Dept. Phys. Chem., The University, Leeds, England; No. 3, April 1969; No. 4, December 1969; No. 5, July 1970.

Hunt, B. G. (1966) J. Geophys. Res. 71:1385.

References

Kasner, W.H., and Biondi, M.A. (1968) Phys. Rev. 174:139.

Kaufman, F. (1969) Canad. J. Chem. 47:1917.

Kebarle, P., Searles, S.K., Zolla, A., Scarborough, J., and Arshadi, M. (1967) J. Amer. Chem. Soc. 89:6393.

Keneshea, T.J. (1969) Aeronomy Rpt No. 32, Univ. of Illinois, p. 400.

Larkin, F.S., and Thrush, B.A. (1964) Disc. Far. Soc. 37:113.

Petersen, H.L., and Kretschmer, C.B. (1960) U.S. Dept. Commerce, O.T.S., A.D. 283044.

Puckett, L.J., and Teague, M.W. (1971) J. Chem. Phys. 54:2564.

Schiff, H.I. (1969) Canad. J. Chem. 47:1903.

Schofield, K. (1967) Planet. Space Sci. 15:643.

Smith, D., and Fouracre, R.A. (1968) Planet. Space Sci. 16:243.

Westenberg, A.A., and DeHaas, N. (1965) J. Chem. Phys. 43:1550.

Wong, E.L., and Potter, A.E. (1965) J. Chem. Phys. 43:3371.

Appendix B

Diurnal Variation of Major Species During a PCA Event

The diurnal variation of the 30 MHz vertical absorption and 24 species, mostly positive ions and negative ions, are illustrated below. An ionization rate based on an isotopic proton flux, over the upper hemisphere of $10^4 e^{-P/P_o}$ cm^{-2} sec^{-1} ster^{-1} was considered with the rigidity, P_o = 50 MV. The specific ionization production rates resulting from this flux are 1.02×10^2, 2.67×10^2, 4.75×10^2, 5.90×10^2, 4.80×10^2 and 1.82×10^2 cm^{-3} sec^{-1} for altitudes of 40-90 km, in decade units respectively. (The 40 km ionization production actually used was 1.82×10^2 cm^{-3} sec^{-1}). The computations were performed for a latitude of 60° and a solar declination of 0°. The abscissa of each plot is in time (hours) rather than solar zenith angle, and hence the following solar zenith angles for the corresponding hours (in parentheses) should be kept in mind: 120°(24), 118.8°(1 and 23), 115.7°(2 and 22), 110.7°(3 and 21), 104.5°(4 and 20), 97.42°(5 and 19), 90.00°(6 and 18), 82.55°(7 and 17), 75.52°(8 and 16), 69.30°(9 and 15), 64.35°(10 and 14), 61.15° (11 and 13), and 60.00°(12).

A detailed discussion of the results would be lengthy and premature, since further improvements must be made in D-region chemistry, as noted in the conclusions of the main text. But a few comments appear to be necessary. Note that if an altitude is not plotted in any figure, it means that the values were below the lowest scale in the figure.

Figure B-1 – Negative ions are negligible at 80 and 90 km because of slow formation of O^- and O_2^- ions and the large quantity of O present (Figure B-10)

which frees the electrons (processes 5 and 9). The slight rise of [e] near noon at 90 km is a result of the inclusion of the normal daytime UV and X-ray fluxes. A "hysteresis" effect can be seen at 60 and 70 km in that [e] at 18 hours is larger than at 6 hours for the same solar zenith angle (90°). At 40 km, by night or day, the electron concentration is merely given by the production rate divided by the rate of O_2^- formation (cf Swider et al, 1971).

Figure B-2 – The 30 MHz absorption is calculated by multiplying the [e] values of Figure B-1 by the appropriate number (see Section 2 of text). Maximum absorption appears to take place at 70 km or slightly below.

Figure B-3 – This ion is always in quasi-equilibrium. Note the rise in O^- during the daytime at 60 and 70 km.

Figure B-4 – The rise in O_2^- (and O^-) in the daytime at 60 and 70 km is partly a result of the increased number of electrons, because of processes like 1, 9 and 99 plus the increased capability of degrading the higher affinity negative ions into O_2^-, principally because of the presence of atomic oxygen.

Figure B-5 – Similar to the case of O_2^- except fewer processes involved.

Figure B-6 – This higher affinity ion suffers a depletion during the daytime at 60 and 70 km.

Figure B-7 – CO_3^- has a behavior somewhat like NO_2^-.

Figure B-8 – This ion is generally in quasi-equilibrium, undergoing rapid transitions near twilight.

Figure B-9 – Reasonable daytime values for O_3 are obtained for $Z \leq 70$ km. Recall that constant values were adopted for 80 and 90 km.

Figure B-10 – The results are typical of similar calculations in the literature. Constant values were adopted at 80 and 90 km.

Figure B-11 – The $O_2(^1\Delta)$ results appear to be reasonable, as discussed in the main text. The results at 80 and 90 km should be treated with caution since they are based on constant levels for O_3 and O. The only source of $O_2(^1\Delta)$ in this work is photo-dissociation of O_3, that is, oxygen recombination processes have been ignored as a source of $O_2(^1\Delta)$.

Figures B-12–B-16 – These species are in quasi-equilibrium. The decline of the heavier hydrated NO^+ ions near 70 km in the daytime is a function of the increased daytime [e] level and the proportionately higher (with mass) dissociative recombination coefficients adopted for $NO^+ \cdot (H_2O)_n$ ions.

Figures B-17–B-20 – These species are always in quasi-equilibrium and hardly even vary during twilight periods.

Figures B-21–B-25 – At 40 and 50 km, possibly even 60 km, these ions can be shown to be essentially in thermodynamic equilibrium. At 70 km it can be observed that the heavier ions decline the most in the daytime. As in the case of the

$NO^+ \cdot (H_2O)_n$ ions, $H_3O^+ \cdot (H_2O)_n$ ions have dissociative recombination coefficients which tend to increase with amu (atomic mass unit). The decline of the heavier ions in the daytime apparently is a result of their formation not being sufficient to counter the increased loss in the daytime resulting from their recombination with electrons.

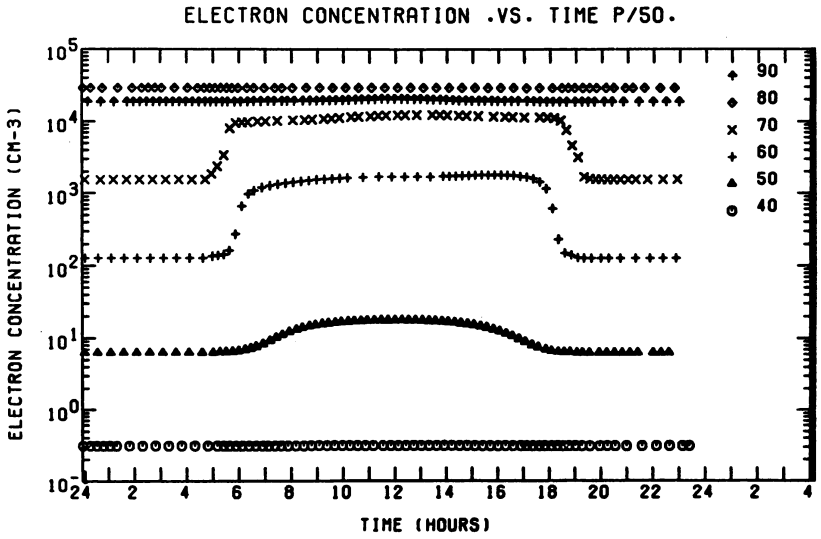

Figure B-1. Diurnal Plot of [e] vs Time

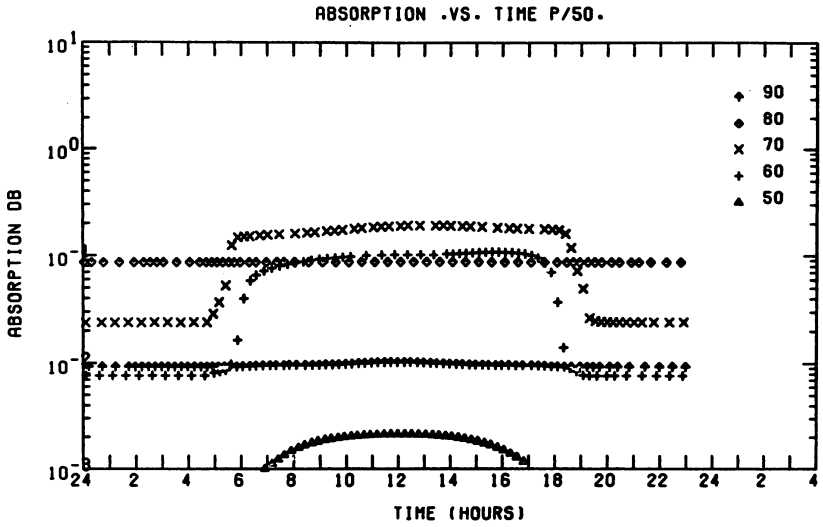

Figure B-2. Diurnal Plot of 30 MHz Vertical Absorption vs Time

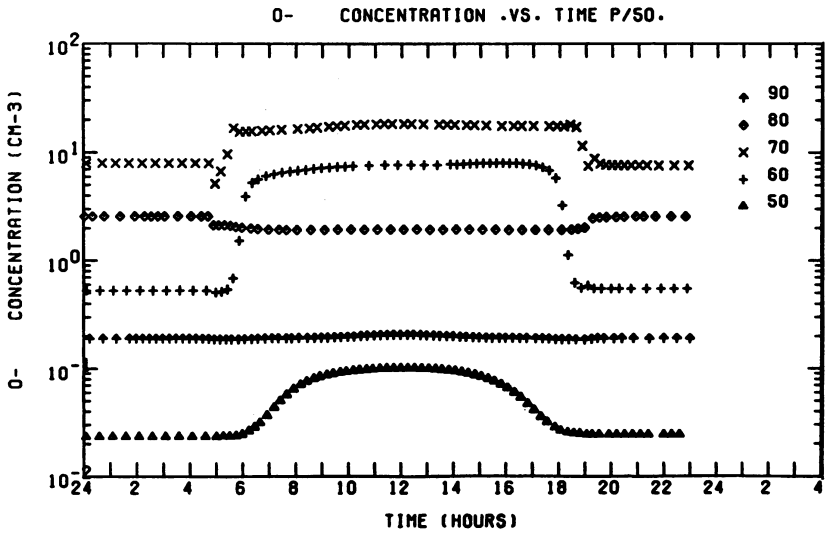

Figure B-3. Diurnal Plot of $[O^-]$ vs Time

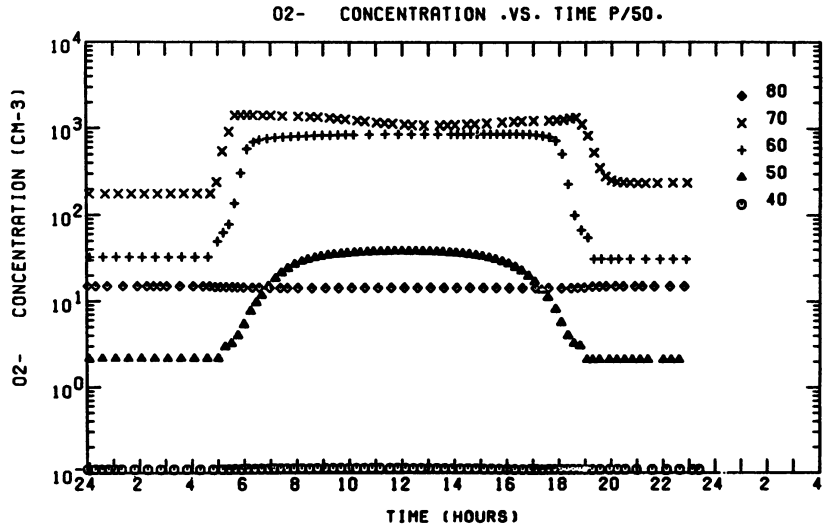

Figure B-4. Diurnal Plot of $[O_2^-]$ vs Time

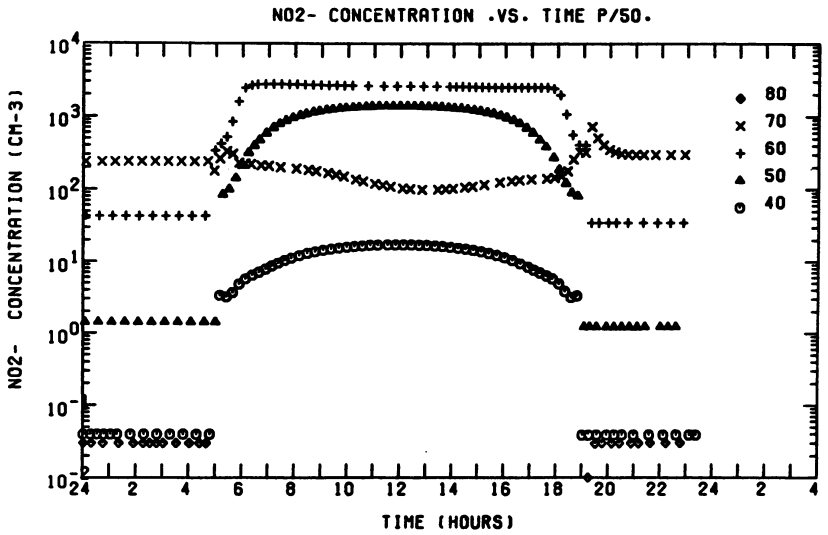

Figure B-5. Diurnal Plot of $[NO_2^-]$ vs Time

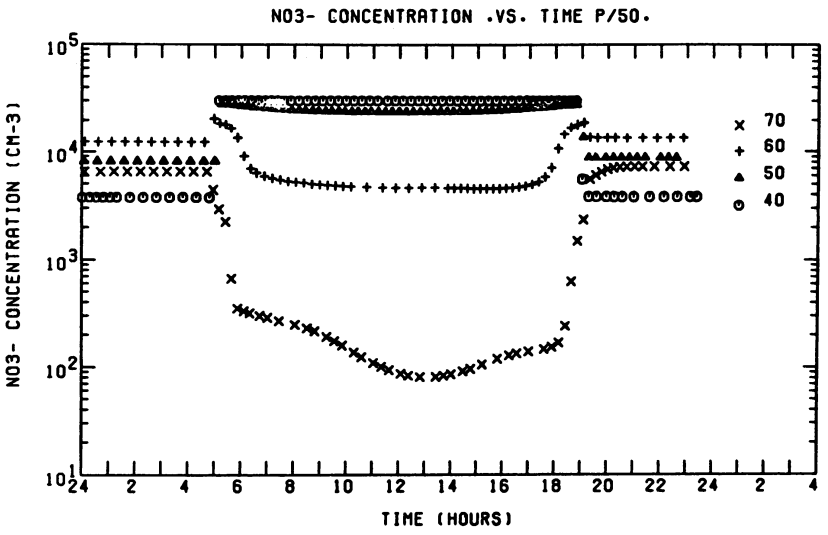

Figure B-6. Diurnal Plot of $[NO_3^-]$ vs Time

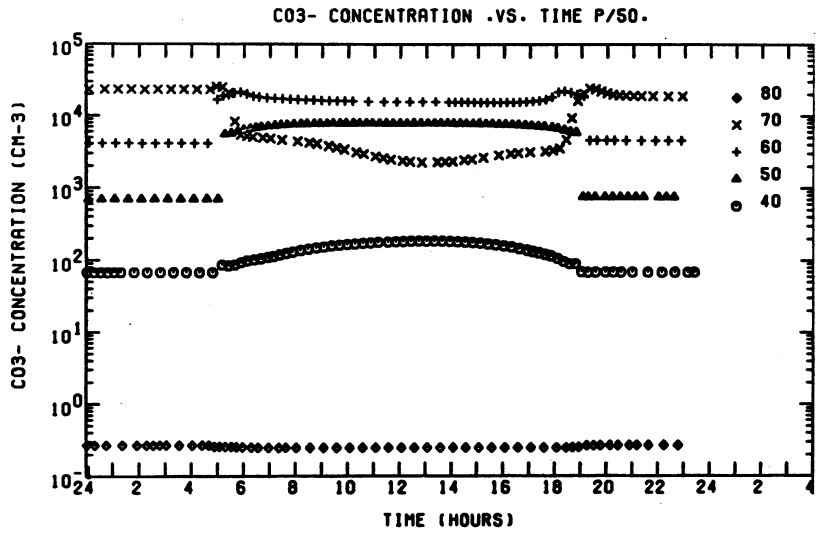

Figure B-7. Diurnal Plot of $[CO_3^-]$ vs Time

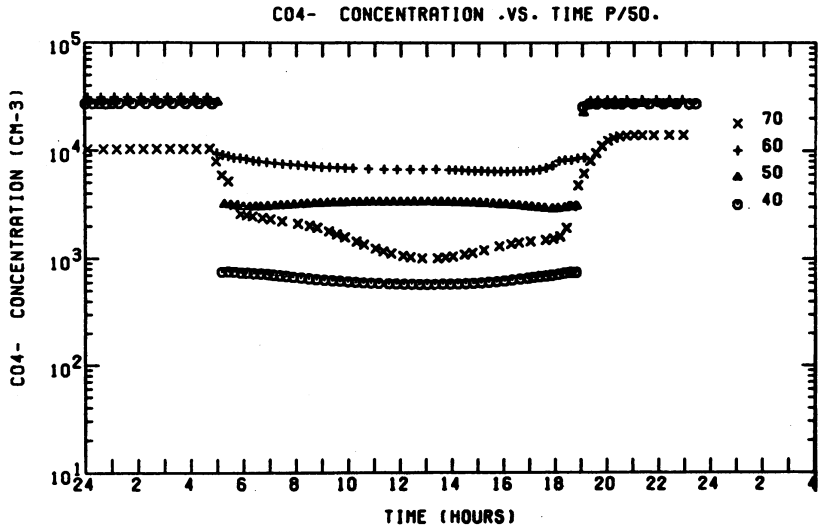

Figure B-8. Diurnal Plot of $[CO_4^-]$ vs Time

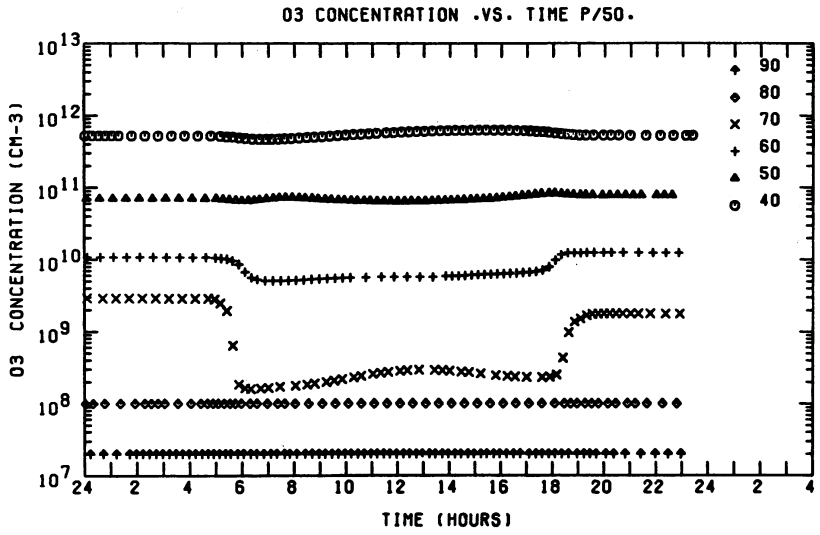

Figure B-9. Diurnal Plot of $[O_3]$ vs Time

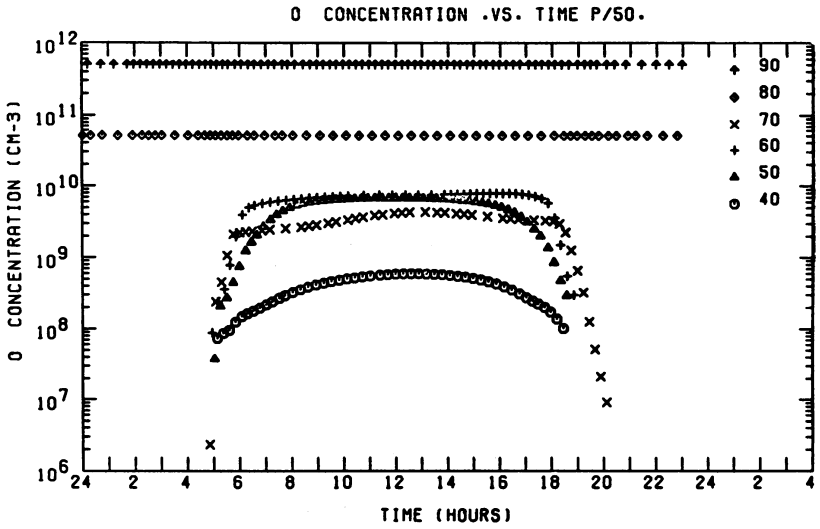

Figure B-10. Diurnal Plot of [O] vs Time

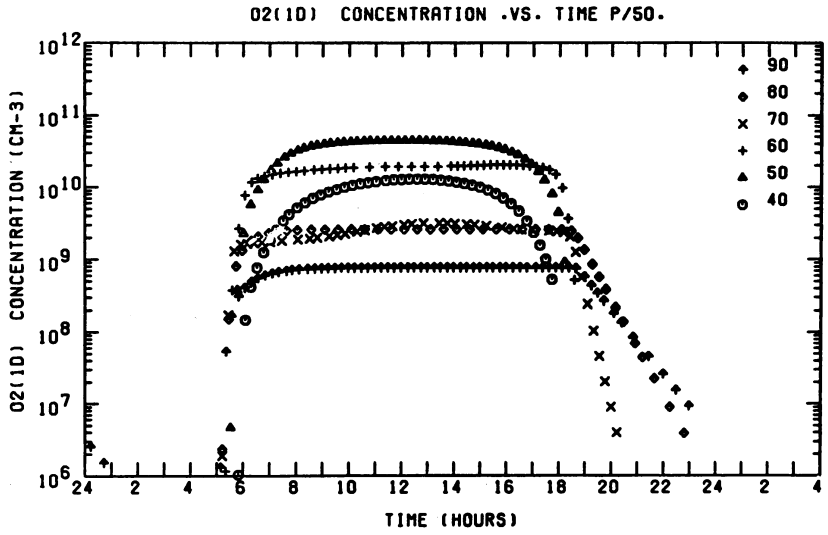

Figure B-11. Diurnal Plot of $[O_2(^1\Delta)]$ vs Time

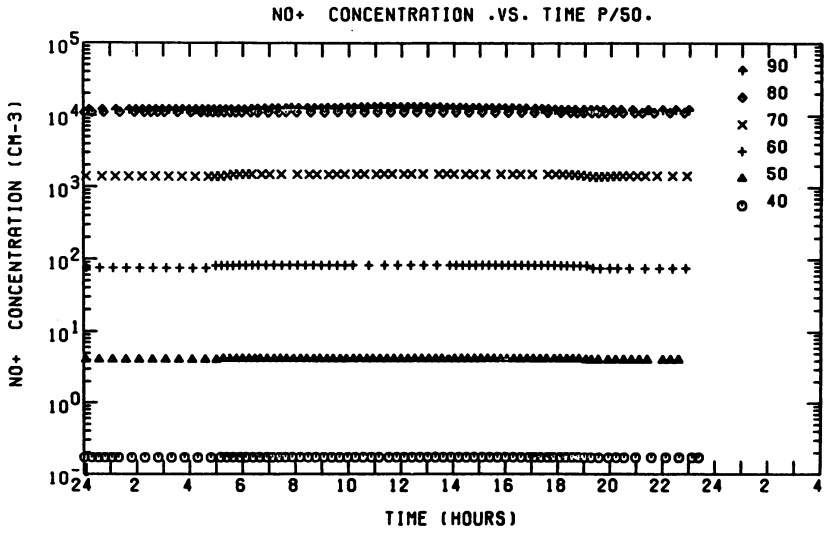

Figure B-12. Diurnal Plot of $[NO^+]$ vs Time

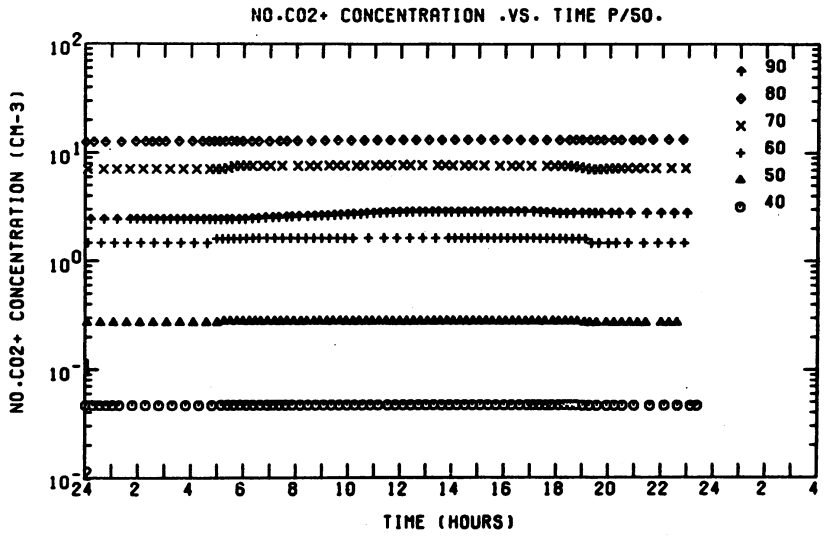

Figure B-13. Diurnal Plot of $[NO^+ \cdot CO_2]$ vs Time

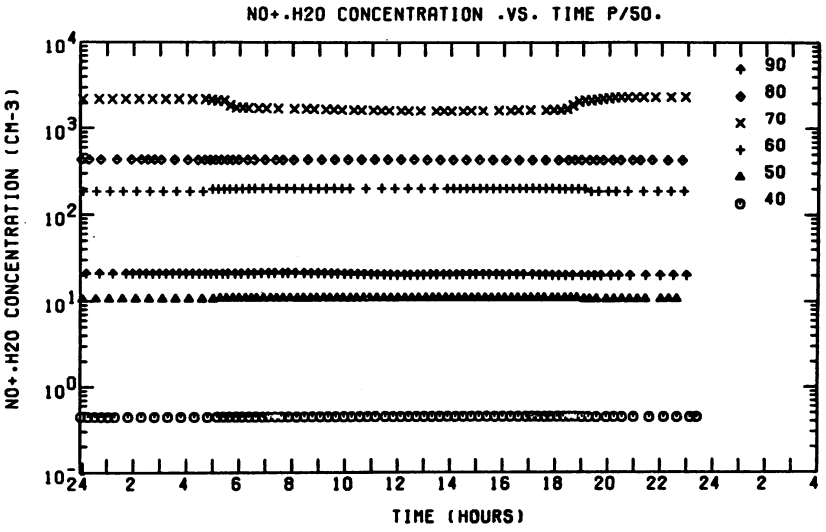

Figure B-14. Diurnal Plot of $[NO^+ \cdot H_2O]$ vs Time

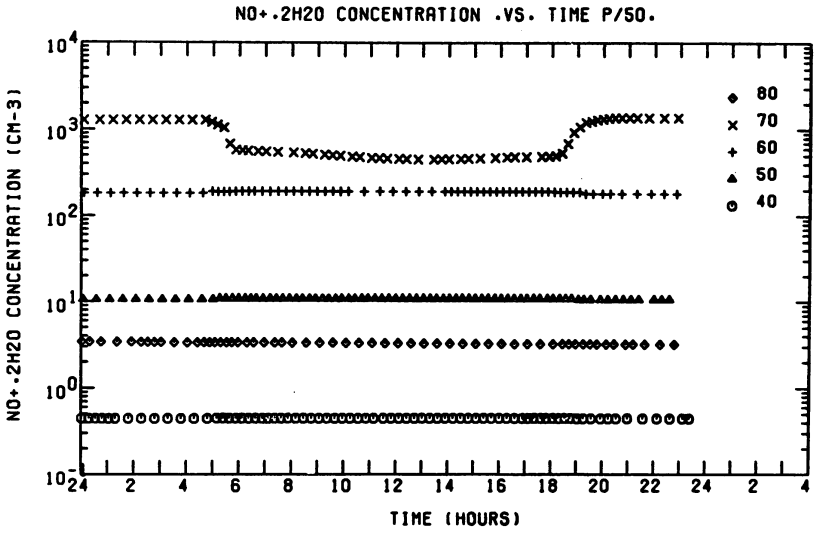

Figure B-15. Diurnal Plot of $[NO^{+} \cdot 2H_2O]$ vs Time

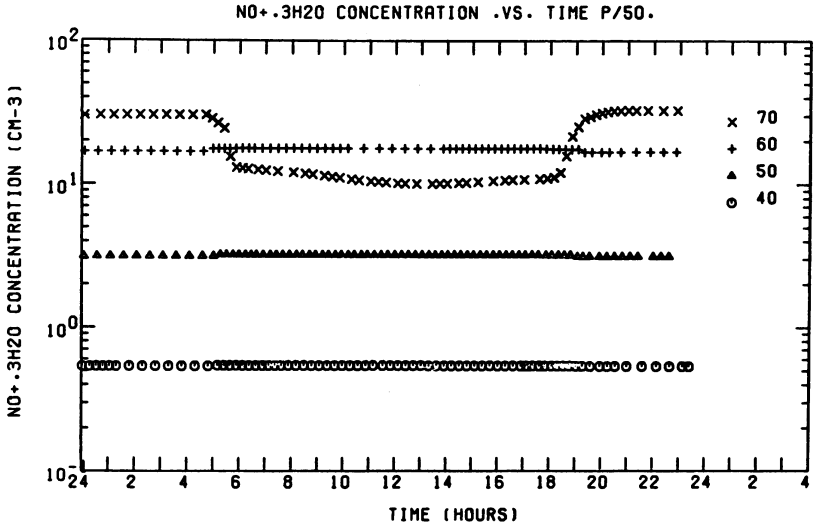

Figure B-16. Diurnal Plot of $[NO^{+} \cdot 3H_2O]$ vs Time

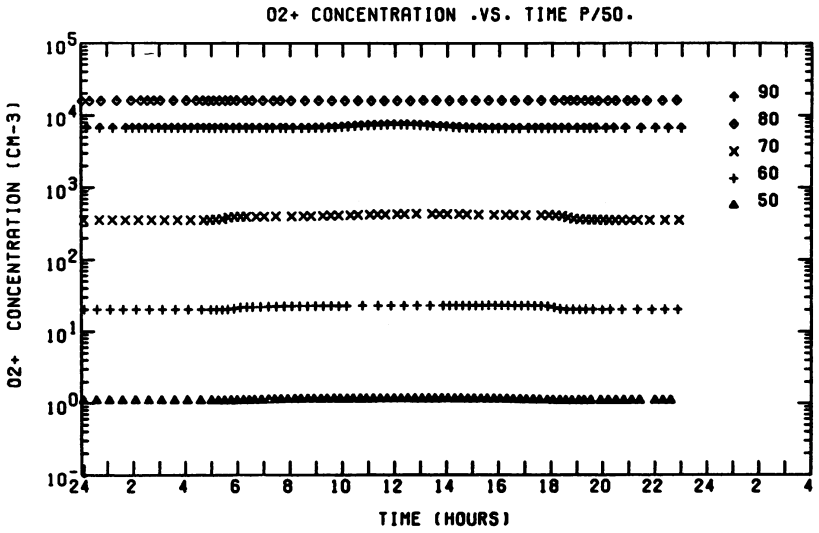

Figure B-17. Diurnal Plot of $[O_2^+]$ vs Time

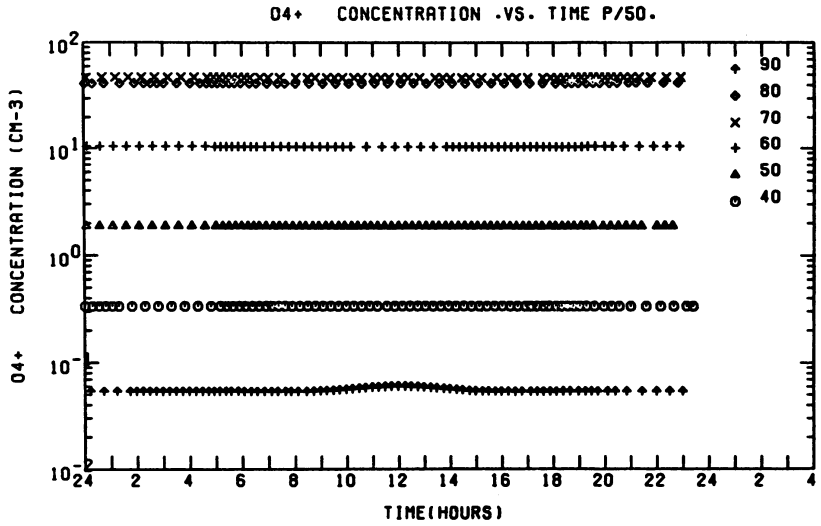

Figure B-18. Diurnal Plot of $[O_4^+]$ vs Time

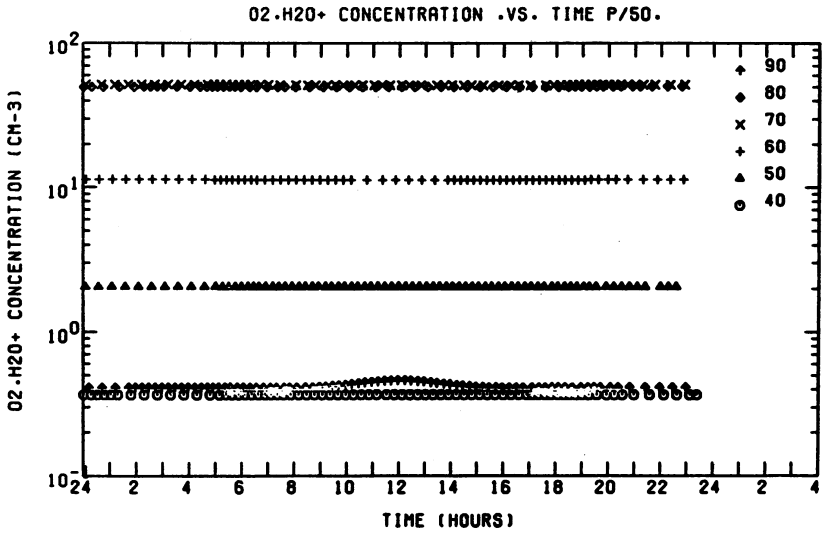

Figure B-19. Diurnal Plot of $[O_2^+ \cdot H_2O]$ vs Time

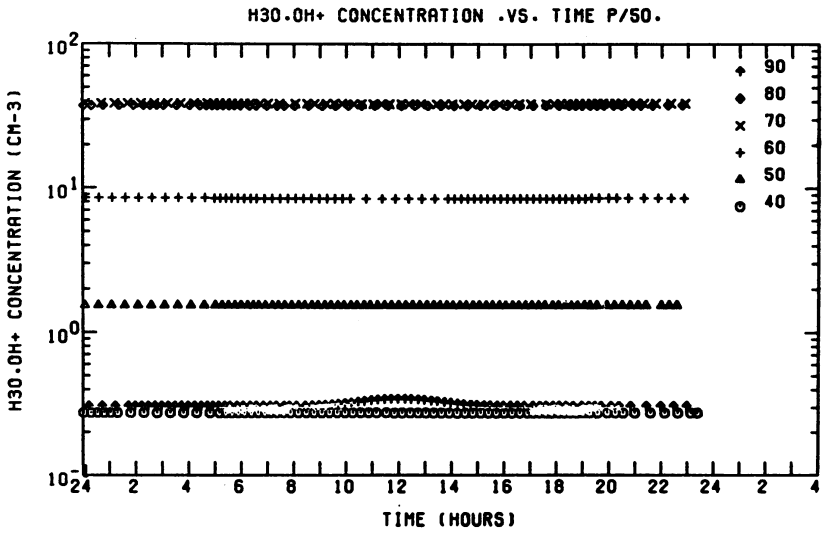

Figure B-20. Diurnal Plot of $[H_3O^+ \cdot OH]$ vs Time

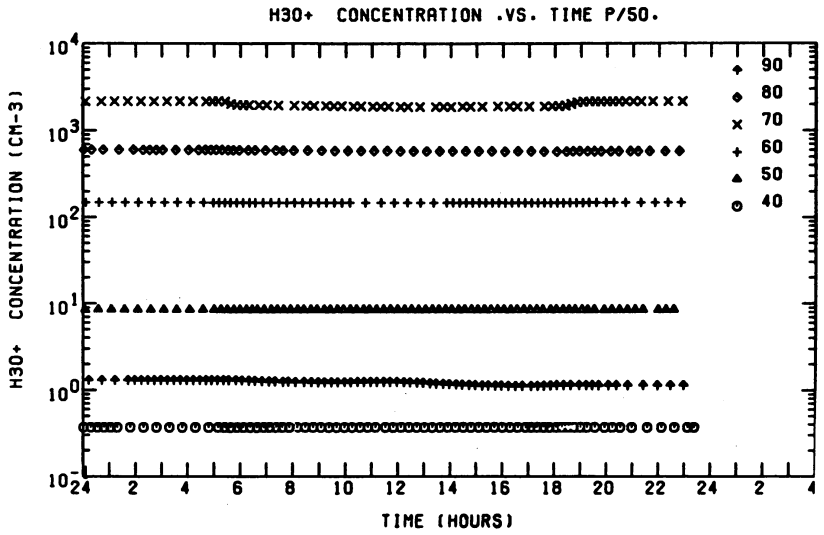

Figure B-21. Diurnal Plot of $[H_3O^+]$ vs Time

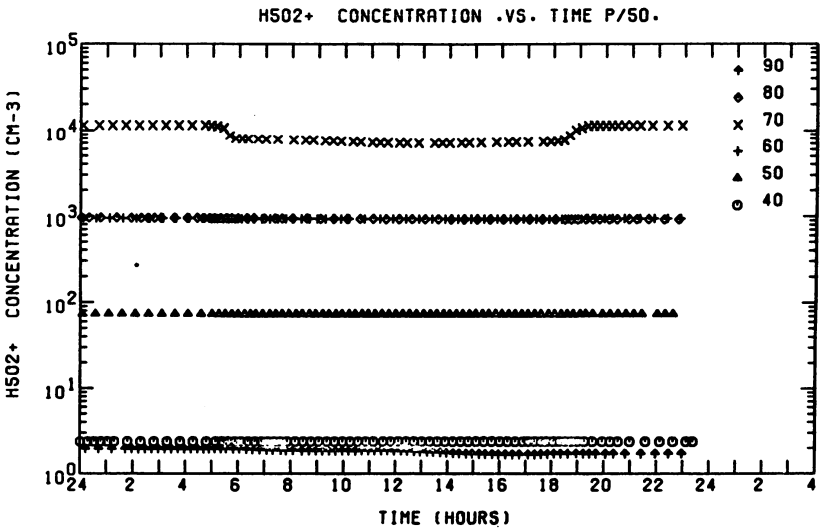

Figure B-22. Diurnal Plot of $[H_5O_2^+]$ vs Time

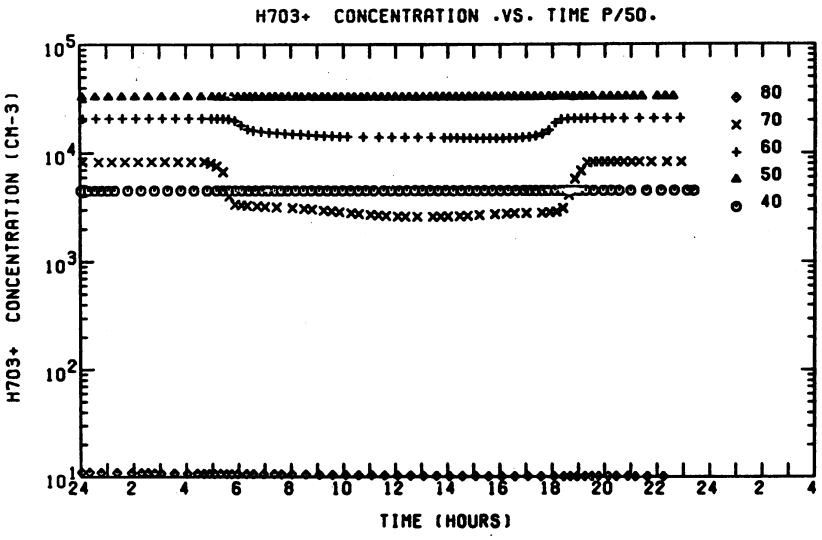

Figure B-23. Diurnal Plot of $[H_7O_3^+]$ vs Time

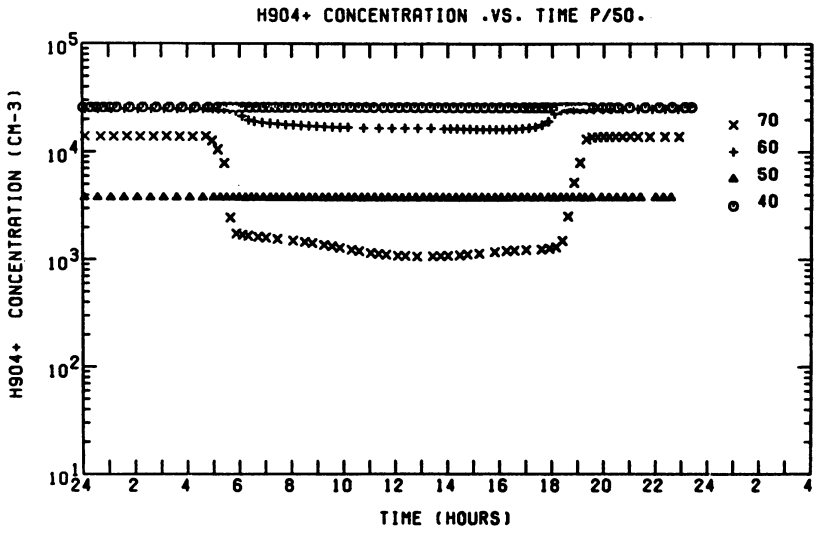

Figure B-24. Diurnal Plot of $[H_9O_4^+]$ vs Time

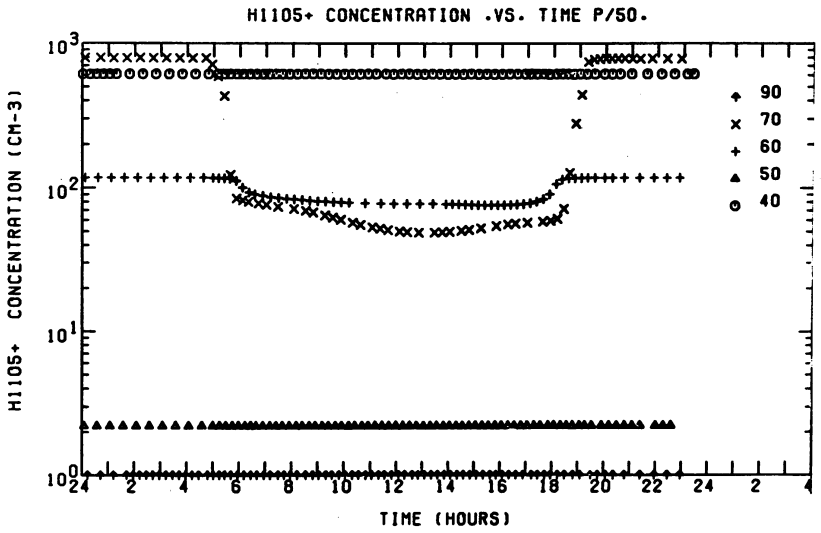

Figure B-25. Diurnal Plot of $[H_{11}O_4^+]$ vs Time

Contents

43. HF and LF Effects in Delhi During November 1969 Solar Proton Events

A. P. Mitra, C. V. Subrahmanyam and L. H. Sarma
Radio Science Division, National Physical Laboratory
New Delhi-12

Abstract

A sizeable decrease in signal strength occurred in the 164 kHz transmission from Tashkent (41° 25N) received in Delhi (28° 35 N), coinciding with the solar proton event of 2 November 1969. The effect began at 1200 U.T. at the time of first increase of proton flux for energies greater than 60 Mev. The signal recovered to its normal value at 1600 U.T., but beginning at 2000 U.T. there was a record decrease (observed on the atmospherics at 164 kHz, the transmission being off) with a minimum at 2200 U.T. coinciding with the large proton flux maximum. This is one of the few cases of solar proton effects known to have occurred at such low latitudes. No effect was observed for the proton flare of 24 November 1969. A curious anomaly, however, existed in the relative magnitudes of SCNA's on the two days; the one occurring on 2 November, being considerably smaller, although the X-ray flux enhancements were unusually large during both the events. For the SCNA of 24 November, SCNA's were observed on both 22.4 and 30 MHz and a comparison of the effects at the two frequencies indicated a substantial lowering of the region to a level not usually reached.

43-1 INTRODUCTION

It is well established that following certain major solar flares the polar regions of the earth are subjected to severe bombardment by charged particle of solar origin.

The ionization caused by them in the lower ionosphere have for long been monitored by groundbased riometers and VLF equipments. In-situ measurements of the nature and distribution of the charged particles by satellites and, of the ionization by rockets are relatively new. These are considerably more valuable, but are essentially limited and, in particular, information on changes in ionization is limited to a few rocket launching locations only. For any one event much of the global information still comes from groundbased measurements.

One of the major limitations in such work is the lack of information on the latitude limit of the ionization effect. There is, in particular, no significant study at low latitude. It is commonly believed that the solar particles have negligible effect on the low latitude D-region because of the large cutoff rigidities at such latitudes.

The present communication incorporates the results of our investigations on the perturbations observed in the field strength measurements in LF at 164 kHz at low latitudes in response to the protons events of 2 November 1969 and 24 November 1969.

43-2 DATA

The proton flux data used in the present analysis to bring out the particle effect at low latitudes are the published measurements on board the Explorer-41 satellite (azimuthal inclination 82.8 degrees and apogee 28 Earth radii).

Following a class of 3B solar flares at 1018 U.T. on 2 November 1969, large increases in the proton flux were recorded on all the three channels of proton counters on board the satellite (>10 MeV, >30 MeV, >60 MeV). The satellite was outside the earth radiation belts at the beginning of the event. The peak proton fluxes recorded on >60, >30 MeV channels were 201 and 737 protons cm^{-2} sec^{-1} $ster^{-1}$ at 1300 U.T. and on >10 MeV channel 1317 protons cm^{-2} sec^{-1} $ster^{-1}$ at 1400 U.T. There was another peak in the proton flux of 3948 protons cm^{-2} sec^{-1} $ster^{-1}$ on >60 MeV channel at 2200 U.T. and of 15482 and 1437 protons cm^{-2} sec^{-1} $ster^{-1}$ on >30 MeV and >10 MeV channels respectively at 2300 U.T. But, at this time the satellite was at the perigee, that is, in the radiation belts.

On 24 November 1969, there was another proton event of a smaller intensity. The recorded increases in the proton fluxes were significant only on the >10 Mev. channel. The peak flux recorded on >10 MeV channel was 3.75 protons cm^{-2} sec^{-1} $ster^{-1}$ at 1700 U.T., following a class 2B solar flare at 0913 U.T. on the >30 MeV channel the peak flux was 1.40 proton cm^{-2} sec^{-1} $ster^{-1}$ at 1500 U.T. on the >60 MeV channel the increase in the proton flux was less than unity.

The Radio Science Division of National Physical Laboratory, New Delhi has round-the-clock field strength recordings of 164 kHz broadcast transmissions from

Radio Tashkent (41° 25N, 69° 12E) and received at Delhi (28° 35N, 77° 5E) and riometers operating on 30 and 22.4 MHz as a part of a regular programme of radio patrol of solar flares.

43-3 RESULTS

In Figure 43-1 is shown a plot of 164 kHz field strength vs time on 2 November 1969 (a continuous curve). The half hourly field strength values averaged for 20 days are shown as the dashed curve (crosses). The dashed curve along with the continuous curve gives the normalized field strength on 2 November 1969 with respect to the average. The proton flux values (>60 MeV) are also shown on a separate scale. An SCNA has occurred at 1015 U.T. Following this, after about one and one-half hours the proton flux has increased to a value of 58 protons cm^{-2} sec^{-1} $ster^{-1}$. This is reflected in the figure as a decrease in field strength beginning at 1200 U.T. reaching a minimum at 1500 hours. It may be observed that the ratio of the field strength on 2 November 1969 to the normalized value, at the minimum is about 0.25.

At 2000 U.T. there is again a significant decrease revealed through the 164 kHz atmospheric noise (the station being switched off at this time). The trend of variation is not consistent in this case and can only be incompletely inferred due to the power failure during 2200 to 2300 U.T. This decrease corresponds to the second peak of proton flux at 2200 U.T. The effect in this case is not well defined due to the lack of reliable values during this period. The large increase in proton flux at 2200 U.T. may not be genuine since the satellite was in the radiation belts at this time, but the average level of proton flux is by far larger than at normal times.

No decrease in the field strength was observed for 24 November 1969, and no significant increase in absorption on 30 MHz was observed during both events.

Figure 43-2 is a comparison between the SCNA's recorded on 30 MHz for 2 November 1969 and 24 November 1969 solar flare events, following which increases in proton flux were observed. It can be seen that the SCNA of 2 November 1969 is significantly smaller. The exact strength of the X-ray flux during these times is not available, since on both the occasions the detectors were saturated, and it is not possible to make a quantitative assessment of the ionization responsible for the two SCNA's. It may be noted that both the solar flares, causing the above-mentioned SCNA's, were followed by proton flux increases. The 2 November 1969 flare was [illegible] by large increases in proton flux, though the SCNA (0.5 db) indicates a [illegible] by flux. On the other hand, the 24 November 1969 solar flare was [illegible] X-rays, as indicated by large SCNA (0.8 db), but followed by low [illegible]. [illegible] large electron-[illegible] [illegible] [illegible] [illegible] [illegible]

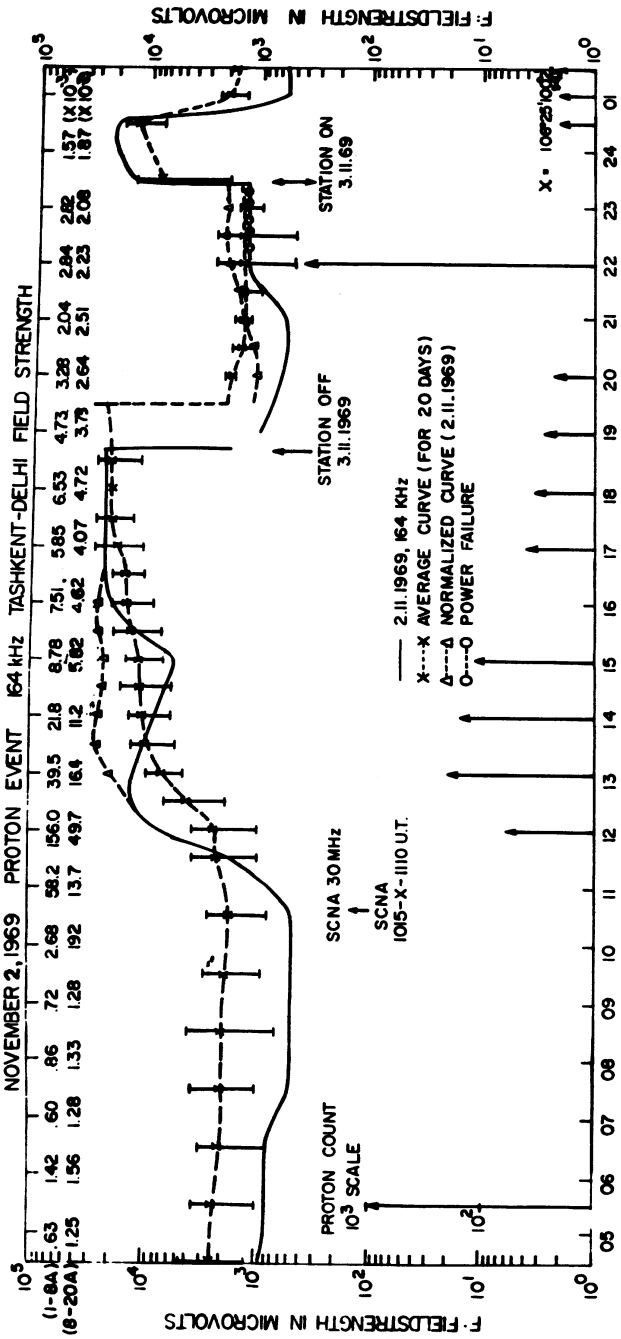

Figure 43-1. Field Strength of 164 KHz Transmissions on 2 November 1969 From Tashkent to Delhi vs Time (U.T.). The proton flux (protons cm^{-2} sec^{-1} $ster^{-1}$) is given on a separate scale. The values given at the top of the diagram are the hourly values of X-ray flux (ergs cm^{-2} sec^{-1}) in (0-8A) and (8-20) range. The χ values for the path mid-point are given at the right hand side bottom corner

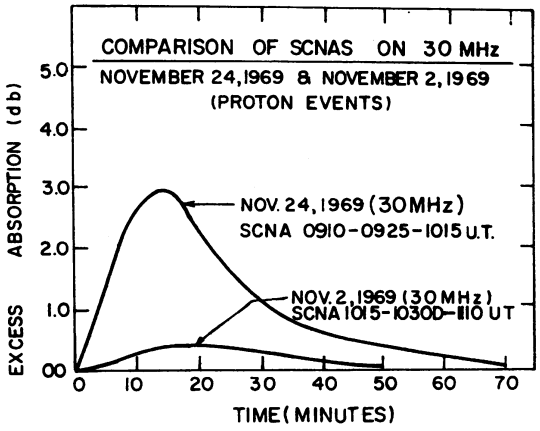

Figure 43-2. Comparison of SCNA's on 2 November 1969 and 24 November 1969, Excess Absorption Against Time

The significantly larger SCNA's recorded on frequencies of 22.4 MHz and 30 MHz on 24 November 1969 as compared to 2 November 1969 has prompted the multifrequency SCNA analysis (Mitra and Deshpande, 1971) to obtain an estimate of electron density with height. In Figure 43-3 is shown the excess absorption for the 24 November 1969 SCNA against time, on 22.4 MHz and 40 MHz. The lower diagram is the ratio of excess absorption on the two frequencies against time. This ratio (Morris, 1960) is indicative of the lowering of the layer responsible for the excess absorption. The method of analysis is briefly given here.

The excess electron density due to enhanced X-ray flux is assumed to be representable by a function,

$$N = N_o (h - h_o)^2$$

where N_o is a constant and h_o is the base level of ionization.

The absorption on a single frequency can be accounted for by assuming any value for the base level h_o. But the absorption on two frequencies can be explained with only one value of the base level h_o, for it is easy to show that

$$\frac{A(f_{e_1})}{A(f_{e_2})} = f(h_o)$$

where $A(f_{e_1})$ and $A(f_{e_2})$ are the absorption suffered by waves of effective frequencies, f_{e_1} and f_{e_2}.

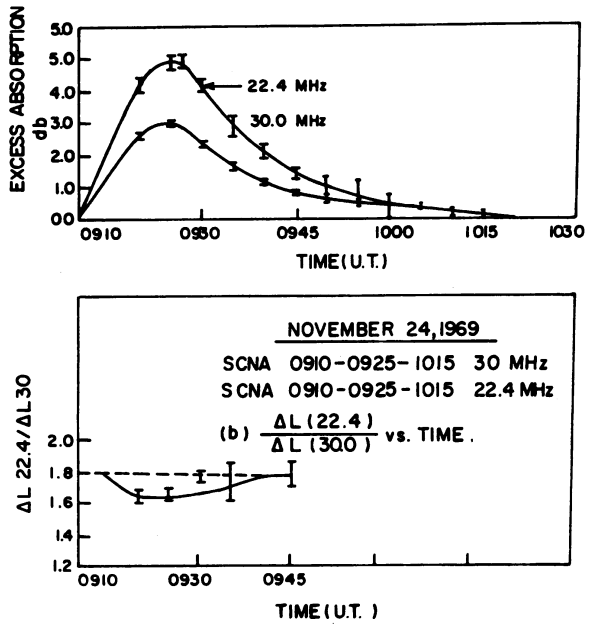

Figure 43-3. SCNA of 24 November 1969 on 22.4 and 30 MHz. The lower diagram is the ratio of excess absorption on the two frequencies drawn against time

Figure 43-4 is the electron density profile obtained from 24 November 1969 SCNA data. The interesting point that comes into light from this analysis is the significant lowering of the layer. This is evident from the value of the base level of ionization, situated at a height of 38.5 km, and such a lowering of the layer is unusual at these latitudes.

43-4 DISCUSSION

The significant decrease in the field strength of 164 kHz transmissions corresponding to the large increases in the proton flux gives evidence to the proton precipitation at D-region heights at low latitudes. Ganguly and Rao (1970), previously, reported the particle effects at low latitudes based on their absorption data by A_1 technique. But their results were doubted by Lanzerotti and Graedel (1970). The cut-off rigidities of these latitudes being very large compared to the particle energies, the results of the present investigation seem not to be not comparable with the existing theories [illegible]

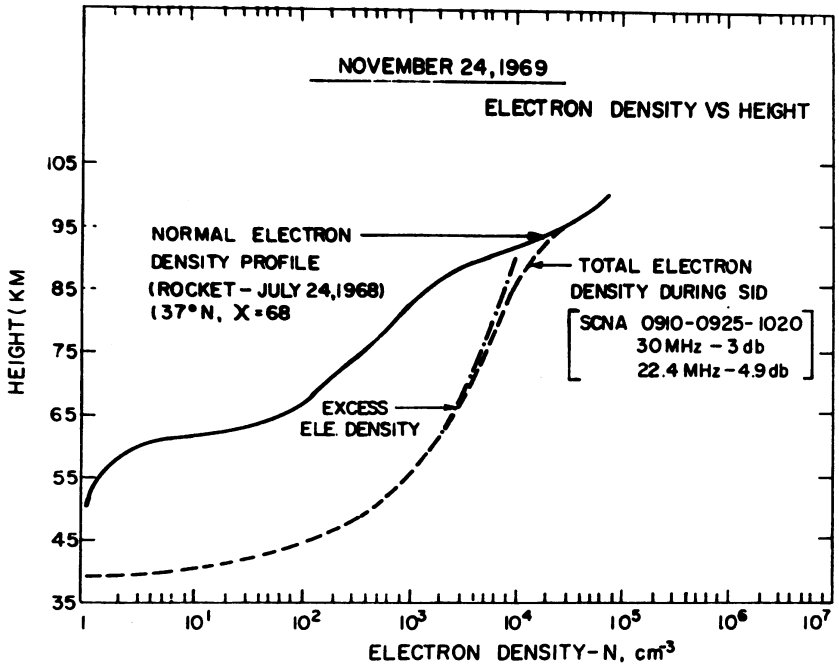

Figure 43-4. The Electron Density Distribution Obtained From Multifrequency SCNA Analysis of 24 November 1969 Event. The dashed curve is the excess electron density obtained from SCNA analysis. The continuous curve is normal time electron density profile from rocket measurement at Wallops Island

Acknowledgments

The authors wish to thank Mr. C. B. Nair for his assistance in scaling the record.

References

Ganguly, S., and Rao, M. (1970) Penetration of solar particles to ionospheric heights at low latitudes, Nature 225:169-170.

Lanzerotti, L. J., and Graedel, T. E. (1970) Penetration of solar particles to ionospheric heights at low latitudes, Nature 228:45.

Mitra, A. P., and Deshpande, S. D. (1971) Electron density profiles from observations of SCNA and VLF phase and amplitude, Scientific Report No. 62, Radio Science Division, National Physical Laboratory.

Morris, R. W. (1960) Observation of sudden ionospheric disturbances, Proc. Phys. Soc. 76:79-91 (London).

Contents

44. The Connection of Solar Proton Fluxes to Airglow and VLF and HF Radio Measurements During the Event of November 2, 1969

T.A. Potemra, A.J. Zmuda, and C.R. Haave
Applied Physics Laboratory
The Johns Hopkins University
Silver Spring, Maryland

Abstract

Solar proton fluxes measured by satellite Explorer 41, (IMP 5), outside the earth's magnetosphere during the event of November 2, 1969 have been quantitatively connected to the following simultaneous observations; (1) N_2^+ emissions at 3914 Å in the north polar cap, (2) electron density profiles measured by rockets from Fort Churchill, Canada, (3) phase disturbances observed on the 17.8 kHz transmission from station NAA in Cutler, Maine, to Thule, Greenland, and on the 23.4 kHz transmission from station NWC in Australia to McMurdo Sound, Antarctica, and (4) 30 MHz riometer absorption measured at Shepherd Bay, Canada and McMurdo Sound. The ionization and radio propagation models previously developed by the authors were used unchanged in this analysis. These models were developed by connecting the proton fluxes measured by the polar-orbiting satellite 1963 38C, at 1100 km altitude, to VLF phase and HF absorption values in 6 major, earlier PCA events.

44-1 INTRODUCTION

Large increases in solar proton intensities were measured near the earth and in interplanetary space following observations of a 3B solar flare on 2 November

1969, by satellites OGO-6 (Masley and Satterblom, 1970), OV1-18 (Reagan and Imhof, 1970; Johnson and Sharp, 1970), Vela 5A (Davenport, 1970), OV5-6 (Yates, 1970), and Explorer 41 (Solar Geophysical Data, 1970; Bostrom, 1970). Ionospheric disturbances coincident with the arrival of these protons were detected by conventional riometer absorption and VLF phase and amplitude measurements in the polar caps, and also by means of the concentrated rocket program called "Operation PCA 69" (Ulwick and Blank, 1970).

We examine here in detail the ionization and radio propagation models previously developed by the authors from several previous events (Potemra et al, 1969; Potemra et al, 1970) by using proton fluxes measured by the joint Applied Physics Laboratory-Goddard Space Flight Center particle experiment on Explorer 41 to compute the following quantities: (1) Intensities of N_2^+ at 3914 Å for comparison with aircraft measurements made in the polar cap on 3 November (Sandford, 1970), (2) Day and night electron density profiles for comparison with profiles measured by rockets launched from Churchill (Ulwick and Blank, 1970), (3) Phase perturbation values observed on the 17.8 kHz transmissions from station NAA in Cutler, Maine, to Thule, Greenland, and on the 23.4 kHz transmission from NWC in North West Cape, Australia to McMurdo Sound, Antarctica, and (4) Riometer absorption at Shepherd Bay, Canada, and McMurdo Sound, Antarctic (Masley et al, 1970). Relationships between the long distance VLF transmissions and timevarying proton cutoff latitudes, and the relation of these cutoffs to storm-time variations (Dst) developed previously by the authors (Zmuda et al, to be published), were also tested here. Ionization and electron density profiles were also computed from the energetic electron fluxes measured during a nighttime rocket flight in the auroral region (Hegblom, 1970).

44-2 PARTICLE DATA

The proton data used in the following calculations are the hourly average fluxes measured by particle detectors with a 2π steradian field of view in the range 1-10 Mev, >10 Mev, > 30 Mev, and > 60 Mev on the Explorer 41 satellite (Solar Geophysical Data, 1970; Bostrom, 1970). This satellite, highly eccentric and inclined at 82.8 degrees, was close to apogee at 175,000 km and outside the magnetosphere at the beginning of this event. Large increases in all proton channels were observed following the 3B solar flare which began at 1028 UT and ended at 1157 UT on 2 November 1969. Peak fluxes in the >60 Mev and > 30 Mev channels equal to 201 and 737 protons cm^{-2} sec^{-1} $ster^{-1}$ respectively, were observed at 1300 UT, in the > 10 Mev channel of 1317 protons cm^{-2} sec^{-1} $ster^{-1}$ at 1400 UT, and in the 1-10 Mev channel of 996 protons cm^{-2} sec^{-1} $ster^{-1}$ at 1500 UT on 2 November.

Second peaks in the proton fluxes were observed in the 1-10 Mev and >10 Mev channels equal to 2700 and 12.7 protons cm^{-2} sec^{-1} $ster^{-1}$ respectively, at 0400 UT on 8 November 1969 before the sudden commencement at 1900 UT on 8 November. No significant enhancements were observed in the > 30 Mev or > 60 Mev channels at this time.

44-3 POLAR AIRGLOW

The transmission of solar protons through the earth's magnetosphere is complex (Paulikas and Blake, 1969) and we do not examine this problem here. But as a measure of the relevance of the Explorer 41 proton measurements to this polar cap analysis, the N_2^+ emission at 3914 Å was computed at various times during this event from these data and are listed in Table 44-1 with the values measured during an airplane flight in the polar cap by Sandford (1970). The computed values were determined by integrating the proton fluxes over the 4 channels described above, using the most recent fluorescence efficiency for the 0-0 band of N_2^+ by energetic particles, 14.1 ion-pairs per photon of 3914 Å (Borst and Zipf, 1970; Hirsh et al, 1970). A correction for the quenching of the N_2^+ emission was not made because the peak ionization and airglow intensity occurred above 70 km where this reduction is less than 10 percent. The good agreement between the computed and observed airglow values listed in Table 44-1 indicates that (at least for a consideration of the total available energy >1 Mev) the fluxes measured by Explorer 41 outside the magnetosphere apply to the polar cap during the times listed in Table 44-1.

44-4 IONIZATION RATES AND ELECTRON DENSITIES

The proton fluxes obtained from Explorer 41 were used to compute ion-pair production rate profiles with the specific rates of Adams and Masley (1965) and with the assumption of isotropic proton fluxes. Day and night electron density profiles were computed from these ionization rates with the ionization models previously developed by the authors (Potemra et al, 1969 and 1970), which for the day case is described by a characteristic effective recombination coefficient. For nighttime conditions a more complicated description is required.

Examples of the electron density profiles computed with our daytime ionization model are shown in Figures 44-1 and 44-2 for comparison with the rocket measured profiles by Dean (1970) and Ulwick (1970) at Churchill, Canada, in the auroral zone. There is good agreement between the computed and observed profiles up to 80 km, above which ionization due to auroral electrons dominates. Electron density profiles

Table 44-1. 3914Å Polar Airglow During 3 November 1969

Time, UT	Total proton energy >1 Mev from Explorer 41, erg cm^{-2} sec^{-1}	I_{3914}, Rayleighs	
		Computed	Observed*
0200	0.22	220	216
0300	0.16	160	213
0400	0.16	160	144
0500	0.13	130	141

*Sandford((1970) and these proceedings) converted from measurements of the 4278Å line using the ratio of emission cross section for (0,0) to (0,1) bands of N_2^+ equal to 3:1.

were computed with our nighttime ionization model using the Explorer 41 proton fluxes and also using the energetic electron fluxes measured in integral channels > 17 kev, >26 kev, >42 kev, and > 90 kev during a rocket flight from Churchill at 0605 UT on 3 November by Hegblom (1970). These computed profiles are shown in Figure 44-3 along with the electron density profile measured during the same rocket flight by Ulwick (1970). The specific ionization rates for energetic electron from Rees (1963) were used for the calculation of the ionization due to energetic electrons. Figure 44-3 clearly shows that the solar protons provide the dominant ionization source at 80 km and below and energetic electrons dominate at the higher altitudes. The good agreement between the computed and observed profiles in Figures 44-1, 44-2, and 44-3 provide the most direct support presently available for our day and night ionization models.

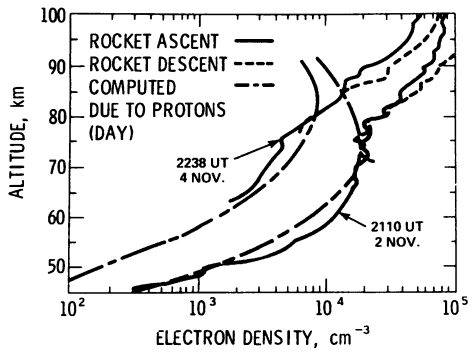

Figure 44-1. Daytime Electron Densities Measured With Rockets Launched From Churchill, Canada by Dean (1970) and Electron Densities Computed From Simultaneous Proton Fluxes Measured by Explorer 41

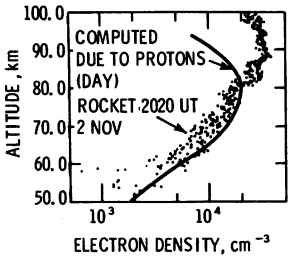

Figure 44-2. Daytime Electron Densities Measured With a Rocket From Churchill by Ulwick (1970) and Electron Densities Computed From Simultaneous Proton Fluxes Measured by Explorer 41

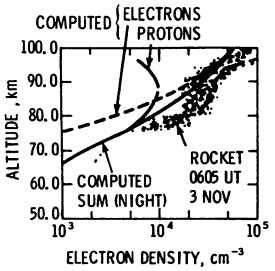

Figure 44-3. Nighttime Electron Densities Measured With a Rocket From Churchill by Ulwick (1970) and Nighttime Densities Computed From Simultaneous Proton Fluxes Measured by Explorer 41 and From the Energetic Electron Fluxes Measured by Hegblom (1970)

44-5 VLF PHASE DISTURBANCES

The electron density profiles described in the previous section were used to compute VLF phase disturbances by the method used in past analyses by the authors (Potemra et al, 1969 and 1970) for the 17.8 kHz transmission from station NAA in Cutler, Maine, to Thule, Greenland, and for the 22.3 kHz transmission from station NWC, North West Cape, Australia, to McMurdo Sound, Antarctica. The computed and observed phase values are shown in Figure 44-4. The VLF calculations involve the use of exponential conductivity profiles determined from the electron density profiles described above, with the full-wave solutions of Wait and Spies (1964 and 1968) and with the multi-wave guide model used previously by the authors to account for the time varying geomagnetic cutoffs. The empirical relation between cutoffs, Λ_c, and magnetic storm time variation Dst (in units of gamma equal to 10^{-5} gauss) from Zmuda et al, (to be published), expressed by the following formulas were used: Λ_c = .027 Dst + 60.4 $\pm$ 2.2 degrees during the main phase and Λ_c = 0.35 Dst + 65.2 $\pm$ 1.8 degrees during the recovery phase of the storm. The magnetic activity throughout this event was relatively quiet with the maximum range of Dst values $\pm$ 20 gammas until 8 November when the sudden commencement occurred. The uncertainty of about $\pm$ 2 degrees in the cutoffs from the empirical relationship above

causes an uncertainty of ± 6 percent in the computed NAA-Thule phase values and is shown as the error bars on the computed values in Figure 44-4. This also causes an uncertainty of only 3 percent for the computed phase values of the longer (6800 km) NWC-McMurdo path and is always less than ± 1 μsec throughout this event. This latter uncertainty is smaller than the dimension of the symbol for the corrected phase shown in Figure 44-4, so no error bars are shown.

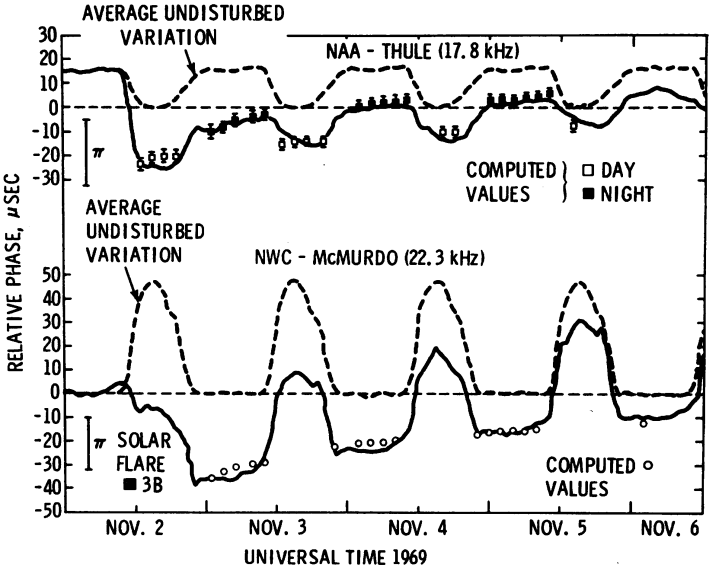

Figure 44-4. Computed and Observed VLF Phase Variations for the NAA to Thule and NWC to McMurdo Transmissions

Approximately 1500 km or 22 percent of the NWC-McMurdo path traverses the Antarctic ice where low ground conductivities ($\sim 10^{-5}$ mho meter^{-1}) and markedly different VLF propagation characteristics, in comparison to propagation over an infinitely conducting ground, have been observed (Webber and Peden, 1970; Westerlund et al, 1969). Full-wave results for these low conductivities were not available for the calculations here, so the empirical results of Westerlund et al, (1969) were extrapolated to the present work.

The NAA-Thule path in the northern polar cap and the NWC-McMurdo path in the southern cap constitute a unique set of VLF data because when one path is in darkness the other is in sunlight and vice versa. The NWC-McMurdo path experienced a very short period of darkness so night phase values were not computed for this path and are not shown in Figure 44-4.

The sensitivity of the VLF phase to solar protons in comparison with the riometer is shown in Figure 44-4 at the end of 5 November, when the NAA-Thule path is perturbed by -10 μsec with respect to the undisturbed night value and the NWC-McMurdo phase is perturbed by -10 μsec with respect to the undisturbed day value, whereas both day and night 30 MHz riometer values are less than 1 db at this time (Masley et al, 1970). Both these paths showed perturbations coincident with the solar flare on 7 November (not shown here) and were disturbed again following the sudden commencement on 8 November. The phase observed on these paths did not return to the undisturbed variation until 10 November.

44-6 RIOMETER ABSORPTION

The day and night electron density profiles computed from the Explorer 41 fluxes and used for the VLF calculation above were used to compute 30 MHz polar cap riometer absorption using the generalized formulas of Sen and Wyller (1960) and are shown in Figure 44-5. The 30 MHz absorption values observed at Shepherd Bay, Canada and at the conjugate station, McMurdo Sound, Antarctica by Masley et al, (1970) are also shown in this figure. The solar zenith angle at McMurdo never exceeded 90° during this event so this station is considered to be in continuous daylight. The solar angle at Shepherd Bay varied between 83° and 126°, causing the diurnal variation in absorption shown in Figure 44-5. No data is available from the Shepherd Bay station from approximately 1000 UT to 1800 on 3 November.

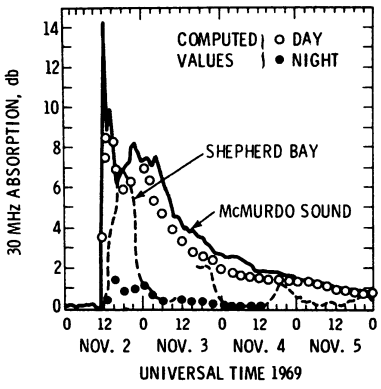

Figure 44-5. Riometer Absorption Observed at Shepherd Bay and McMurdo Sound by Masley et al, (1970) and Computed Values From This Analysis

The large spike in daytime absorption observed at McMurdo shortly after 1200 UT cannot be explained by the values computed from the observed proton fluxes at this time. Nor is this large ionization enhancement evident in any of the VLF phase observations. Also from 1800 UT on 2 November to the end of 4 November the observed McMurdo absorption is systematically greater than the computed absorption. Because of the good agreement of computed electron density profiles and the rocket measured profiles below 80 km discussed earlier and between computed and observed VLF phase values (where the reference height was depressed to as low as 55 km from the undisturbed daytime height of 71.5 km, and to 63 km from the undisturbed night height of 85 km), we conclude that the ionization enhancement causing the excess riometer absorption must occur above 80 km, due possibly to 10–100 kev electrons, or to non-uniform proton precipitation over this station with respect to the rest of the polar cap which cannot be detected by the long-distance VLF paths.

The agreement between computed night riometer absorption and observed values after 1200 UT 4 November are smaller than 0.2 db, very nearly equal to the resolution of the riometer, so these computed values were not included in Figure 44-5 due to the scale limitation.

The "daytime" absorption measured at Shepherd Bay, when the zenith angle is smallest at approximately 1800 UT, is nearly equal to the absorption at McMurdo Sound on 2 and 5 November but is smaller on 3 and 4 November when the computed absorption due to protons is also smaller. This could be attributed to non-uniform particle precipitation over McMurdo in comparison to Shepherd Bay except that effects due to the low daytime zenith at Shepherd Bay cannot be ruled out.

Acknowledgments

This work was supported by the Naval Ordnance Systems Command, Department of the Navy, under contract N00017-62-c-0604. We also thank the staffs of the Physical Science Laboratory of New Mexico State University and DRL, University of Texas for aid in obtaining the VLF data for the NAA-Thule and NWC-McMurdo paths respectively.

References

Adams, G.W. and Masley, A.J. (1965) J. Atmospheric Terrest. Phys., 27:289.

Borst, W.L. and Zipf, E.C. (1970) Phys. Rev. A1:834.

Bostrom, C.O. (1960) Personal Communication.

Davenport, G.R. (1970) Proc. of Meeting on Operation PCA 69, Air Force Cambridge Research Laboratories Rept. (No. 110):29.

Dean, W.A. (1970) Proc. of Meeting on Operation PCA 69, Air Force Cambridge Research Laboratories Rept. (No. 110):87.

Hegblom, R. (1970) Proc. of Meeting on Operation PCA 69, Air Force Cambridge Research Laboratories Rept. (No. 110):59.

Hirsh, M.N. Poss, E. and Eisner, P.N. (1970) Phys. Rev. A1:1615.

Johnson, R.G. and Sharp, R.D. (1970) Proc. of Meeting on Operation PCA 69, Air Force Cambridge Research Laboratories Rept. (No. 110):43.

Masley, A.J. and Satterblom, P.R. (1970) Trans. Am. Geophys. Union, (abstract only) 51:799.

Masley, A.J., McDonough, J.W. and Satterblom, P.R. (1970) Antarctic J. of the U.S. 5:172.

Paulikas, G.A. and Blake, J.B. (1969) J. Geophys. Res. 74:2161.

Potemra, T.A., Zmuda, A.J., Haave, C.R. and Shaw, B.W. (1969) J. Geophys. Res. 74:6444.

Potemra, T.A., Zmuda, A.J., Shaw, B.W. and Haave, C.R. (1970) Radio Sci. 5:1137.

Reagan, J.B. and Imhof, W.L. (1970) Proc. of Meeting an Operation PCA 69, Air Force Cambridge Research Laboratories Rept. (No. 110):39.

Rees, M.H. (1963) Planet. Space Sci. 11:1209.

Sandford, B.P. (1970) Proc. of Meeting on Operation PCA 69, Air Force Cambridge Research Laboratories Rept. (No. 110):171.

References

Sen, H.K. and Wyller, A.A. (1960) J. Geophys. Res. 65:3931.

Solar-Geophysical Data No. 309-Pt. (1970) II:79.

Spies, K.P. (1968) Personal Communication.

Ulwick, J.C. and Blank, C.A. (1970) Proc. of Meeting on Operation PCA 69, Air Force Cambridge Research Laboratories Rept. (No. 110):3.

Ulwick, J.C. (1970) Proc. of Meeting on Operation PCA 69, Air Force Cambridge Research Laboratories Rept. (No. 110):135.

Wait, J.R. and Spies, K.P. (1964) NBS Tech. Note (No. 300).

Webber, G.E. and Peden, I.C. (1970) Radio Sci. 5:655.

Westerlund, S., Reder, F.H. and Abom, C. (1969) Planetary Space Sci. 17:1329.

Yates, G.K. (1970) Proc. of Meeting on Operation PCA 69, Air Force Cambridge Research Laboratories Rept. (No. 110):47.

Zmuda, A.J., Potemra, T.A. and Bostrom, C.O. to be published.

Appendix A

Nighttime Effective Recombination Coefficient Values For the 18 November 1969 Proton Event

T.A. Potemra, A.J. Zmuda and C.R. Haave
Applied Physics Laboratory
The Johns Hopkins University
Silver Spring, Maryland
(Supplement)

As further support for the ionization models developed by Potemra et al, (1969) that were used in the previous paper, values of ionization rates and effective recombination coefficients determined from proton fluxes measured by the 1100 km altitude, polar orbiting, satellite 1963 38C during the proton event of 18 November 1968 are compared with the values measured during a rocket flight from Churchill by Ulwick and Sellers (1970). The electron-ion pair production rate determined from the proton flux measured during a rocket flight from Churchill at 0800 UT on 19 November 1968 is shown as curve Q_1 in Figure 44A-1 which was adopted from Ulwick and Sellers (1970). The ionization rate computed from the integral fluxes measured by satellite 1963 38C in the ranges > 2.2 Mev, > 8.4 Mev, and > 25 Mev on a pass beginning at 0513 on 19 November 1968 are shown as curve Q_2 in this same figure. Specific ionization rates from Adams and Masley (1965) were used in calculations. The rocket determined ionization profile is almost identical with the profile determined from the satellite data.

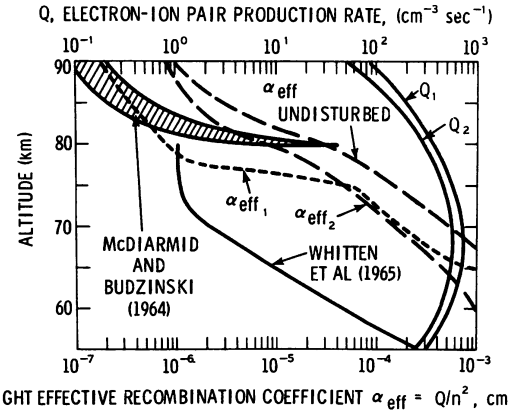

Figure 44A-1. Nighttime Electron-ion Pair Production Rates and Effective Recombination Coefficients. Q_1 and $\alpha_{eff\ 1}$ determined by rocket from Churchill 0800 UT 19 November 1968 (Ulwick and Sellers, 1970). Q_2 and $\alpha_{eff\ 2}$ from this analysis using satellite 1963-38C at 0513 UT 19 November 1968. α_{eff} undisturbed corresponds to undisturbed nighttime conditions (Potemra et al, 1969).

The effective recombination coefficient, α_{eff}, sometimes called the effective electron loss rate, connects ionization rates and electron densities by the formula $n_e = (Q/\alpha_{eff})^{1/2}$. During the night α_{eff} depends on the ionization rate Q (see for example Potemra et al, 1969). Ulwick and Sellers computed a nighttime α_{eff} profile from the ionization rates described above and from the electron densities measured on the same rocket launched on 19 November 1969 and this profile is shown in Figure 44A-1 as curve $\alpha_{eff\ 1}$. The "undisturbed" α_{eff} shown in this figure is determined from our nighttime ionization model, which is essentially a two-ion model described by four effective reactions similar to LeLevier and Branscomb's (1968) and which corresponds to undisturbed nighttime ionization conditions due to galactic cosmic rays and scattered H Ly α. Our α_{eff} profile, which corresponds to the ionization rate Q_2, is shown in Figure 44A-1 and labeled $\alpha_{eff\ 2}$. The values of α_{eff} from an auroral analysis by McDiarmid and Budzinski (1964) and from nuclear burst measurements by Whitten et al, (1965) are also shown in Figure 44A-1.

It is apparent from Figure 44A-1 that extreme care must be exercised when comparing nighttime α_{eff} values because of the dependence on the ionization rate Q. However, for similar ionization conditions, such as during the 18 November 1968 PCA, the nighttime values $\alpha_{eff\ 1}$ and $\alpha_{eff\ 2}$ compare very favorably, at least below 75 km. The smaller α_{eff} above 75 km measured by Ulwick and Sellers' rocket in the auroral zone may be due to the electron densities produced by energetic electrons which if subtracted would increase the values of $\alpha_{eff\ 1}$. The comparison of these two α_{eff}'s is highly significant because of the markedly different ways that they were obtained – in one case from an in situ rocket measurement (although in the auroral region) and in our case from the connection of satellite particle and ground based VLF phase and HF absorption data during previous events. In any case the electron density profile corresponding to Q_2 and $\alpha_{eff\ 2}$

(not shown here) fits the rocket measured profile as well as the profile computed by Ulwick and Sellers using a more complicated model which takes into account about 105 different reaction rates and 30 different species (Keneshea, 1967).

References

Adams, G.W. and Masley, A.J. (1965) J. Atmospheric Terrest. Phys. 27:289.

Keneshea, T.J. (1967) Air Force Cambridge Research Lab. Rept. (No. 67-0221).

LeLevier, R.E. and Branscomb, L.M. (1968) J. Geophys. Res. 73:27.

McDiarmid, I.B. and Budzinski, E.E. (1964) Can. J. Phys. 42:2048.

Potemra, T.A., Zmuda, A.J., Haave, C.R. and Shaw, B.W. (1969) J. Geophys. Res. 74:6444.

Ulwick, J.C. and Sellers, B. (1970) Proc. of Meeting on Operation PCA 69, Air Force Cambridge Research Lab. Rept. (No. 110):201.

Whitten, R.C., Poppoff, I.G., Edmonds, R.S. and Berning, W. (1965) J. Geophys. Res. 70:1737.

Contents

45. The November 1969 Solar Events and Associated Ionospheric Disturbances Over Ahmedabad

R.V. Bhonsle, S.S. Degaonkar, T.S.G. Sastry and J.S. Shirke
Physical Research Laboratory
Ahmedabad -9, India

Abstract

A number of important solar flares occurred in November 1969. Some of these flares were accompanied by electromagnetic emissions covering X-ray, optical and radio wavelengths and energetic particle enhancements. The following phenomena have been recorded at Ahmedabad associated with these solar flares:

(1) sudden enhancements of signals (SES) at 164 kHz from Radio Tashkent;

(2) sudden cosmic noise absorption (SCNA) at 21.3 MHz;

(3) magnetic crochets; and

(4) solar radio bursts.

The paper describes the characteristics of the solar events of 2 November and 24 November 1969 in some detail and presents the quantitative estimates of various disturbances in the terrestrial and solar atmosphere.

45-1 INTRODUCTION

The Physical Research Laboratory, Ahmedabad (lat. 23°N, long. 72°33'E, geographic) has been operating a number of ground-based experiments for studying solar flares and their effects on the earth's ionosphere. These are:

(1) field strength recording of Radio Tashkent at 164 kHz;

(2) riometer at 21.3 MHz;

(3) proton precession magnetometer;

(4) vertical ionospheric sounder; and

(5) solar radio spectroscope (40-240 MHz).

In Table 45-1 are listed the November 1969 solar events as detected by their X-ray effects on the field strength of low frequency transmission at 164 kHz on the Tashkent-Ahmedabad circuit. This paper describes the ground-based observations of the solar events of 2 and 24 November 1969 and their effects on the earth's ionosphere.

Table 45-1. The November 1969 Solar Events as Observed at Ahmedabad on 164 kHz Field Strength Observations of Radio Tashkent

Date	Start	Time in UT		End
		Maximum Enhancement	Minimum*	
2	0956	1030	1200	--
4	0412	0420	0508	--
5	0613	--	0620	--
	0913	0922	--	--
13	0930	--	1045	1145
14	0434	--	0454	--
15	1130	--	1144	1152
18	0711	0717	--	--
19	0410	0424	0436	--
	0454	0505	0515	--
	0526	0541	0530	--
	0704	0711	0740	--
	0813	0821	0845	--
20	0422	--	0426	--
21	0208	--	0214	--
	0652	--	0704	--
	0830	0840	0915	--
22	0925	1010	1100	--
24	0615	0632	0740	--
	0914	0922	--	--

*Minimum Time - Time of the first minimum after the maximum.

45-2 THE SOLAR EVENT OF 2 NOVEMBER 1969

45-2.1 Sudden Enhancement of Signals (Radio Tashkent Field Strength, 164 kHz)

It can be seen from Figure 45-1 that an effect of the solar X-ray flare on the Radio Tashkent field strength was first observed at 0956 UT, with an enhancement

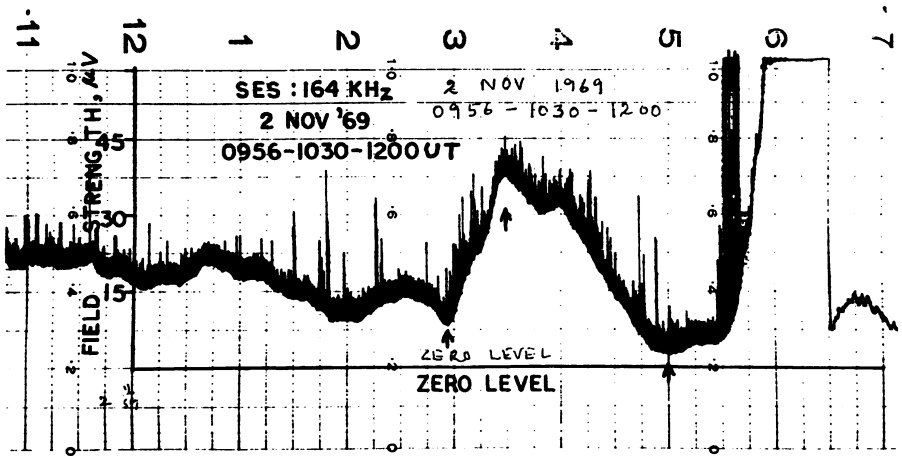

Figure 45-1. Field Strength Recording of Radio Tashkent, 164 KHz Made at Ahmedabad on 2 November 1969

that reached a magnitude of about 13.6 db at 1030 UT. Thereafter a decrease in the field strength followed, which continued until 1200 UT. A subsidiary maximum in enhancement was also observed at about 1100 UT. The low value of field strength continued until 1230 UT, after which time the sunset effect giving the usual rise in field strength was observed. The time taken by this event to reach maximum was 34 minutes, which is more than that of any of the 114 events analyzed by Shirke and Alurkar (1963). Another peculiarity of this event was the long duration (two hours) over which the enhancement in field strength persisted.

45-2.2 Shortwave Fade-Out and Sudden Cosmic Noise Absorption

In spite of the substantially large effect on the low frequency radio propagation, the shortwave fade-out as seen by an ionosonde, as well as the sudden cosmic noise absorption as recorded by a riometer at 21.3 MHz, was comparatively of a very small magnitude corresponding to this solar event. A qualitative explanation for this is given later in this paper.

45-2.3 Magnetic Crochet

It was found that there was no magnetic crochet effect greater than two gammas accompanying the solar flare of 2 November 1969, as seen on the proton precession magnetometer.

45-2.4 Solar Radio Bursts

The solar radio spectroscope operating over a frequency range 40-240 MHz at Ahmedabad indicated that a spectral type IV continuum storm was in progress for the whole day on 2 November 1969. The storm was characterized by strong pulsations in intensity throughout the day. The Radio Astronomy Observatory at Weissenau (G.F.R.) reported a number of groups of spectral type III bursts from 1000 UT to 1050 UT. It may be noted that a spectral type II (slow drift) was altogether absent following this solar flare, which is consistent with the fact that there was no sudden commencement geomagnetic storm in the next few days after 2 November 1969.

45-3 THE SOLAR EVENT OF 24 NOVEMBER 1969

45-3.1 Sudden Enhancement of Signals (Radio Tashkent Field Strength, 164 kHz)

Figure 45-2 shows the field strength recording of Radio Tashkent (164 kHz) made at Ahmedabad on 24 November 1969. It can be seen from the figure that a small solar X-ray flare was noticed beginning around 0615 UT, giving a drop of

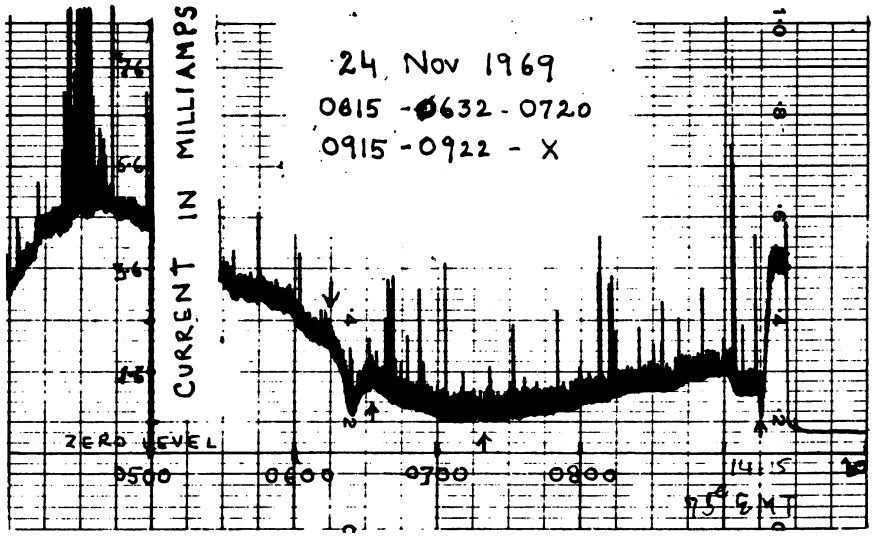

Figure 45-2. Field Strength Recording of Radio Tashkent, 164 KHz Made at Ahmedabad on 24 November 1969

9 db in field strength at 0623 UT. An enhancement of 5 db over this minimum value was reached by 0632 UT. Thereafter a further decrease set in until 0720 UT. It was on the recovery phase of this flare effect that another mild flare effect was observed, giving a decrease of 2.5 db from 0901 UT to 0906 UT. It remained at this level for about eight minutes.

The major X-ray flare event, however, occurred at 0915 UT commencing with an initial drop of 1.5 db and a subsequent sharp enhancement of 11 db in about four minutes, as can be seen in Figure 45-2. The enhanced intensity was maintained for over six minutes, whereafter no data were available due to equipment failure. It may be noted that the commencement of the field strength increase coincided in time with the X-ray flux (1-8 Å) enhancement as observed by Solrad-9 satellite. The X-ray flux of value 4900×10^{-4} ergs/cm^2/sec recorded by the satellite for this event at 0935 UT was by far the maximum during the month of November 1969.

45-3.2 Sudden Cosmic Noise Absorption (SCNA)

Figure 45-3 shows the SCNA which was recorded by means of a riometer operating at 21.3 MHz on 24 November 1969. It started at 0915 UT and caused maximum absorption of 5.1 db at 0922 UT. The absorption remained at this level until 0932 UT. Thereafter, cosmic noise absorption began to decrease and reached its

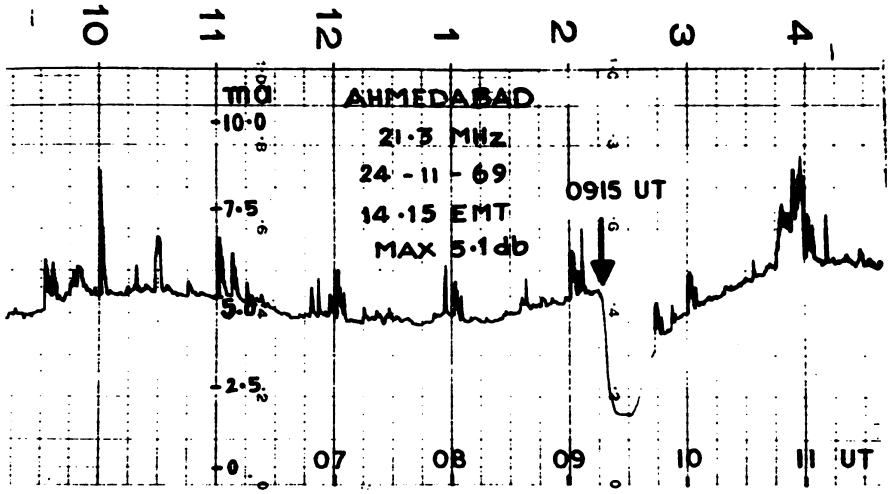

Figure 45-3. Sudden Cosmic Noise Absorption (SCNA) at 21.3 MHz on 24 November 1969. The spikes seen on the trace at 0945, 1000 UT and at other hourly intervals are produced by stray pick up from a nearby transmitter

preflare value by about 1045 UT. The recovery phase of the SCNA lasted from 0932 UT to 1045 UT and exhibited two distinct rates of recovery. The recovery rate was relatively fast from 0932 UT to 0947 UT compared to that in the final stage of recovery. The slow rate of recovery could in part be due to another flare which occurred at 1046 UT.

45-3.3 Magnetic Crochet

Figure 45-4 shows a record of total geomagnetic field at Ahmedabad measured by means of a proton precession magnetometer on 24 November 1969. It can be seen from the figure that the geomagnetic field started to increase suddenly at 0913 UT, reached a maximum of 15 gammas in about five minutes, and remained almost steady until 0926 UT. The field returned to normal by about 0950 UT. It may be noted that the crochet was superimposed on the declining portion of the diurnal curve of the total magnetic field.

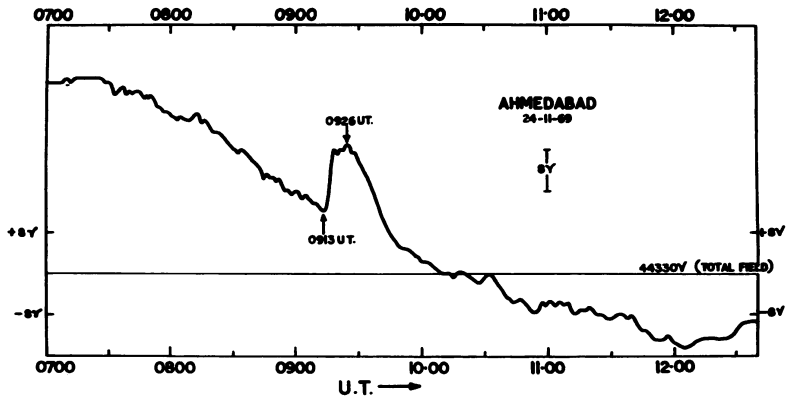

Figure 45-4. Magnetic Crochet on 24 November 1969

45-3.4 Shortwave Fade-out (SWF)

Figure 45-5 shows a set of ionograms on 24 November 1969 recorded by means of an automatic ionospheric vertical sounder. It can be seen that at 0900 UT, the minimum recorded frequency of reflection, f_{min}, was about 2.0 MHz. The next ionogram, taken at 0944 UT during the recovery phase of SWF showed that f_{min} was 5.2 MHz, and it was 4.2 MHz at 1000 UT. The f_{min} returned to normal some time between 1000 and 1100 UT, which confirms that the SCNA continued beyond 1000 UT.

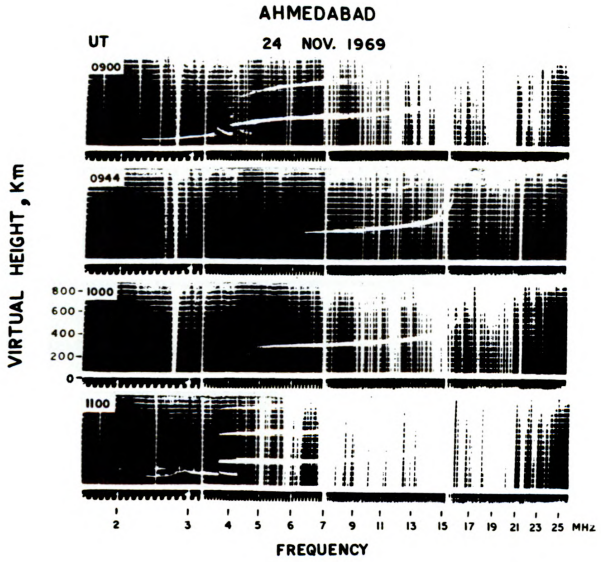

Figure 45-5. Ionograms Showing Shortwave Fade-out on 24 November 1969

45-3.5 Dynamic Spectrum of Solar Radio Burst

Figure 45-6 shows the dynamic spectrum of an intense solar radio burst of spectral type II, recorded by a radio spectroscope on 24 November 1969 at 0919.6 UT, at Ahmedabad. The spectroscope operates over the frequency range 40 MHz to 240 MHz. This slow drift burst had a starting frequency greater than 240 MHz and was most intense until about 0923 UT, although it could be seen at reduced intensity until about 0928 UT. Generally, when a spectral type II (slow drift burst)

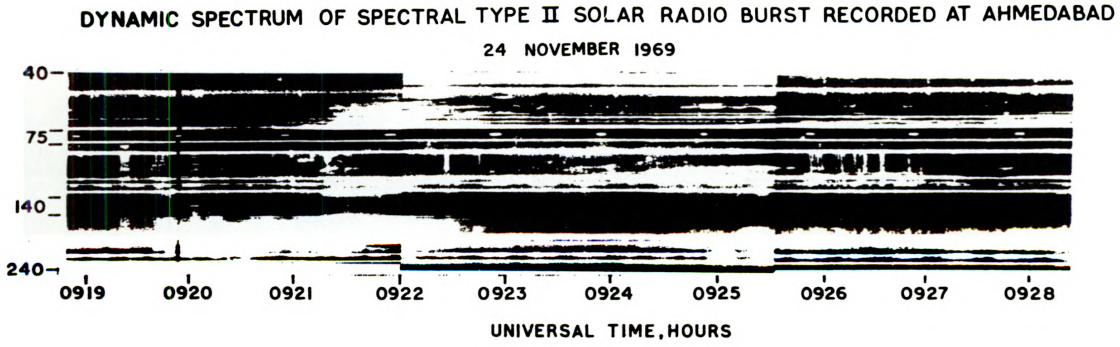

Figure 45-6. Dynamic Spectrum of Spectral Type II Burst on 24 November 1969

has a harmonic structure, both the fundamental and second harmonic radiations do not appear simultaneously (Maxwell and Thompson, 1962). The type II burst radiation was emitted in a single diffuse broad-band of frequencies initially for a period of about one minute. Then, the burst was observed at the subharmonic frequency starting near about 100 MHz at 0921 UT and lasted until 0923 UT. Thereafter, the harmonic structure of the bursts was evident until about 0928 UT but bandwidths were narrower compared to those initially, when intensities were strong. The type II bursts are believed to be generated in the solar atmosphere due to plasma oscillations excited by the outward passage of a shock-front through the overlying corona. It is possible to calculate the radial component of velocity of the shock-front from the knowledge of the rate of frequency drift of the burst and the coronal electron density model. In the present case, the outward radial velocity of the shock front, calculated from the frequency drift between 0920 and 0921 UT, turns out to be of the order of 1000 km/sec. But it appears that the shock-front has suffered some deceleration after 0921 UT, since the frequency drift rate has reduced considerably later on. A geomagnetic storm occurred on 26 November 1969 with a sudden commencement at 1507 UT with a delay of about 54 hours after the solar flare on 24 November 1969 as seen by the Ahmedabad magnetometer. Examination of optical flare data indicates that a number of solar flares occurred around 0600 UT to 0930 UT on 25 November 1969, which could have given rise to the magnetic storm on 26 November 1969. But this can be ruled out because there were no spectral type II and IV bursts associated with these flares. Therefore, it is tempting to identify the solar flare of 24 November 1969 to be the cause of the SC storm on 26 November 1969, since this flare was accompanied by a spectral type II burst.

45-4 DISCUSSION

45-4.1 Time Relationships of the Observed Effects of the Solar Flare of 24 November 1969

The terrestrial effects listed in Table 45-2 started within ±1 minute of 0914 UT which is within the reading accuracy of time from the chart recordings. The initial dip in the field strength starting at 0914 UT is often seen on flare effects observed in winter on Tashkent-Ahmedabad circuit (Shirke and Alurkar, 1963). It can be seen from Table 45-2 that the maximum effect of the solar flare was attained by 0920 ±2 minutes. The maximum effect persisted for the duration close to 8 minutes at substantially the same level for each of the records taken by various techniques. This feature is rather unusual, implying that the steady state of the lower ionosphere persisted for about 8 minutes near the maximum phase of the solar flare.

Table 45-2. Time Relationships of Some of the Observed Effects of the Solar Flare on 24 November 1969

	Start	Maximum	Duration of Max. Phase	Recovery
SES (164 kHz)	0915	0922	7 min.	--
Riometer	0915	0922	8 min.	Between 1000 and 1100
Magnetometer	0913	0918	8 min.	About 0950
Optical	0914	0919		1039

45-4.2 Comparison of the Solar Events of 2 November 1969 and 24 November 1969

Table 45-3 summarizes the knowledge about the solar flares and their observed effects on 2 and 24 November 1969. Although the field strength enhancements of Radio Tashkent have been of comparable magnitude on 2 and 24 November 1969, the times taken by them to reach the maximum have been 34 min and 7 min, respectively. Also, the field strengths remained near the peak value for about 30 minutes on 2 November as against 8 min on 24 November. The field strength enhancement persisted for about 124 minutes on 2 November, which was unusually large. It appears that the X-ray event on 2 November was rather slow in development and of long duration. Although the effect has been large on 164 kHz field strength, the shortwave fade-out as seen on the riometer and ionosonde record on 2 November has been of a comparatively very small magnitude. Solrad-9 X-ray fluxes indicate longer persistence for the 2 November event than that on 24 November. On 2 November the X-ray flux values reached the peak value in 72 min, which is much longer compared to the corresponding time of development of 20 min on 24 November. This observation is consistent with the development times of SES's of 2 and 24 November 1969.

Considering the spectral distribution of X-ray fluxes of the two events, it is found that the fluxes in 0.5 - 3 Å channel were comparable in magnitude in the two cases, whereas the (8-20 Å) channel flux for the 24 November event was more than twice as large as that of the 2 November event. The effect of this difference in the steepness of the X-ray spectrum would be to produce more ionization at higher levels in the ionosphere on the 24 November event than that on 2 November. This appears to be consistent with riometer absorption observations of the two events which showed 5.1 db maximum absorption on 24 November compared to very small absorption on 2 November.

Table 45-3. Comparison of Characteristics of Solar Flares of 2 and 24 November 1969

Effect	Solar Flare of 2 November 1969				Solar Flare of 24 November 1969			
	Start UT	End UT	Max. Effects UT	Remarks	Start UT	End UT	Max. Effects UT	Remarks
164 kHz Radio Tashkent field strength	0956		1030	Gradual rise; rise time, 34 min	0915		0922	Duration of max. phase, 7 min; rise time, 7 min
H α - flare (Mont Mario Obs., Italy)	0955	1008	0959	Location N 14 W 88 Imp -N	0914	1039	0919	Abastumani Observatory Location N 16 W 32 Imp 2N
Solrad -9 X-ray flux				Flux				Flux
(1) 0.5 - 3 Å	0949	2006	1201E	(1) $130,000 \times 10^{-5}$ erg/cm^{2}sec	0915	1619	1225	(1) $130,000 \times 10^{-5}$ erg/cm^{2}sec
(2) 1 - 8 Å			1100E	(2) $3,000 \times 10^{-4}$ " " "			0935	(2) $4,900 \times 10^{-4}$ " " "
(3) 8 - 20 Å			1108	(3) 710×10^{-3} " " "			0929	(3) $1,500 \times 10^{-3}$ " " "
Riometer absorption				Small SCNA	0915	0922	1000-1100	Duration of max. phase, 8 min
Magnetic crochet				No crochet	0913	0918	0950	Duration of max. phase, 8 min
Magnetic storm				No magnetic storm	1507	2200		SC 26 Nov 1969, End 27 Nov 69
Solar radio bursts (only m - λ spectral observations)	1000.1	1039		Weissenau (G.F.R.)	0919.6	0928	0921.5	Ahmedabad spectral Type II burst, harmonic structure;
	1009	1035		Type III (fast drift bursts)	1351	1406		Type I, Harvard
	1043	1050		Ahmedabad Type IV, cont. whole day	1406	1654		Type I, Harvard

When one compares the radio burst spectral data at meter wavelengths accompanying these two solar flares, one finds that on 2 November, only spectral type III bursts and continuum radiation were emitted. There was no evidence of spectral type II bursts accompanying this flare, which implied that particles necessary to produce SC geomagnetic storm were not produced during the solar flare on 2 November. As would be expected, there was no magnetic storm in the next few days following this flare. On the other hand, the 2 November flare has been a very strong source of particles that produced the largest PCA event as recorded by riometer stations at high latitudes. This means that the acceleration mechanism was such as to produce particles of appropriate energy to cause PCA but did not emit particles which could produce magnetic storm. In the case of the 24 November event, however, a spectral type II burst was emitted and an SC type magnetic storm was produced on 26 November 1969. But this flare did not produce enough particles to cause a PCA event, although a small enhancement of particles was seen in space two hours after the flare.

Acknowledgments

We are grateful to Prof. K. R. Ramanathan for critical comments and under whose guidance the work in solar-terrestrial physics at the Physical Research Laboratory, Ahmedabad is being carried out. The financial support for the work reported here came from the Department of Atomic Energy, Government of India.

References

Maxwell, A., and Thompson, A. R. (1962) Spectral observations of solar radio bursts - II. slow drift bursts and coronal streamers, Ap. J. 135 A:138-150.

Shirke, J. S., and Alurkar, S. K. (1963) Solar flare (S. I. D.) effects on the propagation of 164 Kc/s radio-waves from Tashkent to Ahmedabad, Proc. Ind. Acad. Sci. L VII:49-69.

Contents

46. Daily Variation of Geomagnetic Field at the Indian Stations Under the Electrojet During the Period of the July 1966 Proton Flare

T.S.G. Sastry
Physical Research Laboratory
Ahmedabad, India

Abstract

A magnetometer was launched by rocket flight 20.05 from Thumba on 7 July 1966 at 1345 IST (0815 UT) to study the quiet day equatorial electrojet. Results from this flight (Sastry, 1968) indicated that although the day was magnetically quiet, the observed electrojet was abnormal. The vertical current density profile derived from rocket magnetometer data indicated the presence of a second current layer with a broad maximum near 140 km altitude, but the existence of this layer could not be confirmed. An attempt to reconcile ground-based magnetometer observations with rocket magnetometer data taking into consideration the effect of the currents in the main electrojet layer only, suggested an unusually large width for the electrojet. However, subsequent analysis of several magnetometer flights from Thumba and a study of ground H daily variation at Trivandrum and Annamalainagar during 1-10 July 1966 showed that a second current layer was present on 7 July and that the rocket and ground magnetometer measurements could be reconciled if the effect of the second current layer is taken into account. The study further showed that the gradual buildup of H variation amplitude at low latitude stations during 1-6 July prior to the proton flare was due to gradual enhancement of the slowly varying component of ionizing radiation from the sun. It is suggested that the formation of a second current layer observed during flight 20.05 was due to the increased emission of XUV radiation over a wide spectral band during the flare.

46-1 INTRODUCTION

The proton flare event of 7 July 1966 has been extensively studied. The results of this worldwide study have been published in Volume 3 of Annals of IQSY (1968). The week prior to the flare was magnetically quiet. July 7 itself was one of the five international quiet days of the month. This quietness afforded a unique opportunity to study the effects of the flare in detail at the ground based observatories as well as in space. Trivandrum magnetic observatory near the dip equator in India recorded a geomagnetic croche on 7 July. It began at 0026 UT, in time coincidence with the proton flare, and ended by 0200 UT. The croche was accompanied by micropulsation activity. Except for these minor disturbances in the early hours of the day, 7 July was quiet until 2200 UT, when indications of the coming storm were evident on the magnetogram.

A Nike-Apache payload (FL. 20.05) containing a proton precession magnetometer and Langmuir probe was launched from Thumba (8.52°N, 76.87°E, dip latitude 0.47°S) on 7 July 1966 at 0815 UT (Sastry, 1968) to study the nature of the equatorial electrojet. During the flight, the rocket magnetometer encountered a quiet day electrojet extending from 90 km to 118 km in altitude. There were indications in the data of the presence of a weak subsidiary current layer with a broad maximum between 130 and 150 km. The existence of this layer, however, could not be confirmed.

An attempt to reconcile the rocket measurement of the magnetic effect ΔF of the jet with the jet effect ΔH observed at the ground, taking into account the effect of the currents in the main electrojet layer only, showed that the magnetic effect at the ground due to the jet encountered during the flight was almost that due to an infinite current sheet. Thus an abnormality as to the presence of a second current layer or an abnormality in the width of the jet existed on 7 July at the time of the flight. No explanation could be given for the observed abnormality except that it could be due to increased solar activity. Subsequent analysis of the data from similar magnetometer flights from Thumba by Sastry (1970) and the results of analysis of ground magnetometer data from Trivandrum and Annamalainagar for the period 1-10 July 1966 presented here, shows that the unusual nature of the electrojet observed during the flight 20.05 is in fact due to the enhanced XUV emission from the sun during the 7 July 1966 proton flare.

46-2 RESULTS

Table 46-1 shows the estimation of half-width W of the electrojet by the image method. In this method there are two unknown parameters: the depth D underground

of the conducting layer at which the external electrojet gets mirrored, and the width (2W) of the electrojet in the north-south direction. If one of these two parameters is known, the other can be estimated provided ΔF, h, and ΔH can be measured. The change ΔF in the total field due to the external jet and the height, h, of the electrojet center above the ground are determined by rocket measurements. Thumba is almost on the dip equator, and it is assumed that the longitudinal axis of the electrojet passes over Thumba rocket range. The ground magnetometer at Thumba (Trivandrum) measures $\Delta H = (H_e + H_i)$, of which H_e is the contribution due to the external current system, and H_i that due to the induced currents in the ground. ΔH is the departure at the time of the flight of H from midnight levels.

Table 46-1

Flight	Time IST	ΔF Rocket γ	h KM	D KM	w KM	H_e γ	H_i γ	$H_e + H_i$ γ	Trivandrum ΔH γ	H_i/H_e
2001	25 Jan 64 11.00 hrs	67	107.5	507.5	230	24.17	9.08	33.25	33	0.38
2002	27 Jan 64 10.00 hrs	68	107	507	180	22.39	7.38	29.77	30	0.33
2005	7 July 66 13.45 hrs	75	105	505	630	33.57	21.37	54.94	55	0.64
2006	29 Aug 68 11.08 hrs	202	107	507	280	77.55	32.43	109.98	110	0.42
2007	29 Aug 68 14.15 hrs	103	108	508	305	40.34	17.73	58.07	58	0.44
2005*		75	105	505	300	29.46	12.80	42.26	55	0.43

Various factors enter into the estimation of the width of the electrojet by the image method. ΔF is the shift in the total field produced by the electrojet, and h is the height of the center of the electrojet above sea level. ΔF and h are determined from rocket magnetometer measurements. $D = 2d + h$ where d is the depth to the conducting layer. W is the half width of the jet estimated by making $\Delta H = H_e + H_i$. Data tabulated against 2005* gives H_e and H_i values calculated for an assumed W of 300 km for the electrojet encountered during flight 2005.

Average conductivity characteristics of the upper mantle of the earth in the region below the equatorial electrojet has been studied by Rokityanskiy (1969). According to his estimations the depth to the conducting core with a uniform conductivity of 0.2 Ω/m is 200 km in the region around Trivandrum, India. This value of d has been used in calculating W shown in Table 46-1. A change in the value

of d by ±50 km gives rise to a change in the estimated width of about ±10 percent. It is seen from the table that the width of the electrojet and the ratio H_i/H_e are abnormally large for the flight 20.05 conducted on 7 July 1966, compared to the values obtained from other similar flights.

In order to study the possible association of the abnormality in the nature of the electrojet observed during the flight 20.05, the daily variation of the horizontal component H at Trivandrum and Annamalainagar during the period 1 July 1966 to 10 July 1966 was examined. Figure 46-1 shows the daily variation of H at Trivandrum during the above period. It is seen from the figure that ΔH_{max}, the departure of H variation maximum from the midnight level, increases gradually from

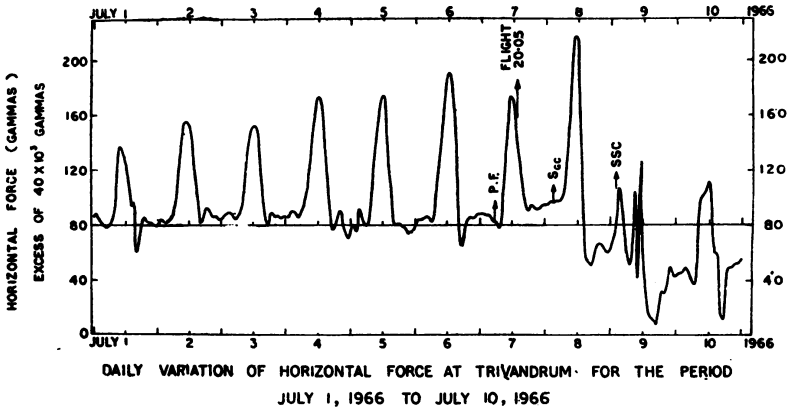

DAILY VARIATION OF HORIZONTAL FORCE AT TRIVANDRUM FOR THE PERIOD JULY 1, 1966 TO JULY 10, 1966

Figure 46-1. Daily Variation of Horizontal Force at Trivandrum for the Period 1 July to 10 July 1966. The time of occurrence of proton flare P.F. (0556 IST), the time of launch of magnetometer payload FL 2005 (13.45 IST), time of onset of prestorm disturbance GSC (0330 IST) on 8 July observed from Trivandrum magnetograms and the time of SSC on 9 July (0232 IST) are marked. The short graduations on the time axis indicate noon and the long ones, midnight

60γ on 1 July to 110γ on 6 July, while the nighttime level remains steady during this period within ±5γ. On 7 July, which is the day of the flare, ΔH_{max} is 87γ and is less compared to that on the day before the flare. July 8 was a disturbed day and the daily variation is superposed on a pre-storm disturbance which started in the early hours before sunrise. A sudden commencement storm followed this disturbance and lasted until 14 July. ΔH_{max} reached a peak value of 160γ on 8 July.

The variation of H at Annamalainagar, about 270 km north of dip equator, follows the same pattern as observed at Trivandrum except that the day-to-day change of midnight level at Annamalainagar is more than it is at Trivandrum.

For the period 1-10 July 1966, Figure 46-2(a) shows the variation of total area A_H of the sunspot group in which the proton flare occurred (McIntosh and Sawyer, 1969); the increase in the S component of solar radio emission at 9400 MHz (Kruger, 1968); the variation of flux density of 10.7 cm wave emission from the sun reported by Banin et al (1968); and the gradual enhancement of the S component of solar X-radiation represented by the summation curve derived from SID effects by Krivsky (1968). Figure 46-2(b) shows the variation of H_R, the range of H daily variation at Trivandrum and Annamalainagar during the same period. In Figure 46-2(c) the gradual increase in the S component of solar X-ray emission in 0-60 Å band as observed by the Explorer 30 satellite (Friedman and Kreplin, 1968) is given. The variation of H_R and the variation seen in Figure 46-1 of ΔH_{max} at Trivandrum, which represents the variation of the strength of the equatorial electrojet, may be compared with the variation of quantities shown in Figures 46-2(a) and 46-2(c).

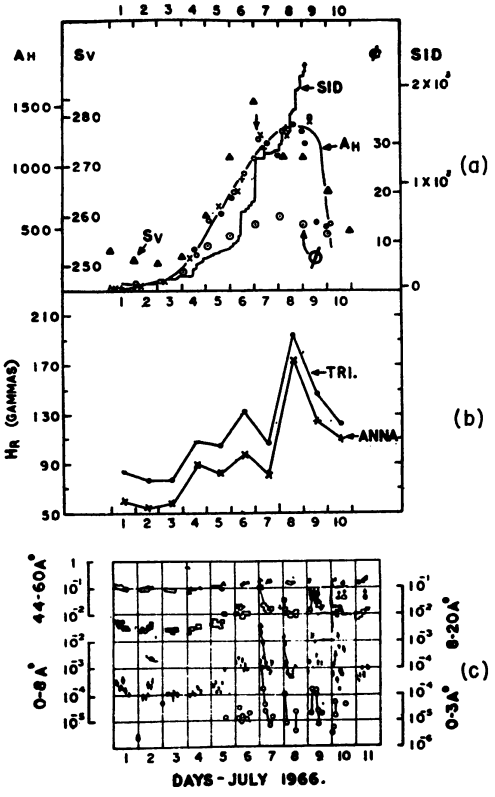

Figure 46-2

(a). Variation of A_H, S_V, SID and ϕ During the Period 1-10 July 1966. A_H is the total area of the sunspot group in which the proton flare occurred, expressed in units of millions of the solar hemisphere. The observations are from ESSA (⊙), solnechyne Daunye (O), U. S. Naval Observatory (+), and Rome (×). The arrow indicates the time of occurrence of the proton flare. S_V is the slowly varying component of solar radio emission at 9400 MHz. The daily means of flux density in units of $W\,m^{-2}\,Hz^{-1} \cdot 10^{-22}$ has been plotted.

SID: Occurrence of sudden ionospheric disturbance (SID) effects of all kinds by flares in the active region of the sun in which proton flare occurred. SID is derived by summing (I × D) of all events during each day where (I = Importance, D = Duration).

ϕ is the flux density of 10.7 cm wave emission from the sun, in the same units as S_V.

(b). Variation of H_R, the range of H daily variation at Trivandrum and at Annamalainagar during 1-10 July 1968.

(c). Buildup of the S component of solar X-ray during 1-10 July 1966 as observed by Explorer 30 satellite.

The general flare activity started on 3 July and reached maximum by 6 July. Just after the proton flare on 7 July, the flare activity reduced considerably but increased again on 8 July.

The source of slowly varying component of radio emission became noticeable by 3 July, and the emission at 9400 MHz steadily increased to a maximum by 7 July. There was little change in the flux density of this source between 7 and 8 July, and after 8 July the intensity decreased slowly. A 10.7 cm solar radio wave intensity which is known to be correlated with solar X-ray emissions responsible for the ionization of the E region, increased steadily from 3 July onwards, reached maximum on 7 July and reduced thereafter.

Gradual enhancement of the S component of solar X-radiation also started on 3 July. On 4 and 5 July, SID activity increased rapidly and reached a maximum by 7 July. There was no increase in SID activity after the flare on 7 July, but on 8 July onwards it increased rapidly again.

Solar X-radiation in the spectral band 5-100 Å is effective in producing ionization in the upper E region. Explorer 30 satellite has provided valuable information concerning the time variation of this component during 1-10 July, which is plotted in Figure 46-2. Between 1 and 3 July, X-ray emission levels were found to be 0.1 erg $cm^{-2} sec^{-1}$ in 44-60 Å band; $3\text{-}10^{-3}$ in 8-20 Å band; and 10^{-4} in 0-8 Å band. First indications of increase of X-ray emission were observed on 4 July and this increase continued through 5 July. By 6 July, X-ray flux levels had increased by factors of 15, 5 and 1.6 in the 0-8, 8-20 and 40-60 Å bands respectively. Large variability in flux intensity was observed before the flare on 6 and 7 July. During the flare, there was large emission of X-rays over a wide spectral band. After the flare, by noon of 7 July, the intensity of X-ray emission reduced to the pre-flare level on 6 July.

Figures 46-1 and 46-2(b) show that the amplitude and the range of daily variation of geomagnetic field at Trivandrum and Annamalainagar increase with the general increase in solar activity. The increase is rapid from 3 July onwards and reaches a maximum on 6 July. Similar increase can be seen in A_H, SID, 9400 MHz and 10.7 cm activity in Figure 46-2(a) and X-ray emission shown in Figure 46-2(c). On 7 July, though the amplitude of H variation is high, it is smaller than the amplitude on pre- and post-flare days. This reduction follows the general reduction in solar activity just after the flare on 7 July. Such reductions can be seen in Figures 46-2(a) and 46-2(c) in A_H, 9400 MHz and X-ray activity. ΔH_{max} reaches a peak on 8 July under the combined influence of ionospheric and magnetospheric effects, and later in the day the SSC storm main phase sets in to reduce the H daily variation peak to a low value.

46-3 DISCUSSION

The close association seen in Figures 46-1 and 46-2 between the rise in solar activity and the increase in the amplitude of H variation at the two low latitude stations indicates that the ionizing radiation from the sun did influence the equatorial ionosphere during the pre-flare days and on the day of the flare. This influence could be the result of direct interaction of the ionizing radiation with the equatorial ionosphere or due to change in electric field due to a charge distribution set up in the ionosphere by the dynamo forces elsewhere as suggested by Akasofu et al (1969). Best et al (1968) have studied the variation of geomagnetic field in the middle and high latitudes during the proton flare event of 7 July 1966. Their study indicates that the average intensity of the Sq system on 7 July was greater than on the days before and after the flare day. This has been ascribed to a general increase of UV radiation around 7 July. The gradual buildup of the amplitude of daily variation of the geomagnetic field from 1 to 6 July at Trivandrum (Figures 46-1 and 46-2), with the gradual enhancement of XUV radiation from the sun during this period, is rather striking and is due to the increase in the intensity of ionospheric currents over Trivandrum. The small reduction in H variation amplitude is due to a general but small reduction of solar activity after the flare, as evidenced in Figure 46-2 by a small reduction of A_H and XUV emission, a fall in 9400 MHz radio emission, and a levelling off of SID activity. Just after the proton flare, the flare activity reduced considerably (Bruzek, 1968) but the average level of XUV activity remained as high as on the pre-flare day.

Explorer 33 plasma probe measurements reported by Lazarus and Binsack (1969) indicate that the solar wind velocity was low (300 km sec^{-1}) on 7 July and increased steadily on 8 July. The daily variation of magnetic field at middle and high latitudes showed no effects attributable to the arrival of high energy particles on 7 July before 2200 UT (Best et al, 1968). Also there was no noticeable disturbance in magnetic field variation at the equatorial stations during the day on 7 July. The onset of disturbance at Trivandrum was noticed only at 2200 UT on 7 July. Hence it can be safely said that the daily variation of geomagnetic field observed at low latitude stations prior to 2200 UT on 7 July is predominently of ionospheric origin.

The abnormality of the electrojet observed during flight 20.05 on 7 July is due to the abnormal state of the ionosphere on that day, brought about by the enhanced ionizing radiation from the sun. The results from flight 20.05 can be reconciled with the ground magnetometer observations either by accepting the existence of a second current layer seen near 140 km in the flight results or by conceding that on the day of flight the width of the electrojet was, in fact, very large.

Enhancement of solar ionizing radiation could result in the increase of ionospheric conductivity, wind velocity or both over a wide area around the equator, thus giving rise to a wider electrojet than usually observed on normal quiet days. However, Figure 46-2 shows that H_R at Annamalainagar is smaller throughout the period 1-10 July compared to H_R at Trivandrum. To see how far the effect of the electrojet extended during the period 1-8 July, the daily variation of H component at Alibag, which is about 1100 km north of dip equator, was examined. It was found that though the variation of ΔH_{max} at Alibag was well correlated with the ΔH_{max} variations at Trivandrum and Annamalainagar during the period 1-8 July, the trend of ΔH_{max} change at Alibag was different from the change observed at the electrojet stations. In particular, ΔH_{max} decreased on 4 July and remained low at Alibag until 8 July, whereas it increased steadily at Trivandrum and Annamalainagar between 3 and 6 July. This shows that the jet effect was not felt at Alibag and the jet did not extend much beyond Annamalainagar.

General enhancement of ionizing radiation from the sun over a wide spectral band could also result in the formation of a second current layer above the main electrojet layer. It appears likely that such a second layer around 140 km altitude was present at the time of flight 20.05 on 7 July. If the magnetic effect of this second current layer is taken into account, the magnetic field departures due to ionospheric currents recorded by the rocket magnetometer during flight 20.05 can be easily reconciled with the ΔH measured at the ground as shown against 20.05* in Table 46-1. Assuming a half width of 300 km for the electrojet observed during the flight, $(H_e + H_i)$ due to this jet at the ground will be 42γ. ΔH at the time of flight was 55γ. Hence, the difference of 13γ must be due to the currents in the second layer and its image underground. The second layer can be expected to produce a departure ΔF of 18γ in the flight record. The actual departure due to the second current layer observed during the flight is $15 \pm 4\gamma$, which agrees will with the 18γ expected from the above calculations.

The buildup of the amplitude of H daily variation during the period 1-6 July could be either due to enhancement of current intensity in the main electrojet layer or due to the formation of a second current layer in addition to the main electrojet. There is no evidence to show that the current layer near 140 km was present all the time during the above period.

46-4 CONCLUSIONS

(1) During the period 1-6 July prior to the 7 July 1966 proton flare, the amplitude of daily variation of the geomagnetic field at the equatorial stations, Trivandrum and Annamalainagar, increased with the general increase of solar activity.

Gradual enhancement of the S component of XUV radiation from the sun during the above period gave rise to enhancement of currents in the equatorial ionosphere, which in turn caused the gradual increase of the amplitude of daily variation of the magnetic field at these stations. The small decrease in the amplitude of H variation on 7 July was probably due to the reduction of solar activity just after the flare on that day. On 8 July the amplitude of H variation reached a maximum under the combined influence of ionospheric and pre-storm effects.

(2) The results from flight 20.05 show that, in addition to the main electrojet layer centered at 107 ± 2 km, a second current layer centered near 140 km altitude was present at the time of the flight on 7 July 1966. Enhancement of XUV emission from the sun over a wide spectral band during the proton flare could have caused the formation of the second layer.

(3) It is important to establish, from further studies, the dependence of the daily variation of magnetic field on the variation of the intensity of the S component of the ionizing radiation from the sun and to confirm from further rocket experiments the presence or otherwise of the second current layer. The outcome of these two studies will help in finding an explanation for the day-to-day variability of the amplitude of daily variation of geomagnetic field seen at the low latitude stations.

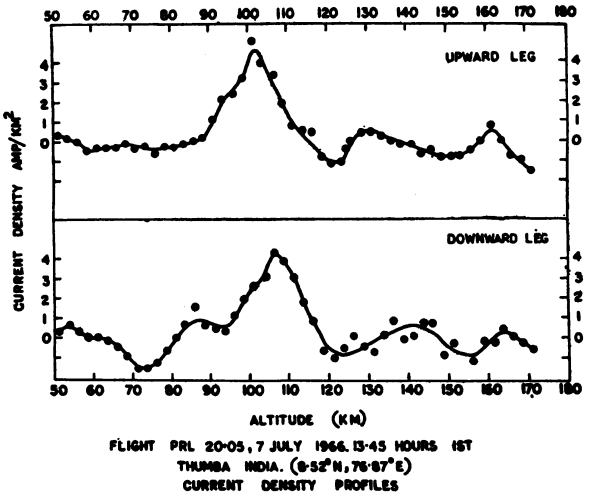

Figure 46-3. Vertical Profiles of Current Density Derived From the Measurements of Total Intensity Measured by a Rocket-Borne Magnetometer During Flight FL 20.05

References

Akasofu, S.I., Meng, C.I., and Chapman, S. (1969) On the causes of the day-to-day variability of the intensity of the equatorial electrojet, Proc. Third Int. Symp. on Eq. Aeronomy 1A:213, Ahmedabad, India.

Balsley, B.B. (1964) Evidence of a stratified echoing region at 150 km in the vicinity of the magnetic equator during daylight hours, J. Geophys. Res. 69:1925-1930.

Banin, V., de Feiter, L.D., Fokker, A.D., Martres, M.J., and Pick, M. (1968) On the development and activity of the active region associated with the proton flare event of 7 July 1966—Summary of observations and conclusions, Ann. IQSY 3:229.

Best, A., Fanselau, G., Grafe, A., Lehmann, H.R., and Wagner, C.U. (1968) The variations of the geomagnetic field in middle and high latitudes during the proton flare event of July 1966, Ann. IQSY 3:413.

Bruzek, A. (1968) Flares in the active region during the proton flare period of July 1966, Ann. IQSY 3:82.

Friedman, H., and Kreplin, R.W. (1968) The slowly varying component of solar X-ray emission in the period 1-15 July 1966, Ann. IQSY 3:78.

Krivsky, L. (1968) Remarks on the development and activity of the active region during the proton flare event of July 1966, Ann. IQSY 3:135.

Kruger, A. (1968) Remarks on the slowly varying component of solar radio emission during the proton flare project period of July 1966, Ann. IQSY 3:70.

Lazarus, A.J., and Binsack, J.H. (1968) Observations of the interplanetary plasma subsequent to the 7 July 1966 proton flare, Ann. IQSY 3:378.

McIntosh, P.S., and Sawyer, C. (1968) Evolution of sunspot group after the proton flare of 7 July 1966, Ann. IQSY 3:169.

Rokityanskiy, I.I. (1969) Experience in magnetic variation sounding at low latitudes, Geomagnetism and Aeronomy 5:726.

Sastry, T.S.G. (1970) Change in the parameters of equatorial electrojet during a magnetically quiet day as observed by rocket-borne magnetometers, sent for publocation to J. Geophys. Res.

References

Sastry, T.S.G. (1968) Quiet day electrojet over Thumba, India, J. Geophys. Res. 73:1789.

Contents

47. Simultaneous Satellite and Riometer Measurements of Particles During Solar Cosmic Ray Events

M.B. Baker, P.R. Satterblom, A.J. Masley, and A.D. Goedeke
Space Sciences Department
McDonnell Douglas Astronautics Company-West
Huntington Beach, California

Abstract

The expected 30 and 50 MHz riometer absorptions have been calculated for three events in 1969 using data from the MDAC-W charged-particle experiment on OGO-6. Several times during each event the satellite passed over the MDAC-W Arctic and Antarctic Geophysical Observatories. The calculated total absorption (using 2 minute averages of the data) agrees well with the measured absorption for the overpasses. The alpha particle and electron contributions usually amount to less than a few percent of the proton absorption. During the large 2 November 1969 event, however, the electrons produced the major part of the absorption up to the peak and a significant contribution during virtually its entire duration. With the two frequencies for which simultaneous riometer data were taken, it is possible to detect the softening of the particle spectra during the events, and the relative hardness differences between the events.

47-1 INTRODUCTION

The McDonnell Douglas Astronautics Company-West (MDAC-W) charged particle experiment on OGO-6 measures the energy spectra of protons between 5.3 and 78 MeV and alpha particles between 17.5 and 84 MeV, and the intensity of electrons

having energies greater than about 350 keV. The instrument has been described by Masley and Satterblom (1970). Between June 1969 and September 1970, measurements were made during solar cosmic ray (SCR) events simultaneously with riometer absorption measurements at 30 and 50 MHz at the MDAC-W conjugate geophysical observatories located at Shepherd Bay, N.W.T., Canada, and McMurdo Sound, Antarctica. The geomagnetic field line at Shepherd Bay is almost vertical at 68.8°N, 93.9°W. Throughout this period the satellite altitude was near 1000 km over the south polar cap; the field line originating at McMurdo is situated at 78.8°S, 170°E at 1000 km altitude. Since the maximum latitude reached by OGO-6 was 82°, it passed within a few hundred km of the McMurdo field line on four or five consecutive orbits each day. An example of some passes is shown in Figure 47-1. On north polar passes, however, the satellite could come close to the Shepherd Bay field line twice per day at most. These near overpasses were examined during the three largest events (that is, those having the highest peak measured riometer absorption) between June 1969 and December 1969: 7 June, 25 September, and 2 November.

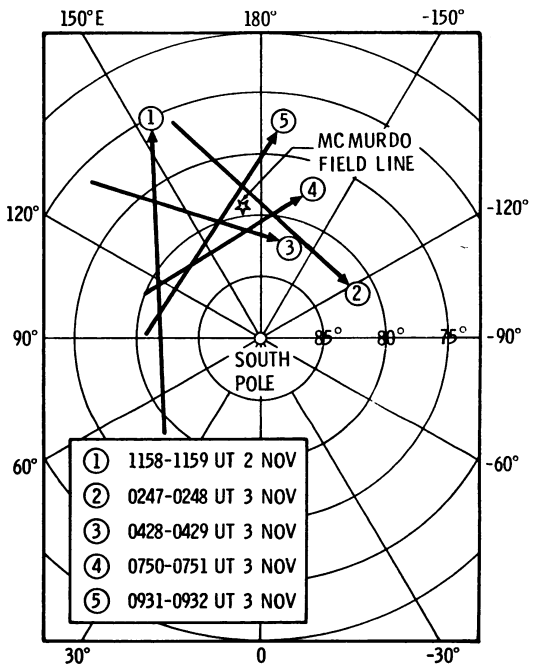

Figure 47-1. OGO-6 Trajectories Over the South Polar Region. The star marks the position at 1000 km altitude of the geomagnetic field line passing through the McMurdo Sound riometer station

47-2 DISCUSSION

A computer program was written, based on the work of Adams and Masley (1966a), which calculates the riometer absorption from satellite-measured proton and alpha-particle spectra. The absorption due to electrons was calculated using the methods of Bailey (1968). The electron energy spectra measured on Explorer 41 (Lanzerotti and MacLennan, 1971) were used. The antenna correction factor (to convert from a pencil beam to the actual riometer antenna pattern) used was 1.4.

Two-minute averages of the OGO-6 particle data were used to calculate the 30 and 50 MHz absorption for all possible near overpasses. Since the analysis of Adams and Masley was carried out for the sunlit ionosphere, only daytime overpasses were used for this study. Other overpasses were deleted because of lack of either particle or riometer data. The results for 30 MHz for the remaining near overpasses during the events of 7 June 1969 and 25 September 1969 are shown in Table 47-1. "Distance" is the approximate minimum distance between the OGO-6 orbit and the geomagnetic field line passing through the riometer station.

Table 47-1. Simultaneous 30 MHz Absorption, 8 June and 25 September 1969 Events

Date	UT	Distance (km)	Riometer Station	Measured Abs. (dB)	Calculated Abs. (dB)
8 June	0218	70	SB	0.56	0.48
9	1143	190	SB	0.90	0.98
10	0231	190	SB	0.67	0.62
11	0145	170	SB	0.39	0.35
25 Sept.	1208	110	SB	0.50	0.98
26	0714	300	McM	0.30	0.28
26	0855	160	McM	0.30	0.25
28	0722	170	McM	0.80	0.76
28	2140	360	SB	0.65	0.92
29	0635	360	McM	1.50	0.94
29	0817	240	McM	0.70	0.61
29	2054	40	SB	0.20	0.15

The electron intensities during the events were quite small and the absorption produced by them insignificant. Similarly, in all cases the alpha particle contribution to the calculated 30 MHz absorption never amounted to as much as one percent of the total. This confirms the conclusion given by Adams and Masley (1966b) that the alpha particle constituent in SCR events usually does not contribute significantly to measured riometer absorption. The agreement for the June and September 1969 events is very good.

The 2 November 1969 event was by far the largest during the period studied, and considerable intensities of solar electrons were detected (Masley and Satterblom, 1971). During this event the sun was up continually at McMurdo Sound. There were seven near overpasses of the McMurdo riometer for which good data

were obtained, all of which were late in the event, past the time of peak absorption. One earlier overpass occurred during the initial rise in absorption which was somewhat further away from the McMurdo field line than the others. There were no usable overpasses of Shepherd Bay.

The results for this event are shown in Table 47-2. "A" is 30 MHz absorption; "P" is protons; "P + α" is protons and alpha particles; "e" is electrons; and "t" is total. "A_t Measured" is the absorption measured at McMurdo when OGO-6 was at its closest approach.

Table 47-2. Simultaneous 30 MHz Absorption, 2 November 1969 Event

Date	UT	Distance (km)	A_p OGO-6	$A_{p+\alpha}$ OGO-6	A_e OGO-6	A_t Calculated	A_t Measured
2 Nov	1158	800	4.3 dB	4.3 dB	7.3 dB	8.2 dB	6.1 dB
3	0248	160	6.3	6.4	2.3	6.8	7.2
3	0428	240	5.4	5.5	2.0	5.8	6.2
4	0201	400	2.3	2.3	1.1	2.6	2.6
4	0341	100	2.2	2.2	1.0	2.4	2.5
4	0523	340	2.1	2.1	0.8	2.3	2.2
4	0703	360	2.0	2.0	1.1	2.2	2.2
4	0844	120	1.9	1.9	0.6	2.0	2.1

The proton and alpha particle absorption, electron absorption, and total 30 MHz absorption calculated from OGO-6 particle data, and the simultaneous measured 30 MHz riometer absorption are shown in Figure 47-2. The tabulated values (the near overpasses) are open circles. The intervening points are calculated from averages of the particle data during southern polar passes. The early absorption before the peak is produced primarily by electrons, while the broad shoulder in the absorption curve during the second seven hours of the event is due primarily to protons. The agreement is excellent. The apparent large differences between 1200 UT and 1800 UT on 2 November are no doubt due to large variations in particle intensities (especially protons) over the polar cap as observed by OGO-6. Changes larger than those shown in Figure 47-2 were seen in much shorter times in both the riometer and OGO-6 data.

Both 30 and 50 MHz absorptions were calculated for a large number of other times during polar passes for the events investigated. The ratio of 50 to 30 MHz absorption was examined to see if information on the particle energy spectra could

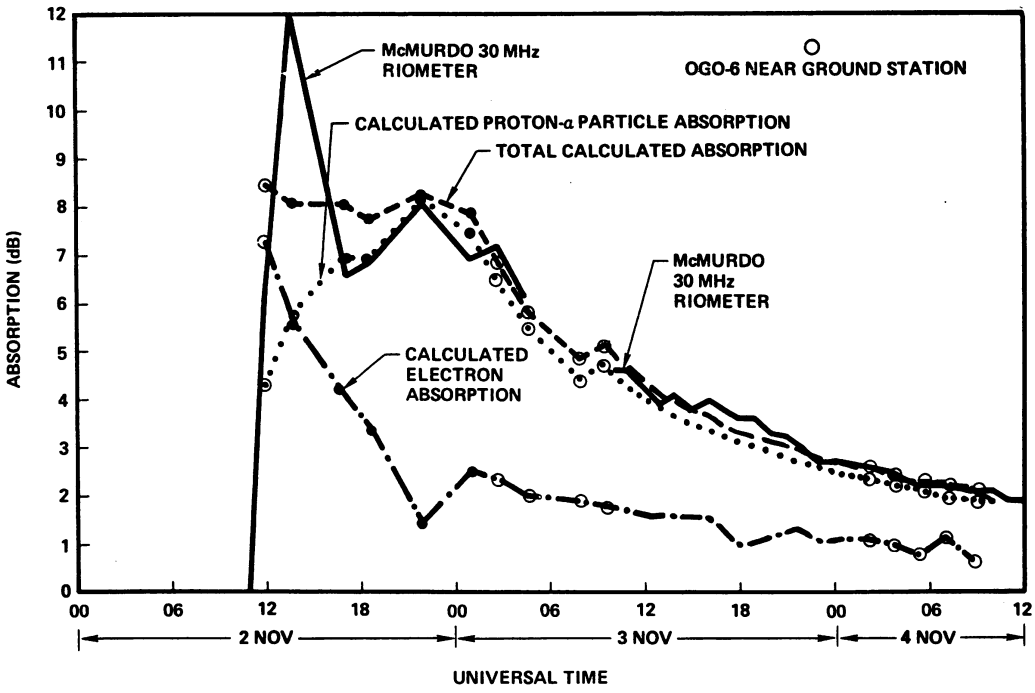

Figure 47-2. Calculated (OGO-6) and Measured 30 MHz Absorption, 2 November 1969 Event. Open circles are two minute averages at the times of near overpasses of the McMurdo Sound riometer station; other points are averages over the intervening south polar passes

be determined from absorption at two frequencies. The theoretical basis for this is discussed by Adams and Masley (1966a). The large 2 November 1969 event is the only one investigated during which the proton and alpha particle spectra softened appreciably. The 50 to 30 MHz absorption ratio (for the protons and alpha particles) decreased by more than 10 percent, which could have been detected by the riometers if there had not been the electron component of absorption present. The minimum unambiguously detectable difference in energy spectra would probably be that which causes a change of 10 percent in the 50 to 30 MHz absorption ratio. A change in differential energy spectrum from $\gamma = 5$ to $\gamma = 3$, for comparison, causes an increase in the ratio of about 8 percent, and from $\gamma = 3$ to $\gamma = 2$ a further increase of 8 percent. A change from $\gamma = 7$ to $\gamma = 5$, however, changes the ratio by less than 1 percent.

47-3 SUMMARY

Excellent agreement is found between measured polar cap riometer absorption during three solar cosmic ray events and absorption calculated from detailed particle data measured on a satellite passing over the riometer. Electrons are found to contribute the greater part of the 30 MHz absorption before the peak of the 2 November 1969 event; at all other times protons produce most of the absorption. For proton events it would be possible to estimate the hardness of the energy spectrum by examining the ratio of 50 to 30 MHz absorption.

Acknowledgments

The OGO-6 experiment was supported by the National Aeronautics and Space Administration (Contract NAS 5-9324), and the operation of the Arctic and Antarctic Geophysical Observatories was supported by the National Science Foundation (Contract NSF-C393). This study has been supported by the McDonnell Douglas Independent Research and Development Program.

References

Adams, G. W., and Masley, A. J. (1966a) Planet. Space Sci. 14:277.

Adams, G. W., and Masley, A. J. (1966b) Recent Advances in Cosmic Ray Research 11:201, Western Periodicals Co., N. Hollywood, Ca.

Bailey, D. K. (1968) Rev. Geophys. 6:289.

Lanzerotti, L. J., and MacLennan, C. G. (1971) Presented at the COSPAR Symposium on the November 1969 Solar Particle Event.

Masley, A. J., and Satterblom, P. R. (1970) Proc. 11th Int. Conf. on Cosmic Rays, 1969; Acta Physica Acad. Sci. Hungaricae 29:(Suppl. 2)513.

Masley, A. J., and Satterblom, P. R. (1971) Conf. Papers, 12th Intl. Conf. on Cosmic Rays 5:1849, Hobart, Australia.

48. Observations During the 2 November 1969 Solar Cosmic Ray Event

A.J. Masley and P.R. Satterblom
McDonnell Douglas Astronautics Company-West
Huntington Beach, California

Abstract

The 2 November event was one of the largest observed since November 1960. Observations made by the polar orbiting OGO-6 satellite and the polar riometers will be discussed. The OGO-6 experiment is a solid state detector telescope which measures the intensity and energy of protons from 5 to 80 MeV in 14 energy intervals and alpha particles from 18 to 160 MeV in 12 intervals every 0.8 seconds.

At 0943, 2 November, about one day behind the limb, a major flare occurred according to the ESSA Preliminary Report. Importance 2 loops, a large 10 cm radio noise burst and the most energetic X-ray event of the year were observed. The southern riometer saw the event start at about 1100 UT in daylight. The first OGO-6 observation was a northern polar pass at 1100. Particles were observed only in the greater than 80 MeV channel. On the following southern polar pass at 1150, particles over the entire energy range were present, with the spectrum peaking at 35 MeV.

From the beginning of the event to about 1200 on 3 November, the intensity was consistently higher in the northern polar cap ranging from 300 percent to 50 percent. After 1200 it was similar in the two polar caps. During the first southern polar pass there were large variations across the polar cap. The variation was nearly 100:1 for the 1330, 2 November southern pass. The distinctive stable features can be followed for about 12 hours to about 0000 3 November, the variation decreasing from 100:1 to 6:1 over this period. The lack of response on neutron monitors indicates essentially no > 500 MeV particles, although there were significant numbers of > 80 MeV particles throughout the event

49. Topside Polar Cap During November 1969 Proton Event

R.C. Sagalyn and M. Smiddy
Air Force Cambridge Research Laboratories
Bedford, Massachusetts

and

M. Ahmed
Regis College
Weston, Massachusetts

Abstract

Positive ion densities in the energy range 0 to 50 eV and ion temperatures were measured throughout the period of the solar proton disturbance of 2–4 November 1969, by means of a spherical electrostatic analyzer mounted on the ISIS-I Satellite. Data were acquired at the rate of 8 hours per day from this polar-orbiting satellite (inclination 88.4) over the altitude range 578 km to 3526 km. Positive ion results obtained over the polar cap and at latitudes greater than 50° during this event have been analyzed. Time variations in the position of ion troughs, plasma rings and auroral boundaries as well as the temporal and spatial behavior of the high latitude topside ionosphere, energetic particle injection and motions deduced from these results are discussed.

Appendix A

Summary of Operation PCA 69

J.C. Ulwick
Air Force Cambridge Research Laboratories
Bedford, Massachusetts

C.A. Blank
Defense Nuclear Agency
Washington, D.C.

Abstract

An overview at Operation PCA 69 is presented. A short discussion is given of Polar Cap Absorption (PCA) for background and the rationale for the program presented. The rocket phase of the investigation is presented in some detail and the supporting satellite, aircraft and ground measurements conducted are specified. Tables and figures are presented that summarize the investigations that were accomplished for Operation PCA 69.

A1. INTRODUCTION

Polar Cap Absorption (PCA) refers to the abnormally high absorption of hf and lower vhf frequencies in their passage through a highly-disturbed polar mesosphere. The events are the result of the bombardment of the lower ionosphere by

solar cosmic ray particles following certain major solar flares. The particles are mainly protons in the 1 to 100 MeV energy range, although in a few events an alpha particle flux of considerable intensity has been observed. These particles give rise to abnormally high ionization of atmospheric constituents with a consequent increase in the ambient free electron density. The influence of the geomagnetic field normally excludes these particles from latitudes below the auroral zone. The absorption is thus a feature of high latitude, above approximately 65 deg, and is considerably uniform over the whole polar cap. For typical events the ionospheric absorption of cosmic radio noise as indicated by riometers begins an hour or so after a major flare. Riometer records of absorption recorded when the polar region is in permanent sunlight show the rapid rise (several hours) of the absorption to a peak and then the slow decay over a period of several days due to the decay of the proton flux. The proton flux spectrum responsible is especially energetic and variable in the early time of the event, and the effects of variation in ionization are in the lowest D region. As time increases, the spectrum becomes softer, less penetrating and more stable. When there is a night and day variation, the absorption decreases markedly at night, and the change between night and day causes a distinct modulation of the otherwise smooth form of the absorption profile.

The study of atmospheric effects on radio propagation techniques, for example, riometers, ionosondes, vhf scatter techniques, and trans-polar cap vlf transmissions has shown the general nature of PCA events (Bailey, 1964; and Obayashi, 1964). In recent years, satellites have been used to measure directly the bombarding particle fluxes which are responsible for the PCA. These observations, compared with riometer absorption measurements, have increased the knowledge of solar-terrestrial interactions (Van Allen et al, 1964; Leinback et al, 1965; Chivers and Burrows, 1966; and Reid and Sauer, 1967). The radio wave attenuation and the mechanisms for ionization by the proton flux are understood fairly well, but the physical chemistry of the D region is still very uncertain. The fact that during a PCA the ionization is increased to such a large extent by a source whose intensity can be readily measured, offers an excellent opportunity to study atmospheric chemical and physical processes occurring in the lower D region. This is especially true during the decay period of the event when there is little change in the incoming energy spectrum, and the variation in absorption is due essentially to the varying sunlight. Specifically the study of the so-called "Twilight Anomaly" (that is, the change of the absorption with solar zenith angles during sunrise and sunset) (Eriksen et al, 1960; Reid and Leinback, 1961; and Reid, 1961), and the study of the ratio of the daytime absorption to that at night, by direct simultaneous measurement of the altitude variation of the negative and positive ion composition, electron and ion density, the proton and electron flux, neutral air density and temperature,

and other important parameters would be especially revealing. The coordinated rocket, satellite, aircraft, and ground measurement program known as Operation PCA 69 was designed to conduct these studies.

A2. OPERATION PCA 69

The rocket program consisted of 36 scientifically instrumented rockets to be launched sequentially into a major PCA event. In addition, 11 rockets were to be fired to provide certification and background information. The basic philosophy of the rocket measurement program during the PCA event was: (1) to measure the primary source of atmospheric ionization during a PCA event; these include protons and alpha particles, and other ionizing sources such as X-rays, Lyman-alpha radiation, and energetic electrons; and (2) to measure the effects on the atmosphere of the ionizing particles. Such effects include ionization, light emission, positive and negative ion composition changes, and neutral density and temperature changes. The studies were to be carried out utilizing a series of rocket-borne probes which would measure the PCA event parameters in four phases; that is, (a) daylight conditions, (b) nighttime conditions, and two transition periods, (c) sunrise, and (d) sunset.

The rocket program was conducted at the Churchill Research Range located in Manitoba, Canada on the shore of the Hudson Bay (Figure 47-1). Although located within the auroral oval where auroral energetic electrons would be an additional complicating production source, this range, probably the foremost research rocket range in the world, offered the personnel, support and capability to accomodate Operation PCA 69. Planning for the program between participants, range personnel and sponsoring organizations began about a year and a half prior to execution. The rocket project personnel, payloads, and equipment arrived at Ft. Churchill on 14 July 1969 to begin payload checkouts to prepare for an operational readiness date of 9 August 1969. The project was prepared to be in a readiness state for a three month period of time with a termination date of 4 November 1969 if no PCA occurred within that time. The time frame was more dictated by operational, logistical and financial considerations than any knowledge a priori that a PCA would occur during this period. Nevertheless, since the previous three major PCA events occurred in time intervals of about four to five months (June 1968, November 1968 and April 1969) and since the time period statistically had been good for PCA events, it appeared to be as good as could be obtained under any planning consideration. It should be noted that during this solar cycle the sunspot numbers were substantially less than the previous cycle and correspondingly the number of PCA events were fewer.

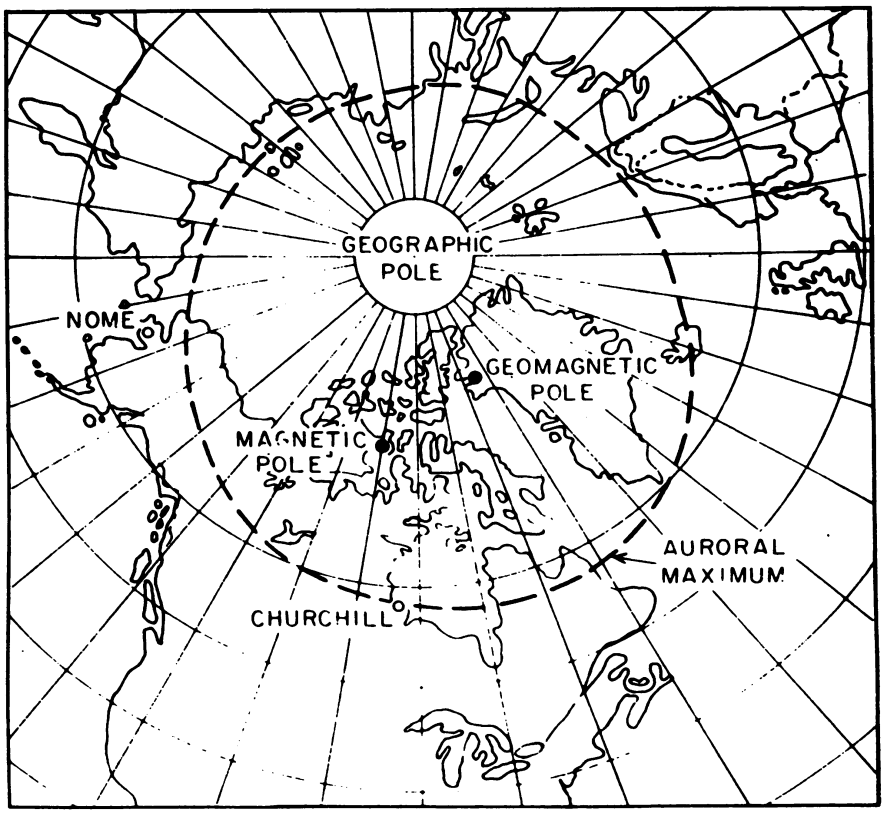

Figure A1

Since the countdown schedule required the launch of 38 rockets within a 24-hour period, dry runs of the operation were a most important prerequisite in order to achieve operational readiness. The countdown schedule was broken down into four separate phases: night (12 rockets), sunrise (8 rockets), day (8 rockets) and sunset (10 rockets) with separate countdowns for each phase. The severest requirements were for the study of the twilight anomaly (sunrise and sunset) where the rockets were to be launched, dependent on the solar zenith angle of the sun. Many practice countdowns of each phase were conducted prior to 9 August 1969, and then on a regular basis throughout the waiting period in order to maintain proficiency. Certification of rockets, payloads and experiments, as well as acquiring background data was also a prerequisite to readiness state. In some cases this was accomplished well in advance of the field operation such as the successful launch of a Black Brant rocket during the 18 November 1968 PCA event, which certified the payload and gave results on ionospheric parameters during a PCA event (Ulwick et al, 1970). Also of note was the achievement of a negative ion composition experiment

in time for the PCA event. This experiment in the development stages was fired three times during the waiting period. Not only was certification of the rocket and experiment achieved, but the first altitude profiles of the negative ion composition were made (Narcisi et al, 1969). For the most part the 11 certification/background rockets were fired during practice countdown phases to provide more complete and realistic checks.

The ground measurement program consisted mostly of experiments already in operation at CRR. At the Auroral Observatory, polar riometer, zenith riometer magnetometer, all-sky camera, photometer and spectrometer measurements were available to support the program. The Canadian Department of Communications partial reflection experiment near the Observatory was operational throughout the program. They also operated riometers at nearby Landing Lake where the CRR ionosonde is located. The only ground experiment conducted specifically in support of the rocket program was a partial reflection experiment (at different operating frequencies than the Canadian experiment) by Cornell Aeronautical Laboratories.

The satellite program consisted in turning on instruments capable of measuring energetic proton and electron fluxes on satellites already in orbit. The OV 1-18 satellite, which had a full array of energy measuring experiments, a working tape recorder, and a favorable orbit was considered the primary satellite, although much data were achieved from other satellites. The Vela and ATS satellites, because of their orbits in deep space, were especially important for early warning and confirmation of the occurrence of a solar proton event.

Two KC-135 aircraft, used in AFCRL auroral and optical research programs, were included in the operation. Since the PCA event was not predictable, the probability of aircraft participation was considerably reduced due to crew rest and, in particular, aircraft maintenance requirements. Both aircraft were able to participate in certification and checkout phases, but during the 2 November 1969 PCA event the auroral aircraft was not available due to ground maintenance check requirements.

A3. PCA 69 PROGRAM

The launch phase of the rocket program began at 2020 GMT on 2 November 1969 with the successful launch of a Black Brant rocket and was completed on 4 November 1969 at 2357 GMT with the launch of an Arcas rocket. The rocket firing sequence is shown in Table A1. The 11 certification rockets that were launched are also shown. As presented, there were 44 successful rocket flights and three failures for the total program. The planned investigation of the sunset transition on 3 November 1969 was cancelled after one vehicle failed to fire, one

rocket broke up shortly after launch, and the surface winds became very high. The sunset rockets were launched the following day after two rockets were flown to establish daytime conditions.

Table A1. Rocket Firing Sequence

		No. of Rockets	Vehicle Performance
A. Certification and Background	Nov 1968 to Nov 1969	11	1 Vehicle Failure 10 Successful
B. PCA			
1. Early Time	2 Nov	3	3 Successful
2. Late Time			
Night	2 Nov	7	7 Successful
Sunrise	3 Nov	7	7 Successful
Day	3 Nov	8	1 Vehicle Failure 7 Successful
Sunset	3 Nov	2	1 Vehicle Failure 1 Successful
Day	4 Nov	2	2 Successful
Sunset	4 Nov	7	7 Successful

The launch times, the solar zenith angles and the vehicle launched are summarized in Table A2. The NIROS rockets labelled MSP and MSN refer to the mass spectrometer measurements of positive and negative ion composition respectively. The NIROS rockets labelled NDT refer to the measurement of neutral density and temperature. The Arcas rockets carried blunt probes for the measurement of positive ion and electron density. The Sidewinder Arcas instrumentation measured ozone. The Black Brant and Nike Javelin rockets carried multi-experimented payloads but the principal measurements were ionization, production sources, and optical emissions on the Black Brant and electron density, absorption and proton flux on the Nike Javelin rockets. Table A3 shows the extensive satellite coverage which provided significant information on this particular event.

Table A2. PCA 69 Rocket Launches During the 2 November 69 Event

Date and Phase	Time (GMT)	Solar Zenith Angle	Vehicle
2 November 69 (Early Time)	2020	79.0°	Black Brant
	2110	83.2°	Nike-Javelin
	2211	89.5°	Sidewinder Arcas
3 November 69 (Night)	0455	134.6°	Met
	0535	136.0°	Arcas
	0605	136.2°	Black Brant
	0629	135.9°	Niros-MSN
	0642	135.5°	Niros-NDT
	0700	134.8°	Arcas
	0730	133.1°	Niros-MSP
3 November 69 (Sunrise)	1228	99.1°	Arcas
	1232	98.6°	Niros-NDT
	1257	95.5°	Nike-Javelin
	1311	93.8°	Met
	1330	91.6°	Nike-Javelin
	1352	89.1°	Black Brant
	1405	87.7°	Arcas
3 November 69 (Day)	1629	76.1°	Arcas
	1711	74.5°	Black Brant
	1730	74.1°	Niros-MSP
	1747	73.9°	Niros-MSN
	1840	74.3°	Niros-NDT
	1854	74.7°	Nike-Javelin
	1902	75.0°	Met
	2130	85.4°	Met
3 November 69 (Sunset)	2245	93.7°	Black Brant
	2308	96.5°	Niros-NDT
4 November 69 (Day)	1943	77.2°	Arcas
	2130	85.7°	Nike-Javelin
4 November 69 (Sunset)	2206	89.5°	Sidewinder Arcas
	2220	91.1°	Arcas
	2238	93.2°	Nike-Javelin
	2250	94.6°	Niros-MSP
	2308	96.8°	Black Brant
	2325	98.9°	Arcas
	2357	102.9°	Arcas

Table A3. Satellite Measurements During the 1969 PCA

Satellite	Particle Measurements		
	Protons	Alpha Particles	Electrons
OV-18 (Polar-Orbiting)	1.2-46 MeV	7-20 MeV	0.4-1.9 MeV
OGO-6 (Polar-Orbiting)	5-80 MeV	18-160 MeV	
OV5-6	1.25-100 MeV	20-100 MeV	>300 keV
OV1-19 (Polar-Orbiting)	0.43-126 MeV		53 keV-5.1 MeV
Explorer 41 (Imp G)	0.47-19.7 MeV	1.0-21.4 MeV/ nucleon	>0.35, >0.6, >1.1 MeV
HEOS-AI	6-1500 MeV		
ESRO IA (Polar-Orbiting)	>500 keV, 1-30 MeV		>40 keV
ESRO IB (Polar-Orbiting)	>500 keV, 1-30 MeV		>40 keV
ESRO II (Polar-Orbiting)	26-400 MeV		
Vela (4 and 5)	.46-29 MeV		

References

Bailey, D.K. (1964) Planet. Space Sci. 12:495-541.

Chivers, H.J.A., and Burrows, J.R. (1966) Planet. Space Sci. 14:131-142.

Eriksen, K.W., Holt, O., and Landmark, B. (1960) J. Atmos. Terr. Phys. 18:78.

Leinback, H., Venkatesan, D., and Parthasarathy, R. (1965) Planet. Space Sci. 13:1075-1095.

Narcisi, R.S., Bailey, A.D., Dellaluccy, L,E., and Sherman, C. (1969) Measurement of negative ion in the lower ionosphere, Trans. Am. Geophys. Union 50:654.

Obayashi, J. (1964) J. Geophys. Res. 69:861-867.

PCA Operational Requirements, Space Data Corp., SDC TM 268.

Reid, G.C. (1961) J. Geophys. Res. 66:4071.

Reid, G.C., and Leinback, H. (1961) J. Atmos. Terr. Phys. 23:216.

Reid, G.C., and Sauer, H.H. (1967) J. Geophys. Res. 72:197-208.

Ulwick, J., Baker, K., and Sellers, B. (1970) Space Res. 10.

Van Allen, J.A., Lin, W.C., and Leinback, H. (1964) J. Geophys. Res. 69:4481-4491.

Unclassified
Security Classification

DOCUMENT CONTROL DATA - R&D

(Security classification of title, body of abstract and indexing annotation must be entered when the overall report is classified)

1. ORIGINATING ACTIVITY *(Corporate author)* Air Force Cambridge Research Laboratories (LI) L.G. Hanscom Field Bedford, Massachusetts 01730	2a. REPORT SECURITY CLASSIFICATION Unclassified 2b. GROUP

3. REPORT TITLE
PROCEEDINGS OF COSPAR SYMPOSIUM ON SOLAR PARTICLE EVENT OF NOVEMBER 1969

4. DESCRIPTIVE NOTES *(Type of report and inclusive dates)*
Scientific. Interim.

5. AUTHOR(S) *(First name, middle initial, last name)*
James C. Ulwick, Editor

6. REPORT DATE 11 August 1973	7a. TOTAL NO. OF PAGES 690	7b. NO. OF REFS 649
8a. CONTRACT OR GRANT NO.	9a. ORIGINATOR'S REPORT NUMBER(S) AFCRL-72-0474	
b. PROJECT, TASK, WORK UNIT NOS. 76630101		
c. DOD ELEMENT 62101F	9b. OTHER REPORT NO(S) *(Any other numbers that may be assigned this report)* Special Reports, No. 144	
d. DOD SUBELEMENT 681000		

10. DISTRIBUTION STATEMENT
Approved for public release; distribution unlimited.

11. SUPPLEMENTARY NOTES Symposium on Solar Particle Events held at Boston College at Chestnut Hill, Massachusetts on 16, 17, and 18 June 1971.	12. SPONSORING MILITARY ACTIVITY Air Force Cambridge Research Laboratories (LI) L.G. Hanscom Field Bedford, Massachusetts 01730

13. ABSTRACT

A COSPAR-sponsored Symposium on Solar Particle Events was held at Boston College at Chestnut Hill, Massachusetts on 16, 17, and 18 June 1971. The purpose of the symposium was to present measurements and observations made during the November 1969 Solar Proton Event. This particular event was unique in that extensive solar, magnetospheric and aeronomic measurements by rocket, satellite and ground based techniques were made to provide a comprehensive picture of the phenomenology and morphology of this event. In addition, present knowledge of solar proton events and their effects on the polar ionosphere was reviewed and discussed. This included theoretical studies as well as results from investigations of other solar proton events. The symposium comprised invited as well as contributed papers. A total of 49 papers presented at the symposium are included in these proceedings.

DD FORM 1 NOV 65 1473

Unclassified
Security Classification

14. KEY WORDS	LINK A		LINK B		LINK C	
	ROLE	WT	ROLE	WT	ROLE	WT
Polar cap absorption D-region aeronomy Solar particle events Rocket investigations of D-region Satellite energetic particle measurements						

☆ U. S. GOVERNMENT PRINTING OFFICE: 1973-704-141/12 REGION #1